



HAL
open science

Three-dimensional numerical modeling of ductile fracture mechanisms at the microscale

Modesar Shakoor

► **To cite this version:**

Modesar Shakoor. Three-dimensional numerical modeling of ductile fracture mechanisms at the microscale. Mechanics of materials [physics.class-ph]. Université Paris sciences et lettres, 2016. English. NNT : 2016PSLEM049 . tel-01744733

HAL Id: tel-01744733

<https://pastel.hal.science/tel-01744733>

Submitted on 27 Mar 2018

HAL is a multi-disciplinary open access archive for the deposit and dissemination of scientific research documents, whether they are published or not. The documents may come from teaching and research institutions in France or abroad, or from public or private research centers.

L'archive ouverte pluridisciplinaire **HAL**, est destinée au dépôt et à la diffusion de documents scientifiques de niveau recherche, publiés ou non, émanant des établissements d'enseignement et de recherche français ou étrangers, des laboratoires publics ou privés.

THÈSE DE DOCTORAT

de l'Université de recherche Paris Sciences et Lettres
PSL Research University

Préparée à MINES ParisTech

Three-dimensional numerical modeling of ductile fracture mechanisms at the microscale

Modélisation numérique tridimensionnelle des mécanismes de rupture ductile à l'échelle microscopique

Ecole doctorale n°364 Sciences Fondamentales et Appliquées
Spécialité Mécanique Numérique et Matériaux

Composition du jury :

M. Nicolas MOËS
EC Nantes, Président du jury

M. R.H.J. PEERLINGS
TU Eindhoven, Rapporteur

M. Jean-François REMACLE
UC Louvain, Rapporteur

M. François HILD
ENS Paris-Saclay, Examineur

M. Thilo MORGENEYER
MINES ParisTech, Examineur

M. Marc BERNACKI
MINES ParisTech, Examineur

M. Pierre-Olivier BOUCHARD
MINES ParisTech, Examineur

Soutenue par **Modesar SHAKOOR**
le 4 novembre 2016

Dirigée par **Pierre-Olivier BOUCHARD**
et **Marc BERNACKI**



Acknowledgments

First of all, I would like to express my sincere gratefulness to the members of my PhD thesis committee, Mr. Nicolas Moës, Mr. Ron Peerlings, Mr. Jean-François Remacle, Mr. François Hild and Mr. Thilo Morgeneyer. I am especially grateful to Mr. François Hild for his thorough proof-reading.

Of course, I am equally grateful to my advisors Marc Bernacki and Pierre-Olivier Bouchard for their numerous reviews of this thesis, but also for a lot more. Advising a PhD student means providing a complex balance of help and autonomy, control and freedom, and I must say that you found the perfect balance for me. All the discussions at work and during travels helped me build my opinion on a wide range of topics that go far beyond ductile fracture, and I would like to thank you for sharing your knowledge of all these topics with me. This experience with you played a key role in my decision to pursue a career in academic research. I am thankful for your guidance and support in reaching my objectives during these three years and even after.

Discussions with many researchers at the center and at conferences were very interesting and fruitful. I cannot list all of them here. I would like to thank in particular Daniel Pino Muñoz for our numerous discussions on numerical methods and fracture and contact mechanics, which had a major influence on some chapters of this thesis. I would also like to express my gratefulness to Thomas Toulorge for our fruitful discussions on numerical methods, and Lionel Fourment for sharing his knowledge and passion for computational solid mechanics.

A lot of knowledge and passion was shared at project meetings, for which I would like to express my sincere gratefulness to François Hild and Thilo Morgeneyer. Special thanks are due to their PhD student Ante Buljac for all our discussions, scientific or not, which made this joint project a real pleasure. Additionally, I would like to thank Thilo Morgeneyer for inviting me to one of his synchrotron experiments, which was a unique experience for me. I do not forget Victor Trejo, who will have the burdensome responsibility to pursue this work.

I gratefully acknowledge the help of Elizabeth Massoni, François Bay, Patrick Coels, Marie-Françoise Guenegan, Genevieve Anseeuw and all staff members for welcoming me in the center and helping me with all administrative procedures. Special thanks to the Scientific Computing and Software team, who take great care of our computational resources, and answered all my requests with patience and kindness.

I would never have started a PhD thesis if my path had not met that of Fikri Hafid at EISTI and Guillaume Enchéry at IFPE. I would like to express my gratefulness to you for sharing your passion for research and numerical methods, and inspiring me to do a PhD thesis.

Because Paris always comes first, I would like to first express my deepest appreciation to all my friends in Paris. Thanks to Yannick, Clément, Fabio, Daniel and Abdel for visiting me in the Riviera. Thanks again to Daniel and also to Nishanth for taking me on post-thesis-writing holidays. My thoughts and appreciation also go to Alexis, Florian, Charles, Priscilla and Delphine, to whom I will have to explain again and again what ductile fracture is about. Then, I would like to thank all the friends I met on the Riviera for these wonderful three years, and send them all my love and encouragements, especially to those who are currently writing their thesis or preparing their defense.

Finally, I would like to express my sincere gratefulness and love to my father, mother and sisters. Thanks for helping me settle in the Riviera, and preparing all these wonderful meals and pastries every time I came back to Paris. I dedicate this thesis to you, and to all the pastries to come...

Frédéric, assure-toi qu'elle n'y manque pas ! Dima, je te promets un régime alimentaire à l'américaine pour mon retour ! Colin, prévois une version censurée de ton manuscrit, que je puisse le lire ! Ivan, mon stagiaire préféré...
when it does not work, the issue most probably comes from the user. Luis, Victor, ¡No olviden recordarle eso! Ante, do not forget to remind Victor all the things I left for him to do! Laure, appelle-moi à ton pot de thèse, c'est moi qui enverrai le message.
Benjamin, je t'apaise encore d'une humiliation aux échecs par tes garçons. Pierre-Olivier, je te souhaite d'assumer enfin ton amour du PSG, et des artistes parisiens à lunettes de soleil. Benjamin, je t'apaise encore d'une humiliation aux échecs par tes garçons. Pierre-Olivier, je te souhaite d'assumer enfin ton amour du PSG, et des artistes parisiens à lunettes de soleil.
Marie-Agathe, laisse-le participer au financement des prochains blockbusters ! Stéphanie, merci pour cette affiche de thèse géniale, vivement ma vengeance ! Daniel, Marc, ne crains pas que je prenne la grosse tête, je me souviens encore d'une humiliation aux échecs par tes garçons. Marie-Agathe, laisse-le participer au financement des prochains blockbusters ! Stéphanie, merci pour cette affiche de thèse géniale, vivement ma vengeance ! Daniel, Marc, ne crains pas que je prenne la grosse tête, je me souviens encore d'une humiliation aux échecs par tes garçons.
règle, faudra qu'on refasse le compte des kilomètres parcourus et pages écrites. Marie-Agathe, laisse-le participer au financement des prochains blockbusters ! Stéphanie, merci pour cette affiche de thèse géniale, vivement ma vengeance ! Daniel, Marc, ne crains pas que je prenne la grosse tête, je me souviens encore d'une humiliation aux échecs par tes garçons.

Contents

Introduction	9
Metal forming	9
Ductile fracture: physics	11
Ductile fracture: models	13
Objectives and outline	15
Publications	17
1 Literature review	21
Introduction	24
1.1 Experimental methods	25
1.1.1 X-ray imaging	25
1.1.2 Void nucleation	27
1.1.3 Void growth and coalescence	29
1.1.4 Digital Volume Correlation	32
1.2 Theoretical and numerical methods	34
1.2.1 Finite Element scheme	34
1.2.2 Homogenization theory	40
1.2.3 Homogenization in porous plasticity	45
Conclusion	50
2 Mesh adaptation with enhanced volume conservation	53
Introduction	56
2.1 Meshing internal interfaces	60
2.2 Volume-conserving mesh adaptation	62
2.2.1 Anisotropic mesh adaptation	62
2.2.2 Mesh adaptation with internal interfaces	67
2.2.3 Robustness improvement	69
2.2.4 Concluding remarks	70
2.3 Mesh motion and transport	72
2.3.1 Mesh motion	72
2.3.2 Transport of history variables	72
2.4 Results	75
2.4.1 Large displacements: sphere rotation	75
2.4.2 Large deformations: sphere stretching	78
2.4.3 Topological changes: sphere stacking	80
2.4.4 Robustness investigation	82
2.5 Parallel implementation	84
2.6 Extension to computational fracture mechanics	86
Conclusion	88
3 Computation and use of signed distance functions	91
Introduction	94
3.1 Curvature-based mesh adaptation	95
3.1.1 Metric fields	95
3.1.2 Error estimators	96
3.1.3 Gradient and Hessian recovery	98

3.1.4	Results	99
3.2	Level-Set reinitialization	103
3.2.1	Introduction	103
3.2.2	Algorithm	104
3.2.3	Results	110
3.2.4	Conclusion	118
3.3	Connected Components identification	120
3.4	Image immersion and meshing	124
3.4.1	Method	124
3.4.2	Results	125
	Conclusion	133
4	Micromechanical modeling of void nucleation	135
	Introduction	138
4.1	Macroscopic criteria	140
4.1.1	Argon criterion	140
4.1.2	Beremin criterion	140
4.1.3	Landron criterion	141
4.1.4	Weibull formula	142
4.2	Microscopic criteria	143
4.2.1	Lee and Mear analysis	143
4.2.2	Local criteria	144
4.3	Proposed models	145
4.4	Boundary conditions and stress state control	148
4.4.1	Choice of boundary conditions	148
4.4.2	Stress state control	148
4.4.3	Consequences on the fracture criteria	151
4.5	Results	153
4.5.1	Numerical ingredients	153
4.5.2	Material	154
4.5.3	Numerical validation	156
4.5.4	Representative Volume Element size	171
4.5.5	Importance of void nucleation modeling	176
4.5.6	Conclusion	183
	Conclusion	184
5	Micromechanical modeling of void coalescence	187
	Introduction	190
5.1	Plasticity driven void coalescence	191
5.2	Plasticity and damage driven void coalescence	192
5.3	Proposed model	194
5.4	Results	197
5.4.1	Identification of damage parameters	197
5.4.2	Effect of intervoid ligament length	199
5.4.3	Effect of number of holes	200
5.4.4	Effect of holes orientation	204
5.4.5	Random arrangements	204
	Conclusion	209

6	A numerical validation framework for micromechanical simulations based on synchrotron 3D imaging	211
	Introduction	214
6.1	Method	217
6.1.1	Introduction	217
6.1.2	Experimental analyses	219
6.1.3	Finite Element simulations	223
6.1.4	Quantitative comparisons	227
6.1.5	Conclusion	233
6.2	Comparison with other methods	235
6.2.1	Introduction	235
6.2.2	Experiments	236
6.2.3	Boundary conditions	238
6.2.4	Results	240
6.2.5	Conclusion	249
	Conclusion	250
7	Conclusions and outlook	253
7.1	Achievements	254
7.2	Suggestions for future work	256
7.2.1	Mesh generation and adaptation	256
7.2.2	Level-Set reinitialization	257
7.2.3	Computational contact mechanics	260
7.2.4	Micromechanical models and computational fracture mechanics	260
7.2.5	Multiscale methods	262
A	An adaptive immersed approach to contact/impact mechanics	267
	Introduction	270
A.1	Contact detection	272
A.1.1	Literature review	272
A.1.2	Proposed method	272
A.2	Contact formulation and solution	276
A.2.1	Literature review	276
A.2.2	Chosen method	277
A.3	Results	280
A.3.1	Contact	280
A.3.2	Impact	282
	Conclusion	284
	Bibliography	285

Nomenclature

Abbreviation	Description
nD	n Dimension(s)
CAD	Computer Assisted Design
CC	Connected Component
Cemef - MINES ParisTech	Center for Material forming - MINES ParisTech
CL	Computed Laminography
CPU	Central Processing Unit
CR	Convection-Reinitialization
CT	Computed Tomography
CZM	Cohesive Zone Model
DF	classical Distance Function
DIC	Digital Image Correlation
DNS	Direct Numerical Simulation
DR	Direct Reinitialization
DRT	Direct Reinitialization with Trees
DVC	Digital Volume Correlation
ESRF - Grenoble	European Synchrotron Radiation Facility - Grenoble
FE	Finite Element
FLAG _c	Fitted Lagrangian Level-Set with volume conservation constraint
GTN	Gurson-Tvergaard-Needleman
H-J	Hamilton-Jacobi
HRBCs	Hill-Reuss Boundary Conditions
HTDF	Hyperbolic Tangent Distance Function
IEUL	Implicit Eulerian Level-Set
ILAG	Implicit Lagrangian Level-Set
KUBCs	Kinematic Uniform Boundary Conditions
LS	Level-Set
NRO	Number of Remeshing Operations
P1	First order (linear) finite element
PBCs	Periodic Boundary Conditions
ROI	Region Of Interest
RVE	Representative Volume Element
SEM	Scanning Electron Microscopy
sFE	strong Finite Element
SPR	Superconvergent Patch Recovery
SR	Synchrotron Radiation
SUBCs	Static Uniform Boundary Conditions
TVBCs	Taylor-Voigt Boundary Conditions
wFE	weak Finite Element
X-FEM	eXtended Finite Element Method

Introduction

Metal forming

Metallic materials are extensively used in the transport and energy industries among others. These materials can be high-performance metal alloys, as in turbine engines of planes and ships. Since these alloys have large production costs, metals of lower performance can be preferred, such as iron and aluminum alloys. A last category of metallic materials, called metal matrix composites, are composed of a main component called the matrix, which is a metal alloy, and other microscopic components. These other components, called reinforcements, inclusions, particles or fibers depending on their properties, are used to improve some specific characteristics such as strength, resistance to corrosion etc., with respect to the matrix material alone.

For all those metallic materials, from composites to high-performance alloys, failure is an important issue that has to be predicted and controlled. Indeed, a better prediction of failure would enable more efficient forming processes, reducing both the cost and the environmental impact of fabrication. Additionally, in many sectors such as the transport industry, a better understanding and modeling of failure mechanisms would permit the use of advanced composite materials, reducing the weight of the products and their energetic consumption.

The occurrence of failure is highly linked to the flawlessness of the material. Even in high-performance alloys, defects can be found, as voids or inclusions may be trapped inside the material during its forming, or may appear during heat treatments due to chemical reactions. For alloys and composites, the defects are linked to the reinforcements themselves, or the different components of the alloy. Indeed, the bond between the different components may fail, or the difference of strength between the components may induce local stress increase and eventually failure. This failure of some components of the microstructure or the bonds between these components due to mechanical loading gives rise to microscopic voids that are at the origin of materials' damage.

Depending on several aspects of the microstructure, such as anisotropy, density of each component, arrangement and shapes of the components, voids may nucleate and grow in very complex patterns. This complexity will be strongly increased if loading itself is complex. Indeed, final pieces are generally the product of several forming stages, each relying on various loading modes (compression, tension, shear). These modes may be combined or applied consecutively in different directions. Such a loading path is very frequent in metal forming and is referred to as non proportional and complex loading path.

Last but not least, metal forming processes are based on irreversible and large deformations, and hence plasticity. In general, plasticity and damage will develop concurrently in the whole material, and will localize in some regions. This localization may be desired or not depending on the forming process, hence it needs to be accurately predicted, controlled, and sometimes avoided. In particular, simulations tools should determine accurately the local distributions of

plasticity and damage.

Both plasticity and damage will have an effect on the materials behavior, as plasticity will generally lead to hardening, while damage will generally lead to softening. For realistic forming simulations, both these effects have to be modeled. More complex aspects of plasticity and damage could also have to be modeled depending on the material and the loading conditions: anisotropy, competition between localization events at multiple scales, dependence on temperature and pressure, etc.

Recently, a global effort was initiated at the Center for Material forming - MINES ParisTech (Cemef - MINES ParisTech) with the aim of developing innovative and efficient numerical simulation tools for predicting and modeling the influence of forming processes on metals, and in particular on their microstructure. This focus on the microscale is motivated by previous works at Cemef - MINES ParisTech where these processes were addressed only at the macroscale, raising important limitations, and experimental results showing the importance of the microstructure [1]. Ultimately, these simulation tools should account for all aspects that interest industrial partners, based on appropriate numerical models for static and dynamic recrystallization [2, 3], crystal plasticity [4], and ductile fracture [5, 6]. Virtual microstructures can be generated based on statistical data [7], but real microstructures based on experimental observations are also targeted [6]. In the case of damage and fracture, generalization of these developments to other materials, such as polymer matrix composites, is not discarded, as these materials are also intensively studied at Cemef - MINES ParisTech and are of great interest for industrial partners [8]. Finally, in many applications, not only should the influence of macroscopic loading conditions on the microstructure be modeled, but also the influence of this evolving microstructure on the macroscopic behavior of the material.

The micromechanisms of ductile fracture are briefly described hereafter, based on experimental approaches. Theoretical and numerical approaches are then considered, including existing models to predict the occurrence and growth of damage. An emphasis is made on previous work at Cemef - MINES ParisTech regarding micromechanical modeling and its limitations in order to introduce the objectives of the present work.

Ductile fracture: physics

The increasing use of metals and metal forming in the twentieth century has led researchers to investigate ductile damage through the nucleation and growth of voids, using both experimental and numerical means. With the development of advanced observation tools based on electrons or X-rays, the microstructure of materials and the microscopic defects can be observed both in two dimensions (2D) [9, 10, 11, 12, 13, 14] and three dimensions (3D) [15, 16, 17, 18, 19, 20]. These techniques enable to reconstruct the microstructure in 2D or 3D, including the crystal structure of metals [15], with a high resolution (0.1 μm to 1 μm). With advanced loading devices, the nucleation and growth of defects can be observed *in-situ* [17, 19, 20, 21, 22], which is very important as the same microstructure is then observed throughout loading. As opposed to destructive imaging techniques, these *in-situ* techniques avoid all issues linked to experiments reproducibility, thus easing results interpretation and modeling. Experimental images obtained using these advanced observation techniques are presented in Figure 1.

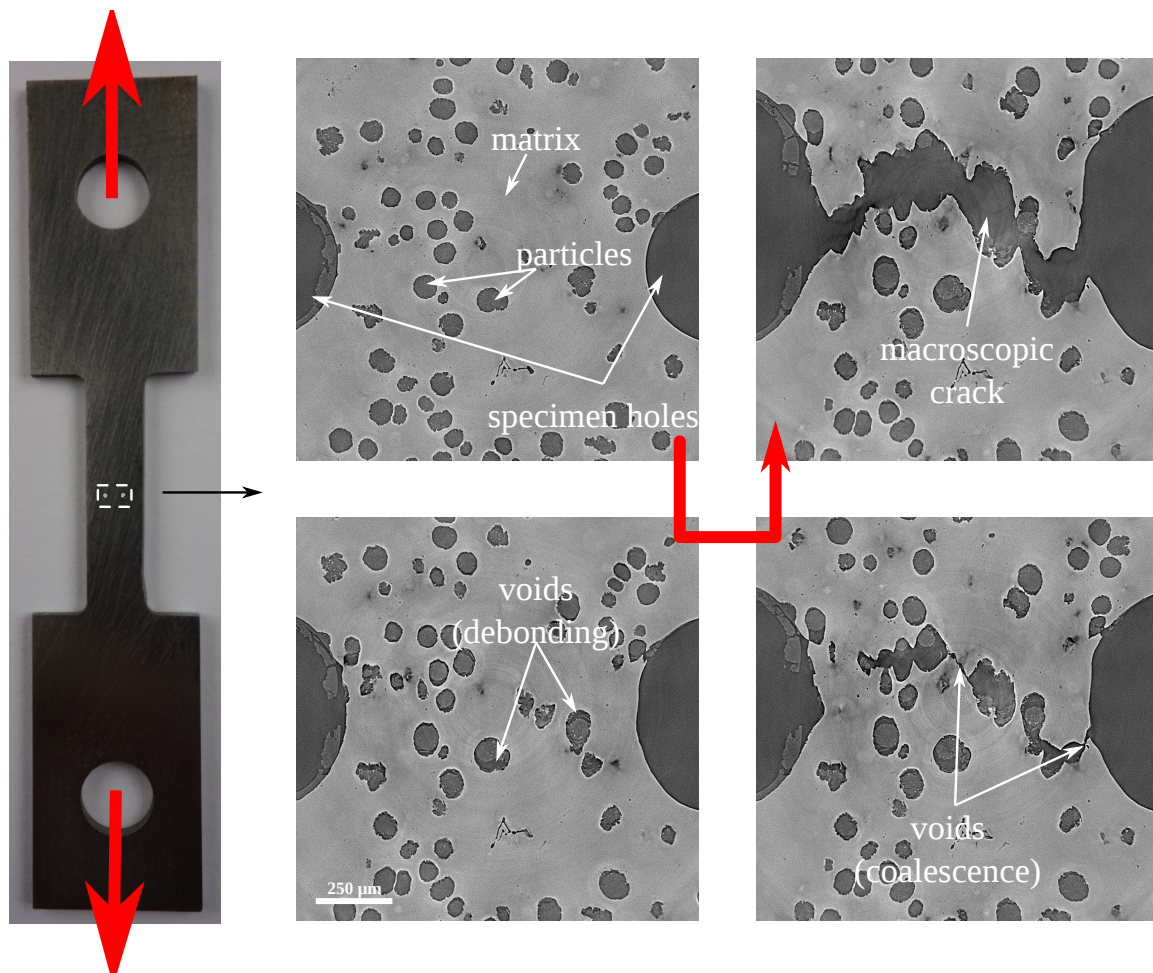


Figure 1 – Failure of a nodular cast iron specimen observed with Synchrotron Radiation Computed Laminography (SRCL) during an *in-situ* tensile experiment. The distance between the two holes is 1 mm. Courtesy of T. F. Morgeneyer.

These images correspond to a flat specimen of nodular cast iron, which at the microscale features a ferritic steel matrix and graphite inclusions. In this material, damage nucleates under

tension by debonding of the inclusions from the matrix. The nucleated voids then grow independently from each other, until void growth starts to accelerate between neighboring voids. This acceleration is the onset of void coalescence, which accumulates until the initiation of a macroscopic crack. This crack will propagate until final failure of the specimen.

Ductile damage is defined by these void nucleation, growth and coalescence mechanisms, that are highly dependent on the microstructure of the material. Due to the microscopic voids that are present and growing in the material, its load carrying capacity will be progressively affected, which will translate into softening of its mechanical response, as shown in Figure 2. This softening may be more or less pronounced depending on the material and loading conditions. While void nucleation and growth occur all along loading and lead to a progressive softening of the mechanical response, void coalescence leads to an acceleration of this softening effect which is significant only at large plastic strain.

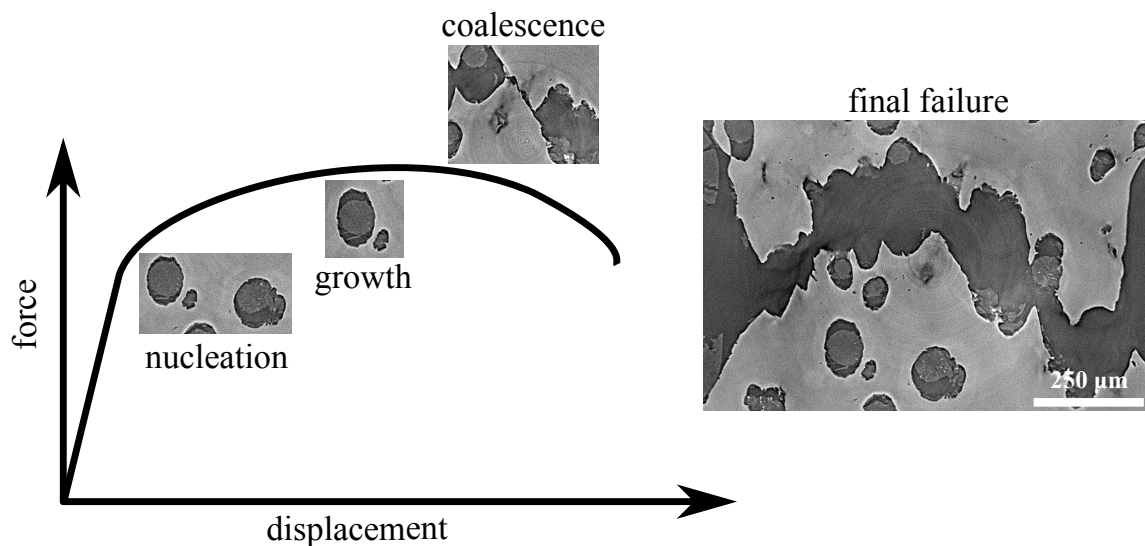


Figure 2 – Typical force/displacement curve of a ductile material under tensile loading. The micromechanisms of void nucleation, growth and coalescence occur during the whole loading path, but each mechanism is dominant at different loading steps. X-ray images are a courtesy of T. F. Morgeneyer.

Finally, the initiation of the macroscopic crack, well-known as the damage to fracture transition, is the final step of ductile fracture. Modeling this step is only important for some forming processes such as self-pierce riveting [23] or cutting [24], as in other processes macroscopic cracks tend to be avoided.

Ductile fracture: models

In this section, ductile fracture modeling is reviewed, with an emphasis on the limitations of macroscopic models, and the necessity to look at the microscale. A first category of models, known as uncoupled models, or damage indicators, can be found in the literature. These models can have an empirical basis, such as the Latham & Cockcroft model, or a theoretical basis, such as the McClintock [25] and Rice & Tracey [26] models. The application of these damage indicators remains limited to situations where damage accumulates without influencing the material's load carrying capacity (softening is neglected).

In the second half of the twentieth century, a new theory, known as continuum damage models, has been developed, enabling to predict the initiation and growth of damage and its impact on the material's elastic and plastic response, until fracture [27, 28]. Both damage indicators [24, 29, 30] and continuum damage models [23, 24, 31, 32] have been applied at Cemef - MINES ParisTech to various metal forming processes where softening or ductile fracture had to be predicted accurately. These studies have shown that in some loading conditions, these models can be calibrated in order to obtain accurate predictions.

However, for complex loading conditions, some modifications are necessary. For instance, the continuum damage model proposed initially by Lemaitre [28] is well-known to give poor predictions when the material is locally subjected to compression. A modified version has hence been used for some forming processes in recent works [23, 31]. Generalized versions of the Lemaitre model have also been investigated [32]. These modifications are however phenomenological, which makes difficult to link the notion of damage to the physical mechanisms of voids nucleation, growth and coalescence in ductile materials.

Homogenization theory enables to overcome this specific difficulty. A study at the microscale of the growth of a single void embedded in an infinite matrix was performed by Gurson [33], inspired by previous works of McClintock [25] and Rice & Tracey [26]. An analytical solution was derived thanks to quite restraining assumptions, and averaged in order to deduce a porous plasticity load surface taking into account both plasticity and porosity. Among these assumptions, the matrix was defined as rigid plastic, and the Representative Volume Element (RVE) used for homogenization did not take into account neighboring voids. The widely used Gurson-Tvergaard-Needleman (GTN) model introduces three phenomenological parameters in order to adjust this load surface [34] and completes Gurson's void growth model with two contributions corresponding to void nucleation and coalescence [35]. The Gologanu-Leblond-Devaux model [36] extends the GTN model to non-spherical voids, improving predictions under shear, where voids do not grow but mainly rotate.

The GTN model has been used at Cemef - MINES ParisTech [32], and especially its extensions to shear loading. These extensions typically introduce numerous parameters that require advanced identification procedures [32]. Additionally, while the model proposed by Gurson is micromechanical and accounts for the physical mechanism of void growth, all extensions based on the GTN model add phenomenological parameters to the model. Thus, while these extensions give more realistic results regarding plasticity and softening, the link between model predictions and the physical micromechanisms of ductile fracture is deteriorated. Another important limitation is that because each extension of the Gurson model targets a specific loading configuration, and a general model that could handle all possible loading conditions accurately is yet to be formulated, applications to non proportional loading paths are limited.

As a conclusion, there is a need to understand the limitations of common damage models, and develop damage models taking into account the microstructure and allowing for an accurate

characterization of the microstructure and the potential defects.

In this aim, Finite Element (FE) analysis is often conducted at the microscale [37, 38]. These investigations are performed in conditions close to the ones used by Gurson in his homogenization methodology. The main advantage of numerical approaches is that they do not require too restraining assumptions since solution is performed numerically and not analytically. However, most works generally do not address the nucleation and coalescence of voids in the RVE. In case of nucleation, FE analysis is performed on an RVE containing particles, and nucleation is predicted after the simulation based on average stress measurements. In the same way, coalescence is studied with an RVE containing voids instead of particles. These works do not allow to raise any conclusions regarding the possible interactions between void nucleation, growth and coalescence, especially in the case of realistic microstructures where particles are distributed randomly, and can have various shapes and sizes.

Based on these observations on existing works, an FE framework was developed at Cemef - MINES ParisTech in order to perform simulations taking into account realistic microstructures and modeling ductile fracture mechanisms at the microscale. The goal was to include micromechanical models accounting for the whole ductile fracture process, from void nucleation to final failure of the RVE due to void coalescence.

This work was based on advanced numerical tools available in the laboratory FE code [5], which were extended in order to model fracture events [6]. Promising results were obtained in 2D, as real microstructures could be meshed and subjected to various loading conditions, proving qualitatively the influence of loading path on ductile fracture. However, several limitations were encountered, especially for 3D applications.

In particular, these developments relied on the LS method, which is described in details farther in this work. This method helps the modeling of interfaces at large deformations and with complex topological events such as voids coalescence. However, it has the main flaw of raising volume conservation issues when it is combined with remeshing, which is necessary in order to reach large plastic strains. Very fine FE meshes were used in previous developments to prevent the geometry from being diffused. As the Level-Set (LS) method was also used to represent cracks, sharp cracks could not be represented and were replaced by spherical nuclei, which were initially given a quite large radius in order to avoid them being also diffused.

Then, the LS method does not include an interface modeling technique. The transition between different material behaviors at interfaces was modeled using mixture laws, which are quite complex to formulate for very different behaviors such as an elastic inclusion and a plastic matrix, or a void and a solid.

Additionally, the remeshing technique relied on some specific properties of the LS method, which require a reinitialization technique in order to be maintained during deformation. No robust and efficient technique was available in the FE code to perform this operation.

Finally, some important aspects of solid mechanics such as contact were neglected, and the fracture criteria used to model the micromechanisms of ductile fracture had yet to be extended to 3D.

Due to these limitations, very fine FE meshes and hence high computational resources were necessary in order to reach large plastic strains in 2D. Consequently, applications to complex 3D microstructures could not be considered. The latter are necessary not only to study the influence of complex three-dimensional loading paths on ductile fracture micromechanisms, but also to validate micromechanical models. Previous developments at Cemef - MINES ParisTech did not address the challenging problem of validating micromechanical FE simulations with respect to experiments since it was difficult to get reliable and accurate data all along loading history.

Objectives and outline

The aim of the CORTEX Carnot Mines project was twofold: improving the FE method for micromechanical modeling of ductile fracture, ideally to enable 3D simulations on real microstructures, and validating quantitatively the developments. The pursuit of the second objective was largely aided by the start of the ANR COMINSIDE project during the second year of the present study, which involved teams from the Centre des Matériaux (MINES ParisTech) and the LMT Cachan (ENS Cachan). This manuscript details the contributions of the work done within the Carnot CORTEX project and their use in the frame of the ANR COMINSIDE project.

- A literature review is first proposed in Chapter 1, with a more thorough description of micromechanical modeling and homogenization theory. As micromechanical calculations are often conducted with the FE method, a brief description of this method and the numerical scheme used at Cemef - MINES ParisTech is given. The Gurson model and its extensions are discussed, with an emphasis on studies relying on numerical calculations.
- Before introducing any material behavior law or fracture criteria, important numerical issues have to be answered. Among them, an appropriate methodology has to be introduced in order to represent the microstructure in an FE context. This methodology should be compatible with the numerous and complex void nucleation, growth and coalescence events that will occur during the simulation, as shown in Figure 1. The numerical method presented in Chapter 2 and proposed in the present work to solve this problem relies on two main tools, namely the LS method and mesh adaptation. In particular, results are presented to prove that the proposed mesh adaptation technique improves significantly a major defect of the LS method, which is volume conservation. However, it is shown that the advantages of the LS method are preserved, with no significant increase of the computational cost. The application of this method in the frame of computational fracture mechanics and the meshing of sharp cracks during the simulation is also described.
- In the aim of addressing real microstructures, three important ingredients are added to the numerical method in Chapter 3, and applied to real microstructure meshing, based on 3D X-ray data. The first ingredient is an error estimator, enabling to achieve better accuracy in the representation of the microstructure's geometry. This estimator has been found in the literature and implemented in the FE library developed at Cemef - MINES ParisTech. The two other ingredients are necessary in order to address void growth at large plastic strain, and ductile fracture modeling. Indeed, a LS reinitialization procedure is needed to maintain the regularity of the LS method, especially when large deformations occur. Such procedure was already implemented in the FE code, but its robustness and computational cost were quite limiting for 3D applications. A new procedure is proposed in the present work, and its efficiency both in terms of accuracy and computational cost is compared to existing approaches. This method is completed with a connected components identification algorithm, which is necessary in order to assess fracture criteria individually for each inclusion or void. Finally, these three ingredients are used to mesh real microstructures based on 3D X-ray data, where the geometry is accurately captured thanks to the error estimator. The regularity of the LS method is enforced thanks to LS reinitialization, and the different inclusions and voids of the microstructure are identified thanks to connected components identification.

- With the enhanced LS method and its additional ingredients detailed in Chapter 2 and Chapter 3, simulations can be conducted with microstructures that undergo large deformations and complex topological events such as fracture or coalescence. The remaining open questions are linked to constitutive modeling. As the focus is on damage modeling, a simple plasticity model is used for the matrix material, while a more thorough bibliographic study is conducted to develop appropriate fracture criteria to predict and model void nucleation. These models are presented in Chapter 4, and used in micromechanical calculations conducted in the frame of homogenization theory. Convergence results are presented with respect to numerical parameters and RVE size, and the importance of modeling simultaneously void nucleation, growth, and coalescence mechanisms is demonstrated.
- While void coalescence is assumed to be purely driven by plastic localization in Chapter 4, recent experimental observations suggest that this phenomenon may be more complex. These experimental studies are reviewed in Chapter 5, and a micro-cracking criterion is proposed to predict the initiation of micro-cracks in intervoid ligaments. This criterion is used in 2D simulations and compared to experimental results found in the literature.
- Validation with respect to 3D data acquired during *in-situ* experiments is addressed in Chapter 6. Thanks to the experimental-numerical framework presented in this chapter, 3D numerical simulations taking into account real microstructures and measured boundary conditions are conducted and compared locally with 3D observations during loading. To the author's best knowledge, this is the first time such simulations are conducted, and that local error measurements with respect to experiments are considered in the case of ductile fracture.
- Finally, Chapter 7 sums up the main developments and achievements of this work and highlights several ideas of improvement related to the field of ductile fracture. Applications of the numerical tools developed in this work to other materials (*e.g.*, polycrystals, polymer matrix composites) and challenging research problems (*e.g.*, static and dynamic recrystallization, fluid-structure interaction, multiphase flow) are also considered.

Publications

This work has led to the publication of 5 papers (and 2 submitted) and to presentations in several international and national conferences.

Articles in peer-reviewed international journals

As lead author

- M. Shakoor, B. Scholtes, P.-O. Bouchard, and M. Bernacki. “An efficient and parallel level set reinitialization method – Application to micromechanics and microstructural evolutions”. In: *Applied Mathematical Modelling* 39.23-24 (2015), pages 7291–7302. doi: [10.1016/j.apm.2015.03.014](https://doi.org/10.1016/j.apm.2015.03.014)
- M. Shakoor, M. Bernacki, and P.-O. Bouchard. “A new body-fitted immersed volume method for the modeling of ductile fracture at the microscale: Analysis of void clusters and stress state effects on coalescence”. In: *Engineering Fracture Mechanics* 147 (2015), pages 398–417. doi: [10.1016/j.engfracmech.2015.06.057](https://doi.org/10.1016/j.engfracmech.2015.06.057)
- M. Shakoor, P.-O. Bouchard, and M. Bernacki. “An adaptive Level-Set Method with enhanced volume conservation for simulations in multiphase domains”. In: *International Journal for Numerical Methods in Engineering* (2016). doi: [10.1002/rme.5297](https://doi.org/10.1002/rme.5297)
- M. Shakoor, A. Buljac, J. Neggers, F. Hild, T. F. Morgeneyer, L. Helfen, M. Bernacki, and P.-O. Bouchard. “On the choice of boundary conditions for micromechanical simulations based on synchrotron 3D imaging”. In: *International Journal of Solids and Structures* (Submitted)

As co-author

- E. Roux, M. Shakoor, M. Bernacki, and P.-O. Bouchard. “A new finite element approach for modelling ductile damage void nucleation and growth—analysis of loading path effect on damage mechanisms”. In: *Modelling and Simulation in Materials Science and Engineering* 22.7 (2014), page 075001. doi: [10.1088/0965-0393/22/7/075001](https://doi.org/10.1088/0965-0393/22/7/075001)
- B. Scholtes, M. Shakoor, A. Settefrati, P.-O. Bouchard, N. Bozzolo, and M. Bernacki. “New finite element developments for the full field modeling of microstructural evolutions using the level-set method”. In: *Computational Materials Science* 109 (2015), pages 388–398. doi: [10.1016/j.commatsci.2015.07.042](https://doi.org/10.1016/j.commatsci.2015.07.042)
- A. Buljac, M. Shakoor, J. Neggers, M. Bernacki, P.-O. Bouchard, L. Helfen, T. F. Morgeneyer, and F. Hild. “Numerical Validation Framework for Micromechanical Simulations based on Synchrotron 3D Imaging”. In: *Computational Mechanics* (Submitted)

Participations in international conferences

As presenting author

- M. Shakoor, M. Bernacki, and P.-O. Bouchard. “Numerical modelling of ductile damage at the microscale in a level set framework”. In: *International CAE Conference (CAE)*. Verona (Italy), Oct. 27–28, 2014

- M. Shakoor, M. Bernacki, and P.-O. Bouchard. “An adaptive body-fitted monolithic method for modeling the fracture of heterogeneous microstructures”. In: *International Conference on Computational Modeling of Fracture and Failure of Materials and Structures (CFRAC)*. Paris (France), June 3–5, 2015
- M. Shakoor, M. Bernacki, and P.-O. Bouchard. “Modeling of ductile fracture mechanisms at the microscale using a new adaptive body-fitted monolithic method”. In: *International Conference on Computational Plasticity (COMPLAS)*. Barcelona (Spain), Sept. 1–3, 2015
- M. Shakoor, M. Bernacki, and P.-O. Bouchard. “An adaptive body-fitted monolithic method for modeling the fracture of heterogeneous microstructures”. In: *World Congress on Computational Mechanics (WCCM)*. Seoul (Korea), July 24–29, 2016

As co-author

- M. Shakoor, M. Bernacki, E. Roux, and P.-O. Bouchard. “Numerical modelling of the effect of non-proportional loading on ductile fracture at the microscale”. In: *European Conference on Fracture (ECF)*. Trondheim (Norway), June 30–July 4, 2014
- M. Shakoor, M. Bernacki, and P.-O. Bouchard. “Analysis of void clusters arrangements on coalescence using a new body-fitted immersed volume method for the modeling of ductile fracture at the microscale”. In: *IUTAM Symposium: Ductile Fracture and Localization*. Paris (France), Mar. 27–28, 2015
- B. Scholtes, M. Shakoor, N. Bozzolo, P.-O. Bouchard, A. Settefrati, and M. Bernacki. “Advances in Level-Set modeling of recrystallization at the polycrystal scale - Development of the Digi- μ software”. In: *International ESAFORM Conference on Material Forming (ESAFORM)*. Graz (Austria), Apr. 15–17, 2015
- M. Shakoor, M. Bernacki, and P.-O. Bouchard. “Micromechanical modelling of ductile fracture mechanisms using a new body-fitted immersed volume method”. In: *International Conference on Computational Modeling of Fracture and Failure of Materials and Structures (CFRAC)*. Paris (France), June 3–5, 2015
- P.-O. Bouchard, M. Shakoor, V. M. Trejo Navas, and M. Bernacki. “Numerical modeling of failure mechanisms in complex heterogeneous microstructures”. In: *European Conference on Fracture (ECF)*. Catania (Italy), June 20–24, 2016
- D. Pino Muñoz, M. Shakoor, M. Bernacki, and P.-O. Bouchard. “Towards a mesh independent fracture modeling method using cohesive elements”. In: *European Conference on Fracture (ECF)*. Catania (Italy), June 20–24, 2016
- V. M. Trejo Navas, M. Shakoor, M. Bernacki, and P.-O. Bouchard. “Ductile fracture – Influence of heterogeneous microstructure on nucleation, growth and coalescence mechanisms”. In: *International Conference on Numerical Methods in Industrial Forming Processes (NUMIFORM)*. Troyes (France), July 4–7, 2016
- D. Polychronopoulou, N. Bozzolo, D. Pino Muñoz, J. Bruchon, M. Shakoor, Y. Millet, C. Dumont, I. Freiherr von Thüngen, R. Besnard, and M. Bernacki. “Introduction to the level-set full field modeling of laths spheroidization phenomenon in α/β titanium alloys”. In: *International Conference on Numerical Methods in Industrial Forming Processes (NUMIFORM)*. Troyes (France), July 4–7, 2016

Participations in national conferences

As presenting author

- M. Shakoor, P.-O. Bouchard, and M. Bernacki. “Modélisation numérique de l’endommagement ductile à l’échelle des microstructures”. In: *Journées Matériaux Numériques (JMN)*. St-Aignan-sur-Cher (France), Feb. 3–5, 2015
- M. Shakoor, M. Bernacki, and P.-O. Bouchard. “Une nouvelle méthode de volume immergé pour la modélisation numérique de l’endommagement ductile à l’échelle des microstructures”. In: *Colloque national en calcul des structures (CSMA)*. Giens (France), May 18–22, 2015

As co-author

- P.-O. Bouchard, M. Shakoor, and M. Bernacki. “3D modeling of ductile fracture at the microscale using a new body-fitted mesh adaptation technique”. In: *Workshop SF2M/MECAMAT*. Paris (France), Nov. 30–Dec. 1, 2015
- A. Buljac, M. Shakoor, J. Neggens, M. Bernacki, P.-O. Bouchard, L. Helfen, T. F. Morgeneyer, and F. Hild. “Micromechanical simulations based on laminography 3D imaging: experimental/numerical framework”. In: *Workshop SF2M/MECAMAT*. Paris (France), Sept. 15–16, 2016
- V. M. Trejo Navas, M. Shakoor, M. Bernacki, and P.-O. Bouchard. “Ductile fracture - Influence of heterogeneous microstructure on nucleation, growth and coalescence mechanisms”. In: *Workshop SF2M/MECAMAT*. Paris (France), Sept. 15–16, 2016

Chapter 1

Literature review

You can't go walking through
Mordor in naught but your skin.

Samwise Gamgee

- Introduction 24
- 1.1 Experimental methods 25
 - 1.1.1 X-ray imaging 25
 - 1.1.2 Void nucleation 27
 - 1.1.3 Void growth and coalescence 29
 - 1.1.4 Digital Volume Correlation 32
- 1.2 Theoretical and numerical methods 34
 - 1.2.1 Finite Element scheme 34
 - 1.2.2 Homogenization theory 40
 - 1.2.3 Homogenization in porous plasticity 45
- Conclusion 50

Résumé en français

Tout matériau métallique est hétérogène à l'échelle microscopique, que ce soit à cause de sa structure cristalline, des renforts, ou encore des défauts. Ainsi, la microstructure de ces matériaux est composée de plusieurs phases métalliques, souvent elles-mêmes séparées par des particules non métalliques et des cavités. Les interfaces entre ces différentes composantes sont des sites de concentration de contraintes pendant le chargement, ce qui mène à la germination de cavités. Ce phénomène de germination peut se manifester par la décohésion, qui est due à la rupture d'une interface entre deux composants, ou par la fragmentation, qui est due à la rupture d'un des composants.

Les cavités ainsi germinées croissent indépendamment les unes des autres pendant le chargement, jusqu'à un certain point critique où elles commencent à interagir entre elles. Ce point critique est le début de la coalescence des cavités. Il est marqué par une accélération de la croissance des cavités s'avoisinant, jusqu'à leur liaison totale, qui est parfois accompagnée de micro-fissures. L'accumulation de ces liaisons entre paires de vides mène à la formation d'une macro-fissure, et à la rupture ductile finale du matériau.

Ainsi, la rupture ductile est complexe par nature, car des fissures se développent à deux échelles. Par ailleurs, de récentes études à la fois expérimentales et théoriques mentionnent que plus de deux échelles pourraient être impliquées, de par l'existence de cavités de taille inférieure au micromètre qui pourraient avoir une influence majeure sur la coalescence des cavités de taille supérieure. Les études expérimentales ont un rôle clé et ont beaucoup aidé à la compréhension de la rupture ductile, grâce notamment aux techniques d'imagerie par rayons X. Ces techniques permettent aujourd'hui l'observation *in situ* de la rupture ductile, pour des éprouvettes jusque quelques millimètres d'épaisseur et une résolution proche du micromètre.

Des algorithmes de suivi automatique de cavités ont été développés pour obtenir des mesures locales de la croissance des cavités à partir de ces données tridimensionnelles (3D). Il y a un fort besoin pour ces techniques de pointe à cause de la distribution aléatoire des cavités dans le matériau, et de la distribution également aléatoire de leurs tailles. Afin d'éviter ces difficultés, certains auteurs ont étudié la conception de matériaux modèles avec des trous percés au laser.

Ajouté à cette nature complexe et multiéchelle de l'endommagement, l'interaction de ce dernier avec la plasticité représente un défi supplémentaire pour les scientifiques à la fois en expérimentation et en modélisation numérique. L'extension récente des techniques de corrélation d'image à la 3D est prometteuse car les mécanismes de localisation plastique peuvent maintenant être mesurés localement. Ces résultats suggèrent que dans certains matériaux la plasticité se développe de manière significative avant toute coalescence de cavité.

La modélisation de phénomènes multiéchelles requiert une théorie mathématique multi-échelles. L'application analytique de la théorie de l'homogénéisation à la rupture ductile représente une des pistes les plus prometteuses dans l'objectif d'obtenir des critères de plasticité et d'endommagement inspirés de l'échelle microscopique, mais s'appliquant à l'échelle macroscopique. La revue bibliographique conduite dans ce chapitre à propos de ces calculs analytiques se restreint au modèle de Gurson, qui ne prend en compte que la croissance de cavités. Les aspects germination et coalescence sont abordés de manière plus détaillée dans les chapitres 4 et 5.

Le modèle de Gurson et ses extensions sont basés sur des hypothèses très contraignantes en ce qui concerne la microstructure des matériaux considérés, les lois constitutives utilisées à l'échelle microscopique, et les conditions de chargement. Afin de quantifier les erreurs produites par ces modèles, et contribuer à leur amélioration, les approches multiéchelles numériques sont d'un

grand intérêt.

Ces approches numériques empruntent la même théorie multiéchelles que celle utilisée pour l'homogénéisation analytique. La différence principale réside dans le fait que la solution du problème d'homogénéisation est calculée numériquement, le plus souvent en utilisant la méthode des éléments finis, qui consiste à représenter toutes les inconnues à l'aide d'un maillage et de variables discrètes portées par les nœuds de ce maillage. Ainsi, on peut s'atteler à la modélisation de microstructures complexes, avec des lois constitutives avancées à l'échelle microscopique, et des conditions de chargements arbitraires.

Cependant, la plupart des analyses éléments finis existantes dans la littérature se restreignent à des microstructures idéales. Les volumes élémentaires représentatifs utilisés ne contiennent en général qu'un seul vide, avec des conditions aux limites périodiques. Certaines études ont également considéré les inclusions, mais les mécanismes de germination sont souvent idéalisés, notamment en faisant l'hypothèse d'une décohésion initiale ou d'une inclusion pré-fragmentée. En effet, des méthodes numériques et modèles micromécaniques avancés restent à développer pour la prise en compte d'inclusions de formes, tailles et distributions arbitraires, et des mécanismes de germination, croissance et coalescence complexes engendrés par de telles microstructures, pour de large déformations plastiques. Le développement de telles méthodes fait partie des défis à relever dans cette thèse, ce qui est abordé dans les chapitres suivants.

Introduction

This literature review is split into two main parts. The first one addresses ductile fracture as a physical phenomenon that calls for advanced experimental means. Thanks to the latter, the voids nucleation, growth and coalescence mechanisms can be observed in two dimensions (2D) and three dimensions (3D) in various loading configurations. In the second part, the modeling of these mechanisms is considered. As proposed in the fundamental works of McClintock [25] and Rice & Tracey [26], ductile fracture calls for micromechanical modeling, because the influence of macroscopic loading conditions on the microstructure has to be studied. Mathematically sound principles have to be introduced in order to make this transition from macro to micro. Additionally, in the work of Gurson [33], this mathematical reasoning was elaborated further in order to also include an influence of the microstructure on the macroscopic behavior. These different steps are described herein, including a review of previous works at the Center for Material forming - MINES ParisTech (Cemef - MINES ParisTech).

1.1 Experimental methods

In this section, the void nucleation, growth, and coalescence mechanisms are described based on experimental observations. In particular, a focus is made on the physical phenomena that lead to these damage events under various loading conditions, while their modeling is addressed in Chapter 4 and Chapter 5.

As ductile fracture is still an open research topic, many questions are raised in this section and multiple assumptions are proposed to explain the different phenomena. Thanks to the numerical modeling tools and the experimental-numerical framework proposed in this work, the validity of these assumptions can be studied for various conditions.

1.1.1 X-ray imaging

Since the ultimate objective of the present work is comparison with experiments in 3D at the scale of a Region Of Interest (ROI) containing up to hundred inclusions and voids, it is important to discuss the experimental means that permit the acquisition of 3D data. Although the present work focuses solely on numerical modeling, a 3D description of the materials microstructures is required to start calculations, and voids have to be observed during loading to compare with experiments.

Most techniques used in recent experimental studies on ductile fracture are based on X-ray imaging. As used for example in medicine, an X-ray Computed Tomography (CT) scan consists in an X-ray source and X-ray sensors placed around an object (which is a part of the human body in medicine) that needs to be scanned [9, 17, 19, 20, 21]. Since X-ray absorption is different depending on the materials, the attenuation of the X-ray beam between the source and the sensors will vary spatially, and the resulting 2D X-ray image will show this contrast. By rotating either the object or the source and the sensors, multiple scans can be acquired. These multiple 2D radiographs can be used to reconstruct a 3D view of the object, using a filtered back projection algorithm [62].

Due to a significant X-ray absorption of some metallic materials, even using very high energy beams, and the very small size of the features to observe (microscopic voids), even using high resolution sensors, only small regions of $\approx 1 \text{ mm}^3$ can be observed. Since the beam has to go through all sections of the specimen in order to obtain projections during a whole rotation, the thickness of the samples is also limited. Therefore, tomography is typically applied to round tensile samples of radius up to $\approx 1 \text{ mm}$ in the region crossed by X-rays, as illustrated in Figure 1.1(a). In fact, these very high energy X-ray beams can only be obtained thanks to specific X-ray sources such as synchrotron radiation, which are difficult and expensive to access.

Even using Synchrotron Radiation Computed Tomography (SRCT), the restriction of round samples is quite limiting. An alternative, known as Synchrotron Radiation Computed Laminography (SRCL), has been proposed in order to overcome this limitation. Small sections are still required, but only in one direction, hence enabling the use of flat specimens, that are interesting in ductile fracture experiments as localization events at multiple scales are studied [16, 22, 63, 64, 65]. The use of these flat specimens is possible because the rotation of the material is no more done around the tensile direction, as illustrated in Figure 1.1(b).

Apart from the developments of these imaging technologies, an important difficulty raised by ductile fracture is the reproducibility of experiments. Since only a small region is observed, the failure of this region will be significantly influenced by the local microstructure, and results such

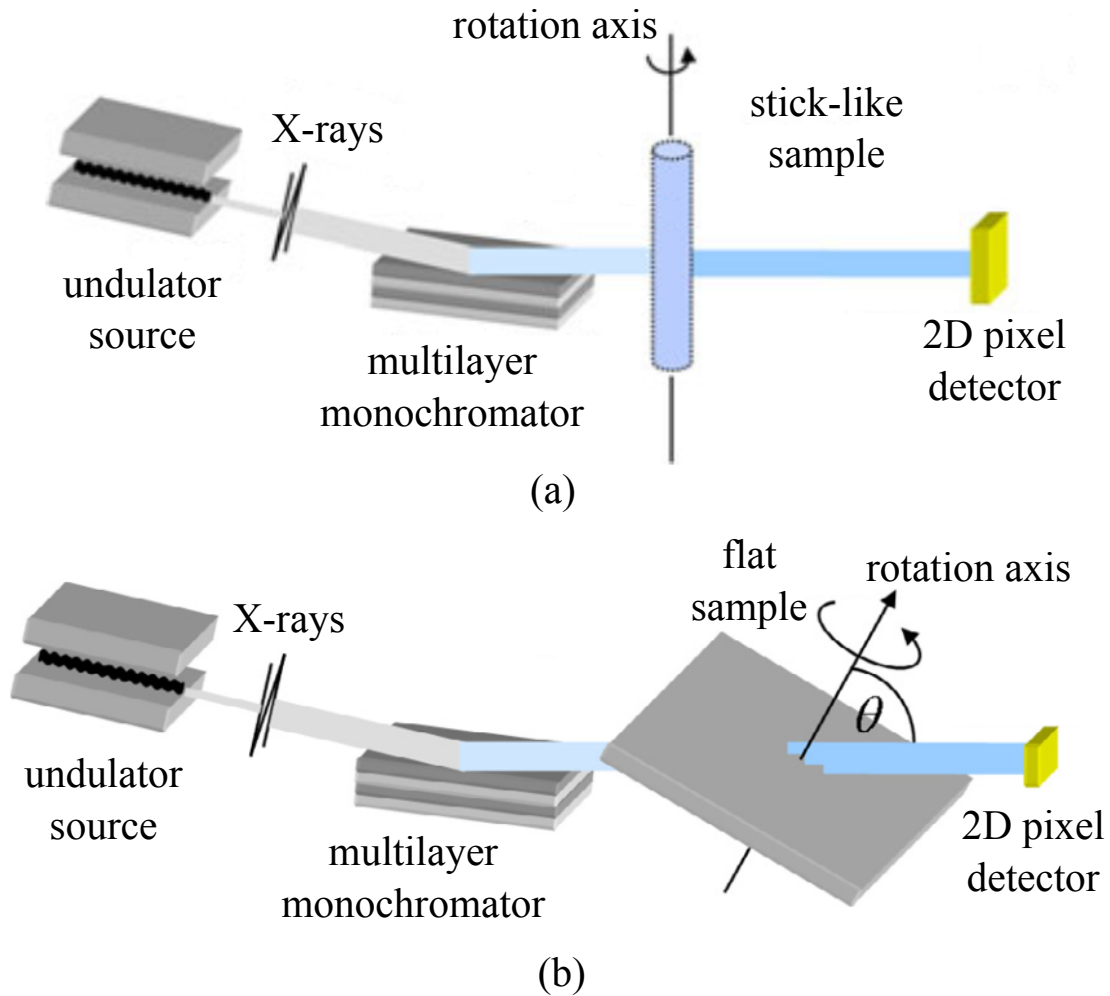


Figure 1.1 – Schematic drawing of: (a) a typical Synchrotron Radiation Computed Tomography (SRCT) setup, (b) a typical Synchrotron Radiation Computed Laminography (SRCL) setup, $\theta \approx 60^\circ$. Figures reproduced respectively from [63] and [22].

as crack propagation patterns will vary from one experiment to another. In order to understand the progressive damage and failure phenomena that will occur, it is important to observe them at different loading steps, for the same microstructure. This challenge has led to the development of *in situ* experimental procedures that rely on advanced loading machines [17, 19, 20, 22]. In the case of tomography and laminography experiments, the main difficulty in the development of these machines is that they will be placed on a rotating stage, hence limiting their size and weight.

Results obtained during *in situ* tensile experiments and using X-ray imaging procedures on various materials are presented in Figure 1.2. The microstructure is clearly distinguishable, together with the subsequent void nucleation, growth and coalescence mechanisms. The influence of each material's X-ray absorption properties on the contrast of the final image also appears in this figure. For instance, the distinction between the void phase and the particle fragments in Figure 1.2(b) is not obvious. This issue is problematic for some materials, which therefore cannot be studied with these X-ray techniques.

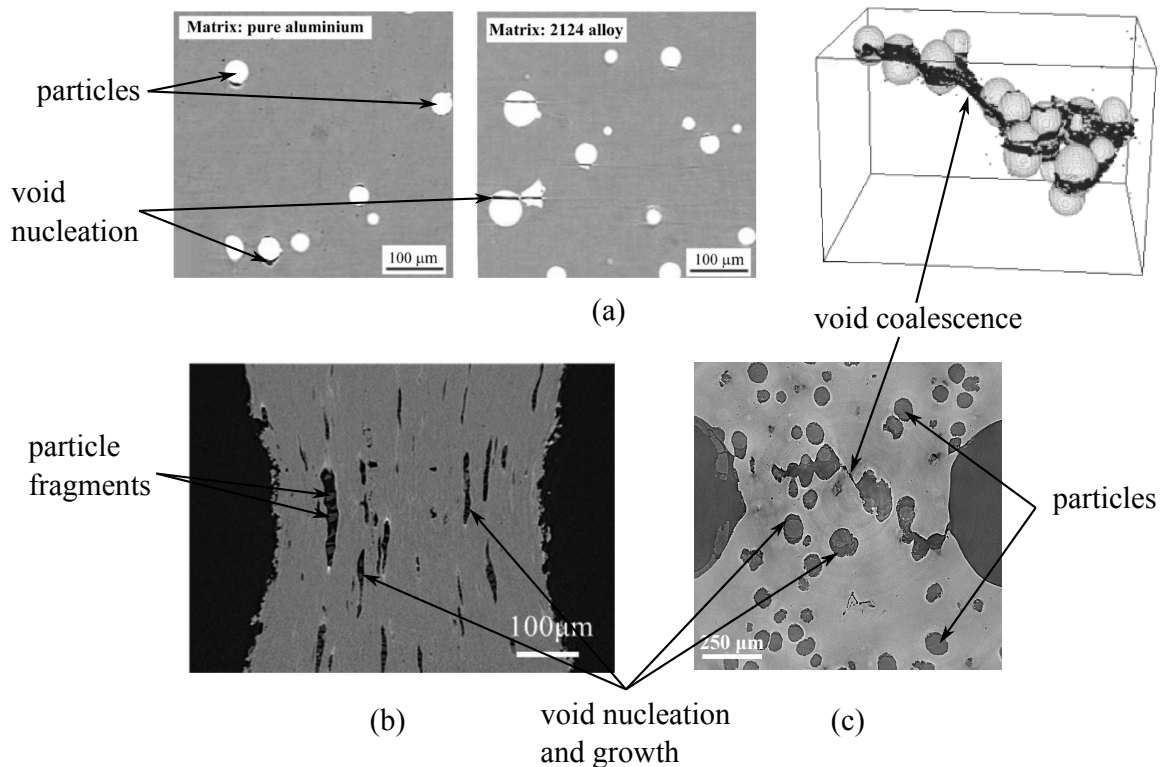


Figure 1.2 – X-ray images: (a) Computed Tomography (CT) images of aluminum alloys reinforced with zirconia/silica (ZrO_2/SiO_2) particles, figures reproduced from [66], (b) CT image of a steel sample containing manganese sulfide (MnS) particles, figure reproduced from [67], (c) Computed Laminography (CL) image of nodular cast iron, courtesy of T. F. Morgeneyer.

1.1.2 Void nucleation

In the following, experimental results obtained using the techniques described in the preceding section are presented, with a focus on void nucleation. As stated in the introduction of this manuscript, the microstructure of metal alloys is composed of a matrix, which is the main component of the alloy, particles, that are the different components of the alloy, and voids, that are the physical sign of damage. Void nucleation occurs either by particle fragmentation or particles/matrix interfaces debonding [21, 37, 68, 69, 70, 71].

In Figure 1.3, Scanning Electron Microscopy (SEM) images featuring both void nucleation modes are shown. These pictures correspond to an aluminum alloy reinforced with aluminum oxide (Al_2O_3) and silicon carbide (SiC) particles [72], meaning that particles can be of different compositions. Additionally, it is clear from the SEM images that particles can also be of different sizes, shapes, and arrangements. These properties of the microstructure have a large influence on void nucleation, that has been studied in the literature. Other external conditions, such as temperature and loading type have also been studied.

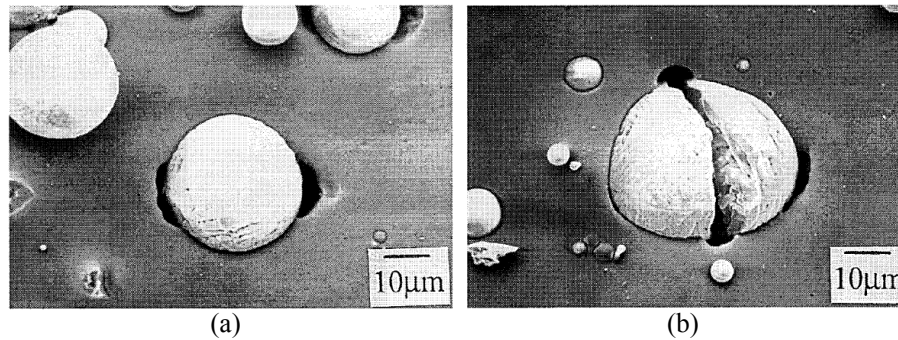


Figure 1.3 – SEM images of: (a) particle/matrix interface decohesion, (b) particle fragmentation. Loading was tension in the horizontal direction. Figures reproduced from [72].

1.1.2.1 Loading direction / particles orientation

Based on [73, 74], it is clear that under tensile loading particles elongated along the loading direction tend to break whereas interface debonding is favored for particles elongated in the transverse direction. However, there is no such conclusion for intermediate orientations or complex loading paths. Though experiments on randomly oriented particles have already been carried out [70, 71, 75, 76], there is a lack in Finite Element (FE) modeling of these situations and comparisons with experiments.

1.1.2.2 Particles size and shape

The effect of particle size was observed in some studies [74, 77, 78]. It appears that bigger particles tend to break earlier during loading than smaller ones. This can be explained statistically as bigger particles contain more defects. Shape is related to the effect of particle orientation that has already been described. Furthermore, it has been observed that the most elongated particles are more prone to breaking than spherical ones [74, 78, 79]. This is also called the aspect ratio effect.

1.1.2.3 Temperature

The influence of temperature was first observed in Reference [73]. A more precise study was made in Reference [80] by *in situ* observation of void nucleation in a metal matrix composite containing titanium carbide (TiC) inclusions. The experiments at different temperatures showed that interface decohesion is the major mode of void nucleation at higher temperatures ($> 800^\circ\text{C}$ for the considered material) whereas particle fragmentation is observed at lower temperatures. Similar discussions can be found in Reference [70].

1.1.2.4 Matrix/particles properties mismatch

The strong dependence between void nucleation modes and mechanical properties of both phases (particle and matrix) has been mentioned above. In the case of an elastic-plastic matrix containing elastic inclusions, the effect of matrix hardness has been studied by some authors [21, 68, 78, 79]. A qualitative conclusion is that a harder matrix favors particle fragmentation, while a harder particle favors decohesion. The same conclusion was raised in Reference [81] for elastic inclusions in an elastic matrix.

1.1.2.5 Particles volume fraction and distribution

This effect is somehow related to the effect of properties mismatch. Indeed, it is clear that if the matrix contains more reinforcement, it can be modeled as a harder material when considering an isolated particle. Then, the conclusion that a harder matrix favors particle fracture can be applied [71, 78].

However, literature also mentions other effects, as the effect of stress relaxation caused by void nucleation [69, 74]. In recent studies [75, 76], it has been observed by means of SEM imaging of an aluminum alloy matrix containing SiC inclusions that void nucleation by particle fragmentation or interface debonding favors void nucleation in neighboring reinforcements. This effect was also studied in Reference [69].

1.1.3 Void growth and coalescence

While void nucleation is clearly defined as it occurs in two precise modes of fragmentation and debonding, it is less obvious to distinguish the different modes of void growth and coalescence. First, void growth is characterized by the fact that the void does not interact with any neighboring voids. In particular, in the absence of coalescence, there is no acceleration or deformation of the free surface that could indicate the presence of a neighboring void. On the contrary, void coalescence is characterized by an acceleration of void growth, and in particular the accelerated growth of a singularity on the free surface. This distinction is illustrated in Figure 1.4 for cylindrical voids under tension or shear. The shape of the voids at the onset of void coalescence may vary because the latter does not generally occur at the same instant in all materials. For instance, the rotation of the voids may be more or less significant before void coalescence occurs in the shear case in Figure 1.4(b). The distinction between void coalescence under tension and shear, including the 3D aspects, are detailed in the following.

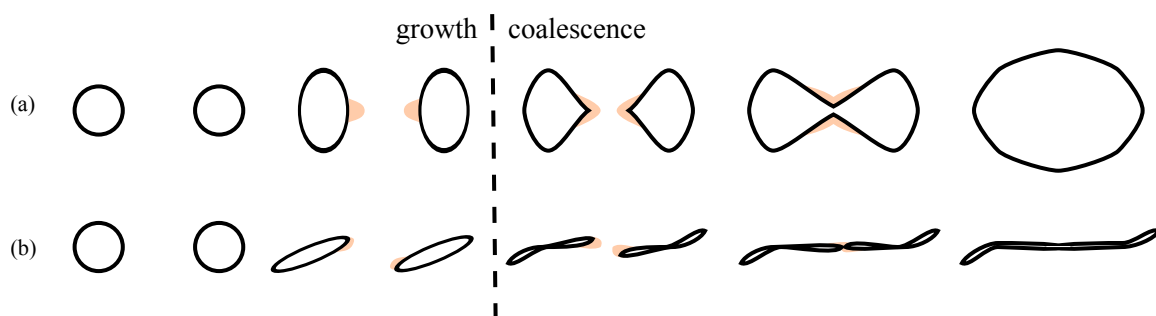


Figure 1.4 – Schematic drawing of the distinction between void growth and coalescence for two cylindrical voids under: (a) tension, (b) shear.

The main challenges regarding void coalescence modeling are the prediction of the singularity on the free surface and its location depending on void arrangements and loading type. In the case of complex loading paths, loading history is also an important factor.

From an experimental point of view, voids are generally randomly distributed and hence difficult to observe [22, 66, 82]. In Reference [83], the authors have proposed to manually insert holes in test materials (an aluminum alloy, a copper alloy, and pure copper) by means of laser drilling. Based on this technique, 2D experiments were carried out with two or more holes, where hole spacing and positioning could be controlled, and void growth and coalescence were observed using SEM [83]. This procedure was also extended to 3D experiments [84], using CT observations [10, 17, 85, 86]. These results have shown that there are at least two distinct void coalescence mechanisms under tensile loading, depending on hole arrangements. When the holes are aligned perpendicular to the tensile direction, voids grow towards a diamond shape, with a significant necking of intervoid ligaments, until final failure of these ligaments. As shown in Figure 1.5, this effect is observed both in 2D and 3D.

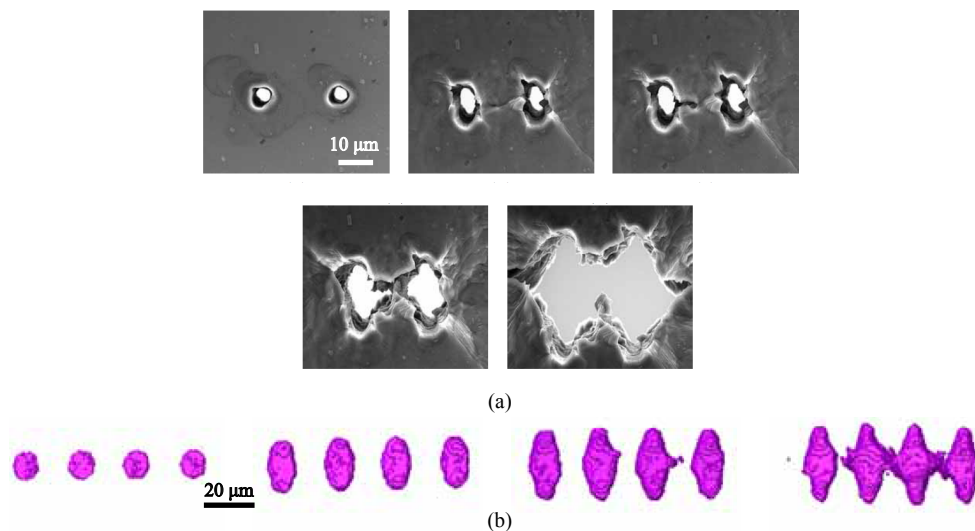


Figure 1.5 – Experimental observation of void coalescence by intervoid ligament necking: (a) SEM images of a 2D test using an aluminum alloy, (b) CT reconstruction of a 3D test using a copper alloy. Figures reproduced from [87].

When the holes are aligned at 45° with respect to the tensile direction, a localization mechanism takes place between neighboring holes aligned in bands at 45° . This localization in shear bands leads to failure along these bands. Another main aspect of this shear coalescence mechanism is that if coalescence occurs at sufficiently large plastic strain, especially if the void spacing is large, the voids rotate and flatten in the direction of the shear band. This mechanism is specific to shear-dominated loading, and raises the issue of modeling a major change in void morphology, with no significant change in void volume. As shown in Figure 1.6, shear-band coalescence is observed both in 2D and 3D, but the flattening of the voids can be more or less pronounced, and the amount of growth the voids undergo before coalescing also varies.

Due to these two mechanisms of intervoid ligament necking and shear-band coalescence, voids rarely coalesce along the tensile direction. However, this mechanism does exist, especially if voids are very elongated along the tensile direction (for example if voids nucleated around particles that were already very elongated in that direction). This mechanism, known as voids

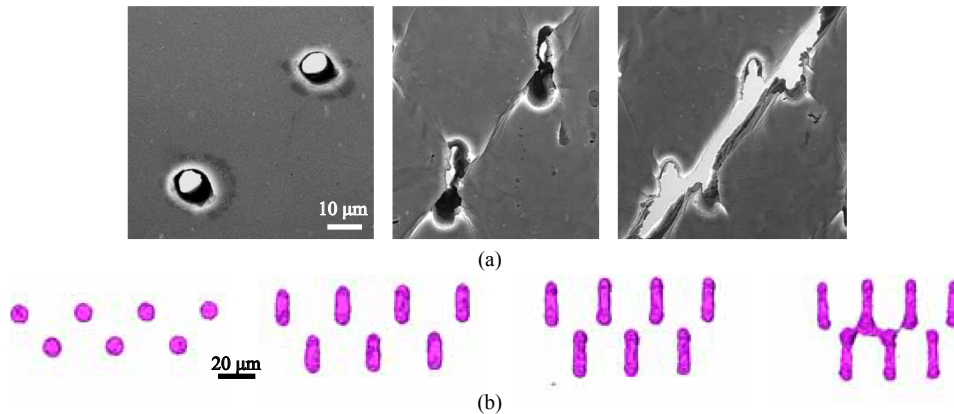


Figure 1.6 – Experimental observation of void coalescence by strain localization in shear bands: (a) SEM images of a 2D test using an aluminum alloy, (b) CT reconstruction of a 3D test using a copper alloy. Figures reproduced from [87].

collapse, or necklace coalescence [37, 88], is illustrated in Figure 1.7. Because this mechanism is linked to pre-existing anisotropy of the microstructure in the initial material, it has been often disregarded for void coalescence modeling.

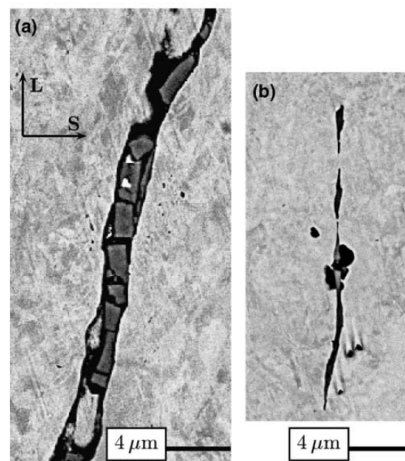


Figure 1.7 – Experimental observation of necklace coalescence during tensile tests (in the vertical direction) on a steel alloy. Figures reproduced from [88].

Recent works on void coalescence modeling focused on modeling void coalescence by intervoid ligament necking and shear-band coalescence in the presence of plasticity, hardening, and general loading conditions. A physical interpretation of these phenomena is that plasticity localizes at least at two scales. The first scale leads to plastic localization bands that include totally multiple voids, while the second scale is finer and leads to plastic localization bands between voids. This second category includes plastic localization due to necking or shear between neighboring voids [38, 89].

Going further with this interpretation, damage could also occur concurrently at these two scales. The first population of voids would be totally included in the first category of localization bands, while the second category of voids would be totally included in the second category of bands. This second void population would hence be of submicron size for typical metal alloys. The presence of these smaller voids would mean that intervoid ligament necking and shear-band coalescence would not only be explained by plasticity, but also damage at a lower scale. An attempt to classify these different ductile fracture modes is shown in Figure 1.8.

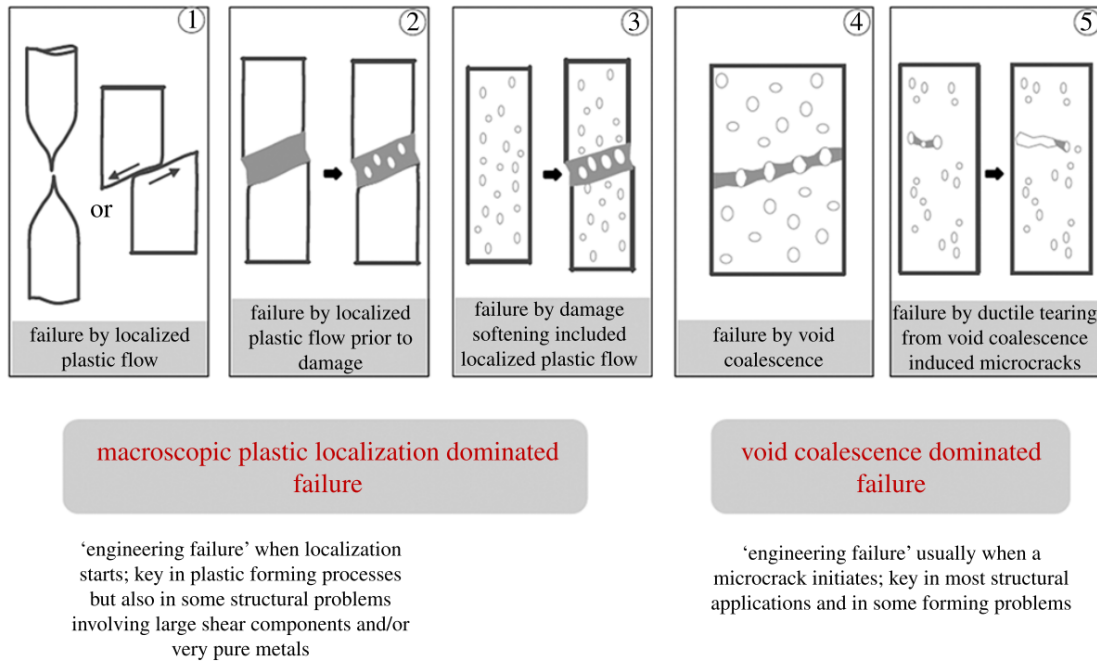


Figure 1.8 – Classification of ductile fracture modes depending on the balance between plasticity and damage at multiple scales. Figure reproduced from [89].

To prove or discard these theories, yet more advanced experimental means are necessary. As explained above, recent X-ray imaging techniques typically have a resolution of the micrometer. In order to validate the presence of submicron sized voids, it would be necessary to apply nanotomography or nanolaminography techniques to ductile fracture experiments. An additional difficulty would be to simultaneously quantify plasticity together with damage [22].

1.1.4 Digital Volume Correlation

An interesting aspect offered by *in situ* experiments is that 3D images of the same microstructure at consecutive loading steps are available. While most authors rely only on averaged information, such as the total porosity over each image [1, 20, 21, 64], the possibility of considering inclusions and voids individually based on manual [64] or automatic [20] procedures is now being considered. The purpose of this approach is to study the participation of isolated voids in the coalescence and failure process.

While these techniques are based on geometrical information, such as the volume of each void and its change, a more global approach is offered by Digital Volume Correlation (DVC). This technique is the 3D extension of Digital Image Correlation (DIC). The latter is now available in multiple commercial codes and is used extensively to identify material properties, especially

when damage models are involved [90, 91, 92].

DIC relies solely on 2D images of the surface of the specimen, where contrast is usually enhanced by speckling the specimen. Consecutive images are compared and a least-squares problem is solved, where the variable is the 2D displacement field \mathbf{u} to go from the first image to the second one, and the objective function to minimize is the gray level residual. This residual is defined as the difference between the first image deformed by the given displacement field $g(\mathbf{x} + \mathbf{u}(\mathbf{x}))$, and reference image $f(\mathbf{x})$. It is coined gray level residual because the colors of the two images are directly subtracted and summed on the whole domain.

In most cases, this problem is ill-defined. For instance, if the speckle is too coarse with respect to the mesh used to discretize the displacement field, the contrast may be insufficient and poor compared to the number of unknowns to determine. This problem is drastically increased in DVC [93, 94, 95, 96], as it is impossible to speckle inside the specimen. The method hence relies directly on the microstructure in order to obtain contrast. It can work only for materials with a significant density of particles and voids, and the mesh used to discretize the 3D displacement field will generally be of size comparable to that of these features [65, 97, 98, 99]. Additionally, the space of possible solutions can be reduced by adding continuity and mechanical admissibility constraints [100].

The important aspects are that DVC yields 3D displacement fields between consecutive 3D X-ray images, and that the resolution of these displacement fields is usually limited because the formulation on which DVC is constructed is ill-defined in the absence of contrast. As mentioned above, regularization methods have been proposed in order to help the solution of this problem, by adding constraints to restrict the solution space, these constraints generally being progressively relaxed during the solution [100, 101]. Additionally, while the accuracy of a DVC result can be assessed by studying gray level residuals, the residuals themselves rely on the presence of contrast.

With the obtained displacement fields, the formation of strain localization patterns can be studied [22, 63]. These surprising results show that the correlation between plasticity and damage may be more complex than what is usually assumed in the literature, and that ductile fracture may be ruled mostly by plasticity for some materials, with negligible void growth [22, 89].

1.2 Theoretical and numerical methods

Theoretically, a material's mechanical response at the microscale could be studied using Direct Numerical Simulation (DNS). This would mean meshing the microstructure of the whole material, and then applying macroscopic boundary conditions directly on this mesh. It seems obvious that such an approach would have a huge cost and could be applicable only in the case of very small specimens. Hence, for larger specimens and industrial applications, researchers have studied methods where micromechanics could be taken into account, without the huge computational cost of DNS. These methods are based on the so-called homogenization theory, that is detailed in this section, with an emphasis on its application to ductile fracture.

Added to the macroscopic domain, which is the industrial piece or ingot that is being studied, homogenization theory introduces a microscopic domain, through a Representative Volume Element (RVE). While the macroscopic domain is considered homogeneous, the RVE takes into account explicitly the microstructure of the material. Most numerical studies address RVEs containing only voids [102, 103, 104, 105, 106, 107], but computational approaches taking into account the particles, their load-carrying capacity, and the subsequent void nucleation events can also be found in the literature [108, 109, 110, 111, 112]. The strain and stress fields in the macroscopic domain vary depending on loading and geometric conditions, but these variations are small when considered at the scale of the RVE. Therefore, some macroscopic mechanical variables can be approximated by a Taylor expansion (a polynomial) at the scale of the RVE. This assumption is called scale-separability, and its validity depends on the ratio between the characteristic length ℓ_M of the macroscopic domain, and the size ℓ_{RVE} of the RVE.

An added difficulty is that the RVE has to be representative of the real microstructure of the material. It has to be large enough so that any mechanical variable averaged on the RVE does not depend on the choice of RVE. This means that RVE size will be larger than the average size of an inclusion or a void ℓ_m . As a conclusion, RVE size has to be large enough to enable a sufficient number of realizations of the microstructure and void nucleation, growth and coalescence events, but small compared to the structure

$$\ell_M \gg \ell_{RVE} \gg \ell_m. \quad (1.1)$$

In most metal forming applications, ℓ_M is of the order of the millimeter, while ℓ_m is of the order of the micrometer. For small pieces and especially for the small specimens used in tomography, scale-separability is questionable since the millimeter is the size of the structure.

Once these characteristic lengths have been defined, numerous possibilities are still open. Homogenization theory has led to a wide range of so-called homogenization schemes that all allow for analytical or numerical solution. While all these schemes rely on similar mathematical principles, the validity of these principles depends on scale-separability, and the choice of boundary conditions. For a detailed review of all these schemes, the reader is referred to [112]. In the following, the FE code developed at Cemef - MINES ParisTech is described to understand how continuum mechanics equations are formulated and numerically solved. Then, some classical homogenization schemes are presented.

1.2.1 Finite Element scheme

In this part, the FE library developed at Cemef - MINES ParisTech is described in the case of an homogeneous material. This code is the result of numerous works on the FE method and its

application to continuum mechanics for solid materials undergoing plastic flow [23, 32, 113, 114, 115] and then Newtonian and non-Newtonian fluids [116, 117, 118].

1.2.1.1 Continuum mechanics

In continuum mechanics, the domain $\Omega \subset \mathbb{R}^d$ ($d = 2, 3$) is a material or structure that moves or deforms due to external forces. When $d = 2$, the continuum mechanics equations will still be written in 3D, but strains will be assumed to remain planar. In the present work, Ω will generally be the RVE. The unknown is hence the displacement u .

The FE code developed at Cemef - MINES ParisTech considers the so-called small deformation theory, which is implemented within an updated Lagrangian formulation. Strains are measured by a linear approximation ε , which is the symmetric part of the displacement gradient

$$\varepsilon = \frac{1}{2} (\nabla u + \nabla^t u).$$

This approximation ε is called strain tensor hereafter (though it is only an approximation of the strain tensor). The relation between this strain tensor and external forces relies on the definition of the Cauchy stress tensor σ , which is defined as the internal forces per unit area induced by the deformation of the material. The balance equation in the static case is given by

$$\nabla \cdot \sigma = 0. \quad (1.2)$$

Defining the hydrostatic pressure $p = -\frac{1}{3} \text{tr}(\sigma)$ and the deviatoric stress tensor $s = \sigma + pI$, where I is the identity matrix in \mathbb{R}^d , this balance equation can be expressed as

$$\nabla \cdot s - \nabla p = 0. \quad (1.3)$$

The link between σ and ε is material dependent, and coined constitutive model, or behavior law. For instance, in the case of isotropic linear elasticity, it is given by Hooke's law

$$\sigma = 2\mu\varepsilon + \lambda \text{tr}(\varepsilon)I, \quad (1.4)$$

where μ and λ are the Lamé coefficients, and are proper to each material. They are linked to Young's modulus E and Poisson's coefficient ν through the relations

$$\mu = \frac{E}{2(1+\nu)}, \lambda = \frac{E\nu}{(1-2\nu)(1+\nu)}, \mathcal{X} = \lambda + \frac{2}{3}\mu,$$

where \mathcal{X} is the bulk modulus. Inserting these relations in Equation (1.4), the latter can be expressed in terms of s and p

$$\begin{cases} s &= 2\mu \left(\varepsilon - \frac{1}{3} \text{tr}(\varepsilon)I \right) \\ p &= -\mathcal{X} \text{tr}(\varepsilon) \end{cases} \quad (1.5)$$

where $\text{tr}(\varepsilon) = \nabla \cdot u$. In the case of small deformation elasto-plasticity, an additive decomposition of the strain tensor into an elastic part ε^{el} and a plastic part ε^{pl} is assumed

$$\varepsilon = \varepsilon^{el} + \varepsilon^{pl}.$$

In the case of incompressible plasticity (non porous plasticity), $\text{tr}(\varepsilon^{pl}) = 0$, which leads to $\text{tr}(\varepsilon) = \text{tr}(\varepsilon^{el})$. The constitutive equations regarding the elastic part are

$$\begin{cases} s &= 2\mu \left(\varepsilon^{el} - \frac{1}{3} \text{tr}(\varepsilon) \right) \\ p &= -\mathcal{X} \text{tr}(\varepsilon) \end{cases} \quad (1.6)$$

while the plastic part depends on the definition of the yield surface $f = f(\sigma, \varepsilon)$. Defining the von Mises equivalent stress $\bar{\sigma}$, the von Mises equivalent plastic strain rate $\dot{\bar{\varepsilon}}^{pl}$, and the von Mises equivalent plastic strain $\bar{\varepsilon}^{pl}$

$$\bar{\sigma} = \sqrt{\frac{3}{2} s : s}, \quad \dot{\bar{\varepsilon}}^{pl} = \sqrt{\frac{2}{3} \dot{\varepsilon}^{pl} : \dot{\varepsilon}^{pl}}, \quad \bar{\varepsilon}^{pl} = \int_0^t \dot{\bar{\varepsilon}}^{pl},$$

the von Mises (or J_2) yield surface is

$$f(\sigma, \varepsilon) = \bar{\sigma} - \sigma_0(\bar{\varepsilon}^{pl}),$$

where $\sigma_0(\bar{\varepsilon}^{pl})$ is the yield stress of the material, which will depend also on $\bar{\varepsilon}^{pl}$ in case of viscoplasticity. The yield surface defines the condition for plasticity, hence three situations can be met:

- purely elastic loading if $f < 0$,
- plastic flow if $f = 0$ and $\frac{\partial f}{\partial \sigma} > 0$,
- elastic unloading if $f = 0$ and $\frac{\partial f}{\partial \sigma} \leq 0$.

When the conditions for plastic flow are met, associative plasticity yields

$$\dot{\varepsilon}^{pl} = \dot{\bar{\varepsilon}}^{pl} \frac{\partial f}{\partial \sigma} = \frac{3}{2} \dot{\bar{\varepsilon}}^{pl} \frac{s}{\sigma_0},$$

where $\dot{\bar{\varepsilon}}^{pl}$ appears as the plastic multiplier. Inserting this last relation into Equation (1.6) requires an objective time-derivative of the deviatoric stress tensor s . The Jaumann rate is implemented in the FE code

$$\overset{\Delta}{s} = \dot{s} + s \cdot \omega - \omega \cdot s, \quad (1.7)$$

where $\omega = \frac{1}{2} (\nabla u - \nabla^t u)$. This objectivity is only applied explicitly, meaning that balance equations are first solved as if $\overset{\Delta}{s} \approx \dot{s}$, and the deviatoric stress tensor is corrected afterwards by using Equation (1.7). Thus, the constitutive equations in the case of elasto-plasticity can be written as

$$\begin{cases} \dot{s} &= 2\mu \left(\dot{\varepsilon} - \frac{3}{2} \dot{\bar{\varepsilon}}^{pl} \frac{s}{\sigma_0} - \frac{1}{3} \text{tr}(\dot{\varepsilon}) \right) \\ \dot{p} &= -\mathcal{X} \text{tr}(\dot{\varepsilon}) \end{cases} \quad (1.8)$$

where both time derivatives \dot{s} and \dot{p} are discretized with an implicit Euler scheme. The balance equations can then be formulated as

$$\begin{cases} \nabla \cdot s(\dot{\varepsilon}(v)) - \nabla p &= 0 \\ \dot{p} + \mathcal{X} \text{tr}(\dot{\varepsilon}(v)) &= 0 \end{cases} \quad (1.9)$$

where s is given by a nonlinear relation in terms of $\dot{\varepsilon}$ in Equation (1.8), which is itself a linear function of v .

1.2.1.2 First order Lagrange Finite Element method

The FE method, as described for example in Reference [119] or Reference [120], consists in a discretization of unknown or known functions thanks to polynomial interpolation. With standard Lagrange FE basis functions, the function ends up being uniquely represented by its values at some particular locations. These locations, together with the basis functions, are carried by an FE mesh.

Although the latter can be quite complex in a general FE setting, the FE code developed at Cemef - MINES ParisTech relies solely on unstructured linear simplex meshes. A linear simplex is a triangle in 2D, and a tetrahedron in 3D. The vertices of these simplexes are called nodes of the mesh, while the simplexes themselves are called elements of the mesh.

For the mesh to be conform (*i.e.*, compatible with the Lagrange FE method), the intersection of any pair of elements (*i.e.*, simplexes) must be a common node, edge or face to both elements. If such mesh is built so as to cover the whole domain Ω , any continuous function such as the pressure p can be approximated by its values at mesh nodes, and its value at any point of the domain can be obtained by linear interpolation

$$p(\mathbf{x}) \approx p_h(\mathbf{x}) = \sum_{i \in \text{nodes}} p_i N_i(\mathbf{x}), \mathbf{x} \in \Omega. \quad (1.10)$$

The interpolation is linear because the basis functions N_i are linear. If the function is regular enough ($p \in H^1(\Omega)$), its derivatives can also be approximated, simply by using the derivatives of the basis functions

$$\nabla p(\mathbf{x}) \approx \nabla_h p_h(\mathbf{x}) = \sum_{i \in \text{nodes}} p_i \nabla N_i(\mathbf{x}), \mathbf{x} \in \Omega. \quad (1.11)$$

While p_h is continuous, the derivatives $\nabla_h p_h$ are discontinuous across element boundaries. The basis functions and their derivatives are known and implemented in the FE code for a reference element (a triangle or tetrahedron aligned with the Cartesian frame), and they are computed on each element of the mesh through a linear mapping (this mapping being linear because the simplexes are linear). In case of vectors such as the velocity v , the interpolation can be defined component-wise, and the same principles apply.

This interpolation technique is already very interesting for many scientific and computer graphics applications where complex functions have to be approximated at random points. However, the FE method shows its full potential when applied to the numerical solution of partial differential equations.

1.2.1.3 Mixed Finite Element method

In the case described in Equation (1.9), the functions v and p are unknown, but they can still be approximated directly in the partial differential equation by the approximations v_h and p_h . Then, instead of being functions, the unknowns are vectors composed of the unknown values at mesh nodes. This transition from continuous variables and equations to their discrete versions relies on a weak form of the balance equations

$$\begin{cases} \int_{\Omega} s(v) : \dot{\varepsilon}(w) - \int_{\Omega} p \operatorname{div} w = \int_{\partial\Omega} w \cdot (\sigma n), \forall w \in \mathcal{V}, \\ - \int_{\Omega} q \operatorname{div}(v) - \int_{\Omega} \frac{\dot{p}}{\chi} q = 0, \forall q \in \mathcal{P}. \end{cases} \quad (1.12)$$

This weak form, coined mixed form due to the presence of two unknowns v and p , is obtained by "testing" the strong form of the balance equations given in Equation (1.9) with test functions

w and q , and integrating on Ω . Integration by parts can then be applied, which introduces the outgoing normal vector n to the boundary of the domain $\partial\Omega$. The solutions v and p are assumed to belong respectively to $\mathcal{V} = H^1(\Omega)^d$ and $\mathcal{P} = H^1(\Omega)$.

The variables and integrals in Equation (1.12) are approximated in discrete spaces \mathcal{V}_h and \mathcal{P}_h so that a discrete weak form is obtained. An important restriction is that the choice of \mathcal{V}_h and \mathcal{P}_h is not open, as the discrete weak formulation is well-defined only for some adequate choices [121]. In particular, locking issues arise when the material is incompressible.

The FE code implements the so-called $P1^+$ element, also called MINI element, or bubble element. Each component of the velocity is approximated in this discrete space, while the pressure is approximated in a standard P1 space, which is the space spanned by simplex-wise linear basis functions. There are 3 basis functions per element in 2D, and 4 in 3D. Each of them is equal to one at one of the nodes of the simplex, and zero at the others. The $P1^+$ space is obtained by adding a basis function (and an additional unknown) at the center of each simplex. This basis function is equal to one at the center of the simplex, and zero on its boundary. The additional unknown is eliminated by a static condensation process, therefore no additional unknown is actually introduced in the formulation.

Once the domain Ω , the normal vector n , the continuous spaces \mathcal{V} and \mathcal{P} , and the unknowns v and p have been replaced by their approximations, the discrete weak mixed formulation is obtained

$$\left\{ \begin{array}{l} \int_{\Omega_h} s_h(v_h) : \dot{\varepsilon}(w_h) - \int_{\Omega_h} p_h \operatorname{div} w_h = \int_{\partial\Omega_h} w_h \cdot (\sigma_h n_h), \forall w_h \in \mathcal{V}_h, \\ - \int_{\Omega_h} q_h \operatorname{div}(v_h) - \int_{\Omega_h} \frac{\dot{p}_h}{\mathcal{X}} q_h = 0, \forall q_h \in \mathcal{P}_h. \end{array} \right. \quad (1.13)$$

This system is nonlinear due to a nonlinearity in the expression s_h in Equation (1.8). The Newton-Raphson procedure used to solve this nonlinearity relies on a first order approximation of this term. Given a current approximation of the velocity field v_h^0 , a better approximation $v_h = v_h^0 + \delta v_h$ is obtained by solving the following equations

$$\left\{ \begin{array}{l} \int_{\Omega_h} \left(\frac{\partial s_h}{\partial v_h}(v_h^0) : \dot{\varepsilon}(v_h) \right) : \dot{\varepsilon}(w_h) \\ \quad - \int_{\Omega_h} p_h \operatorname{div} w_h = \int_{\Omega_h} \left(\frac{\partial s_h}{\partial v_h}(v_h^0) : \varepsilon(v_h^0) \right) : \dot{\varepsilon}(w_h) \\ \quad - \int_{\Omega_h} s_h(v_h^0) : \dot{\varepsilon}(w_h) \\ \quad + \int_{\partial\Omega_h} w_h \cdot (\sigma_h n_h), \forall w_h \in \mathcal{V}_h, \\ - \int_{\Omega_h} q_h \operatorname{div}(v_h) - \int_{\Omega_h} \frac{\dot{p}_h}{\mathcal{X}} q_h = 0, \forall q_h \in \mathcal{P}_h. \end{array} \right. \quad (1.14)$$

where the nonlinear term has been approximated by $s_h(v_h) \approx s_h(v_h^0) + \frac{\partial s_h}{\partial v_h}(v_h^0) : \dot{\varepsilon}(\delta v_h)$. Replacing v_h and p_h in Equation (1.14) with their expressions based on Equation (1.10) and Equation (1.11) (with bubble basis functions for v_h), and applying numerical quadrature rules to evaluate the integrals, a nonlinear system in terms of discrete variables is obtained. More information on the $P1^+/P1$ and the static condensation process implemented in the FE code can be found in previous publications [122, 123]. These publications also detail the solution of the nonlinear velocity-pressure system thanks to a Newton-Raphson procedure at the global level and also at the local (element) level for the return mapping of an elastic trial stress onto the plastic yield surface [124].

1.2.1.4 Parallel computing

An important aspect of the FE code developed at Cemef - MINES ParisTech is that it is implemented in a distributed computing context [125]. This means that the mesh of the domain is divided into multiple partitions, each distributed to a different process. The processes are likely to be executed on different machines and therefore a process can access information known by another process only through network communications.

The partitioning of the mesh is done element-wise first, meaning that each element of the mesh is agglomerated into distinct partitions. Each process knows the connectivity of its elements, and all variables stored in these elements. Regarding the nodes, each process knows the coordinates of all the nodes of its elements, and also of all variables stored at these nodes. However, if a node is shared by multiple processes, it is associated to only one of them, and cannot be modified by the others.

This partitioning strategy is illustrated in Figure 1.9. In this example, the colors for the two nodes at the extremities are determined directly by the coloring of the elements, while the nodes on the edge shared by the two triangles could have been arbitrarily colored in green or orange by the partitioning algorithm. Though only green can modify the value stored on the green node of this edge, orange can read data from this node. The same remark applies for the orange node of this edge.

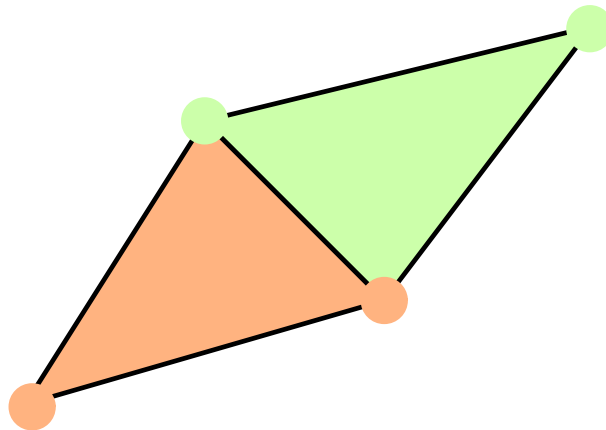


Figure 1.9 – Example of partitioning of a 2D mesh containing two triangles. The two partitions both in terms of elements and nodes are distinguished in orange and green.

The FE code implements some functions in order to define new operations element-wise or node-wise, and computes quantities such as derivatives element-wise. Note that with linear elements and linear FE fields, there is only one quadrature point per element. Other operations enable to sum values from all nodes or elements to a scalar variable, or to sum values to a node from its neighboring elements. These operations can be a sum but also a minimum or maximum computation.

Other operations must be implemented carefully as communications between multiple processes may have to be considered if data located on different partitions have to be accessed. This is systematic for all operations that require to access a node's neighbors, an element's neighbors, and the elements containing a given node.

Regarding FE solvers, all numerical integration, static condensation, nonlinear and linear solution operations are implemented element-wise in the FE code, with no difficulty linked to distributed computing, while global assembly and linear solution and the subsequent network

communications are handled by the PETSc library [126].

Although an FE code allowing only linear simplexes and linear interpolations may be quite restricting, it has the main advantage that all communications can be prepared very efficiently, as the length of each message is fixed. This will be illustrated for example in Section 3.2. However, the implementation of several key algorithms becomes quite complex in a distributed computing context (Section 2.5, Subsection 3.1.3 and Subsection 3.2.2). This remark also applies to the implementation of boundary conditions for homogenization calculations.

1.2.2 Homogenization theory

Once the RVE V has been defined, homogenization theory can be used to study the influence of a forming process on the microstructure, by transferring the macroscopic stress or strain state to the boundaries of the RVE. This technique is referred to as hierarchical approach in the following. However, the homogenization theory can also be used to identify material parameters for a given macroscopic constitutive model based on RVE simulations. Indeed, damage models have a limited applicability to complex and non proportional loading paths, and require a targeted identification for each type of loading. If RVE simulations could be proved to be predictive for multiple types of loading paths, with the same material parameters, one could use RVE simulations to automatically correct a macroscale constitutive model. This second and more advanced utilization of homogenization theory is referred to as concurrent approach in the following.

In the homogenization approach used in previous works [5, 6], the boundary conditions and the definition of the RVE corresponded to an embedded cell approach [127, 128, 129]. In this approach, the RVE is embedded in a larger computational domain ($V \subset \Omega, V \neq \Omega$), and the microscopic material behavior is considered only inside the RVE, while a homogeneous behavior is defined outside. Some limitations were pointed out such as controlling the stress state inside the RVE or defining the homogeneous behavior in the rest of the domain. Additionally, this method led to perturbations and stress concentrations at the transition between the homogeneous material and the RVE. As a consequence, only the core of the RVE could be considered for homogenization, which made difficult the setting of the initial particle volume fraction or void volume fraction inside the RVE.

The definition of the homogeneous constitutive law used in the rest of the domain could be highly helped by extending the hierarchical embedded cell approach to a concurrent approach, thanks to a self-consistent scheme [127, 128]. In this incremental scheme, the macroscale constitutive model used for the out-of-RVE material is first set using an initial guess of material parameters. After solving balance equations, a first guess of the RVE's mechanical response is obtained and averaged in order to be compared to the macroscale constitutive model. Based on this sensitivity analysis, material parameters for the macroscale constitutive model are corrected and the whole process is iterated until convergence. The last step of this incremental scheme contains not only an RVE simulation in a given macroscopic strain or stress state, but also material parameters for the macroscale constitutive model adapted to this strain or stress state.

In the following, other widely used boundary conditions are presented, with a restriction to homogenization methods where the RVE is the whole computational domain ($V = \Omega$), therefore any relevant information such as stress state or void volume fraction can be easily computed. The computational cost is also reduced because compared to an embedded cell approach only

the RVE itself is meshed.

These methods are considered in this work for a hierarchical use, where local stress or strain fields are extracted from a macroscale experimental or numerical experiment and applied on the boundaries of the RVE. This could allow to follow and understand the consequences of mechanical treatments performed by a metal forming process on the microstructure. Concurrent schemes where these microscale simulations are used to correct macroscale constitutive models are not considered yet.

The main focus of the present work is to validate RVE calculations directly at the microscale, and then exploit these simulations in a hierarchical scheme. FE-FE schemes where the macroscale simulation takes into account microscale physics are not considered in this work. These FE-FE schemes have their own challenges, such as a huge computational cost, that has led for instance to the use of model reduction techniques [130, 131, 132]. In the case of ductile fracture, plasticity and damage localization also raise a number of issues that are being addressed for instance using higher-order homogenization schemes [102, 103, 104, 106, 109, 133] and multiscale cohesive zone models [107, 110, 111].

Some of the approaches mentioned in this section are illustrated in Figure 1.10. Green arrows represent macroscopic variables that are transferred from macroscopic experimental measurements or simulations to the RVE. Red arrows represent RVE-averaged variables that can be used directly (FE-FE) in a macroscopic simulation, or indirectly by identifying material parameters for a macroscopic constitutive model.

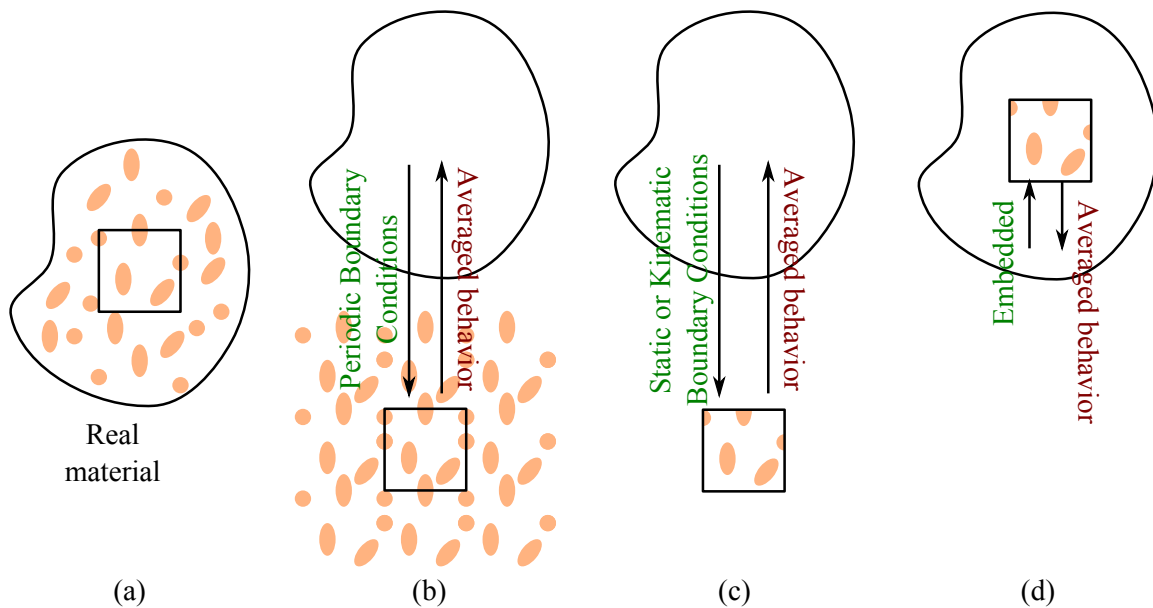


Figure 1.10 – Heterogeneous material (a), and examples of multiscale methods: (b) periodic unit cell, (c) windowing approaches, (d) embedded unit cell. Classification inspired from [112].

In order to describe linear (first order) homogenization theory, some basic definitions are reminded [112, 134, 135]. The mechanical response of the RVE, or unit cell, is split into a slow contribution, which would be the exact response in the absence of heterogeneity, and a fast contribution resulting from the perturbation due to heterogeneity. The volume average of a variable f over the RVE V is defined as

$$\langle f \rangle = \frac{1}{|V|} \int_V f. \quad (1.15)$$

In an embedded cell approach, $V \neq \Omega$, while in the other approaches presented in this section, $V = \Omega$. Two identities obtained using integration by parts have to be reminded regarding the displacement field u and the stress field σ

$$\begin{aligned} \langle \nabla u \rangle &= \frac{1}{|V|} \int_V \nabla u = \frac{1}{|V|} \int_{\partial V} u \otimes n, \\ \langle \sigma \rangle &= \frac{1}{|V|} \int_V \sigma = \frac{1}{|V|} \int_{\partial V} \mathbf{x} \otimes (\sigma \cdot n). \end{aligned} \quad (1.16)$$

where n is the outgoing normal vector. The second identity uses the fact that the mechanical problem to be solved is

$$\nabla \cdot \sigma = 0 \text{ in } V,$$

and hence the stress field is divergence-free. Boundary conditions are yet to be defined to close this problem. The aim of these conditions is to fulfill Hill-Mandel's lemma, which is the fundamental basis of homogenization theory (not satisfied yet)

$$\langle \sigma : \varepsilon \rangle = \frac{1}{|V|} \int_V \sigma : \varepsilon = \frac{1}{|V|} \int_{\partial V} u \cdot (\sigma \cdot n) = \langle \sigma \rangle : \langle \varepsilon \rangle \quad (1.17)$$

where integration by parts has been used once again. Boundary conditions that fulfill the lemma in Equation (1.17) are described in the following. In the case of Taylor-Voigt Boundary Conditions (TVBCs), Kinematic Uniform Boundary Conditions (KUBCs) and Periodic Boundary Conditions (PBCs), loading is strain-controlled, while in the case of Hill-Reuss Boundary Conditions (HRBCs) and Static Uniform Boundary Conditions (SUBCs), it is stress-controlled. Mixed boundary conditions that are often used in the literature [112, 135] are not considered in this work.

1.2.2.1 Taylor-Voigt Boundary Conditions

In the case of strain-controlled boundary conditions, the displacement and strain fields u and ε in the RVE admit the following additive decomposition

$$\begin{aligned} u &= E \cdot \mathbf{x} + u^\# \quad \text{in } V \\ \langle \varepsilon \rangle &= E + \langle \varepsilon(u^\#) \rangle \end{aligned} \quad (1.18)$$

where E is a prescribed homogeneous strain, usually equal to the strain field at a Gauss point of a macroscopic simulation, and $u^\#$ is coined fast part of the displacement field. The particularity of TVBCs is that this fast part $u^\#$ is assumed to be zero on the whole RVE

$$\begin{aligned} u^\# &= 0 \quad \text{in } V, \\ \langle \varepsilon \rangle &= E. \end{aligned}$$

As a consequence, it is easy to prove that the lemma in Equation (1.17) is satisfied

$$\begin{aligned} \langle \sigma : \varepsilon \rangle &= \frac{1}{|V|} \int_{\partial V} u \cdot (\sigma \cdot n) = \frac{1}{|V|} \int_{\partial V} (E \cdot \mathbf{x}) \cdot (\sigma \cdot n) \\ &= E : \left(\frac{1}{|V|} \int_{\partial V} \mathbf{x} \otimes (\sigma \cdot n) \right) = \langle \sigma \rangle : E = \langle \sigma \rangle : \langle \varepsilon \rangle. \end{aligned}$$

1.2.2.2 Kinematic Uniform Boundary Conditions

A less restrictive definition of strain-controlled boundary conditions with the additive decomposition in Equation (1.18) is given by KUBCs, where the fast part of the displacement field is assumed to be zero only on the boundary of the RVE

$$\begin{aligned} u^\# &= 0 \quad \text{on } \partial V, \\ \langle \nabla u^\# \rangle &= \frac{1}{|V|} \int_{\partial V} u^\# \otimes n = 0 \Rightarrow \langle \varepsilon \rangle = E. \end{aligned}$$

The proof of the lemma in (1.17) is identical to the one for TVBCs, because the fast part vanishes at boundaries

$$\langle \sigma : \varepsilon \rangle = \frac{1}{|V|} \int_{\partial V} u \cdot (\sigma \cdot n) = \frac{1}{|V|} \int_{\partial V} (E \cdot \mathbf{x}) \cdot (\sigma \cdot n) + \frac{1}{|V|} \int_{\partial V} u^\# \cdot (\sigma \cdot n) = \langle \sigma \rangle : \langle \varepsilon \rangle.$$

1.2.2.3 Periodic Boundary Conditions

PBCs are also based on the additive decomposition in Equation (1.18), with the restriction that the fast part of the displacement field is assumed to be identical on opposite sides of the RVE, while the normal stress is assumed to be opposite. This implies that the RVE has a particular geometry, which is usually chosen to be a cube or a hexagon [136, 137]. Based on this restriction, the boundary ∂V of the RVE can be split into two sets of faces S_1 and S_2

$$\langle \nabla u^\# \rangle = \frac{1}{|V|} \int_{S_1} u^\# \otimes n + \frac{1}{|V|} \int_{S_2} u^\# \otimes n = 0 \Rightarrow \langle \varepsilon \rangle = E$$

due to the fact that $u^\#$ is equal on opposite faces, but the normal vectors n go in opposite directions. This decomposition into two sets of faces also has the following consequence

$$\int_{\partial V} u^\# \cdot (\sigma \cdot n) = \int_{S_1} u^\# \cdot (\sigma \cdot n) + \int_{S_2} u^\# \cdot (\sigma \cdot n) = 0.$$

This result extends the proof of Hill-Mandel's lemma to all types of strain-controlled boundary conditions.

1.2.2.4 Hill-Reuss Boundary Conditions

It can be shown that though both strain-controlled and stress-controlled calculations converge to a unique mechanical response, the first type of boundary conditions yields upper bounds on effective material properties while the second type yields lower bounds [112, 134, 135]. The use of both strain-controlled and stress-controlled RVE calculations can hence be interesting to check the validity of a result.

HRBCs are the stress-based equivalent of TVBCs, so that instead of assuming a homogeneous strain in the RVE, a homogeneous stress Σ is assumed

$$\begin{aligned} \sigma &= \Sigma \text{ in } V, \\ \langle \sigma \rangle &= \langle \Sigma \rangle = \Sigma. \end{aligned}$$

Proof of the lemma in Equation (1.17) is easily obtained

$$\begin{aligned} \langle \sigma : \varepsilon \rangle &= \frac{1}{|V|} \int_V \sigma : \varepsilon = \frac{1}{|V|} \int_V \Sigma : \varepsilon \\ &= \Sigma : \left(\frac{1}{|V|} \int_V \varepsilon \right) = \Sigma : \langle \varepsilon \rangle = \langle \sigma \rangle : \langle \varepsilon \rangle. \end{aligned}$$

1.2.2.5 Static Uniform Boundary Conditions

SUBCs are the stress-based equivalent of KUBCs, so that instead of assuming a homogeneous strain at RVE boundaries, a homogeneous normal tension $\Sigma.n$ is assumed

$$\begin{aligned}\sigma.n &= \Sigma.n \text{ on } \partial V, \\ \langle \sigma \rangle &= \frac{1}{|V|} \int_{\partial V} \mathbf{x} \otimes (\sigma.n) = \frac{1}{|V|} \int_{\partial V} \mathbf{x} \otimes (\Sigma.n) = \langle \Sigma \rangle = \Sigma.\end{aligned}$$

Proof of the lemma in Equation (1.17) uses the same reasoning as above

$$\begin{aligned}\langle \sigma : \varepsilon \rangle &= \frac{1}{|V|} \int_{\partial V} u.(\sigma.n) = \frac{1}{|V|} \int_{\partial V} u.(\Sigma.n) \\ &= \Sigma : \left(\frac{1}{|V|} \int_{\partial V} u \otimes n \right) = \Sigma : \langle \varepsilon \rangle = \langle \sigma \rangle : \langle \varepsilon \rangle.\end{aligned}$$

1.2.2.6 Numerical aspects

Because they are too restrictive and cannot take into account local events such as void growth and coalescence, it can be assumed that TVBCs and HRBCs would give too loose lower and upper bounds. This remark also applies to SUBCs and KUBCs, but only at RVE boundaries. Thus, for large RVEs, these boundary effects decrease and a realistic mechanical response is obtained.

Difficulties arise with PBCs because of multiple reasons.

First, the microstructure in the RVE has to be periodic, which requires specific digital microstructure generation tools. These tools are usually quite advanced in order to satisfy prescribed particle distribution and size statistics corresponding to a given material [7, 138]. Adding a periodicity constraint leads to a very complicated problem, which may not always have a satisfactory solution for a given RVE size, especially for materials with high density [112, 139].

Then, mesh generation and adaptation, which plays a key role in the present developments, also becomes quite troublesome when dealing with periodic meshes [140, 141].

Finally, parallel computing, which becomes necessary when using large RVEs, also raises technical difficulties because linear constraints between nodes on opposite faces have to be added to the discrete balance equations. These constraints also have a negative effect on the sparsity pattern of the matrices obtained by discretisation of balance equations [134], affecting the performance of standard iterative linear solvers [126].

Though these technical difficulties may seem to penalize PBCs, they are actually widely used because the mechanical response is known to converge more rapidly with increasing RVE size [135]. Therefore, smaller RVEs can be used. Additionally, in some configurations, illustrated in green in Figure 1.11, PBCs can be simplified thanks to symmetries. Indeed, if both the microstructure and the loading are symmetric, only one fourth (or one eighth in 3D) of the RVE can be simulated, with symmetry boundary conditions on two faces (three in 3D). Normal displacements can then be applied on the remaining faces in order to constrain them to remain planar, resulting in periodicity.

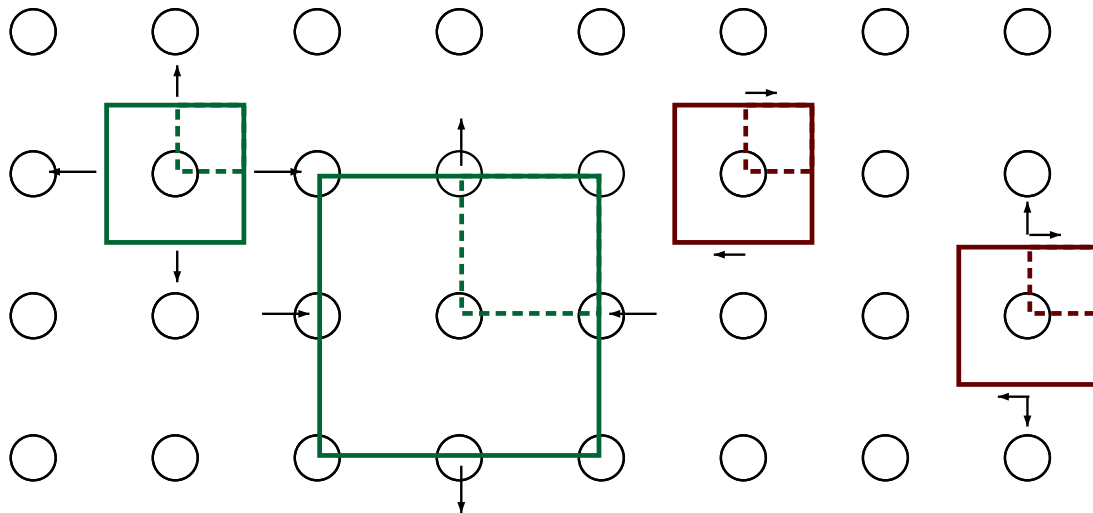


Figure 1.11 – Simple periodic microstructure and different choices of PBCs. In green, boundary conditions that can be implemented easily thanks to symmetries. In red, boundary conditions that require to constrain displacements between nodes on opposite faces.

1.2.3 Homogenization in porous plasticity

1.2.3.1 Gurson model's derivation

In this section, the homogenization theory described above is applied in the case of porous plasticity, as done by Gurson [33]. This approach is similar to the micromechanical calculations of McClintock [25] and Rice & Tracey [26], as it yields a void growth law, but it also uses homogenization theory in order to deduce a macroscopic yield surface taking into account the presence of a porosity. Opposed to numerical approaches, the RVE response is computed analytically, with the advantage of resulting in a closed-form model, which can be implemented and used directly at the macroscale in standard FE codes. Nevertheless, closed-form solutions can only be obtained for simple RVEs, with very restrictive assumptions that may have a major influence on the relevance of the final model.

In the sequel, the derivation of Gurson's model is summarized, based on [37, 142, 143, 144], with a particular care regarding the assumptions that it requires. First, Gurson considered *a spherical RVE of radius b with a spherical void of radius a at its center*, as illustrated in Figure 1.12. The porosity f is defined as the ratio between void volume and RVE volume, namely, $f = \frac{a^3}{b^3}$.

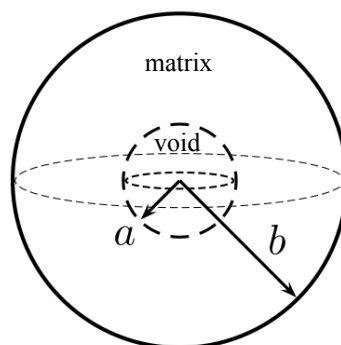


Figure 1.12 – RVE consisting of a single spherical void included in a spherical domain used by Gurson [33]. Figure reproduced from [37].

In Gurson's work, KUBCs are considered as in Equation (1.18), but since these boundary conditions are still too general to analytically derive a solution, a *specific velocity field* of the following form is assumed

$$v = v^A + v^B, v^A = \dot{E}_m \frac{b^3}{r^2} e_r, v^B = \dot{E}' \mathbf{x} \text{ in } V \quad (1.19)$$

where \dot{E} is a prescribed homogeneous strain rate, $\dot{E}_m = \frac{\text{tr}(\dot{E})}{3}$ and $\dot{E}' = \dot{E} - \dot{E}_m I$ are respectively its mean and deviatoric parts, and e_r is the first vector of the spherical basis.

The procedure used by Gurson consists in expressing the microscopic trial plastic work and averaging it on the whole RVE using Equation (1.15) and Equation (1.17). Though the computation of this integral is eased by the fact that *von Mises perfect plasticity* is assumed, it remains quite complex and relies on a Taylor series expansion of one of the terms to integrate (not detailed here). In Reference [144], the authors showed that based on Cauchy-Schwartz's inequality, it can be proved that the first order approximation of this term used by Gurson is restrictive. Performing a second order Taylor expansion, they proved that a closed-form solution can still be obtained, with more accurate results. A third order expansion was also performed, but with no significant improvements on the results.

The macroscopic trial plastic work obtained with this integration has then to be derived with respect to the macroscopic strain rate in order to obtain the macroscopic Cauchy stress tensor Σ . In the *isotropic plasticity* case, this is eased as both the macroscopic strain rate and stress tensors are diagonal in the same basis. Derivation is hence carried out in that basis, and both the mean part Σ_m of Σ and the macroscopic von Mises equivalent stress $\bar{\Sigma}$ can be expressed in function of \dot{E}_m and \dot{E}' . The combination of these two relations and the elimination of the dependence on \dot{E}_m and \dot{E}' gives the final expression of the Gurson yield surface

$$\frac{\bar{\Sigma}^2}{\bar{\sigma}^2} + 2f \cosh\left(\frac{3}{2} \frac{\Sigma_m}{\bar{\sigma}}\right) - 1 - f^2 = 0. \quad (1.20)$$

Several comments can be made on that result. First, the dependence on the macroscopic triaxiality ratio $\eta = \frac{\Sigma_m}{\bar{\sigma}}$ is not artificially added such as in empirical or phenomenological models, but emerges naturally from homogenization of the initial microscopic problem. This result already appears in the Rice & Tracey void growth model [26].

In Reference [144], the authors proved that a better approximation during the computation of the macroscopic trial plastic work enabled to naturally introduce the normalized Lode angle $\bar{\theta} = 1 - \frac{2}{\pi} \arccos\left(\frac{27}{2} \frac{\det(\Sigma')}{\bar{\sigma}^3}\right)$ in Equation (1.20). These results have not been validated experimentally yet, but a clear advantage of this approach is that the dependence on both invariants of the Cauchy stress tensor stems naturally from a micromechanical calculation, and not from macroscopic considerations.

1.2.3.2 Restrictive assumptions

In the summarized derivation of the Gurson yield surface presented above, multiple points have been highlighted in *italic*. These points are assumptions and potential sources of errors for industrial applications where the Gurson model does not provide realistic solutions.

- A first restrictive assumption is the choice of an RVE containing a single spherical void, since real microstructures feature multiple voids and inclusions. Models accounting for the presence of inclusions have been considered by some authors [145, 146]. These are important for the modeling of void nucleation, which is discussed in more details in Chapter 4.

The shape of the void is also restrictive, as it has been mentioned in this manuscript that under shear voids may rotate and flatten. This influence of shape has been taken into account for instance in the Gologanu-Leblond-Devaux model [36] and its extensions [146, 147, 148, 149]. Studies specifically targeting shear loading have also been carried out [89, 106, 148, 150, 151, 152]. Regarding the influence of neighboring inclusions and voids, it has been the object of multiple void coalescence models proposed in the literature, which are discussed in Chapter 5.

- Assuming von Mises perfect plasticity, and hence no elasticity and no hardening restricts the applications for real materials where both these phenomena can be important [33, 147, 148, 153]. Other plasticity models have been investigated in the literature, as plasticity at this scale could be influenced significantly by the crystal structure of the metal [154, 155, 156, 157], especially if the size of the grains is comparable to that of the voids. Anisotropic plasticity models have also been considered [158, 159, 160]. Moreover, porous plasticity models and higher-order approaches have been investigated in order to model the presence of a secondary void population in the RVE and size effects due both to plasticity and damage [106, 137, 161, 162, 163, 164].

A more complete review of the Gurson model and its extensions can be found in recent reviews [37, 38].

1.2.3.3 Numerical approaches

The different limitations of the Gurson model have led researchers to rely extensively on numerical procedures. When a damage model gives incorrect results with respect to an experiment or an industrial application, it is difficult to understand the differences and explain them. However, the main advantage of the Gurson model and its extensions, is that the differences can be directly compared at the microscale.

For instance, it is mentioned above that the derivation of Gurson's model is based on a Taylor series expansion. Indeed, Gurson used only a first order approximation of the microscopic trial plastic work. In Reference [144], the authors considered second order and third order approximations. A numerical solution however, does not require such approximations. Thus, the error induced by Gurson's approximation, and the improvements obtained using higher-order approximations, can be quantified with respect to the numerical solution. In Reference [144], the authors conducted FE simulations using the same RVE as Gurson (Figure 1.12) and the same KUBCs (Equation (1.19)). Because Gurson's model (Equation (1.20)) depends explicitly on the macroscopic triaxiality ratio η , it is important to conduct computations where η is fixed. As higher-order approximations depend on the Lode angle θ , the latter should also be fixed. A relevant macroscopic variable such as the porosity rate \dot{f} can be used to assess the validity of an analytic approximation, as in Figure 1.13. In this example, it can be seen that there is a nearly 20 % difference between the higher-order approximations and Gurson's initial one. Additionally, as Gurson's model does not depend on the Lode angle θ , it is very sensitive to the latter and the error becomes significant for some values.

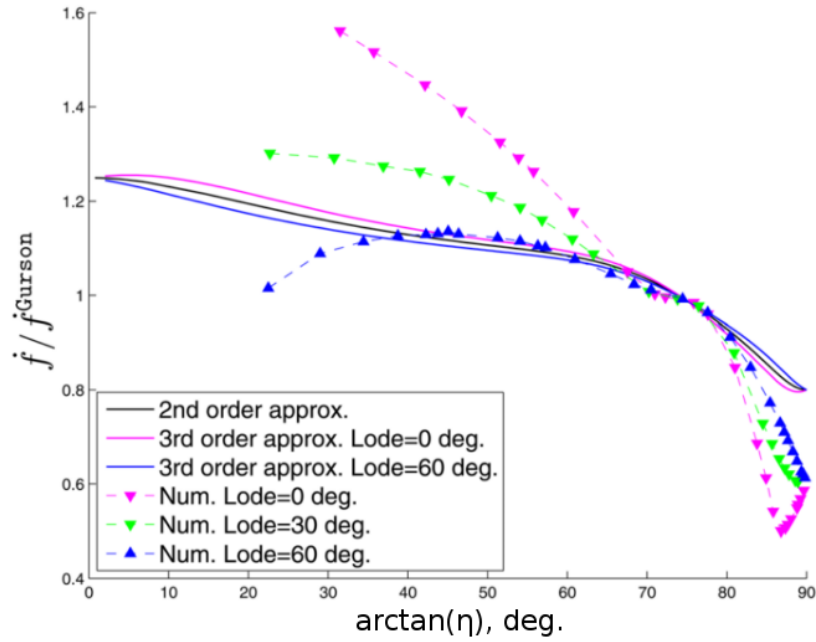


Figure 1.13 – Comparison between the porosity rate \dot{f} obtained using several analytic or numerical methods and Gurson’s initial approximation \dot{f}_{Gurson} . These comparisons consider various stress states, represented by the angle $\arctan \eta$ and the Lode angle $\theta = \frac{27 \det(\Sigma')}{2 \bar{\sigma}^3}$. Figure reproduced from [144].

This comparison nevertheless considers the same spherical RVE with a spherical void as Gurson, the same von Mises perfect plasticity model, and the same loading. Thanks to numerical methods, more complex configurations have been considered in the literature [37].

- In Figure 1.14(a), the RVE with pre-fragmented inclusions and hence penny-shaped voids used in Reference [145] is shown. In this study, the effect of particles on load carrying capacity was investigated, as well as void shape. This study nevertheless considered only periodic arrangements of particles or voids, while real materials feature complex particles and voids arrangements, including particles and voids clusters.
- The same remark regarding periodic arrangements applies to the RVE considered in Reference [164], as shown in Figure 1.14(b). However, this study included the effect of a secondary void population, which may lead to matrix softening in intervoid ligaments. Instead of representing explicitly the secondary voids, they were homogenized using a Gurson model in the matrix.
- The same method was used in Reference [108], as shown in Figure 1.14(c). This study considered RVEs of randomly positioned particles. A Gurson model was used in the matrix to model a secondary void population. A debonding criterion was used to predict and model the initiation and propagation of cracks at the interface between the matrix and particles. However, fragmentation mechanisms were not modeled. The number of particles was also quite small (up to 10), and no sensitivity analysis was conducted with respect to RVE size.

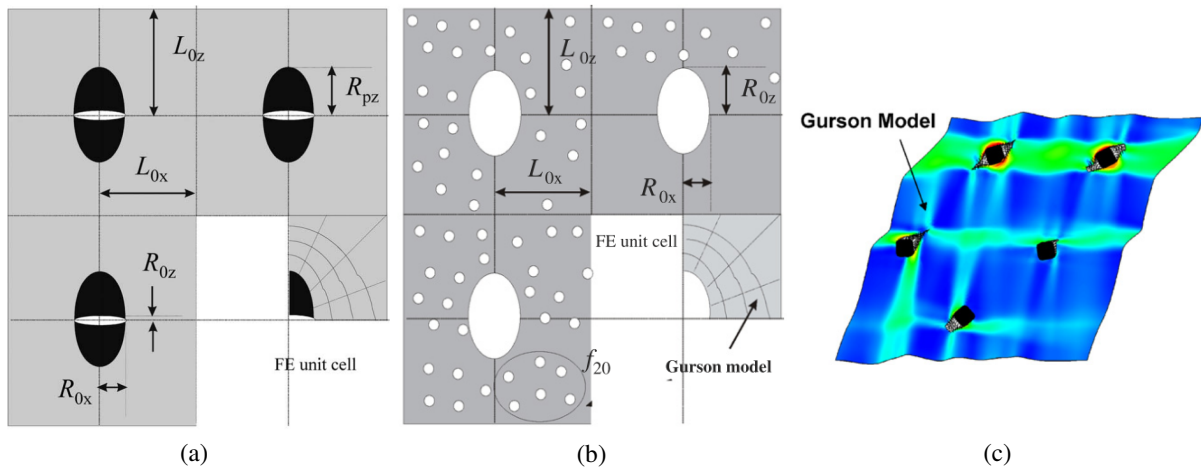


Figure 1.14 – RVEs used by various authors: (a) periodic arrangement of initially fragmented particles, figure reproduced from [145], (b) periodic arrangement of voids with a secondary void population in the matrix, figure reproduced from [164], (c) random arrangement of debonded particles, figure reproduced from [108].

Other authors have considered more general loading conditions [148], or the instantaneous fragmentation of some inclusions for small plastic strains [112].

These studies however do not consider several key micromechanical aspects of ductile fracture. When random arrangements of voids or particles are used instead of periodic ones, no sensitivity analysis regarding RVE size is conducted. Such analysis would be important to prove that the chosen RVEs are indeed representative of the studied materials. It can be postulated that such analysis would prove that the considered number of particles and voids is not sufficient.

Additionally, most works consider only voids. When particles are taken into account, both particle fragmentation and debonding mechanisms are not considered simultaneously, while in real materials and general loading conditions both phenomena may be observed (Subsection 1.1.2).

Finally, though some works taking into account the effect of a secondary void population can be found, the damage to fracture transition in the matrix material is not modeled. In particular, void linkage events between pairs of voids have been observed in the literature at large plastic strains (Subsection 1.1.3). These phenomena are sometimes accompanied by micro-cracks, which would require a transition from a continuous damage model to a discontinuous fracture model. As a conclusion, numerical methods taking into account large microstructures with complex arrangements of particles and voids are yet to be developed. Particles of complex shapes should be considered. There is also a need for numerical methods enabling the modeling of void nucleation events with a competition between particle fragmentation and debonding. Conducting such simulations at large plastic strains would require an advanced damage and fracture criterion in the matrix in order to model the coalescence and linkage of voids.

Conclusion

All metallic materials are heterogeneous at the microscale, due to their crystalline structure, reinforcements, and defects. Hence, there are multiple metallic phases, sometimes separated by non-metallic particles and voids. The interfaces between these different components are sites of stress localization during loading, which leads to the nucleation of voids. This nucleation phenomenon can occur either by debonding, which is the failure of an interface between two components, or fragmentation, which is the failure of one of the components.

Voids grow independently from each other during loading, up to a certain critical point where they start to interact. This critical point is called the onset of void coalescence. It is marked by an acceleration of void growth between neighboring voids, up to linkage of these voids, which is sometimes accompanied by micro-cracks. The accumulation of void linkage events leads to the formation of a macro-crack, and the final ductile fracture of the material.

Ductile fracture is hence complex by nature, because cracks develop at two scales. Recent experimental and theoretical studies mention that more than two scales could have to be considered, as submicron size voids may also develop and have a major influence on void coalescence. Experimental studies are of great interest and have importantly helped the understanding of ductile fracture, thanks to recent X-ray imaging techniques. These techniques now allow for an *in situ* observation of ductile fracture for millimeter-thick specimens, with a resolution close to the micrometer.

Automatic void tracking algorithms have been developed to obtain local measurements of void growth based on these three-dimensional (3D) data. The need for these advanced procedures is due to the random distribution of the voids, and their random sizes. Some studies have addressed the manufacturing of model materials with laser drilled microscopic holes to avoid these issues. Added to this multiscale and complex aspect of damage, its interaction with plasticity is also a challenging problem for both experimental and numerical modeling scientists. The recent extension of image correlation techniques to 3D is promising as strain localization can be measured locally. Results obtained using these techniques suggest that in some materials plasticity may develop and localize significantly before void coalescence occurs.

The modeling of multiscale phenomena calls for multiscale mathematical frameworks. The analytic application of homogenization theory to ductile fracture is of great interest to derive microscale-based plasticity-damage constitutive models that can be used at the macroscale. The literature review in this chapter regarding these analytic derivations was restricted to the Gurson model, which only accounts for void growth. Discussions about void nucleation models are presented in Chapter 4, while void coalescence modeling is considered in Chapter 5.

The Gurson model and its extensions are based on very limiting assumptions regarding the microstructure of the studied materials, the constitutive models used at the microscale, and the loading conditions. In order to quantify the errors produced by these models, and help their improvement, numerical multiscale approaches are worth considering.

Numerical approaches follow the same multiscale framework that is used for analytic homogenization. The main difference is that the solution is computed numerically, most often using the Finite Element (FE) method, which relies on a representation of all unknowns by a mesh, and discrete variables carried at the nodes of this mesh. Thus, complex microstructures, advanced microscale constitutive models, and general loading conditions can be accessed.

However, most FE analysis studies found in the literature consider only simple microstructures. The used Representative Volume Elements (RVEs) generally contain only a single void, with Periodic Boundary Conditions (PBCs). Some works have also considered inclusions but the

subsequent void nucleation mechanisms are often simplified, by assuming initial debonding or a pre-fragmented inclusion for instance. Advanced numerical methods and micromechanical models are yet to be developed in order to take into account randomly positioned and shaped inclusions, and the subsequent complex void nucleation, growth and coalescence events up to large plastic strains. Numerical tools developed in the present work to address such challenges are presented in the following chapters.

Chapter 2

Mesh adaptation with enhanced volume conservation

The fight is won or lost far away
from witnesses - behind the lines, in
the gym, and out there on the road,
long before I dance under those
lights.

Muhammad Ali

Introduction	56
2.1 Meshing internal interfaces	60
2.2 Volume-conserving mesh adaptation	62
2.2.1 Anisotropic mesh adaptation	62
2.2.2 Mesh adaptation with internal interfaces	67
2.2.3 Robustness improvement	69
2.2.4 Concluding remarks	70
2.3 Mesh motion and transport	72
2.3.1 Mesh motion	72
2.3.2 Transport of history variables	72
2.4 Results	75
2.4.1 Large displacements: sphere rotation	75
2.4.2 Large deformations: sphere stretching	78
2.4.3 Topological changes: sphere stacking	80
2.4.4 Robustness investigation	82
2.5 Parallel implementation	84
2.6 Extension to computational fracture mechanics	86
Conclusion	88

Résumé en français

La modélisation de microstructures telles que celles étudiées dans cette thèse se fait généralement dans un cadre Lagrangien. La méthode des fonctions de niveau est intéressante car elle permet de modéliser très simplement des phénomènes topologiques complexes comme la liaison de vides. Néanmoins, pour de grandes déformations, les opérations de remaillage, indispensables dans un cadre Lagrangien, sont généralement perçues comme trop coûteuses numériquement. Dans ce chapitre, en associant un algorithme de mouvement de maillage avec un critère de qualité et de retournement d'élément, il est montré que la fréquence des opérations de remaillage peut être réduite. Ainsi, une méthode Lagrangienne avec fonctions de niveau peut devenir plus qu'intéressante vis-à-vis d'une méthode Eulérienne avec fonctions de niveau, aussi bien pour de grandes déformations que pour des changements topologiques complexes.

Le principal défaut de la méthode Lagrangienne est alors une tendance à diffuser de manière importante les interfaces et le volume de chaque phase lors des opérations de remaillage. La nouvelle méthode de remaillage avec contrainte de conservation de volume présentée dans ce chapitre permet de contrôler et réduire cette diffusion, menant ainsi à des résultats très prometteurs pour de grands déplacements. En comparaison avec les deux premières approches, cette nouvelle méthode ajoute également le maillage explicite des interfaces, ce qui est connu pour poser des difficultés lorsque de grandes déformations et des modifications topologiques doivent être prises en compte. À l'aide de l'utilisation des fonctions de niveau comme intermédiaires, il est montré que cette méthode est capable de prendre en compte de tels événements, sans augmentation significative de l'erreur d'approximation ou du temps de calcul.

À la connaissance de l'auteur, ceci est la première fois que de tels résultats sont obtenus avec des interfaces maillées explicitement, et en ayant recourt exclusivement à de l'adaptation de maillage. Cela est d'un grand intérêt notamment d'un point de vue du coût numérique et de l'utilisation de cet algorithme pour le calcul parallèle, car l'adaptation de maillage s'appuie uniquement sur des opérations locales.

Il serait intéressant d'étudier l'application de cette méthode à d'autres phénomènes physiques, comme les écoulements multiphasiques, où la tension de surface et les discontinuités fortes aux interfaces sont difficiles à modéliser lorsque les interfaces ne sont pas maillées explicitement. Cette difficulté a été notée également lors de la modélisation des phénomènes de recristallisation statique et surtout dynamique, avec le défi supplémentaire lié aux joints multiples. Ces problèmes sont discutés dans le chapitre 7.

Pour conclure, cette méthode adaptative avec fonctions de niveau et conservation de volume améliorée est un outil robuste qui peut être utilisé pour le suivi d'interfaces dans des simulations où tous types d'événements ont lieu (grands déplacement, grandes déformations, modifications topologiques). Cette robustesse permet également d'utiliser des maillages moins raffinés ou d'améliorer la conservation de toutes les échelles de variation d'une géométrie, incluant les échelles les plus fines. Les développements réalisés dans ce chapitre s'étendent aisément au calcul parallèle, bien que l'étape de génération du maillage explicite des interfaces nécessite certaines précautions.

Combinées, ces méthodes parallèles de génération et adaptation de maillages peuvent être utilisées pour générer des maillages explicites depuis des fonctions de niveau à la volée pendant la simulation. Ainsi, des applications liées à la mécanique de la rupture sont accessibles. En comparaison avec des travaux précédents, cette approche préserve la possibilité de modéliser et propager des fissures de formes arbitraires, évitant ainsi toute dépendance pathologique envers la discrétisation. Bien que cette méthode engendre une perte de masse, due au volume artificiel

donné au germe inséré à chaque initiation ou propagation de fissure, cette perte de masse est drastiquement réduite grâce au maillage explicite des interfaces. Par ailleurs, la pointe de fissure peut être discrétisée avec précision sans raffinement excessif du maillage.

Un point important de cette méthode de mécanique numérique de la rupture est que la technique d'adaptation de maillage mentionnée ci-dessus peut être appliquée à la phase vide, puisque les fissures, et donc la phase vide, sont représentées par des fonctions de niveau et maillées explicitement. En effet, une limitation connue de la méthode des éléments finis étendus (X-FEM) est l'impossibilité de modifier arbitrairement les éléments portant la fissure, à cause de leur enrichissement. En conséquence, l'application des techniques X-FEM aux grandes déformations induites par la croissance des cavités et à leur coalescence est limitée. De telles difficultés ne sont pas rencontrées avec la méthode proposée dans ce chapitre, qui permet d'adapter le maillage automatiquement depuis l'amorçage des fissures jusqu'à leur coalescence, en passant par leur croissance en vides sphériques (chapitres 4 et 5). Un problème intéressant lié à la présence de fissures est le déclenchement de phénomènes de contact et de pénétration aux lèvres des fissures, incluant des possibilités d'auto-contact. Ce problème est étudié dans l'annexe A.

Introduction

Finite Element (FE) simulation in multiphase domains arises in many applications of computational solid and fluid mechanics. At a macroscopic scale, fluid-structure interaction involves a heterogeneity that is due to the presence of a solid structure, usually in rigid body motion, surrounded by a fluid, usually in turbulent flow [165, 166]. At a smaller scale, all materials are heterogeneous. For example, one may cite the microstructure of dual-phase steels or particle-reinforced composites, which contain a main phase, the matrix, second-phase particles, and defects [6, 167]. Metal phases can themselves be decomposed into a heterogeneous grain structure [43, 168].

Once the initial mesh is generated, a challenging problem arises in transient simulations: tracking moving and deforming interfaces. Depending on the magnitude of these displacements and deformations from one time increment to another, various methods may be used. Lagrangian methods can be based on explicit meshes of interfaces or implicit representations [169], where the interfaces are carried by FE fields stored at mesh nodes (Level-Set [170], Phase-Field [171, 172]), or at mesh elements (Volume Of Fluid [173]).

A focus is made in the following on the Level-Set (LS) method in particular, as the Phase-Field and Volume Of Fluid methods are not suited for fracture mechanics applications where crack tips have to be discretized (though the Phase-Field method is gaining an increasing interest for computational damage mechanics applications [174, 175]). Advanced representations have also been proposed in the literature, for example by coupling two of these methods [176], or enhancing an Eulerian LS method with Lagrangian particles [177, 178], or with remeshing techniques [168, 179, 180, 181].

Large displacements and deformations are difficult to handle using Lagrangian techniques because of the risk of element flipping. While many commercial codes implement remeshing techniques to prevent element flipping at domain boundaries, it is less common to remesh internal boundaries. Even with implicit interfaces, remeshing is difficult because of the risk of diffusing the FE fields carrying these interfaces.

When the interfaces move or deform too fast as in fluid mechanics, or when their topology becomes too complex to be followed as in recrystallization [168], it is common to resort to fixed mesh methods. In this last category of methods, convection is not solved by mesh motion as in Lagrangian methods but through convection equations that involve the FE fields carrying the interfaces. The solution of such equations with LS functions raises volume conservation and stabilization issues. Although these issues are sometimes addressed using topological mesh adaptation in order to improve the interfaces description [168, 180], the term "fixed mesh methods" will be used in this chapter to refer to all Eulerian methods, regardless of whether they are coupled to topological mesh adaptation or not.

Finally, an interesting compromise between Lagrangian and Eulerian methods is offered by Arbitrary Lagrangian-Eulerian methods. The aim of these methods is to avoid as much as possible the volume conservation and stabilization issues raised by Eulerian LS methods, by activating Eulerian convection only in areas where the deformations are too large to be followed by pure mesh motion. Regarding interfaces, explicit representations require the interfaces to remain purely Lagrangian throughout the simulation (otherwise the mesh of the interface would be delayed with respect to the interface itself). This choice was made, for example, in Reference [182] and also in Reference [183], with the major consequence that it restricted the range of applications to simulations where no large stretching or topological change occurred.

The particularity of the simulations targeted in this thesis is the presence of at least three phases: the matrix, which is the main phase of the alloy, particles, and voids. The number of phases may be larger if the crystalline structure of the matrix is taken into account, or if particles of different nature (and therefore different behavior) are present. Since the aim is to address forming processes, large plastic strains occur and deformations are significant, especially around the void phase, due to void growth. Interfaces between each of the three or more phases do not only deform significantly, but also appear and disappear due respectively to void nucleation and linkage.

All possible events that have to be handled are illustrated in Figure 2.1. This list does not apply only to ductile fracture but to a wide range of multiphase applications.

- From Figure 2.1(a) to Figure 2.1(b), two objects have merged, or linked, together. In ductile fracture, this phenomenon takes place between voids due to necking or shear bands, but in other applications such as multiphase flow, it takes place between gas and liquid bubbles due to the flow, with the importance of surface tension.
- From Figure 2.1(a) to Figure 2.1(c), the motion was omitted and replaced by the propagation of a crack through the objects. This situation is not only linked to ductile fracture but to material science and solid mechanics in general.
- Finally, from Figure 2.1(a) to Figure 2.1(d), an external motion pushed the two objects towards each other, but the interface is still present. This situation is well described by contact mechanics, which can take into account not only the reaction force preventing the two objects from penetrating each other, but also friction forces.

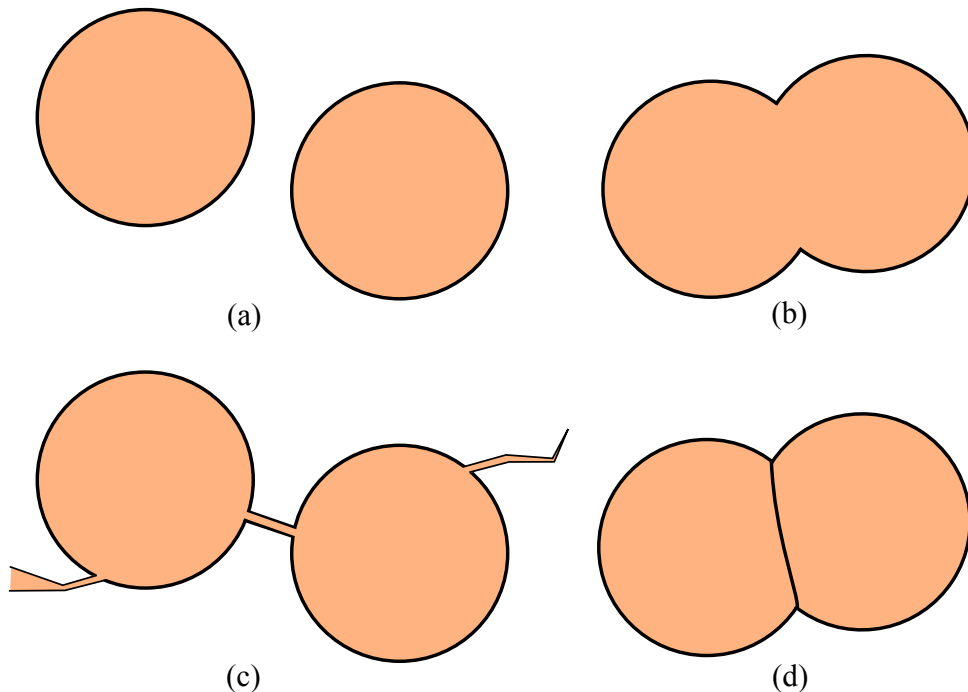


Figure 2.1 – Complex topological events that need to be addressed in this chapter: (a) initial topology of two spheres, (b) linkage, (c) crack propagation, (d) contact.

In a previous work [5], a Lagrangian LS method was chosen as it eased computations with the linkage event in Figure 2.1(b), which is naturally handled by the LS method given that all

phases, including the void phase, are embedded in a single mesh. However, this event cannot be controlled in an LS framework, and any pair of objects of the same phase, including particles, link the same way as voids [6]. As illustrated in Figure 2.2, this is not physical as particle interfaces should behave as in the contact situation in Figure 2.1(d). Additionally, a special care has to be taken when using the LS method to represent cracks [169].

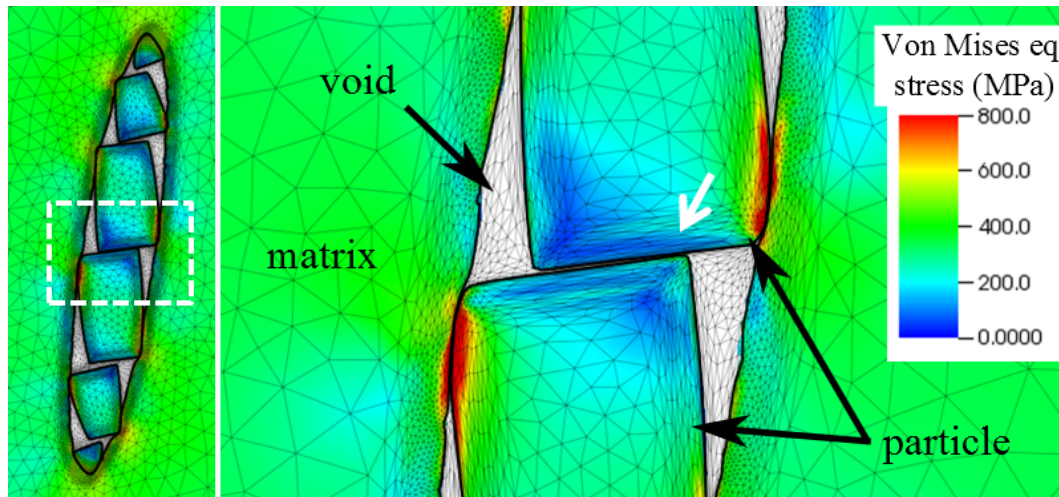


Figure 2.2 – Example of a fragmented elliptic particle where contact between fragments (white arrow) was not taken into account by the used Lagrangian LS method, and may have led to a non physical closure and healing of the particle. Figure adapted from [6].

Computational fracture mechanics is a prolific research topic and multiple strategies have been proposed to model the initiation and propagation of a crack in homogeneous or heterogeneous materials. These strategies can be distinguished into two categories, depending on whether a loss of mass is induced or not.

On the one hand, the crack may be modeled by explicitly splitting faces and therefore inserting a discontinuity in the mesh, or by inserting zero-thickness elements as in a Cohesive Zone Model (CZM) [184]. Both techniques are well-known to produce mesh dependent results when they are used between existing faces of the mesh. Indeed, the crack propagation path is then highly influenced by the orientations of the faces of the mesh. Techniques based on remeshing operations have been proposed in the literature to avoid this mesh dependency [114, 185, 186, 187], by aligning the mesh onto arbitrary directions. The latter ones are determined thanks to appropriate crack propagation criteria. In the case of small deformations, one may prefer to avoid remeshing by using the eXtended Finite Element Method (X-FEM) [169, 188], which can also be enhanced with a CZM.

On the other hand, cracks may be modeled by removing a part of the mesh, instead of splitting it. The kill-element method consists in removing elements along the crack direction. This technique is well-known to produce mesh dependent results, as once again the crack propagation path is determined by the shape of the elements of the mesh.

In a previous work [6], because all phases, including the void phase, were embedded in a single mesh, cracks could be initiated and propagated simply by modifying the LS function to the void phase. This was an important improvement over the kill element method, as the proposed method enabled to remove arbitrary shapes, hence avoiding any mesh dependency.

Because voids were represented by a single LS function, very fine anisotropic meshes were used to represent cracks and especially crack tips (Figure 2.2). These very fine meshes had important

consequences on the computational cost.

Moreover, this method shared with the kill-element method the limitation of generating a loss of mass at each initiation or propagation. To reduce this loss of mass, the nuclei of arbitrary shapes that were used to modify the LS function to the void phase were defined as small as possible, which required even finer meshes, and even higher computational requirements.

In this chapter, a mesh generation procedure is presented in order to obtain a conform FE mesh (with explicit interfaces) from LS functions (Section 2.1).

Then, a new mesh adaptation technique that combines both explicit meshing of interfaces and implicit LS representation is presented (Section 2.2). Compared with a standard LS method with moving or fixed mesh, it is shown that this method reduces drastically the diffusion of interfaces during convection and remeshing.

Although this approach relies on Lagrangian mesh motion (Section 2.3), it is proven that it remains competitive for large displacements and deformations, especially regarding volume conservation. An advantage of the whole procedure is that it is purely topological, and may be applied in all dimensions, including space-time frameworks. To meet this requirement, the method is restricted to first-order simplex meshes, a simplex being a line segment in one dimension (1D), a triangle in two dimensions (2D), a tetrahedron in three dimensions (3D), and a pentachoron in four dimensions (4D).

Numerical experiments are proposed with interfaces that undergo large displacements or deformations, and topological changes (Section 2.4).

The integration of these developments in the distributed computing framework developed at the Center for Material forming - MINES ParisTech (Cemef - MINES ParisTech) is then considered (Section 2.5).

Finally, a computational fracture mechanics methodology is built over these parallel mesh generation and adaptation methods (Section 2.6), with applications to crack insertion and propagation in heterogeneous materials.

2.1 Meshing internal interfaces

Choosing an appropriate interface discretization does not only have consequences on the difficulty of interface tracking. The numerical solution of equilibrium equations, constitutive models, and other physical problems is also highly impacted by this choice, in terms of difficulty, accuracy and computational cost. The most simple and straightforward approach is doubtlessly explicit interface meshing. Having a conform FE mesh at interfaces does not require any specific treatment during the solution, apart from the use of different constitutive models depending on which phase an element belongs to. However, as stated above, most interface tracking methods do not maintain conform FE meshes at interfaces.

In particular, the LS method only addresses interface tracking, and has to be coupled to mixture laws or the X-FEM for interface modeling. In some fluid-structure interaction problems, the deformation of the solid phase can be neglected as the focus is made on the flow or on thermal exchanges. Hence, nullity of the solid's deformation rate can be imposed by defining its behavior as a fluid with penalized viscosity [189, 190]. Consequently, the elements that are crossed by the LS function have their behavior defined by a mixture law taking into account both fluid and solid behaviors. As both fluid and solid phases are modeled by a fluid behavior, this mixture law simply consists in mixing the viscosities, yielding the same result as a Volume Of Fluid method. When the deformation of the solid is of interest, this principle can also be applied for nonlinear behavior such as visco-plasticity. When mechanical properties other than viscosity come into play, such as in visco-elasticity [191] or crystal plasticity [4], homogenizing both fluid and solid behavior becomes more complex. Additionally, this technique is known to decrease the order of convergence at interfaces [169], which is often compensated by aggressive local mesh refinement at interfaces [4, 166, 168, 189, 190, 191]. This strategy was used in previous work [5, 6] and resulted in a large computational cost, limiting 3D applications.

As an alternative to mixture laws and explicit interface meshing, X-FEM is widely used in computational solid mechanics. Compared to mixture laws, this method actually represents the discontinuity in behavior at the interface and has been shown to improve the order of convergence [169]. Indeed, the geometry of the interface, which is only carried by the LS functions, is accurately taken into account through enriched basis function and quadrature rules.

However, applications of X-FEM to large deformations remain limited. Since the latter typically require repetitive remeshing operations, a method such as X-FEM that is specifically designed to avoid remeshing operations is not adapted. For the present applications with large plastic strains, an explicit interface meshing methodology has been preferred. Hence, interface modeling is quite easily achieved, while interface tracking requires advanced mesh adaptation techniques, as described in the following sections.

For the generation of these conform FE meshes at an interface, standard tools based on the Delaunay criterion or a frontal approach can be used [192]. However, if the geometry is generated on-the-fly, for example during crack propagation, or if it is not based on a Computer Assisted Design (CAD) file, as in image immersion, then alternatives are necessary. LS functions are well-suited to play this role, as any analytic geometry can be represented by an LS function, and images can be converted to signed distance functions using appropriate algorithms (Section 3.4).

Once these LS functions are defined, a procedure is necessary to generate a conform FE mesh at the interfaces they represent. This operation, known as fitting, or cutting, is inspired from the cut-cell method [193]. In the present case, the domain Ω of dimension d is the union of N

subdomains Ω_i corresponding to the N phases, each having its own LS function ϕ_i defined as

$$\forall t, \forall \mathbf{x} \in \Omega(t), \phi_i(\mathbf{x}, t) = \begin{cases} +\text{dist}(\mathbf{x}, \partial\Omega_i(t)), & \mathbf{x} \in \Omega_i(t), \\ -\text{dist}(\mathbf{x}, \partial\Omega_i(t)), & \mathbf{x} \notin \Omega_i(t). \end{cases}$$

Fitting consists in browsing all edges of the mesh and splitting into two the edges where an LS function ϕ_k takes two different signs. At such edges, the intersection S^{ij} between the interface and the edge (i, j) is obtained by means of linear interpolation based on its two vertices S^i and S^j

$$S^{ij} = S^i - (S^i - S^j) \frac{\phi_k(S^i)}{\phi_k(S^i) - \phi_k(S^j)}.$$

Applying this procedure to all edges and all LS functions results in a mesh that is conform to internal interfaces, but is likely to be of very poor quality, and requires to be adapted.

2.2 Volume-conserving mesh adaptation

Depending on the application, various definitions can be used to represent the interface in implicit methods. LS functions are widely used in multiphase fluid dynamics, where they are discretized on a fixed mesh, and convected through a convection equation. Although this allows to reduce the dependence on mesh adaptation, it raises a major issue regarding volume conservation. In solid mechanics, this issue may be circumvented by using a Lagrangian mesh, which naturally convects interfaces through mesh motion. Because this process may deteriorate element quality, it is usually combined with remeshing. Mesh adaptation may also be employed together with appropriate error estimators, both in moving and fixed mesh methods.

The aim of the method proposed hereafter is to reduce volume loss and interface diffusion caused by the remeshing process itself. Although it is presented in the case where the interface is carried both by a LS function and by the mesh, it can easily be generalized to pure LS representations (Subsection 2.2.4).

2.2.1 Anisotropic mesh adaptation

Mesh adaptation is an open research field that has motivated various approaches. Most techniques consist in defining a certain set of operators, and applying them one by one in order to improve mesh quality. In the present work, the quality is defined for any simplex T as [194]

$$Q(T) = \min \left(c_0 \frac{|T|_M}{h_M^d}, h_M^d, \frac{1}{h_M^d} \right), \quad (2.1)$$

where

- c_0 is a normalization factor so that a regular simplex would have a quality of 1, $c_0 = \frac{d!}{\sqrt{d+1}} 2^{d/2}$,
- $|T|$ is the volume of T and $|T|_M = |T| \sqrt{\det(M(T))}$,
- h_M is the Euclidean norm of edge lengths $h_M = \sqrt{\left(\frac{1}{c_1} \sum_{(i,j) \in \mathcal{N}(\{T\}), i < j} \|S^j - S^i\|_{M(T)}^2 \right)}$, with $\mathcal{N}(\{T\})$ being the set of the nodes of T ,
- c_1 is the number of edges in a simplex, $c_1 = \frac{d(d+1)}{2}$,
- $\|v\|_A = \sqrt{v^t A v}$, $v \in \mathbb{R}^d$, $A \in \mathbb{R}^d \times \mathbb{R}^d$.

In these formulae, M is a metric field defined at mesh nodes which drives anisotropic mesh adaptation, and $M(T)$ is the interpolation of M at the center of T . Although the presented algorithms enable anisotropic meshes, only isotropic meshes are used in this work, as stretched elements are difficult to maintain in a Lagrangian framework, due to the risk of element flipping.

Thus the metric field is defined as $M = \text{diag}\left(\frac{1}{h^2}\right)$, where h is a prescribed mesh size. For further details on metric fields and how they can be used to adapt not only the size but also the shape of mesh elements, the reader is referred to Section 3.1.

Summing up Equation (2.1), an over-sized, under-sized or ill-shaped element has a quality close

to 0, and an appropriately sized and shaped element has a quality close to 1. Though this criterion takes into account both element shape and size, it is possible in the implementation to define different regions in the mesh so that the full expression in Equation (2.1) is considered for some regions, while only the shape term (*i.e.*, $c_0|T|_M/h_M^d$) is considered in other regions.

Regarding the set of operators used to adapt the mesh, many propositions can be found [182, 195], for example: node smoothing, edge swapping, edge splitting, edge collapsing. As detailed in Reference [196], edge swap itself can be declined into many different versions in 3D. Most techniques consider local patches of elements in the mesh, and try to improve them with each one of these operators. These techniques often distinguish the optimization of mesh size from the optimization of element quality by first applying edge split and collapse to reach an optimal size on every edge of the mesh, and then trying to improve element shape using node smoothing and edge swap [182, 195].

In the present work, the technique introduced in Reference [194] is preferred. This technique is presented in Algorithm 1. All nodes and edges of the mesh are considered one by one. Although considering nodes and edges proves to be sufficient in practice, this method can also deal with the faces of the mesh. The patch of elements to improve is defined as all elements that contain the given node or edge (line 12). The external faces of this patch are extracted easily by searching for the faces that belong to only one element of the patch. Then, for each node of the patch, the generic operator consists in connecting all the external faces to this node (line 16). The qualities of the elements built by this procedure are computed for each tested candidate, and the winner is the one having its worst element with the highest quality (line 17).

This generic operator, named *star-connection* operator, has the advantage of considering all swapping, splitting, and collapsing operations at once. Node insertion and smoothing are implemented by adding the center of the patch to the list of candidates (line 15). Although no comparison has ever been performed with classical approaches, a possible drawback of considering all operations altogether is that some operations may be redundantly tested.

An example of patch for a nodal target is described in Figure 2.3(a). After extraction of the external faces, as shown in Figure 2.3(b), several candidates are tested (Figure 2.3(c-h)), with swapping operations that cover a larger set of topological possibilities than a simple edge swap. Finally, the node smoothing candidate in Figure 2.3(h) seems to be preferable (in the isotropic case).

A similar example is described in Figure 2.4, but with the target being an edge of the mesh. While the candidate in Figure 2.4(e) is equivalent to an edge split, the candidates in Figure 2.4(c) and Figure 2.4(d) are equivalent to a simple edge swap. Moreover, these two candidates consist in the same topological modification, which is an example of the redundant operations performed by Algorithm 1.

This algorithm has certain advantages compared to classical approaches.

- When edge length optimization is uncoupled from element shape optimization, there might be a risk of infinite loop [182, 195], as element shape improvement may require to collapse edges that were split during edge length optimization. Uncoupling edge coarsening and refining also raises the same risk [182, 195].

In the proposed method, because the quality criterion takes simultaneously into account both objectives, such issues are avoided, and convergence is obtained without restricting the maximum number of iterations in any way.

Algorithm 1 Quality maximization through local topological operations, lines 12 and 17 contain key operations that are enhanced in the present work.

```

1: function MESHADAPT(Mesh mesh)
2:   Node node
3:   Element element, target
4:   ElementList queue
5:   Mesh patch, candidate, winner
6:
7:   queue.addAll(mesh.nodes())
8:   queue.addAll(mesh.edges())
9:
10:  while queue.notEmpty() do
11:    target ← queue.poll()
12:    patch ←  $\bigcap_{\text{node} \in \text{target.nodes}()} \{ \text{node.neighbors}() \}$ 
13:
14:    winner ← patch
15:    for node ∈ ({ patch.nodes() } ∪ { patch.barycenter() }) \ { target.nodes() } do
16:      candidate ← patch.starConnect(node)
17:      if candidate.isConform() and candidate > winner then
18:        winner ← candidate
19:      end if
20:    end for
21:
22:    if winner ≠ patch then
23:      mesh ← (mesh \ patch) ∪ winner
24:      queue.addAll(winner.nodes())
25:      queue.addAll(winner.edges())
26:    end if
27:  end while
28:  return mesh
29: end function

```

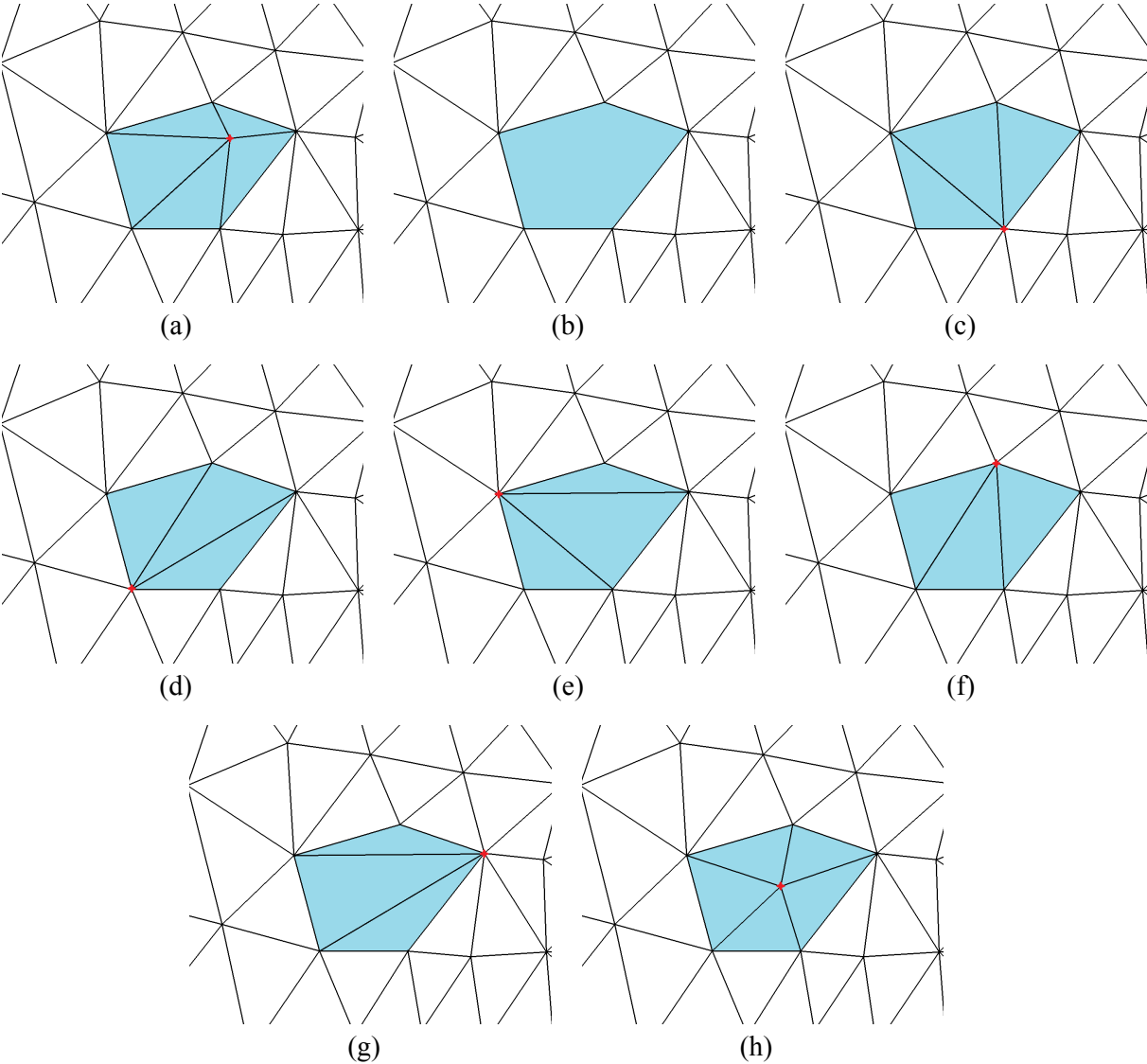


Figure 2.3 – Example of patch at the neighboring of a node: (a) initial patch, (b) external faces extraction, (c-h) candidates.

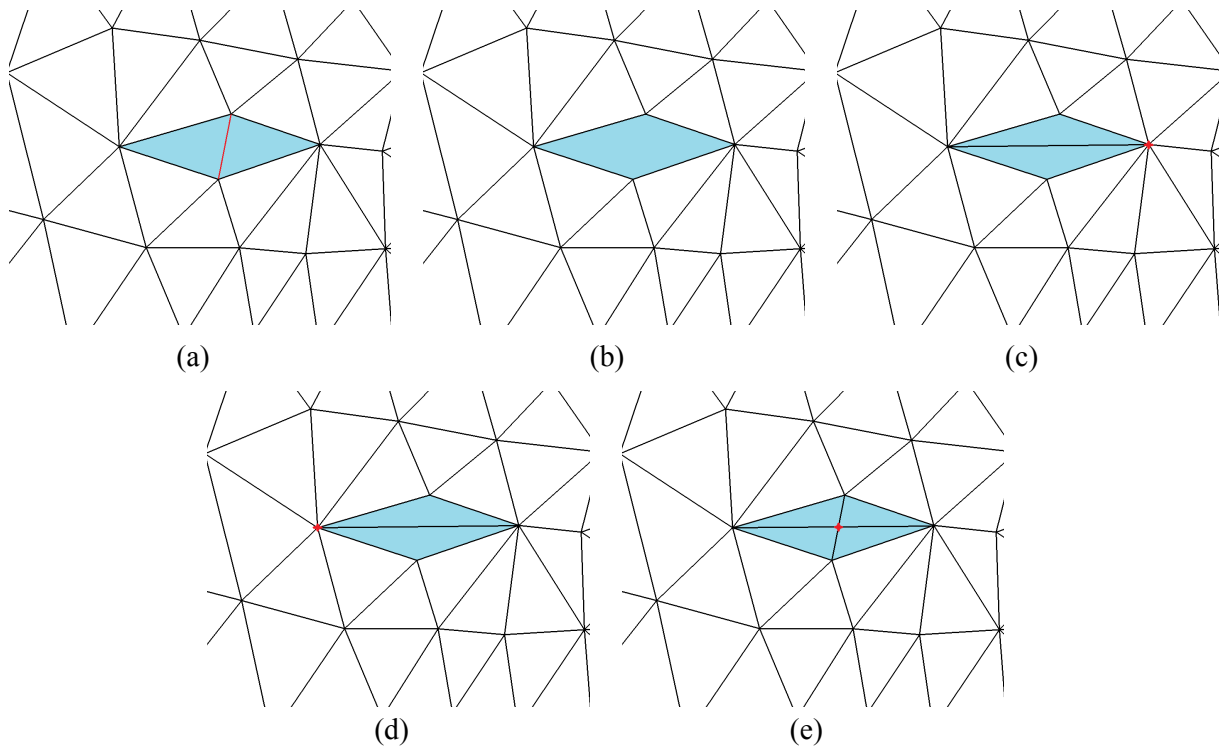


Figure 2.4 – Example of patch at the neighboring of an edge: (a) initial patch, (b) external faces extraction, (c-e) candidates.

- The proposed method is purely topological. This point is essential for the implementation in order to avoid classical programmer mistakes inherent to the implementation of geometric procedures. In particular, Algorithm 1 is far easier to implement than classical remeshing algorithms. Another major consequence of avoiding geometric operations is the extension to space-time methods, and, in particular, to remeshing in four dimensions (see Appendix A of [116]).
- Any other local remeshing operation can be introduced without significant programming effort. The only modification to make in order to add new operations is to change the patch definition at line 12 of Algorithm 1. The algorithm works for any patch of connected elements. The latter means that the domain formed by the patch has to consist in one Connected Component (CC).

Regarding implementation details, they are hidden behind the undefined structures and functions used in Algorithm 1. In the C (as of [197]) implementation of this algorithm developed in the present work, two arrays are used to store the mesh, one containing each node's coordinates and the other each element's connectivity. The elements neighboring each node are stored in an additional two-dimensional array, which enables to increase the number of neighbors for one node without modifying the whole structure. The *Mesh* structure contains these three arrays. Though using arrays may seem inappropriate for a problem like remeshing which implies significant changes in the number of nodes and elements, they are preferred because they avoid repetitive memory allocations. When at any point of the algorithm, it is tried to add a new item to an array which has already reached maximum capacity, this array is reallocated with twice its current capacity. This functioning is similar to the C++ class vector, and the number of reallocations is proven to be negligible and independent from the number of nodes or elements. The *Node* structure is just an integer referring to a node's position in the coordinates array. The

Element structure is a small connectivity array used to store an element. It can also be used to store faces, edges, or nodes. This enables the *ElementList* structure used for queuing to contain faces, edges or nodes. This structure itself is a linked list.

Based on these structures, the functions *addAll()* and *nodes()* at line 7 of Algorithm 1 are easy to implement. The function *edges()* at line 8 consists in collecting all edges of the mesh and eliminating duplicates. This last operation requires to sort the edges. Sorting is used repetitively in Algorithm 1, and the quick-sort algorithm has been chosen to perform this task. Function *notEmpty()* at line 10 is obvious, together with *poll()* at line 11, which removes the last item from the queue and returns it. Operation *neighbors()* is solved directly by the neighbor array, and the intersection at line 12 is based on sorting and dichotomic search. At the same line, *patch* is not actually a complete mesh, since neighbors do not have to be computed.

The barycenter of the patch is computed by function *barycenter()* at line 15, and *starConnect()* at line 16 has already been detailed. The external faces of the patch only have to be extracted once for all candidates. At line 17, the comparison criterion has already been explained, and the function *isConform()* is a key point of the proposed algorithm which is detailed in the next subsection. Finally, line 23 implies replacing obsolete elements with new ones in the connectivity array, and possibly inserting a new node in the coordinates array.

2.2.2 Mesh adaptation with internal interfaces

The extension of the previous algorithm to conserve preexisting internal boundaries is implemented in the function *isConform()* at line 17 of Algorithm 1. In the standard definition, this function only has to verify that the new candidate is a conform (in an FE sense) mesh of the domain defined by the previous patch. By construction, this candidate is a well-defined topology: it has same external faces as the previous patch, and none of its faces has more than two neighbors. For this topology to be conform, two constraints have to be added: the new elements have to be correctly oriented (*i.e.* positive volume), and the total volume of the candidate patch has to match the volume of the previous patch. This constraint prevents element overlapping and flipping, while element degeneration is prevented by the quality criterion.

In Figure 2.5, two variants of an initial 2D topology (Figure 2.5(a)) are presented. Both variants have the same total volume as the initial patch, but they are not considered. Element 4 in Figure 2.5(b) has a negative volume (flipped element). Element 6 in Figure 2.5(c) corresponds to a degenerated element and hence does not maximize the quality criterion.

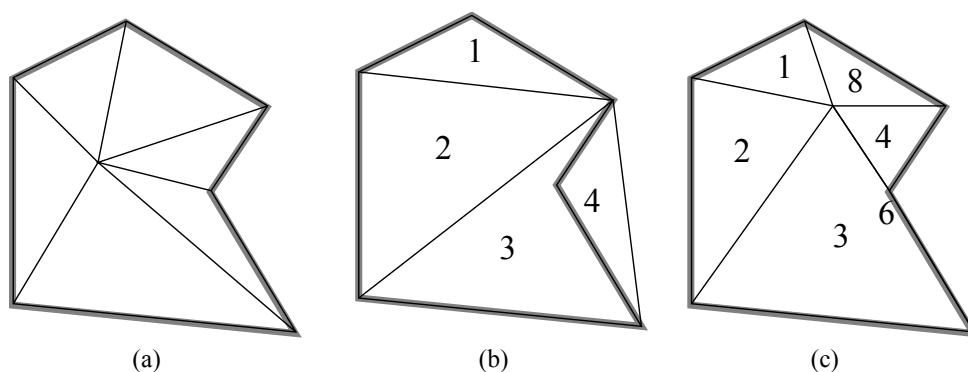


Figure 2.5 – Initial patch (a) and forbidden remeshing operations: (b) element 4 has negative volume, (c) the flat element 6 has a quality that is lower than the initial patch's worst quality. External faces of the patch are highlighted in light gray.

To address the conservation of internal interfaces, LS functions come into play. Inside the initial patch, an element is attributed to a phase if the associated LS function is positive or null at its barycenter. If multiple LS functions are null for the same element (pathological case), this element is attributed to the phase which has lower index. In Figure 2.6(a) and Figure 2.7(a), two 2D examples (respectively with 2 and 3 phases) are shown where the colors indicate which phase an element belongs to. Based on this attribution, the interface faces corresponding to a phase are the faces that separate an element of this phase from elements belonging to other phases. In Figure 2.7(a), interface faces are pointed out by markers, but there is no marker for the blue phase because it has no LS function.

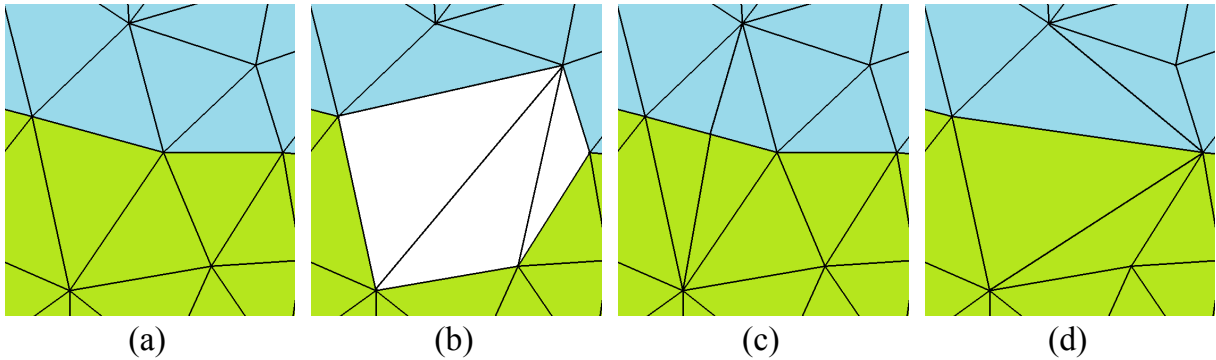


Figure 2.6 – Mesh adaptation with two phases: (a) initial patch, (b) illegal operation, (c) conform operation, (d) relaxation of the phase volumes conservation constraint.

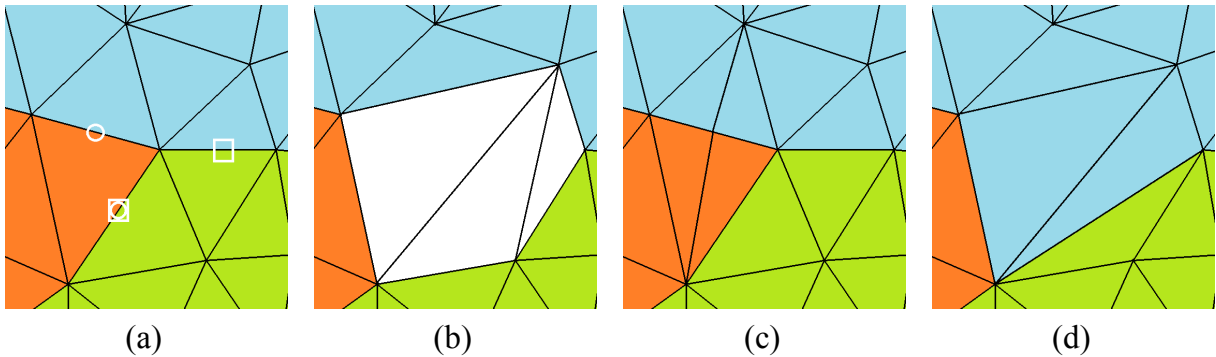


Figure 2.7 – Mesh adaptation with three phases: (a) initial patch with the interface between orange and other phases pointed out by white circles, and the interface between green and other phases pointed out by white squares, (b) illegal operation, (c) conform operation, (d) relaxation of the phase volumes conservation constraint.

The first constraint added to the operation *isConform()* is: if there are any interface faces inside the patch, the candidate chosen at line 16 has to belong to all of them. For example, the operation illustrated in Figure 2.6(b) does not conform with this new definition. The fact that the candidate has to belong to all interfaces extends this constraint to any number of phases, as illustrated in Figure 2.7(b).

For the 3D applications addressed in the present work, this constraint proves to be insufficient because it authorizes aggressive interface remeshing, leading to significant diffusion. Therefore, another constraint is added by comparing the distribution of phase volumes in the initial patch and in the new patch. The tolerance on relative change ϵ_Q for the volume occupied by each phase

inside the patch is given by a Gaussian law based on two parameters Q_μ and Q_σ

$$\epsilon_Q(Q_{min}) = \begin{cases} \exp\left(-\frac{1}{2}\left(\frac{Q_{min} - Q_\mu}{Q_\sigma}\right)^2\right), & Q_{min} > Q_\mu, Q_\sigma > 0 \\ 0, & Q_{min} > Q_\mu, Q_\sigma = 0 \\ 1, & Q_{min} \leq Q_\mu \end{cases} \quad (2.2)$$

where Q_{min} is the worst quality of the initial patch. This constraint is really restrictive and nearly blocks interface remeshing for shapes with high curvature when element quality is acceptable, while it is relaxed to prevent issues during FE solution when element quality is poor. For example, the operations in Figure 2.6(c) and Figure 2.7(c) are always conform, while only relaxation can enable the operations in Figure 2.6(d) and Figure 2.7(d).

In practice, both values Q_μ and Q_σ are chosen empirically as small as possible, to prevent excessive diffusion, but high enough so that the influence on the conditioning of the FE problems is negligible. Typical values are $0.05 \leq Q_\mu \leq 0.1$, $0 \leq Q_\sigma \leq 0.1$. For higher values, relaxation would be too important and volume conservation would be severely affected. For lower values, convergence of the FE solvers would be affected, depending on whether metric anisotropy is significant. Exceptions are presented in Appendix A, where a setting $Q_\mu = Q_\sigma = 0$ is used (no relaxation) because interfaces are not remeshed. These exceptions actually cover a wide range of structural problems, including fluid-structure interaction problems where the boundary of the structure does not deform significantly.

Both interface and volume conservation constraints do not actually require node-wise signed distance functions, and only element-wise tags such as the colors in Figure 2.7 would have been sufficient as interfaces are explicitly meshed. LS functions are only required in order to build the initial mesh (Section 2.1) or initiate and propagate cracks (Section 2.6). However, the proposed remeshing algorithm will often be coupled to error estimators based on distance functions (Section 3.1). Thus, there is an interest for a remeshing algorithm that automatically updates these distance functions when remeshing interfaces. This is also simpler for the user who only has to keep track of these node-wise signed distance functions instead of alternatively using LS functions and element-wise tags.

2.2.3 Robustness improvement

Ideally, thanks to the strategy defined in the preceding section, no element should have a quality lower than Q_μ after remeshing. In practice, numerical experiments with domains involving more than two phases reveal that this situation can occur at intersections between multiple phases. Improving the robustness of the method is essential to avoid the presence of very low quality elements that may reduce the conditioning of the FE solution and hence increase computation time. It is also essential to the remeshing strategy itself: if the remeshing algorithm is efficient enough, relaxation of the volume preservation constraint should happen very rarely.

To achieve this aim, new operations are added to the remeshing process. As stated in Subsection 2.2.1, this is easily done by adding a new possibility, called wide gather, to the patch definition at line 12 of Algorithm 1. This definition is activated only when the following conditions are met at the end of an iteration of the remeshing loop: the target was an edge, no modification was performed (the condition at line 22 was not verified), and the patch contains an element with quality under Q_μ . Under these conditions, at the next iteration, the target is kept to the same edge, but the intersection operator \cap at line 12 is replaced by a union operator \cup .

This simple change adds a wide range of new topological modifications, including edge collapse.

Since, by construction, the patch still consists in one CC, the FE conformity and volume conservation criteria remain valid. An example of patch constructed using this new definition is pictured in Figure 2.8(a) and Figure 2.8(b). Among all candidates, the patch pictured in Figure 2.8(i) is aesthetically interesting, but is not reachable directly using the standard patch definitions of Figure 2.3 and Figure 2.4.

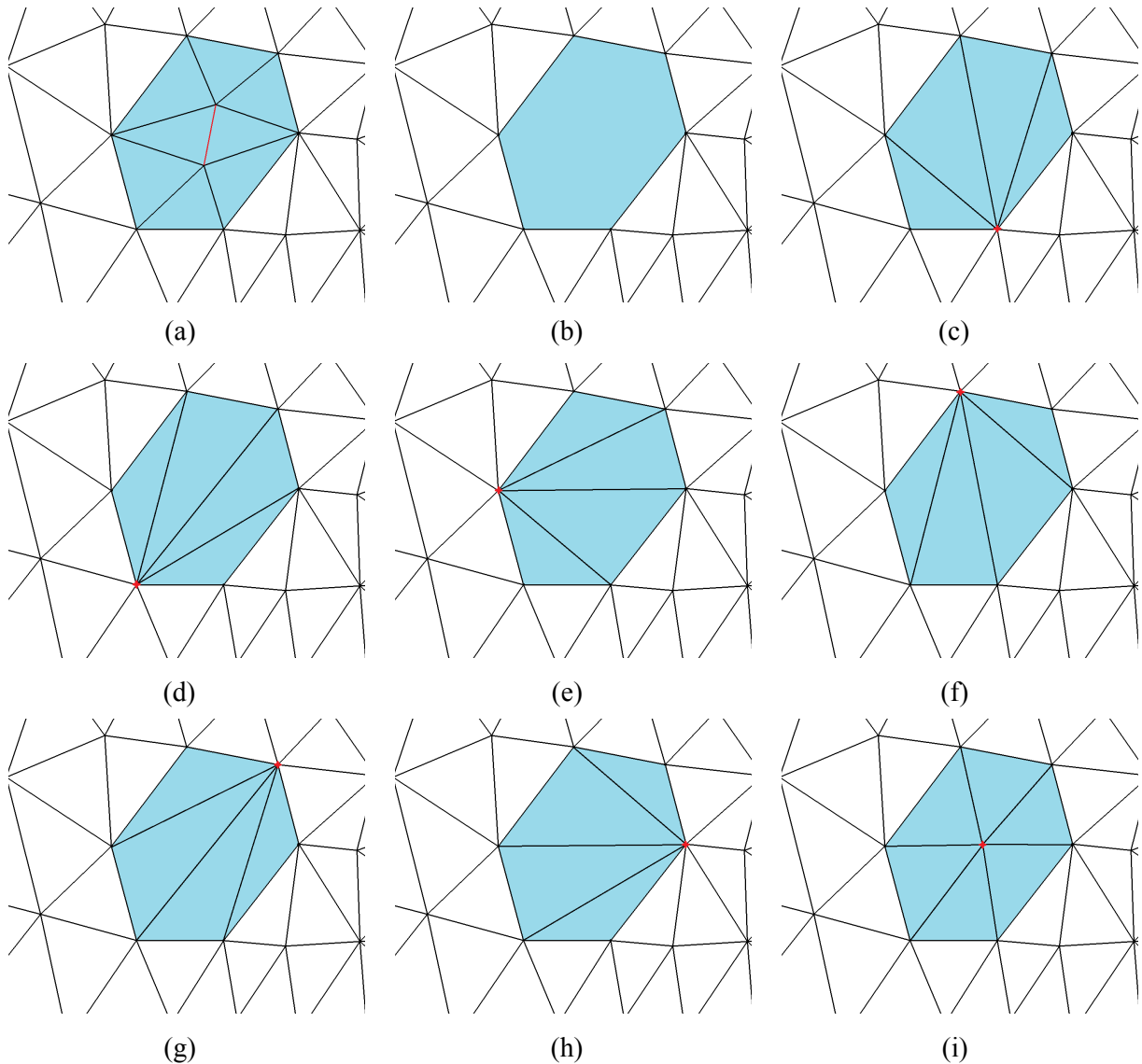


Figure 2.8 – Example of patch at the wide gathered neighboring of an edge: (a) initial patch, (b) external faces extraction, (c-i) candidates.

2.2.4 Concluding remarks

After discussion of the limitations of previous developments [5, 6] and the state of the art, it is chosen to use an FE method with conform interface meshing, as illustrated in Figure 2.6. This is essential for the accuracy of the FE solution at the interface, especially at crack tips. For small deformations, a comparable accuracy could also be obtained using X-FEM, as described in Reference [169].

Though only explicit meshes are used in this work, it is important to precise that since the volume conservation condition defined in Subsection 2.2.2 is purely based on the distribution

of phase volumes, it is readily applicable to implicit methods. If interfaces were implicit, these volumes could be accurately computed by subdividing the elements crossed by the interfaces, as already required by X-FEM [169]. Because there would be no interface faces, only the volume conservation constraint would apply, and the interface preservation constraint would be dropped. In relaxation mode, all operations would be allowed. Hence, implicit methods would ease the remeshing process, with the advantage of volume conservation.

Additionally, element subdivision can be performed by pure edge splitting, as defined in Section 2.1. Thus, it can be observed that the implementation of the volume conservation constraint is purely topological, and in particular, the whole algorithm remains dimension-independent.

Such an approach with implicit interfaces would be interesting for other applications than ductile fracture, such as multiphase flow or grain growth, where the computational cost of following interfaces with explicit meshes may be too high. Explicit meshes should nevertheless not be discarded too promptly, as they allow a better discretization of singularities, which are smoothed with implicit methods. This is important for instance at multiple junctions in grain growth modeling (Chapter 7).

2.3 Mesh motion and transport

In this section, a simple iterative technique is described in order to move mesh nodes, based on a given displacement field, without triggering element flipping. This technique is not different from usual procedures implemented in commercial codes or used for example in Reference [182]. However, its coupling with the relaxation method defined in the preceding section gives a powerful tool that can handle large deformations and complex entanglements of interfaces. The problem of transporting history variables after each remeshing process is also addressed in this section.

2.3.1 Mesh motion

Since convection is modeled by mesh motion in Lagrangian methods, there is a risk of element flipping locally if an element is misaligned with respect to the direction of the displacement increment, or if an element is small with respect to the magnitude of the displacement increment. This is illustrated in Figure 2.9(a) and Figure 2.9(b), where the displacement field is voluntarily singular (only one node is moving). The best way to avoid such situation is to maintain every element as close as possible to a regular simplex [196]. This is the reason why mesh anisotropy is generally avoided in Lagrangian methods, or at least controlled carefully in the regions where the displacement field is known *a priori* to be oscillatory.

In Algorithm 2, a method is proposed to operate mesh motion progressively, with a constant checking of element flipping and quality decrease. This checking is based on the operations *coordinates()*, *volumes()* and *qualities()*, which are directly solved from the coordinates and connectivity arrays. Under the assumption that the initial mesh does not contain any flipped element, the condition at line 15 of Algorithm 2 ensures that no element flipping occurs during mesh motion. It is avoided by rolling back when it occurs, and starting again with a smaller displacement increment, as shown respectively in Figure 2.9(c) and Figure 2.9(d).

Of course, the same problem would appear even if small increments are used, hence the mesh has to be adapted at some point. This is triggered at line 17 if at least one of the two following conditions were met during mesh motion: element flipping was detected, or the worst quality of the mesh decreased too significantly. For example, the remeshing operation in Figure 2.9(e) solves the problem in Figure 2.9(b), as shown in Figure 2.9(f). The procedure *MeshTransport* at line 20 is a standard operation which consists in transporting all fields stored at nodes and elements from the old mesh to the new mesh after remeshing. This operation includes the correction for multiphase domains detailed in Subsection 2.3.2.

2.3.2 Transport of history variables

History variables are mainly present in solid mechanics, where updated Lagrangian formulations require the knowledge of stress and strain states element-wise, throughout the simulation. To describe the issue addressed in this subsection, the following element-wise Heaviside functions are defined for each phase i

$$H_i(\mathbf{x}) = \begin{cases} 1 & \text{where } \phi_i(\mathbf{x}) \geq 0, \\ 0 & \text{elsewhere.} \end{cases}$$

These H_i functions are computed on the elements of the initial mesh, and are transported by a basic transport method after remeshing: for each element of the new mesh, the value of any element-wise field is taken from the closest element of the initial mesh (distance is computed

Algorithm 2 Mesh motion with element flipping prevention, β is a user-defined tolerance on quality decrease, Q_{old} is a user-defined initial quality, or the quality obtained after the last remeshing, the lines in bold contain key operations that are enhanced in the present work.

```

1: function MESHMOVE(Mesh mesh, NodeField  $X_{obj}$ , Real  $\beta$ , Real  $Q_{old}$ )
2:   Real  $\alpha$ ,  $Q_{new}$ 
3:   NodeField  $X_{old}$ ,  $X_{new}$ 
4:   Mesh meshold
5:
6:   repeat
7:      $X_{old} \leftarrow$  mesh.nodes().coordinates()
8:      $X_{new} \leftarrow X_{obj}$ 
9:      $\alpha \leftarrow 2$ 
10:    repeat
11:      mesh.nodes().coordinates()  $\leftarrow X_{new}$ 
12:       $X_{new} \leftarrow \frac{X_{old} + X_{new}}{2}$ 
13:       $\alpha \leftarrow \frac{\alpha}{2}$ 
14:      until min(mesh.elements().volumes()) > 0
15:       $Q_{new} \leftarrow$  min(mesh.elements().qualities())
16:      if  $\alpha \neq 1$  or  $Q_{new} < \gamma Q_{old}$  then
17:        meshold  $\leftarrow$  mesh
18:        mesh  $\leftarrow$  MESHADAPT(meshold)
19:        MESHTRANSPORT(mesh, meshold)
20:         $Q_{old} \leftarrow Q_{new}$ 
21:      end if
22:    until  $\alpha = 1$ 
23:    return mesh
24: end function

```

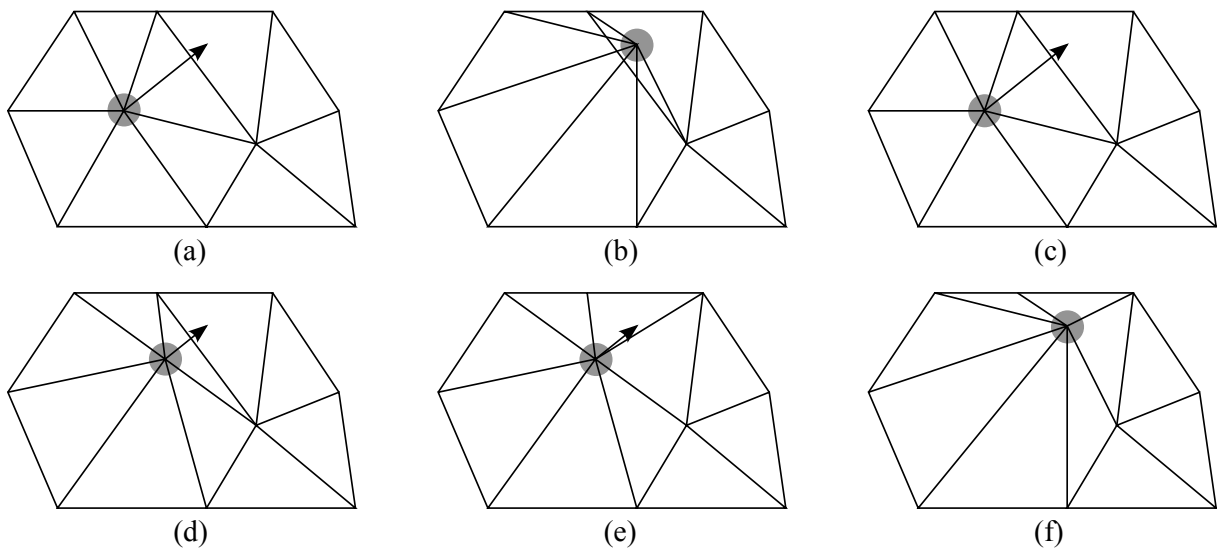


Figure 2.9 – Example of node motion (highlighted in light gray) provoking element flipping: (a) initial mesh, (b) mesh after motion, (c) rollback, (d) new try with half motion, (e) remeshing by edge swap, (f) final motion.

from center to center). Although the present method has the aim of conserving internal interfaces, some local optimizations of these interfaces may change their position, for example in the aggressive case illustrated in Figure 2.7(d). Thus, for some elements, recomputing Heaviside functions \tilde{H}_i from the LS functions modified by the remeshing process may yield a result different from H_i . As a consequence, an element may be attributed history variables from a phase it does not belong to, which is wrong from a thermomechanical point of view. This is illustrated in Figure 2.10, where an expected blue element of the new mesh has its barycenter (marked by a white star in Figure 2.10(b)) located in an element of the initial green phase (highlighted in white in Figure 2.10(b)), which makes it wrongfully considered as a green element.

To correct this mistake, two strategies seem possible: moving the interfaces in order to agree with the transported history variables, or correct the transport method in order to agree with the interfaces. In the present framework, it seems appropriate to leave interface tracking to the mesh motion and adaptation algorithms, and modify the transport of history variables. To correct this method, for each phase i , history variables of elements where transported H_i is different from recomputed \tilde{H}_i are corrected by projecting the history variable of the closest element which has $\tilde{H}_i = H_i = 1$. To perform this operation efficiently, the barycenters of all elements where $\tilde{H}_i = H_i = 1$ are stored in a specific structure described in Subsection 3.2.2. For each element where \tilde{H}_i is different from recomputed H_i , the cost of finding the closest element in this structure is logarithmic on the number of elements in the structure. Consequently, the cost of the present treatment is negligible. An example of corrected result is illustrated in Figure 2.10(c).

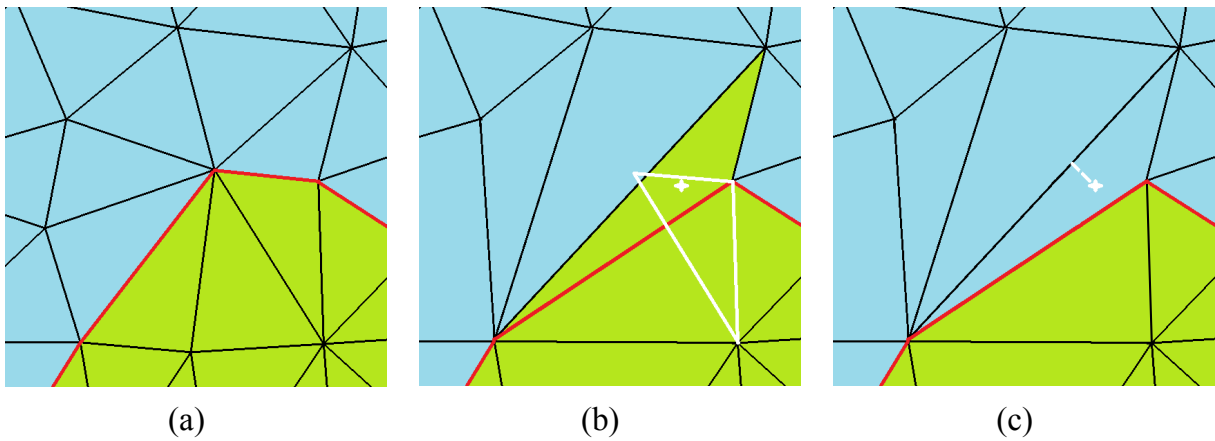


Figure 2.10 – Example of an incorrect transport of history variables: (a) initial mesh, (b) adapted mesh, (c) corrected transport. The two phases are colored in green and blue according to the H_i functions, and the interface is highlighted in red according to the ϕ_i functions.

2.4 Results

In this section, the proposed method is applied to track interfaces in multiphase simulations. Though these test cases are academic, they correspond to real and challenging computational solid and fluid mechanics problems. The efficiency of the algorithms presented in this chapter is investigated in terms of mesh quality and computation time. All computations are performed on a 1.2 GHz Intel Xeon processor. The volume conservation parameters are fixed to $Q_\mu = 0.05$, $Q_\sigma = 0$.

In an attempt to establish a panel of applications where the method presented in Section 2.2 and Section 2.3 could be competitive and preferable compared to standard approaches, several test cases are proposed. A particular attention is given to volume conservation and computation time for small and large displacements and deformations. Topological changes such as linkage of objects are also addressed. Unless otherwise mentioned, the domain Ω is the 3D box $[0, 1]^3$, an unstructured uniform isotropic mesh is used, and the time step is fixed to 0.01, all spatial and temporal data being nondimensionalized.

- IEUL refers to an Eulerian LS method where all interfaces are implicitly described by LS functions, the mesh remains fixed during the whole simulation, and convection is operated by solving $\frac{\partial \phi}{\partial t} + v \nabla \phi = 0$, with a first order implicit Euler scheme, a first order Lagrange FE and SUPG stabilization. More advanced and recent stabilization methods, such as [198], could be used, but it is reasonable to suppose that the chosen stabilization method would not change the conclusions raised in this section.
- ILAG refers to a Lagrangian LS method where all interfaces are implicitly described by LS functions, and convection is operated by mesh motion using Algorithm 2 with $\beta = 0.5$, but regardless of the interfaces and their conservation.
- FLAGc refers to the method proposed in this chapter, which is the same as ILAG, but with explicit interface meshing and enhanced volume conservation.

For the comparison to be fair, the initial mesh is the same for all methods, but in the case of FLAGc an explicit interface is obtained using the interface fitting procedure described in Section 2.1. As mesh quality is likely to be deteriorated after this operation, it is followed by a mesh adaptation step using Algorithm 1. This ensures that the initial interpolation error is the same for all methods, though this initial adaptation step may induce some volume loss at the initial state for the FLAGc method if relaxation occurs.

Computation time measurements consider only the solution of the convection equation in the IEUL case, and the whole cost of Algorithm 2 in the ILAG and FLAGc cases, which includes mesh motion, remeshing, and transport of FE fields. For comparisons between these last two methods, the Number of Remeshing Operations (NRO) is also reported.

2.4.1 Large displacements: sphere rotation

Though in this chapter no material behavior is defined, this first problem has to be seen as a rigid sphere rotating inside a fluid in turbulent flow. Hence, the displacements and the deformations inside the fluid cannot be modeled by a Lagrangian mesh. However, an Arbitrary Lagrangian-Eulerian method could be used to track the rotation of the sphere by mesh motion [182, 183]. The presently proposed method falls in this category. In this test, only the IEUL and the FLAGc

methods are compared, and in the case of the FLAGc method mesh motion is applied only where $\phi \geq 0$.

The set-up is directly inspired from [177], where an enhanced LS Method was proposed, which consisted in adding Lagrangian markers on an Eulerian LS, also to reduce LS diffusion during convection. The sphere is placed at $(0.5, 0.75, 0.5)$, has a radius of 0.15, and its rotation is ruled by the velocity field

$$v(\mathbf{x}) = (-2\pi(0.5 - x_2), 2\pi(0.5 - x_1), 0).$$

This case is illustrated in Figure 2.11.

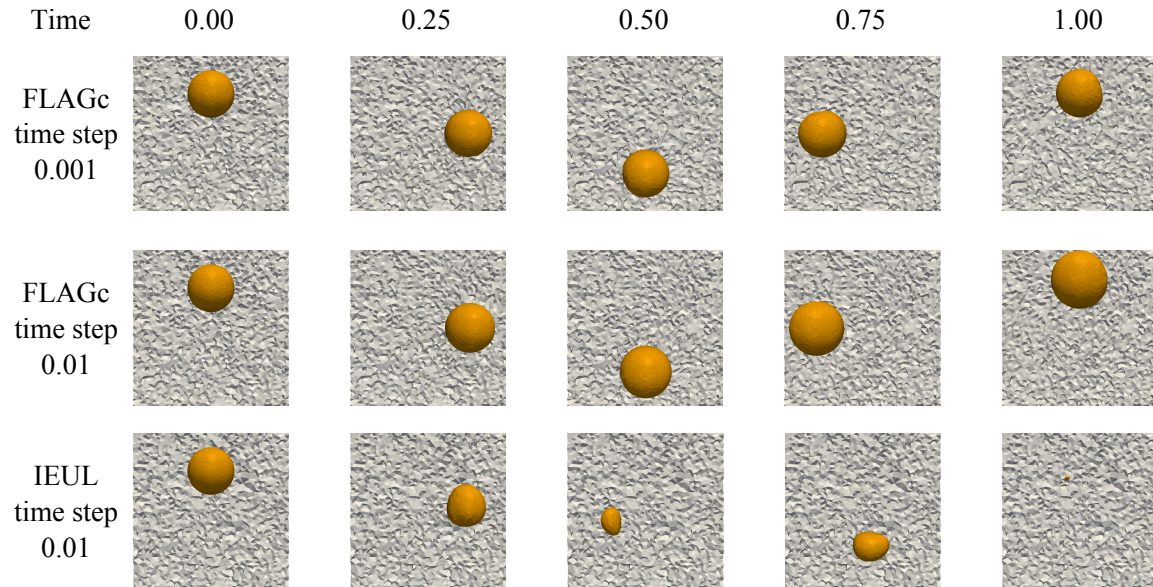


Figure 2.11 – Sphere rotation with a mesh size of 0.025 using the FLAGc method with two different time steps and the IEUL method.

It can already be observed in Figure 2.11 that diffusion is way more significant for the IEUL method, while it is controlled using the FLAGc method. On the one hand, this poor performance for the IEUL method was expected, as the meshes used in this section are not as fine as the finite difference grids used in Reference [177] for example, or the structured 2D FE meshes used in Reference [198]. On the other hand, the performance of the FLAGc method could be improved by starting with an explicit mesh of the interface directly built from a proper meshing tool [192], and fixing Q_μ to 0 since there is no interface deformation. Volume conservation would then be optimal, as demonstrated in Appendix A.

However, it seems obvious that other moving mesh techniques such as [182] or [183] would certainly yield the same result with far less computation time. These techniques consist in defining artificial velocity fields for the nodes inside the fluid phase, in order to maintain a good quality as long as possible, and delay the use of computationally expensive algorithms such as Algorithm 1.

Another possibility for rigid body motions would be embedded mesh techniques [199], where the interfaces are implicit, and carried not by FE fields on the computational mesh, but by separate surface meshes. Nevertheless, these approaches are restricted to rigid body motions or small deformations, while the LS methods (FLAGc, ILAG and IEUL) considered in this section cover a wider range of applications.

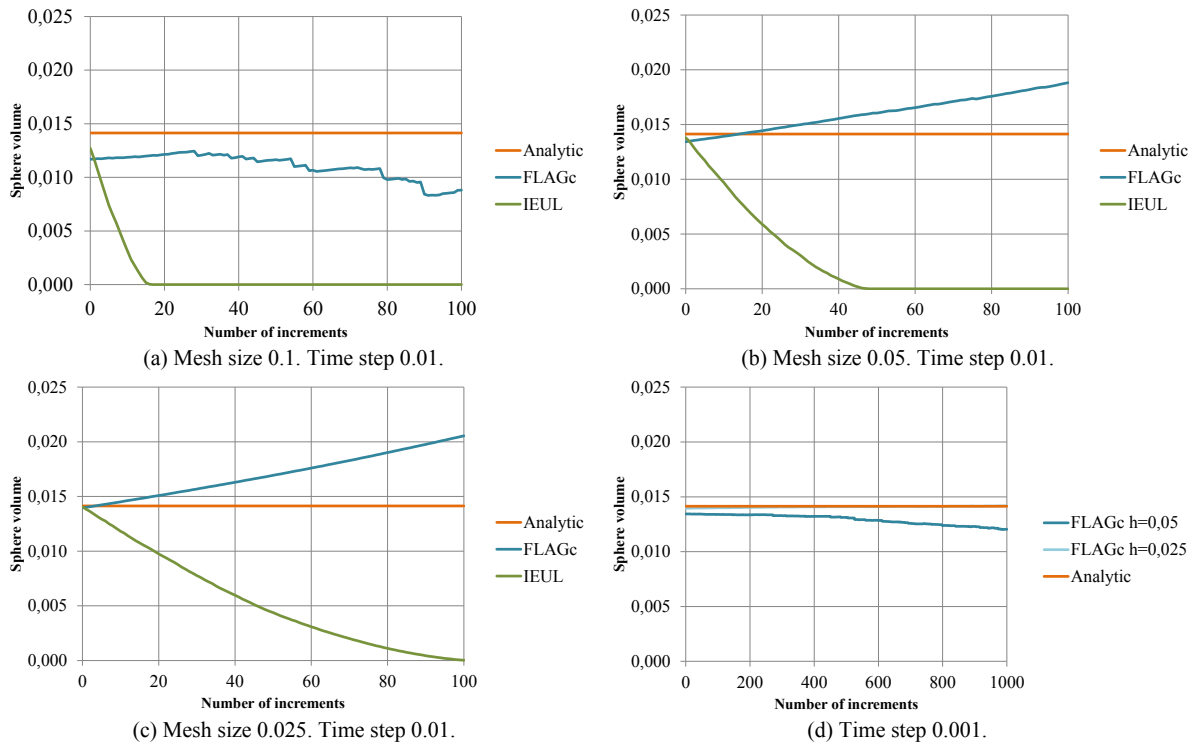


Figure 2.12 – Evolution of sphere volume during a full rotation using the reference time step and a mesh size of: (a) 0.1, (b) 0.05, (c) 0.025. (d) Evolution of sphere volume during a full rotation using a time step of 0.001.

In Figure 2.12(b) and Figure 2.12(c), the IEUL method shows first order convergence, but the results regarding the FLAGc method are surprising, as the volume goes increasing, and so does the error. These startling results are due to the fact that between Figure 2.12(a) and Figure 2.12(b), there is a major change in the composition of the volume error: the temporal error becomes dominant over the spatial one. This is confirmed by Figure 2.12(d), which is the same numerical experiment, but with a time step 10 times smaller. Additionally, in Figure 2.12(a), increments where remeshing was operated can be clearly recognized as the points where sphere volume drops abruptly. Indeed, a larger mesh size reduces the number of calls to the remeshing procedure. On the contrary, in Figure 2.12(b) and Figure 2.12(c), the drops of the sphere volume are reduced both by the fact that the mesh is finer, and that remeshing is more frequent, and are hence less visible.

More precise information is summarized in Table 2.1, which also reports the computation time for each simulation. The relative error is computed based on the sphere volume, and the measurements are performed after 20 increments (resp. 200 increments for the cases of Figure 2.12(d)). While the FLAGc method is approximately 10 times costlier, it is also more accurate. In particular, it is robust and gives a satisfactory solution, even for the coarsest mesh size, while the sphere did not survive 20 increments for the IEUL method. Using a mesh size of 0.1 for the FLAGc method and 0.025 for the IEUL one, the computation time is inverted and the IEUL method is approximately 10 times costlier, for an error that is more than 3 times bigger than the one obtained with the FLAGc method.

Note that since in this case, there are no continuum mechanics equations to solve, the computation time for the finer meshes is underestimated. In practice, if one had to use finer meshes to avoid diffusion, the cost of all other operations (Navier-Stokes solution, output writing, etc.) would

increase the advantage of the FLAGc method. Therefore, for coarse meshes, or when the interfaces show multiple scales of variations, the FLAGc method would be significantly more interesting than the IEUL one in preserving all variations during the simulation, including the smallest ones.

Method	Mesh size	Time step	Computation time (s)	Error (%)
FLAGc	0.1	0.01	62	15.8
	0.05	0.01	570	10.0
	0.025	0.01	8935	15.3
	0.05	0.001	580	6.5
	0.025	0.001	6909	0.3
IEUL	0.1	0.01	9	100
	0.05	0.01	98	93.6
	0.025	0.01	808	57.8

Table 2.1 – Computation time and relative error on the volume of the sphere after 40% of rotation for the two methods, the three used mesh sizes, and the two used time steps.

2.4.2 Large deformations: sphere stretching

This case is representative of an heterogeneous material with multiple phases that are likely to deform at comparable rates. A sphere of radius 0.15 is placed at the center of the box, and an incompressible vertical stretching is applied by defining the velocity field as

$$v(\mathbf{x}) = \left(-\frac{1}{2}(x_1 - 0.5), 1(x_2 - 0.5), -\frac{1}{2}(x_3 - 0.5) \right).$$

With such stretching of the interface, pure moving mesh techniques such as [182] or [183] do not apply anymore, since interfaces need to be remeshed. This case is illustrated in Figure 2.13. The evolution of the volume of the sphere during stretching is presented in Figure 2.14 for three different mesh sizes. There is a clear difference of accuracy between the IEUL method, which diffuses at each increment, and the ILAG method, which diffuses only at remeshing. The diffusion at remeshing is then drastically reduced with the FLAGc method (note that remeshing is not triggered at the same increments for the ILAG and FLAGc methods).

Additionally, convergence can be observed on these graphs for the three methods, as diffusion is reduced by mesh refinement. This is confirmed in Table 2.2, where the relative error is computed based on the sphere volume after 100 increments. For the FLAGc and ILAG methods, the gap between the error using the coarsest mesh size and the intermediary one is big due simply to the fact that the first mesh size is too coarse for such stretching. Then, a first order convergence is obtained. The same observation can be made for the IEUL method, with the difference that the sphere is totally diffused using the coarsest mesh, as illustrated in Figure 2.14(a).

Finally, measurements of computation time in Table 2.2 must be considered carefully since they highly depend on the number of remeshings triggered for the ILAG and FLAGc methods. Though this number is low in the present case, it could be more significant depending on the magnitude of the deformation the mesh undergoes at each time step. The main conclusion that can be raised from these results is that the volume preservation constraint does not induce a significant cost increase, as at equal NRO, the computation time of the FLAGc method is comparable to the one of the ILAG method.

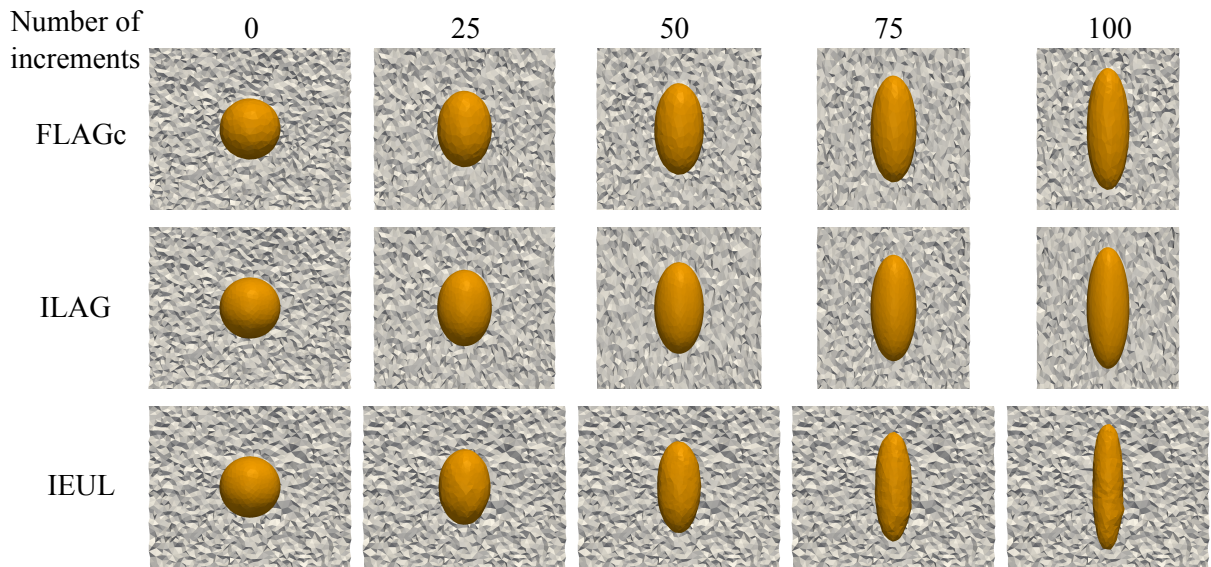


Figure 2.13 – Sphere stretching with a mesh size of 0.025 using the three different methods.

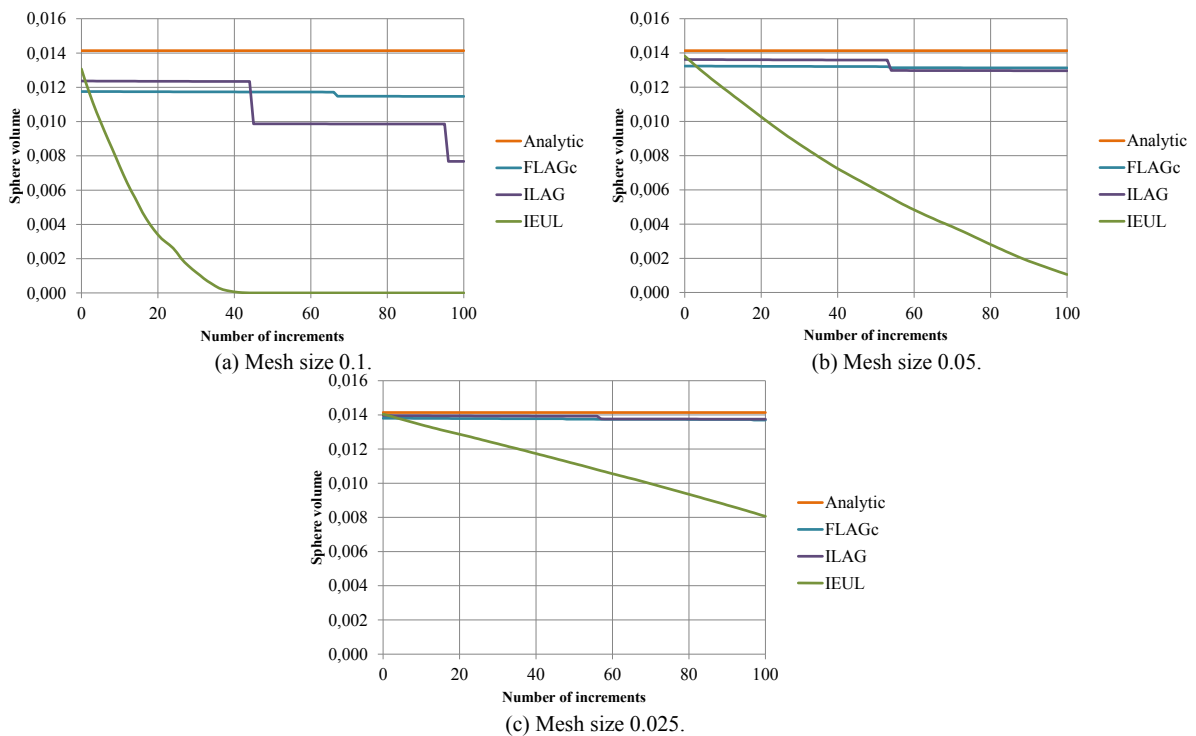


Figure 2.14 – Evolution of the volume of the sphere during its stretching. After 100 increments, the major diameter is doubled, while the other two are divided by $\sqrt{2}$. The mesh size is: (a) 0.1, (b) 0.05, (c) 0.025.

Method	Mesh size	Computation time (s)	Error (%)	NRO
FLAGc	0.1	6	18.9	2
	0.05	49	7.2	2
	0.025	820	3.1	3
ILAG	0.1	10	45.7	3
	0.05	46	8.3	2
	0.025	422	2.7	2
IEUL	0.1	23	100	
	0.05	252	92.5	
	0.025	2101	43	

Table 2.2 – Computation time and relative error on the volume of the sphere after full stretching for the three methods and the three used mesh sizes.

2.4.3 Topological changes: sphere stacking

Applications where topological changes occur do not restrict to crack propagation, where crack branching and merging are difficult to handle from a meshing point of view [114], but easily modeled using an implicit interface. Other examples are recrystallization [168], where grains may appear or disappear during the simulation, or polymer injection, where bubbles may nucleate and link [191, 200]. Generally, in all these applications, explicit interface meshing becomes very difficult and is generally avoided [191, 200].

The present test aims at showing that the present method can handle complex topological changes and, more importantly, maintain a good element quality when they occur. It is designed to reproduce what happens during void linkage in ductile fracture.

The domain contains three spheres of identical radius 0.15 which are placed at (0.3, 0.2, 0.5), (0.7, 0.2, 0.5) and (0.5, 0.5, 0.5), and the lower face of the box is of the same material as the spheres (ϕ is zero on this face). In this test, a Stokes problem is solved using the mixed $P1^+/P1$ FE method described in Subsection 1.2.1 at each time step, with homogeneous Dirichlet boundary conditions for the velocity, and homogeneous Neumann boundary conditions for the pressure. The parameters of this problem are the nondimensional viscosity and gravity, which are set respectively to 1000 and (0, -1000, 0) inside the spheres, and 10 and (0, -10, 0) in the rest of the domain. As illustrated in Figure 2.15, the spheres and the plane are expected to link altogether (as in polymer injection for example). Due to the significant computational cost of the Stokes solver (not reported here), the configuration with a mesh size of 0.025 is not considered for this test.

For the coarsest mesh, the results in Figure 2.16(a) show a poor performance of the FLAGc method. Maintaining a body-fitted mesh raises complicate issues when the spheres start to touch, consequently the NRO is greater than with the ILAG method (Table 2.3), and volume relaxation is omnipresent. Then, when the spheres have linked (after ≈ 500 increments), mesh quality seems to have been restored, as volume is better conserved. The main difference between the FLAGc method and the ILAG one is that the ILAG method diffuses approximately the same amount of volume whatever the encountered deformation or topological change, while the FLAGc method controls this diffusion.

In fact, if the FLAGc method was used with an implicit interface, one could assume that remeshing would be less frequent, and a better performance could be recovered. Although

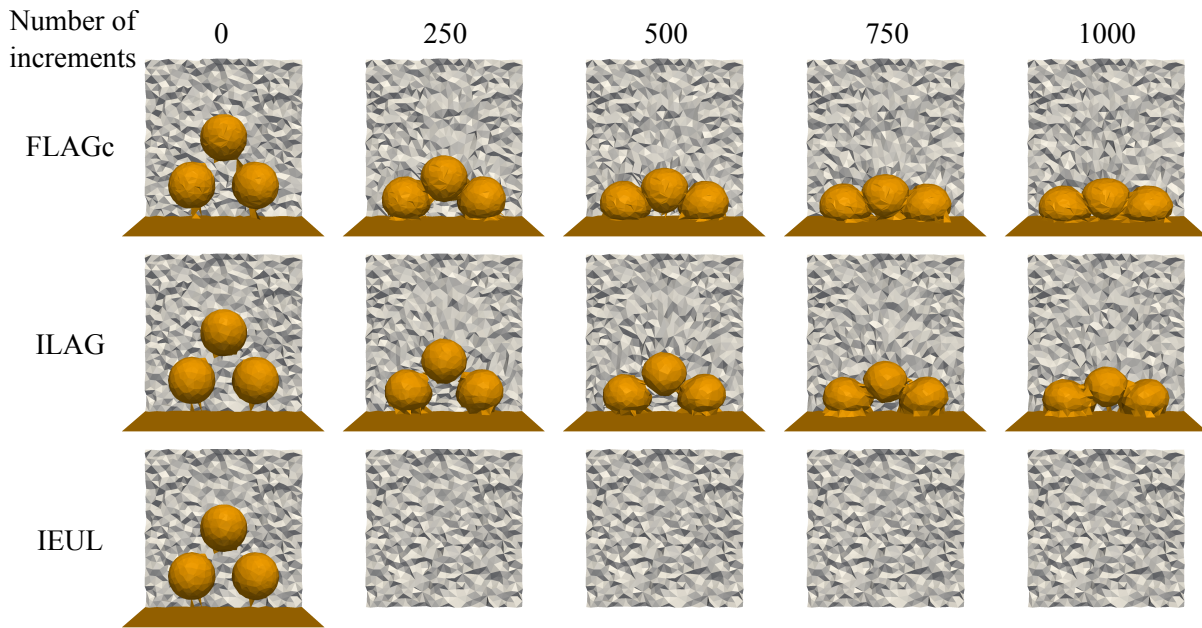


Figure 2.15 – Spheres stacking with a mesh size of 0.05 using the three different methods.

such experiment is not performed in this section, the results in Figure 2.16(b) with a finer mesh prove that the FLAGc method controls indeed volume diffusion, while the ILAG method keeps releasing the same amount of volume at each remeshing.

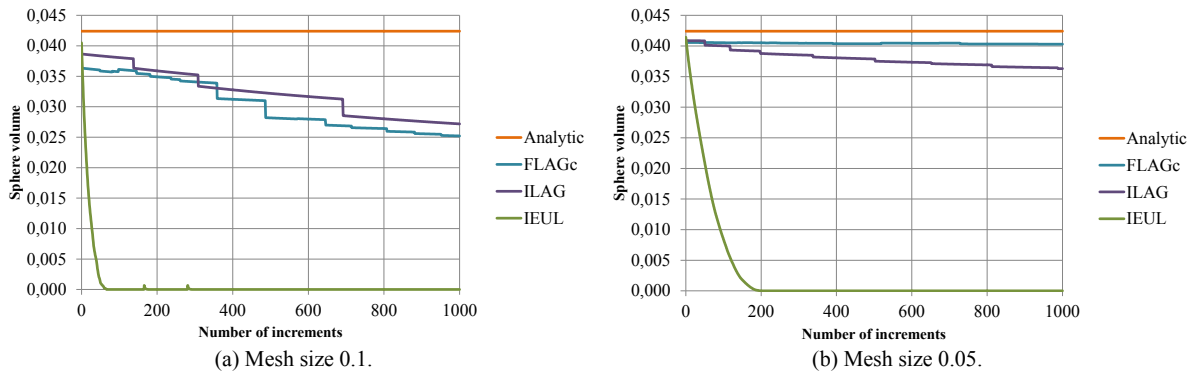


Figure 2.16 – Evolution of the volume of the spheres during stacking for a mesh size of: (a) 0.1, (b) 0.05.

Regarding the IEUL method, the conclusions are the same as in the preceding sections: convergence is of first order, but the difference with the other methods is large. An interesting point is that the IEUL method is way costlier in this case, as reported in Table 2.3. This is due to the fact that the cost of the ILAG and FLAGc methods is mainly due to Algorithm 1. Decreasing the time step has no reason to influence significantly the NRO and hence to change significantly computation time. However, the IEUL method relies on the solution of a convection equation at every time step. Although a preconditioned conjugate residual iterative method is used and the number of iterations decreases with the time step, there is still an irreducible cost at each solution.

Method	Mesh size	Computation time (s)	Error (%)	NRO
FLAGc	0.1	103	40.6	16
	0.05	889	5.0	22
ILAG	0.1	62	35.9	4
	0.05	600	14.4	9
IEUL	0.1	251	100	
	0.05	2940	100	

Table 2.3 – Sphere stacking test: computation time and relative error on the volume of the spheres after 1000 increments for the three methods and the two used mesh sizes.

2.4.4 Robustness investigation

For all preceding numerical experiments, a particular attention was given to volume conservation and computation time. Because the method proposed in this chapter is based on a mesh adaptation algorithm, it is also important to verify that this algorithm is efficient. In that purpose, element quality, as defined in Equation (2.1), is computed at each increment and integrated over time for all tests performed with the FLAGc method.

This quality distribution is expected to be concentrated around two peaks corresponding respectively to the elements of the domain far from any interface, and the elements having their quality deteriorated by the presence of a neighboring interface. As most histograms presented in Figure 2.17 feature only one peak, a first qualitative conclusion is that, in most cases, element quality is not deteriorated significantly by the volume conservation constraint.

First, in the sphere rotation case in Figure 2.17(a), it can be seen that element quality is efficiently restored after the passing of the sphere, as element quality is concentrated around 0.7 for all used mesh sizes. Regarding the sphere stretching case in Figure 2.17(b), the histogram is slightly shifted to the left because the whole domain is stretched and remeshing is not operated frequently enough to maintain higher quality; hence, the quality of some elements is allowed to decrease. The fact that there are very few ill-shaped elements is nevertheless satisfactory and remeshing based on a quality decrease criterion seems appropriate.

Finally, element quality distribution for the spheres stacking case is the only distribution that clearly exhibits two distinct concentration points: one around 0.3 and one around 0.7 (Figure 2.17(c)). This suggests that a whole part of the domain is represented with elements of inferior quality and that these elements are kept in the mesh for a long time. This is most likely due to the small space between the spheres that progressively narrows down and then disappears. The numerous contact areas between the spheres and the plane and between the spheres themselves could also explain this decrease of mesh quality.

A zoom on the sphere in the lower left corner is presented in Figure 2.18. It is important to point out that the FLAGc method handles very well the linkage events between the different objects, hence preserving the advantages of the LS method. While in the literature mesh regeneration techniques have been used to address such problems in Lagrangian frameworks [114, 181], to the author's best knowledge, this is the first time that such results are obtained with body-fitted interfaces, based purely on mesh adaptation. This is interesting in a point of view of computational cost and parallel computing, as mesh adaptation relies only on local operations.

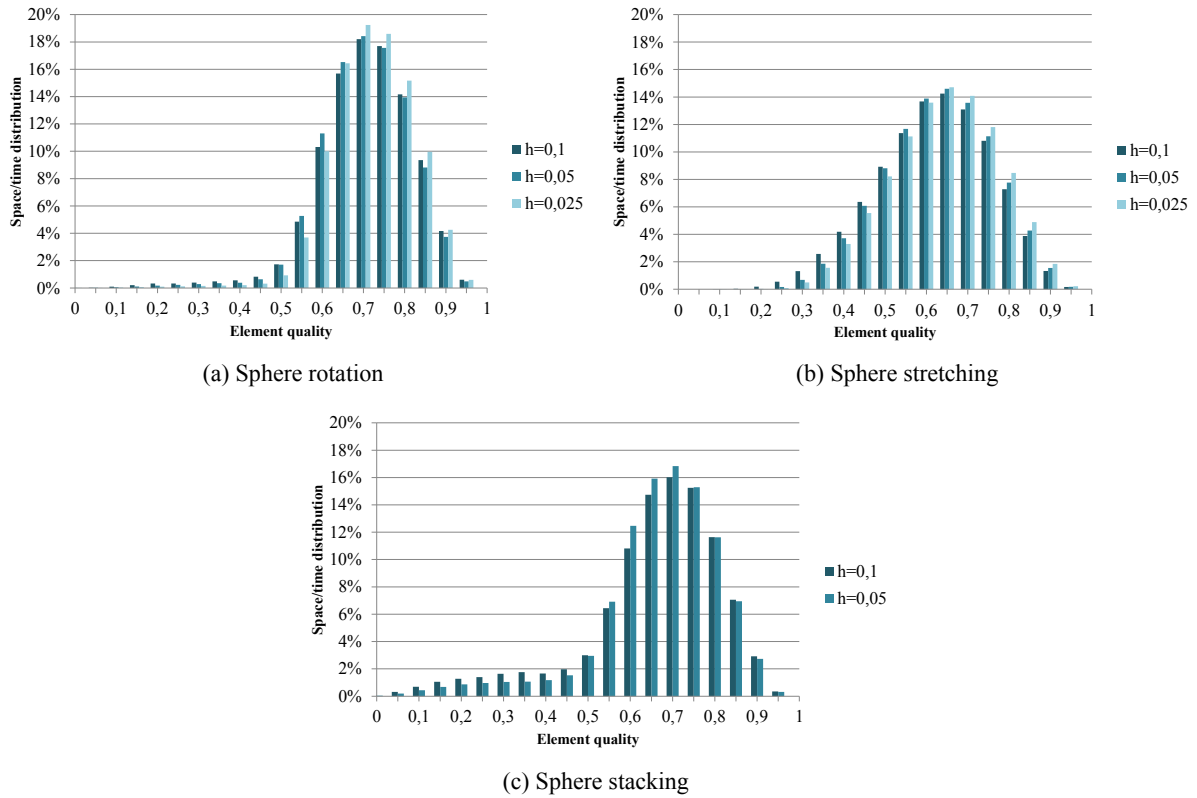


Figure 2.17 – Distribution of element quality integrated on all increments for: (a) the sphere rotation case, (b) the sphere stretching case, (c) the spheres stacking case.

Number of increments

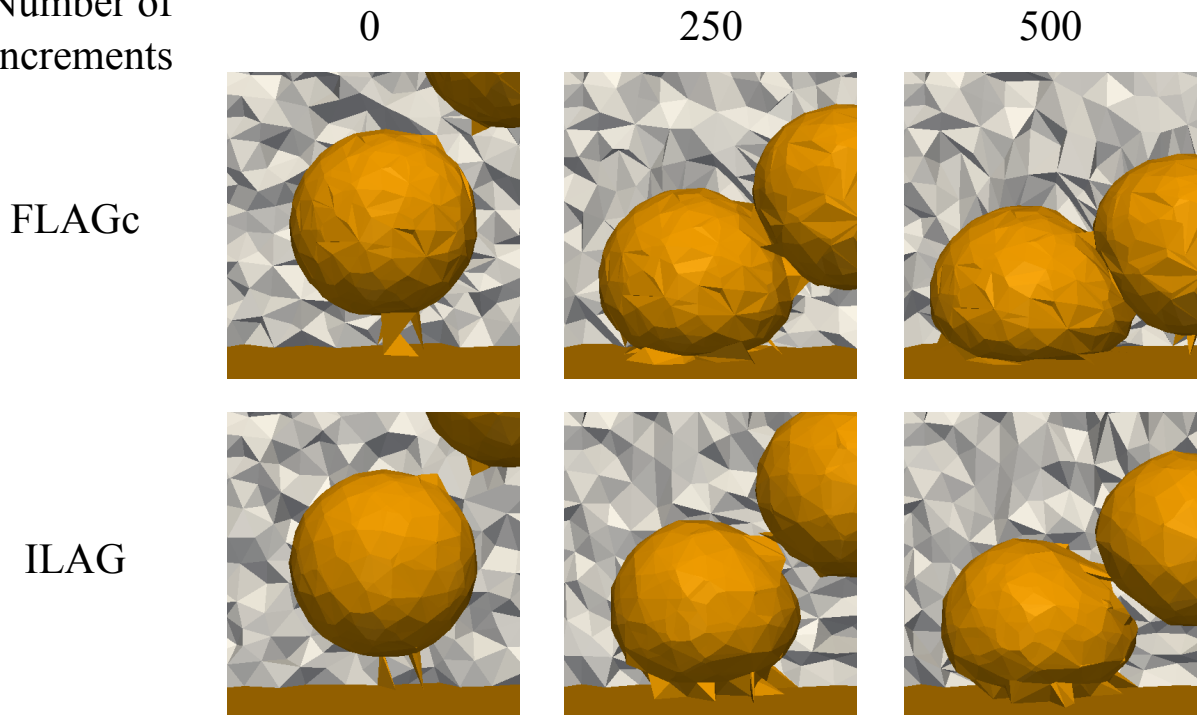


Figure 2.18 – Spheres stacking with a mesh size of 0.05 using the two Lagrangian methods, zooming in on the lower left corner.

2.5 Parallel implementation

As described in Subsection 1.2.1, the FE code in which all the present developments are integrated is based on a distributed computing paradigm. Because the mesh is partitioned among multiple processes, mesh modifications have to be undertaken carefully. In particular, it would be very technical to implement mesh modification operations on patches containing nodes that are shared among multiple partitions. Although it is stated in Subsection 1.2.1 that the FE code lacks methods to ease the development of such operations, it is not true in the case of mesh adaptation, which is at the core of this FE library [125].

The methodology implemented in this library for parallel remeshing consists in first remeshing independently each partition, inter-partition boundaries being blocked. Then, repartitioning is performed so that poor quality elements land far away from these inter-partition boundaries, using the methodology introduced in Reference [125], and remeshing is applied independently again. As illustrated in Figure 2.19, this cycle is repeated several times. Thus, all methods presented in Section 2.1 and Section 2.2 can be implemented in a totally sequential manner, with no regard with respect to the parallel aspects, apart from the fact that inter-partition boundaries are tagged and blocked. All parallel aspects, mainly repartitioning, are handled by the existing FE code.

However, in order to ensure that all edges of the mesh are actually reached by the fitting procedure described in Section 2.1, the quality of the elements with edges that are not conform to all interfaces is penalized. The repartitioning procedure will then move inter-partition boundaries far from these elements, so that they can be remeshed. Additionally, the method proposed in Reference [125] established a fixed number of remeshing/repartitioning cycles, which did not necessarily allow for a global adaptation of the whole mesh. An additional iteration was hence added so that these cycles are repeated until all nodes and elements of the mesh have been actually reached by the algorithms presented in Section 2.1 and Section 2.2.

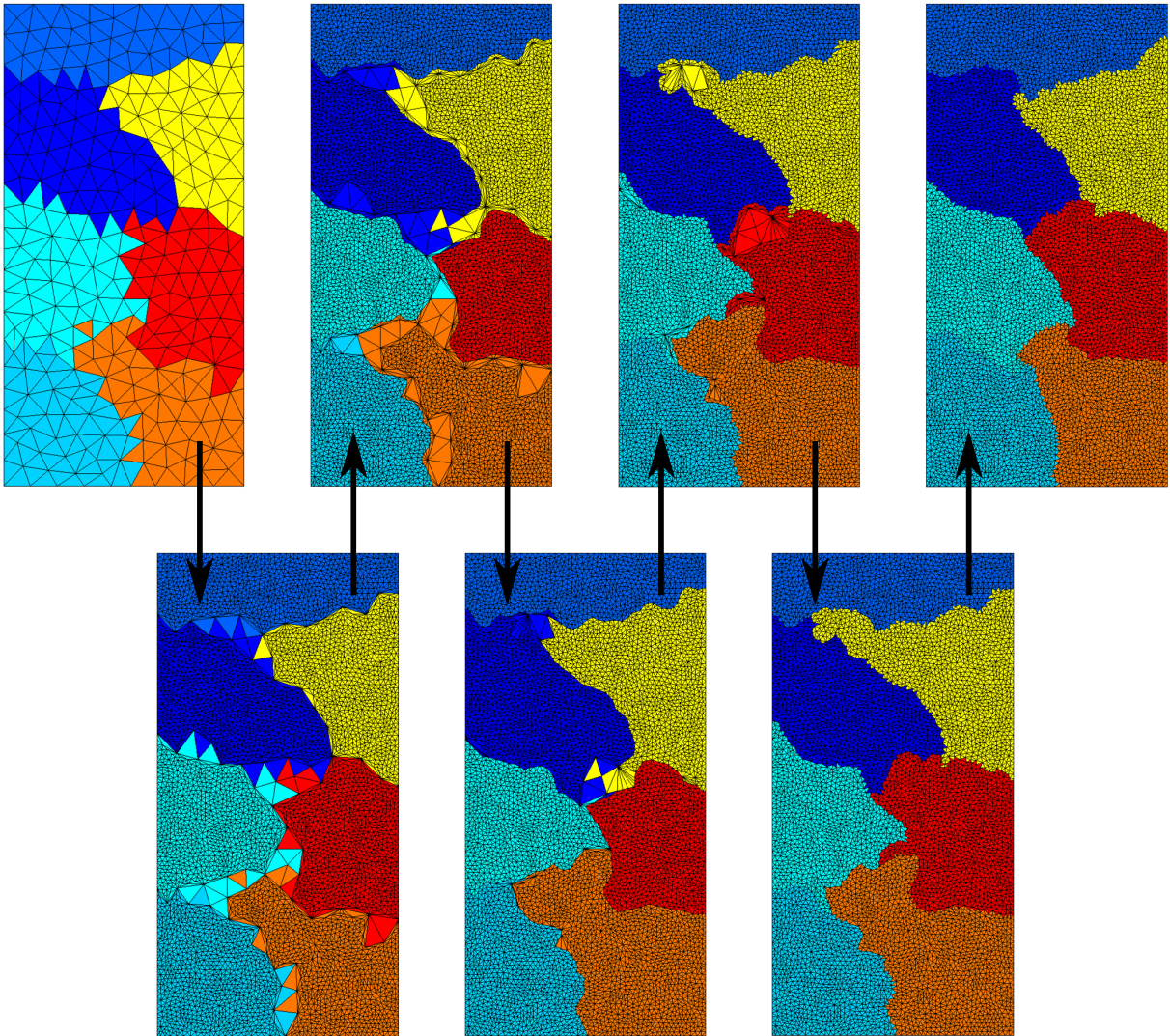


Figure 2.19 – Application of the parallel remeshing procedure to a 2D mesh, arrows pointing downward represent remeshing steps, while arrows pointing upward represent repartitioning steps. Partitions are distinguished by the coloring. Figure reproduced from [201].

2.6 Extension to computational fracture mechanics

Insertion of new interfaces during simulations with explicit representations is usually done either by splitting existing faces of the mesh, or generating a new mesh carrying the new interfaces [114, 185, 186]. In this section, a method requiring only mesh adaptation is proposed, hence avoiding to modify the mesh in regions far from the crack.

To insert a crack, three LS functions are defined, as illustrated in Figure 2.20. Two of these LS functions define the two faces of the crack, while the third one defines a filter enabling to propagate the crack progressively instead of letting it cross the whole domain. These functions are defined analytically using appropriate crack initiation or propagation criteria (Chapter 4 and Chapter 5), then the interface fitting procedure is applied only in the regions selected by the filter LS function.

For example, a small portion of the matrix/particle interface can be debonded as in Figure 2.20(b), or a particle can be fragmented without affecting neighboring particles as in Figure 2.20(c). The use of LS functions aims at simplifying fracture modeling, which does not need to implement mesh modification operations, as these operations are already implemented in Algorithm 1. These operations are only local, which enables to reduce drastically the computational cost with respect to a global mesh generation procedure [114].

It would be tempting and more rigorous to define only two LS functions, namely one for the filter and one for the crack, mesh the latter using the technique in Section 2.1, and then split the faces carrying it to insert the free surface. However, a key aspect of the present developments is the ability to handle void linkage, which requires to mesh the void phase, as in Subsection 2.4.3. Hence, it is necessary to define two crack faces and have them slightly separated by a small (one order below mesh size) numerical thickness ϵ_l so that the elements belonging to the intersection between the three LS functions do not have a zero volume. These elements are added to the LS function of the void phase, and removed from other LS functions, so that the mesh adaptation algorithm can be applied.

An important issue raised by this approach is that these elements that are inserted between the two crack faces are likely to be of very poor quality, due to the small numerical thickness ϵ_l . Thus, the volume conservation constraint defined in Subsection 2.2.2 is likely to be relaxed in these elements, leading to crack closure. To avoid this, the authorized relative change ϵ_Q for the volume occupied by the void phase inside each patch during mesh adaptation, given by Equation (2.2), is modified by replacing each quality parameter (Q_μ , Q_σ) and variable (Q_{min}) by volumes (V_μ , V_σ , V_{min}). For instance, the volume threshold V_μ under which the volume conservation constraint is totally relaxed for the void phase will be $\ll \epsilon_l^3$. Numerical examples using this computational fracture mechanics with LS-based crack modeling and remeshing are presented in Chapter 4 and Chapter 5.

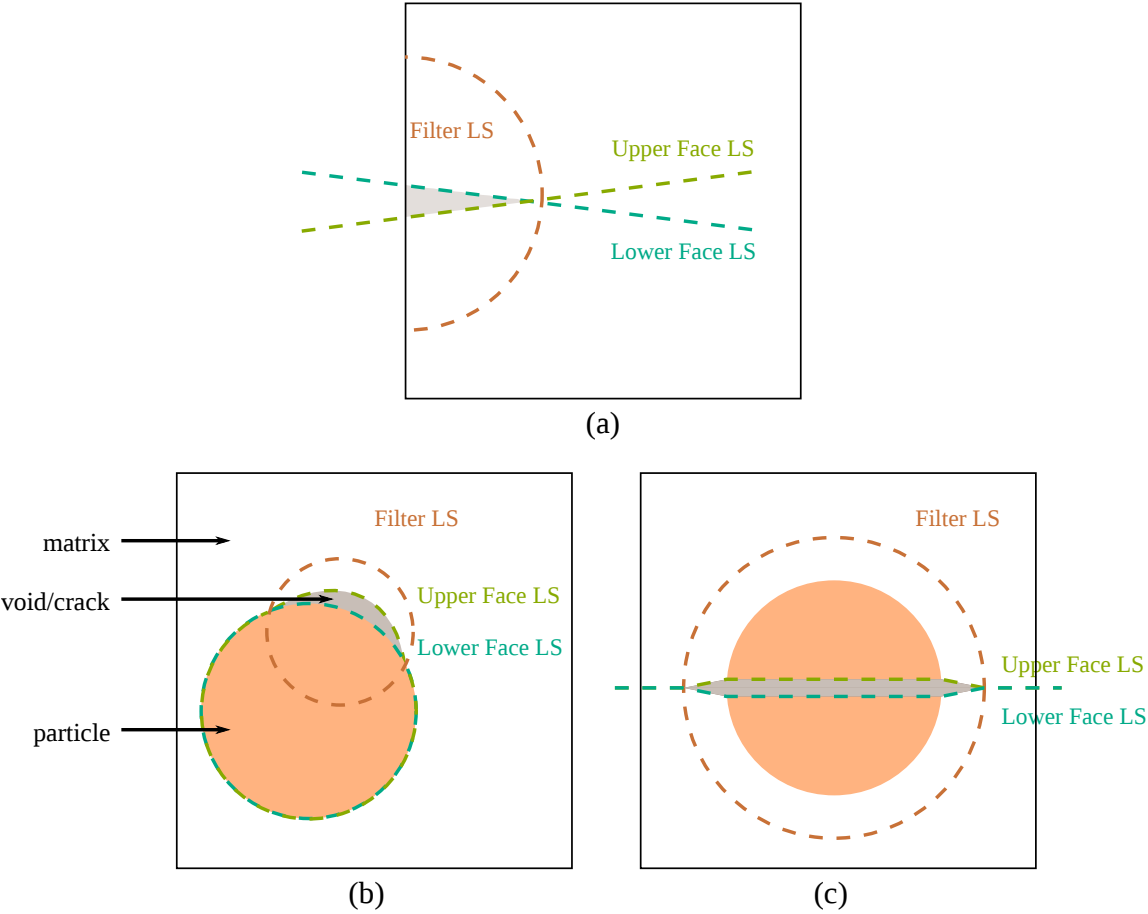


Figure 2.20 – Insertion of a crack (in gray) using three LS functions: (a) crack initiation at a free boundary, (b) debonding crack, (c) fragmentation crack. The numerical thickness separating the two faces is exaggerated in these illustrations.

Conclusion

Modeling microstructures such as those found in metal alloys is generally carried out in a Lagrangian framework. The Level-Set (LS) method is an interesting numerical tool as it enables to model easily complex topological changes, such as void linkage. However, for large deformations, remeshing operations, which are necessary in Lagrangian simulations, are usually pointed out to be too computationally demanding. In this chapter, coupling a mesh motion algorithm with a quality and element flipping criterion (Section 2.3), it is proved that remeshing can be delayed enough so that a Lagrangian LS method becomes more than interesting compared with an Eulerian LS method, even when large deformations and topological changes occur (Subsection 2.4.2 and Subsection 2.4.3).

The main defect of the Lagrangian method is the tendency of significantly diffusing the interfaces and the volume at each remeshing operation. The new remeshing method with volume conservation constraint presented in this chapter (Section 2.2) is then proved to control and reduce this diffusion, and promising results are obtained for large displacements (Subsection 2.4.1). Compared to the first two approaches, this new method also adds explicit interface meshing (Section 2.1), which is well-known to raise difficulties when large deformations and topological changes occur. Thanks to the intermediary use of LS functions, the method is proved to be able to handle such events without a significant loss of accuracy or increase of computation time.

To the author's best knowledge, this is the first time that such results are obtained with explicitly meshed interfaces, based purely on mesh adaptation. This is interesting in a point of view of computational cost and parallel computing, as mesh adaptation relies only on local operations. It would be interesting to apply this method to other applications, such as multiphase flow, where surface tension and high discontinuities at interfaces are difficult to capture when interfaces are not explicitly meshed. This problem also appears in static and especially dynamic recrystallization modeling, with the added difficulty that multiphase junctions have to be handled. Such topics are considered in Chapter 7.

As a conclusion, this adaptive LS Method with enhanced volume conservation is a robust tool that can be used to track interfaces in simulations where all types of events occur (large displacements, large deformations, topological changes). This robustness also allows to use coarser meshes or to improve the conservation of all scales of variations of the interfaces, including the smallest ones. These features are easily extended to distributed computing, though some issues linked to the mesh generation procedure have to be addressed (Section 2.5).

Coupled together, these parallel mesh generation and adaptation techniques can be used to generate body-fitted meshes from LS functions, enabling fracture mechanics applications where new interfaces can be captured on-the-fly during the simulation (Section 2.6). Compared to previous work, this approach preserves the ability to initiate and propagate cracks of arbitrary shapes, hence avoiding any mesh dependency. Although there is still a loss of mass, as the inserted nuclei is given an artificial volume, this loss of mass is drastically reduced thanks to body-fitted meshing. Additionally, crack tips are captured with no excessive mesh refinement. An important aspect of this computational fracture mechanics approach is that, because the cracks and hence the void phase are represented by LS functions and meshed, the adaptive LS method discussed above can be applied to the void phase. For instance, a well-known issue with eXtended Finite Element Method (X-FEM) techniques is that the elements carrying the crack cannot be remeshed due to their enrichment. Thus, applications of these techniques to the large deformations induced by void growth and coalescence are limited. Such issues are not encountered with the proposed method as remeshing operations are used to track the transformation of

a sharp crack into a spherical void, and then its coalescence with neighboring voids (Chapter 4). An interesting problem raised by the presence of cracks is the occurrence of contact and penetration problems, including self-contact. These issues are addressed in Appendix A.

Section 2.1 and Section 2.5 are highly inspired from results published in Reference [40], while the remaining sections of this chapter, with the exception of Section 2.6, are highly inspired from results published in Reference [41].

Chapter 3

Computation and use of signed distance functions

There's always a bigger fish.

Qui-Gon Jinn

- Introduction 94
- 3.1 Curvature-based mesh adaptation 95
 - 3.1.1 Metric fields 95
 - 3.1.2 Error estimators 96
 - 3.1.3 Gradient and Hessian recovery 98
 - 3.1.4 Results 99
- 3.2 Level-Set reinitialization 103
 - 3.2.1 Introduction 103
 - 3.2.2 Algorithm 104
 - 3.2.3 Results 110
 - 3.2.4 Conclusion 118
- 3.3 Connected Components identification 120
- 3.4 Image immersion and meshing 124
 - 3.4.1 Method 124
 - 3.4.2 Results 125
- Conclusion 133

Résumé en français

Dans ce chapitre, trois outils numériques supplémentaires sont ajoutés à la méthode éléments finis. Parmi les objectifs figurent l'import de données acquises par imagerie à rayons X vers le maillage éléments finis et la génération de maillages adaptés à ces données. La technique d'import d'images décrite dans ce chapitre requiert des opérations de traitement d'image assez coûteuses, mais qui ne sont appliquées qu'une fois pour chaque image. Afin de limiter ces coûts à la fois en termes de consommation mémoire et temps de calcul, ces traitements sont systématiquement exécutés à l'aide du code éléments finis lorsque cela est possible. Ainsi, les algorithmes parallèles implémentés dans ce code sont exploités au maximum de leurs capacités.

L'adaptation du maillage aux géométries trouvées dans les images, et plus généralement à la morphologie des microstructures, s'appuie sur un recouvrement de la matrice hessienne de chaque fonction de niveau. Ce recouvrement est réalisé à l'aide d'une implémentation distribuée d'une technique de recouvrement par patches superconvergent de second ordre détaillée dans ce chapitre. Certaines valeurs propres des matrices hessiennes des fonctions de niveau représentent les courbures principales locales des interfaces et sont utilisées pour raffiner le maillage dans les régions à haute courbure principale maximale.

Cet estimateur d'erreur est validé numériquement sur des cas tests où il est couplé avec l'algorithme d'adaptation de maillage vu au chapitre précédent. Des ordres de convergence proches de ceux prédits par la théorie sont obtenus. Pour des géométries singulières, ces ordres de convergence sont amoindris, ce qui est également en accord avec la théorie.

Pour que l'estimateur d'erreur soit fiable, il est important que les fonctions de niveau restent aussi proches que possible de leur définition initiale de fonctions distance signée à l'interface. En effet, une irrégularité de ces fonctions mènerait à une mauvaise estimation des courbures principales locales, et ensuite à un maillage trop fin ou trop grossier dans certaines régions. Afin de maintenir cette propriété de distance signée, une procédure de réinitialisation des fonctions de niveau est proposée dans ce chapitre.

En s'appuyant sur divers cas d'application, il est montré que cette méthode est très intéressante en termes de temps de calcul et précision en comparaison avec d'autres approches proposées dans la littérature. En particulier, des géométries correspondant à des matériaux du vivant et des composites observés par imagerie à rayons X peuvent être immergées dans un maillage éléments finis à l'aide de cette méthode de réinitialisation de fonctions de niveau. Le coût de calcul est alors largement dominé par les opérations d'adaptation du maillage aux courbures principales locales de la géométrie, tandis que la méthode de réinitialisation a un coût négligeable.

Avec les outils développés dans ce travail, l'import des images vers le maillage et l'adaptation de ce dernier à la géométrie, à l'aide de fonctions de niveau réinitialisées, peuvent être suivis par une étape de génération de maillage explicite aux interfaces. Un outil supplémentaire présenté dans ce chapitre permet également de distinguer les différentes composantes connexes d'une phase représentée par une unique fonction de niveau. Cette opération est complexe dans un contexte de calcul distribué mais est indispensable pour effectuer certaines mesures statistiques ou considérer des critères de rupture par vide ou par inclusion.

A l'aide des différents outils développés dans ce chapitre, des maillages éléments finis conformes et de bonne qualité peuvent être générés et adaptés à toute géométrie. En particulier, ces outils permettent d'accéder aux applications liées à la biologie et à la science des matériaux,

où l'utilisation de l'imagerie par rayons X en trois dimensions (3D) est prépondérante. En outre, la procédure de génération et adaptation de maillage proposée dans ce chapitre a un temps de calcul raisonnable et peut être ajustée par l'utilisateur pour obtenir différents niveaux de précision grâce à un estimateur d'erreur.

Introduction

Though it is based on a conform Finite Element (FE) meshing of interfaces, the mesh generation and adaptation methodology introduced in Chapter 2 still relies heavily on the Level-Set (LS) method. Hence, some aspects of this method have to be addressed.

First, results obtained using the volume conservation constraint introduced in Chapter 2 show that some numerical diffusion remains, and converges to zero linearly with mesh size, but it is drastically reduced. Thus, thanks to explicit interface meshing and enhanced volume conservation, the very fine meshes used in previous works [5, 6] are no longer required, but local mesh refinement could still be used. The accuracy of the mechanical solution at the interface could be improved, as mechanical fields are more likely to vary there than in the rest of the domain. The geometry of the interface and all its scales could also be better captured if the mesh size depended on geometrical quantities such as the principal curvatures. Error estimators and metric-based mesh adaptation strategies to refine the mesh depending on the principal curvatures are detailed in Section 3.1.

Then, the robustness of any LS method depends importantly on a key operation, known as LS reinitialization. Multiple approaches have been proposed in the literature to solve this operation, but numerical experiments showed that not all of them guarantee the same level of accuracy. As described in Section 3.2, these experiments and the literature on the topic motivated the study of a novel approach to the problem, applicable to the case of unstructured meshes distributed among several processes.

Since in most LS frameworks, multiple objects of the same phase are embedded in a single LS function, it is no longer possible to identify how many components are represented by an LS function. For example, in the present study, the number of particles and their distribution in size and space are not so easy to obtain, because all particles are embedded in the same LS function. The same remark applies to voids, which makes it difficult to consider void coalescence criteria that usually apply between pairs of voids. In other applications, the number of grains, bubbles, fibers, and other physical components has to be retrieved for statistical or modeling purposes. In Section 3.3, an algorithm is introduced in order to solve this problem, by identifying each Connected Component (CC) inside the same LS function with a unique tag. The difficulty of this problem is mainly linked to its parallel implementation.

Finally, image immersion techniques are necessary in the present study as experimental validation on real three dimensional (3D) microstructures is targeted. Meshing real microstructures from 3D images is a complex and challenging problem that is significantly simplified in the present work thanks to the LS reinitialization and mesh generation and adaptation procedures presented in Section 3.2 and Chapter 2. In Section 3.4, these tools are used to import geometries by transforming a gray scale 3D image to an LS function on an FE mesh, the latter being adapted thanks to curvature-based error estimators as in Section 3.1. The images used in these example span over a wide range of materials including human bone, polycrystals and fiber-reinforced polymers.

3.1 Curvature-based mesh adaptation

3.1.1 Metric fields

Before defining any error estimator, it is necessary to give some details about metric fields and metric-driven mesh adaptation, especially regarding how anisotropic meshes are obtained. The reader is referred to Chapter 2 for details about the mesh adaptation algorithm. In particular, in Subsection 2.2.1, an element-wise definition of mesh quality is given, with a reference to a metric field M . This metric field is actually a second order tensor that is defined node-wise and interpolated element-wise for quality computation, where it is used to distort the usual Euclidean definitions of volume and length, hence defining a Riemannian space. Depending on M , the remesher will see some edges longer or shorter than they are, and because the remesher is trying to have the average edge length in each element as close as possible to 1, mesh anisotropy will result.

An example is given in Figure 3.1 in the isotropic case. The initial mesh of a square domain $[0, 1]^2$ in Figure 3.1(a) is adapted with a metric field

$$M = \begin{pmatrix} \frac{1}{0.1^2} & 0 \\ 0 & \frac{1}{0.1^2} \end{pmatrix}.$$

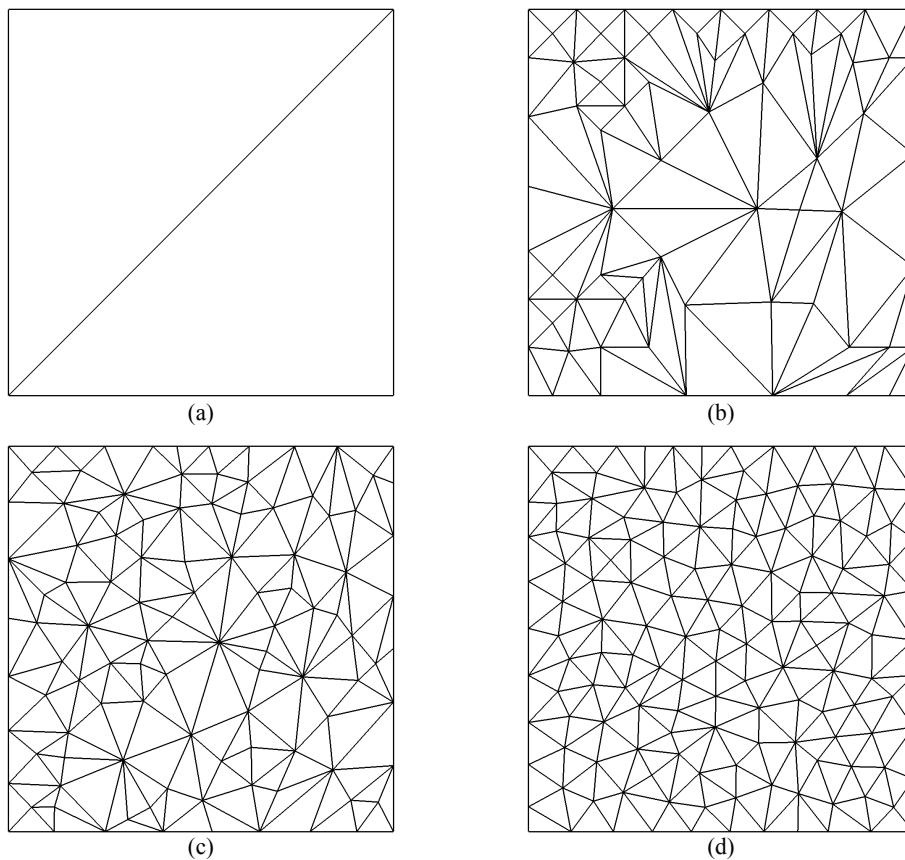


Figure 3.1 – Metric-driven mesh adaptation applied to a two dimensional (2D) isotropic example: (a) initial mesh, (b,c) progressive adaptation, (d) final mesh.

The small topological changes performed by Algorithm 1 progressively refine the mesh so that all edges have a length close to 0.1 without inducing poorly shaped elements. An example with anisotropy is given in Figure 3.2, using the metric field

$$M = R \begin{pmatrix} \frac{1}{h_1^2} & & \\ & \ddots & \\ & & \frac{1}{h_d^2} \end{pmatrix} R^T = \begin{pmatrix} 1 & 0 \\ 0 & 1 \end{pmatrix} \begin{pmatrix} 1 & 0 \\ 0 & \frac{1}{0.1^2} \end{pmatrix} \begin{pmatrix} 1 & 0 \\ 0 & 1 \end{pmatrix}$$

where R is a rotation matrix, and the values h_i are the mesh sizes prescribed in the directions defined by the column vectors of R . In this example, R is the identity hence the directions are the Cartesian directions, and the mesh sizes are 1 in the x direction, and 0.1 in the y direction.

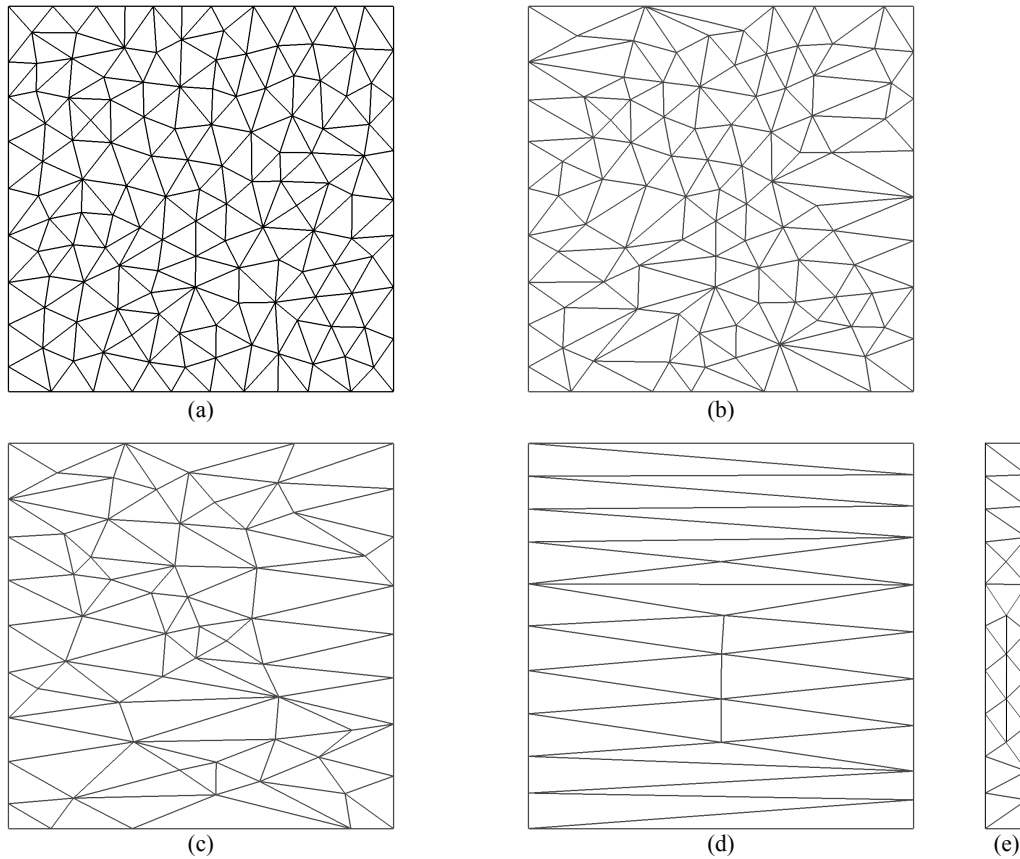


Figure 3.2 – Metric-driven mesh adaptation applied to a 2D anisotropic example: (a) initial mesh, (b,c) progressive adaptation, (d) final mesh, (e) final mesh as the remesher sees it.

The comparison between the result displayed in the Euclidean space in Figure 3.2(d) and its representation in the Riemannian space defined by M in Figure 3.2(e) reveals the effect of the metric field on the remesher.

3.1.2 Error estimators

The purpose of error estimators is two-fold, namely, obtaining an estimate of the error produced by a numerical approximation, and then giving some insights into how this approximation could

be improved in order to reduce the error. In an FE context, there are two ways of influencing the error. The first way is to change the order of the FE method, and the second way is to change mesh size. Both techniques can be applied locally. The former is known as p -adaptivity while the latter as h -adaptivity. Both can of course be combined. In the present work, p -adaptivity was discarded because it requires major changes in the FE code, while h -adaptivity only requires appropriate error estimators and a mesh adaptation tool, the latter being already implemented in Chapter 2.

Therefore, error estimators that could help predict locally the approximation error are investigated. What is of interest in this section is the approximation error linked to the approximation of a geometry by an LS function ϕ . The reader is referred to [119, 120] for a more thorough introduction to numerical errors produced by the FE method and their estimation. As a consequence of Céa's lemma, the approximation error is bounded by the interpolation error, which is the error between the exact LS function to the geometry, and its FE interpolation. Given that the geometry is regular enough, the interpolation error can be related to the Hessian matrix of the exact LS function to the geometry. Further details on this error estimator can be found in Reference [166]. Because the objective is to describe the geometry more accurately, this estimator is only used in a small layer around the interface. While local mesh refinement would enable to improve the accuracy only in this small layer, anisotropic mesh adaptation would enable to improve the accuracy differently depending on prescribed directions.

The anisotropic error estimator introduced in Reference [166] aims at refining the mesh in the normal direction to the interface in order to better capture material heterogeneity, while mesh size in the tangential direction(s) to the interface will depend on local principal curvature(s). The number of principal curvatures depends on the dimension d . In the normal direction n to the interface, a linear transition is defined between a mesh size h_{max} at a distance ϵ_h from the interface, and a mesh size h_{min} on the interface, with $h_{min} \leq h_{max} \leq \epsilon_h$. The one ($d = 2$) or two ($d = 3$) other directions are given by the eigenvectors of the Hessian matrix that are not colinear with n , and mesh size in these directions is related to the corresponding eigenvalues. This anisotropic error estimator has been applied to fluid-structure interaction problems in Reference [166]. Anisotropic meshes are however not suited for the present Lagrangian simulations. Hence, an isotropic error estimator is derived by considering only the maximum eigenvalue λ_{max} of the Hessian matrix of the exact LS function (*i.e.*, the maximum principal curvature). Mesh size is then defined as

$$h = \max\left(\min\left(\frac{h_c}{\lambda_{max}} + \left(h_{max} - \frac{h_c}{\lambda_{max}}\right)\frac{\phi}{\epsilon_h}, h_{max}\right), h_{min}\right), M = \text{diag}\left(\frac{1}{h^2}\right). \quad (3.1)$$

The role of bound h_{min} is to ensure that when the geometry is singular (at corners and sharp edges of the interface), mesh size will not degenerate to a very low value. For a planar geometry with $\lambda_{max} \rightarrow 0$, the role of bound h_{max} is to ensure that mesh size will not degenerate to a very high value. Apart from these bounds, Equation (3.1) defines a linear transition from a curvature-dependent mesh size at the interface, to a mesh size of h_{max} at a distance of ϵ_h from the interface.

The curvature-dependent mesh size is a ratio between a meshing parameter h_c and the maximum eigenvalue λ_{max} of the Hessian matrix of the exact LS function. All normalization coefficients were voluntarily omitted in this formula, hence h_c is a parameter that permits to refine the mesh if it is decreased, and coarsen the mesh if it is increased. This effect is independent from the principal curvatures, thus discretization should be scale-independent, apart from the influence of parameters h_{min} and h_{max} .

In the present work, because multiple LS functions ϕ_i are defined, Equation (3.1) is first applied independently on each LS function to obtain a mesh size h_i . Then the minimum of these mesh sizes is taken as final value.

Additionally, because the geometry is evolving due to deformation and fracture, the exact LS functions are not known. Therefore, a procedure is necessary in order to recover an accurate estimate of the exact Hessian matrix of each LS function.

3.1.3 Gradient and Hessian recovery

Gradient recovery and Hessian recovery problems have both been discussed in the literature, especially with the objective of building accurate error estimators. Hessian recovery is also necessary to solve problems with curvature-driven interface motion such as grain growth (Paragraph 3.2.3.2). The techniques proposed in the literature consist in first building a higher-order approximation of the initial approximation thanks to a least squares formulation, and then using this approximation to compute the desired Gradient or Hessian matrix [120].

For a given first order FE approximation, a higher-order approximation can be obtained using a modified Superconvergent Patch Recovery (SPR) technique [202, 203]. For each node, this technique consists in collecting the values of the given variable on every element containing this node. Then, a second order Hermite interpolation of the variable is fitted on these values in a least squares sense.

A common issue with a second order SPR technique is the significant number of unknowns, namely, the value of the field, the d values for its gradient, and the $d(d+1)/2$ values for its Hessian matrix. In order to well-define the least squares problem, the patch must then contain enough data ($1 + d + d(d+1)/2$).

In the frame of the present work, a parallel algorithm was developed to reach this purpose. As pictured in Figure 3.3(a), this algorithm consists in first collecting two sets at every node of the mesh: the *data*, which contain the values of the field on the neighboring elements, and the *ghost*, which contains the nodes connected to the considered node. Until *data* do not contain $1 + d + d(d+1)/2$ elements, the two sets are fed by collecting the data and the ghost of the nodes already located in *ghost*, as shown in Figure 3.3(b).

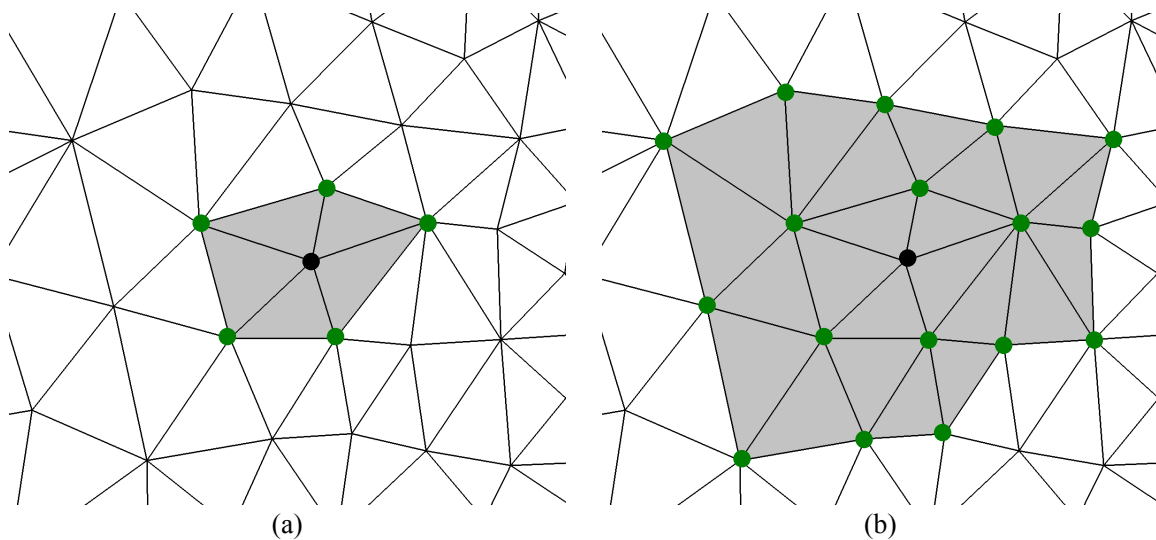


Figure 3.3 – Illustration of the patch, or *data* (light gray) and the *ghost* (green dots) for a considered node (black dot) at the first (a) and second (b) iterations of the feeding algorithm.

Once the least squares problem is solved, node-wise gradients and Hessian matrices can be extracted directly from the node-wise second order Hermite polynomials. Equation (3.1) can then be solved and mesh size defined in the whole domain.

3.1.4 Results

In this section, meshes are adapted to different geometries thanks to the error estimator presented above, and the accuracy and convergence of this procedure is proved numerically. The goal is not to validate the SPR technique, which has already been validated by other authors [202, 203, 204], but to validate the use of this SPR technique to construct an isotropic error estimator and then a metric field, which are used to adapt the mesh thanks to Algorithm 1. In particular, results will be affected if the adaptation algorithm fails at producing meshes that answer the requirements specified by arbitrary metric fields.

These tests are carried out in the case of a regular geometry and then a geometry incorporating a singularity. For both geometries, the domain Ω is the 3D box $[0, 1]^3$, discretized initially by an unstructured mesh of uniform isotropic size 0.08, all data being nondimensionalized. There is only one LS function, associated with a sphere of radius 0.3 centered with respect to the box for the first geometry. It is replaced by a Zalesak sphere for the second geometry. The meshing parameters are set to $\epsilon_h = 1$, $h_{max} = 0.16$, $h_{min} = 0.01$, and h_c is varied. The goal is to verify that the error converges to zero with decreasing h_c , and that the order of convergence in L^2 norm is 2. The exact interpolation error is measured by the $L^2(\mathcal{T}_\Gamma)$ norm of the difference between the exact LS function ϕ_s and the interpolated LS function $\phi_{s,h}$, this difference being directly computed at Gauss points (it is zero at mesh nodes). The interface Γ is not explicitly meshed, and the set \mathcal{T}_Γ contains all the elements of the mesh that are crossed by the interface (*i.e.*, ϕ_s takes opposite signs on one of their edges).

3.1.4.1 Sphere

The LS function ϕ_s associated with the sphere is given by

$$\phi_s(\mathbf{x}) = 0.3 - \sqrt{\sum_{k=1}^d (x_k - 0.5)^2}.$$

In order to verify that the remesher produces a mesh that satisfies the requirement specified by the error estimator, it is necessary to have a converged error estimate. This is guaranteed by performing 5 iterations of LS computation, error estimation, and remeshing. For the sphere test, in the last two iterations, the number of elements does not vary significantly, so that the 5th mesh can be considered as a converged result.

The results for this first geometry are presented in Table 3.1. An order of convergence slightly higher than 2 is obtained, which means that the estimator may overestimate the error in some cases. Since this overestimation is not significant, this is not a major issue.

h_c	Error in $L^2(\mathcal{T}_\Gamma)$ norm	Order of convergence	Number of elements
0.32	1.280×10^{-3}		5940
0.16	2.015×10^{-4}	2.67	27679
0.08	4.819×10^{-5}	2.06	119467
0.04	9.015×10^{-6}	2.42	496844

Table 3.1 – Convergence results for the error estimator based on LS functions. Sphere test.

Because no parallel implementation of the SPR technique was available in the FE code, other methods have been used in previous work at Cemef - MINES ParisTech for gradient and Hessian recovery operations. The most widely used was through node-wise averaging. First, the gradient was computed at Gauss points based on FE shape functions. Then, at each node, a node-wise gradient was obtained by averaging the gradients of all elements containing this node. These two steps were reiterated in order to obtain node-wise Hessian matrices. Results for the sphere test using this node-wise averaging technique are reported in Table 3.2.

h_c	Error in $L^2(\mathcal{T}_\Gamma)$ norm	Order of convergence	Number of elements
0.32	1.631×10^{-3}		4424
0.16	8.137×10^{-4}	1.01	12665
0.08	2.828×10^{-4}	1.53	43591
0.04	5.850×10^{-5}	2.28	173658

Table 3.2 – Convergence results for the error estimator based on LS functions, using a node-wise averaging gradient/Hessian recovery technique instead of SPR. Sphere test.

A more conventional approach that was available in the FE code is global least squares fitting. This approach is similar to SPR, with the difference that only first order polynomials are used, and the least squares problem is solved globally. Because linear polynomials are used, this operation must be performed twice to obtain the Hessian matrices. Results for the sphere test using this global least squares technique are reported in Table 3.3.

h_c	Error in $L^2(\mathcal{T}_\Gamma)$ norm	Order of convergence	Number of elements
0.32	1.209×10^{-3}		5743
0.16	4.341×10^{-4}	1.48	21729
0.08	1.160×10^{-4}	1.91	86784
0.04	2.329×10^{-5}	2.33	358566

Table 3.3 – Convergence results for the error estimator based on LS functions, using a global least square gradient/Hessian recovery technique instead of SPR. Sphere test.

It is important to point out that these techniques are known to produce less accurate results. The present tests aim at showing the influence of these inaccuracies on mesh adaptation. The results show that the order of convergence is deteriorated, especially using coarse meshes, while it should be optimal for this regular geometry. Thus, a second order SPR technique is not only relevant for gradient and Hessian recovery, but also for obtaining optimal meshes.

3.1.4.2 Zalesak sphere

The LS function ϕ_z associated to the Zalesak sphere is given by

$$\phi_s(\mathbf{x}) = \min \left(0.3 - \sqrt{\sum_{k=1}^d (x_k - 0.5)^2}, -\min(x_1 - 0.30, 0.55 - x_2, x_2 - 0.45) \right).$$

For this geometry, the presence of several singularities means that h_{min} will be reached in some regions of the domain. Thus, more than 5 iterations are necessary to reach convergence of the error

estimator. The results obtained at convergence (*i.e.*, when the number of elements does not vary significantly between two iterations of error estimation and remeshing) are presented in Table 3.4.

h_c	Error in $L^2(\mathcal{T}_\Gamma)$ norm	Order of convergence	Number of elements
0.32	5.539×10^{-4}		113412
0.16	1.893×10^{-4}	1.55	245052
0.08	5.071×10^{-5}	1.90	375837
0.04	2.953×10^{-5}	0.78	710522

Table 3.4 – Convergence results for the error estimator based on LS functions. Zalezak sphere test.

There is a clear increase in the number of elements, when compared with Table 3.1, due to a more complex geometry. The order of convergence is inferior because the mesh only varies in the regions close to the spherical part of the geometry. This was theoretically expected and confirms the role of the h_{min} and h_{max} bounds, which is summarized in Figure 3.4.

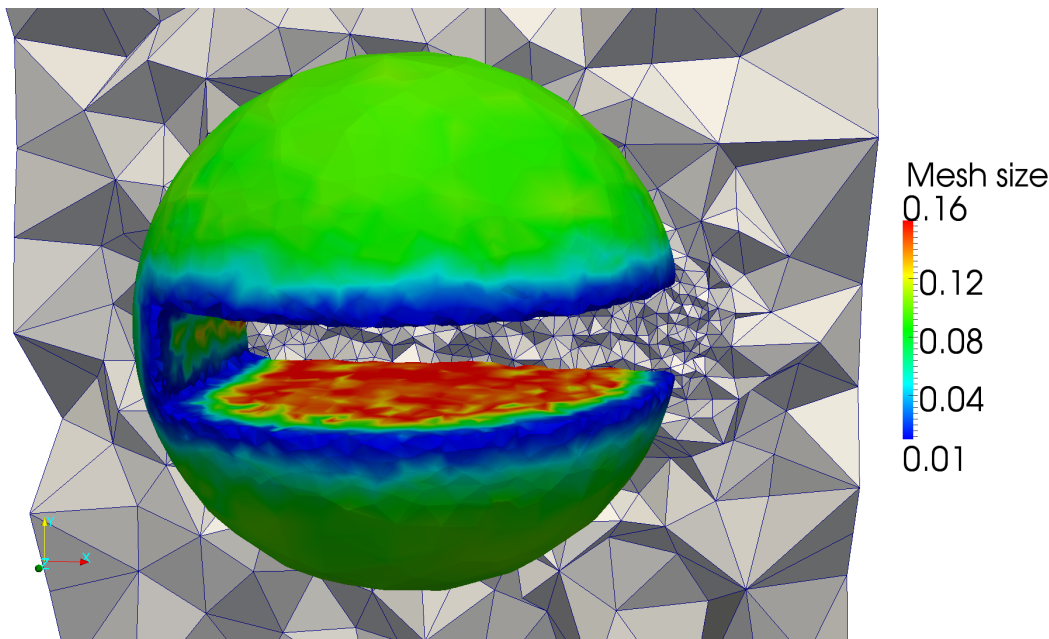


Figure 3.4 – Converged mesh for the Zalezak sphere test with $h_c = 0.32$. The interface is colored with respect to mesh size: regions in red have $\lambda_{max} \rightarrow 0$ (mesh size is h_{max}), regions in blue have $\lambda_{max} \rightarrow \infty$ (mesh size is h_{min}), and remaining regions are regular (mesh size depends on h_c and the local λ_{max}).

As a conclusion, an error estimator is presented in this section in order to adapt the mesh close to interfaces based on the interpolation error on LS functions. This error is directly linked to geometrically relevant information, namely, the maximum principal curvature λ_{max} , which is estimated thanks to an SPR technique. The implementation of the latter in a distributed computing framework is addressed. An isotropic metric field is constructed based on this SPR technique and the error estimator, and is used to drive mesh adaptation.

Results show that both the SPR technique and the mesh adaptation algorithm perform satisfactorily, as an order of convergence close to the theoretical one is obtained. When the geometry is

of low λ_{max} , an upper bound on the mesh size prevents it from going to infinity, while for high or infinite λ_{max} , a lower bound on the mesh size guarantees the best discretization possible, as defined by the user. The influence of these bounds and the geometrical error parameter h_c is verified numerically.

As a consequence to this influence of λ_{max} , it is important that the LS function remains as close as possible to a signed distance function. A loss of regularity would lead to undesired results such as a very high local refinement in regions where it is not needed, or the opposite. This regularity is maintained thanks to LS reinitialization, which is addressed in the next section.

3.2 Level-Set reinitialization

3.2.1 Introduction

The LS method has been employed to simulate a wide variety of mechanical and metallurgical phenomena [166, 169, 181, 205, 206]. A major drawback of this formulation lies in the fact that after transport (in both Eulerian and Lagrangian cases), in general, the function is no longer a distance function. This is particularly problematic when a specific remeshing technique depending on the distance property is used at the interface (Section 3.1). In addition, some phenomena, such as curvature-driven interface motions, require a distance function at least in a thin layer around the interface in order to compute properly the corresponding velocity field [207]. Finally, the conditioning of the transport problem solved in Eulerian methods also depends on the regularity of the LS function [2].

For these reasons, the distance function needs to be reinitialized. Restoring the metric property is equivalent to solving the following eikonal equation for a given LS function ϕ to an interface Γ

$$\forall t \begin{cases} \|\nabla\phi(\mathbf{x}, t)\| = 1, \mathbf{x} \in \Omega(t), \\ \phi(\mathbf{x}, t) = 0, \mathbf{x} \in \Gamma(t). \end{cases} \quad (3.2)$$

There exist different approaches to solve this equation including the well-known fast marching method introduced by Sethian [208], which propagates a front from the interface and ensures directly a gradient equal to unity. Though this approach has been later extended to unstructured meshes [209], its implementation becomes extremely complicated when it comes to consider anisotropic (*i.e.*, obtuse) triangulations [210]. The latter relies on the insertion of numerical supports for obtuse triangle and is mentioned as "cumbersome" in Reference [210].

Another major drawback of the fast marching method lies in the parallel implementation. More specifically, the algorithm has to be performed several times on each partition to synchronize the values between the processors, which requires significant implementation effort and poor parallel efficiency.

In Reference [211], a Hamilton-Jacobi (H-J) formulation equivalent to Equation (3.2) was proposed in order to correct iteratively the LS values around the interface by solving a partial differential equation. This method thus requires the definition of a purely numerical parameter known as the fictitious time step for reinitialization $\Delta\tau$. This quantity is generally of order of the mesh size h in the direction normal to the interface. For convenience we assume in the following that $\Delta\tau = h$. By noting ϵ_r the reinitialized thickness, $\epsilon_r/\Delta\tau$ increments are then needed to reinitialize completely the layer $\phi \in [-\epsilon_r, \epsilon_r]$.

More recently, coupled Convection-Reinitialization (CR) methods emerged wherein the LS function is automatically reinitialized during the solution of the transport equation [2]. Their main advantage lies in the fact that only one solution step is needed for the simulation instead of two for the classical H-J technique.

The signed distance function can also be replaced by any smooth function that satisfies the metric property, at least in a thin layer around the interface. In the following these two variants will be mentioned: the former using a classical distance function (CR-DF) and the latter working with a hyperbolic tangent distance function $\tilde{\phi} = \epsilon_r \cdot \tanh(\phi/\epsilon_r)$ (CR-HTDF). Since the hyperbolic tangent function has a gradient close to one only in the neighborhood of zero, the truncation thickness ϵ_r has to be chosen big enough to verify the metric property at least in a thin layer around the interface.

Finally, a natural way to reinitialize LS functions consists in using a brute force algorithm to perform a complete reconstruction of the distance function. This technique works in two steps: discretize the interface (zero-isovalue of the LS function) into a collection of simple elements and, for every node, compute the distance to all elements of the collection and store the smallest one that becomes the updated value of the distance function.

Though it guarantees optimal accuracy, this Direct Reinitialization (DR) technique is generally mentioned as extremely greedy in terms of computational requirements in the literature [211, 212]. Hence it is carefully avoided in most implementations, with the exception of [181]. In Reference [213], a review of various improvements to this method proposed in the literature to overcome this difficulty can be found. These works generally address only regular grids or hierarchical meshes [214].

In the following, the DR method is investigated and a new parallel and efficient implementation is proposed for unstructured and possibly anisotropic meshes. It is then compared to other approaches in terms of accuracy and numerical performances. Applications addressed in this section cover not only the topic of the present work but also full field grain growth modeling. The algorithms and the examples do not use the explicit interface meshing technique presented in Chapter 2 but rely on standard Eulerian and Lagrangian LS methods.

3.2.2 Algorithm

As stated above, the DR method that is a basis for the present work starts from a simple idea, which is illustrated in Figure 3.5. In the frame of P1 (linear by element) interpolation, the LS function is represented by its values at mesh nodes. On each element crossed by the interface, a discrete representation of a portion of the interface is constructed giving in the end a mesh of the whole interface. In 2D, this element-wise discrete representation is an edge, while in 3D it is one or two triangles. For sake of clarity, the initial FE mesh is hereafter referred to as mesh, while the 1D or 2D interfacial mesh is referred to as collection.

Hence, reinitialization of the signed distance function can be performed at any mesh node by searching the closest edge or triangle in the collection. As the computation of the distance to an edge or a triangle will be a critical operation in this part of the algorithm, the optimal implementations detailed in Reference [215] are used. The sign of the reinitialized function can then be taken as the one of the initial LS function.

It can be seen that opposed to H-J approaches mentioned above, the DR method is way more accurate: given a P1 representation of an LS function, the DR method performs a geometric solution. Nevertheless, this method, if used as is, has large costs.

In the following, n represents the number of nodes in the mesh, and e the number of elements in the collection. Using these notations, collection construction is of complexity $\mathcal{O}(n)$, while distance computation is of complexity $\mathcal{O}(n \cdot e)$. Hence, this last operation is too costly and makes the algorithm unsuitable for computations, especially in 3D. This is basically the reason why H-J methods are usually preferred.

Based on techniques widely used in computer graphics, data mining, and other domains, a new DR method can be proposed, where the cost of distance computation is significantly reduced. This optimization is based on a space partitioning technique. Such technique consists in dividing the space, *i.e.*, the collection, in several parts, thanks to a suitable criterion. More precisely, hierarchical space partitioning techniques consist in dividing the space into p parts, and applying

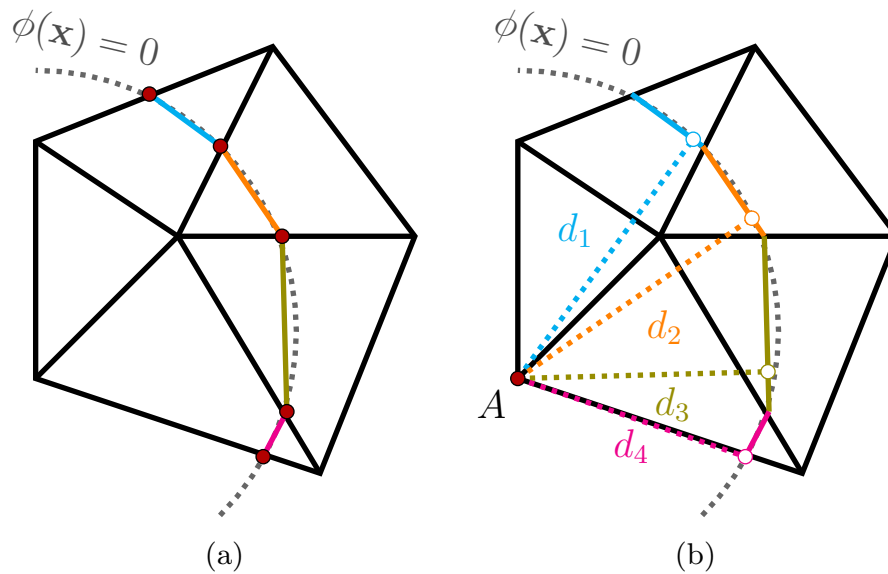


Figure 3.5 – DR method on a P1 mesh: (a) collection construction, (b) distance computation.

the same procedure to these parts, and so on, until small parts are obtained where searching or pruning can be performed at acceptable costs.

The number p is a constant inherent to the used methodology. For example, one may cite quad-trees in 2D, with $p = 4$, where the whole space is placed in a bounding box, which is divided in 4 boxes of identical dimensions, corresponding to the four quarters of the initial box (these boxes are then divided again, and so on). Using such systematic division, one or several boxes may be empty at some stage, and the division may not be optimal, especially in the present case with unstructured and possibly anisotropic meshes. The same statement can be made regarding oc-trees ($p = 8$), which are the 3D equivalent to quad-trees.

That is the reason why it is chosen to partition the space hierarchically using a k -dimensional (k - d) tree, where the division is always made into $p = 2$ parts, using a criterion that depends on the considered set of elements. This structure was first introduced in Reference [216], with examples of potential applications. Among these applications, a focus is made in the following on nearest neighbor searches: for each node of the mesh, the nearest element in the collection has to be found. In the following a methodology, named Direct Reinitialization with Trees (DRT), is explained, which reduces the complexity of distance computation to $\mathcal{O}(n \log e)$.

Opposed to systematic methods, the chosen division criterion is based on an analysis of the space that is to be divided. In the present case, this space is the initial collection, or a sub-set of it, which can both be addressed as a set of elements, and division in 2 parts will be obtained using a division plane. Optimally, this plane should divide the given set into 2 sub-sets containing the same number of elements. To narrow such result without adding too large costs, it is chosen to use planes normal to the Cartesian axis, and centered respectively to the set of elements. This centering is obtained by computing the barycenter of each element, and choosing a plane that goes through the barycenter of these points. The whole process of tree construction is given below:

- (b.1) Set the division plane (line in 2D) as the plane going through the barycenter of all elements and having its direction alternatively defined by the x , y and z directions depending on the depth in the tree.

- (b.2) Compute the signed distance from the vertices of all the elements in the collection to this plane.
- (b.3) Build a left child to the current tree by going back to (b.1) with all the elements having at least a vertex with negative plane distance.
- (b.4) Build a right child to the current tree by going back to (b.1) with all the elements having at least a vertex with positive plane distance.

As illustrated in Figure 3.6, this process recursively builds a binary tree. As observed in Figure 3.6(c), it ends when at steps (b.3) and (b.4) one of the two subtrees contains the other. In such situation, a leaf is created, and instead of containing a plane and two subtrees, this leaf contains only the remaining elements of the collection.

Regarding the division plane, it is easy to find geometric configurations where the used simple definition does not divide the elements in two balanced subtrees. However, such situations are not met in practice, and tests have shown that this definition leads to a globally balanced tree.

Regarding costs, the computation of the barycenter is performed in linear time, and because at each stage the number of considered elements should be divided by 2, the global tree construction operation is of optimal complexity $\mathcal{O}(e \log e)$.

Searches can then be performed for each node of the mesh using the following algorithm at the root of the tree:

- (b.5) Compute the signed distance from the node to the division plane.
- (b.6) If it is negative, go back to (b.5) with the left subtree.
- (b.7) If it is positive, go back to (b.5) with the right subtree.

This recursive process will reach a leaf, where distance computation will be performed by considering one by one all the elements stored in this leaf. Then, it may appear at steps (b.6) or (b.7) that the resulting distance is bigger than the distance to the division plane. In such case, it is required to go back to (b.5) with the other subtree.

Though this operation is implemented to ensure consistency, it is not met often if the planes are well defined, as in most applications. Moreover, due to all the divisions, the set of elements stored in any leaf should be small enough to consider that distance computation is of optimal complexity $\mathcal{O}(n \log e)$.

In the examples shown in Figure 3.7 and Figure 3.8, the distance from a point \mathbf{x} to the interface needs to be computed. At each stage of the search, the notation d_p is the distance to a division plane, obtained at an intermediary node of the tree, the distance d_e is the distance to an element, obtained at a leaf of the tree, and d^+ is the final result.

In the first case (Figure 3.7), the point is optimally located since it is close enough to the interface. Hence, browsing two levels of the tree in (a) and (b) leads directly to the correct leaf in (c), and since when browsing back in (d) and (e), the obtained distance is smaller than the distance to any of the division planes, this distance is the final result.

In the second case (Figure 3.8), a worst case scenario occurs. The point is located in a leaf (b) which gives a distance greater than the distance to the first division plane (a). Hence, the other part of the tree has to be browsed (c). In this part of the tree, an optimal situation is met as the recursive browsing (d) and (e) gives the final result.

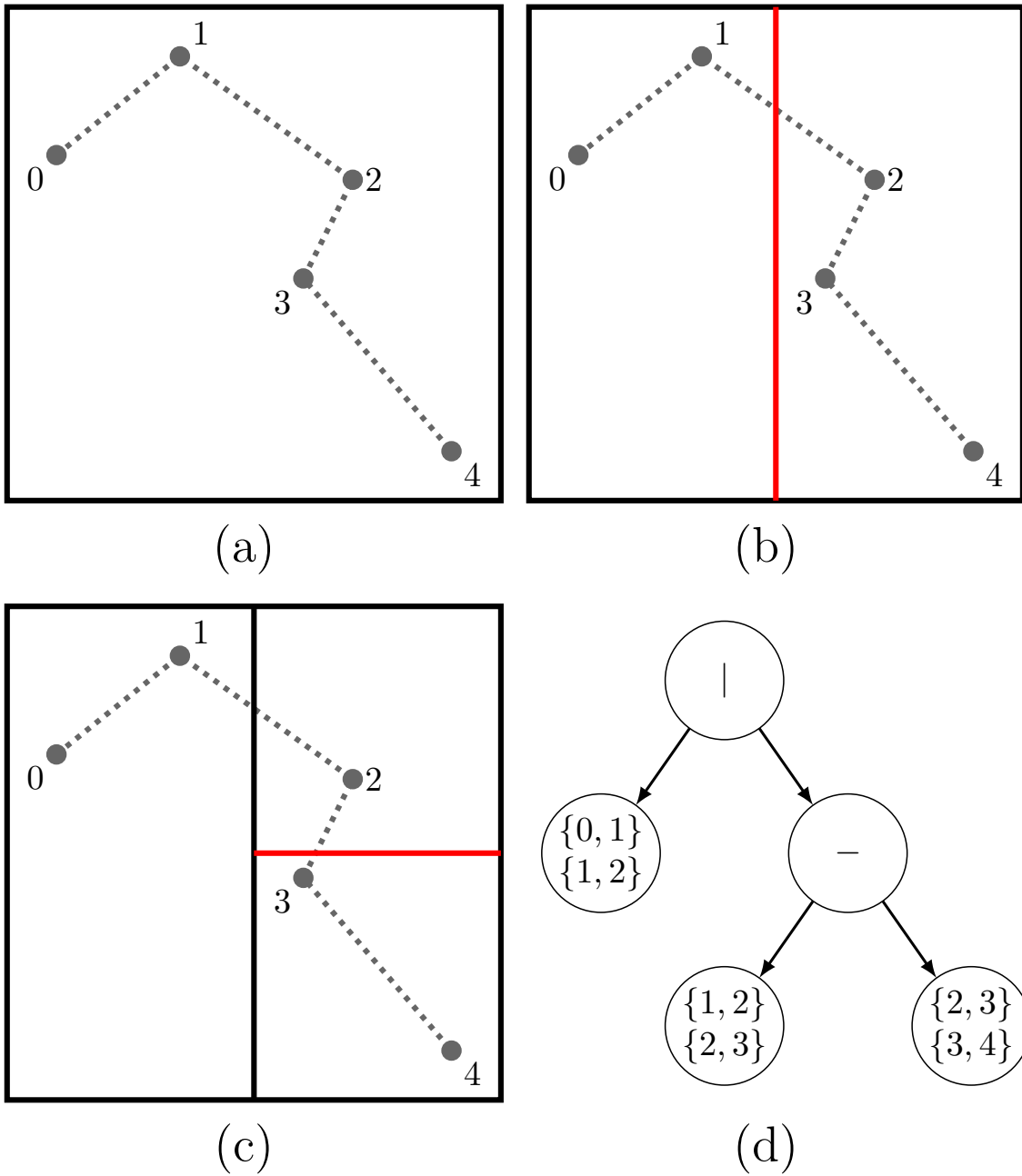


Figure 3.6 – Example of recursive tree construction in 2D.

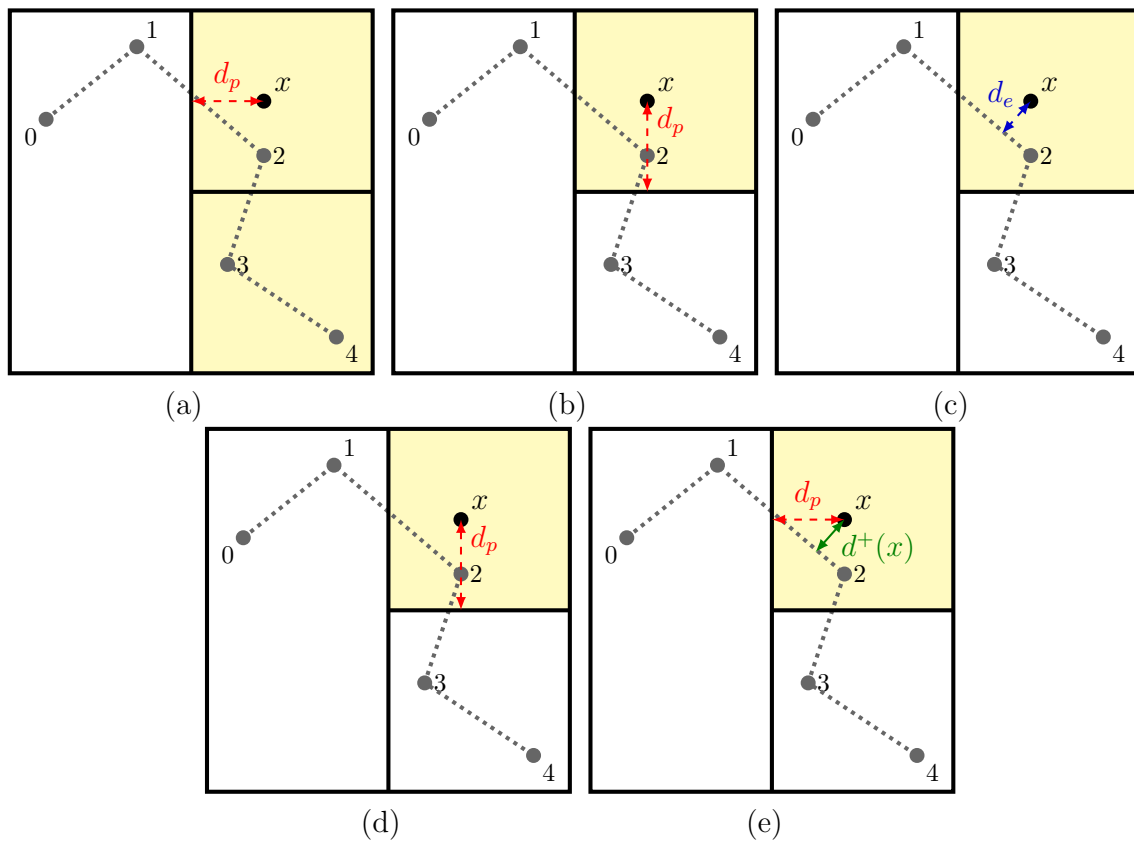


Figure 3.7 – Example of recursive distance computation in 2D with the DRT method, best case scenario.

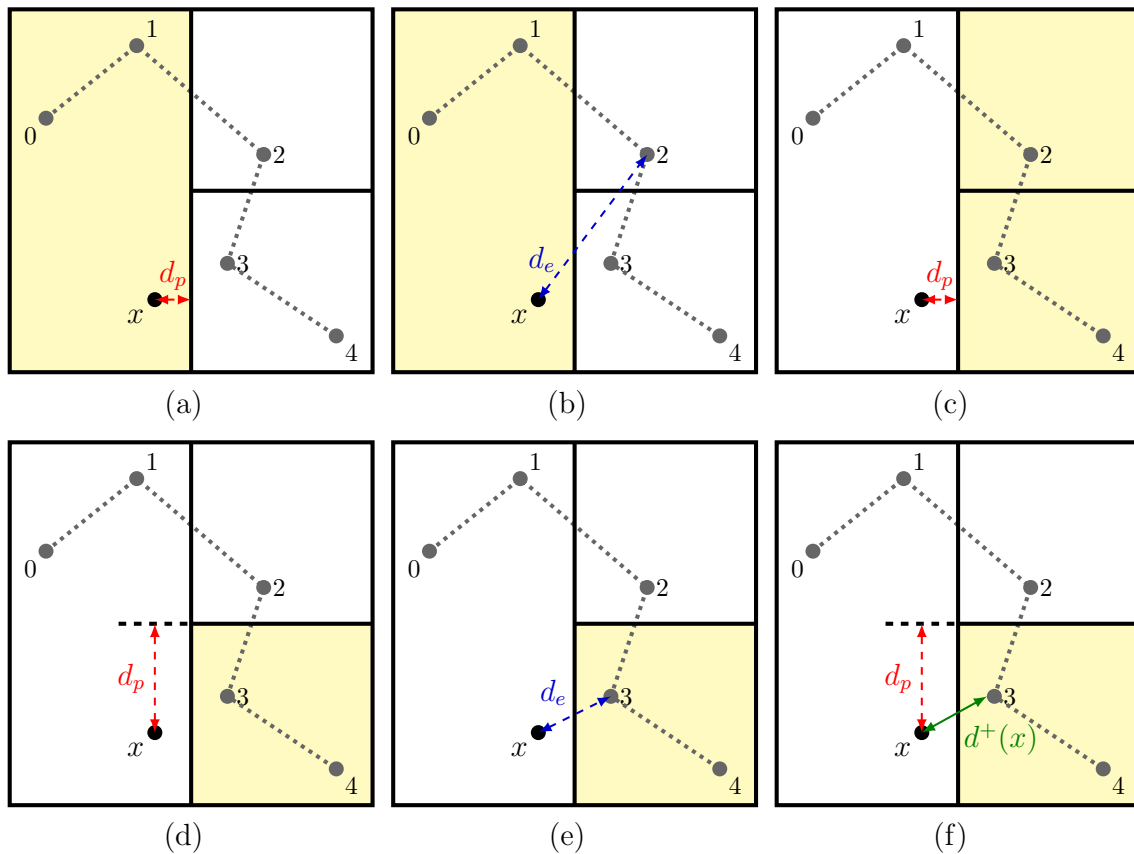


Figure 3.8 – Example of recursive distance computation in 2D with the DRT method, worst case scenario.

In the introduction, it was mentioned that H-J approaches, because of prohibitive costs, are usually applied only in a small thickness around the interface. Implementing the same optimization to the DRT method can drastically reduce distance computation costs. The first step of the implementation consists in executing searches only for the nodes located in the reinitialization zone. Then, at steps (b.6) and (b.7), if the resulting distance raises a need to look in the other subtree but the distance to the plane is bigger than the thickness used for reinitialization, this operation can be skipped.

Because in practice the thickness is small enough to reduce the order of n to the same order as e , the final complexity of the new DRT method is expected to be $O(e \log e)$. Moreover, using this optimization it appears that the best case scenario illustrated in Figure 3.7 occurs more often than the worst case, because the point x will always be located close to the interface.

Massively multi-domain computations often require a significant computational power to obtain a good accuracy. The same remark can be drawn for 3D computations. For this kind of simulations, a classical choice is parallelization using the distributed memory paradigm. Opposed to shared memory, distributed memory enables each parallel unit, called process, to have a separate memory, and to be possibly located on a different machine. This last point is essential for large scale computations, where the whole mesh cannot be stored on a single machine.

This paradigm nevertheless raises an issue in our case: since each process will only have the knowledge of a part of the mesh, it will only be able to build a part of the collection; hence it will not be able to compute distances to the collection. To solve this issue, one could simply gather

the full collection on each process, and then build the *k-d tree* on each process. Experiments have showed that though this method has a good performance for a small number of processes (up to 20), it has a poor parallel speed-up.

To retrieve parallel efficiency, a more advanced technique has been developed. In this method, each process builds its own collection and its own tree, ignoring other processes. Then, a bounding box system is used. Each process computes the minimal box aligned to the Cartesian axis that can contain completely its collection. At the step of distance computation, each process will compute first the distance using its tree, and then will interrogate one by one the processes when they can improve this distance.

This parallel implementation is summarized in Figure 3.9. In this illustration, distance computation to point A is local since it is shorter than the distance to the box associated to Beige. Regarding point B, the distance to the box associated to Orange is shorter than the local distance computation performed inside Beige. Hence, the distance from B to Orange's collection is computed and chosen as it is shorter than the previous one.

This parallel space partitioning technique is also extended to the case when reinitialization is only performed in a small layer around the interface. In practice, this avoids interrogating other processes when the distance to their box is larger than the reinitialization thickness.

It can already be seen on the example in Figure 3.9 that bounding boxes are not optimal, as Orange's box includes a wide area around the interface. It is however expected that for a large number of processes and a good repartition of the interface, communications will be minimized and optimal parallel efficiency reached.

This bounding box technique at the global level completes the *k-d tree* optimization used at the local level, and the DRT method can now be applied to perform LS reinitialization in parallel.

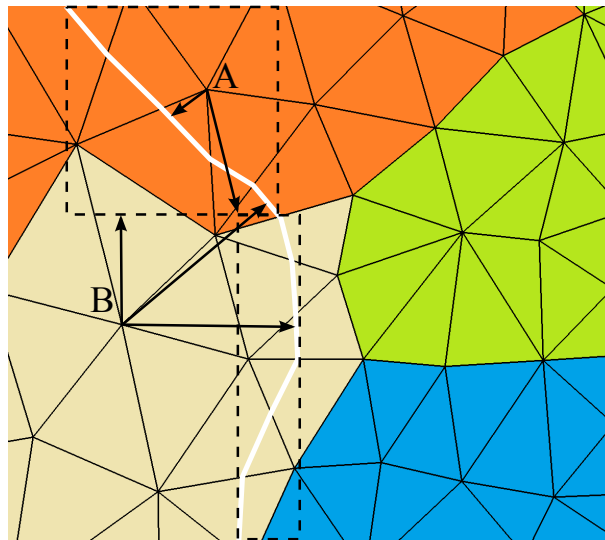


Figure 3.9 – Bounding boxes (broken line) on a 2D example with 4 processes (identified by the color code). The solid white line is the interface, and the arrows represent distance computation steps.

3.2.3 Results

In this part, numerical results obtained with the new DRT method are provided. Both DR and DRT methods were implemented within the parallel C++ library Cimlib [2]. Regarding the H-J, CR and CR-HTDF methods that are used for comparison, parallel implementations were already

provided by the library. All the following computations were performed on the same 1.2GHz Intel Xeon Linux cluster.

3.2.3.1 Academic cases

The first test case proposed is a square (respectively a cube in 3D) centered in a 1×1 (respectively $1 \times 1 \times 1$ in 3D) domain and subjected to a velocity field equal to the LS function gradient $\vec{v} = \nabla\phi$, all data being nondimensionalized for this test. The parameter ϵ_r for the CR-HTDF solver is set to $\epsilon_r = 20h$ and $\epsilon_r = \epsilon_r$ is kept for all methods in order to perform a fair comparison. The theoretical values of the LS function $\phi_{theo}(\mathbf{x}, t)$ and the theoretical internal area (respectively volume in 3D) \mathcal{A}_{theo} are calculated through

$$\begin{cases} \phi_{theo}(\mathbf{x}, t) = \phi(\mathbf{x}, 0) - t, \\ \mathcal{A}_{theo}(t) = (l_0 - 2t)^d, \end{cases}$$

with $t \in [0, l_0/2]$. The term l_0 corresponds to the initial edge length of the square/cube, which is chosen equal to 0.5 both in two and three dimensions. The simulation time step is calibrated separately so that the following global error on the internal area remains lower than 1 %

$$L^2 = \frac{\|\mathcal{A}_{theo}(t) - \mathcal{A}(t)\|_2^{t \in [0, 0.25]}}{\|\mathcal{A}_{theo}(t)\|_2^{t \in [0, 0.25]}}.$$

These first simulations are carried out within an Eulerian LS context (IEUL method in Chapter 2).

3.2.3.1.1 Shrinking square (Two Dimensions) In this two-dimensional test case, a fixed unstructured and homogeneous mesh is used. The number of elements is equal to 150000, which corresponds to an average mesh size $h \approx 0.004$. The main results of this set of simulations are summarized in Table 3.5.

Method	H-J	CR-DF	CR-HTDF	DRT
Δt	0.01	0.0001	0.0001	0.001
$t_{transport}$ (s)	6.4	85.1	86.7	5.8
t_{reinit} (s)	133			0.4

Table 3.5 – Results of shrinking square simulations run on 4 Central Processing Units (CPUs). For the CR solvers, the LS function is automatically reinitialized during the transport, so there is only one time for these two steps.

The new algorithm appears to be clearly the most efficient among all methods and is up to 300 times faster than the H-J approach. The CR solvers are proving more effective than the H-J method but require a very small time step to guarantee scheme stability. Let \mathcal{N} be the set of nodes belonging to the layer $\pm 5h$ around the interface, the relative discretization error $\mathcal{R}(t)$ between the exact and computed LS functions is calculated through

$$\mathcal{R}(t) = \frac{\|\phi_{theo}(\mathbf{x}, t) - \phi(\mathbf{x}, t)\|_2^{\mathcal{N}}}{\|\phi_{theo}(\mathbf{x}, t)\|_2^{\mathcal{N}}} \quad \text{with} \quad \|u(\mathbf{x}, t)\|_2^{\mathcal{N}} = \sqrt{\sum_{n \in \mathcal{N}} u(\mathbf{x}_n, t)^2}.$$

Such small layer is chosen because both CR methods are only valid close to the interface [2].

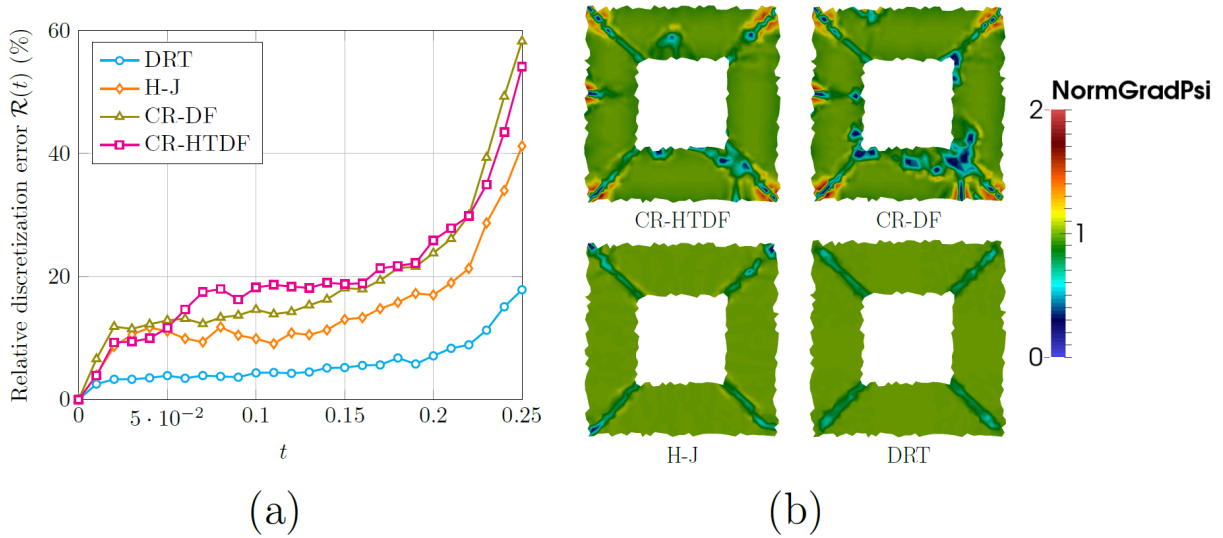


Figure 3.10 – Shrinking square test case: (a) relative discretization error $\mathcal{R}(t)$ between the exact and computed distance functions around the interface $\pm 5h$, (b) values of $\|\nabla\phi\|$ for each method at $t = 0.08$.

Figure 3.10(b) illustrates the inability of the CR solvers to properly maintain the metric property, especially in the corner vicinity. On the other hand, the DRT and H-J methods exhibit a high level of accuracy. This first 2D test case thus demonstrates that the proposed algorithm is both extremely fast (Table 3.5) and accurate (Figure 3.10).

3.2.3.1.2 Shrinking cube (Three Dimensions) A similar case is now investigated in 3D. In order to limit the number of elements, a remeshing operation is performed at each time step using the *a posteriori* error estimator and remeshing algorithms presented in Reference [217]. With this estimator, elements located near the interface are stretched to form a refined and anisotropic layer with thickness $2\epsilon_r$ around the zero iso-level. Outside this zone, the mesh is kept coarse (Figure 3.11).

For this set of simulations, the total number of elements in the domain is equal to 500000. The local mesh size h in the refined layer thus constantly evolves during the simulation. The parameters ϵ_r and $\Delta\tau$ are therefore updated at each time step in order to maintain $\epsilon_r = \epsilon_t = 20h$ and $\Delta\tau = h$. The time steps for all methods are chosen identical to the ones calibrated for the two-dimensional case (Table 3.5).

In addition to the use of an anisotropic mesh, this case is also critical for non-direct approaches because the gradient is poorly defined along bisecting planes and diagonals. Hence, the linear problems built by the H-J solver also have a poor conditioning (on average 430 iterations are performed by the used GMRES iterative solver in 3D compared to around 20 in 2D). During the simulation, one observes furthermore the appearance of a parasitic phase outside the cube because oscillations start polluting the FE solution of the convection solver (Figure 3.12). It proves the function becomes too irregular to be properly reinitialized leading to a modification of sign of the LS function. The interface of this parasitic phase is then automatically detected and captured by the remesher which adapts the mesh around it. As the total number of elements is fixed, the calculation accuracy then falls because fewer elements are used to represent the cube interface.

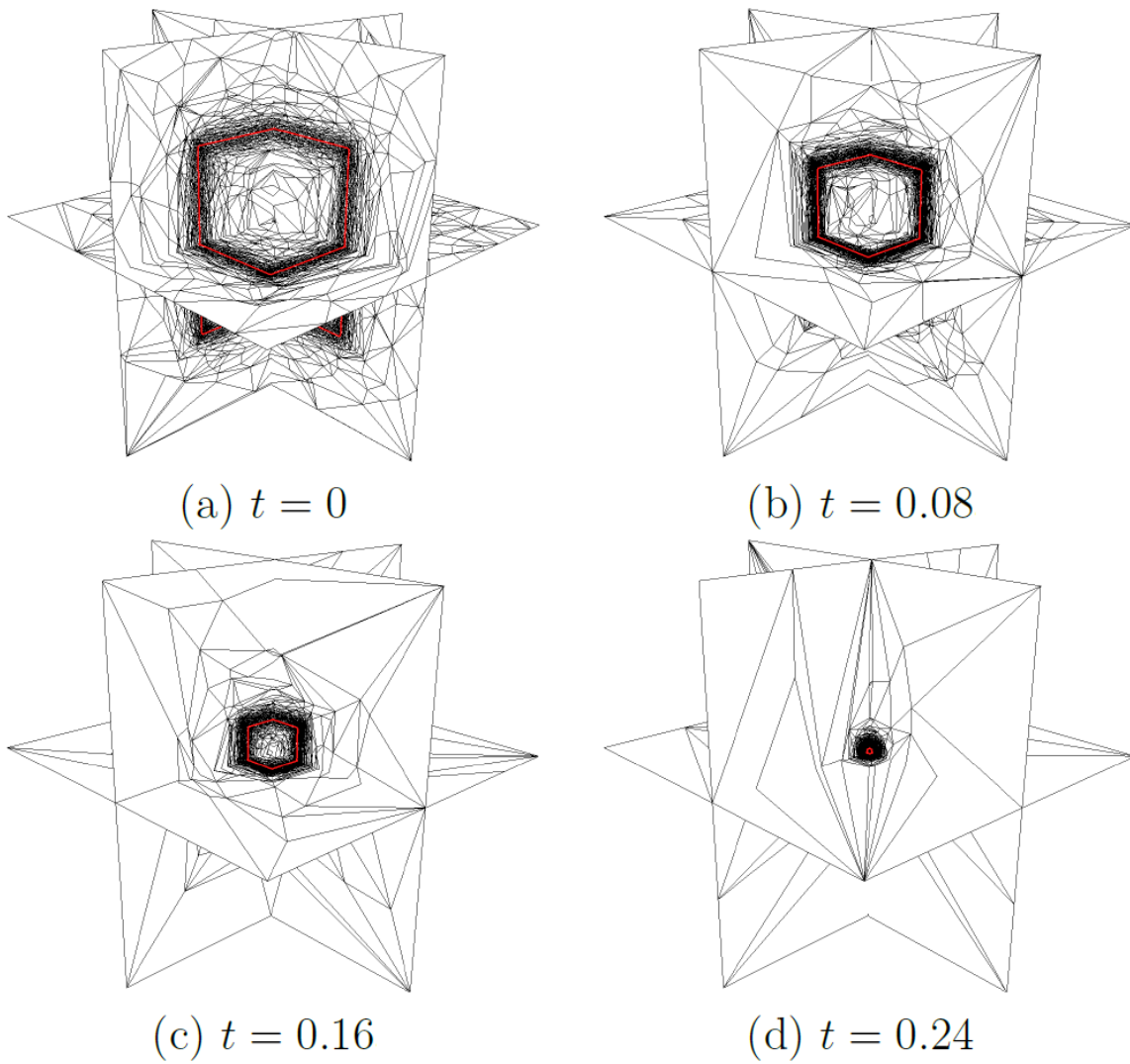


Figure 3.11 – Anisotropic mesh used for the shrinking cube test case. The red thick line indicates the zero contour.

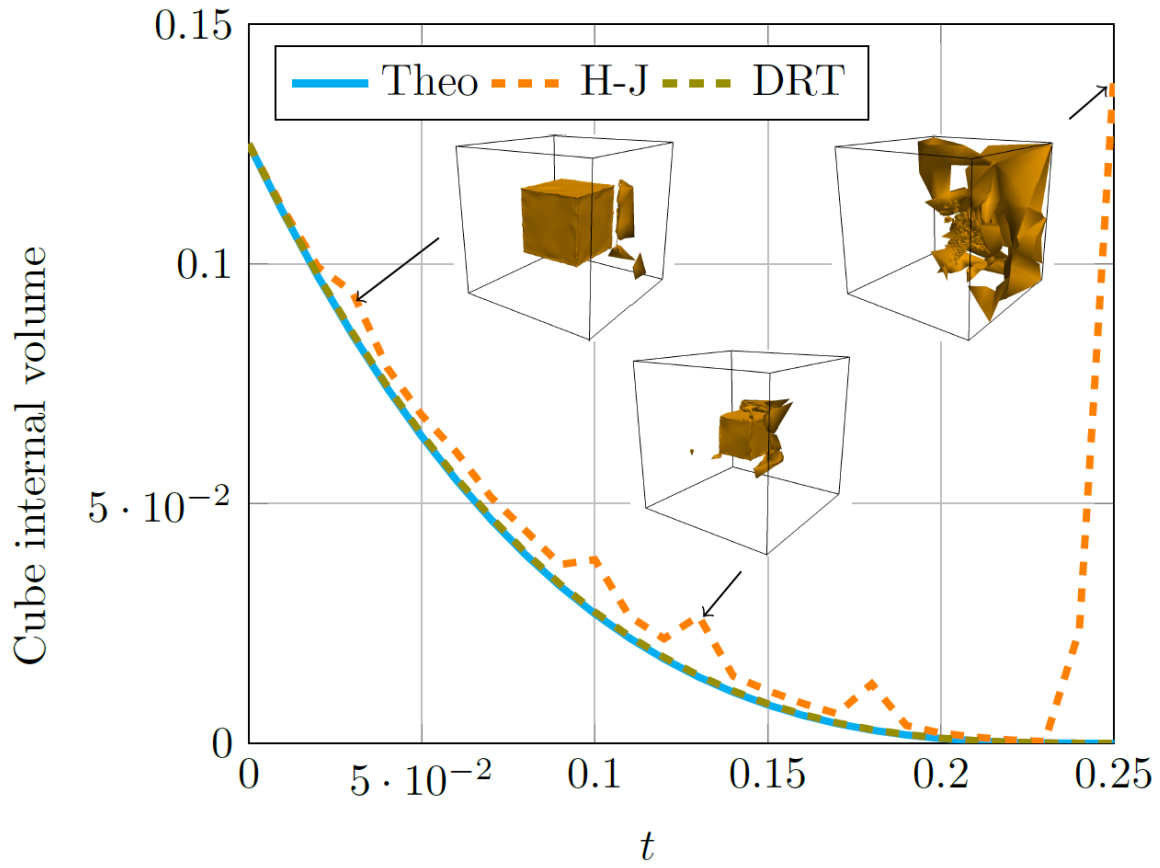


Figure 3.12 – Evolution of the cube internal volume and appearance of a parasitic phase with the H-J approach due to an unsatisfactory reinitialization of the LS function.

The CR solvers exhibit unstable behaviors although the simulation time step remains an order of magnitude lower than the mesh size in the refined zone (no violation of the stability condition). These approaches seem therefore to be less robust than the H-J and direct ones. In addition they require a good knowledge of the parameters needed for the stabilization. Results obtained with the direct and H-J approaches are summarized in Table 3.6.

Method	H-J	DRT
$\mathcal{R}(t)$ (%)	57	0.54
t_{reinit} (s)	263.6	52.8

Table 3.6 – Results of shrinking cube simulations run on 20 CPUs.

In 3D, the DRT algorithm appears to be around five times faster than the H-J approach, while keeping a very high accuracy. The gain in terms of computational performances is smaller than in 2D. Nevertheless, this configuration is particularly unfavorable to the proposed algorithm. During the simulation, the cube rapidly shrinks and becomes very small compared to the size of the domain. Considering the proposed partitioning strategy and the number of processors involved (20 CPUs for the cube shrinking case), the whole interface is poorly distributed across the CPUs. The parallel implementation described earlier thus becomes far less efficient. This is no longer true for massively multiphasic systems such as discussed in the next section wherein

interfaces are naturally spread in a balanced way across the processes.

As a conclusion, these simple academic test cases confirm the superiority of the proposed algorithm and demonstrate its robustness. It appears to be also well-suited with particular triangulations (anisotropic meshes) and does not require any calibration, contrary to other classical methods that require at least one numerical parameter.

3.2.3.2 Ideal grain growth

The second test case is an extremely popular problem in material science, namely, ideal grain growth. This problem is particularly interesting because it can involve a large number of LS functions $N_f \gg 1$. An efficient reinitialization of the LS functions is then essential when it comes to reduce the computation time.

During grain growth, the normal velocity of the grain boundaries (*i.e.*, interfaces delimiting the grains) of all grains represented by the same LS function ϕ_i is proportional to their mean local curvature κ that can be expressed as follow

$$\vec{v} = m\gamma\kappa\vec{n} = -m\gamma\nabla \cdot \left(\frac{\nabla\phi_i}{\|\nabla\phi_i\|} \right) \frac{\nabla\phi_i}{\|\nabla\phi_i\|},$$

with \vec{n} the unit outward normal vector and $m\gamma$ a material parameter set to $8.28 \times 10^{-7} \text{ mm}^2 \text{ s}^{-1}$, which is representative of a 304L austenitic steel at 1050°C [207]. In a P1 framework such as used in the present work, computing the mean curvature would rely on a Hessian recovery technique that would induce unacceptable errors using the Hessian recovery methods already available in the FE code [206]. It is thus impossible to use the CR solvers for this application. Tests using the SPR method to compute the mean curvature have not been conducted yet and are an interesting prospect (Chapter 7).

An alternative approach consists in reformulating the problem as a pure diffusion one solved on a fixed mesh, by assuming each LS function satisfies $\|\nabla\phi_i\| = 1$ around the interface. LS reinitialization is therefore fundamental for this application. Further details can be found in previous works [206, 207]. In order to remove kinematic incompatibilities a particular treatment is performed on each LS function $\phi_i(\mathbf{x}, t)$

$$\tilde{\phi}_i(\mathbf{x}, t) = \frac{1}{2} \left(\phi_i(\mathbf{x}, t) - \max_{j \neq i} (\phi_j(\mathbf{x}, t)) \right).$$

This treatment removes vacuum regions at multiple junctions (with a precision equal to the local mesh size) but also strongly alters the LS functions outside the grains, leading to catastrophic results if LS functions are not reinitialized (second column in Table 3.7). Another strategy to deal with these kinematic incompatibilities would be to rely on explicit meshing techniques such as those developed in the present work (Chapter 7).

This set of simulations is performed on a $8 \times 8 \text{ mm}^2$ domain with a fixed homogeneous mesh composed of one million elements. The initial microstructure contains around 3600 grains represented by only 27 LS functions thanks to a graph coloring technique (Figure 3.13). The evolution of the mean grain size is tracked and the well-known Burke & Turnbull mean field model [218] is used as reference solution (denoted Theo). The reinitialized thickness is fixed to $\epsilon_r = 20 \mu\text{m}$.

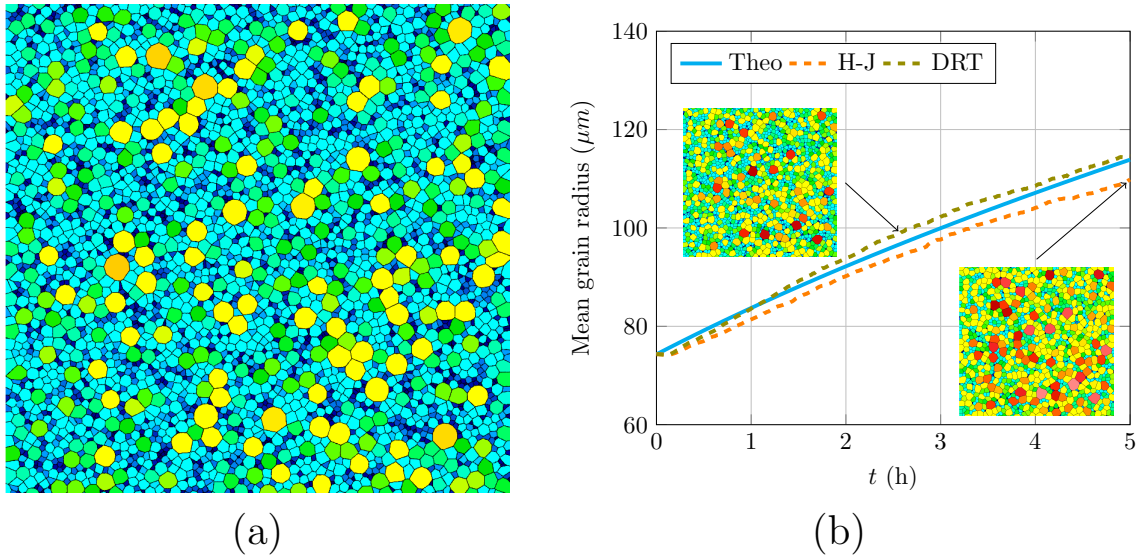


Figure 3.13 – (a) 2D initial microstructure used for grain growth. The color scale corresponds to the grain size; (b) evolution of the mean grain size and coarsening of the microstructure.

This benchmark is also used to compare the optimized (DRT) and non-optimized (DR) versions of the proposed algorithm, which have respective complexity of $\mathcal{O}(n \log e)$ and $\mathcal{O}(n \cdot e)$. The parallel implementations are challenged by running simulations on 4, 8 and 16 CPUs.

Method	Without reinit	H-J	DR	DRT
Comparison with Theo (%)	72		< 3	
t_{reinit} (h)				
4 CPUs		7.74	4.2	0.09
8 CPUs		5.02	3	0.07
16 CPUs		2.48	1.52	0.03
Speedup (4/16 CPUs)		3.12	2.76	3

Table 3.7 – Results of 2D grain growth simulations. The total duration of the heat treatment is equal to 5h.

It appears both the direct and H-J methods are in good agreement with the Burke & Turnbull model. The reinitialization times for the H-J and DR approaches are of the same order while the DRT one is around 80 times faster than the H-J method between 4 and 16 CPUs. The interest of using a *k-d tree* appears clearly in these results. The latter ones also validate the parallel implementation of the proposed DRT algorithm, as it exhibits a speedup comparable to the H-J solver.

3.2.3.3 Void growth

For this last test case, modeling of ductile damage at the scale of a Representative Volume Element (RVE) is addressed using the numerical framework developed prior to the present thesis [5]. An isotropic mesh refinement is used to progressively refine the mesh from the boundaries of the RVE to its center, where a void arrangement is located. At the interfaces between matrix and voids, an anisotropic mesh is built using the error estimator proposed in Reference [166]. Close to the interface, a small mesh size is fixed in the normal direction, and the refinement in

the other directions depends on local principal curvatures.

To compute the normal vector to the interface and the principal curvatures, the gradient and the Hessian matrix of the LS function representing the void phase are estimated thanks to the SPR technique described in Subsection 3.1.3.

The particularity of this framework is that it is Lagrangian hence the LS function is convected directly by mesh motion (ILAG method in Chapter 2). Since the voids grow and may even change shape during simulation, no LS reinitialization may lead to improper mesh adaptation.

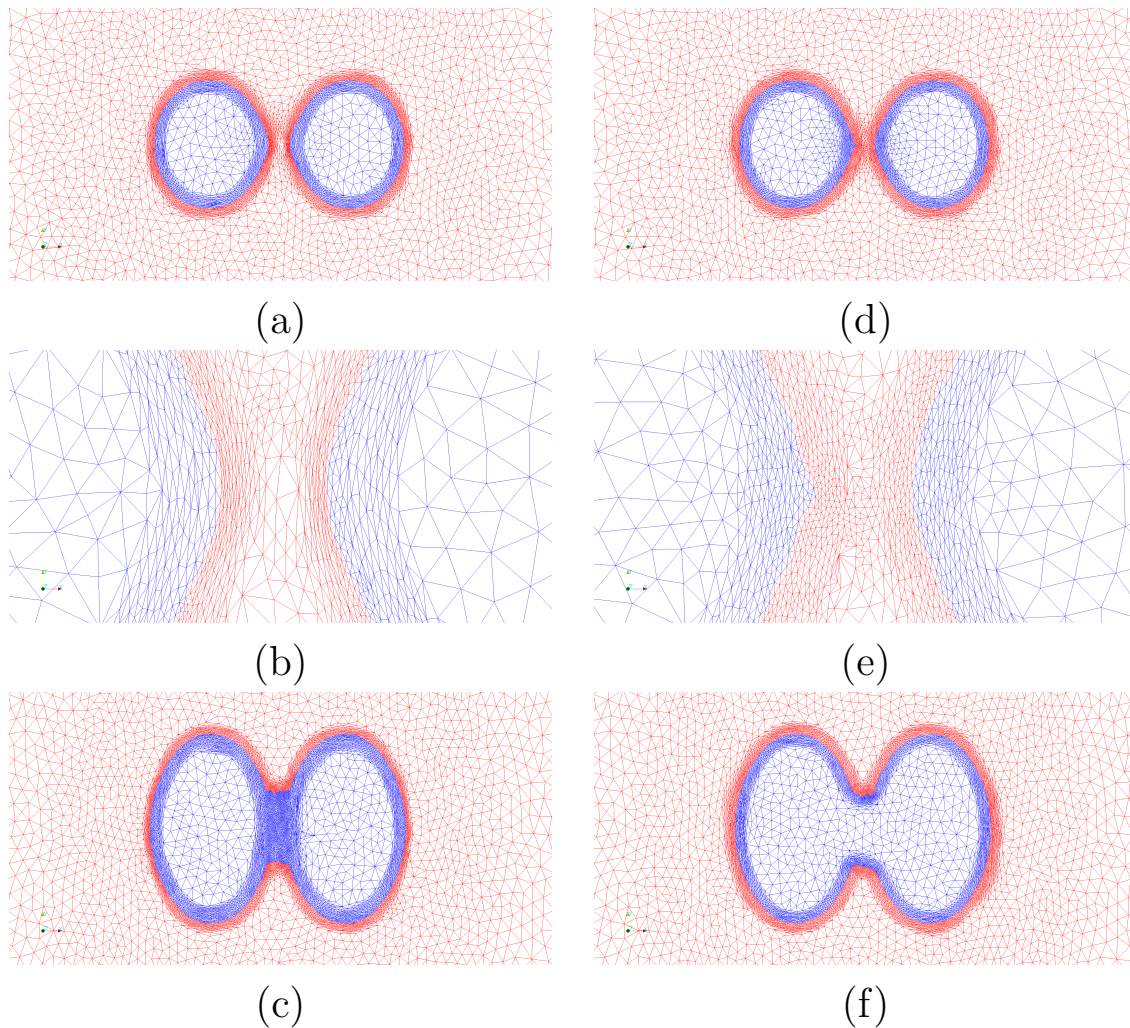


Figure 3.14 – 2D example of void (in blue) coalescence without (a,b,c) and with (d,e,f) reinitialization using the DRT method.

In the 2D example shown in Figure 3.14, a void coalescence simulation is performed without (a,b,c) and with (d,e,f) LS reinitialization. In pictures (a) and (d), it can be seen that due to the vertical tension applied on the RVE, necking appears at the intervold ligament. Pictures (b) and (e) show a zoom on this ligament. Without reinitialization, the mesh is tightened, while with a proper distance function, the mesh can be adapted identically on the whole interface. After coalescence, growth in the tensile direction is accelerated and leads to pictures (c) and (f). Obviously, only LS reinitialization can enable for a correct tracking of interfaces.

Since the framework is Lagrangian, the CR method cannot be used. Hence, both the new DRT

and the classical H-J approaches are applied to the 3D version of the configuration presented in Figure 3.14. A $1 \times 1 \times 1 \text{ mm}^3$ RVE is subjected to vertical tension at a constant velocity with a sticking boundary condition. On this 3D case, no coalescence is triggered, and the resulting void shapes at 20% of elongation are shown in Figure 3.15.

To reach 20% of elongation of the RVE, which corresponds to 200 time steps and LS reinitializations, the H-J method takes 127 minutes on 16 processors, while the new DRT method takes 23 minutes in the same configuration. Though the efficiency of the DRT method compared to the H-J method was already proven in previous simulations, this test case confirms the superiority of the DRT approach when the reinitialization thickness becomes large.

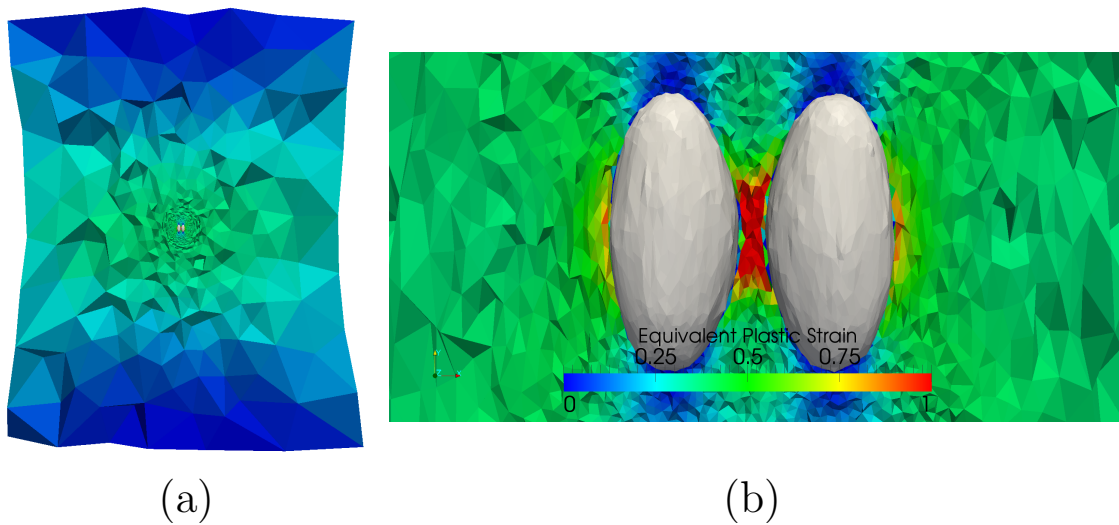


Figure 3.15 – Equivalent plastic strain and void shape after 20% of vertical elongation using the DRT method.

3.2.4 Conclusion

Although indirect methods to reinitialize LS functions were historically developed to avoid the computational costs required by direct methods, it is proved in this section that this idea is questionable. For example, it is proved that simple DR through a brute force algorithm can compete with an H-J approach in terms of performance for massively multiphasic problems such as grain growth in polycrystalline aggregates.

Then, based on a *k-d tree* sorting of the interface discretization, a new DRT method is proposed and applied to three different test cases arising from different contexts. The novelty of this method relies in its parallel implementation, its capability to reinitialize efficiently the LS function only in a small layer around the interface with a direct approach, and its compatibility with unstructured anisotropic meshes.

This parallel and optimized DRT approach is proved to be as accurate as a classical DR method, while being up to 20 times faster. Computation time reduction is also observed compared to an H-J formulation, with speed-ups between 5 in 3D and 300 in 2D. Additionally, direct methods, including the new DRT technique, reveal being the most accurate in theory as in practice.

All tests are performed with unstructured 2D or 3D meshes, and anisotropic mesh adaptation for the third one, to illustrate that the proposed method remains as efficient in all these configurations.

However, it is mentioned that the efficiency of the bounding boxes method used for the parallel implementation highly depends on mesh partitioning. Taking the interface into account inside the mesh partitioning algorithm should be considered in order to further improve the parallel performance of the proposed algorithm for general applications.

3.3 Connected Components identification

In this section, the problem at hand is to identify each CC of a given LS function ϕ . This is a necessary step before computing any statistical data regarding the inclusions and voids and their distribution. It also plays a key role in void nucleation and coalescence modeling, where each inclusion or void has to be considered individually.

The approach chosen to solve this problem is based on a CC identification algorithm where the FE mesh is considered as a graph, namely, mesh nodes are considered as graph vertices, and mesh edges as graph edges. While this problem seems trivial, especially in the field of graph theory, it becomes quite complex in a distributed computing context. Since the mesh, and hence the graph, are distributed among several processes, a single CC may be partitioned among multiple processes.

Before addressing these difficulties linked to the parallel implementation, the problem is first formalized and then solved using a sequential algorithm. The objective is to create an FE field at mesh nodes, noted \mathcal{I} , in which each CC has a unique identifier (id). To achieve this goal, Algorithm 3 is proposed.

Algorithm 3 Recursive tagging of the CCs.

```

function TAG(Mesh mesh, Field  $\phi$ ) : Field  $\mathcal{I}$ 
  Node seed
  Integer id
  for seed  $\in$  mesh.nodes() do
    if  $\phi(\text{seed}) \geq 0$  then
       $\mathcal{I}(\text{seed}) \leftarrow -1$ 
    else
       $\mathcal{I}(\text{seed}) \leftarrow 0$ 
    end if
  end for
   $id \leftarrow 1$ 
  for seed  $\in$  mesh.nodes() do
    if  $\mathcal{I}(\text{seed}) = -1$  then
      PROPAGATE_TAG( $\mathcal{I}$ , seed, id)
       $id \leftarrow id+1$ 
    end if
  end for
end function
function PROPAGATE_TAG(Field  $\mathcal{I}$ , Node seed, Integer id)
  Node new_seed
   $\mathcal{I}(\text{seed}) \leftarrow id$ 
  for new_seed  $\in$  seed.neighbor_nodes() do
    if  $\mathcal{I}(\text{new\_seed}) = -1$  then
      PROPAGATE_TAG( $\mathcal{I}$ , new_seed, id)
    end if
  end for
end function

```

The notations are the same as in Algorithm 1, with the addition of the function `neighbor_nodes()` that gives the set of the nodes connected to a given node by an edge. Unrolling this algorithm, when a node located inside the LS function (*i.e.*, $\phi \geq 0$) is found, it is assigned an integer value *id*. Its neighbors are then recursively contaminated until the interface is reached (*i.e.*, when ϕ becomes negative). The variable *id* is finally incremented and the procedure continues with the remaining unlabeled nodes, as illustrated in Figure 3.16. This algorithm has a complexity which is almost linear.

It is obvious the previous algorithm does not work in parallel because a process cannot access the nodes located on another partition. This difficulty is detailed by the example in Figure 3.17(a).

In this worst case scenario, three partitions P_0 , P_1 and P_2 share two CCs. One is totally located on P_2 while the other is shared by the three partitions. Moreover the latter is seen as two distinct components by P_1 . To solve this situation and any other situations that may occur with more processes or components, the following divide and conquer procedure is proposed

1. each process performs Algorithm 3 independently, leading to independent tags, possibly redundant,
2. in Algorithm 3, when an exterior (located on another partition) neighboring *Node* is met, it is stored in a set,
3. this set is communicated between processes,
4. each process receives messages of type "Process *X* wanted to tag your *Node* *N* with tag *id*"; if *Node* *N* already has a not null *id*, the conflict is communicated to the root process,
5. the root process solves the conflicts by applying Algorithm 3 on the tags instead of the nodes,
6. the root process finally broadcasts the new global tags to the other processes.

Let Figure 3.17(b) be the result of the first step of this procedure on the proposed worst case scenario. P_0 has recognized one CC, tagged as " P_0 's 1", while both P_1 and P_2 have a number 1 and a number 2 CC. During its tagging loop, P_0 has seen that some of its nodes are connected (by an edge) to nodes located on P_1 and P_2 , and the same for the other two. To prevent redundancy, a conflict is detected only if the identifier of the neighboring partition is higher than the one of the current partition.

For example on partition 1 (corresponding to the process P_1), if a *Node* of P_0 is met, there is no conflict because $1 > 0$. If a *Node* of P_2 is met, the conflict is detected and stored in the set. A description of all possible situations can then be established (the item letters correspond to the element edges represented in Figure 3.17(b))

- (a) P_1 has a *Node* with no tag that P_0 sees as tag 1 \rightarrow there is no conflict,
- (b) P_1 has a *Node* with tag 2 that P_0 sees as tag 1 \rightarrow the conflict " P_0 1 means P_1 2" is stored,
- (c) P_2 has a *Node* with no tag that P_0 sees as tag 1 \rightarrow there is no conflict,
- (d) P_2 has a *Node* with no tag that P_1 sees as tag 1 \rightarrow there is no conflict,
- (e) P_2 has a *Node* with tag 2 that P_0 sees as tag 1 \rightarrow the conflict " P_0 1 means P_2 2" is stored,

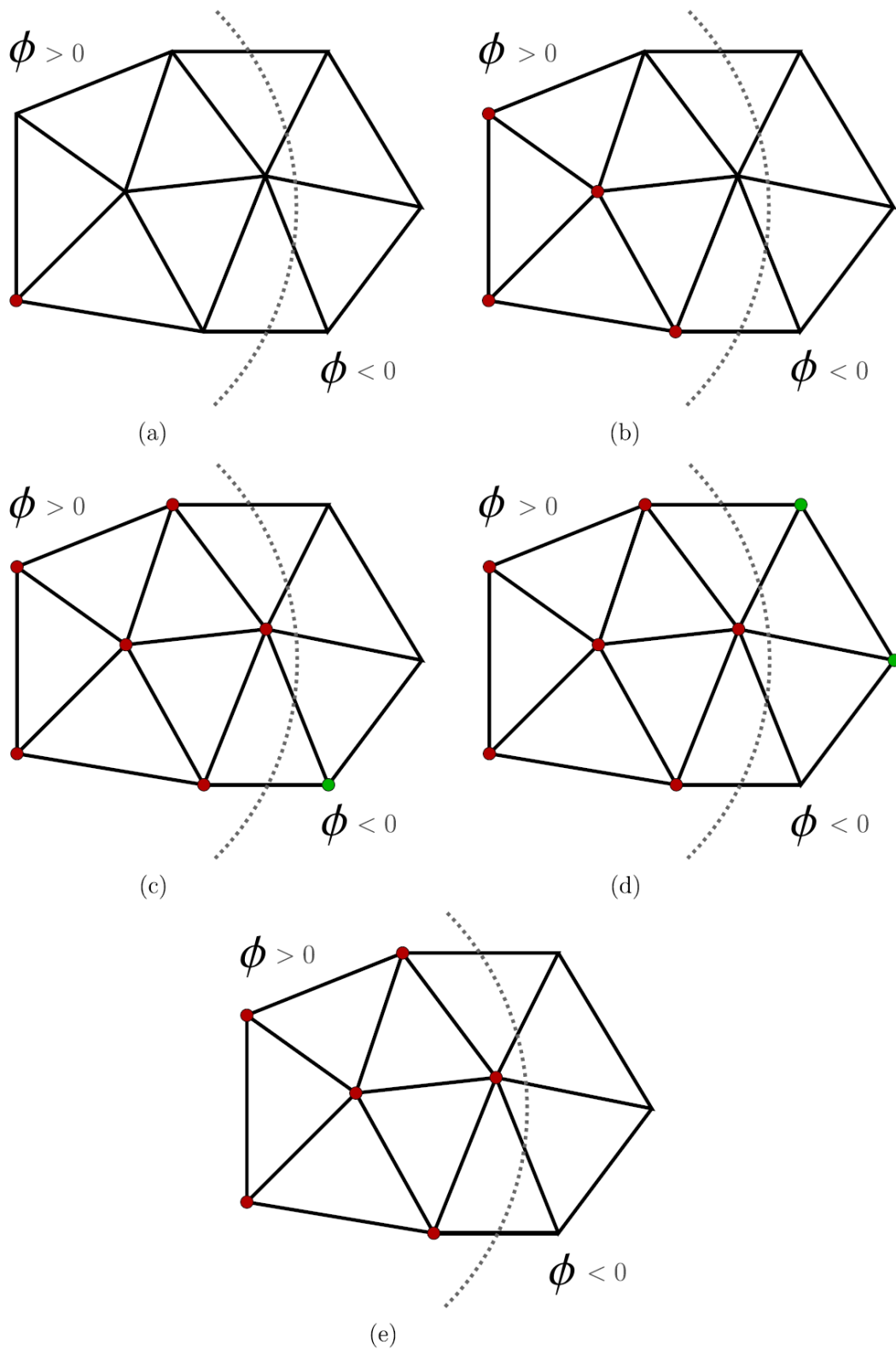


Figure 3.16 – Tagging procedure. The recursive propagation stops when a node satisfactory $\phi < 0$ is met, which means that the interface has been crossed (green nodes in (c-d)).

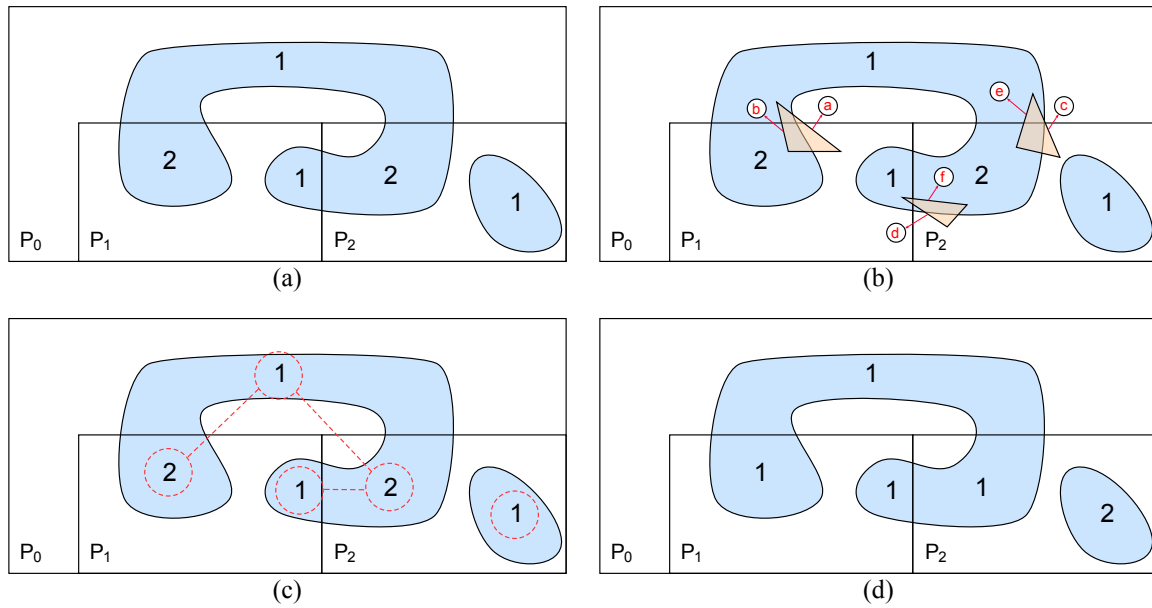


Figure 3.17 – Example presenting: (a) a worst case scenario for tagging in a distributed computing context, (b) local tags after employing Algorithm 3 independently on each partition, (c) graph giving the tag conflicts, (d) final global tags.

(f) P_2 has a *Node* with tag 2 that P_1 sees as tag 1 \rightarrow the conflict " P_1 1 means P_2 2" is stored.

The next step of the algorithm is, for each process, to send its tags along with these conflicts to the root process. All redundancies are then treated by applying Algorithm 3 on a specific graph constructed by the root process in which the nodes are the local tags of each process and there exists a connection between two nodes if there is a conflict between them, as illustrated in Figure 3.17(c). After performing the algorithm on this graph, global tags that are unique for each CC are obtained. The matching table between local and global tags is finally broadcast to all processes, which then correct their numbering, as in Figure 3.17(d).

This step of the algorithm is thus critical because all the conflicts are treated by the root process. Nevertheless, its complexity depends on the number of CC represented by the LS function, which is several order of magnitude lower than the number of mesh nodes. Hence, the computational cost of the algorithm is negligible with respect to other operations such as remeshing, or mechanical solution.

3.4 Image immersion and meshing

The numerical tools presented in the preceding sections and in Chapter 2 can be used to mesh any geometry for which an LS function can be computed, and then adapt the mesh during deformation. For most simple geometries (*e.g.*, planes, spheres, triangles) analytic formulas can be found. For more complex entities such as those found in Computer Assisted Design (CAD) files, a preprocessing step may be used to transform the CAD file into a surface mesh, and then compute LS functions based on this surface mesh.

For biology and materials science applications however, the use of CAD files is not possible because the data are acquired using X-ray techniques. As the objectives of the present work include comparisons with experimental data, a method has to be developed in order to mesh real microstructures from X-ray data.

3.4.1 Method

Meshing heterogeneous domains is a difficult task that is however necessary for multiple applications. Although robust and fast solutions can be found for first order triangular or tetrahedral mesh generation from CAD files [192, 219], their extension to arbitrary element types and orders are still being developed [220]. Additionally, in many applications such as medicine or materials science, the input is not a CAD file or a parametric description, but a 2D or 3D image of the object. Mesh generation from this kind of data is an open and prolific research topic, for which various approaches have been proposed [203, 221, 222].

A direct method would consist in first thresholding the image, applying a contour detection algorithm to build a surface mesh of all interfaces and then building a volume mesh around them [203]. The method presented in this section consists in first building a volume mesh of the domain Ω , usually of a box for the present applications. This mesh will generally be structured with a uniform isotropic mesh size equal to h_{max} if one wants to progressively refine the mesh in some regions, as in Subsection 3.1.4, or h_{min} if one wants to capture directly all details of the image, and then coarsen the mesh in some regions. The choice between these two approaches will generally be based on the complexity of the geometry; for instance, a high density of interfaces with significant tortuosity will favor the second method.

Standard image processing operations [223, 224] are applied on the image to smooth the data, threshold a selected phase, and then convert these binary data to a signed distance function. The latter is interpolated to the FE mesh using a trilinear FE interpolation procedure where the image is considered as a hexahedral grid, voxels being nodes.

It may seem preferable to compute the signed distance function on the FE mesh rather than on the image, using LS reinitialization. The algorithm applied on the image does not benefit from the distributed computing capabilities of the FE code, and is highly memory-consuming. However, poor results are obtained when gray levels or binary data are directly interpolated from the image to the FE mesh [222]. In particular, oscillations are obtained at the interface, which is a major issue not only for mechanical computations but also for the mesh adaptation procedure, which depends on local principal curvatures. Therefore, the LS function is computed directly on the image, which may be a limiting part of the procedure, though it is only applied once for each image.

After this LS function is interpolated to the FE mesh, LS reinitialization is generally applied in order to have a distance field that is relevant with respect to the interface that was actually interpolated on the FE mesh (some regions may have vanished due to a coarse mesh size).

This LS function is used as an intermediary to locate the interface and construct an explicit representation (Section 2.1). This mesh generation step is combined with an adaptation step taking into account the local maximum principal curvature of the interface (Section 3.1).

A similar procedure was used for example in Reference [222], but with an indirect LS reinitialization method, and no conform meshing of the interface. The quality of the interpolation from the image to the mesh is also improved. The whole procedure is summarized with an example in Figure 3.18. For applications with multiple phases and LS functions, it is just repeated for each phase. If it is chosen to progressively adapt the mesh, steps (b-d) are repeated from 5 to 10 times until no significant change in the number of elements is noticed.

Compared to classical approaches [203, 221], the main difference in the proposed method is that both LS reinitialization and conform mesh generation steps rely on contour extraction algorithms applied on the FE mesh, and not on the image. Recent X-ray imaging techniques produce high resolution images, which are generally several orders finer than the FE mesh that will be used for computations. While classical approaches always start from a surface mesh as fine as the image, and then coarsen it if the user prescribes a coarse mesh size, in the proposed method only the coarse mesh is used, and all algorithms are applied only on this mesh, except for the image processing operations mentioned above.

Reducing the number of operations performed on the image and implementing them in the FE code also has the benefit of enabling the use of the distributed computing capabilities of this code, especially regarding parallel LS reinitialization (Section 3.2) and mesh adaptation (Section 2.5). In order to increase even more the efficiency of this approach, it would be interesting to study the issue mentioned above regarding interpolation of the data from the image to the FE mesh, especially for applications to very large images.

3.4.2 Results

In this section, applications are proposed in order to illustrate the capabilities of the image meshing procedure. The computations start with an initial structured mesh of the domain, with a mesh size equal to h_{min} , so that the image importation procedure in Figure 3.18 is performed as is. In particular, no iterative process consisting in importing the image several times to progressively adapt the mesh before the construction of the final conform mesh is used. As a consequence, computational cost and memory consumption could be reduced for the following computations, because the initial mesh is very fine compared to the desired one. Volume conservation parameters are set to $Q_\mu = Q_\sigma = 0.05$. All computations were performed on the same 1.2GHz Intel Xeon Linux cluster.

3.4.2.1 Stanford Bunny

The Stanford Bunny is a well-known geometry proposed by the Stanford University Computer Graphics Laboratory and used extensively in the meshing and computer graphics communities to illustrate their algorithms. A Computed Tomography (CT) scan of a Stanford terra-cotta bunny provided by Marc Leroy of Stanford CS was performed by Terry Yoo of the National Library of Medicine, using a scanner provided by Sandy Naper and Geoff Rubin of Stanford Radiology. The data consists of 360 scans of 512×512 voxels, which is also the size of the domain. This first test is purely illustrative, though real animals and insects are typical examples of "objects" for which CAD files are not easy to find or construct, while CT scans are possible.

A first mesh obtained with adaptation parameters $h_{curv} = 0.2$, $h_{max} = \epsilon_h = 50$, $h_{min} = 10$ is shown in Figure 3.19(a). The discretization varies from a very fine mesh of size h_{min} (blue) in regions

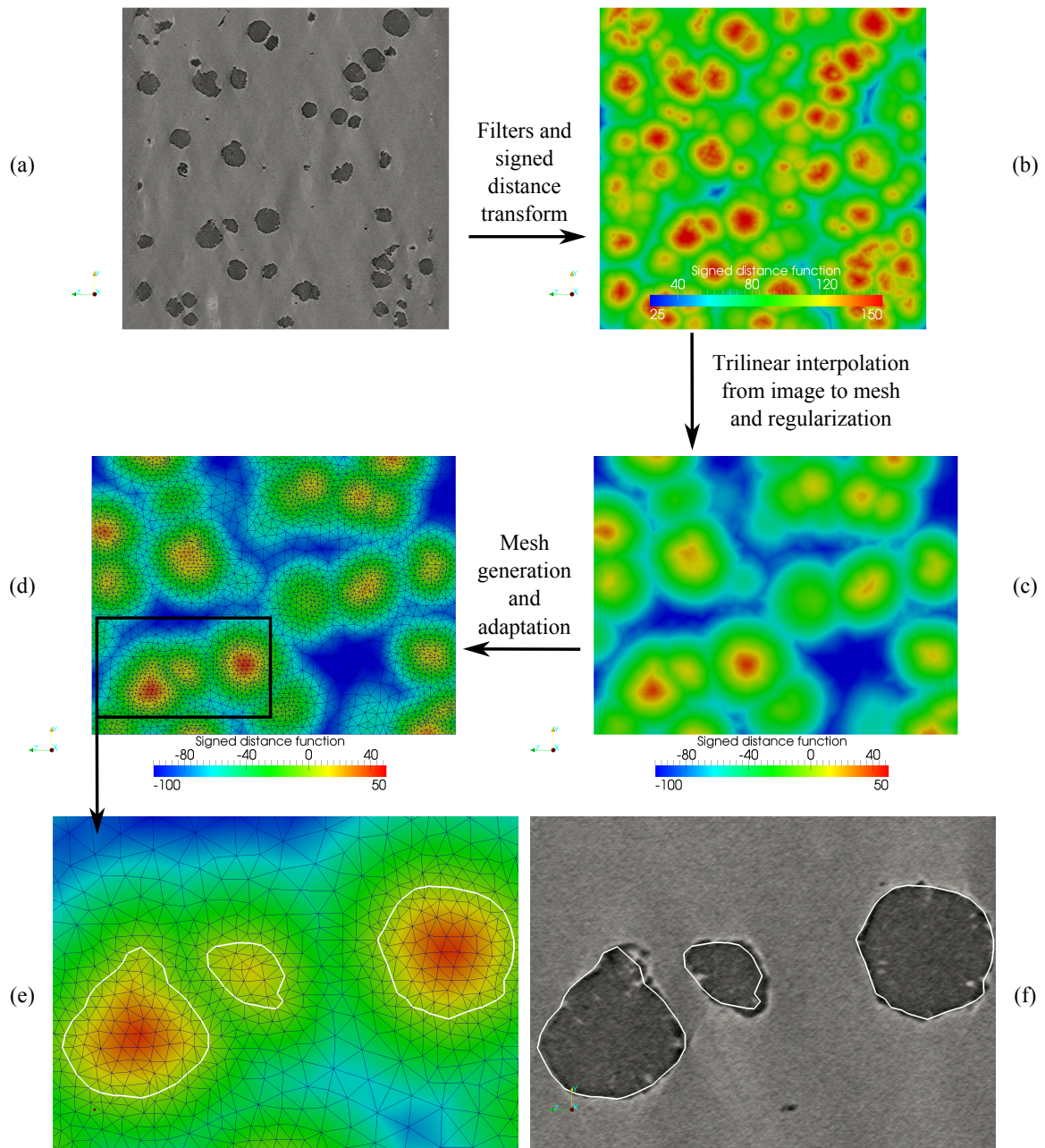
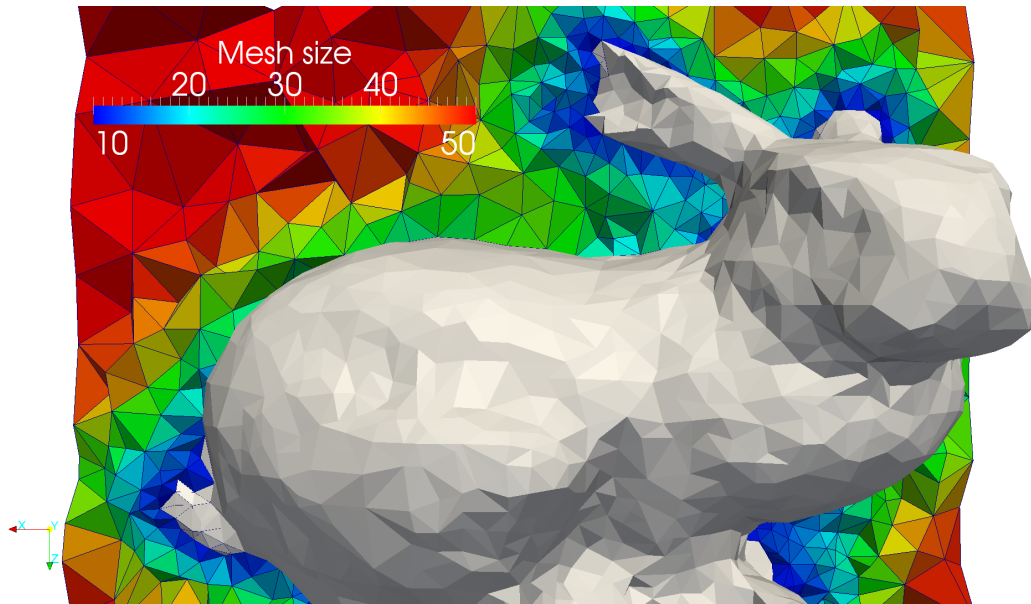
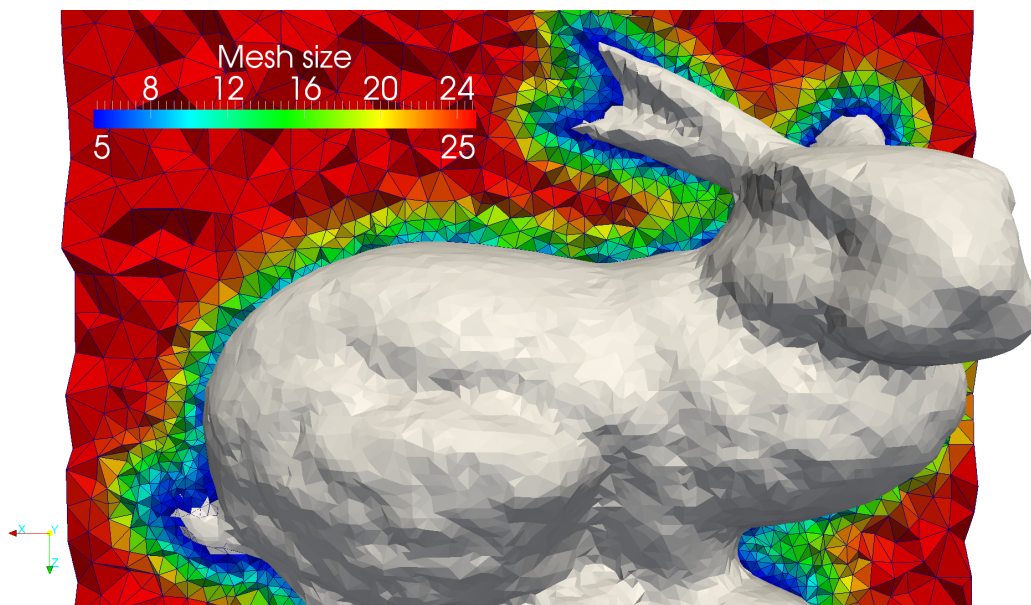


Figure 3.18 – Image immersion and meshing: (a) initial X-ray image, (b) signed distance function computed thanks to image processing, (c) signed distance function interpolated and regularized on the FE mesh, (d) conforming FE mesh generated and adapted to interfaces and the local maximum principal curvature, (e) zoom on the FE mesh, (f) comparison between initial X-ray image and interfaces in the final FE mesh (in white). Figure reproduced from Reference [42].

with high principal curvatures such as the tail, while coarser elements (green) are obtained in regions with lower principal curvatures such as the back. Far from the interface, a mesh size of h_{max} (red) is retrieved.



(a)



(b)

Figure 3.19 – Mesh generation from the Stanford bunny CT scan: (a) coarse mesh, (b) fine mesh.

To show the flexibility of the technique and its ability to capture finer details by varying mesh adaptation parameters, a finer setting $h_{curv} = 0.1$, $h_{max} = \epsilon_h = 25$, $h_{min} = 5$ is used to obtain the result in Figure 3.19(b). Comparing the two results, it can be seen that details are more accurately represented with the fine mesh. This has a direct influence on computational cost, which is of 2 min for the coarse mesh of 84660 elements, and 34 min for the fine mesh of 550502 elements, on 8 CPUs.

3.4.2.2 Bone

At the intersection between medical science and materials science, the study of bone behavior is important to understand the cause of bone fracture, and the impact of some illnesses such as osteoporosis. In a recent work [225], CT scans were acquired from mandibular bone samples. As illustrated in Figure 3.20(a) and Figure 3.20(b), this part of the human skeleton is heterogeneous as it is composed of cortical bone and spongy cancellous bone. Because these two materials have different material properties, it is complex to determine a homogenized Young's modulus. For accurate results, distribution and shapes of these pores should be taken into account, by performing full field numerical simulations on RVEs and comparing them with homogenized results.

As a first step towards such simulations, the image immersion method is applied to a volume extracted from this 3D image. The size of the domain is set to $100 \times 100 \times 100$ voxels, which is the resolution of the extracted 3D volume. The mesh adaptation parameters are set to $h_{curv} = 0.4$, $h_{max} = \epsilon_h = 10$, $h_{min} = 2$ for a first coarse setting, and $h_{curv} = 0.2$, $h_{max} = \epsilon_h = 5$, $h_{min} = 1$ for a second fine setting. The generated meshes are shown in Figure 3.20(c) and Figure 3.20(e).

Due to the high density of interfaces and their numerous variations, most portions of the interface are discretized with h_{min} . Comparison between Figure 3.20(b), Figure 3.20(d) and Figure 3.20(f) shows once again the effect of the meshing parameters. The importance of smoothing the data in the images is also shown in these images, as the artifacts in Figure 3.20(b) do not appear in Figure 3.20(f). The mesh obtained with the fine setting in Figure 3.20(e,f) seems to be both accurate regarding the description of the interface and of good quality for FE computations.

This is confirmed in Figure 3.21, where mesh quality distribution is investigated. The histogram is slightly shifted to the right with the fine mesh, as the proportion of elements close to interfaces gets lower. The important observation that can be made on this graph is that no element has a quality under $Q_\mu = 0.05$, which proves that the volume conserving mesh adaptation algorithm is robust enough to recover from the ill shaped elements created by the fitting procedure.

Regarding computation time, it is of 5 min for the coarse mesh of 360410 elements, and 24 min for the fine mesh of 2289614, on 32 CPUs. Approximately 85 – 90% of this cost is due to the mesh adaptation algorithm, and less than 3% to LS reinitialization. Comparison between the coarse and fine settings shows that computation time is nearly proportional to the number of elements. This proves that Algorithm 1 converges rapidly, without browsing the mesh too many times. Finally, computation time for both results is reasonable as the number of elements is significant in both cases.

3.4.2.3 Fibers

The study of the microstructures of composites is of great interest in order to determine the macroscopic mechanical behavior of these heterogeneous materials. As in the preceding case, this requires computations on small RVEs, which can be either real or virtual (generated based on statistics).

In this test, the RVE is a small volume extracted from Synchrotron Radiation Computed Tomography (SRCT) images obtained at beamline ID16 of the European Synchrotron Radiation Facility - Grenoble (ESRF - Grenoble) during a previous work [226]. The material is a polymer reinforced by glass fibers, with a dominant orientation that can be seen in Figure 3.22(a). The size of the domain is set to $100 \times 100 \times 200$, which is the resolution of the extracted 3D volume.

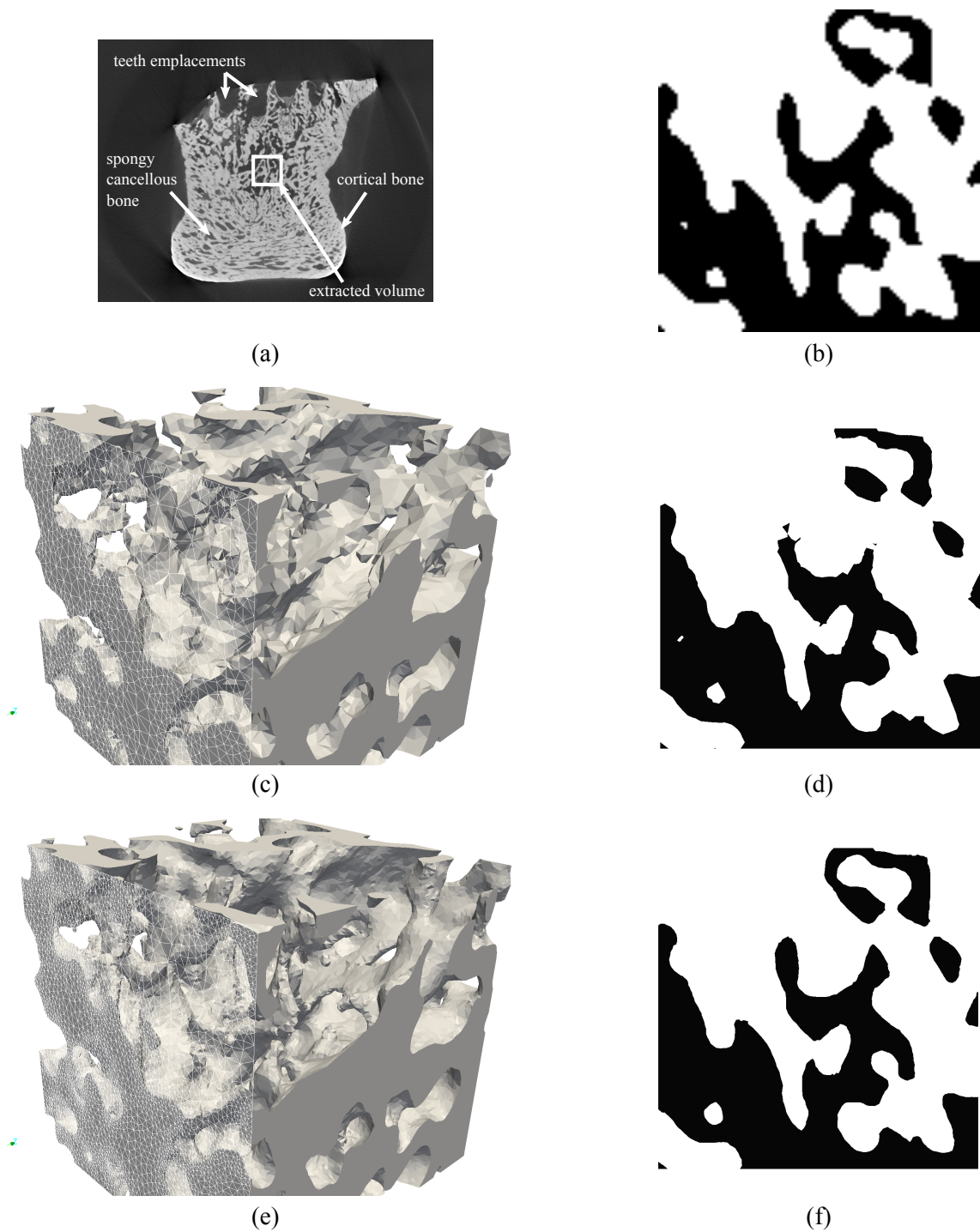


Figure 3.20 – Mesh generation from mandibular bone tomography images: (a) slice of the initial image, courtesy of Y. Tillier [225], (b) middle slice of the volume extracted from the initial image with cortical bone in black, (c) surface view of the cortical bone in the generated coarse mesh, (d) middle slice of the coarse mesh with cortical bone in black, (e) surface view of the cortical bone in the generated fine mesh, (f) middle slice of the fine mesh with cortical bone in black.

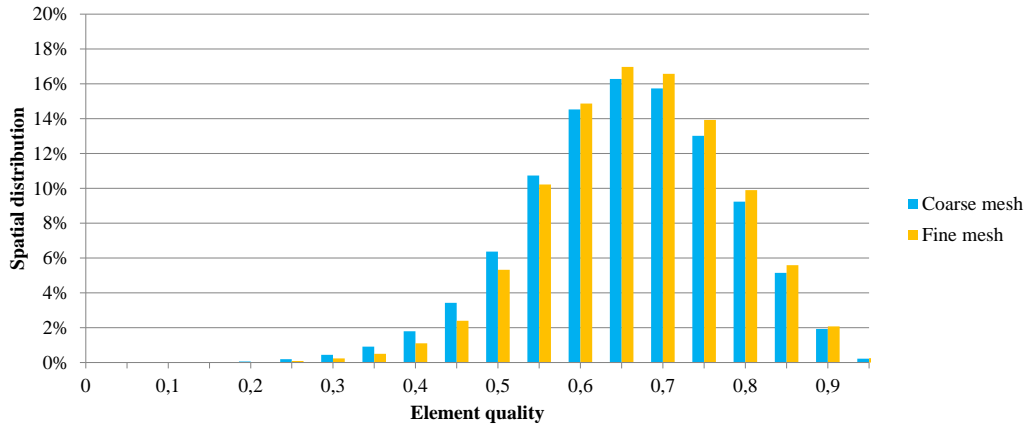


Figure 3.21 – Quality distribution in the meshes generated from mandibular bone CT scans.

The two sets of mesh adaptation parameters are the same as in the preceding section. The results are presented in Figure 3.22(c-f). Because all reinforcements are of same shape and size, mesh size at the interface is nearly constant, apart from some contact areas between neighboring fibers. These contact areas cannot be modeled with the image meshing technique proposed in this chapter. In fact, some fibers cannot be distinguished in the images due to the resolution of the SRCT imaging technique (Figure 3.22(b)), and they cannot be distinguished in the meshes either (Figure 3.22(d,f)). Modeling contact mechanisms between these fibers that are very close to each other would require a different approach, for instance one based on digital microstructures and CAD files [8].

Regarding quality distribution, the same trends as in Figure 3.21 are observed and the graphs are hence not reported here. In particular, no element with a quality lower than $Q_\mu = 0.05$ is present in the final meshes, and the histogram is slightly shifted to the right with the fine mesh, due to a higher proportion of elements far from interfaces. For the same reason, computation time is not reported either. It is observed to be proportional to the the number of elements, with a significant mesh adaptation cost, and negligible costs for all other operations. As a conclusion, this test shows the flexibility of the proposed method when the addressed microstructure changes. Neither the quality of the result nor the cost of the method were severely affected by the change of morphology. In particular, the present microstructure contains elongated features, which have a simple geometrical shape (cylindrical) but with multiple contacts, while the preceding microstructure featured a more tortuous and geometrically complex arrangement.

3.4.2.4 Nodules

As a last test case for the image importation procedure, Synchrotron Radiation Computed Laminography (SRCL) images of nodular cast iron are used. As calculations and error measurements with different meshes are carried out in Chapter 6 using these images, the present test only focuses on illustrating the capabilities of the CCs identification procedure detailed in Section 3.3. Due to the large number of nodules, the computation is run on 40 CPUs. Thus, the distributed computing implementation of the CCs identification algorithm is used to its full extent. The

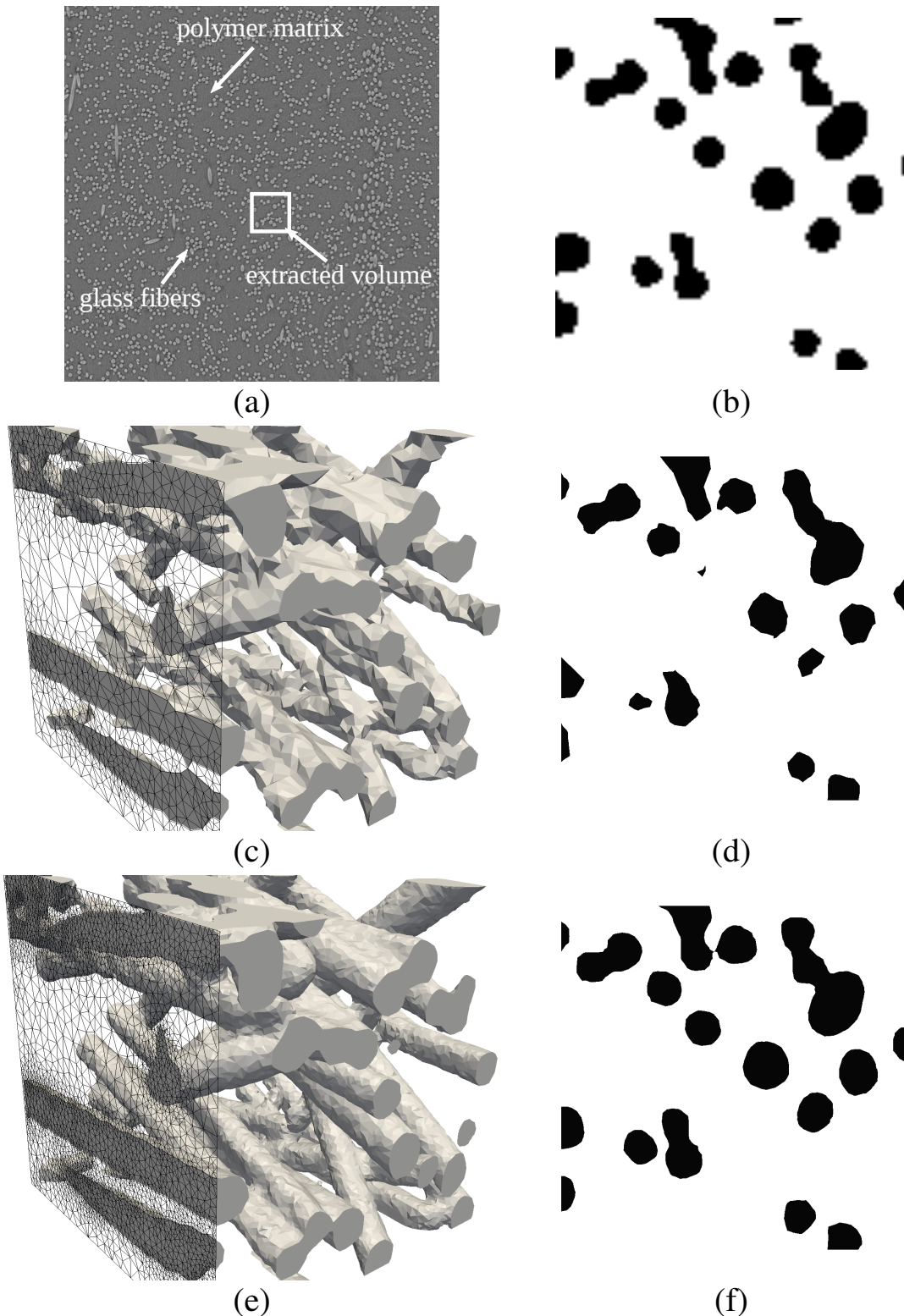


Figure 3.22 – Mesh generation from composite SRCT images: (a) slice of the initial image, courtesy of V. Fabre [226], (b) middle slice of the volume extracted from the initial image with glass fiber reinforcements in black, (c) surface view of fibers in the generated coarse mesh, (d) middle slice of the coarse mesh with glass fiber reinforcements in black, (e) surface view of fibers in the generated fine mesh, (f) middle slice of the fine mesh with glass fiber reinforcements in black.

result is shown in Figure 3.23. The different CCs are identified with different colors. The number of nodules is close to the hundred, but some nodules are in contact, leading to false results. For instance, the arrow in Figure 3.23 points to three nodules that form as a single CC and will hence be considered as a single nodule for the fragmentation criterion. If the nodules are not in contact in the initial image, this issue could however be avoided using a finer mesh, in order to have some nodes between the nodules. If the nodules are in contact in the initial image, then it is quite difficult to distinguish them. Physically, the importance of such treatment would depend on whether load is transferred totally or partially between the nodules. Such advanced modeling is not addressed in the present work. Hence, for these "connected" nodules, sticking contact is assumed, and fragmentation is considered for the whole CC.

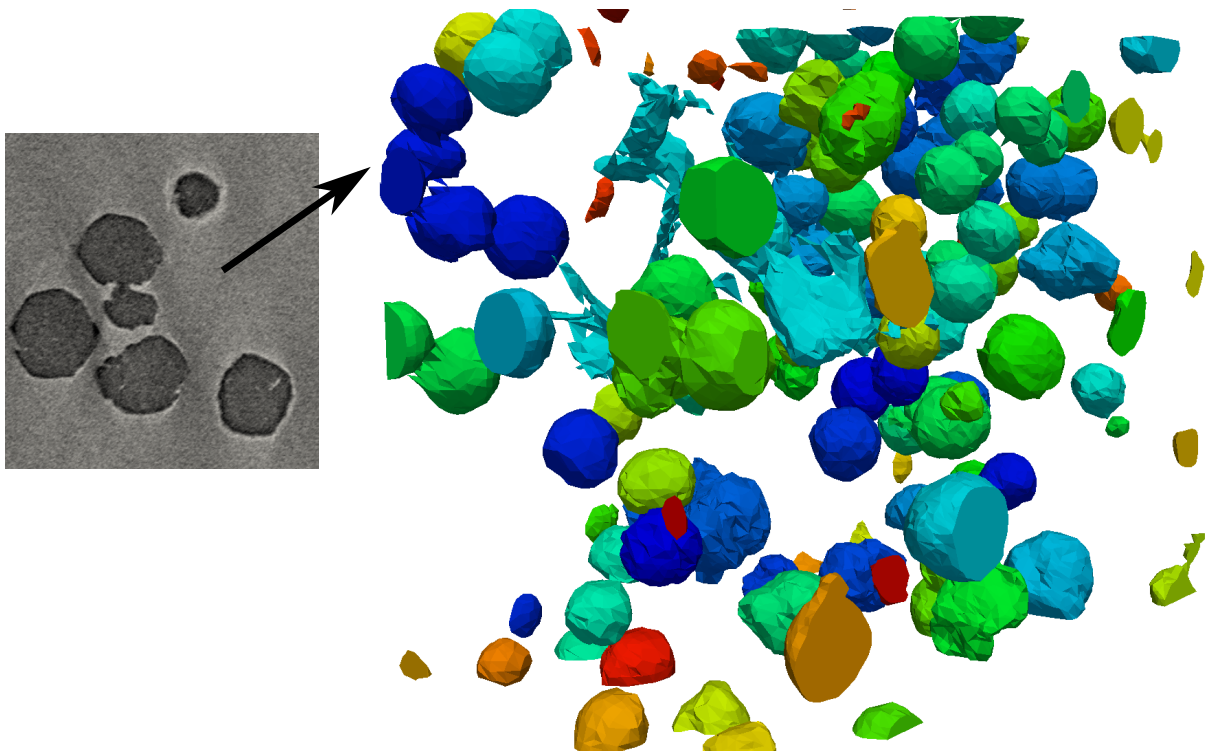


Figure 3.23 – Mesh generation from nodular cast iron SRCL images, final mesh with CCs identification. The nodules pointed out by the arrow are tagged with the same identifier because they are very narrow and in contact at some points in the initial X-ray image.

Conclusion

In this chapter, three numerical ingredients are added to the Finite Element (FE) framework with the aim of importing X-ray data to the FE mesh and generating meshes that are adapted to these data. The image importation procedure described in Section 3.4 is based on some image processing operations, performed once for each image. Due to the cost both in terms of memory consumption and computation time of these operations, treatments are systematically performed using the FE code when possible. The distributed computing capabilities of this code are hence exploited as much as possible.

The adaptation of the mesh to the geometry extracted from images, and microstructures in general, relies on an Hessian recovery step. The latter is solved using a distributed computing implementation of a second order Superconvergent Patch Recovery (SPR) technique, as detailed in Section 3.1. The eigenvalues of the Hessian matrices of Level-Set (LS) functions are used to estimate the local principal curvatures close to interfaces, and refine the mesh in regions with high maximum principal curvature.

Numerical experiments prove that the coupling between this error estimator and the mesh adaptation algorithm yields convergence rates that are close to the theoretical ones. For geometries with singularities, these convergence rates are deteriorated, as could be expected.

For the error estimator to be relevant, it is important that the LS functions remain as close as possible to signed distance functions. An irregularity would lead to a wrong estimation of the local principal curvatures, and then to a mesh that is locally too fine or too coarse. Hence, an LS reinitialization procedure is proposed in Section 3.2.

Numerical experiments prove that this algorithm is very interesting in terms of computation time and accuracy with respect to other methods proposed in the literature. Applications on X-ray images of biological materials and composites show that the cost of this operation is negligible with respect to mesh adaptation.

Once images are imported to the FE mesh and regularized with LS reinitialization, the mesh is adapted to interfaces, with an implicit or explicit representation. Identifying the different components of the microstructure, for statistical or modeling purposes, is carried out thanks to a parallel Connected Components (CCs) identification algorithm presented in Section 3.3.

Thanks to these different ingredients, FE meshes that are both conform and of good quality are generated and adapted to various geometries corresponding to a wide range of applications where three-dimensional (3D) imaging techniques are used extensively. This procedure has reasonable computation time, and can be tuned for different levels of accuracy thanks to an error estimator.

Section 3.1 is partially inspired from [40]. Section 3.2 is highly inspired from [39]. Section 3.3 is highly inspired from [43]. Section 3.4 is partially inspired from [42, 44].

Chapter 4

Micromechanical modeling of void nucleation

Comment voulez-vous gouverner
un pays où il existe 258 variétés de
fromage ?

Charles de Gaulle

- Introduction 138
- 4.1 Macroscopic criteria 140
 - 4.1.1 Argon criterion 140
 - 4.1.2 Beremin criterion 140
 - 4.1.3 Landron criterion 141
 - 4.1.4 Weibull formula 142
- 4.2 Microscopic criteria 143
 - 4.2.1 Lee and Mear analysis 143
 - 4.2.2 Local criteria 144
- 4.3 Proposed models 145
- 4.4 Boundary conditions and stress state control 148
 - 4.4.1 Choice of boundary conditions 148
 - 4.4.2 Stress state control 148
 - 4.4.3 Consequences on the fracture criteria 151
- 4.5 Results 153
 - 4.5.1 Numerical ingredients 153
 - 4.5.2 Material 154
 - 4.5.3 Numerical validation 156
 - 4.5.4 Representative Volume Element size 171
 - 4.5.5 Importance of void nucleation modeling 176
 - 4.5.6 Conclusion 183
- Conclusion 184

Résumé en français

Ce chapitre s'appuie fortement sur les outils numériques développés dans les chapitres précédents afin de traiter des simulations éléments finis de matériaux hétérogènes où la microstructure est maillée explicitement.

Un matériau avec une microstructure initialement composée d'une matrice élasto-plastique et de particules élastiques fragiles est étudié. A partir de la littérature, des critères de rupture sont proposés afin de modéliser la décohésion et la fragmentation de ces particules lors de la phase de germination. La décohésion est prédite à partir d'un critère local sur la contrainte normale critique, tandis que la fragmentation est prédite à partir d'un critère moyenné par inclusion sur la contrainte principale maximale. Ce dernier fait appel à l'algorithme d'identification de composantes connexes développé dans ce travail pour distinguer chaque inclusion. La méthode des fonctions de niveau aide grandement la modélisation des fissures, tandis que l'adaptation de maillage et la réinitialisation des fonctions de niveau sont utilisées pour suivre la déformation des surfaces libres ainsi créées. Cette déformation mène à l'apparition progressive de larges cavités qui finissent par interagir et coalescer.

Les simulations rendues possibles par ces développements et modèles sont validées numériquement en deux dimensions (2D) et trois dimensions (3D) à partir d'une analyse de sensibilité sur des quantités moyennées. Les variables locales, comme le chemin de propagation de fissure, sont moins évidentes à valider. L'énergie de rupture devrait être contrôlée à l'aide de modèles plus avancés, comme les modèles de zone cohésive.

Néanmoins, l'homogénéisation et la comparaison avec des modèles à champ moyen ne nécessite que des quantités moyennées. Dans la littérature, ces comparaisons considèrent en général des volumes élémentaires représentatifs assez simples. En particulier, ceux-ci ne prennent généralement pas en compte les formes, tailles et arrangements arbitraires que les particules et les vides peuvent avoir dans une vraie microstructure. Dans les simulations présentées dans ce chapitre, des microstructures avec des particules sphériques de tailles et positions aléatoires sont utilisées. En imposant certaines restrictions quant à ces microstructures et aux types de chargements qui leur sont appliqués, des conditions aux limites périodiques peuvent être implémentées assez simplement. Les problèmes liés au positionnement et à la numérotation arbitraires des nœuds dans le cadre éléments finis adaptatif et parallèle utilisé dans ce travail sont ainsi évités. En outre, l'état de contrainte macroscopique dans le volume élémentaire représentatif peut être contrôlé.

Ces calculs micromécaniques sur volumes élémentaires représentatifs statistiques révèlent des phénomènes de rupture complexes, dus à la germination d'une multitude de cavités dans la microstructure. En conséquence de certaines agglomérations de particules dans le volume élémentaire représentatif, et de leur alignement particulier avec la direction de traction, la plasticité se localise dans certaines régions. La croissance et la coalescence des cavités est favorisée dans ces régions, y compris pour des déformations assez faibles. La capacité de charge du matériau est sévèrement compromise par ces phénomènes de rupture locale de la microstructure.

Les simulations conduites dans ce chapitre ont un coût numérique assez élevé, surtout en 3D. Celui-ci pourrait être réduit en simplifiant les conditions aux limites, ou en optimisant l'implémentation parallèle de certains algorithmes, en particulier en ce qui concerne le remaillage. Toutefois, il serait certainement augmenté drastiquement si des lois constitutives plus complexes étaient utilisées pour modéliser la microstructure et sa rupture, comme des lois cohésives par

exemple.

Par conséquent, il est primordial de montrer que les résultats obtenus avec l'approche numérique développée dans ce travail diffèrent significativement de ceux obtenus dans la littérature en utilisant des outils moins avancés et donc moins coûteux. En effet, la plupart des études existantes considèrent des particules pré-fragmentées, ou remplacent les particules par des vides dans la microstructure initiale. Des comparaisons entre des simulations prenant en compte les particules et leur rupture progressive par décohésion et fragmentation, et des simulations avec des particules pré-fragmentées ou des vides sont effectuées dans ce chapitre. Ces comparaisons montrent que la croissance des cavités est sous-estimée avec les approches conventionnelles. De plus, la capacité de charge du matériau est sous-estimée dans la première partie du chemin de chargement, et surestimée dans la seconde partie. Une propriété remarquable est que ces différences sont plus ou moins importantes selon le rapport de triaxialité macroscopique.

Pour conclure, la prise en compte de la décohésion et de la fragmentation des particules pendant le chargement est indispensable pour prédire de manière fiable l'influence des procédés de mise en forme des métaux sur la microstructure de ces derniers. Ces calculs micromécaniques 3D sont également indispensables pour prédire l'influence des micro-fissures et des cavités présentes dans la microstructure sur le comportement macroscopique du matériau. Les outils numériques et les modèles de germination de cavités développés dans ce travail sont très intéressants car des microstructures complexes peuvent être modélisées, y compris les phénomènes de rupture complexes en découlant. L'application de ces outils de simulation et modèles à des trajets de chargement complexes est une piste à explorer.

Introduction

The mixed weak form of continuum mechanics equations, taking into account all the constitutive models discussed in previous chapters, is recalled

$$\left\{ \begin{array}{l} \int_{\Omega_h} \left(\frac{\partial s_h}{\partial v_h}(v_h^0) : \dot{\varepsilon}(v_h) \right) : \dot{\varepsilon}(w_h) \\ \quad - \int_{\Omega_h} p_h \operatorname{div} w_h \\ + \rho_c \int_{\Gamma_{c,h}^+} (D_h(v_h) \cdot n_h) (D_h(w_h) \cdot n_h) = \int_{\Omega_h} \left(\frac{\partial s_h}{\partial v_h}(v_h^0) : \varepsilon(v_h^0) \right) : \dot{\varepsilon}(w_h) \\ \quad - \int_{\Omega_h} s_h(v_h^0) : \dot{\varepsilon}(w_h) \\ \quad + \int_{\partial\Omega_h} w_h \cdot (\sigma_h n_h) \\ \quad + \rho_c \int_{\Gamma_{c,h}^+} (D_h(v_h^0) \cdot n_h) (D_h(w_h) \cdot n_h) \\ \quad - \rho_c \int_{\Gamma_{c,h}^+} (P_h(v_h^0)) (D_h(w_h) \cdot n_h), \forall w_h \in \mathcal{V}_h, \\ - \int_{\Omega_h} q_h \operatorname{div}(v_h) - \int_{\Omega_h} \frac{\dot{p}_h}{\mathcal{X}} q_h = 0, \forall q_h \in \mathcal{P}_h. \end{array} \right.$$

Notations are detailed in Subsection 1.2.1. As discussed in Appendix A, this formulation includes contact terms arising from penalization of the constraint P_h and its derivative D_h with respect to the velocity field. Remeshing operations, especially at void linkage events, and the detection and discretization of contact terms are helped by the fact that the void phase is meshed. However, there is no constitutive model in these elements, apart from contact terms, and both the velocity and the pressure unknowns are fixed using Dirichlet boundary conditions for nodes that are only carried by void phase elements.

Regarding solid phases, Hooke's law for linear isotropic elasticity is already mentioned in Subsection 1.2.1, together with the additive decomposition between elasticity and plasticity that is assumed for small deformations. Particles are generally considered as purely elastic and brittle in the literature [69, 79, 108, 227], though dual phase steels and other materials with multiple ductile phases have also been studied [71, 228, 229, 230]. Ductile fracture modeling of these materials calls for crystal plasticity models and appropriate intragranular and intergranular fracture criteria [231, 232, 233, 234]. The study of these materials and the application of the mesh adaptation techniques proposed in this work to the discretization of grain boundaries will be considered in a future work (Chapter 7).

In this chapter, it is assumed that particles debond from the matrix or fail before yielding can occur [69, 79, 108, 227], and appropriate fracture criteria are investigated to model both phenomena. Experimental results and observations presented in Subsection 1.1.2 indicate that void nucleation occurs in the neighborhood of particles. They can debond locally and progressively from the matrix, or experience internal failure [37, 68, 69, 70, 71]. Criteria are hence necessary to model the initiation and propagation of cracks at the matrix/particle interface, and through the particles.

These criteria should have the capability to predict that particle fragmentation is favored for particles elongated in the tensile direction, or a hard matrix, while particle debonding is favored

for particles elongated perpendicular to the tensile direction [73, 74, 78, 79], or a soft matrix [21, 68, 78, 79]. Particle size is affected by void nucleation in a similar manner, as in a microstructure with particles of various sizes, larger particles tend to fragment, while smaller particles tend to debond [74, 77, 78]. Clustering effects are also of interest in the present work as real microstructures and random particle arrangements will be considered [69, 74, 75, 76].

Regarding the matrix material, a simple von Mises plasticity model with isotropic hardening is considered. As first applications, simulations performed in the frame of homogenization theory using Periodic Boundary Conditions (PBCs) are considered.

Note that all constitutive models are discussed and used in the frame of cold forming (*i.e.*, at room temperature) and quasi-static loading conditions.

4.1 Macroscopic criteria

It is important to point out that most studies found in the literature do not address crack initiation and propagation in the Representative Volume Element (RVE). Calculations are hence conducted with no fracture modeling. The averaged stress and strain fields are used to predict the amount of failed particles. These criteria do not systematically make the distinction between debonding and fragmentation. These works aim at improving macroscopic constitutive models, such as Gurson-like models, by adding void nucleation laws. That is the reason why averaged quantities are used instead of microscopic ones.

Although the aim of the present work is to model these phenomena in the RVE and pursue simulations after the onset of void nucleation, the reasoning behind these criteria is of interest. Therefore, a literature review is first conducted and then discussed in the frame of the present developments.

4.1.1 Argon criterion

One of the first criteria found in the literature is the so-called Argon criterion, which aims at predicting particle/matrix interface debonding [235]. An important remark made in this paper is that a certain limit of elastic energy must be reached before interface debonding can occur, but this condition is not sufficient [70, 71, 236]. This is the reason why a criterion was proposed to predict when the interface strength is reached.

A spherical non-deformable particle included in an elastic-ideally plastic matrix and subjected to pure shearing was considered. The strain and stress fields obtained by Finite Element (FE) calculations were studied to formulate the following criterion that accounts for a possible hydrostatic pressure by superposition

$$\Sigma_m + \bar{\Sigma} = \Sigma^A \leq \Sigma_c^A, \quad (4.1)$$

where Σ_m and $\bar{\Sigma}$ are respectively the macroscopic mean stress and the macroscopic von Mises equivalent stress. The term Σ_c^A is the critical stress at which debonding is predicted. A modification of this criterion was proposed by the same authors to account for particle shape, it is expressed as follows

$$\Sigma_m + k^A \bar{\Sigma} = \Sigma^A \leq \Sigma_c^A,$$

where k^A is a coefficient depending on particle shape. This criterion has been used and discussed by numerous authors [37, 71, 73, 77, 235, 236].

It was proved by experiments and *post-mortem* Scanning Electron Microscopy (SEM) observations that the Argon criterion can also be used as a particle fragmentation criterion [77]. The material used was a quenched and tempered steel containing manganese sulfide (MnS) and titanium nitride (TiN) inclusions. Void nucleation was observed by interface debonding or fragmentation of TiN inclusions in the case of notched specimens under uniaxial tension. Empirical values were determined for k^A and Σ_c^A . Another important remark made in Reference [37] is that the critical stress Σ_c^A will not have the same value for predicting both phenomena. This will be evidenced more clearly in the case of the Beremin criterion.

4.1.2 Beremin criterion

A few years after the Argon criterion was proposed, the Beremin team studied cavity formation in an A508 steel containing elongated MnS inclusions during tensile tests [73]. They made *post-*

mortem observations on notched specimens of different notch radii, under various temperatures and loading directions. When the inclusions were elongated in the tensile direction, most particles broke before interface debonding could occur, while when they were elongated in the perpendicular direction nucleation occurred by interface debonding between particles and matrix. Although they evidenced these two different mechanisms, they formulated a unique criterion for void nucleation

$$\Sigma_1 + k^B (\bar{\Sigma} - \Sigma_0) = \Sigma^B \leq \Sigma_c^B,$$

where Σ_1 is the maximum macroscopic principal stress ($\Sigma_1 \geq \Sigma_2 \geq \Sigma_3$) and Σ_0 is the macroscopic yield stress. The coefficient k^B depends on particle shape and loading direction. Calibration of this coefficient is quite difficult, though closed-form expressions can be found for some special cases in Reference [37].

Experiments at different temperatures led the Beremin team to remove the yield stress from the equivalent stress to make their criterion temperature-independent. However, when omitting this operation, it is proved in Reference [73] that the Beremin criterion is equal to the Argon one in the case of uniaxial tension. Although this remark proves that these two criteria have a similar nature, it is important to remind that the k^B coefficient and the critical stress Σ_c^B defined in the Beremin criterion are different in definition as in observation from the ones defined in the Argon criterion [37, 71].

Moreover, the Beremin team identified two different values of the critical stress Σ_c^B for predicting void nucleation depending on loading direction, namely one value corresponding to the onset of interface debonding and the other one to particle fragmentation. This may be limiting for applications to non proportional loading paths, where the loading direction can vary. Examples of use of the Beremin criterion can be found in several studies [37, 70, 71, 73, 78, 236].

4.1.3 Landron criterion

In a recent study of the micromechanisms of damage in dual phase steels using advanced observation technologies like X-ray Computed Tomography (CT) [71], a new criterion based on the Argon one was proposed [228]. The experiments consisted in *in situ* tensile tests under different stress triaxialities. This idea of using specimens with different notch radii already appeared in the Beremin paper [73], which mentions that void nucleation is favored by higher stress triaxiality ratio. The effect of triaxiality was also confirmed in other studies [26, 33, 79, 237].

The first step [71, 228] was to reveal explicitly the triaxiality in the Argon criterion

$$\Sigma^A = \Sigma_m + \bar{\Sigma} = \bar{\Sigma} (1 + T),$$

where $T = \frac{\Sigma_m}{\bar{\Sigma}}$ is the stress triaxiality and k^A is chosen equal to 1 as in the original Argon criterion. A work similar to [73] is then performed to include the effect of strain inhomogeneity between particle and matrix in the criterion. Moreover, based on a study of titanium alloys presented in Reference [236], this effect can be taken into account by using a local formula for the stress triaxiality ratio, which accounts for the effect of kinematic hardening X . The latter was included in the model because it was showed that it affects the local stress triaxiality ratio at the interface between matrix and particles in dual phase steels [236]. The resulting Landron criterion is [71, 228]

$$\Sigma^L = \bar{\Sigma} \left(1 + T \frac{\bar{\Sigma}}{\bar{\Sigma} - X} \right) \leq \Sigma_c^L.$$

A direct identification with the Argon criterion (Equation (4.1)) leads to $k^A = k^A(\bar{\Sigma}, X) = \frac{\bar{\Sigma} - X}{\bar{\Sigma}}$.

This reveals the phenomenological nature of the parameter k^A , which reminds the parameters added in the Gurson-Tvergaard-Needleman (GTN) model and its extensions, with respect to the initial model of Gurson (Subsection 1.2.3). Hence, there is a need for models that take into account all aspects of ductile fracture, including advanced plasticity and hardening phenomena.

4.1.4 Weibull formula

Another example of method that can be used to improve the previous criteria in order to take into account important aspects of ductile fracture is the Weibull formula. This formula consists in adding statistical considerations into a given macroscopic criteria. For instance, in Reference [21], the authors considered the maximum average principal stress in each particle $\Sigma_{1,p}$, and used a Weibull formula to take into account the effect of particle size

$$P_W(V_p, \Sigma_{1,p}) = 1 - \exp\left(-\frac{V_p}{V_u} \left(\frac{\Sigma_{1,p}}{\Sigma_u}\right)^m\right),$$

where V_p is the volume of the particle. The term Σ_u corresponds to the critical value of Σ_1 for which $1 - e^{-1} \approx 63\%$ of particles of reference size V_u would break. The Weibull modulus m measures stress dispersion. For instance, a low modulus prevents an overestimation of stress concentration in particles and an early prediction of fragmentation [68].

When this probability is close to 100%, particle fragmentation is predicted. An experimental procedure to identify this criterion parameters is presented in Reference [78]. The Weibull criterion was successfully applied to predict the fragmentation of silicon carbide (SiC) particles included in a metal matrix composite in Reference [74]. Applications to aluminum and aluminum alloy matrix composites with ceramic particles can be found in other studies [21, 68, 238].

Similar Weibull criteria can also be found in the literature for the prediction of interface debonding. This probabilistic approach is an attempt to avoid the difficulties that appear when one tries to predict particle failure based on the averaged stress Σ . The difficulties lie in the calibration of the Weibull modulus m , which actually accounts for size and shape effects on void nucleation, and, implicitly, any other differences between particles. Hence, a more precise study of void nucleation prediction considering the local stress field in and around the particle is necessary.

4.2 Microscopic criteria

A common aspect of all criteria presented above is that they are stress-based. These criteria are based on the average stress Σ , and are not suited for the present developments where crack initiation and propagation has to be predicted and modeled locally in the RVE. In the following, a study of local stress fields around an inclusion is presented, and then used as a basis for the development of microscopic void nucleation models.

4.2.1 Lee and Mear analysis

In Reference [79], the authors performed a study of stress concentration in an elastic spheroidal particle subjected to tension along its three axes. They computed the following variables κ^I and κ^P by FE calculations

$$\begin{aligned}\kappa^I &= \frac{1}{S} \max_{\Gamma_p} \sigma_n, \\ \kappa^P &= \frac{1}{S} \max_{\Omega_p} \sigma_1,\end{aligned}$$

where S is the stress applied along the z direction, which corresponds to the particle's elongation direction, Ω_p the particle, and $\Gamma_p = \partial\Omega_p$. As shown in Figure 4.1, an inferior remote stress T is applied along both other directions. The normal (microscopic) stress at the interface is noted σ_n and the maximum (microscopic) principal stress σ_1 .

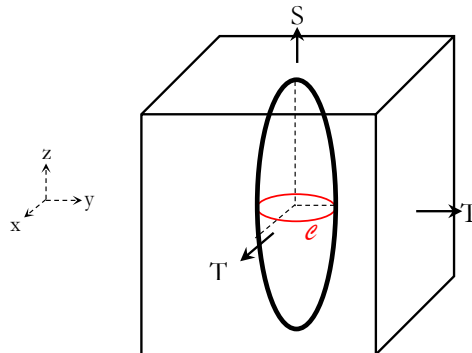


Figure 4.1 – Spheroidal particle model used by Lee and Mear [79].

This study reveals that for an elastic-plastic matrix, the stress field is not uniform. Although the critical value for κ^P is always reached at the outer edge C indicated in Figure 4.1, there is no similar rule for κ^I . The interfacial normal stress reaches its maximum in different points depending on particle aspect ratio (it will be at the pole for a very elongated particle, and in a larger area around the pole for a spherical particle).

Moreover, calculations reveal that the stress field is more or less uniform in the disk corresponding to the circle C . This result indicates that particle fragmentation is likely to occur instantaneously for the whole particle. On the other hand, the significant variations of the stress field on the interface justifies the progressive nature of interface debonding, the critical value being met at one point at a given time.

As a conclusion, criteria based on the maximum principal stress averaged per particle seem to be appropriate to model particle fragmentation, and this phenomenon can be considered as

instantaneous. Regarding particle debonding, it has to be considered locally at each point of the interface, as it is a progressive phenomenon. These conclusions apply only for particles of nearly spheroidal shape, and more complex criteria will certainly have to be studied for materials with more complex microstructure.

4.2.2 Local criteria

Simple criteria to model void nucleation can be deduced from those implicitly used by the authors of Reference [79] in their study. To model particle fragmentation, they considered the maximum principal stress σ_1 and studied the points or areas where it reaches its critical values. Regarding particle/matrix interface debonding, they considered the normal stress at the interface. These two criteria have been used together to predict void nucleation in Reference [69], where they were successfully compared with experimental results of a copper matrix containing tungsten (W) inclusions. In Reference [70], the first criterion was used to predict both modes of void nucleation, but the calculations made in Reference [79] show that the point of critical maximum principal stress is not generally located where interface debonding will start. In the case of Reference [79], it would mean that debonding first occurs at the outer edge C (Figure 4.1), which is not consistent with observations.

In Reference [239], an improved version of the debonding criterion was proposed. If a point of the interface is submitted to a shear stress σ_t , then a negative normal stress σ_n (assuming the normal is outgoing with respect to the particle) will make debonding difficult, whereas a positive normal stress will favor it. This reasoning led to the following criterion

$$\sigma_n + k^F |\sigma_t| = \sigma^F \leq \sigma_c^F.$$

The choice of linear combination was verified on a fiber reinforced composite during uniaxial tensile tests with various orientations. A description of the experimental procedure used to identify the parameters k^F and σ_c^F can be found in Reference [239]. An application of this criterion to a polyester matrix composite with glass fibers and a metal matrix composite with SiC inclusions can be found in Reference [74]. Both materials were observed by means of SEM during tensile tests to verify the criterion's efficiency.

Basing the criterion on the normal stress at the interface to predict debonding has already been justified [69, 70, 79]. However, the superposition of the shear stress has yet to be investigated.

This superposition of the two stresses reminds what is known as Cohesive Zone Models (CZMs) [184]. In these methods, a nodal force or normal stress criterion is used as a trigger to insert so-called cohesive elements at the interface. These elements have zero volume initially, and their opening is ruled by a traction-separation law, which takes into account both normal and shear stress. Applications of these methods to particle debonding can be found in the literature [37, 237, 238].

These approaches and the use of the shear stress have been implemented but are not considered in the present work due to the difficulty of identifying the additional material properties at the microscale. However, as discussed in Chapter 7, this problem could be revisited in the future thanks to the procedure presented in Chapter 6.

4.3 Proposed models

Based on the preceding literature review, two distinct criteria are proposed to predict particle debonding and fragmentation. The debonding criterion is no other than the one proposed by Lee and Mear [79]

$$\sigma_n \leq \sigma_c^D, \quad (4.2)$$

where the normal stress σ_n at the interface can be computed easily from the Level-Set (LS) function ϕ_p associated with particles

$$n = \frac{\nabla\phi_p}{\|\phi_p\|_2}, \sigma_n = n^t \sigma n.$$

When the critical value σ_c^D is reached, the numerical method presented in Section 2.6 is applied. In particular, the geometry used for the filter LS function ϕ_f is a sphere centered on the point where σ_c^D was reached, and with radius the length ℓ^D . This criterion hence introduces one additional material parameter σ_c^D and one numerical parameter ℓ^D .

As detailed in Section 2.6, the LS functions associated with the two crack faces ϕ_p and $\phi_p + \epsilon_l$ are meshed only in the region where ϕ_f is positive. The LS functions and the numerical parameters are illustrated in Figure 4.2(a). Then, the LS function ϕ_v associated to the void phase and the LS function ϕ_m associated to the matrix are modified as follows

$$\phi_v = \max(\tilde{\phi}_v, \min(-\phi_p, \phi_p + \epsilon_l, \phi_f)), \phi_m = \min(\tilde{\phi}_m, -\phi_v), \quad (4.3)$$

where $\tilde{\phi}_v$ and $\tilde{\phi}_m$ are the initial LS functions, before nucleation. Consequently, the small volume (due to the artificial thickness ϵ_l) of the crack is added to the void phase, and removed from the matrix phase, leading to a small loss of volume that will be investigated in Section 4.5. After this modification of the LS functions, the mesh is adapted, and the microstructure is modified due to the new crack geometry.

Particle fragmentation modeling requires a nonlocal criterion, because it is considered as instantaneous. This criterion is based on the particle-wise average maximum principal stress

$$\frac{1}{\int_{\Omega_{p_i}} \chi(\sigma_1)} \int_{\Omega_{p_i}} \sigma_1 \chi(\sigma_1) = \sigma_1^{p_i} \leq \sigma_c^F, \quad (4.4)$$

where $\chi(x) = \begin{cases} 1 & , x > 0 \\ 0 & , x \leq 0 \end{cases}$, and Ω_{p_i} the volume occupied by particle i . This distinction between particles is obtained thanks to the Connected Components (CCs) identification algorithm presented in Section 3.3. This fragmentation criterion is also inspired from the Lee and Mear analysis, but the particularity is that the crack position and orientation remain to be defined. First, the position of the crack is given by the point

$$G_{p_i} = \frac{1}{\int_{\Omega_{p_i}} \sigma_1 \chi(\sigma_1)} \int_{\Omega_{p_i}} \sigma_1 \chi(\sigma_1) \mathbf{x}. \quad (4.5)$$

In the present first order FE context, σ_1 is computed by diagonalization of σ , which is defined element-wise. The coordinates \mathbf{x} in Equation (4.5) are hence the coordinates of the barycenter of each element. The elements with zero or negative maximum principal stress are not considered in order to ignore the parts of the inclusion that are under compression, and hence do not carry

any tensile load. Fragmentation is not predicted if G_{p_i} does not belong to an element of Ω_{p_i} with positive σ_1 .

The first principal direction (the eigenvector associated to the eigenvalue σ_1) is chosen as the normal vector to the fracture plane. The LS function to this plane ϕ_{pl} defines the LS functions associated with the two crack faces $\phi_{pl} - \frac{\epsilon_l}{2}$ and $\phi_{pl} + \frac{\epsilon_l}{2}$, while the filter LS function is ϕ_{p_i} . The latter is constructed by combining the LS function to inclusions ϕ_p and the CC identifiers. Thanks to these LS functions, particle fragmentation can be triggered by modifying the LS functions to voids $\tilde{\phi}_v$ and inclusions $\tilde{\phi}_p$

$$\phi_v = \max\left(\tilde{\phi}_v, \min\left(-\left(\phi_{pl} - \frac{\epsilon_l}{2}\right), \phi_{pl} + \frac{\epsilon_l}{2}, \phi_{p_i}\right)\right), \phi_p = \min(\tilde{\phi}_p, -\phi_v). \quad (4.6)$$

In practice, in order to make sure that the inclusion is totally broken in two, and that the inserted crack is penny-shaped with sharp edges in three dimensions (3D), and two crack tips in two dimensions (2D), the LS function ϕ_{p_i} is corrected to $\phi_{p_i} + \ell^F$. This numerical parameter ℓ^F has the consequence that the LS function to the matrix phase is also affected by particle fragmentation ($\phi_m = \min(\tilde{\phi}_m, -\phi_v)$).

This is illustrated in Figure 4.2(b). Thus, particle fragmentation leads to crack tips in the matrix phase, which has been observed for some materials and loading configurations where cracks propagate simultaneously in the matrix and the particles. However, in most situations, fragmentation is restricted to the particle, hence a very small ℓ^F should be used. This raises numerical difficulties since mesh size has to be inferior to ℓ^F . An improved crack insertion technique is considered in Chapter 7.

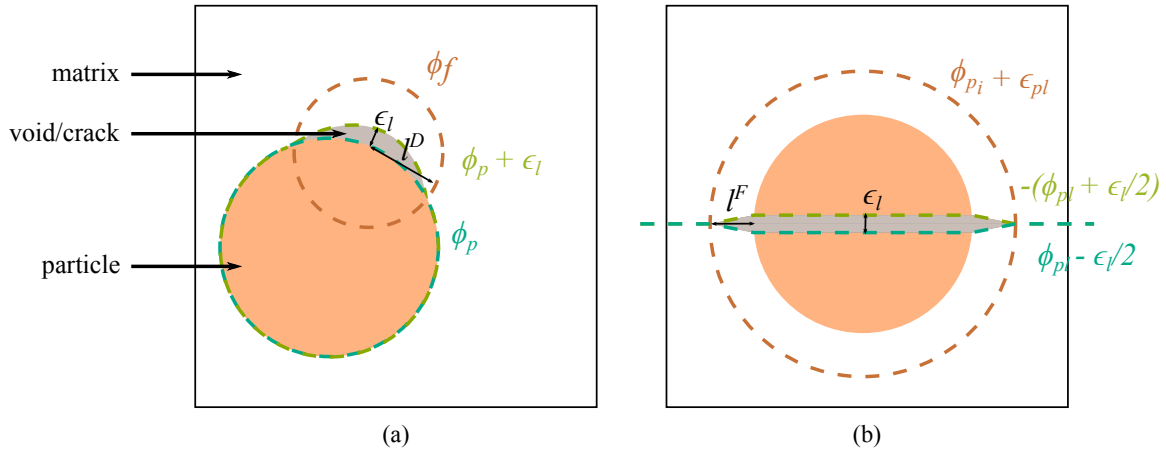


Figure 4.2 – LS functions and numerical parameters used for void nucleation modeling by: (a) particle debonding, (b) particle fragmentation.

As a conclusion, two fracture criteria based on microscopic stresses are formulated in this section. Debonding is predicted based on the normal stress at the interface, and leads to a crack at a portion of the matrix/particles interface. This model adds two parameters σ_c^D and ℓ^D . Fragmentation is predicted based on the average maximum principal stress per particle, and leads to a crack across a whole particle. This model also adds two parameters σ_c^F and ℓ^F . The numerical method used to insert these cracks through LS functions and mesh adaptation requires a numerical parameter ϵ_l .

All parameters are summarized in Table 4.1. Thanks to these models, the two modes of void nucleation can be predicted and modeled during RVE simulations. This evaluation of the criteria

and the subsequent modifications on LS functions and the mesh is performed at the beginning of each time increment, based on stresses σ_n obtained at the preceding time increment. A mechanical solution is then conducted to obtain the new stresses σ_{n+1} , resulting in a weak coupling between the nucleation models and balance equations.

critierion	material parameter(s)	numerical parameter(s)
debonding	σ_c^D (MPa)	ℓ^D (μm), ϵ_l (μm)
fragmentation	σ_c^F (MPa)	ℓ^F (μm), ϵ_l (μm)

Table 4.1 – Numerical and material parameters for the void nucleation criteria.

4.4 Boundary conditions and stress state control

4.4.1 Choice of boundary conditions

In Section 1.2, various possibilities were listed regarding boundary conditions for RVE calculations. In addition, the numerical validation framework based on Digital Volume Correlation (DVC) measurements presented in Chapter 6 should also be considered. It is disregarded in this section as it can only be applied to small specimens. Thus, it could be used to experimentally validate and calibrate microscopic models, but an alternative is necessary to exploit these models in industrial applications. Direct Numerical Simulation (DNS) is clearly too computationally expensive and cannot be applied in the case of meter-scale metallic structures such as ingots or industrial parts in general.

Homogenization schemes are an interesting possibility. An embedded cell technique would allow to mesh the microstructure only in some Region Of Interest (ROI) of the structure, while using a macroscopic constitutive model in the rest of the structure. Using a self-consistent scheme, material properties for the latter would be identified as a result of the computation. Such scheme would be really interesting for industrial applications, but some technical difficulties arise, such as non physical localization phenomena at the transition zone between the homogeneous material and the RVE.

Simpler approaches are hence considered. Taylor-Voigt Boundary Conditions (TVBCs) and Hill-Reuss Boundary Conditions (HRBCs) are likely to lead to large errors regarding void coalescence, as linear strain or stress fields are imposed in the RVE. The same remark applies for Kinematic Uniform Boundary Conditions (KUBCs) and Static Uniform Boundary Conditions (SUBCs), but only at RVE boundaries. It can be assumed that very large RVEs would be necessary to reduce the influence of these boundary effects. Therefore, PBCs are considered.

The main difficulty raised by PBCs consists in applying constraints between unknowns located on opposite faces of the RVE. In particular, the use of distributed computing and mesh adaptation randomize the positioning and numbering of mesh nodes. However, as mentioned in Subsection 1.2.2.6, under some assumptions, the implementation of PBCs can be simplified. Restricting the 2D (resp. 3D) RVE to symmetric microstructures, only one fourth (resp. one eighth) of the RVE has to be simulated, with symmetry boundary conditions on two (resp. three) of the faces. The velocities of the two (resp. three) remaining faces are to be fixed to normal velocities, so that all faces of the RVE are constrained to remain planar.

Opposed to KUBCs, the tangential velocities at RVE boundaries are not constrained, thus localization and void coalescence are possible. Although the use of symmetric microstructures may have an influence on results, this setting still allows to access any stress state. An example of RVE with these geometrical restrictions is given in Figure 4.3. The whole RVE (in light color) is not meshed, but only the highlighted part, thanks to symmetry boundary conditions. Loading is not represented in this figure as it is described more thoroughly in the next paragraph.

4.4.2 Stress state control

Experimental evidence and existing damage models suggest that at fixed temperature and pressure conditions, damage change is mainly driven by plastic strain and stress state [37, 38]. In order to obtain relevant results for analysis, it is important to perform simulations at a constant stress state, or at a stress state that corresponds to a targeted application, and then measure damage change with respect to plastic strain. For instance, in the case of metal forming, the stress state

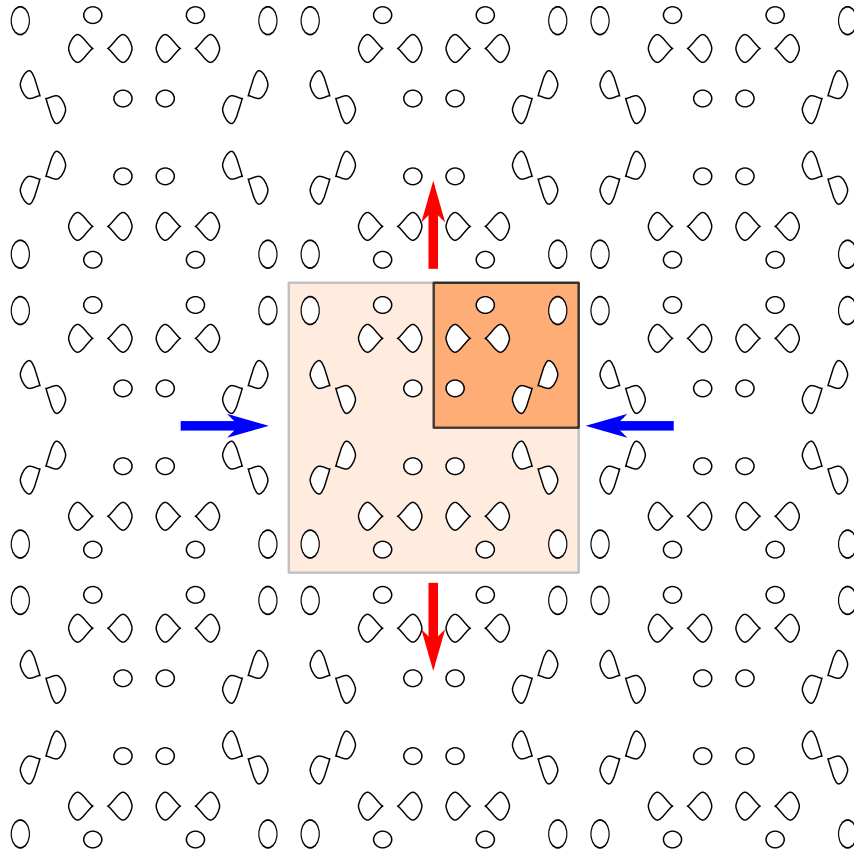


Figure 4.3 – Example of periodic microstructure with symmetries that simplify the implementation of PBCs. Thanks to symmetry boundary conditions, the part in light color is not meshed (loading must also feature these symmetries).

at a critical point could be measured during the whole loading path, and then RVE calculations could provide quantitative information on how the experimentally observed macroscopic plastic strains would affect the microstructure for this stress state.

To identify a stress state, definitions of the three invariants of the macroscopic stress tensor Σ and its deviatoric part Σ' have to be reminded (Subsection 1.2.3)

$$\begin{aligned}\Sigma_m &= \frac{\text{tr}(\Sigma)}{3}, \\ \bar{\Sigma} &= \sqrt{\frac{3}{2}\Sigma'_{ij}\Sigma'_{ij}} = \sqrt{\frac{1}{2}((\Sigma_1 - \Sigma_2)^2 + (\Sigma_2 - \Sigma_3)^2 + (\Sigma_3 - \Sigma_1)^2)}, \\ J_3 &= \det(\Sigma'),\end{aligned}\tag{4.7}$$

where Σ_m is the macroscopic mean stress, $\bar{\Sigma}$ the macroscopic von Mises equivalent stress, Σ_i the macroscopic principal stresses, and J_3 the third invariant of the deviatoric stress tensor. The first two invariants Σ_m and $\bar{\Sigma}$ appear in the definition of the macroscopic stress triaxiality ratio η

$$\eta = \frac{\Sigma_m}{\bar{\Sigma}},\tag{4.8}$$

and the third invariant appears in the definition of the macroscopic normalized Lode angle $\bar{\theta}$

$$\bar{\theta} = 1 - \frac{2}{\pi} \arccos\left(\frac{27 J_3}{2 \bar{\Sigma}^3}\right).\tag{4.9}$$

A detailed presentation of η and $\bar{\theta}$ and their values for some widely used specimen geometries can be found in Reference [240]. In particular, axisymmetric compression is identified by $\bar{\theta} = -1$, while axisymmetric tension is identified by $\bar{\theta} = 1$. A plane stress setting yields $\bar{\theta} = 0$. The stress triaxiality ratio can then favor the situation already set by the normalized Lode angle. A triaxiality ratio $\gg \frac{1}{3}$ will favor tension with increasing tensile stresses in the directions perpendicular to the loading direction, while a triaxiality ratio $\ll -\frac{1}{3}$ will favor compression with increasing compressive stresses in the directions perpendicular to the loading direction. The remaining range between $-\frac{1}{3}$ and $\frac{1}{3}$ corresponds to combined compression-shear or tension-shear situations if $\bar{\theta} = \pm 1$, and pure shear if $\bar{\theta} = 0$.

All these settings are interesting as they can be met locally in various material forming processes, and no model existing in the literature succeeds in predicting damage change for any $\bar{\theta}$ and any η [240, 241]. RVE calculations with more and more accurate microscopic models are hoped to give some clues on how to build such a model.

In the present framework, the degrees of freedom in 3D are the three normal velocities applied to the three faces of the domain that are not subjected to symmetry conditions. As mentioned above, the goal is to use these three degrees of freedom to reproduce loading conditions at a point of an industrial part during a forming process. These conditions will generally be computed using a macroscopic FE simulation at the scale of the part, or measured experimentally.

Because damage is mainly influenced by the plastic strain and the stress state, the quantities of interest to be computed or measured are the macroscopic strain rate E_α in the loading direction, and the stress state characterized by η . In order to simplify the problem, the normalized Lode angle $\bar{\theta}$ is not considered yet and will be assumed to be equal to ± 1 (*i.e.*, axisymmetric tension or compression).

First, the velocity v_α of the upper face of the domain is fixed in order to obtain constant elongation rate E_α . Second, the two remaining velocities are fixed to the same value v_β in order to set the normalized Lode angle $\bar{\theta}$ to ± 1 . This velocity v_β is then the only remaining degree of freedom. Note that there would be two degrees of freedom if an arbitrary $\bar{\theta}$ was considered. This is summarized in Figure 4.4, where the velocities in red are fixed to the same predefined value, and the velocities in blue have the same unknown value.

This unknown value is found using a linear search algorithm where the objective is to yield a desired η . This algorithm is quite costly as a significant number of iterations (up to 20) is necessary to reach an acceptable approximation of η at the beginning of the simulations. Although the obtained solution can be used as an initial guess for the following time increments, requiring only up to 2 linear search iterations, any fracture event in the RVE induces major changes that increase momentarily the number of iterations.

Improving this linear search algorithm to reduce this significant computational cost will be considered in the future. Generalizing it to 2 degrees of freedom would certainly be also interesting in order to address a wider range of stress states with varying $\bar{\theta}$ (Chapter 7). Note that in 2D, plane strains are assumed, so that $\bar{\theta}$ is free and η is fixed using the linear search algorithm. Table 4.2 sums up the two settings used in this work. In both settings, v_α is a predefined constant velocity, and v_β is computed by the line search procedure in order to reach a desired triaxiality ratio. Note that v_β should never be higher than v_α in magnitude.

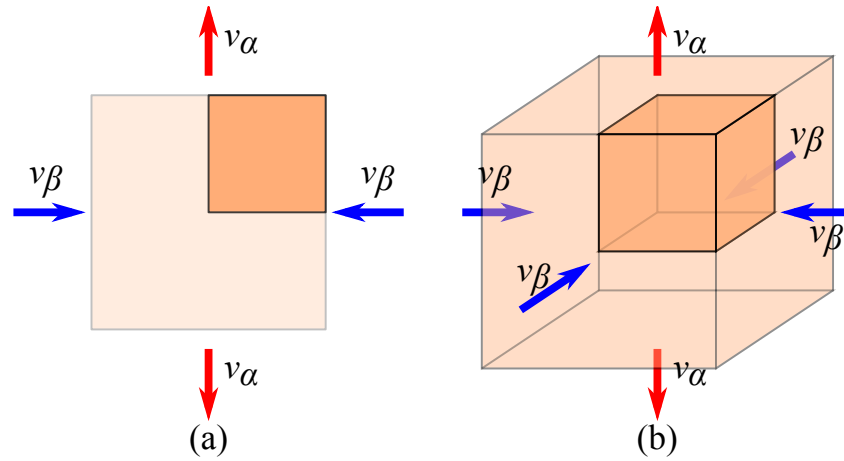


Figure 4.4 – RVE under axisymmetric tension in: (a) 2D, (b) 3D. Thanks to symmetry boundary conditions, the part in light color is not meshed.

	axisymmetric	tension compression	plane strain	tension compression
\dot{E}		$\begin{pmatrix} v_\beta & 0 & 0 \\ 0 & v_\alpha & 0 \\ 0 & 0 & v_\beta \end{pmatrix}$		$\begin{pmatrix} v_\beta & 0 & 0 \\ 0 & v_\alpha & 0 \\ 0 & 0 & 0 \end{pmatrix}$
$\bar{\theta}$		+1, $v_\alpha > 0$ -1, $v_\alpha < 0$		free
η		user-defined		user-defined

Table 4.2 – Macroscopic strain rate \dot{E} and macroscopic normalized Lode angle $\bar{\theta}$ for the two stress states imposed in RVE calculations.

4.4.3 Consequences on the fracture criteria

The use of PBCs is not without consequences regarding fracture modeling. Because it is local, the debonding criterion is not affected. However, due to its non local nature, the fragmentation criterion should consider the fact that symmetry boundary conditions are used at some RVE boundaries, while periodicity is applied at the remaining ones. This is quite complex to implement, especially in a distributed computing framework (the implementation of both criteria already being quite technical). To avoid this difficulty, particles are placed at a certain distance from RVE boundaries. This ensures that the fragmentation criterion does not require any special treatment due to the choice of boundary conditions.

Void coalescence may also lead to numerical difficulties due to these PBCs. Plasticity may localize in the ligament between a void and the boundary of the RVE, leading to its necking. This is illustrated in Figure 4.5. When elements in the intervoid ligament become degenerated, the mesh adaptation technique diffuses the ligament, hence naturally modeling void linkage. This is not possible at RVE boundaries, because the boundary of the domain does not belong to the void phase. Thus, elements are significantly stretched, leading to a numerical issue. This is solved by setting the LS function to the void phase to zero ($\phi_v = 0$) for boundary nodes that are neighboring a node of $\partial\Omega_v$. Since such situation can only arise when the topology of the mesh is modified, this treatment is applied after each remeshing operation. The result is shown in Figure 4.5. Because this treatment is applied across an edge of the mesh,

it is likely to be mesh dependent. Its effect can however be assumed negligible, because for large RVEs failure will be mainly driven by the nucleation and coalescence of voids inside the RVE.

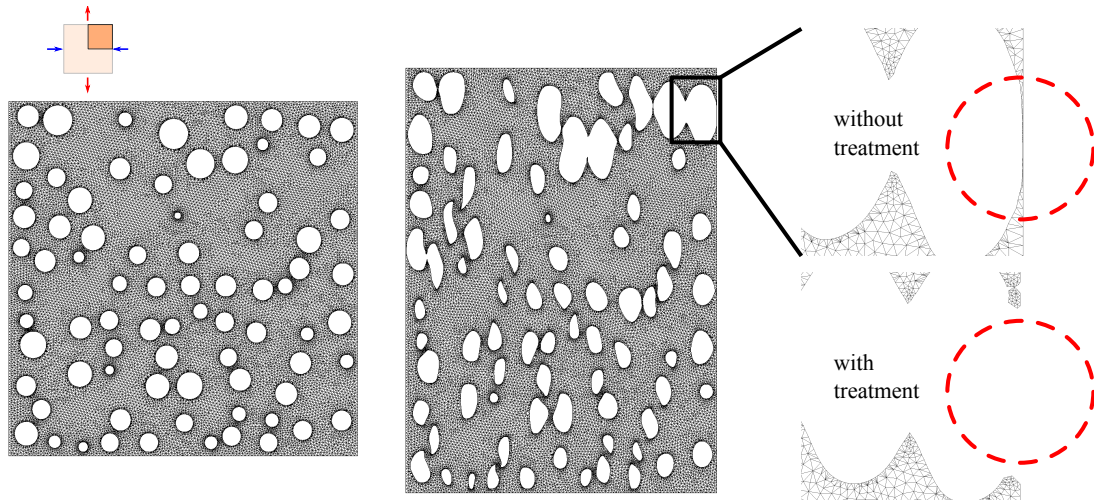


Figure 4.5 – Mesh of a microstructure of voids with multiple purely plasticity-driven void coalescence and linkage events. Remeshing diffuses well the intervoid ligament when it is between voids, but a numerical issue (outlined in red) arises for ligaments between a void and the boundary of the RVE. This is corrected with the numerical treatment.

4.5 Results

In the following, the two void nucleation models presented in this section are first validated, and then used to study various aspects of ductile fracture. This study focuses on the influence of particles and the subsequent failure mechanisms. Regarding the matrix material, it is modeled using a simple rate-independent isotropic hardening model, based on a power law [242]

$$\sigma_0(\bar{\varepsilon}^{pl}) = \sigma_y + K \left(\bar{\varepsilon}^{pl} \right)^n, \quad (4.10)$$

where σ_y is the yield stress, K the plastic consistency and n the hardening exponent. This hardening law is a parameter of the model and could be replaced by any other local plasticity model, including rate-dependent plasticity. All material parameters E , ν , σ_y , K and n are defined element-wise, and are discontinuous because multiple phases are present in the domain. Simulations are also carried out to show the interest of using an advanced computational fracture mechanics approach, especially at large plastic strain.

4.5.1 Numerical ingredients

Because multiple numerical tools were developed in the previous chapters, it is important to point out which of them are used in this section, and how.

First, the microstructures used in this section are not extracted from X-ray images, thus no image processing technique is used (Section 3.4). The LS functions associated with the particles and/or voids of the initial microstructure are computed analytically.

However, the initial mesh is generated using the edge splitting algorithm presented in Section 2.1, and the volume-conserving mesh adaptation algorithm detailed in Section 2.2, coupled to the curvature-based error estimator described in Section 3.1. In order to reach large plastic strains, simulations rely extensively on the mesh motion and transport algorithms presented in Section 2.3, and the LS reinitialization procedure introduced in Section 3.2.

The fracture criteria described in this section require the identification of each particle with a single identifier (Section 3.3) and the modeling of cracks (Section 2.6).

The computational contact mechanics methodology introduced in Appendix A is used, but due to its limitations, it is not used to its full extent. In particular, the Lagrange multipliers are omitted, so that only penalization terms with a coefficient $\rho_c = 1$ are accounted for. The mesh adaptation step that should be triggered before each mechanical solution to ensure contact detection is also omitted. Instead, it is assumed that because the mesh is regularly being adapted due to the mesh motion algorithm, and the fracture criteria, the mesh in the void phase remains of good quality throughout the simulation.

Thanks to all these numerical tools, simulations of complex microstructures with multiple particle and void clusters are possible. Because the subsequent complex fracture events are likely to localize, some parts of the microstructure may totally fail while other parts still have a significant load carrying capacity. In particular, some parts of the microstructure may totally relax before the end of the simulation, thus authorizing numerically problematic rigid body modes (*e.g.*, a fully debonded particle).

Due to the choice of boundary conditions, these abnormal solutions can be detected by tagging CCs (Section 3.3) of the solid phase. At the beginning of the simulation, there will generally be only one CC, but due to the nucleation of cracks some solid parts may separate totally. A CC of the solid phase is said to be a rigid body if it does not have at least one node on each of the following boundaries:

- either the bottom or the top face of the RVE,
- either the left or the right face of the RVE,
- either the back or the front face of the RVE (only in 3D).

As illustrated in Figure 4.6, these phases are eliminated from the computation and considered as voids during mechanical solution. However, their volume is not accounted for in the calculation of the porosity f .

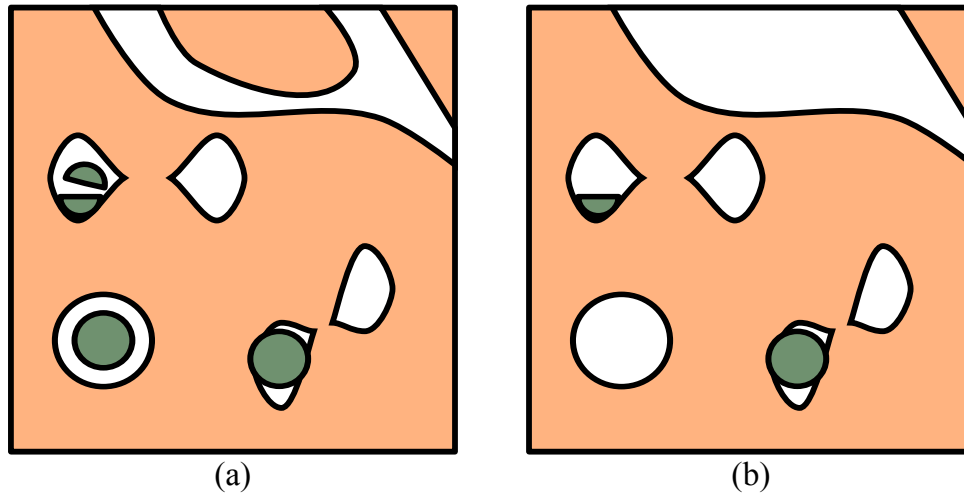


Figure 4.6 – Elimination of CCs of the solid phase that could lead to rigid body modes during mechanical solution: (a) initial microstructure with rigid body modes, (b) resulting microstructure after the numerical treatment.

This treatment is problematic for some non proportional loading paths that could include compression. To generalize the present numerical framework to such situations, a more robust contact formulation should be investigated, including an alternative to this treatment of rigid body modes.

4.5.2 Material

An interesting study on void nucleation can be found in Reference [66], where ductile fracture of a particle reinforced aluminum alloy was investigated. This material is composed of an aluminum matrix reinforced with 20% of Zirconia-Silica (ZS) particles. Particle fragmentation is the dominating void nucleation mechanism, as shown in Figure 4.7. Some voids can be seen in the initial microstructure in black in Figure 4.7(a) but are neglected in the present study.

In Reference [66], material parameters were identified for the matrix by carrying tensile tests on purely matrix material specimens, and for the inclusions by using nanoindentation. Some uncertainties may arise due to the limitations of these identification techniques. First, the forming process is different for the purely matrix material and the reinforced one, so the behavior of the matrix may also be different. Second, nanoindentation can only be applied to the inclusions at the surface of the specimen, hence some differences may apply due to polishing for instance. Nevertheless, such advanced identification is not commonly found in the literature. In particular, the fracture properties of the inclusions were also determined and are given in Table 4.3. These

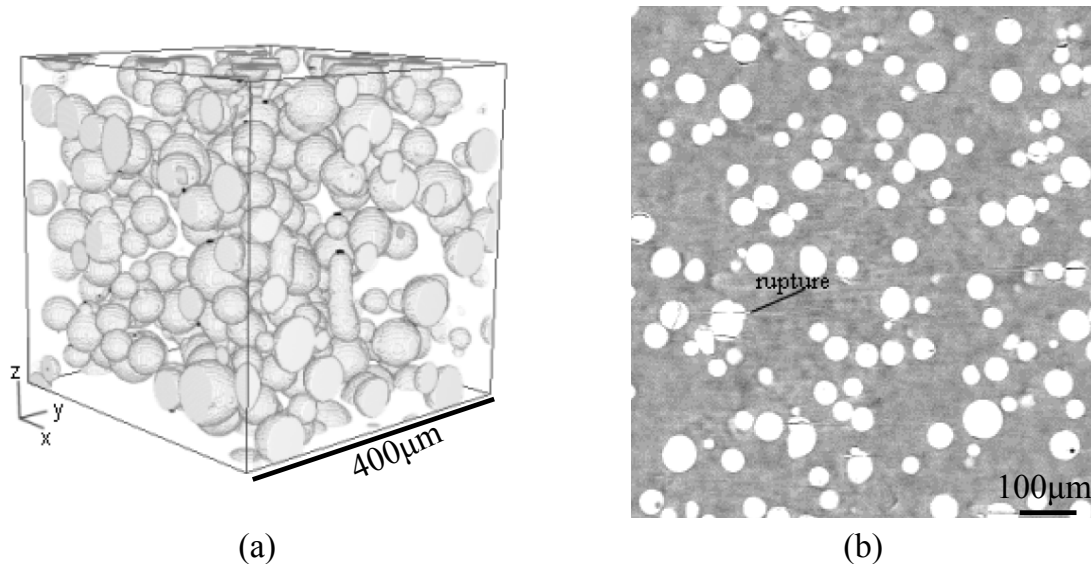


Figure 4.7 – Tomography images of the particle reinforced aluminum alloy: (a) 3D view of the initial microstructure, (b) view of a section showing particle fragmentation mechanisms at 4 % of true plastic strain. Figures reproduced from Reference [66].

properties were determined by comparing X-ray tomography data acquired *in situ* with RVE calculations. The latter considered a single inclusion with periodic boundary conditions. The equivalent plastic strain was identified by measuring the section reduction of the specimen, while the triaxiality was determined using Bridgman’s formula.

The limitations of this identification methodology are discussed in Chapter 6, and a promising alternative is proposed. Properties given in Table 4.3 may vary depending on heat treatments and particle volume fraction [68], but they are assumed constant to allow for comparisons.

Material behavior	Phase	E (MPa)	ν	σ_y (MPa)	K (MPa)	n
	Matrix	72000	0.33	270	580	0.54
Fracture criteria	Particles	123000	0.23	∞		
	Phase	σ_c^D (MPa)	ℓ^D (μm)	σ_c^F (MPa)	ℓ^F (μm)	
	Particles	1060	10	700	10	

Table 4.3 – Material parameters for the Al2124 matrix and the ZS particles, including fracture criteria parameters [66], to which are added the two numerical parameters ℓ^D and ℓ^F .

For the calculations in this section, statistical RVEs are used. Inclusions are considered as spherical, with radii distributed according to a normal law of mean 20 μm and standard deviation 5 μm [68].

To generate virtual microstructures, a set of particle radii is first generated based on the given normal law. The size of the RVE is a user-defined parameter. Particles are consecutively placed randomly in this RVE, with a safety minimum distance of 8 μm between each other, and between each of them and the boundary of the RVE. These constraints are important for the CC identification algorithm on which the particle fragmentation criterion is based (Paragraph 3.4.2.4). When it is not possible to place inclusions anymore without having the volume fraction exceed the prescribed one, the generation is stopped and the resulting RVE is returned. For 2D calculations, a surface fraction is imposed, and plane strains are assumed.

Unless otherwise mentioned, boundary conditions as defined in Section 4.4 are used and the macroscopic stress triaxiality ratio η is maintained to 0.33.

4.5.3 Numerical validation

To begin with, numerical parameters such as meshing parameters and the time step are chosen and validated. The time step is dimensionless because all calculations are performed in static loading conditions, and material constitutive laws are rate-independent. The single-particle RVE used for numerical validation has a size of $80\ \mu\text{m}$ in 2D, and $55\ \mu\text{m}$ in 3D. The reference numerical parameters setting uses:

- remesher parameters $Q_\mu = Q_\sigma = 0.05$, $V_\mu = V_\sigma = 10^{-3}\ \mu\text{m}^3$ in 2D and $V_\mu = V_\sigma = 10^{-6}\ \mu\text{m}^3$ in 3D (Subsection 2.2.2), a mesh motion parameter $\beta = 0.5$ (Subsection 2.3.1),
- meshing parameters $\epsilon_h = 12\ \mu\text{m}$, $h_{curv} = 0.2\ \mu\text{m}$, $h_{max} = 6\ \mu\text{m}$, $h_{min} = 2\ \mu\text{m}$ (Section 3.1),
- a crack thickness $\epsilon_l = 0.2\ \mu\text{m}$ (Section 2.6),
- a contact thickness $\epsilon_c = 0.1\ \mu\text{m}$ (Section A.2) (Section 4.3),
- a time step $\Delta t = 0.001$, which is decreased by a factor of two every 20 iterations of the Newton-Raphson algorithm if convergence was not reached.

The particle has a radius of $20\ \mu\text{m}$ both in 2D and 3D. A sensitivity analysis is conducted by varying numerical parameters and investigating the influence of this variation on relevant mechanical variables.

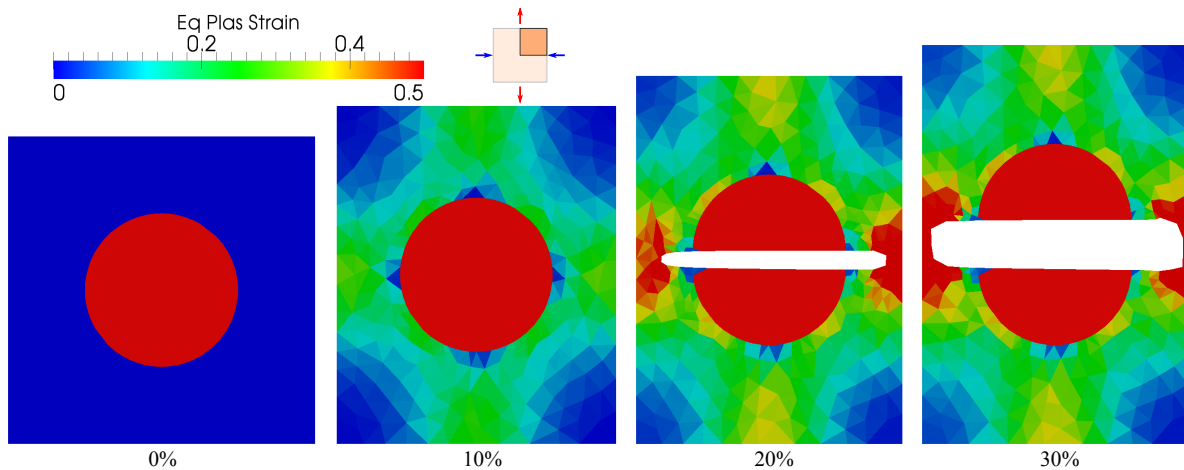
Remesher parameters only have an influence on volume conservation, which can be assessed by considering the porosity and its increase during loading. A significant increase indicates that volume diffusion is negligible, while a stagnation or a decrease is likely to be due to significant numerical diffusion. Because the present framework relies extensively on remeshing operations, all parameters that depend on mesh size are expected to have a significant influence.

Results may also be sensitive to the time step, because the discretization of the extra terms resulting from the Jaumann derivative in Equation (1.7) and the fracture criteria are explicit. Additionally, the uncertainty on macroscopic stress triaxiality ratio control is likely to be increased with large time steps.

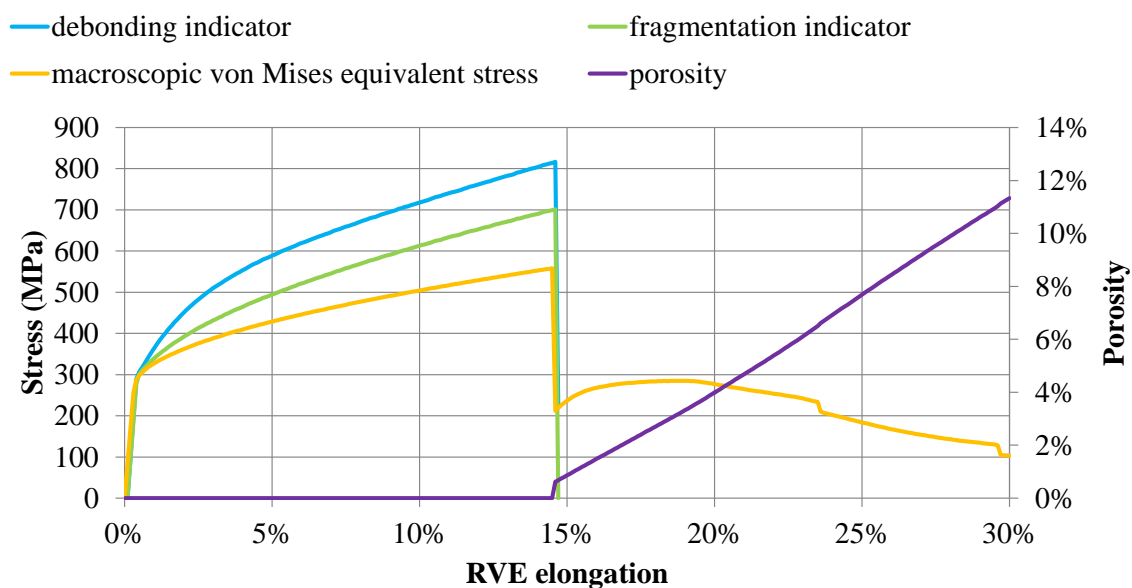
For comparisons with mean field models such as the GTN model, only averaged quantities such as the porosity f and the macroscopic von Mises equivalent stress $\bar{\Sigma}$ are of interest. However, for comparisons with experiments, convergence on local variables is also important. This is verified based on the maximum normal stress at the matrix/particle interface σ_n (Equation (4.2)) and the particle-wise average maximum stress σ_1^p (Equation (4.4)). The present sensitivity analysis includes both averaged and local quantities. Sensitivity to mesh size is assessed using a coarse mesh setting with ϵ_h , h_{curv} , h_{max} , h_{min} , ϵ_l and ϵ_c multiplied by a factor of 2, and a fine mesh setting with a factor of 0.5. Sensitivity to the time step is assessed using time steps of 0.01 and 0.0001.

4.5.3.1 Particle fragmentation reference results

The results obtained using the reference numerical parameters in 2D and 3D are shown in Figure 4.8 and Figure 4.9.



(a) Microstructure at different RVE elongations, with particle in red and voids in white.



(b) Evolution of the particle debonding indicator σ_n (threshold at 1060 MPa), the particle fragmentation indicator σ_1^p (threshold at 700 MPa), the macroscopic von Mises equivalent stress $\bar{\Sigma}$, and the porosity f .

Figure 4.8 – Reference result in 2D plane strain featuring only particle fragmentation.

As observed in these figures, using the material and fracture criteria parameters given in Table 4.3, only particle fragmentation is predicted, both in 2D and 3D. This is in agreement with experimental observations (Figure 4.7(b)). Both σ_n and σ_1^p increase up to values that are close to the critical thresholds, but the fragmentation threshold is reached first, at nearly 15 % of RVE elongation in 2D, and at nearly 3 % in 3D.

Regarding the fragmentation crack, The 2D and 3D results are very similar, with a horizontal fracture plane, which is also in agreement with experimental observations (Figure 4.7(b)). In 3D, because of a smaller RVE size, due to the fact that the particle volume fraction is initially fixed to 20 %, the plane is already in contact with the RVE boundary at its nucleation. This is not physical and is linked to the numerical parameter ℓ^F , whose influence is investigated in Paragraph 4.5.3.3.

Additionally, fragmentation cracks could be accompanied with a debonding of the matrix/particle interface close to the fragmentation crack tip (Figure 1.3(b)). Although this is not the case for

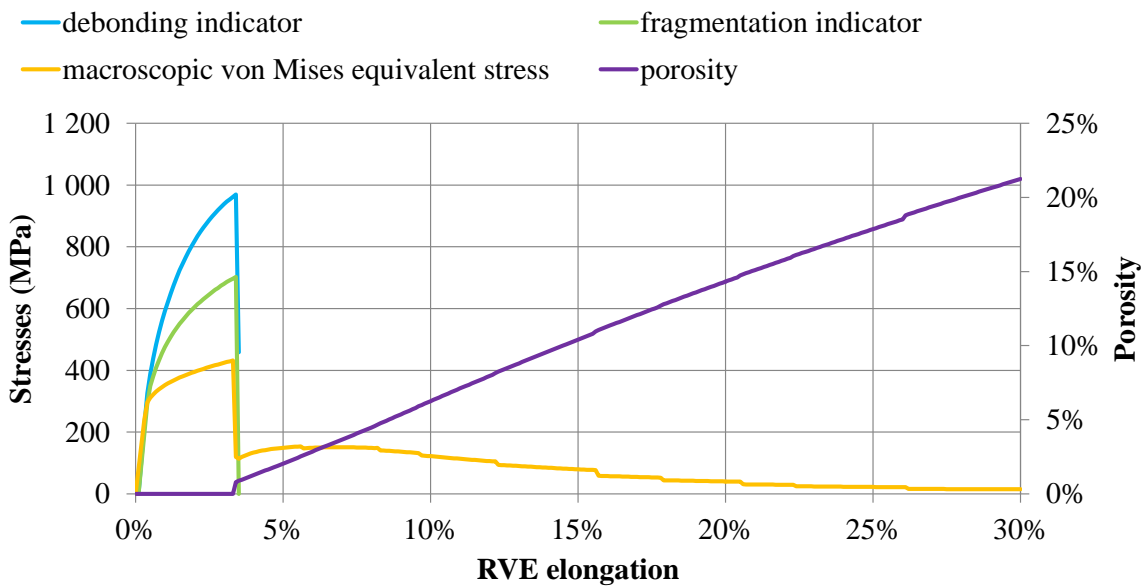
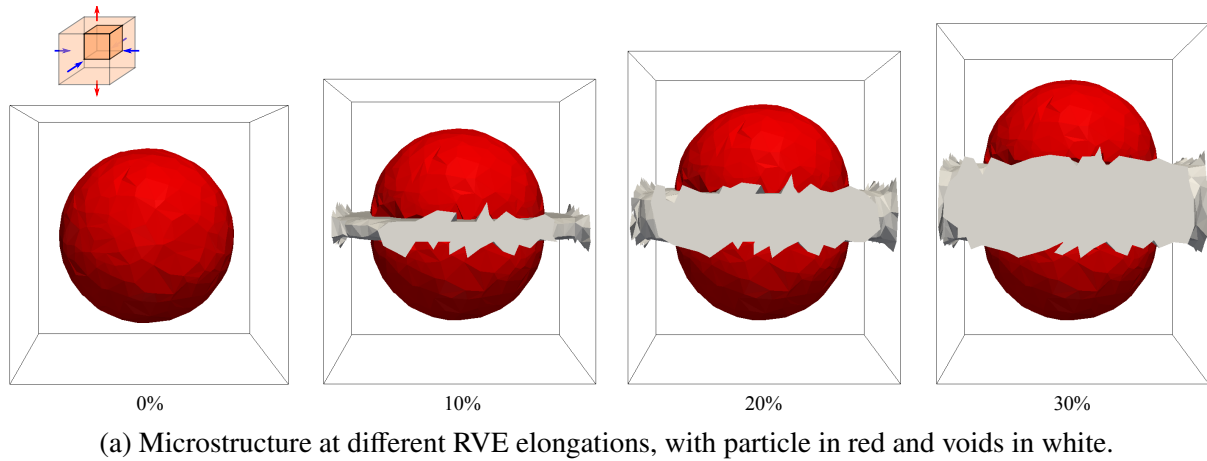


Figure 4.9 – Reference result in 3D featuring only particle fragmentation.

the present material (Figure 4.7(b)), the presence of a quite large part of the fragmentation crack inside the matrix would prevent this phenomenon both in 2D and 3D. Thus, it will be important in the future to improve the fragmentation criterion in order to avoid this numerical parameter ℓ^F (Chapter 7).

Regarding the crack thickness parameter ϵ_l , its influence cannot be seen directly in Figure 4.8(b) and Figure 4.9(b). Since the fracture criteria are considered at the beginning of each time increment, the porosity shown in these figures includes both the artificially inserted porosity due to ϵ_l and the porosity due to crack opening.

In order to distinguish the two, the artificial porosity is computed separately during the simulation. It is equal to 0.18 % in 2D and 0.30 % in 3D at the onset of particle fragmentation. It then decreases because no additional artificial porosity is inserted, while the global void volume increases due to void growth.

This is a major improvement over previous work at Cemef - MINES ParisTech, where a mesh

size at least ten times finer was required to reduce the artificial porosity to similar values in 2D [6]. Moreover, this artificial porosity is negligible when compared to the final porosity, which is close to 10 % in 2D and 20 % in 3D.

The porosity curves in Figure 4.8(b) and Figure 4.9(b) show no oscillations after the onset of particle fragmentation, which proves that void volume is well conserved. Hence, remesher parameters V_μ and V_σ are small enough and well-suited for the present study.

While volume is very well conserved, it is not the case for history variables. This can be observed by looking at the macroscopic von Mises equivalent stress in Figure 4.8(b) and Figure 4.9(b). At the onset of particle fragmentation, the load carrying capacity is severely affected, but it is partially preserved because the fragmentation crack does not entirely cut the RVE into two halves. Even in 3D, the crack intersects lateral boundaries but not the corners. Due to void growth and coalescence, the thickness of these regions is progressively reduced and the load carrying capacity tends to zero. During this process, small jumps can be observed in the macroscopic von Mises equivalent stress curve (e.g., slightly before 25 % and 30 % of RVE elongation in Figure 4.8(b)).

These are not caused by a fracture event or the treatment of rigid body modes described in Subsection 4.5.1, as shown in Figure 4.8(a) where the only void is the fragmentation crack. Thus, these jumps are due to remeshing operations and in particular to numerical diffusion during the transfer of history variables. Although these jumps are not significant globally, they may have an influence locally. It will be important to improve the field transfer method in future work (Chapter 7).

4.5.3.2 Particle fragmentation criterion

Based on the reference result discussed in Paragraph 4.5.3.1, a sensitivity analysis is conducted in the present paragraph regarding numerical parameters.

In Figure 4.10, it is verified that reference results are converged regarding the onset of particle fragmentation.

The fact that σ_1^p is null for the first loading step both in 2D and 3D is simply due to the fact that the fragmentation criterion is computed at the beginning of each time increment. This also explains why at the onset of particle fragmentation the load carrying capacity seems to be lost progressively.

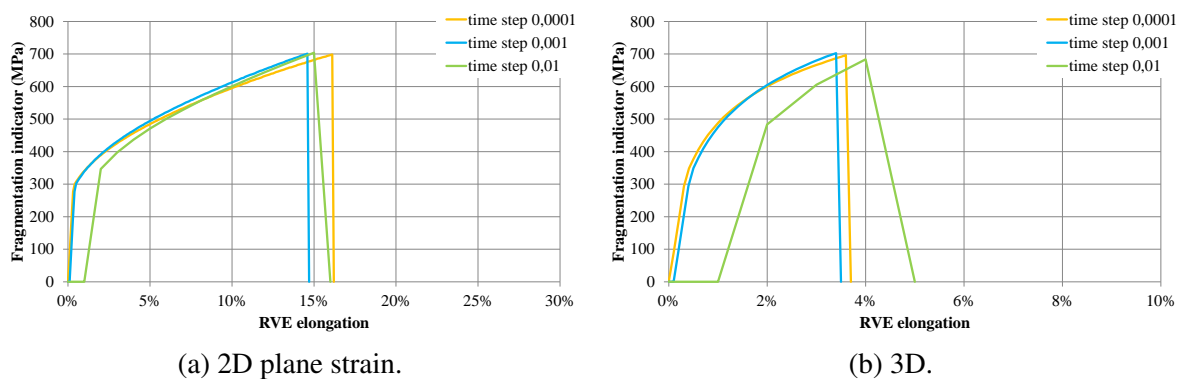


Figure 4.10 – Sensitivity of the particle fragmentation indicator σ_1^p during loading with respect to the time step. Note that the scales of the graphs differ from 2D to 3D.

However, the threshold for particle fragmentation is never reached in the 3D simulation using the coarse time step. This means that this time step is too large to enable for the modeling of the competition between the two void nucleation mechanisms. Particle debonding is predicted in this simulation. It is hence discarded in the remaining of this analysis.

The differences between the curves using the reference and fine time steps are small, especially in 3D. The measured absolute uncertainty of 1.5 % (2D) and 0.08 % (3D) of RVE elongation regarding the prediction of particle fragmentation is nevertheless acceptable using the reference time step.

In Figure 4.11, the influence of this uncertainty on porosity change is assessed (the result using the coarse time step in 3D is not reported).

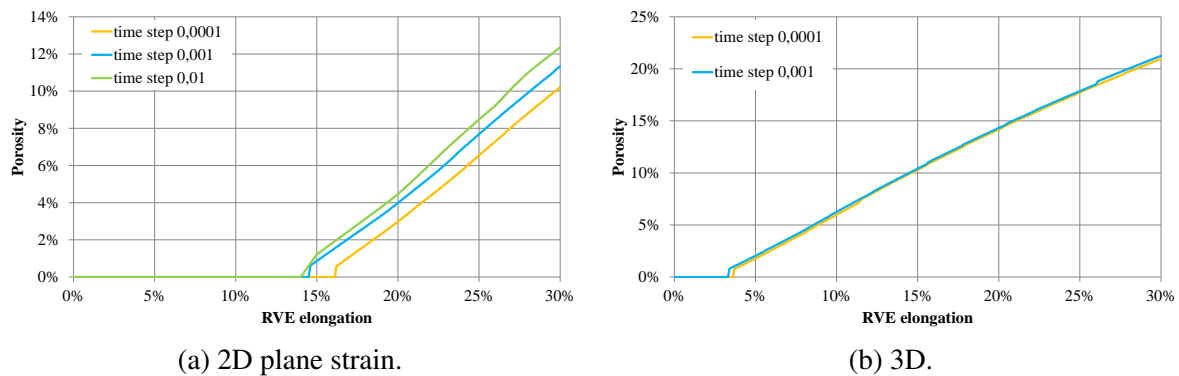


Figure 4.11 – Sensitivity of the porosity during loading with respect to the time step.

No significant influence of the time step on void growth can be observed. The slopes of the curves obtained using the reference time step correspond well to the slopes obtained using the fine time step. The main differences are due to the delay regarding the prediction of the onset of particle fragmentation. The corresponding absolute error on the porosity at 30 % of RVE elongation is 1.1 % in 2D and 0.1 % in 3D. This is acceptable for the present material with high porosity, but should be investigated further for industrial materials where the porosity is lower. The influence of mesh size on the prediction of the onset of particle fragmentation is assessed in Figure 4.12.

Opposed to simulations with varying time steps, particle fragmentation is predicted in all these simulations. However, the onset of particle fragmentation is underestimated using coarse meshing parameters both in 2D and 3D. The absolute uncertainties on RVE elongation at the onset of particle fragmentation for the reference mesh remain small, namely 0.8 % in 2D and 1.0 % in 3D.

The influence of these uncertainties on void growth is shown in Figure 4.13.

The results are similar to those obtained in the time step sensitivity analysis. Particle fragmentation is delayed but this does not affect void growth, as the slopes of the curves correspond well between the reference result and the result with fine mesh. The absolute uncertainties on the porosity at 30 % are 0.02 % in 2D and 0.04 % in 3D. The reference results are hence well-suited for the present material. Moreover, the fact that these uncertainties are very small indicates that the crack thickness parameter ϵ_l has, in the end, a very low influence on the results.

As a conclusion, absolute errors regarding the prediction of the onset of particle fragmentation

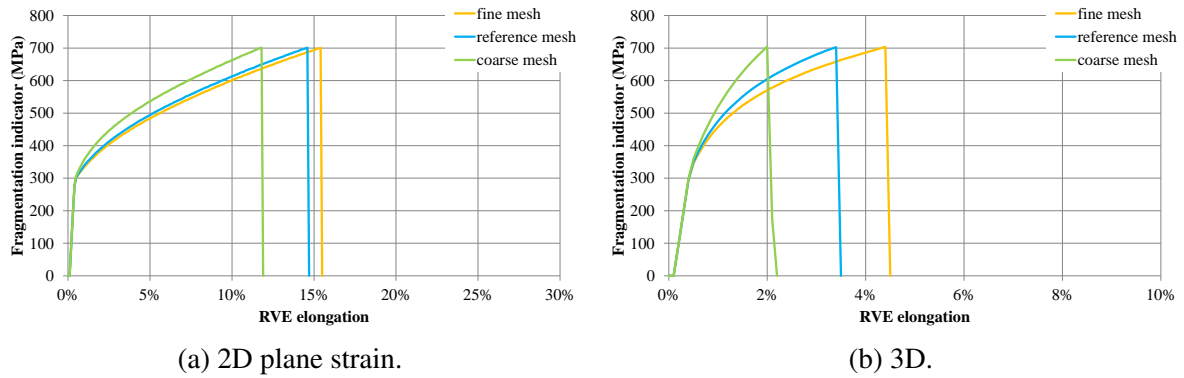


Figure 4.12 – Sensitivity of the particle fragmentation indicator σ_1^D during loading with respect to mesh size.

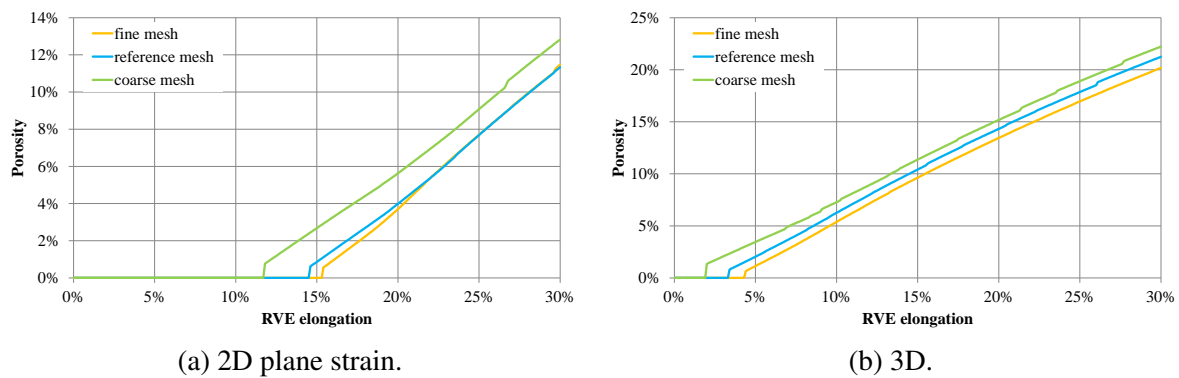


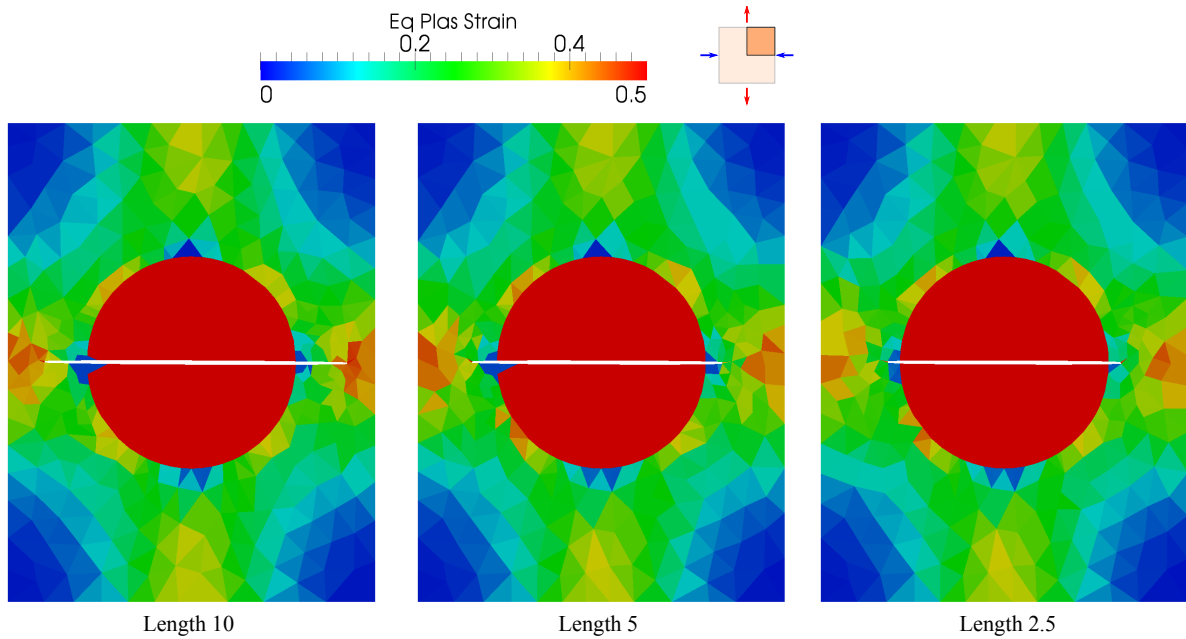
Figure 4.13 – Sensitivity of the porosity during loading with respect to mesh size.

close to the percent are obtained using reference numerical parameters. These uncertainties mainly delay void growth, but do not affect significantly the slope of the porosity change curves. The absolute uncertainty on the final porosity is hence also close to the percent.

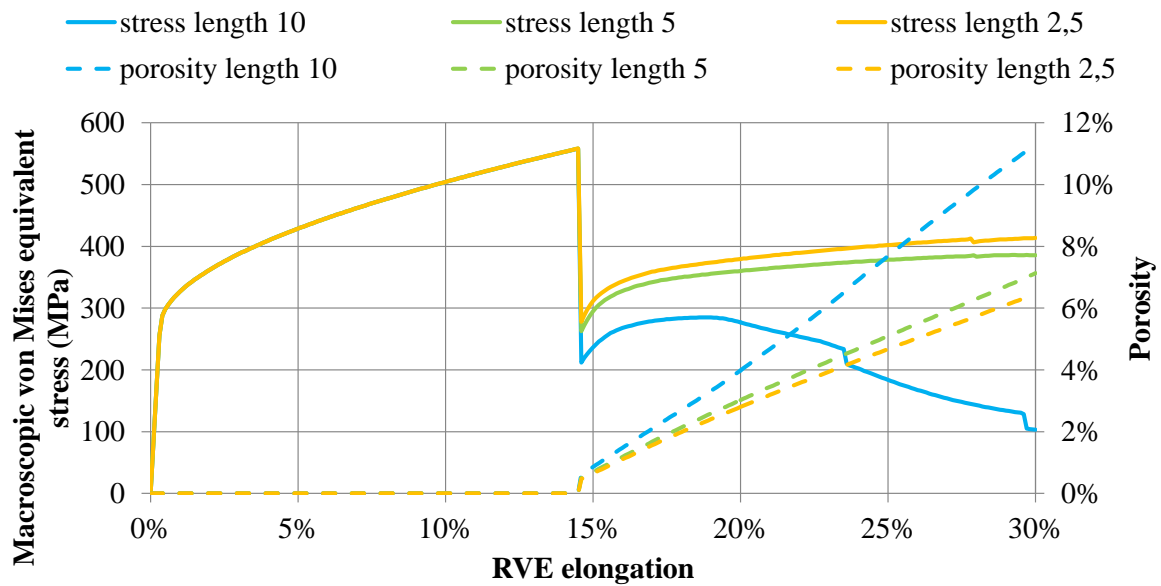
Although these results validate the particle fragmentation criterion, the fact that the onset of particle fragmentation is systematically delayed with fine numerical parameters remains to be investigated. With a coarse mesh or time step, an underestimation of stress localization in the particle would be expected, instead of an overestimation. This is investigated in the case of particle debonding in Paragraph 4.5.3.6.

4.5.3.3 Particle fragmentation crack extension length ℓ^F

As mentioned in Paragraph 4.5.3.1, the numerical implementation of the particle fragmentation criterion includes a length ℓ^F that leads to non physical result. The fragmentation crack is extended in the matrix material, which does not correspond to experimental observations in Figure 4.7(b). In this paragraph, 2D and 3D simulations with the reference numerical parameters but varying ℓ^F are conducted to study the influence of this parameter. Results are reported in Figure 4.14 for the 2D case.



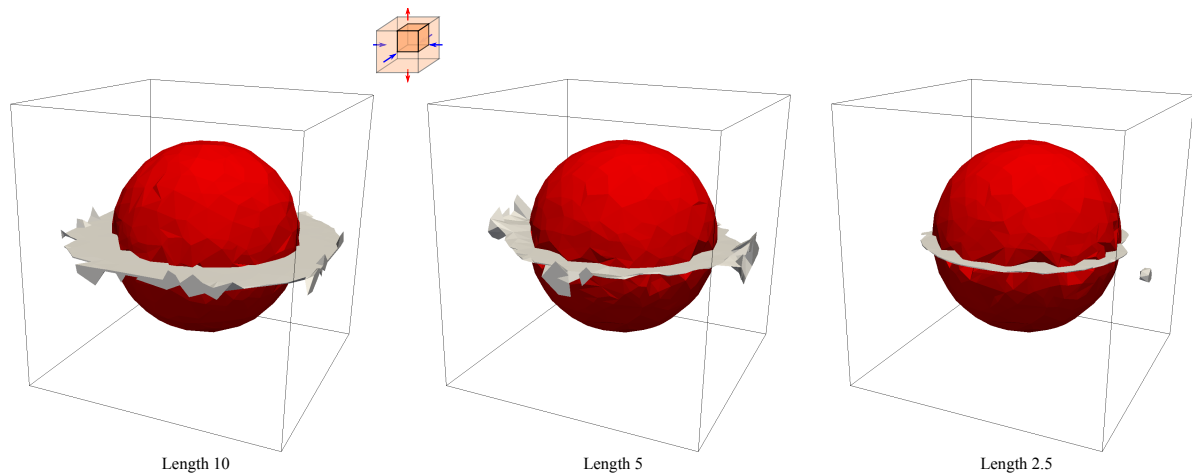
(a) Microstructures at the onset of particle fragmentation, with particle in red and voids in white.



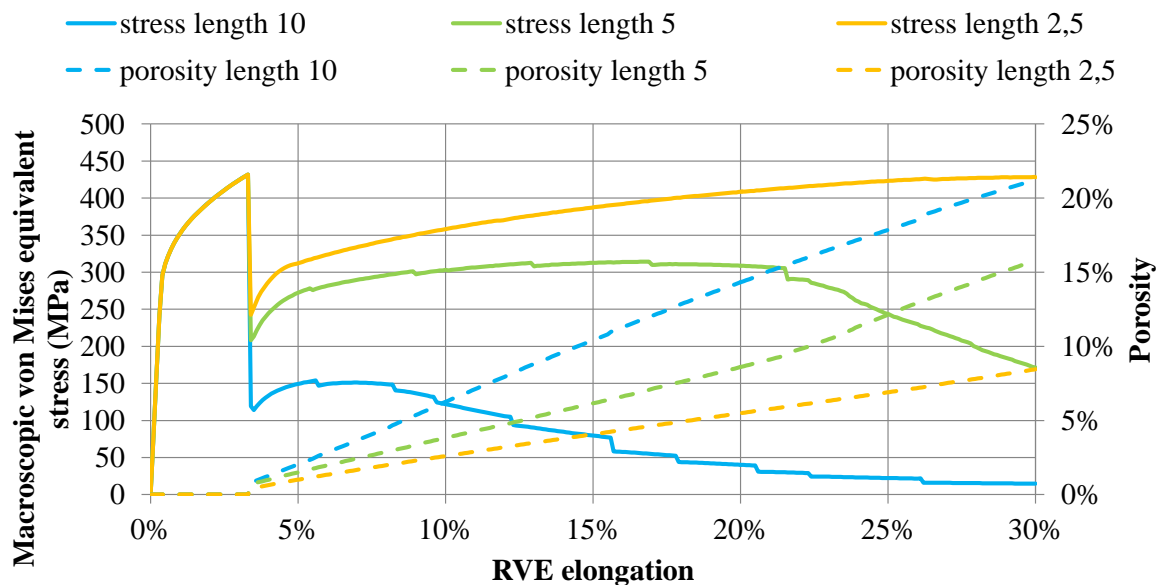
(b) Evolution of the macroscopic von Mises equivalent stress $\bar{\Sigma}$ and the porosity f .

Figure 4.14 – Sensitivity of the results with respect to the fragmentation crack extension length ℓ^F in 2D plane strain.

There is a significant influence for $\ell^F = 10\ \mu\text{m}$, which shows that with a too large crack extension length the thickness of the intervoid ligament is severely reduced and void coalescence is overestimated. This is corrected with smaller lengths both regarding the porosity and the load carrying capacity of the intervoid ligament (the particle being broken). This study is extended to 3D in Figure 4.15.



(a) Microstructures at the onset of particle fragmentation, with particle in red and voids in white.

(b) Evolution of the macroscopic von Mises equivalent stress $\bar{\Sigma}$ and the porosity f .Figure 4.15 – Sensitivity of the results with respect to the fragmentation crack extension length ℓ^F in 3D.

In 3D, with the used mesh size, the numerical treatment for void linkage at RVE boundaries described in Subsection 4.4.3 is triggered even with $\ell^F = 2.5 \mu\text{m}$. Small void phase elements are visible at the right boundary of the RVE for $\ell^F = 2.5 \mu\text{m}$ in Figure 4.15(a). This could be avoided by using a smaller mesh size. However, the macroscopic von Mises equivalent stress curve in Figure 4.15(b) for the result with $\ell^F = 2.5 \mu\text{m}$ shows that the load carrying capacity is preserved. Hence, this activation of the numerical treatment for void linkage does not have a dominant effect.

This is not true for the other two calculations, although void coalescence and linkage with RVE boundaries is pronounced only after 20 % of RVE elongation with $\ell^F = 5 \mu\text{m}$.

Therefore, due to a smaller intervoid ligament thickness, the sensitivity to ℓ^F is very high in 3D, both regarding the load carrying capacity and the porosity, due to an overestimation of void coalescence. Although a converged result seems to be obtained in 2D with $\ell^F \leq 5 \mu\text{m}$, the

pictures in Figure 4.14(a) show that plasticity localizes very early in the core of the intervoid ligament. In particular, there is neither plasticity nor stress localization in the corners of the particle fragments in these pictures, even using the smallest ℓ^F .

As a conclusion, the present sensitivity analysis indicates that the numerical parameter ℓ^F should be exactly zero in order to obtain an accurate and physical modeling of particle fragmentation. It will hence be necessary to improve the crack insertion method in the future in order to avoid the use of this parameter (Chapter 7).

4.5.3.4 Particle debonding reference results

For particle debonding to be predicted instead of fragmentation, the particle fragmentation criterion is deactivated. Debonding is then triggered both in 2D and 3D, but for larger strains, as shown in Figure 4.16 and Figure 4.17.

While particle fragmentation in Paragraph 4.5.3.1 is predicted at an RVE elongation of nearly 15 % in 2D and 3 % in 3D, particle debonding does not occur until 25 % in 2D and 5 % in 3D. Note that the competition between fragmentation and debonding is hence tighter in 3D, which explains why debonding is predicted instead of fragmentation in Paragraph 4.5.3.2 using a too large time step in 3D.

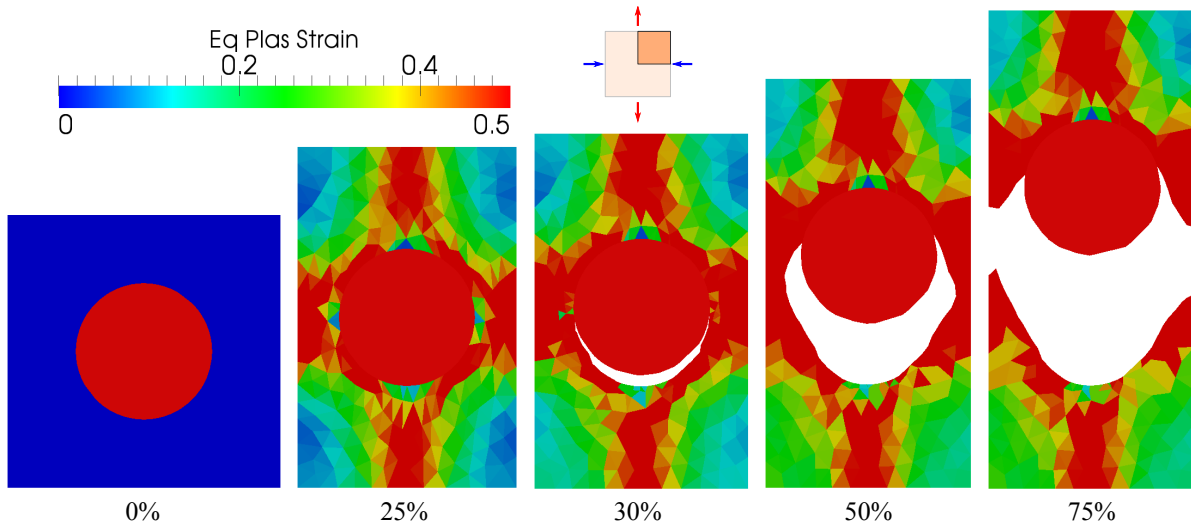
An important observation is that debonding occurs only in the bottom of the inclusion in the 2D reference result, while it is observed both in the top and bottom parts in the 3D reference result. Although this effect is revealed in these simulations only due to the fact that the debonding criterion is local, the same result would have been obtained if particle fragmentation had been considered for two particles in a symmetric microstructure. Depending on numerical errors, one particle or the other would have fragmented (or both), with no possibility to obtain a converged result. Such perfectly symmetric results cannot be found in nature, as residual stresses and nanoscopic defects are likely to favor one crack propagation pattern or the other. An application to a random microstructure is presented in Paragraph 4.5.3.7 to verify that convergence can be obtained regarding the crack propagation path.

An interesting study is to compare the effect of particle debonding on the load carrying capacity to the effect of particle fragmentation. For instance, in 3D, the macroscopic von Mises equivalent stress curve in Figure 4.17(b) can be compared to that in Figure 4.15(b) using a particle fragmentation crack extension length $\ell^F = 2.5 \mu\text{m}$. The two curves are very similar, regarding the beginning and the end.

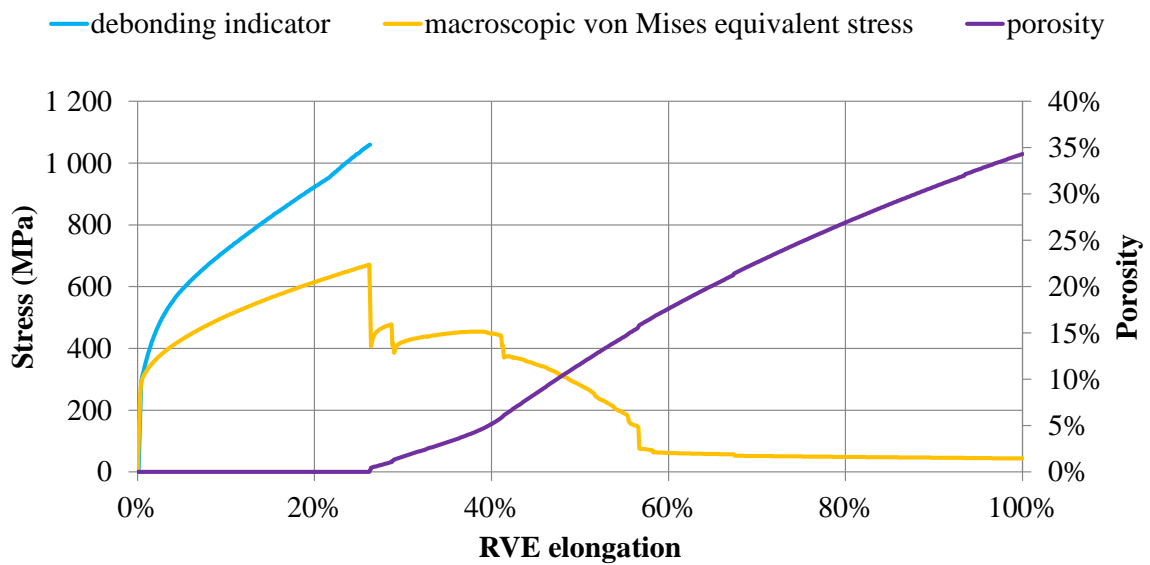
However, particle fragmentation leads to a more severe and instantaneous drop of the load carrying capacity ($\bar{\Sigma} \approx 250 \text{ MPa}$ at 3 % of RVE elongation) while this is less significant and more progressive in the case of debonding ($\bar{\Sigma} \approx 300 \text{ MPa}$ at 5 % of RVE elongation). Void growth is also slowed down in the case of debonding, as the porosity reaches 10 % at 50 % of RVE elongation (Figure 4.17(b)), while this occurs at only 30 % of RVE elongation (Figure 4.15(b)) in the particle fragmentation case with $\ell^F = 2.5 \mu\text{m}$. Thus, while particle fragmentation leads to an instantaneous void nucleation mechanism, particle debonding is more progressive.

This effect is not necessarily due to the fact that debonding cracks may still be propagating at the onset of void coalescence. This is the case in the 2D simulation, which can be seen for instance between 30 % and 50 % of RVE elongation in Figure 4.16(a), where necking is clearly visible in the ligament between the void and lateral boundaries, but debonding is still going on. Multiple drops of the macroscopic von Mises equivalent stress curve are also visible in Figure 4.16(b).

However, it is not true for the 3D simulation, as only one void nucleation mechanism appears clearly in Figure 4.17(b). Debonding cracks are propagating during the whole simulation (Figure

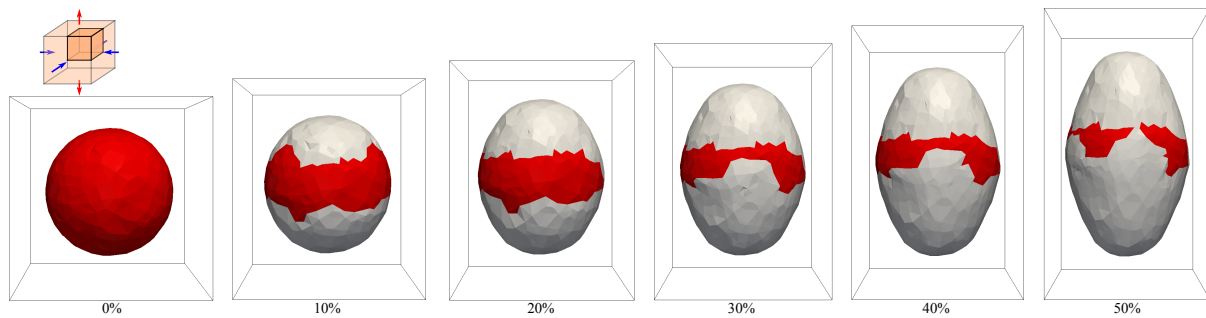


(a) Microstructure at different RVE elongations, with particle in red and voids in white.

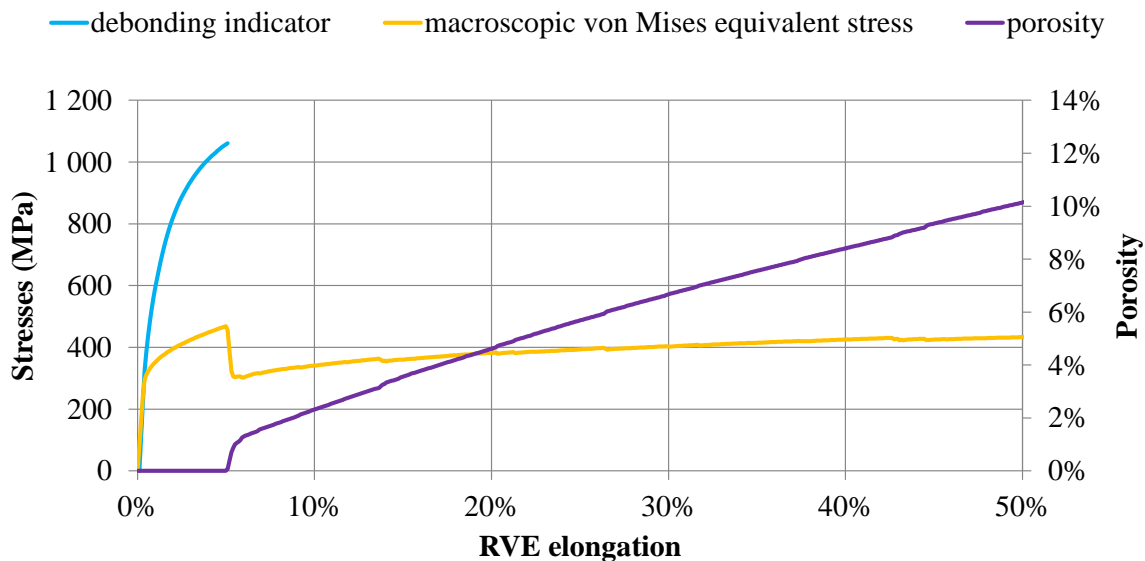


(b) Evolution of the particle debonding indicator σ_n (threshold at 1060 MPa), the macroscopic von Mises equivalent stress $\bar{\Sigma}$, and the porosity f .

Figure 4.16 – Reference result in 2D plane strain, featuring only particle debonding, the fragmentation criterion being deactivated.



(a) Microstructure at different RVE elongations, with particle in red and voids in white.



(b) Evolution of the particle debonding indicator σ_n (threshold at 1060 MPa), the macroscopic von Mises equivalent stress $\bar{\Sigma}$, and the porosity f .

Figure 4.17 – Reference result in 3D featuring only particle debonding, the fragmentation criterion being deactivated.

4.17(a)), but only the first debonding event at 5% of RVE elongation affects clearly the load carrying capacity. Later debonding cracks propagate along the lateral boundaries of the particle. Although these cracks do not affect the load carrying capacity in the present case, their effect cannot be neglected as it would certainly be very important for non proportional loading paths with varying loading direction.

4.5.3.5 Particle debonding criterion

Simulations with deactivated particle fragmentation criterion are numerically validated in this paragraph. First, the time step is varied (Figure 4.18).

The absolute errors on the onset of particle debonding using the reference time step are 5.8% in 2D and 1.8% in 3D. While the 3D result is acceptable, the error is quite high for the 2D one. It is important to check the influence of this error on porosity change (Figure 4.19).

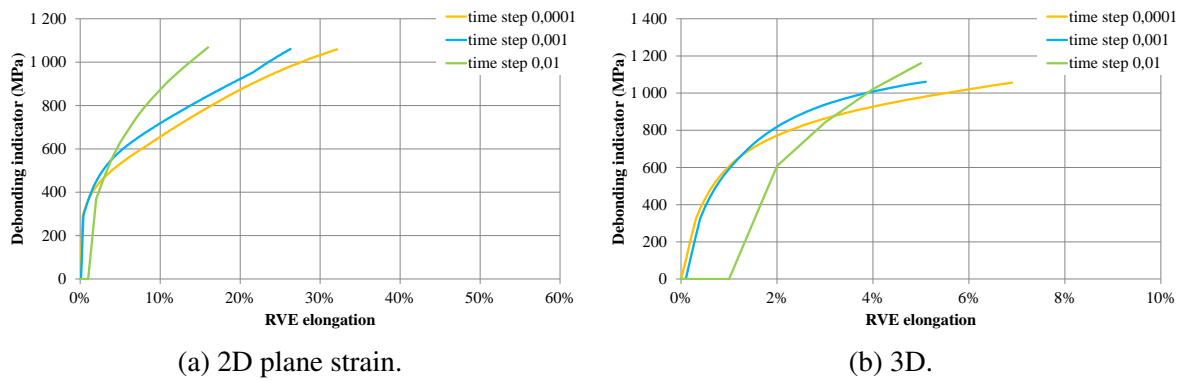


Figure 4.18 – Sensitivity of the particle debonding indicator σ_n during loading with respect to the time step.

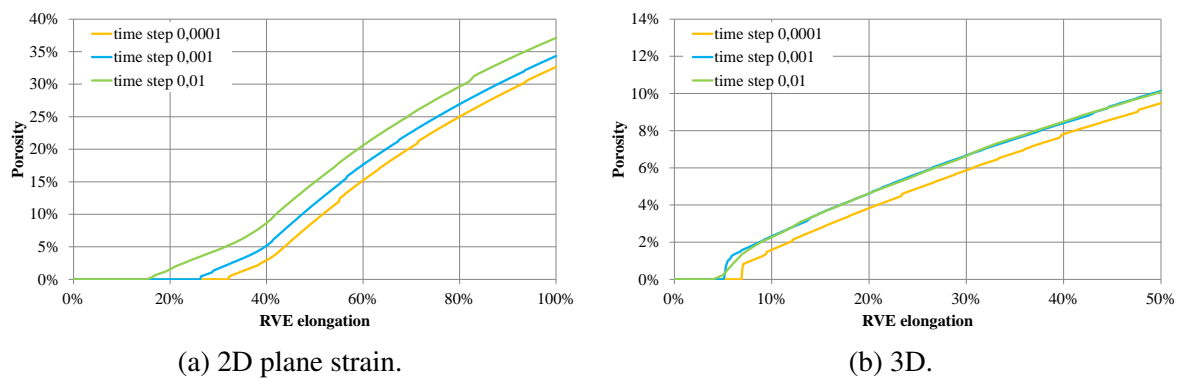


Figure 4.19 – Sensitivity of the porosity during loading with respect to the time step.

The same remarks as for particle fragmentation apply. In particular, the delay regarding the onset of void nucleation does not seem to affect void growth, as the slopes of the porosity change curves correspond for all used time steps. The absolute error on the porosity at 100 % of RVE elongation in 2D using the reference time step is 1.7 %. It is 0.7 % in 3D at 50 % of RVE elongation. These results validate the use of the reference time step for further FE analysis. The dependence on mesh size is assessed in Figure 4.20.

The absolute uncertainties regarding the prediction of the onset of particle debonding using the reference mesh are very low both in 2D (0.2 %) and 3D (0.01 %). However, porosity change curves in Figure 4.21 show that the 3D results may be influenced by mesh size more significantly than 2D ones.

A possible explanation is the sensitivity of the particle debonding site with respect to numerical parameters. While a good convergence is obtained regarding the particle debonding indicator, the latter reaches values very close to the critical threshold at multiple points of the interface. The debonding of one of these points instead of the other is purely linked to numerical errors. This effect is illustrated in Figure 4.22, and investigated further in Paragraph 4.5.3.7.

The results with coarse meshes either underestimate stress localization (2D), especially at lateral boundaries of the particle, or overestimate void coalescence (3D) due to a small number of elements between the particle and lateral RVE boundaries. This explains the quite large difference between the results obtained using coarse meshes and the other results in Figure 4.21.

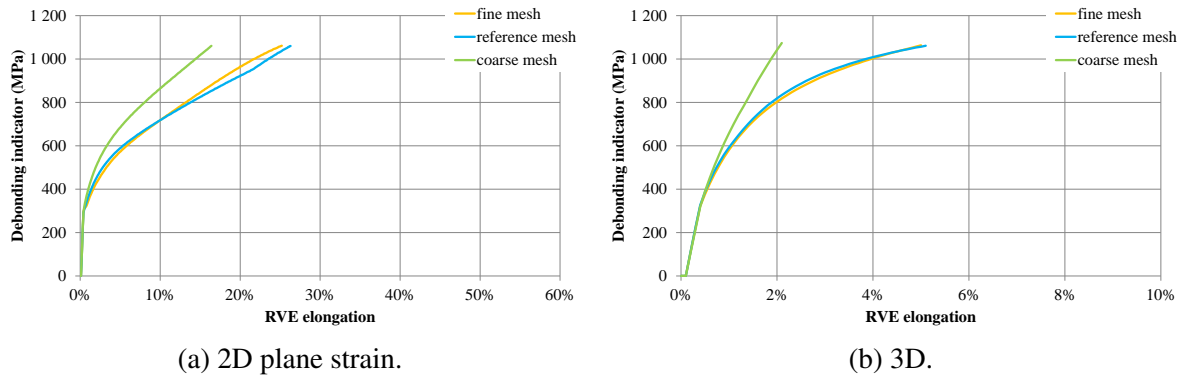


Figure 4.20 – Sensitivity of the particle debonding indicator σ_n during loading with respect to mesh size.

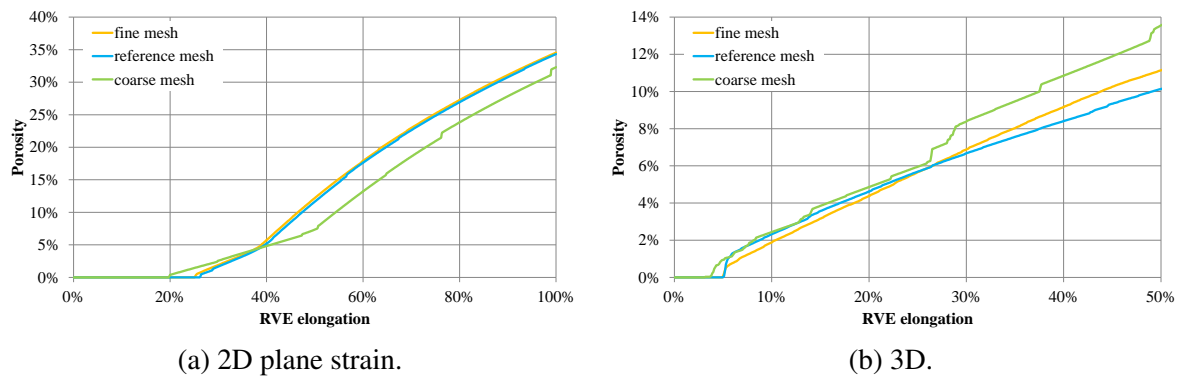


Figure 4.21 – Sensitivity of the porosity during loading with respect to mesh size.

The small difference between the reference and fine results in 2D in Figure 4.21(a) is explained by the fact that debonding occurs at only one side of the particle in both simulations. This is not the case in 3D as debonding occurs at both sides using the reference meshing settings. This explains the difference observed regarding porosity change in Figure 4.22. In Paragraph 4.5.3.7, it is verified whether this has an effect on the prediction of the crack propagation path for random microstructures.

4.5.3.6 Delay of void nucleation using fine numerical parameters

An important remark regarding the void nucleation prediction is that it is systematically delayed using finer numerical parameters (time step and mesh size). This result is quite surprising because the use of explicit fracture criteria and remeshing operations with a diffusive field transfer operator would theoretically imply an underestimation of plasticity and stress localization with coarse meshes.

This surprising result hence suggests that the dominating error is not due to remeshing or the explicit nature of the fracture criteria, but to the FE solution of balance equations. This is investigated in Figure 4.23(a,b), where the plastic strain rate and the pressure are shown for the 2D simulation with the fine mesh at 0.5 % of RVE elongation.

It can be seen that because the initial mesh is generated using the fitting procedure followed by mesh adaptation, some elements with poor quality remain at the matrix/particle interface. These elements are voluntarily not eliminated in the present work because they do not affect

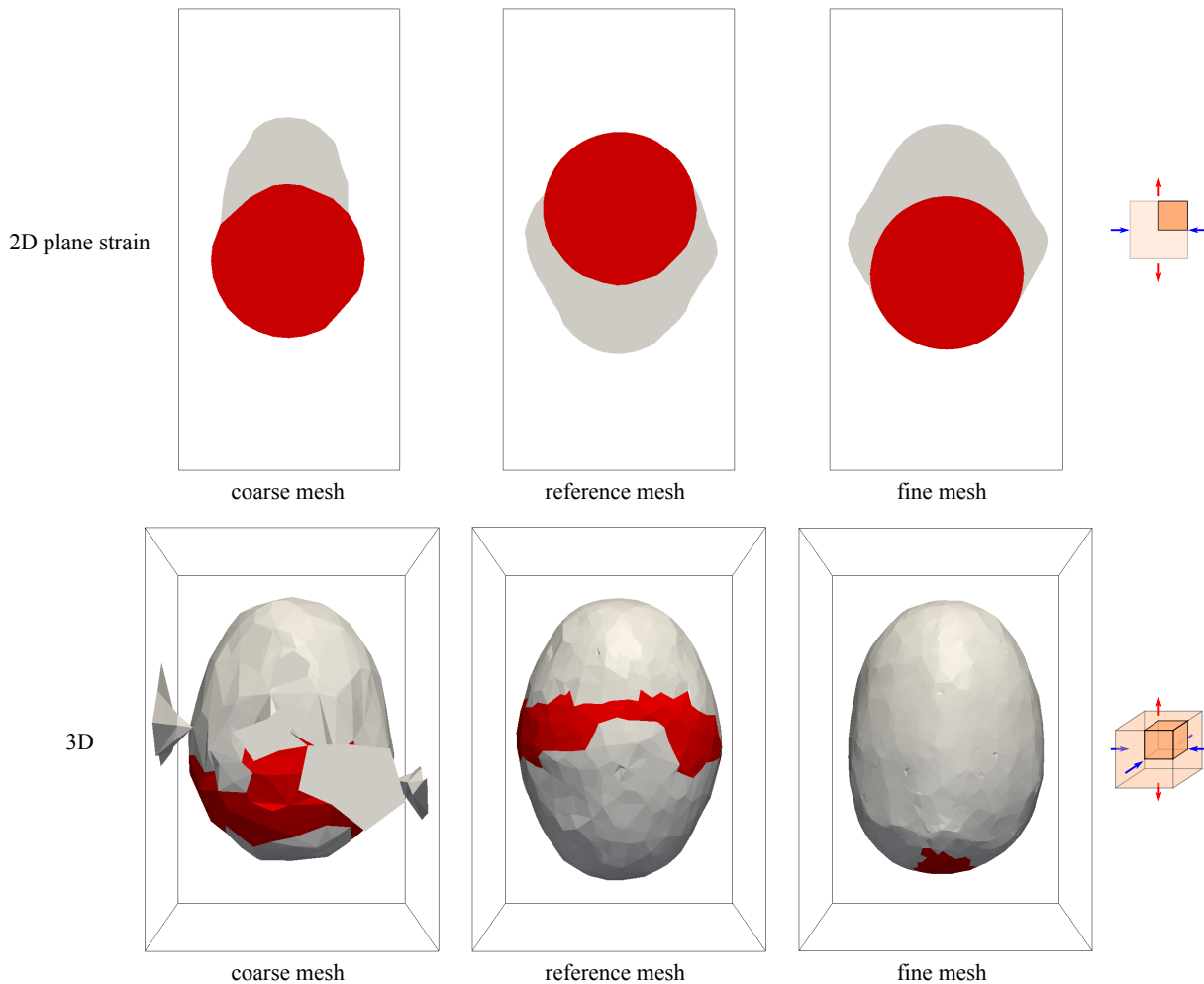


Figure 4.22 – Microstructures in 2D plane strain and 3D using various meshing parameters, with particles in red and voids in white.

severely the conditioning of the linear systems associated with the balance equations (Subsection 2.2.2), and plasticity does not seem to be affected (Figure 4.23(a)).

However, the pressure field (Figure 4.23(b)) seems to be affected by the presence of these elements. This is verified by conducting FE simulations with an initial mesh of uniform size $2\mu\text{m}$ where the particle is initially meshed more regularly using a mesh generation software [192]. The result is shown in Figure 4.23(c) regarding the pressure field. Although oscillations are still present, they are reduced.

Regarding the convergence rate, it is significantly improved as simulations with varying time step predict an onset of particle fragmentation at 3.5 %, 3.59 %, and 3.594 %. The absolute error is hence also significantly reduced compared to what is measured in Paragraph 4.5.3.5. This improved convergence rate proves that the onset of particle fragmentation is delayed due to oscillations of the pressure field at the matrix/particle interface, which seem caused by the presence of elements of poor quality in this region of the mesh.

Although these oscillations are reduced with meshes of better quality, the fact that they are still present incites to reconsider the used $P1^+/P1$ scheme for the solution of the balance equations (Subsection 1.2.1), and not the mesh adaptation method. The fact that oscillations of the pressure field are still present even with meshes of very high quality (Figure 4.23(c)) will be

problematic in the future as pressure-dependent plasticity models will be used.

The cause of these oscillations could be attributed to the use of the bubble element for the velocity approximation. However, the concentration of these oscillations at the interface, and the fact that neither the velocity field nor its gradient (shown through the plastic strain in Figure 4.23(a)) are affected by these oscillations indicates that the problem could be purely linked to the approximation of the pressure.

Comparisons between the $P1^+/P1$ element and elements with discontinuous pressure could be interesting to validate these observations.

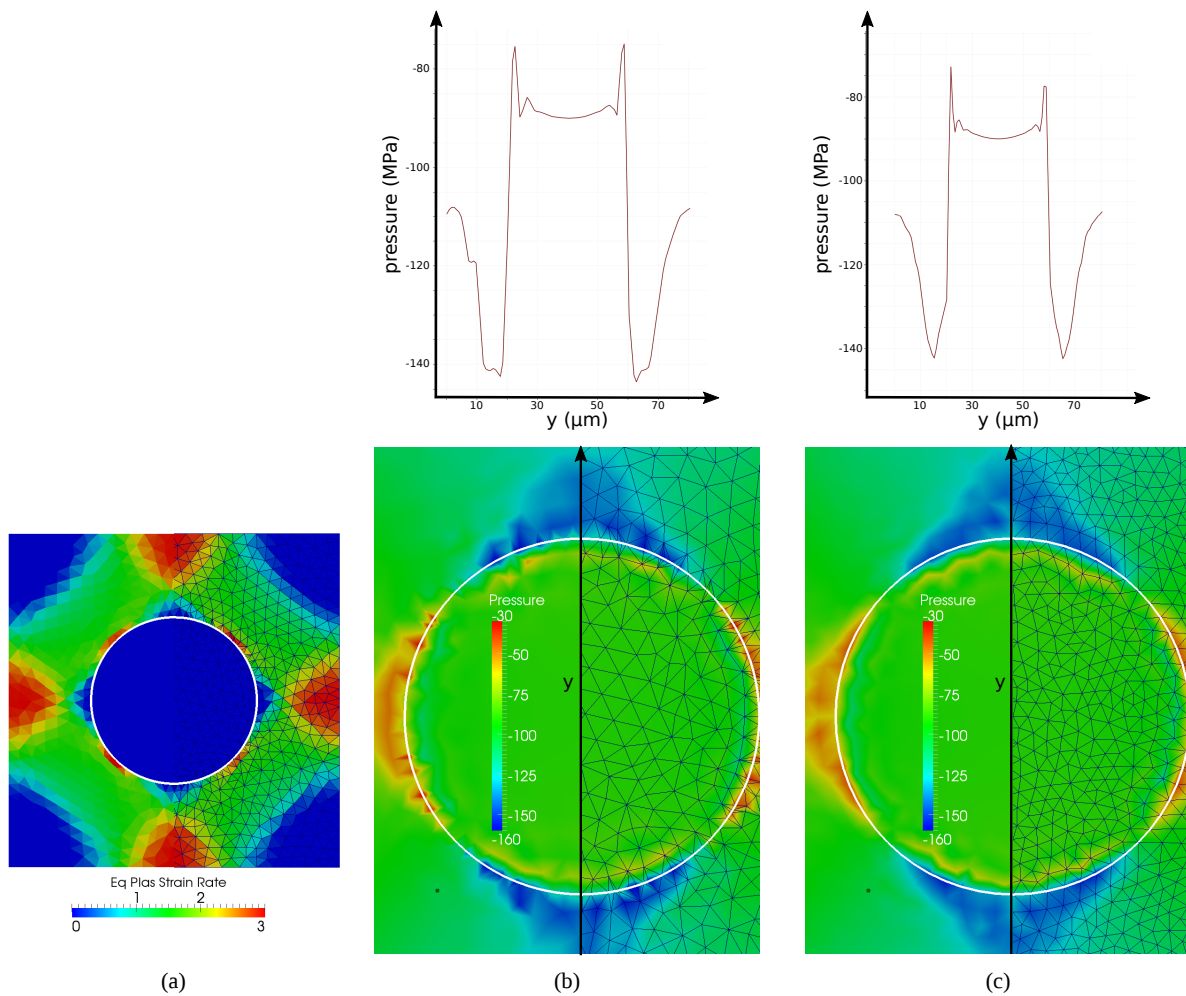


Figure 4.23 – Simulation result in 2D plane strain at 0.5 % of RVE elongation: (a) equivalent plastic strain rate using the fine meshing setting, (b) pressure field using the fine meshing setting, (c) pressure field using an initial mesh of uniform size $2\ \mu\text{m}$ where the particle is initially meshed using a mesh generation software [192]. In (b,c), oscillations of the pressure at the matrix/particle interface are evidenced by the graphs.

4.5.3.7 Crack propagation path

Using a 2D statistical RVE of size $240\ \mu\text{m}$, idealistic and symmetric configurations such as in Figure 4.17 are avoided. Thus, it can be assumed that void nucleation will occur in the same region of the RVE, and in the same mode, which will not depend on numerical parameters. In Figure 4.24(a), this 2D microstructure is simulated using the reference time step and meshing parameters for the result in the top left corner ($h2\ dt0.001$). Going to the right, a time step ten times

($dt0.0001$) and then a hundred times ($dt0.00001$) smaller is used. Going to the bottom, meshing parameters ϵ_h , h_{curv} , h_{max} , h_{min} , ϵ_l and ϵ_c twice ($h1$) and then four times ($h0.5$) smaller are used.

The changes of the fracture indicators are shown in Figure 4.24(b) for fragmentation (σ_1^p), and in Figure 4.24(c) for debonding (σ_n). All curves are stopped at the first fragmentation or debonding event, because then it is not possible to know to which particle the values correspond to. In particular, all curves shown in these figures correspond to the particle in the top right corner of the microstructure in Figure 4.24(a).

At fixed time step, refining the mesh can have opposite effects. For $dt0.001$ (in blue in Figure 4.24(b) and Figure 4.24(c)), refining excessively the mesh delays void nucleation ($h0.5 dt0.001$). For $dt0.0001$ (in green in Figure 4.24(b) and Figure 4.24(c)), mesh refinement does not seem to have a significant effect, so results can be assumed to be converged. For $dt0.00001$ (in orange in Figure 4.24(b) and Figure 4.24(c)), mesh refinement leads to an earlier prediction of void nucleation ($h2 dt0.00001$).

At fixed mesh size, varying the time step gives very different results. However, the gaps are reduced with finer meshes. For instance, the gaps between the dotted lines are far smaller than the gaps between the solid lines in Figure 4.24(b) and Figure 4.24(c).

An important remark is that the curves in Figure 4.24(b) and Figure 4.24(c) seem to be converging towards the results obtained with time step $dt0.0001$. However, depending on mesh size, different results are obtained with this time step. The particle at the top right corner of the microstructure (Figure 4.24(a)) debonds in $h2 dt0.0001$, fragments and debonds in $h1 dt0.0001$, and solely fragments in $h0.5 dt0.0001$. The same remark can be made regarding the results on the diagonal in Figure 4.24(a) ($h2 dt0.001$, $h1 dt0.0001$, and $h0.5 dt0.00001$).

The computational cost increases significantly with finer time steps and mesh sizes. For instance, the computation times up to 15 % of RVE elongation for the simulations on the diagonal in Figure 4.24(a) are of 5 min for $h2 dt0.001$ (6000 elements), 42 min for $h1 dt0.0001$ (20000 elements), and 44 h for $h0.5 dt0.00001$ (70000 elements). At least 90 % of this time is devoted to mechanical solution.

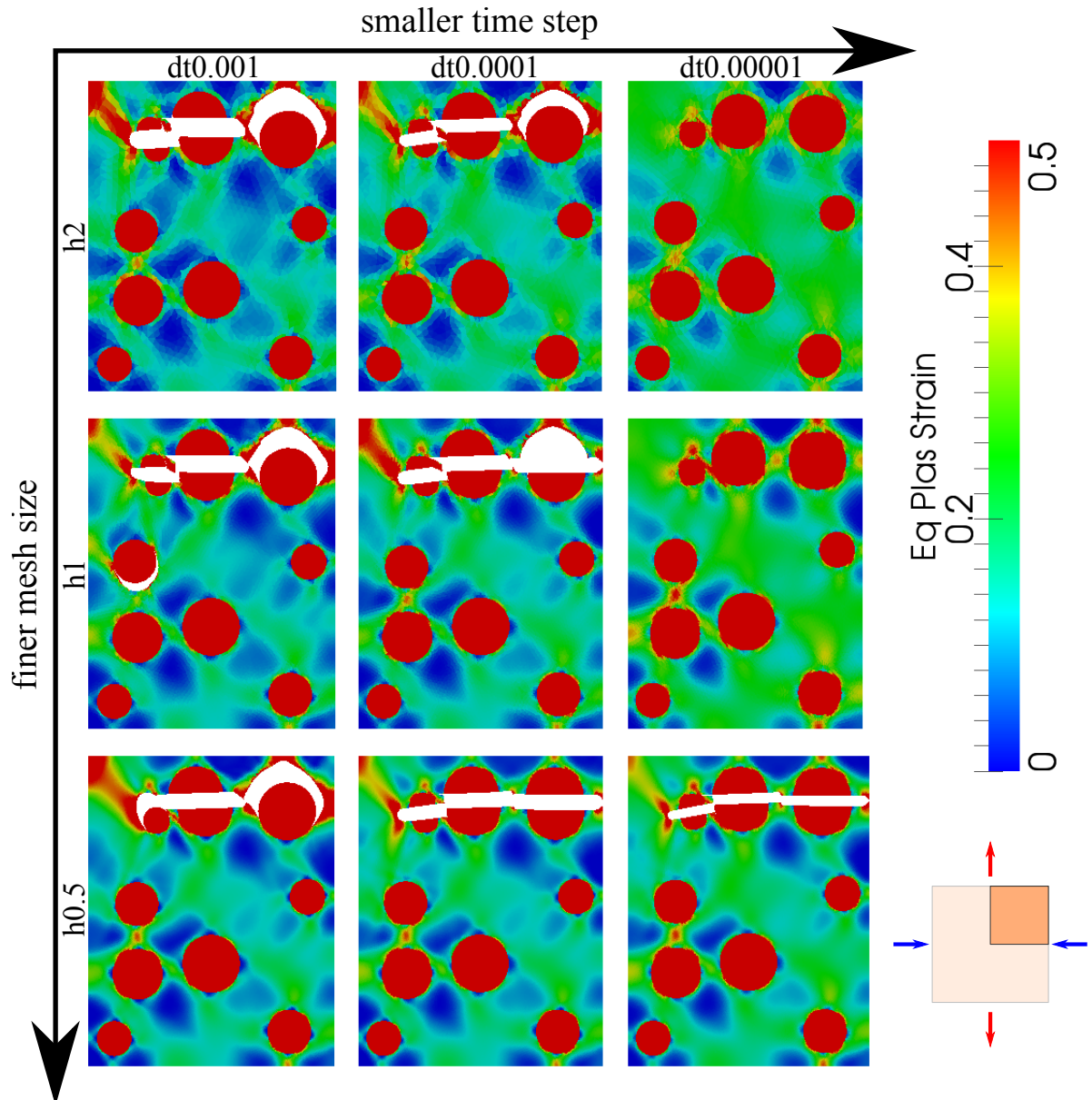
As a conclusion, the present analysis shows that convergence on nucleation modes and crack propagation path could be obtained, but at the expense of an increased computational cost. The latter is mainly due to the fact that both the time step and mesh size need to be refined simultaneously to obtain relevant results. Some uncertainties remain regarding the prediction of the void nucleation mode. These are not due to the mesh generation and adaptation methodology used to model cracks, but could come from the oscillations due to the FE scheme mentioned in Paragraph 4.5.3.6.

The absence of a control of the strain energy release after the first void nucleation event could also lead to uncertainties regarding the following nucleation events.

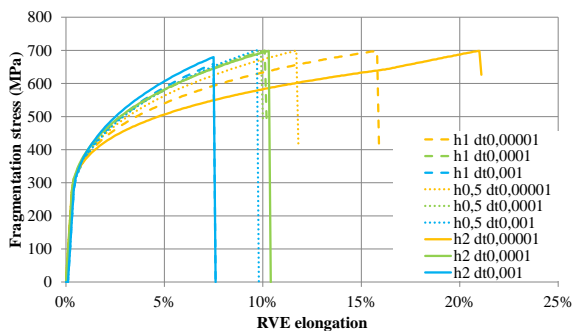
The reference numerical parameters are kept in the following as only averaged quantities are of interest in this section. For validation of the proposed void nucleation criteria using local comparisons with experiments (Chapter 6), the limitations mentioned in this paragraph will have to be investigated more thoroughly.

4.5.4 Representative Volume Element size

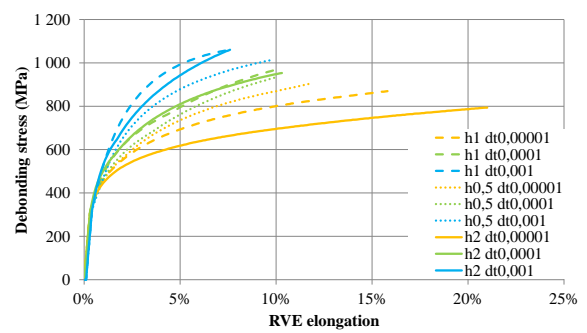
RVE size can also be considered as a numerical parameter, introduced by the homogenization scheme. While a too large RVE is not an issue in this section because no macroscopic structure is considered (though computational cost may be a limitation), a too small RVE will yield results



(a) Microstructure at 15 % of RVE elongation, with particles in red and voids in white.



(b) Sensitivity of the particle fragmentation indicator σ_1^p during loading.



(c) Sensitivity of the particle debonding indicator σ_n during loading.

Figure 4.24 – Influence of time step and mesh size on void nucleation criteria for a random 2D microstructure.

that are not representative of the material. Added to the two 2D RVEs of sizes $80\ \mu\text{m}$ (1 particle, Figure 4.8(a)) and $240\ \mu\text{m}$ (9 particles, Figure 4.24(a)), and the 3D RVE of size $55\ \mu\text{m}$ (1 particle, Figure 4.9(a)) already used in previous calculations, additional RVEs are generated. All these RVEs (except the single-particle RVEs) are shown in Figure 4.25. The *bis* 2D RVEs are used further in this analysis.

It is reminded that due to symmetry boundary conditions, the dimensions and numbers of particles mentioned in Figure 4.25 should be multiplied by 4 in 2D and 8 in 3D. In this figure, only the meshed region is represented, and abusively called RVE.

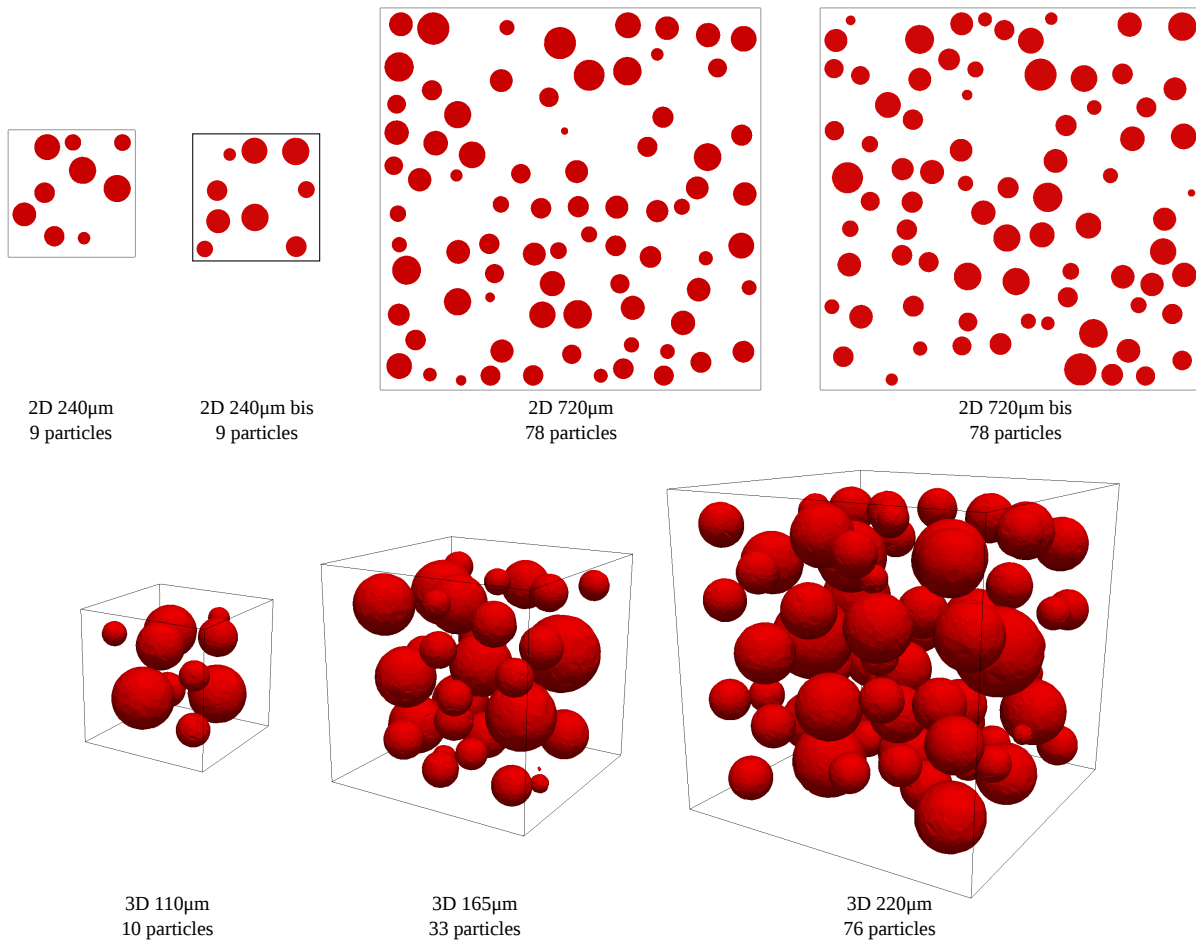


Figure 4.25 – Statistical RVEs used for the validation of RVE size. Particle volume fraction is close to 20 %, and particle radii follow a normal law of mean $20\ \mu\text{m}$ and standard deviation $5\ \mu\text{m}$.

Based on the remarks made in Paragraph 4.5.3.7, only averaged quantities are used for this validation, though full field quantities can be considered qualitatively. Porosity and macroscopic von Mises equivalent stress curves are presented in Figure 4.26 using the different RVE sizes for the 2D simulations.

Convergence seems to be obtained in 2D for an RVE of reasonable size, as the RVE with only 9 particles gives predictions regarding the porosity that are very close to those obtained with 78 particles (Figure 4.26(a)). The elongation for which the RVE reaches its maximum strength also corresponds well between the two largest 2D RVEs, as well as the associated macroscopic von Mises equivalent stress (Figure 4.26(b)).

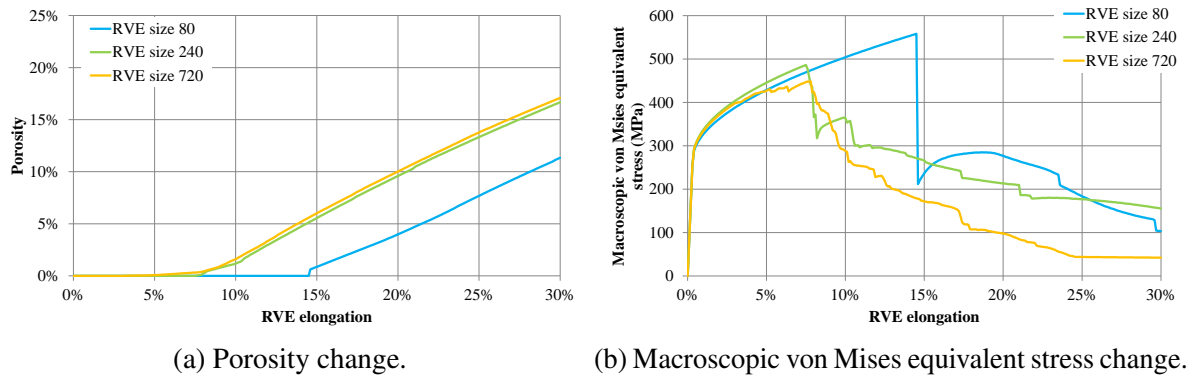


Figure 4.26 – Influence of RVE size in 2D plane strain.

This is surprising because the number of particles is very different between the two RVEs. Thus, these results are verified by considering two alternative RVEs with the same particles, but positioned differently. The two alternative RVEs (*bis*) are shown in Figure 4.25 and the subsequent results are shown in Figure 4.27(a) and Figure 4.27(b).

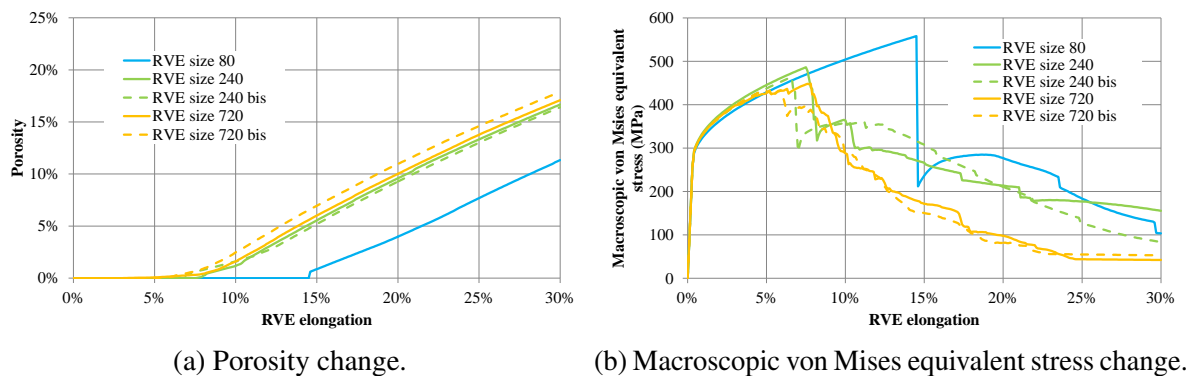


Figure 4.27 – Influence of RVE size in 2D plane strain with alternative RVEs (*bis*).

There is no significant sensitivity of the porosity to particle positioning (Figure 4.27(a)), even for the RVE of size 240 μm . The differences regarding the load carrying capacity are higher but remain acceptable (Figure 4.27(b)). This convergence on RVE size with a small RVE could be due to the fact that this material has a high particle volume fraction, and hence a low ductility. It is promising as the computational time for the calculation with RVE size 240 μm is only a few minutes. However, the main interest of the present work is 3D simulations. Results for the 3D simulations with varying RVE size are shown in Figure 4.28.

In 3D, convergence is only obtained regarding the slopes of the porosity change curves in Figure 4.28(a). There is still a non negligible difference in ductility even with the two largest 3D RVEs, especially regarding the mechanical response (Figure 4.28(b)). For instance, the largest RVE is significantly more ductile than smaller ones. Its final porosity rate corresponds to the final porosity rate of the RVE of size 165 μm only after 20 % of RVE elongation. Hence, void nucleation mechanisms are still occurring in this RVE at 15 % of RVE elongation, while the other RVEs have already reached a state where void growth and coalescence are the dominating damage mechanisms.

This difficulty to converge regarding RVE size in 3D but not in 2D may be linked to higher

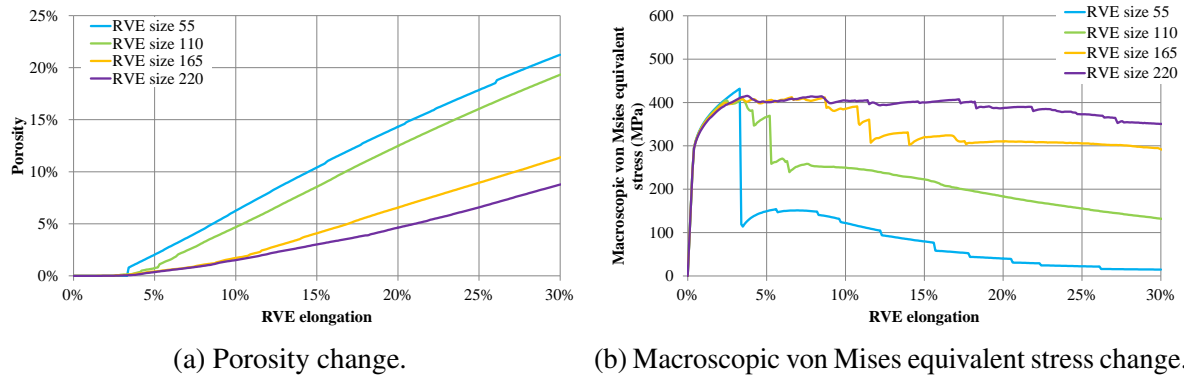


Figure 4.28 – Influence of RVE size in 3D.

clustering effects in 3D. Clusters of particles very close to each other are more likely to be present in the initial microstructure in 3D. It will be important to improve the statistical RVE generation tool in order to control the distribution of particles more closely. In fact, this distribution is only fixed globally in the RVEs shown in Figure 4.25, hence locally distances between particles may not be representative of the real material shown in Figure 4.7.

An additional difficulty is that the limits in computational resources are reached for the largest RVEs. The computation time for the four 3D RVEs is reported in Table 4.4.

RVE size (μm)	CPUs	total	mechanical solution (%)	mesh adaptation (%)
55	8	42 min	72	24
110	25	11 h	63	28
165	79	46 h	49	46
220	148	61 h	36	52

Table 4.4 – Computation time for the 3D calculations with different RVE sizes.

An important issue for the very large RVEs is that the number of elements increases severely during the simulation due to the fracture events. Therefore, it is not possible to predict the optimal number of Central Processing Units (CPUs) at the beginning of the simulation. Instead, the computation is stopped and restarted when the number of elements per partition becomes too large. The number of CPUs indicated in Table 4.4 corresponds only to the median (half or twice this number of CPUs may have been used at some points of the simulation).

Another issue, also linked to distributed computing, is revealed in this table. When the number of elements increases, the distribution of computation time changes. While for small RVEs (and number of CPUs), mechanical solution costs more than mesh adaptation, this tendency is progressively reversed when RVE size increases (and the number of CPUs). This might be due to the parallel implementation of the interface meshing procedure in Section 2.5, or the repartitioning/remeshing algorithm implemented in the FE library [125].

All other algorithms developed in this work do not appear in Table 4.4 because they have negligible cost. These include the computation of the error estimator thanks to Hessian matrix recovery (Subsection 3.1.3), the reinitialization of LS functions (Section 3.2), the correction of the transport of history variables (Subsection 2.3.2), and the identification of the inclusions for the fragmentation criterion (Section 3.3).

As a conclusion, convergence with respect to RVE size is reached even with small RVEs in 2D, which is most probably helped by the use of PBCs. Thus, the implementation of these conditions for more general loading configurations and microstructures would be interesting. In 3D however, the computational cost becomes too large before convergence is reached. While the parallel efficiency of the mechanical solution relies mainly on the PETSc library [126], the parallel remeshing technique should be revisited (Chapter 7). For the following simulations, an RVE size of 240 μm is chosen in 2D, and 165 μm in 3D.

4.5.5 Importance of void nucleation modeling

In the following simulations, the reference numerical parameters chosen in Subsection 4.5.3 are used. It is reminded that using these numerical parameters, converged results are obtained in terms of averaged quantities, but discussions regarding local phenomena such as the crack propagation path can be only qualitative. Additionally, unless otherwise mentioned, the triaxiality ratio η is fixed to 0.33.

4.5.5.1 Two-dimensional analysis

It has been discussed previously that most studies on ductile fracture often disregard the void nucleation mechanism by considering an initial microstructure where particles are replaced by voids, or by initially debonded and/or fragmented particles. For the material studied in this subsection, the dominating void nucleation mechanism is particle fragmentation with fracture planes that are orthogonal to the tensile direction (Figure 4.7). Comparisons are thus proposed between:

- the *nucleation* simulation carried out in Subsection 4.5.4, with a 2D RVE of size 240 μm (9 particles), taking into account both void nucleation mechanisms;
- a *fragmentation* simulation with same RVE, but taking into account only the particle fragmentation mechanism;
- a *pre-fragmentation* simulation with same RVE size, but initially fragmented particles instead of modeling void nucleation during the simulation;
- a *void* simulation with same RVE size, but voids instead of particles.

The four RVEs are shown in Figure 4.29 before and after 15 % of RVE elongation.

One of the voids is very close to the RVE boundary and the numerical treatment for void linkage at RVE boundaries (Subsection 4.5.1) is already active in the initial state for the *void* configuration. This is also the case for two of the fragmentation cracks in the *pre-fragmentation* configuration, due to the crack extension length ℓ^F .

On the one hand, the load is nearly equivalently shared by all voids in the *void* and *pre-fragmentation* simulations. As a consequence, void growth is nearly homogeneous in the whole RVE for these two simulations, apart from some void coalescence and linkage events. Thus, the stress and plasticity localization mechanisms that could take place in some regions of the RVE before the onset of void coalescence are totally neglected.

On the other hand, plasticity is localized in the top region of the RVE in the *pre-fragmentation* and *nucleation* simulations. The microstructure fails due to the three aligned particles at the top of the RVE. The stress first decreases significantly due to the failure of the two big particles

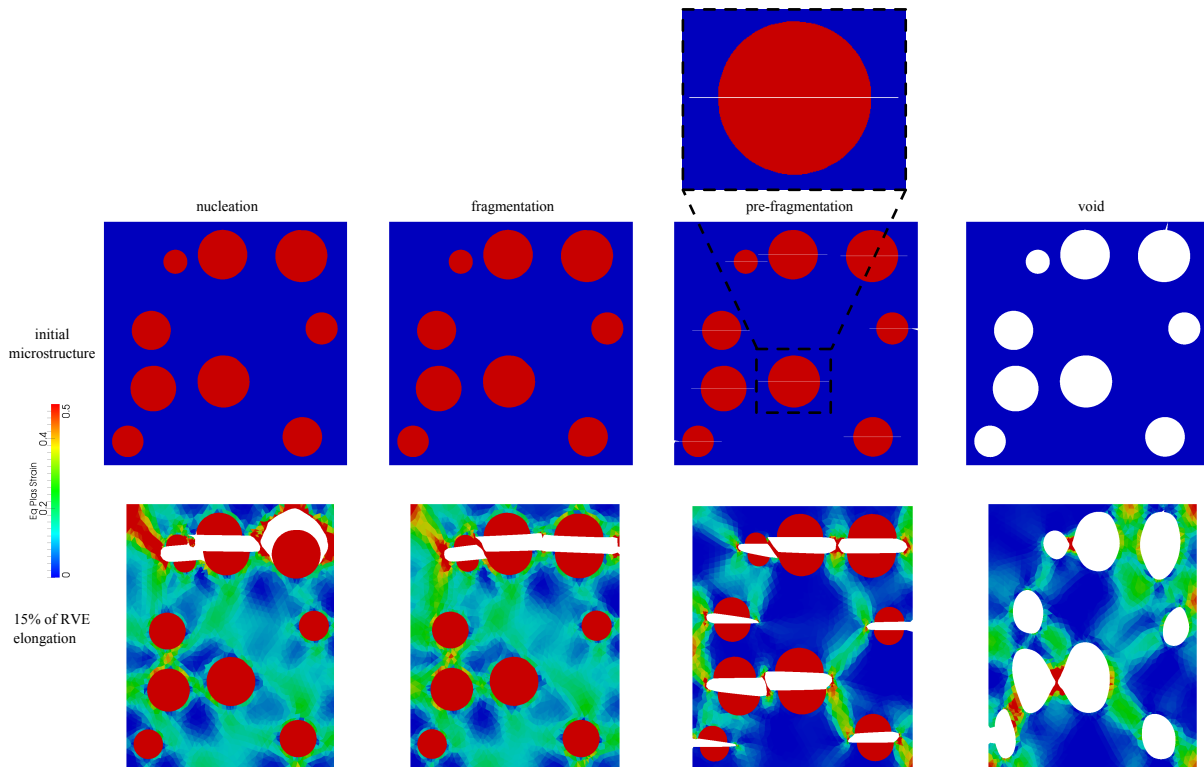


Figure 4.29 – Microstructures before and after 15 % of RVE elongation for the assessment of the importance of void nucleation modeling in 2D plane strain. Particles are shown in red, and voids in white.

($\approx 8\%$ of RVE elongation), and then later a minor decrease is noticed due to the third particle ($\approx 10\%$ of RVE elongation). In fact, nucleation due to debonding or fragmentation of a particle leads to a stress localization phenomenon that is likely to trigger further nucleation events in neighboring particles.

Results with a modeling of nucleation mechanisms (only fragmentation or both) during the simulation are hence qualitatively very different from results with an initial population of voids or pre-fragmented particles. A more quantitative idea is given by the porosity change and macroscopic von Mises equivalent stress change curves in Figure 4.30.

From the point of view of damage (Figure 4.30(a)), the influence of void nucleation modeling is concentrated in the first part of loading, for an RVE elongation less than 10%. Void growth has already started in the *pre-fragmentation* simulation, while no nucleation is predicted in the *nucleation* and *fragmentation* simulations. After significant void growth, this difference decreases and the *nucleation* and *fragmentation* curves progressively join with the *pre-fragmentation* one. The *void* simulation shows a very different damage change as void growth is far lower with respect to the two other simulations.

These differences are explained when looking at the stress curves in Figure 4.30(b). Due to the presence of undamaged particles, the *nucleation* and *fragmentation* RVEs have an ultimate strength twice higher than others. Therefore, a significant part of the strain energy is neglected in simulations that do not consider void nucleation criteria.

The difference between the *nucleation* and *fragmentation* simulations is mainly concentrated in the first nucleation event, which is debonding in the former while it is fragmentation in the latter. As already mentioned in Paragraph 4.5.3.4, debonding has a less significant effect on the load

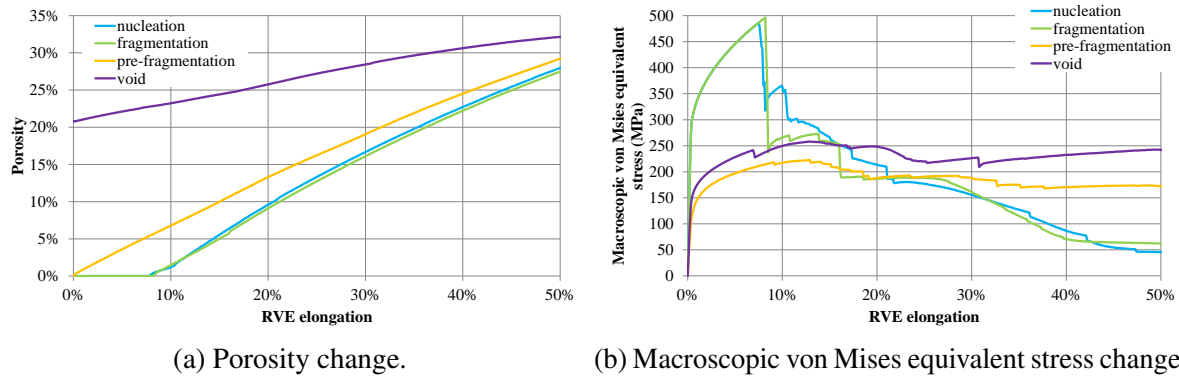


Figure 4.30 – Importance of void nucleation modeling in 2D plane strain.

carrying capacity (at $\approx 8\%$ of RVE elongation in Figure 4.30(b)). This difference does not seem to have a significant effect after 20% of RVE elongation, in the void growth and coalescence stages.

An important aspect is that while the *void* and *pre-fragmentation* simulations show very different void growth curves, with different slopes, the stress/strain curves correspond quite well. This reveals that the difference between penny-shaped voids and spherical voids is not significant under tensile loading. It may nevertheless have a major influence under different loading conditions, such as shear. The presence of particle fragments in the *pre-fragmentation* configuration may also have a significant influence under such loading conditions.

Additionally, the numerical crack extension length parameter ℓ^F may also reduce significantly the influence of particle fragments in these simulations. This may also certainly explain why the macroscopic von Mises equivalent stress in the *pre-fragmentation* result is lower than that in the *void* result in Figure 4.30(b).

As a conclusion, this 2D FE analysis shows that while the particle debonding mechanism may be neglected for the studied material and loading conditions, the fragmentation mechanism has to be accounted for. In particular, a significant part of the strain energy is neglected if particles are assumed to be already fragmented in the initial RVE, or if they are replaced by voids.

4.5.5.2 Three-dimensional analysis

This importance of void nucleation modeling is investigated further in 3D with an RVE of size $165\mu\text{m}$ (33 particles), and varying macroscopic stress triaxiality ratio η . For these 3D simulations, due to a large computational cost, only the two extreme cases are considered, namely the *nucleation* and *void* configurations of Paragraph 4.5.5.1. Results are presented in Figure 4.31 for the *nucleation* RVEs and Figure 4.32 for the *void* RVEs.

First, it can be observed that ductility decreases with higher triaxiality ratios, which is in good agreement with the theory. Independently of whether particles and void nucleation mechanisms are taken into account, larger voids and more numerous void coalescence and linkage events are visible in the results corresponding to $\eta = 0.66$. In particular, most voids in the results with $\eta = 0$ have regular and nearly spherical shapes, which shows that coalescence is not the dominating mechanism yet, even at 50% of RVE elongation.

Although this decrease of ductility is well captured by the *void* simulations, there are significant differences between the *void* and *nucleation* simulations. These differences seem to be increased at lower triaxiality ratios. With $\eta = 0.66$, void coalescence and linkage have led

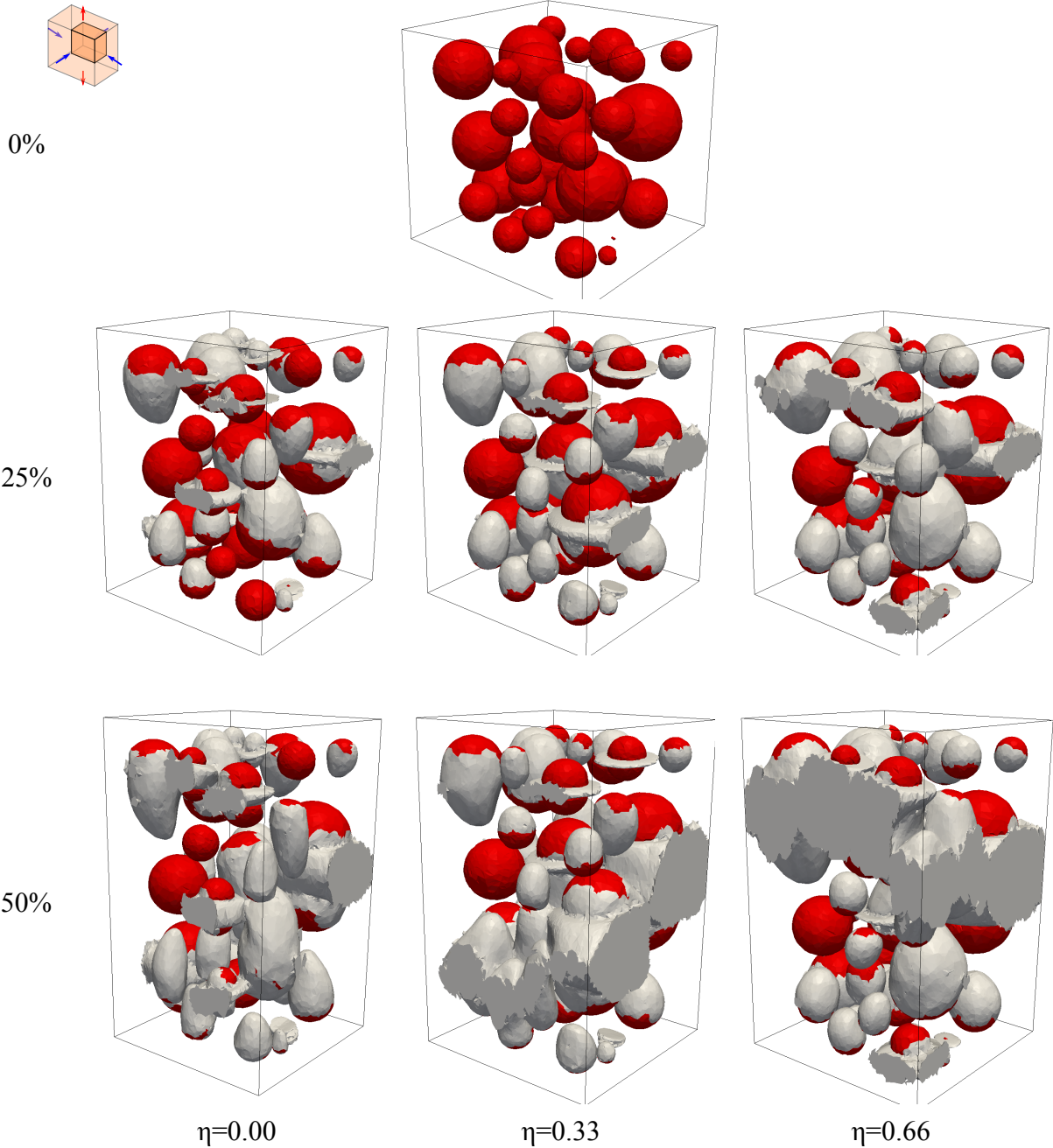


Figure 4.31 – Particles (red) and voids (white) at different RVE elongations for the 3D *nucleation* computations at varying macroscopic stress triaxiality ratio η .

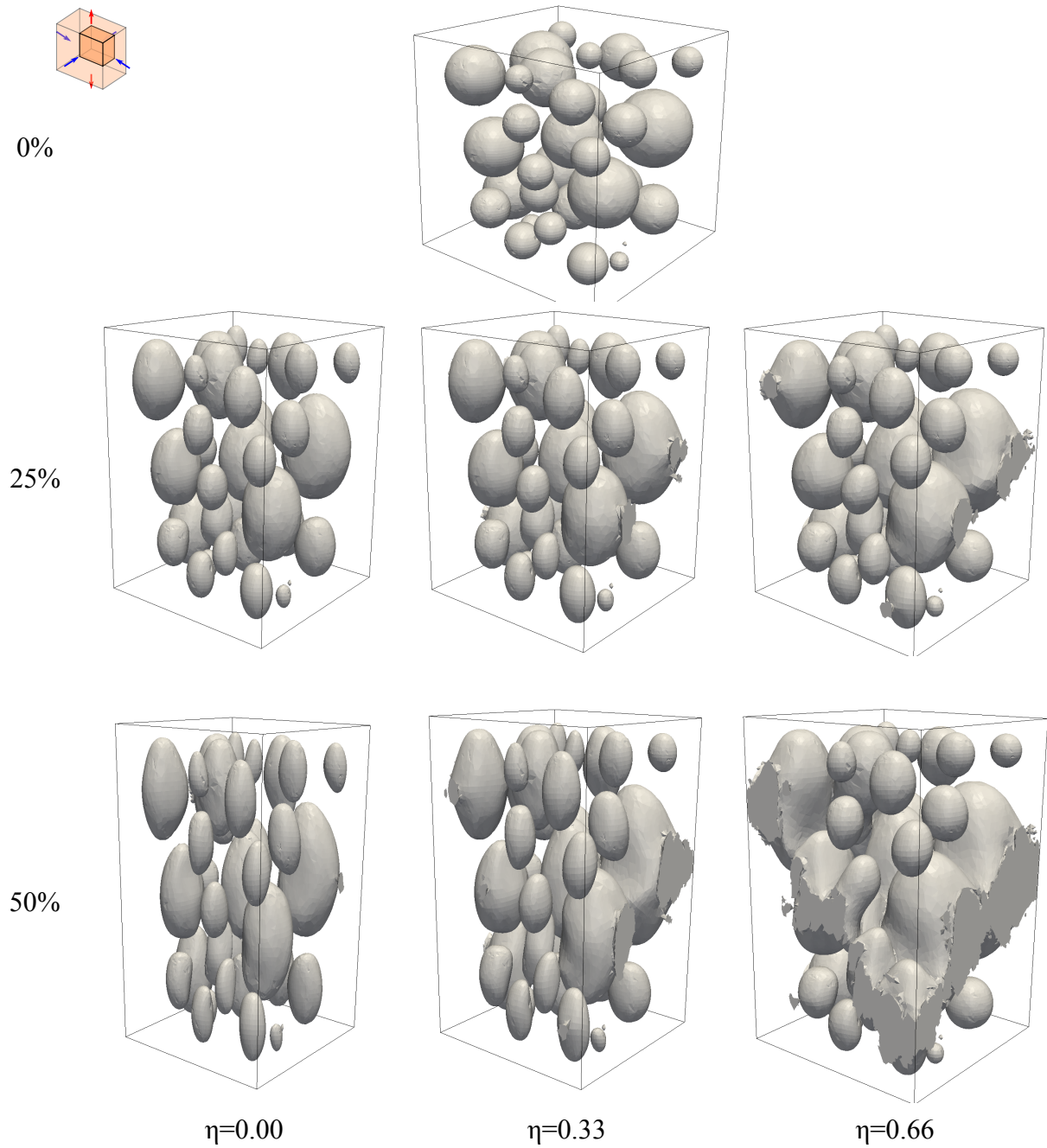


Figure 4.32 – Voids at different RVE elongations for the 3D *void* computations at varying macroscopic stress triaxiality ratio η .

to the localization of damage in a region of the RVE, while void growth out of this region is moderate (Figure 4.32). This is not true for the simulation with $\eta = 0$, where all voids seem to have flattened homogeneously in Figure 4.32, while some undamaged particles are still visible in Figure 4.31 at 50 % of RVE elongation. As a conclusion, these results confirm that early stress and plasticity localization phenomena due to void nucleation are neglected in the *void* simulations. Additionally, the effect of this assumption is increased at low triaxiality ratios. These effects are investigated further in terms of global porosity and load carrying capacity in Figure 4.33.

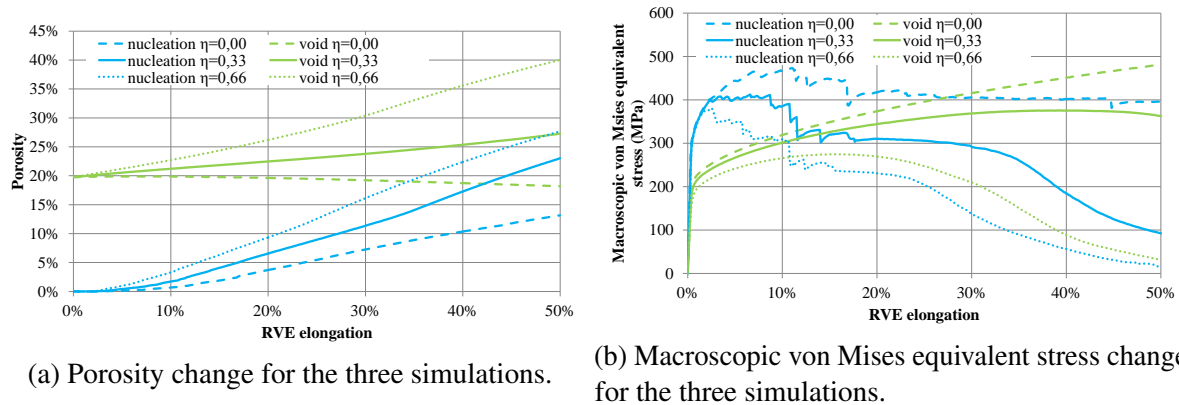


Figure 4.33 – Importance of void nucleation modeling in 3D.

A remarkable result is that for $\eta = 0$, no void growth is observed in the *void* simulation (Figure 4.33(a)). Voids only flatten for $\eta = 0$ in Figure 4.32, but the overall void volume does not vary. This effect is a well-known limitation of the Gurson model (Subsection 1.2.3). This absence of void growth explains that the macroscopic von Mises equivalent stress for $\eta = 0$ does not decrease during the simulation in Figure 4.33(b). However, void flattening in a direction could have an influence if the loading direction varied.

Moreover, the void growth curves for $\eta = 0$ reveal the major influence of the void nucleation mechanisms. Void growth is observed in the *nucleation* simulation (Figure 4.33(a)), with a small loss of load carrying capacity (Figure 4.33(b)). The ultimate strength is also higher due to the presence of particles, hence a significant part of the strain energy is neglected in the *void* configuration.

Note that flattening occurs in the tensile direction, hence no void rotation is observed. This may not be intuitive for comparisons with experiments. It will be important in the future to study a more general implementation of PBCs, in order to access and control extra-diagonal components of the macroscopic strain rate tensor.

At higher triaxiality ratios (Figure 4.33(a)), the differences between the *nucleation* and *void* simulations regarding porosity curves are reduced, as the slope of these curves are similar at large plastic strain. The macroscopic von Mises equivalent stress curves also show similar changes for large plastic strain (Figure 4.33(b)).

This is however not true in the first part of loading, before 10 % of RVE elongation. In these first 10 %, a significant part of the strain energy is still neglected, although this error seems to decrease when the triaxiality ratio increases. This is explained by the fact that void coalescence is the dominant damage mechanism at high triaxiality ratio, and not void nucleation. Small drops in the macroscopic von mises equivalent stress curve in Figure 4.33(b) are only visible for an

RVE elongation below 15 % when $\eta = 0.66$. After 15 % of RVE elongation, the smoothness of the curve indicates that void nucleation is negligible.

It is important to underline that in all Gurson-type models, void nucleation is considered based on the porosity, which considers only void volume (and sometimes also particle volume). Thus, cracks that nucleate but do not open and grow significantly cannot be described with a Gurson-type model, while their influence on the load carrying capacity may not be negligible. In fact, even if this influence was negligible for a given monotonic loading, this would most certainly not be true if the loading direction was then modified, as in most metal forming processes. The plastic localization zone appears more clearly in Figure 4.34, where plastic strain for the uniaxial tension configuration is shown.

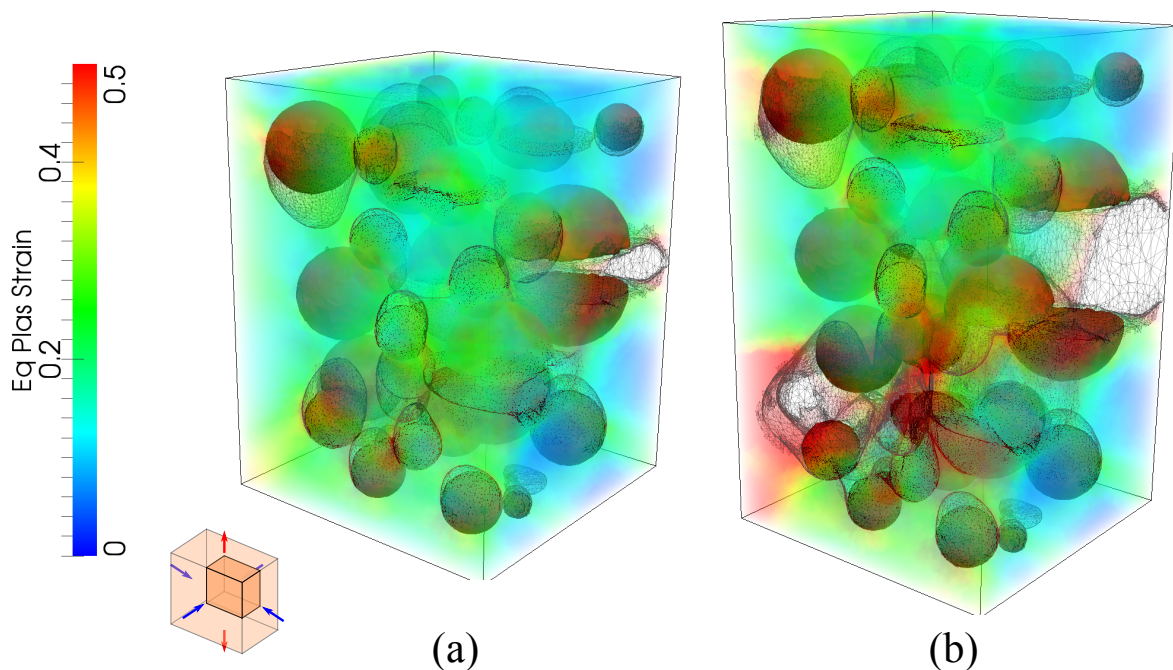


Figure 4.34 – Equivalent plastic strain for the 3D computation taking into account nucleation mechanisms at macroscopic stress triaxiality ratio $\eta = 0.33$ and RVE elongation of: (a) 25 %, (b) 50 %.

This figure reveals several fragmentation and debonding cracks at the top of the microstructure which have merely grown, and are located in a zone with moderate plasticity (in green/blue). While these voids do not participate in the final fracture of the microstructure, they would most certainly have an influence if loading was stopped for instance at Figure 4.34(a), and restarted with a different loading direction. Such calculation is not carried out in the present section due to the numerical uncertainty on the crack propagation path reported in Paragraph 4.5.3.7. It can nevertheless be assumed that the load carrying capacity of the material, and its final mechanical properties, would also be affected by the presence of these microscopic cracks.

Finally, these 3D calculations taking into account the void nucleation mechanisms are interesting for studying macroscopic yield criteria for ductile materials. For instance, looking at the *nucleation* curve for $\eta = 0.33$ in Figure 4.33(b), void nucleation is marked by a progressive loss of load carrying capacity until approximately 10 % of RVE elongation. The macroscopic

von Mises stress then stays at approximately 300 MPa, until severe plastic localization dominates in the RVE, marking the onset of void coalescence and the last decrease of load carrying capacity, up to failure.

The range of RVE elongation between the first failure step (due to nucleation) and the second one (due to coalescence) is larger for low triaxiality ratios, and smaller for high triaxiality ratios. While in classical Gurson-type models, the nucleation and coalescence stages are modeled separately, these results indicate that for high triaxiality ratios this assumption is not valid anymore, and both phenomena should be accounted for simultaneously in a unified criterion.

4.5.6 Conclusion

The numerical validation carried out in this section has revealed some limitations of the numerical methods proposed in the present work. In particular, the numerical particle fragmentation crack extension length should be eliminated, and an alternative to the $P1^+/P1$ scheme used for the solution of the balance equations should be studied.

Micromechanical models should also be improved, mainly regarding the constitutive model used for the matrix material, and the modeling of strain energy release at the onset of particle fragmentation and debonding.

Apart from these limitations, very promising results are obtained. The numerical methods proposed in the present work enable for simulations after the onset of void coalescence (Figure 4.34). Applications to large and complex 3D RVEs with particles of random size and position are possible. Multiple void linkage events occur in these RVEs and are captured by the mesh adaptation procedure (Figure 4.31 and Figure 4.32). The initiation of multiple cracks during simulations due to particle debonding and fragmentation is also modeled. To the author's best knowledge, this is the first time that simulations taking into account all these micromechanisms at large plastic strains are conducted.

When compared to less advanced approaches where particles and/or nucleation mechanisms are neglected, significant differences are observed, hence showing the importance of modeling particles and the subsequent void nucleation mechanisms. It is obvious that these simulation tools are too costly to be applied directly to model plasticity and mechanical behavior at industrial scale. For these applications, classical Gurson-type models are now well accepted to be the most promising approaches. However, these models usually consider the three aspects of void nucleation, growth, and coalescence mechanisms separately, based on micromechanical or phenomenological considerations. In order to improve predictions, these assumptions should be reconsidered.

It is very difficult to engineer materials with given microstructures, for instance with a given initial arrangement of particles or voids. In numerical methods, however, this is greatly simplified. Computational approaches also allow to compute accurately relevant mechanical variables and study relations between them. In the future, the present numerical framework should be used to assess the capabilities of classical Gurson-type models (Chapter 7), especially regarding non proportional loading paths. Such comparisons between full field and mean field models should give insights into the limitations of mean field models, and how they could be improved.

Conclusion

The present chapter relies extensively on the numerical tools developed in previous chapters in order to conduct Finite Element (FE) simulations of heterogeneous materials where the microstructure is meshed explicitly.

A material with a microstructure initially composed of an elastic-plastic matrix and brittle elastic particles is considered. Based on the literature, fracture criteria are proposed to model the debonding and fragmentation of these particles. Debonding is predicted based on a local critical normal stress criterion, while fragmentation is predicted based on a maximum principal stress criterion averaged by inclusion. The latter uses the Connected Component (CC) identification algorithm to distinguish each inclusion. The Level-Set (LS) method helps the modeling of cracks, and mesh adaptation and LS reinitialization are used to track the deformation of the subsequent free surfaces until they change into large voids that start interacting, coalescing, and finally linking.

These simulations are validated numerically both in two dimensions (2D) and three dimensions (3D) regarding averaged quantities, thanks to a sensitivity analysis on numerical parameters. Local variables, such as the crack propagation path, are more complicated to validate. Strain energy release should be controlled more carefully, for instance using Cohesive Zone Models (CZMs).

Nevertheless, only averaged quantities are of interest for homogenization and comparison with mean field models. In the literature, these comparisons usually consider simple Representative Volume Elements (RVEs) that do not account for the arbitrary shapes, sizes, and arrangements of particles and voids in a real microstructure. In the simulations presented in this chapter, spherical particles of random sizes and positions are used. With some restrictions on this microstructure and the loading conditions, Periodic Boundary Conditions (PBCs) can be implemented very simply, even in a parallel and adaptive numerical framework. The macroscopic stress state in the RVE can also be controlled.

These micromechanical calculations with statistically generated microstructures feature complex fracture events, as voids nucleate at multiple critical points in the RVE. Due to local arrangements (clusters) of particles with respect to the tensile direction, plasticity localizes in some regions and the voids in these regions grow and coalesce early during loading. Consequently, the microstructure fails, compromising the load carrying capacity of the material.

These computations have a very high cost, especially in 3D. Although this could be reduced using simpler boundary conditions, and optimizing the parallel implementations, especially regarding remeshing, it would certainly be increased with more advanced constitutive models (*e.g.*, CZMs). Thus, it is important to show that the results obtained using the computational fracture mechanics approach developed in this work differ significantly from what is obtained using more conventional approaches.

In particular, most studies found in the literature have considered initially pre-fragmented particles, or initial microstructures with voids instead of particles. Comparisons between simulations accounting for the particles and their progressive failure during loading and simulations with pre-fragmented particles, or initial voids, are conducted. These comparisons reveal that void growth is underestimated with conventional approaches. Moreover, the load carrying capacity of the material is underestimated at small plastic strains, while it is overestimated at large plastic strains. An interesting aspect is that these differences are more or less significant depending on

the macroscopic stress triaxiality ratio.

As a conclusion, 3D micromechanical calculations accounting for particle fragmentation and debonding during loading are important to predict accurately the influence of metal forming processes on the microstructure. They are also important in order to predict the influence of micro-cracks and voids in the microstructure on the macroscopic behavior of the material. The numerical tools and void nucleation models developed in the present work are very interesting as complex microstructures and the subsequent fracture events can be accounted for. Applications to non proportional loading paths are of great interest for future work.

Chapter 5

Micromechanical modeling of void coalescence

Le savant n'étudie pas la nature parce que cela est utile ; il l'étudie parce qu'il y prend plaisir et il y prend plaisir parce qu'elle est belle. Si la nature n'était pas belle, elle ne vaudrait pas la peine d'être connue, la vie ne vaudrait pas la peine d'être vécue.

Henri Poincaré

- Introduction 190
- 5.1 Plasticity driven void coalescence 191
- 5.2 Plasticity and damage driven void coalescence 192
- 5.3 Proposed model 194
- 5.4 Results 197
 - 5.4.1 Identification of damage parameters 197
 - 5.4.2 Effect of intervoid ligament length 199
 - 5.4.3 Effect of number of holes 200
 - 5.4.4 Effect of holes orientation 204
 - 5.4.5 Random arrangements 204
- Conclusion 209

Résumé en français

Dans ce chapitre, un matériau modèle avec des trous percés au laser est considéré. La plupart des modèles analytiques font l'hypothèse d'une coalescence purement causée par une localisation de la plasticité. Cette hypothèse est également faite dans le chapitre 4. Cependant, de plus en plus d'auteurs considèrent maintenant des analyses par éléments finis prenant en compte l'endommagement de la matrice entre les cavités. L'hypothèse sur laquelle ces analyses sont basées est celle de la présence de cavités de taille inférieure au micromètre, qui germent, croissent et coalescent dans la matrice entre les cavités, et complexifient ainsi grandement la modélisation du phénomène de coalescence de cavités.

Par comparaisons entre simulations et expériences de la littérature, il est montré dans ce chapitre que la croissance des cavités est assez bien décrite avec un simple critère de plasticité de von Mises pour la matrice. Cela n'est néanmoins vrai que jusqu'à une certaine limite dans le chemin de chargement, où la matrice rompt quasi-instantanément entre les cavités. Suite à ces comparaisons, un critère de rupture de la matrice entre cavités est proposé. Un modèle d'endommagement de Lemaitre est utilisé pour prédire l'initiation de la micro-fissure, et un critère géométrique est proposé pour prédire son chemin de propagation.

Les résultats obtenus montrent que le critère proposé peut prédire la rupture de la matrice entre cavités à la fois par striction et par cisaillement. Bien que les simulations conduites sous l'hypothèse de déformations planes diffèrent des expériences, qui elles correspondent à des contraintes planes, certaines propriétés remarquées dans les expériences sont bien prédites par ce critère. Par exemple, une perte de ductilité est observée lorsque la distance entre les trous est diminuée, et lorsque de nombreux trous sont présents dans le matériau, des fissures s'amorcent à plusieurs endroits. Une propriété remarquable observée dans les simulations est que ces fissures se propagent d'abord indépendamment, puis coalescent ensemble, menant à une fissure finale en *zig-zag*.

De plus, des simulations avec des arrangements aléatoires de trous montrent que la ductilité est significativement réduite lorsque des arrangements non périodiques sont considérés. Cette perte de ductilité est causée par une localisation de la plasticité et de l'endommagement au voisinage d'agglomérations de trous très proches initialement les uns des autres. Par conséquent, des micro-fissures s'amorcent plus tôt dans ces agglomérations en comparaison avec les cas périodiques. Cette analyse est d'une importance capitale car la plupart des modèles théoriques de coalescence de vides ne considèrent que des arrangements périodiques.

Pour poursuivre et valider quantitativement cette étude, il sera important dans le futur de développer une implémentation en contraintes planes dans le code éléments finis. Alternative-ment, ces simulations pourraient être conduites en trois dimensions (3D), mais les coûts de calcul seraient alors très importants, en particulier pour les arrangements avec de nombreux trous. De telles comparaisons seront néanmoins nécessaires afin de vérifier la validité du critère d'endommagement de Lemaitre utilisé dans ce chapitre. Afin de modéliser tous les phénomènes observés dans les expériences, un critère de plasticité plus avancé sera très probablement nécessaire, en particulier pour des ligaments entre trous très fins où un modèle de plasticité cristalline d'ordre supérieur devrait être considéré. Un tel modèle s'ajouterait alors à celui de plasticité poreuse d'ordre supérieur, indispensable pour modéliser l'adoucissement des ligaments entre trous, non considéré dans ce chapitre.

Pour finir, le modèle de coalescence de cavités discuté dans ce chapitre soulève de grands défis en ce qui concerne les procédures d'identification des propriétés du matériau à l'échelle

microscopique. Cela concerne également les critères de germination proposés dans le chapitre 4. En effet, les paramètres des critères de germination ont été extraits d'une étude issue de la littérature, où ils ont été identifiés à l'aide de calculs sur un volume élémentaire représentatif avec une seule particule et des conditions aux limites périodiques. L'état de contrainte et de déformation appliqué à ce volume élémentaire représentatif a été mesuré expérimentalement à l'échelle macroscopique.

Ainsi, bien que les simulations sur volume élémentaire représentatif proposées dans le chapitre 4 sont plus réalistes, les incertitudes liées aux propriétés matériaux utilisées sont assez grandes. Pour ce qui est du critère de rupture de la matrice entre cavités, les comparaisons avec des résultats expérimentaux ont été fortement aidées par le fait que la totalité des éprouvettes utilisées a pu être maillée, grâce à l'aspect artificiel de la microstructure (trous percés au laser).

Pour des applications 3D, une approche plus générale reste à établir pour la validation des simulations numériques par rapport aux observations expérimentales. Une telle approche devrait permettre de ne mailler qu'une petite région des éprouvettes, et inclure une méthodologie pour déduire les conditions aux limites à appliquer aux bords de cette région maillée. La mesure automatique des erreurs entre simulations et expériences devrait également être rendue possible. Ceci fait l'objet du chapitre 6.

Introduction

Using a simple von Mises plasticity model, void coalescence is observed in the simulations of Chapter 4, not only at large strains but also at small strains for voids that nucleate early around particles that are very close to each other. This mechanism is caused by a localization of plasticity, and a subsequent acceleration of void growth between pairs of voids. These localization and acceleration mechanisms will mainly be influenced by the initial distance between voids, and the used hardening law for the matrix material.

At the last stage, when the intervoid ligament has a thickness close to zero, the remesher removes it from the simulation, due to the relaxation of the volume conservation constraint introduced in Chapter 2. As detailed in Section 5.1, this coalescence mechanism could be qualified as purely plasticity-driven.

However, as mentioned in Subsection 1.1.3, recent experimental evidence suggests that coalescence could also be driven by damage at smaller scales. In Section 5.2, a particular attention is given to recent experimental results suggesting that the last stage of void coalescence, namely void linkage, can be the result of the nucleation and propagation of micro-cracks across intervoid ligaments.

A criterion is hence formulated in Section 5.3 to model these micro-cracks. Simulations are then carried out in Section 5.3 with varying hole arrangements and spacing. Comparisons between periodic arrangements and random arrangements are conducted to show the errors that are made when the microstructure is idealized.

Note that all constitutive models are discussed and used in the frame of cold forming (*i.e.*, at room temperature), and quasi-static loading conditions.

5.1 Plasticity driven void coalescence

The local von Mises plasticity model used in the present work is close to the one used by Gurson [33], with the addition of isotropic hardening. However, it is questionable, especially for use at the microscale. As discussed in Subsection 1.1.3, void growth is characterized by a low interaction between voids, leading to spherical shapes, while void coalescence is due to important interactions between neighboring voids, leading to singular shapes.

In particular, void coalescence occurs in two main plastic localization modes that are intervoid ligaments necking and shear bands [38, 85, 86, 89]. The former leads to a diamond shape, while the latter leads to void rotation and flattening. A less common void coalescence mode, known as void collapse or necklace coalescence, has also been observed by some authors for voids that are very elongated along the tensile direction [37, 88].

Most theoretical studies on void coalescence focus on applying homogenization theory, as in Gurson's seminal work (Section 1.2.3). However, instead of considering a single void, the RVE is a regular array of cylindrical (2D) or spherical (3D) voids aligned at 90° , and plastic deformation is assumed to be localized in intervoid ligaments (no plastic deformation in the rest of the domain).

The first example of a result obtained using this approach is the Thomason criterion for coalescence by intervoid necking [243]. The matrix is considered as a von Mises material, hardening and elasticity being neglected as in Gurson's work. However, the two approaches lead to two distinct results due to a different choice of RVE. Thomason's RVE features a cylindrical void with square basis and a zone with localized plasticity sandwiched between two rigid zones.

Similarly as for the Gurson model, generalizations of the Thomason model to shear band coalescence and more realistic materials both in terms of behavior and geometry (especially void shape) have been studied in the literature [89, 145, 147, 148, 244, 245]. Attempts to unify the plasticity criteria of Gurson and Thomason into a single flow rule have been studied recently [246].

While in the GTN model a phenomenological criterion based on a critical porosity is used to predict the onset of void coalescence, and the subsequent change in the yield surface, generalizations of the Thomason criterion introduce criteria for the onset of void coalescence that are based on microscopic calculations. Plastic flow and porosity change after this onset are also ruled by microscopically-based criteria. Nonetheless, these models introduce additional parameters, increasing the complexity of Gurson-like models that already feature significant numbers of parameters.

5.2 Plasticity and damage driven void coalescence

Recent experimental evidence suggests that interaction between voids does not only traduce into plastic localization, but also into the nucleation, growth, and coalescence of a minor void population [86, 87, 164]. This is illustrated in Figure 5.1.

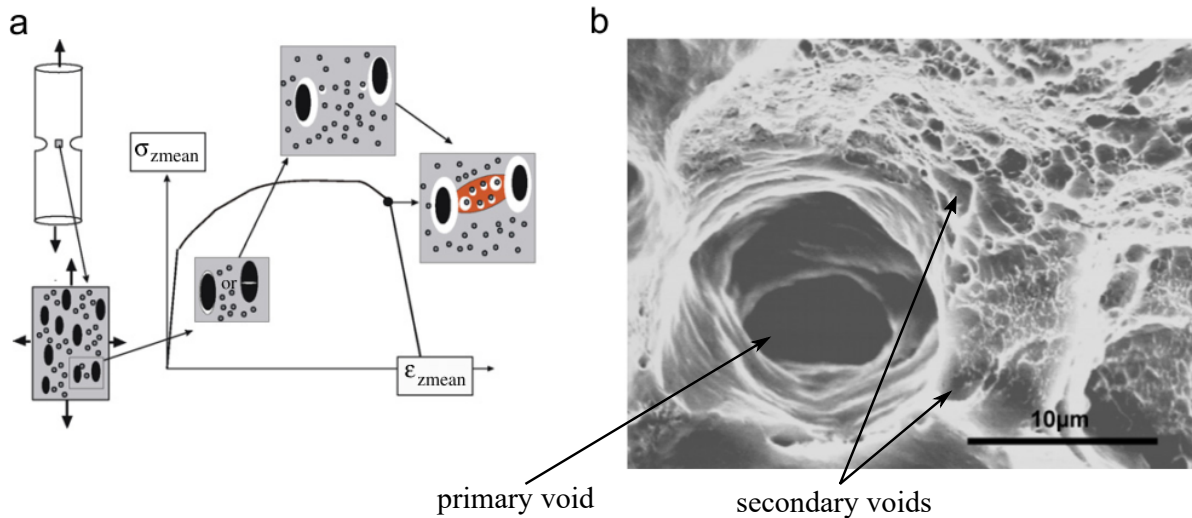


Figure 5.1 – (a) Voids nucleation, growth and coalescence at the neighborhood of primary and secondary particles. (b) Fractography of an aluminum alloy showing these two voids populations. Figure reproduced from Reference [164].

This has led authors to consider micromechanical calculations with RVEs containing a primary population of voids modeled in the FE mesh of the RVE, and a secondary population of voids of minor size that are taken into account by using a Gurson-like model for the matrix material [89, 164, 247, 248]. This requires to introduce a characteristic length scale, in order to define the scale separation between the two populations and the subsequent size effects. This length scale is also necessary in order to regularize damage models when they are coupled to constitutive equations. It is well known that damage localization leads to non-physical and mesh-dependent solutions, and various regularization methods have been proposed in the literature [249, 250, 251, 252].

These discussions are also closely linked to the modeling of the damage to fracture transition, which is the transition from diffuse damage, to localized damage, and then initiation and propagation of a crack. The transition from diffuse plasticity to localized plasticity is also well known to lead to a loss of regularity, and higher-order plasticity theories have been proposed in order to model these size effects [253, 254, 255, 256, 257].

These theories generally introduce additional degrees of freedom associated with the plastic strain, yielding a quite complex FE scheme where a special care has to be given to boundary conditions. In particular, boundary conditions are to be set at the elastic-plastic boundary, which is usually unknown. Non linear boundary conditions hence arise for some of these higher-order theories.

As a conclusion, void coalescence should be considered as the result of a phenomenon that is as complex as ductile fracture itself. It is driven by a competition between plasticity and damage at the microscale, between neighboring voids. This calls for plasticity and damage models that take

into accounts size effects.

5.3 Proposed model

Following the previous discussion, void coalescence can be decomposed into two distinct phases. In the first phase, void growth accelerates and voids develop singular shapes. In the second phase, pairs of voids start linking, by failure of the matrix ligament separating these voids. This failure may be due to the nucleation of a micro-crack between the two voids, or simply by the growth of the two voids towards each other, until the thickness of the ligament continuously tends to zero. Both modes have been observed experimentally, and the occurrence of one or the other depends mainly on the material and the initial distance between the voids [83, 85].

In the model used in Chapter 4, the second void linkage phase is naturally taken into account if it does not include micro-cracks. If micro-cracks initiate in the intervoid ligament before it reaches a thickness close to zero, void coalescence will be underestimated. To predict this void linkage by micro-cracks, a local damage indicator $D = D(\sigma, \varepsilon)$ and a critical damage threshold D^c are defined.

Although this criterion could be based solely on plasticity, for instance by defining $D = \bar{\varepsilon}$, a more advanced damage indicator is preferred. The chosen criterion should take into account the effect not only of plasticity but also of damage in the intervoid ligaments. The uncoupled Lemaitre damage model is used in this section [28] as an example. In the future, different damage criteria could be used and compared, thanks to the numerical validation framework described in Chapter 6.

The first phase of void coalescence is modeled by the simple von Mises plasticity model with the hardening rule given in Equation (4.10) for the matrix. This may be extended by coupling the Lemaitre damage model to the constitutive equations in order to account for softening in the intervoid ligaments. The latter is not considered here, but softening modeling in intervoid ligaments is definitely of interest and will be studied in the future (Chapter 7).

The implementation of the uncoupled Lemaitre damage model used in this section is based on earlier developments at the Center for Material forming - MINES ParisTech (Cemef - MINES ParisTech) [115]. The equation ruling the change of the damage indicator $D \in [0, 1]$ is based on thermodynamics, with a potential explicitly accounting for the triaxiality ratio, which is known to be a factor of major influence on damage [26, 33, 240, 241]. As detailed in Reference [28], the constitutive equation for damage evolution is

$$\dot{D} = \left(-\frac{Y}{S_0} \right)^{s_0} \dot{\varepsilon}^{pl}, \quad (5.1)$$

where the damage strain energy release rate Y is defined as

$$Y(\sigma, D) = -\frac{\bar{\sigma}^2}{2E(1-D)^2} \left[\frac{2}{3}(1+\nu) + 3(1-2\nu) \left(\frac{\sigma_m}{\bar{\sigma}} \right)^2 \right].$$

Two material parameters S_0 and s_0 are introduced. Regarding the discretization, this damage indicator is defined element-wise, and it is updated at the end of each time increment using an explicit scheme

$$D_{n+1} = D_n + \Delta t \left(-\frac{Y(\sigma_{n+1}, D_n)}{S_0} \right)^{s_0} \dot{\varepsilon}_{n+1}^{pl}.$$

In this scheme, D is used only as a damage indicator. In particular, it is not coupled to the constitutive equations for elasto-plasticity, and does not require any regularization. Regarding the damage to fracture transition, it is modeled by considering each pair of voids in the microstructure. The CC identification algorithm described in Section 3.3 is used to identify distinct voids

with a node-wise tag \mathcal{I}_v .

For all pairs of mesh nodes (n_A, n_B) with non zero and different void tags ($\mathcal{I}_v(n_A), \mathcal{I}_v(n_B) \neq 0, \mathcal{I}_v(n_A) \neq \mathcal{I}_v(n_B)$), the closest pair is considered. This means that it is assumed that the coalescence micro-cracks always follow the shortest path between voids.

If the damage indicator D has reached a certain threshold D_c on the whole line segment linking the two closest nodes, a crack is initiated along this line segment. This is sufficient to define the micro-crack in 2D (no 3D simulation is carried out in this section).

In order to represent this line segment, multiple LS functions are used, as in Chapter 4. The LS function ϕ_{pl} associated to the line is completed by a filter LS function ϕ_f to a sphere with center the middle of the two nodes, and with diameter the distance between the two nodes. These LS functions are shown in Figure 5.2.

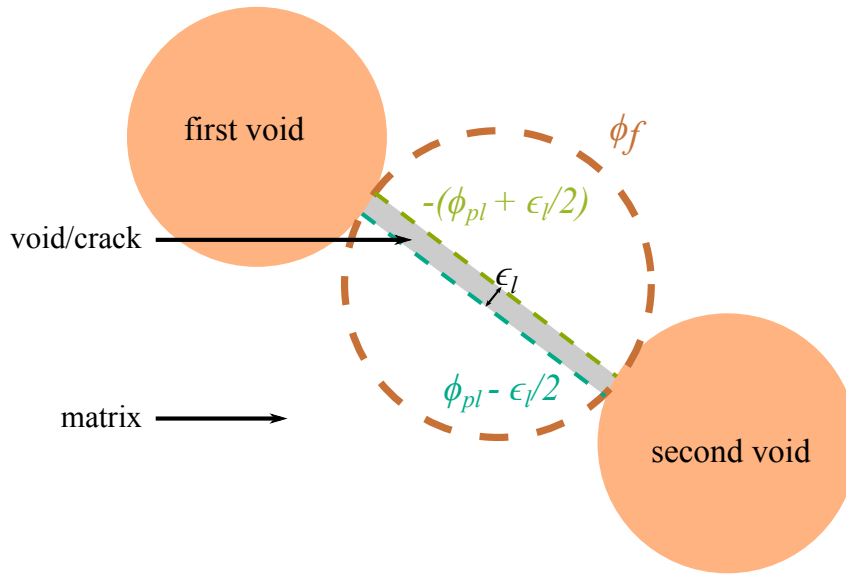


Figure 5.2 – LS functions and numerical parameters used in the void coalescence by micro-cracking model.

As in void nucleation modeling, these LS functions are used to modify the LS functions associated to the void and matrix phases

$$\phi_v = \max\left(\tilde{\phi}_v, \min\left(-\left(\phi_{pl} - \frac{\epsilon_l}{2}\right), \phi_{pl} + \frac{\epsilon_l}{2}, \phi_f\right)\right), \phi_m = \min(\tilde{\phi}_m, -\phi_v), \quad (5.2)$$

and mesh adaptation is then triggered to adapt the mesh to the new interfaces. The application of this coalescence by micro-cracking criterion to intervoid ligament necking and shear band coalescence is illustrated in Figure 5.3. In this figure, it is not specified whether localization is due to plasticity or damage or both. This will depend on materials and loading conditions. In particular, voids may link without the formation of a micro-crack, or with a very late micro-cracking.

As a conclusion, the void coalescence by micro-cracking model relies on a damage indicator, which is given by the Lemaitre damage model. The latter introduces two material parameters S_0 and s_0 . This uncoupled damage model is used as an indicator for the prediction of the damage to fracture transition.

When damage reaches a certain threshold D_c on a whole region between neighboring voids, a

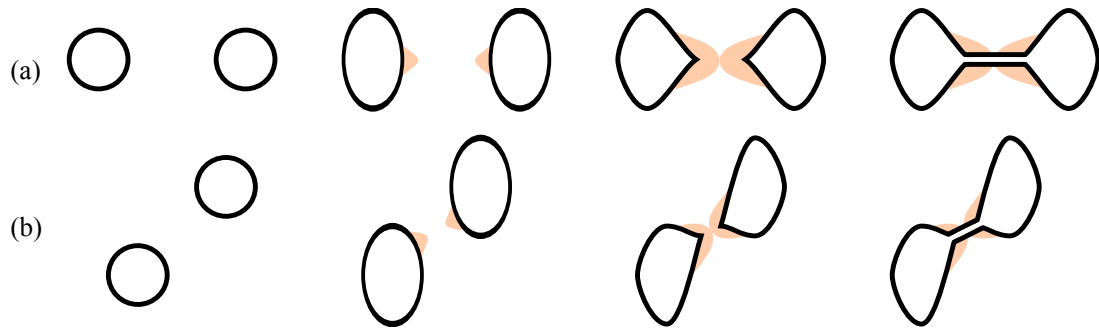


Figure 5.3 – Void coalescence by micro-cracking between two distinct voids under vertical tension progressively forming a single localization region, which leads to a micro-crack: (a) voids aligned at 90° with respect to the tensile direction, (b) voids aligned at 45° .

micro-crack is inserted in the simulation by modifying LS functions and adapting the mesh. This verification of the void coalescence by micro-cracking criterion is carried out alongside void nucleation models, at the beginning of each time increment, while the damage indicator is updated at the end of each time increment.

5.4 Results

While in Chapter 4, a focus is made on the importance of void nucleation modeling, the objective of the present chapter is to show that coalescence of voids is not necessarily purely driven by plastic localization. In particular, for the material and loading configuration studied in this section, void coalescence cannot be modeled without appropriate damage and fracture criteria.

An experimental investigation of void coalescence mechanisms was carried out by Weck *et al.* [87]. Holes were drilled in metallic sheets using an advanced laser drilling technique [84], in order to perform tensile tests with varying hole spacing and arrangement [83]. Different materials were also considered to study the influence of hardening and plastic behavior.

This technique was extended to 3D experiments where holes were drilled in a first sheet, which was then sandwiched between two parts [85]. The resulting holes were nearly spherical. SEM was used for 2D observations, and SRCT for 3D observations.

The 2D experiments are revisited in the following by means of numerical simulation using the coalescence by micro-cracking criterion proposed in the present work. Apart from the holes, which are embedded in the mesh, the material is assumed homogeneous. In particular, no particles and no void nucleation mechanisms are explicitly modeled, as opposed to the simulations in Chapter 4. Calculations are performed at specimen scale under uniaxial tension, hence lateral boundaries are free and no stress state control algorithm is used.

The 2D experiments on an aluminum alloy (AA5052) are used as a basis for the simulations in this section [83, 87]. Because the used aluminum sheets had a small thickness, plane stresses can be assumed. However, the FE code developed at Cemef - MINES ParisTech only includes a plane strain implementation. Thus, although the simulations conducted in this section use the same material and specimen geometries as those proposed in Reference [87], a quantitative match between simulation results and experimental observations is not expected. Damage localizes differently in plane stress and plane strain loading conditions, leading to two different failure modes.

The material parameters are taken from Reference [258] for elasticity, and identified from a true stress/true strain curve given in Reference [87] for plasticity. The resulting parameters are listed in Table 5.1.

	E (MPa)	ν	σ_y (MPa)	K (MPa)	n
Matrix	70000	0.33	150	583	0.696

Table 5.1 – Material parameters for AA5052 [87, 258].

The numerical parameters are inspired from Chapter 4, considering the fact that the diameter of the holes is $10\ \mu\text{m}$, while the average diameter of the particles for the material studied in Chapter 4 is $40\ \mu\text{m}$. Remesher parameters $Q_\mu, Q_\sigma, V_\mu, V_\sigma$, the time step Δt , and the contact penalization coefficient ρ_c are unchanged, while the other parameters are divided by 4. Hence, meshing parameters are set to $\epsilon_h = 3\ \mu\text{m}$, $h_{curv} = 0.05\ \mu\text{m}$, $h_{max} = 1.5\ \mu\text{m}$, and $h_{min} = 0.5\ \mu\text{m}$, the crack thickness to $\epsilon_l = 0.05\ \mu\text{m}$, and the contact thickness to $\epsilon_c = 0.025\ \mu\text{m}$.

5.4.1 Identification of damage parameters

Because the Lemaitre damage model is not coupled to the constitutive equations, the identification of material parameters S_0 , s_0 , and D_c for this model consists in ensuring that the onset of

micro-cracking is well captured. This means conducting simulations with no damage model, and identifying the instant where void growth is not well tracked anymore by the plasticity model. Experiments of Reference [83] are well-suited for such analysis, especially those with only two holes. The major diameter (along the tensile direction) of the holes was measured during loading, and SEM images are available close to the onset of micro-cracking. The setup for these simulations is summarized in Figure 5.4, with two holes aligned at 90° with respect to the tensile direction and then 45° , the initial intervoid ligament thickness ℓ_{lig} being identical ($27\ \mu\text{m}$).

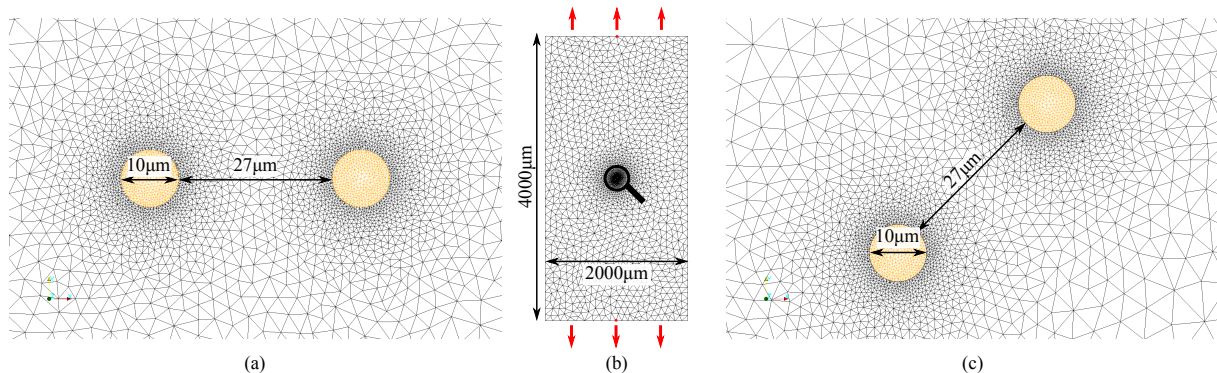


Figure 5.4 – Specimen geometry (b) and microstructure for the simulations with two holes: (a) aligned at 90° , (c) aligned at 45° . Geometry based on specimens used in Reference [83].

Simulation results without any fracture model are shown in Figure 5.5 at the last stages of void coalescence. The shape of the voids in the simulations seems to be qualitatively in accordance with experimental observations in the first images on the left. In the remaining images, micro-cracks nucleate in the experiments and accelerate severely void growth, which is not modeled in the simulations.

The fact that there is no clearly visible mismatch regarding void morphology between experiments and simulations up to the nucleation of these micro-cracks proves that softening in the intervoid ligament is negligible. Thus, it can be assumed that only a micro-cracking criterion would be necessary in order to model the observed coalescence mechanisms.

From this figure, it can be seen that plasticity first localizes at the void/matrix interface, and this localization region then extends into the matrix. At some critical point in the loading path, localization regions from different voids start interacting.

Because the numerical model assumes plane strains, plastic localization bands in an X pattern are observed in the simulation results for holes aligned at 90° with respect to the tensile direction. This does not seem to be the case in the experiments, where the micro-crack propagates perpendicularly to the tensile direction. Despite this difference, it is assumed that the micro-crack would go through the shortest path between holes also in plane strains.

In the following, material parameters for the Lemaitre damage model are set to $S_0 = 0.55\ \text{MPa}$, $s_0 = 0.90$, and $D_c = 0.43$. With these parameters, the engineering strains at ligament failure in the simulations are close to experimental ones for an intervoid ligament thickness $\ell_{lig} = 30 - 40\ \mu\text{m}$. Although quantitative comparisons between experiments and simulations are not possible, this choice ensures that plasticity develops and localizes sufficiently in simulations before the prediction of micro-cracking.

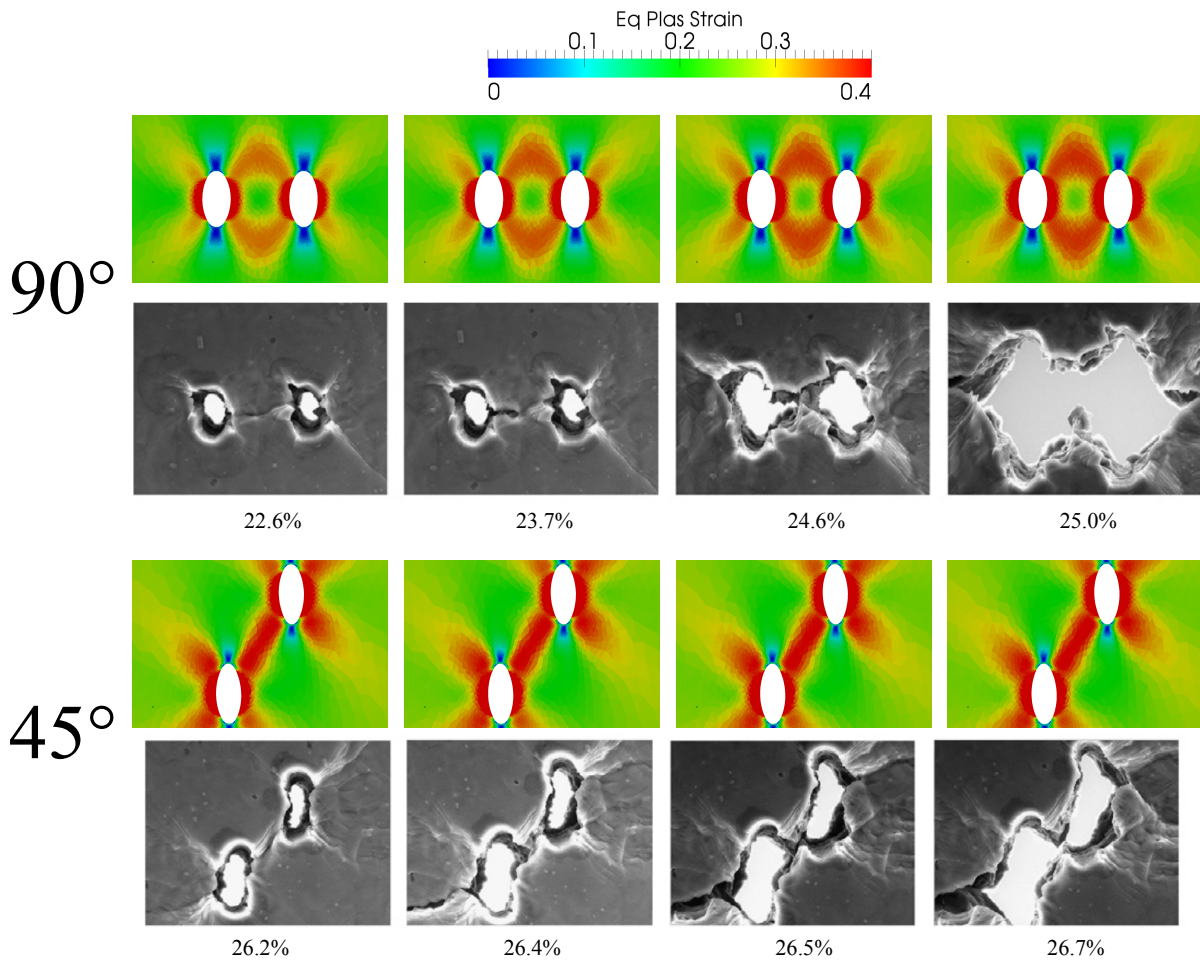


Figure 5.5 – Comparisons between computational results with no micro-cracking modeling and experimental observations at the last stages of void coalescence. Mentioned strains are engineering strains. Experimental images reproduced from Reference [83].

5.4.2 Effect of intervoid ligament length

The engineering strain at ligament failure in the simulation is 0.258 for $\ell_{lig} = 40 \mu\text{m}$, 0.235 for $\ell_{lig} = 30 \mu\text{m}$, 0.113 for $\ell_{lig} = 15 \mu\text{m}$, and 0.015 for $\ell_{lig} = 5 \mu\text{m}$. Thus, micro-cracking is delayed when hole spacing is increased. This has also been observed in experiments in the plane stress case [87].

An important and very interesting result is that even when no micro-cracking criterion is used, void linkage occurs very early in the simulation for $\ell_{lig} = 5 \mu\text{m}$. This is illustrated in Figure 5.6, where results are shown with and without micro-cracking modeling for the three configurations with small intervoid ligament length.

This figure shows that there are two damage localization regions in plane strains. Although damage localizes in an X pattern, there is an additional localization region at lateral boundaries of the holes. Opposed to the X pattern that is already visible far from the holes already in green in Figure 5.6(a) and Figure 5.6(e), the second localization region in red in Figure 5.6(a) and Figure 5.6(e) only develops close to hole boundaries. These two localization regions are also visible for plasticity in Figure 5.5.

Therefore, when holes are very close to each other, ligament failure is driven by an interaction

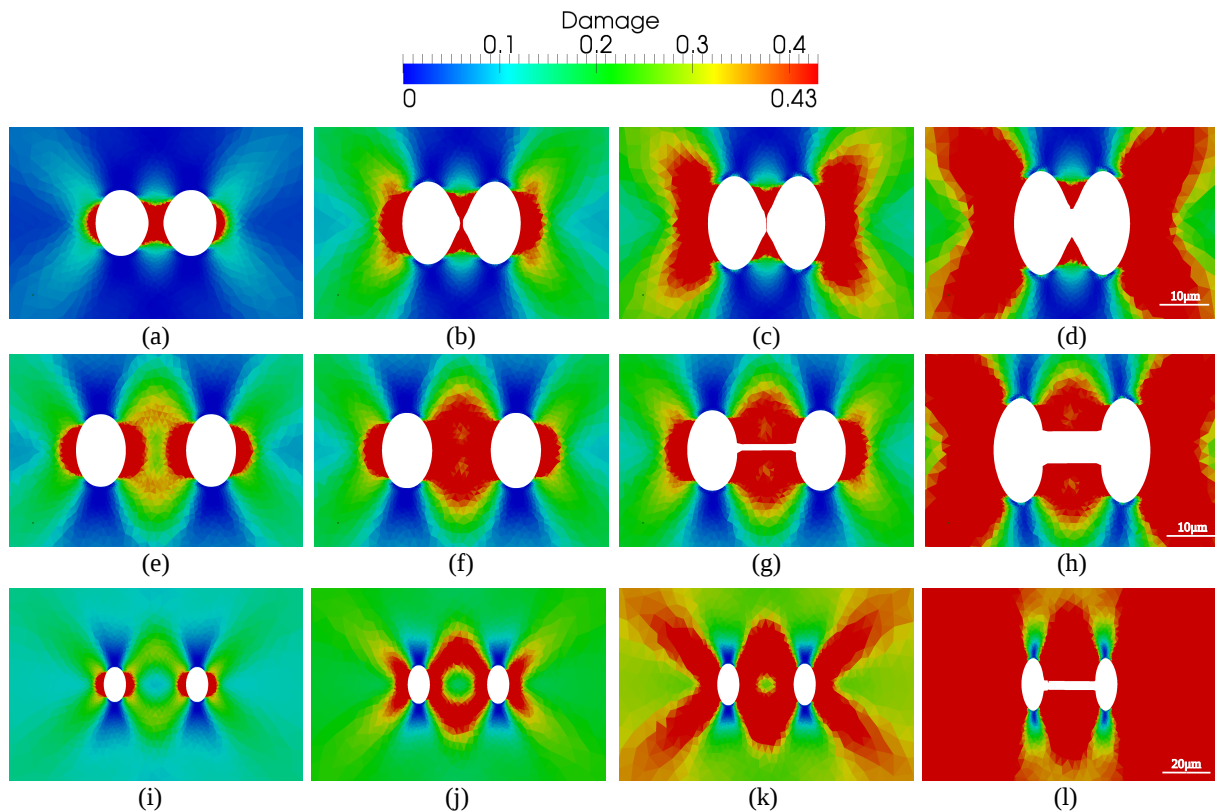


Figure 5.6 – Computational results with two holes aligned at 90° , $\ell_{lig} = 5 \mu\text{m}$ and no micro-cracking modeling at an engineering strain of: (a) 0.050, (b) 0.100, (c) 0.125, (d) 0.150. Computational results with two holes aligned at 90° , $\ell_{lig} = 15 \mu\text{m}$ and micro-cracking modeling at an engineering strain of: (e) 0.100, (f) 0.113, (g) 0.114, (h) 0.150. Computational results with two holes aligned at 90° , $\ell_{lig} = 30 \mu\text{m}$ and micro-cracking modeling at an engineering strain of: (i) 0.120, (j) 0.160, (k) 0.200, (l) 0.240.

between holes due to the second localization region. The modeling of this interaction with very large and very localized plastic strains at small scales may require a more advanced plasticity model than that used in the present work. While recent literature focuses on the modeling of softening in intervoid ligaments to avoid an overestimation of the strain at ligament failure, these results imply that more physical plasticity and hardening models are also of interest.

Crystal plasticity models could be considered. The size and the scales at which the different localization regions develop may also be ruled by length scales associated to a minor void population in the matrix, or its crystalline structure. These should be taken into account in the constitutive models. The determination of the length scales would require advanced strain measurement techniques such as those used in Chapter 6.

5.4.3 Effect of number of holes

With holes aligned at 90° and $\ell_{lig} = 30 \mu\text{m}$, experiments were conducted by varying the number of holes. First by replacing the two holes by a line of 13 holes, and then by multiplying the number of lines. Failure was systematically observed along the lines, with coalescence micro-cracks oriented perpendicular to the tensile direction.

Simulation results in plane strains are shown in Figure 5.7 for 1 and 3 lines of holes. The roman numbers indicate the order in which the ligaments failed.

The first ligament fractures at an engineering strain of 0.217 for the 1 line configuration (I in Figure 5.7(a)). It is reminded that with only two holes, the engineering strain at ligament failure is 0.235. Thus, plasticity and damage localization are favored with a higher number of holes in the line in plane strain.

Additionally, failure does not start at the extremities of the line, hence void growth and coalescence is more pronounced for holes that are surrounded by two neighboring holes instead of one. This was also observed in the plane stress case in Reference [87].

With 3 lines, results in plane stress and plane strain differ. Weck *et al.* observed an increase of ductility with additional lines. In the plane stress case, failure is due to the localization of plasticity and damage in a single line. When multiple lines are present the load is shared between these lines and localized necking phenomena in some intervoid ligaments are delayed. In the plane strain case, because plasticity and damage localize in an X pattern, the presence of multiple lines activates failure mechanisms at 45° with respect to the tensile direction. As mentioned in Subsection 5.4.2, although plasticity and damage are higher in the lateral directions close to the holes, the 45° localization bands develop earlier and propagate farther from the holes. Thus, failure is more likely to occur earlier along these 45° bands than in the perpendicular direction.

Although plasticity localizes earlier in bands aligned at 45° with respect to the tensile direction, failure does not systematically occur along these bands. In the 3 line configuration, the secondary ligament fracture events occur in the perpendicular direction (II in Figure 5.7(b)). This is due to a change in plasticity and damage localization once the first fracture event has occurred. This first event induces a higher localization of damage and plasticity in a certain region of the hole arrangement, and limits the propagation of micro-cracks far from this region. Void growth is also favored close to micro-cracks.

Results with 7 and 13 lines of holes are shown in Figure 5.8. The same effects are observed, namely the first void linkage phenomena occur along shear bands (I in Figure 5.8), but failure by intervoid ligament necking is also observed at larger plastic strains (II and III in Figure 5.8).

An interesting mechanism, which is favored with a higher number of lines, is that independent micro-cracks can nucleate in the hole arrangement. These micro-cracks will then tend to coalesce together in order to propagate as a single final crack. This mechanism has the consequence that the final crack features a zig-zag pattern. This pattern is hence not caused by the propagation of a single crack in an unstable manner, but by the nucleation and coalescence of multiple initially independent cracks oriented in different directions.

Moreover, most studies in the literature have focused on modeling only the first step of this failure mechanism, which is the interaction between cylindrical or spherical voids. Due to the failure of intervoid ligaments, new elongated voids are formed and different void interaction mechanisms have to be modeled.

Finally, for these two simulations with 7 and 13 lines, the influence of the number of lines on ductility seems to be less significant. This may be due to the fact that failure occurs in shear bands in simulations, and hence the bottom of the hole arrangement is reached by cracks at higher strains when the number of lines is increased. The effect of the number of lines may hence be reduced and even reversed for large numbers.

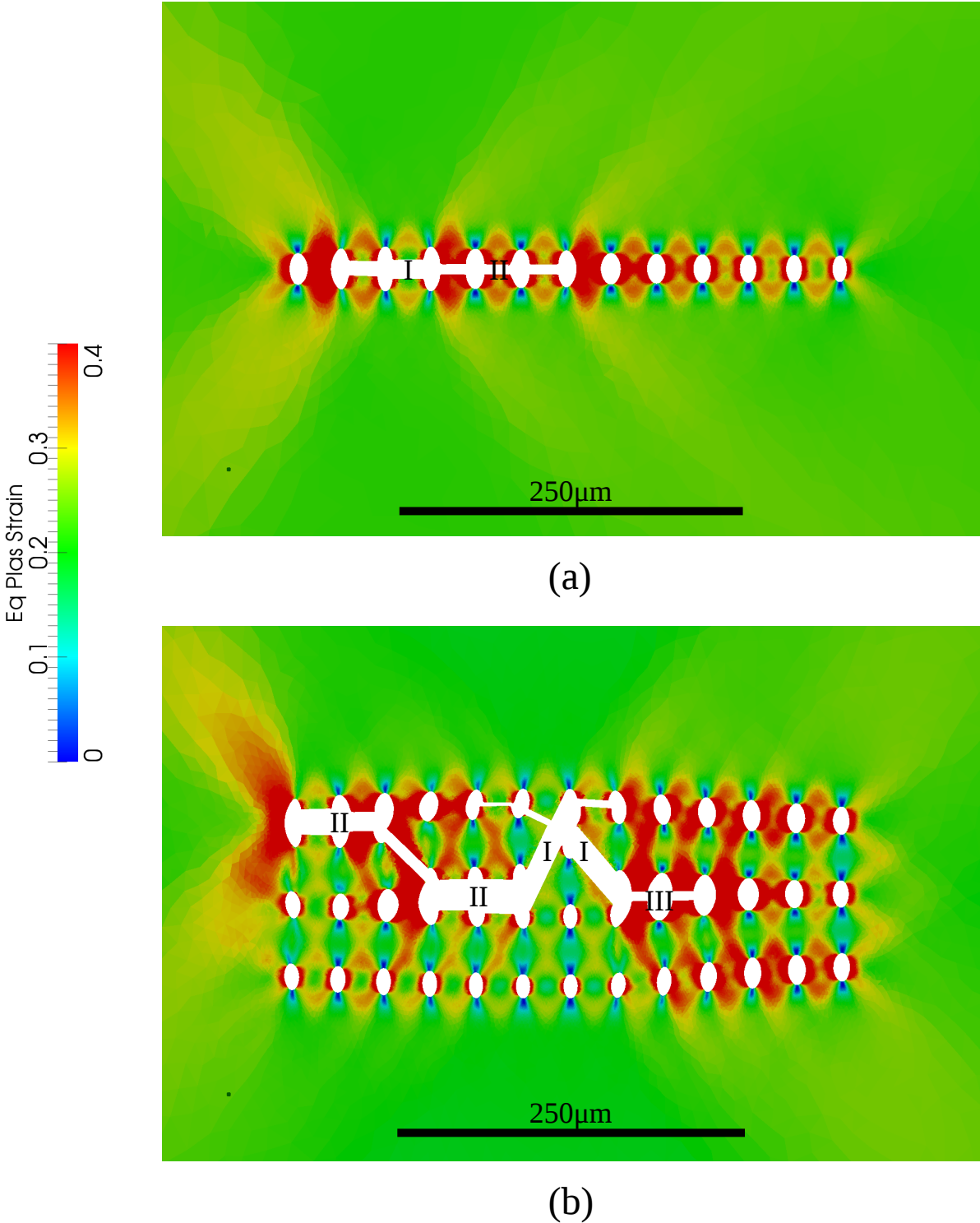


Figure 5.7 – Computational results for 1 and 3 lines of 13 holes at an engineering strain of: (a) 0.219, (b) 0.190.

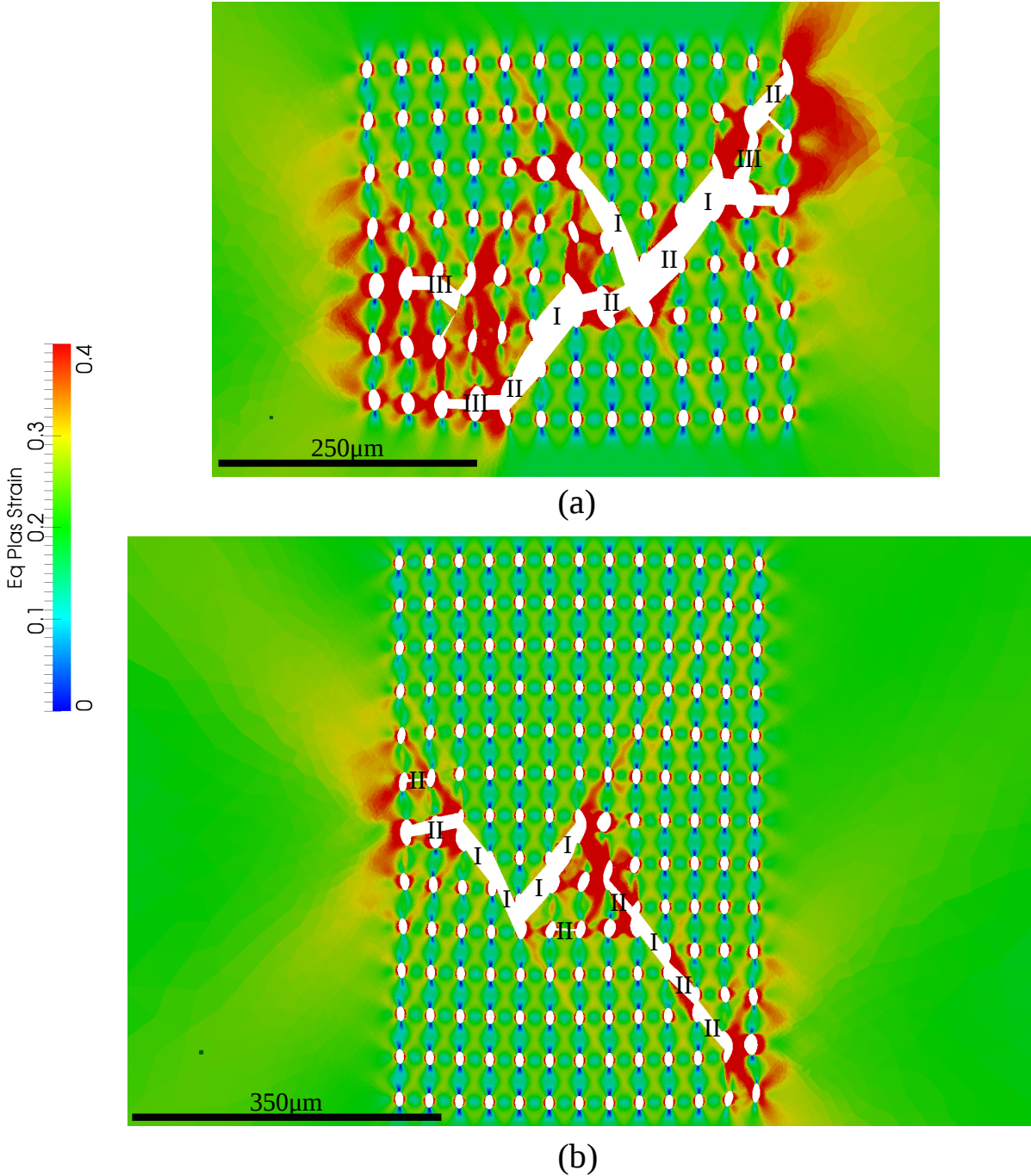


Figure 5.8 – Computational results for 7 and 13 lines of 13 holes at an engineering strain of: (a) 0.175, (b) 0.185.

5.4.4 Effect of holes orientation

Due to the presence of failure mechanisms along shear bands for holes aligned at 90° with respect to the tensile direction, the study of the configuration with holes aligned at 45° is of particular interest. The intervoid ligament length is fixed to $\ell_{lig} = 27 \mu\text{m}$ and holes alignment is varied. As expected based on previous results, ductility is significantly reduced with voids aligned at 45° , as shown in Figure 5.9.

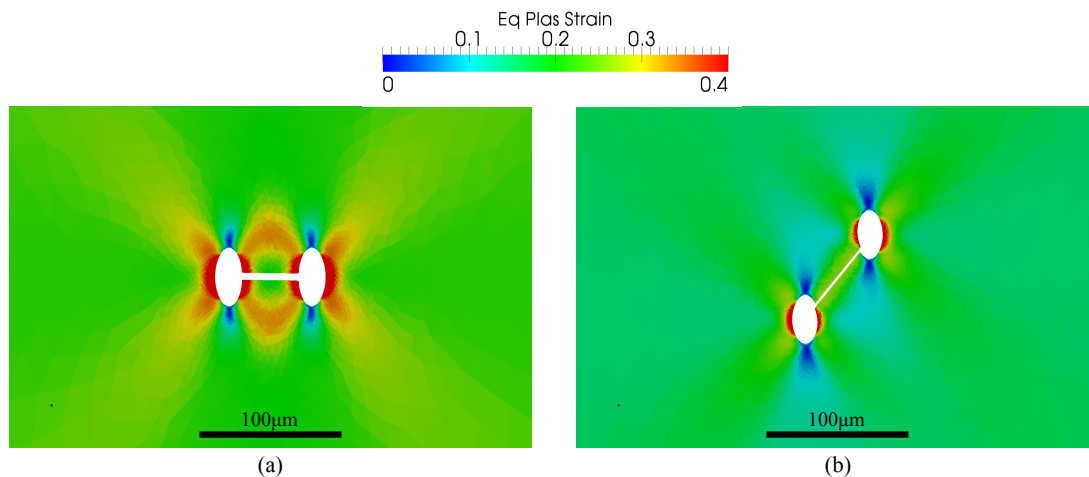


Figure 5.9 – Computational results for different hole orientations at an engineering strain of: (a) 0.218, (b) 0.142.

A comparison between the computational result (Figure 5.9(b)) and the experimental observation (Figure 5.5) with only two holes at 45° shows that the position and orientation of the micro-crack is well captured by the model. The micro-crack is not perfectly centered inside the shear band, but is slightly shifted because it follows the shortest path (Figure 5.9(b)). This is in agreement with the experiment (Figure 5.5), although this should be validated with plane stress simulations.

This analysis of the effect of hole orientation is pursued further with hole arrays ($\ell_{lig} = 38 \mu\text{m}$), as illustrated in Figure 5.10.

Once again, a zig-zag pattern is observed, especially in Figure 5.10(b). As mentioned in Subsection 5.4.3, this is due to the fact that the first micro-cracks initiate independently from each other, in regions of the holes arrangements that may be far from each other. An additional consequence of these independent crack initiation mechanisms is that the coalescence of these micro-cracks may require the formation of micro-cracks aligned along the tensile direction. This is observed in both hole arrays. This mechanism is however still a shear band coalescence mechanism, and not to be confused with necklace coalescence. These shear bands are caused by particular crack geometries and orientations with respect to the tensile direction.

5.4.5 Random arrangements

As discussed in Chapter 1 and Section 5.1, most theoretical studies on void coalescence modeling have considered periodic arrangements of voids. Although the laser drilling technique proposed by Weck *et al.* [83] is very interesting as such idealistic arrangements can be studied experimentally, real materials feature random arrangements [38]. These random arrangements

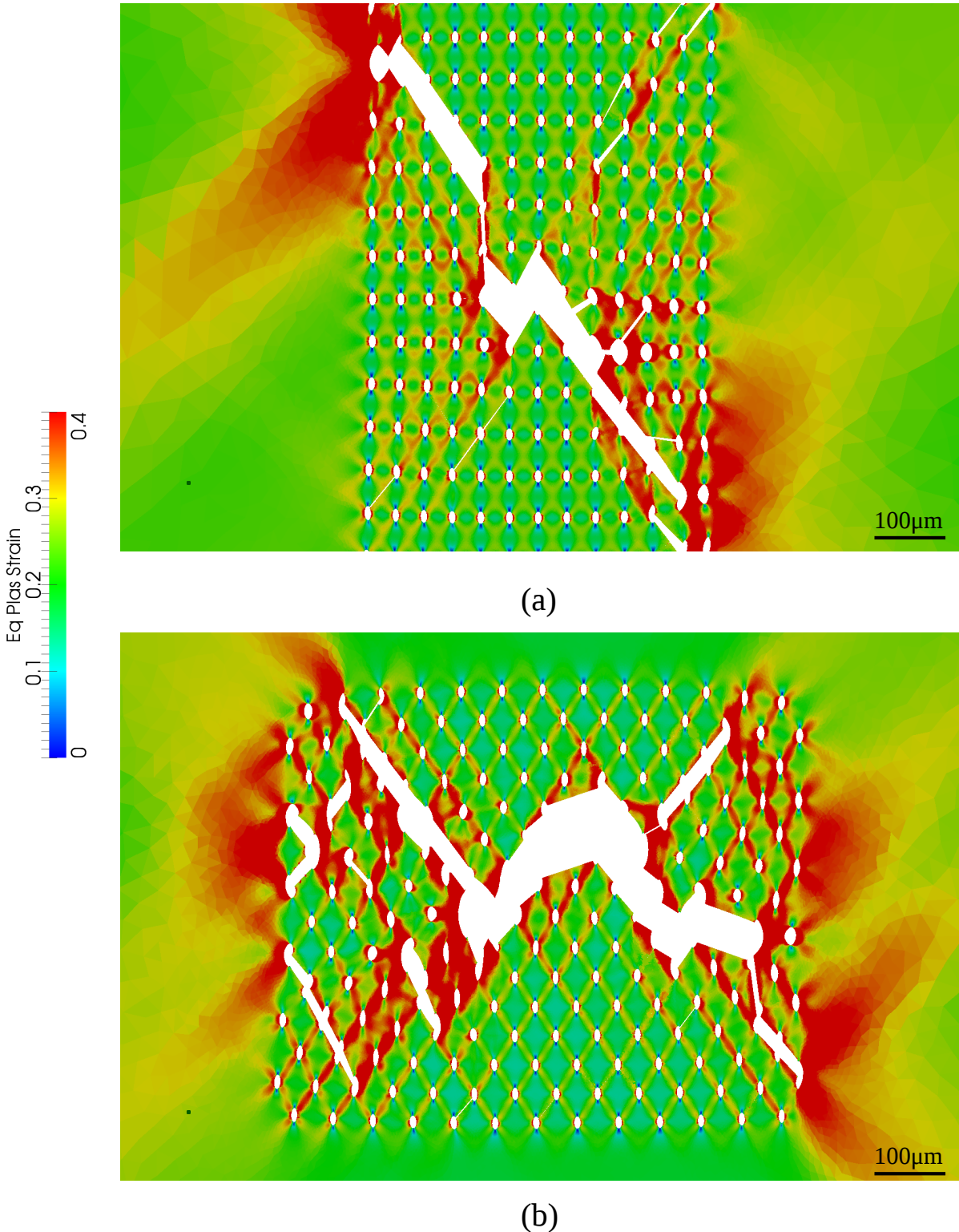


Figure 5.10 – Computational results for arrays of holes with different orientations at an engineering strain of: (a) 0.210, (b) 0.190.

have been studied in Chapter 4 regarding void nucleation.

In the following, random arrangements are considered and their influence of ductility is assessed. These arrangements contain 167 holes of diameter $10\ \mu\text{m}$ packed in a square of dimensions $620 \times 620\ \mu\text{m}^2$ (vs 169 holes in Figure 5.10(a) and 175 holes in Figure 5.10(b)). The intervoid ligament length ℓ_{lig} is greater than or equal to $27\ \mu\text{m}$. Hence, while the overall porosity and the average intervoid distance are comparable to the periodic configurations, holes might be locally closer in the random configurations ($\ell_{lig} = 38\ \mu\text{m}$ in the periodic configurations). All arrangements are shown in Figure 5.11.

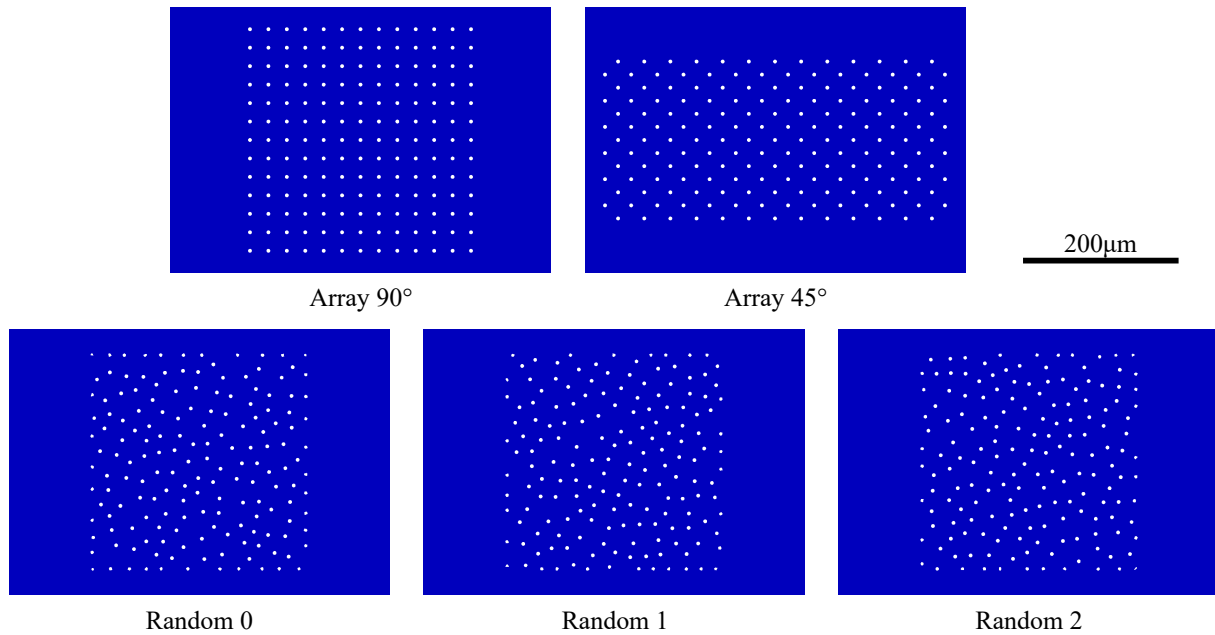


Figure 5.11 – Periodic and random arrangements used in simulations with large number of holes.

Results are first shown in terms of porosity change and engineering stress/strain curves in Figure 5.12. The engineering stress is the stress at the top of the specimens (Figure 5.4) divided by the initial section.

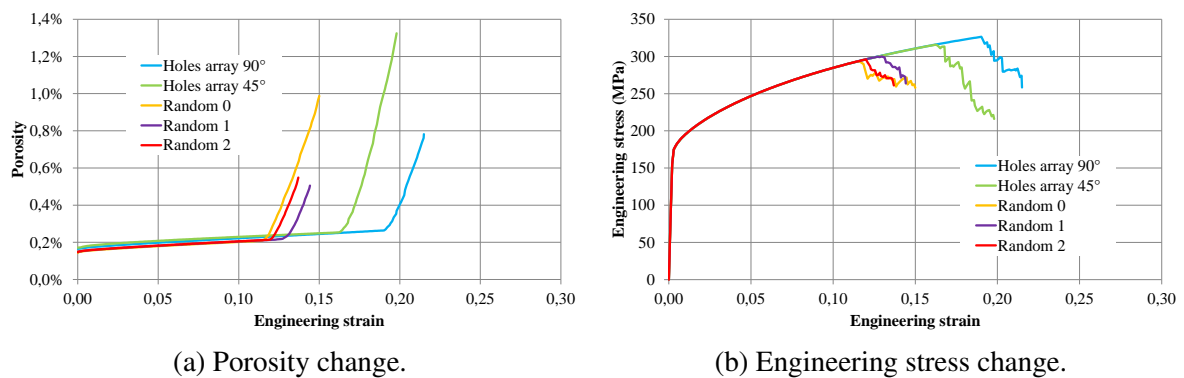


Figure 5.12 – Computational results for random hole arrangements (initial global porosity similar to hole arrays).

These curves show two phases. First, the engineering stress increases up to the ultimate

tensile strength (Figure 5.12(b)), with a moderate void growth (Figure 5.12(a)). Then, the activation of micro-cracking mechanisms leads to a progressive loss of load carrying capacity and a significant acceleration of void growth. In a third phase, not shown in these curves, the engineering stress would start to increase again, because micro-cracking is only detected between pairs of voids. Thus, no failure criterion is used for the regions between the hole arrangements and the lateral boundaries of the specimen. All curves are stopped at the lowest point in the stress/strain curve, after the activation of micro-cracking mechanisms, hence the third phase does not appear in Figure 5.12.

The reduction of ductility with holes aligned at 45° with respect to the tensile direction instead of 90° is shown by these curves, both regarding the porosity and the engineering stress. Ductility is further decreased with random arrangements. Results with these arrangements are shown in Figure 5.13.

For all arrangements, micro-cracking initiates in multiple regions due to voids that are closer to each other than the average intervoid distance, and aligned at 45° with respect to the tensile direction. These early micro-cracks may not necessarily participate in the final crack. For instance, in the *Random 1* arrangement, there is a first micro-cracking event at an engineering strain of 0.125 that does not participate in the final crack, which can be distinguished at an engineering strain of 0.135.

The final crack develops in preferential regions where not only two holes but multiple holes are located close to each other. The alignment of these holes with respect to the tensile direction also plays a role, as shown by the blue regions in Figure 5.13 where cracks cannot propagate. Once micro-cracks accumulate in certain regions of the holes arrangements due to void clusters, plastic localization has the consequence that void growth and coalescence also localize in these regions. Therefore, micro-cracking out of these regions rarefies.

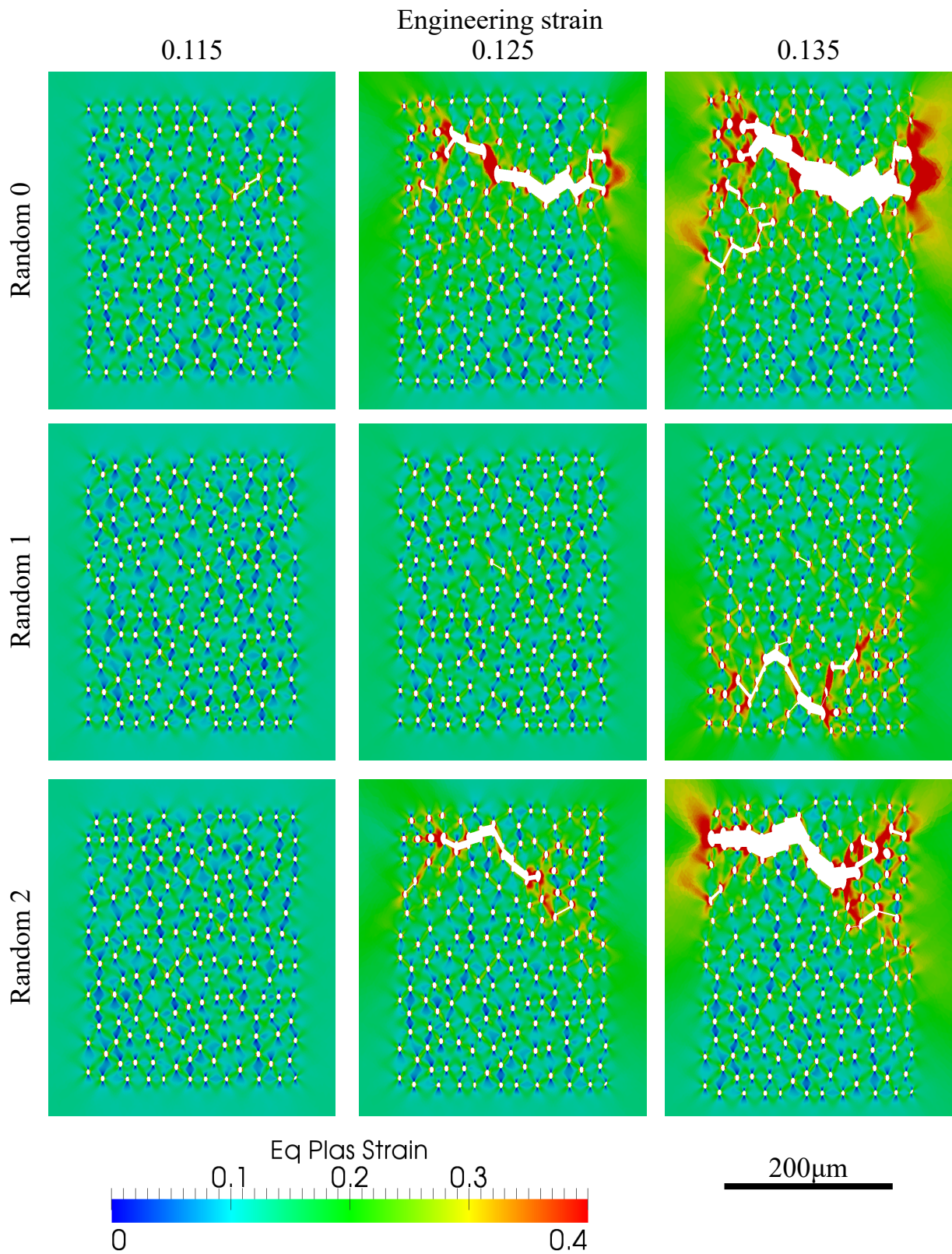


Figure 5.13 – Computational results for random hole arrangements at different engineering strains.

Conclusion

In this chapter, a model material with laser drilled holes is considered. Most analytic models assume that void coalescence is purely driven by plastic localization, as in the calculations conducted in Chapter 4. However, Finite Element (FE) approaches accounting for damage in the intervoid ligaments have been conducted by multiple authors. Submicron size voids may nucleate, grow, and coalesce in intervoid ligaments, hence increasing greatly the complexity of void coalescence modeling.

Based on comparisons between simulation results and experimental observations from the literature, it is shown that void growth is well captured with a simple von Mises plasticity model for the matrix when the initial distance between the voids is sufficiently larger than their diameter. However, at large plastic strain, the intervoid ligaments fail nearly instantaneously. Based on these comparisons, the fracture of the intervoid ligament is predicted and modeled during the simulation, using a Lemaitre damage indicator to predict its onset, and a geometrical criterion to predict its position and orientation.

Applications of this micro-cracking criterion to various hole arrangements prove that it can model the two modes of micro-cracking by intervoid ligament necking and along shear bands between holes. Although simulations differ from experiments because plane strains are assumed instead of plane stresses, some properties observed in experiments are well captured in simulations. For instance, ductility is decreased when holes are placed closer to each other, and when numerous holes are present in the material cracks initiate at multiple points of the hole arrangement. A remarkable property observed in simulations is that these cracks then grow independently, before coalescing together, leading to a zig-zag pattern.

Additionally, simulations with random hole arrangements show that ductility is significantly reduced when the arrangements are no longer periodic. This loss of ductility is caused by a localization of plasticity and damage at the neighborhood of void clusters. Consequently, micro-cracks initiate earlier in these clusters than with periodic arrangements. This is of major importance because most theoretical studies on void coalescence only address periodic arrangements.

In future work, it will be important to develop a plane stress implementation in the FE code in order to allow for quantitative comparisons. An alternative would be to perform these simulations in three dimensions (3D), but the computational cost would then be very high, especially with numerous holes. Such comparison would however be important to check the validity of the Lemaitre damage indicator used in this chapter. For a correct quantitative match between experiments and simulations, an advanced modeling of plasticity may be necessary, especially for small intervoid ligament thicknesses, for instance using higher-order crystal plasticity models. This requirement is independent from the modeling of damage and micro-cracking, which may require to couple the damage model to constitutive equations, for instance using higher-order porous plasticity models.

Finally, the coalescence model discussed in this chapter as well as the nucleation criteria discussed in Chapter 4 raise important challenges regarding identification procedures. In Chapter 4, material properties for the nucleation models are taken from the literature, where they were identified using Representative Volume Element (RVE) simulations with Periodic Boundary Conditions (PBCs) and a single particle. The stress state and the applied strain in these calculations were measured experimentally at the macroscale.

Thus, even if the RVE simulations conducted in Chapter 4 are more realistic, uncertainties on the material parameters used at the microscale are quite high. Regarding the coalescence model,

comparisons with experiments are helped by the fact that the whole specimens are meshed, and the microstructure of the material is artificial.

For 3D applications, a more systematic numerical validation framework is necessary. This framework should enable to mesh only a small region of the specimen, and hence define boundary conditions to apply at the boundaries of this meshed region. An automatic procedure should also be available to quantify errors between simulation results and experimental observations. This is the objective of Chapter 6.

This chapter is partially inspired from [40].

Chapter 6

A numerical validation framework for micromechanical simulations based on synchrotron 3D imaging

You hear about how many fourth quarter comebacks that a guy has and I think it means a guy screwed up in the first three quarters.

Peyton Manning

Introduction	214
6.1 Method	217
6.1.1 Introduction	217
6.1.2 Experimental analyses	219
6.1.3 Finite Element simulations	223
6.1.4 Quantitative comparisons	227
6.1.5 Conclusion	233
6.2 Comparison with other methods	235
6.2.1 Introduction	235
6.2.2 Experiments	236
6.2.3 Boundary conditions	238
6.2.4 Results	240
6.2.5 Conclusion	249
Conclusion	250

Résumé en français

Les techniques expérimentales permettant d'acquérir *in situ* des images tridimensionnelles (3D) des micromécanismes de germination, croissance et coalescence de cavités qui définissent la rupture ductile sont de plus en plus couramment utilisées. Dans le chapitre précédent, il a été montré que les outils numériques et modèles développés dans ce travail permettent des simulations à champ complet de ces mêmes micromécanismes, à l'échelle de microstructures 3D de tailles importantes. Dans le présent chapitre, une méthodologie est développée pour comparer expériences et simulations en champ complet et en 3D.

La méthodologie proposée s'appuie fortement sur la corrélation d'images volumiques. Des données 3D acquises par imagerie à rayons X à différentes étapes du chargement peuvent être corrélées afin de mesurer les déplacements subis par chaque point de la microstructure au cours du chargement. Une analyse d'incertitudes appliquée à deux expériences différentes sur le même matériau confirme la validité de ces mesures et la robustesse de la méthode de corrélation. Le matériau utilisé est de la fonte à graphite sphéroïdal. La microstructure de ce matériau comporte une matrice d'acier ferritique, et des nodules de graphite qui se décolent assez facilement de la matrice en traction. De plus, il a été établi par plusieurs auteurs dans la littérature que ces nodules ont une faible capacité de charge. Ainsi, ils sont considérés comme des vides dans ce chapitre et les mécanismes de germination ne sont donc pas modélisés.

Une fois la microstructure initiale maillée, à l'échelle d'une petite région d'intérêt, les déplacements mesurés par corrélation d'images volumiques sont utilisés comme conditions aux limites de Dirichlet sur toute la frontière de cette région d'intérêt. Ainsi, la corrélation d'images volumiques pilote les simulations éléments finis. Cette méthode permet de reproduire avec grande fidélité le chargement que subit localement la microstructure dans la réalité. Par ailleurs, les déplacements calculés à l'intérieur de la région d'intérêt dans la simulation éléments finis peuvent être comparés avec les mesures obtenues par corrélation d'images volumiques. Cette comparaison permet de quantifier l'erreur commise par les modèles micromécaniques à l'intérieur de la région d'intérêt. Alternativement, la validation de la solution éléments finis peut se faire directement par rapport aux images 3D acquises pendant le chargement par imagerie à rayons X. L'intérêt de la méthodologie proposée consiste donc aussi en la possibilité de quantifier les erreurs localement et avec précision. Cette méthodologie s'appuie fortement sur les outils numériques de maillage et de suivi d'interface développés dans ce travail. En effet, des simulations sur microstructures réelles et dans des conditions de chargement réalistes nécessitent des méthodes numériques avancées permettant de mailler des microstructures de formes arbitraires et de suivre leur déformation.

Ensuite, l'intérêt de la méthodologie proposée dans ce chapitre est démontré à l'aide de comparaisons avec les approches conventionnelles. Cette discussion inclut le problème du choix des conditions aux limites, et des mesures d'erreurs locales. En effet, la plupart des travaux existants utilisent des méthodes multi-échelles pour déduire des conditions aux limites pour les calculs micromécaniques. Indépendamment de la méthodologie utilisée pour coupler simulations macromécaniques et micromécaniques, il est montré dans ce chapitre que la fiabilité de ces méthodes multi-échelles est limitée. En particulier, les résultats indiquent que ces méthodes ne permettent pas de capter les phénomènes de localisation plastique et de coalescence de cavités complexes se déroulant dans la région d'intérêt. Ces conclusions ne peuvent pas être obtenues à l'aide de mesures d'erreurs globales, qui sont

couramment utilisées dans la littérature. Seuls des indicateurs d'erreur locaux, tels ceux basés sur la corrélation d'images volumiques, permettent des mesures précises des erreurs. Ainsi, il est montré que la croissance des cavités est bien prédite en volume mais non en forme avec les méthodes conventionnelles, et que les prédictions sont plus fidèles à la réalité avec la méthodologie proposée dans ce chapitre.

Etant donné qu'un critère de plasticité simple a été utilisé dans ce chapitre pour modéliser la matrice, et que le comportement des nodules a été négligé, les prédictions obtenues avec la méthodologie proposée dans ce chapitre sont parfois éloignées de la réalité. Cela est d'autant plus vrai pour de grandes déformations plastiques, où la coalescence de cavités est prépondérante. Pour améliorer ces prédictions, la piste principale semble être la modélisation des cavités de taille inférieure au micromètre, à l'aide d'un modèle tel que celui discuté au chapitre 5, ou d'un modèle de plasticité poreuse.

Pour d'autres matériaux ou conditions de chargement, le comportement des nodules devrait également être pris en compte, et les critères de décohésion et fragmentation développés dans le chapitre 4 devraient être utilisés. En outre, la méthodologie proposée dans ce chapitre s'appliquerait certainement à d'autres matériaux où la modélisation micromécanique est de plus en plus populaire, comme les mousses métalliques et les composites à matrice de polymère par exemple.

En dernier lieu, les résultats présentés dans ce chapitre sont très prometteurs non seulement pour la modélisation micromécanique, mais également pour l'identification de lois constitutives à l'échelle microscopique. La méthodologie proposée permet dans ce cadre de fournir des conditions aux limites pour des calculs micromécaniques, et ensuite de mesurer les erreurs commises par les modèles micromécaniques utilisés. Par conséquent, la sensibilité des erreurs mesurées par rapport aux paramètres du matériau peut aisément être quantifiée et utilisée pour l'analyse inverse et l'identification de ces paramètres à l'échelle microscopique.

Introduction

In the present work, numerical tools have been developed to access realistic Finite Element (FE) simulations of ductile fracture at the microscale. Several difficulties have been handled, including large plastic strains, void coalescence, nucleation of cracks and contact between crack faces. The goal is not only to perform more realistic micromechanical calculations as presented in Chapter 4, but to reproduce as accurately as possible what is observed in experiments.

This last point calls for a methodology to observe in three dimensions (3D) the void nucleation, growth and coalescence mechanisms, and then conduct FE simulations at the microscale in the same conditions as those of the experiments. The difficulty lies in the fact that these conditions have to be identified at the microscale, and in 3D.

The experiments on which this chapter is based were carried out at the European Synchrotron Radiation Facility - Grenoble (ESRF - Grenoble) by T. F. Morgeneyer¹ and A. Buljac^{2,1}, with the help of L. Helfen^{3,4}. In order to allow for two scales of localization mechanisms, at the macroscale and at the microscale, laminography was used. As mentioned in Section 1.1, this X-ray imaging technique permits the use of flat specimens that can be several millimeters wide, while the thickness is limited depending on the X-ray absorption properties of the material. The presence of iron in the constituents of the materials studied in this chapter restricts this thickness to the millimeter range. An *in situ* tensile loading machine is used to acquire 3D Synchrotron Radiation Computed Laminography (SRCL) scans during loading. The resolution of these images is typically $\approx 1 \mu\text{m}$, for an observed Region Of Interest (ROI) of $\approx 1 \text{mm}^3$. More details on SRCL and the loading machine can be found in previous publications [16, 22, 64, 65]. In order to reproduce what is observed in these 3D X-ray images acquired at different loading steps during the experiment, it is necessary to mesh the ROI and its microstructure observed in the initial state, and identify loading conditions to be applied at the boundaries of this ROI. The first part has been covered by the image meshing procedure presented in Section 3.4. The second part is often solved in the literature based on specimen geometry and other macroscopic measurements.

In many works [66, 67, 83, 259, 260], because the ROI is often located close to a notch, the macroscopic stress state is deduced from approximations such as Bridgman's formula, while the macroscopic equivalent plastic strain is deduced from the section reduction of the specimen. These formulas are used both to apply analytical void growth and coalescence models [25, 26, 243], and conduct FE analysis. In both cases, significant errors can be made, because neither the macroscopic stress state nor the macroscopic equivalent plastic strain can generally be considered as uniform in the ROI [240, 261], due to its significant size relative to that of the specimen (both being of millimeter scale).

This difficulty is directly related to the fact that scale separability cannot be assumed for the specimens used for X-ray imaging. Alternatives that are based on FE simulations at specimen scale raise the same issue. In these techniques [18, 82, 262], macroscopic mechanical fields

¹MINES ParisTech, PSL Research University, Centre des Matériaux, CNRS UMR 7633, BP 87, 91003 Evry, France

²Laboratoire de Mécanique et Technologie (LMT), ENS Cachan/CNRS/Université Paris-Saclay, 61 avenue du Président Wilson, 94235 Cachan, France

³ANKA/Institute for Photon Science and Synchrotron Radiation Karlsruhe Institute of Technology (KIT), D-76131 Karlsruhe, Germany

⁴European Synchrotron Radiation Facility (ESRF), F-38043 Grenoble, France

computed during a first calculation at specimen scale are used as Static Uniform Boundary Conditions (SUBCs) or Kinematic Uniform Boundary Conditions (KUBCs) for a second calculation at the microscale.

Non homogeneous boundary conditions should hence be considered, for instance the embedded unit cell approach, where the ROI with meshed microstructure is embedded directly in the mesh of the specimen, and a single FE simulation is performed using this combined mesh [17, 248, 258, 263, 264, 265]. Microscale constitutive models are used inside the ROI, while a homogenized macroscale constitutive model is used for the out-of-ROI material.

The main difficulty then lies in the choice of macroscale constitutive model. This difficulty can be avoided by using a self-consistent scheme where the constitutive model for the out-of-ROI material is corrected incrementally during the simulation by homogenizing the mechanical response of the ROI [127, 128], but at the sacrifice of a significant additional computational cost.

In this chapter, a new numerical validation framework linking *in situ* 3D X-ray images directly to FE simulations at the ROI scale is presented. This framework relies extensively on Digital Volume Correlation (DVC) measurements performed by A. Buljac^{2,1}, J. Neggers² and F. Hild². These measured displacement fields between consecutive 3D scans are used as Dirichlet boundary conditions for the FE simulations. Added to the fact that this framework avoids any assumption on the macroscopic behavior of the material, and any dependence on macroscopic measurements or simulations, it provides a very promising mean for validating microscale constitutive models.

First, while the displacements at the boundaries of the ROI are controlled by DVC, the kinematic FE solutions inside the ROI can be compared to DVC measurements, giving local error indicators. In fact, most studies only consider global indicators, such as the ROI-averaged porosity [9, 19, 21, 67, 228, 259].

Second, gray level residuals can be computed for FE simulations, in order to have a quantitative indication of the error committed by FE models and its local distribution. Opposed to global indicators, these two local error measurement techniques are extremely relevant when void growth is well predicted in volume, but not in shape. As a consequence, they are promising candidates for inverse analysis, and identification of microscale material parameters, including those associated to the fracture criteria presented in Chapter 4 and Chapter 5.

The studied material is a commercial nodular graphite cast iron (EN-GJS-400), and specimens were supplied by M. Kuna⁵, L. Zybell⁵ and M. Horn⁵. At the microscale, this material features a ferritic steel matrix and graphite nodules, with no significant porosity in the initial state. Then, under tensile loading, ductile fracture is mainly driven by a very early debonding of the nodules from the matrix, and coalescence of the subsequent nucleated voids [266, 267]. Evidence in the literature [266, 267, 268, 269] suggests to model the nodules as voids, as their load carrying capacity is very low under tensile loading. This assumption is made in this chapter and at the microscale the material is considered as a two-phase microstructure with a ferritic matrix and voids.

The proposed numerical validation framework is described in details in Section 6.1 and applied to a test on a flat specimen of nodular cast iron with a central hole. The material and the *in situ* SRCL imaging technique are presented, and DVC measurements are performed on the resulting 3D data. Validation of both the DVC measurements and the FE simulations carried out

⁵TU Bergakademie Freiberg, Institute of Mechanics and Fluid Dynamics, Lampadiusstr. 4, 09596 Freiberg, Germany

based on these measurements is assessed thanks to gray level residuals computation and mutual comparison.

Once this method is validated on this first experiment, where nodule debonding, void growth and coalescence are observed, its interest with respect to other approaches found in the literature remains to be shown. This is the object of Section 6.2, where the proposed methodology is applied to a test on a flat specimen of nodular cast iron with two holes aligned at 45° with respect to the loading direction, and compared with classical approaches found in the literature.

6.1 Method

6.1.1 Introduction

As summarized in Figure 6.1, the methodology proposed to obtain local comparisons between experimental analyses and numerical simulations is based on the following steps:

- X-ray laminography to get 3D pictures of an *in situ* test in a synchrotron facility [270, 271, 272, 273, 274].
- Global DVC to measure displacement fields whose kinematic basis is made of the shape functions of 8-noded elements [97, 98, 99].
- FE simulations at the microscale explicitly accounting for the morphology of the studied two-phase material.
- Comparisons between experimental measurements and numerical simulations based on displacement fields and correlation residuals.

The SRCL setup is based on previous work [270, 271, 272, 273, 274]. The ability to use flat specimens is of particular interest in the field of mechanics of materials since sheet-like samples allow for a wide range of engineering relevant boundary conditions. However, due to the inclination angle with respect to the beam direction, incomplete sampling of the 3D Fourier domain of the specimen is performed and additional artifacts are present [275].

The DVC registration technique used to measure 3D displacement fields in the bulk of samples is based on a recently developed global approach [97, 98, 99]. The gray level residual described in Subsection 1.1.4 is minimized on the whole ROI, using kinematic fields based on FE discretizations.

Most aspects related to FE simulations have already been detailed in previous chapters. In particular, the X-ray image acquired in the undeformed state is discretized with an adapted and conform mesh using the procedure detailed in Chapter 3. Continuum mechanics equations are solved using the parallel FE code described in Subsection 1.2.1, and the hardening law given in Equation (4.10). During loading, the void/matrix interface undergoes large deformations and complex void linkage phenomena that require the use of the mesh adaptation procedure presented in Chapter 2.

In the past, 3D meshes stemming from X-ray tomography data have been created for fatigue loading cases e.g. to assess the stress intensity factors ahead of a crack [98]. In Reference [276] the 3D grain structure and orientation has been assessed via diffraction contrast tomography and subsequently been meshed in 3D to assess the effect of crystallographic orientation on fatigue crack propagation numerically and experimentally. However, to the author's best knowledge, there are no studies that explicitly mesh real microstructures and model microscopic fracture mechanisms for the case of ductile damage.

Three ROIs are illustrated in Figure 6.1. Starting from the laminography data (initial ROI), FE mesh generation (FE ROI) and DVC measurements (DVC ROI) are carried out independently. Then, DVC measurements \mathbf{u}_{DVC} are interpolated on the boundaries of the FE mesh, and material parameters $\{\mathbf{p}_0\}$ are added to conduct FE simulations. The latter yield FE displacement fields \mathbf{u}_{FE} that can be compared to DVC measurements \mathbf{u}_{DVC} , resulting in a first error measurement \mathbf{u}_{diff} . Uncertainties can also be assessed by direct comparisons with the laminography data through the computation of gray level residuals. The latter can be computed both for DVC measurements

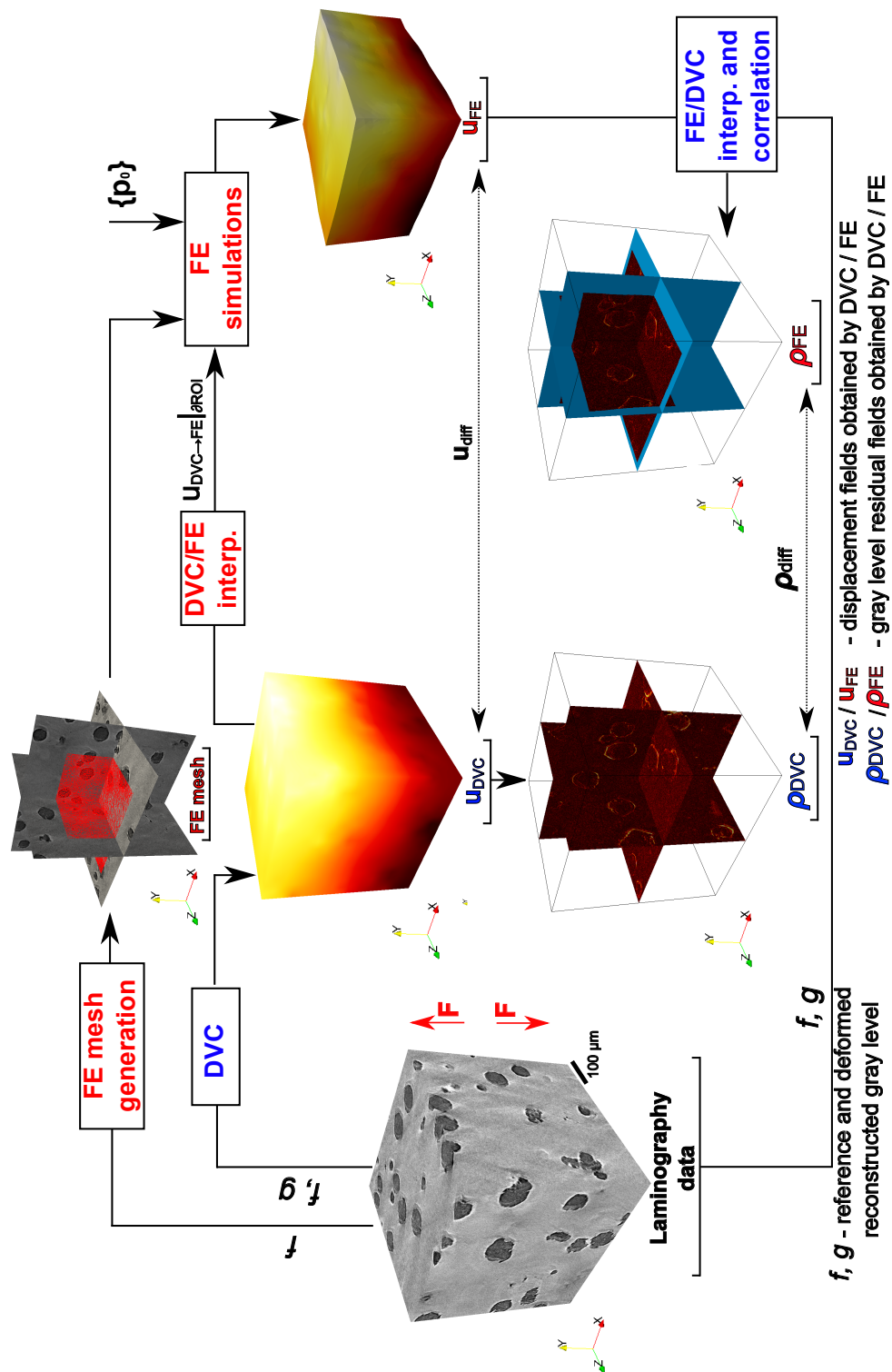


Figure 6.1 – Schematic representation of the methods used in the present chapter for validating numerical simulations at the microscale. Trilinear hexahedral meshes are used for DVC, and linear tetrahedral meshes for FE simulations.

(ρ_{DVC}) and for FE displacement fields (ρ_{FE}). All these operations are described in this section. First, the experimental setup and the laminography imaging technique are introduced. The basic principles of DVC incorporating uncertainty quantification and DVC results are then presented. FE simulation tools including the microstructure meshing procedure and the strategy for applying DVC measured boundary conditions are described next. Last, the results from both methods are compared relatively via kinematic field subtractions and absolutely by computing gray level residuals.

Since the present work focused exclusively on FE simulations and micromechanical modeling, all details regarding the experiments and DVC can be found in the published version of this section [44].

6.1.2 Experimental analyses

6.1.2.1 Synchrotron test

The geometry of the flat specimen with a central hole is shown in Figure 6.2(a). The specimen geometry yields stress triaxialities within the range 0.4-0.5 in the vicinity of the central hole [277]. A stepwise loading procedure resulted in the force-displacement curve shown in Figure 6.2(b).

The 3D images used in this work were obtained at beamline ID15A (ESRF - Grenoble, experiment MA 1932), and have a final size of $1600 \times 1600 \times 1600$ voxels. The physical size (length) of 1 cubic voxel is equal to $1.095 \mu\text{m}$.

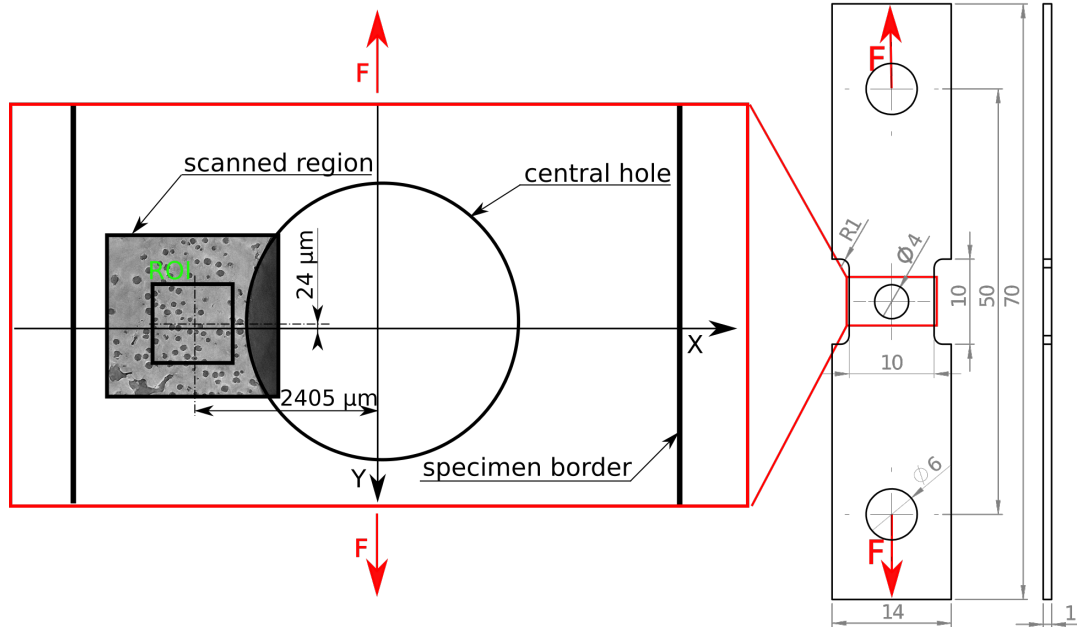
Figure 6.3 shows microstructure sections for the unloaded state and after the first five loading steps. From the reconstructed raw images early nodule debonding from the matrix is noted. Softening becomes significant after the sixth loading step, as shown in the macroscopic load-displacement curve in Figure 6.2(b). Indeed, the final crack has started propagating through the scanned region in Figure 6.3(f). Therefore, results after the sixth loading step, although available, are of less interest for the present numerical modeling procedure. Conversely, the measured kinematic fields for the initial steps are of special interest.

6.1.2.2 Digital Volume Correlation

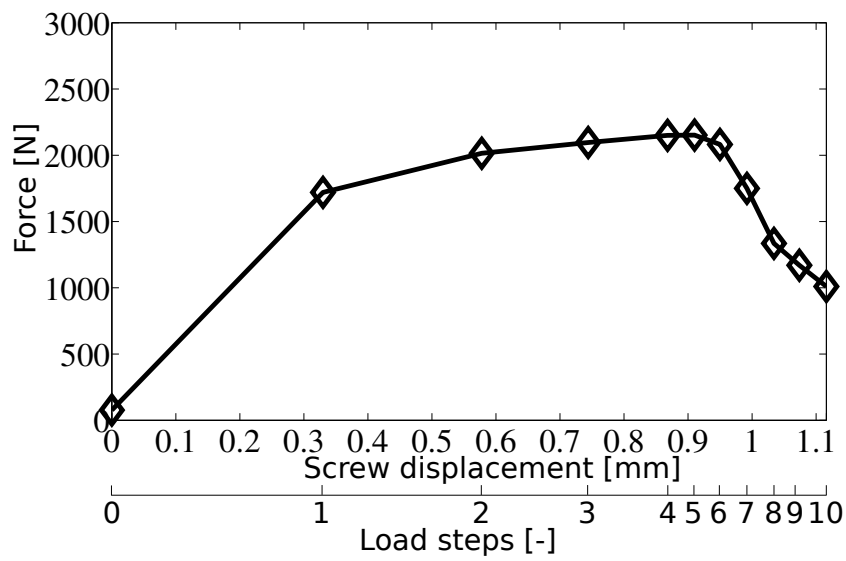
A correlation procedure applied to the whole volume size would be computationally too demanding. Therefore an extracted ROI (*i.e.*, DVC ROI) of size $532 \times 532 \times 532$ voxels is used for DVC analyses. The position of the ROI in the global coordinate system is shown in Figure 6.2(a) while in the z direction the ROI and sample mid-thickness planes coincide.

6.1.2.2.1 Basic principles DVC used herein is an extension of global two dimensional (2D) Digital Image Correlation (DIC) [278, 279]. The reconstructed volume is represented by a discrete scalar matrix of spatial coordinate \mathbf{x} of (in this case 8-bit deep) gray levels determined by the microstructure absorption of X-rays (Figure 6.4). The image contrast is mainly due to graphite nodules of micrometer size.

Due to acquisition noise, reconstruction artifacts [275] and the correlation procedure itself [101], the global minimization of gray level residuals may be numerically difficult. It is helped by using a mechanical regularization procedure [100, 280, 281], where a mechanical admissibility constraint is enforced on the solution. This constraint is successively relaxed so that the final solution is only constrained to be continuous. This last constraint stems from the fact that the displacement field is discretized globally [97] using a FE method with trilinear shape functions



(a)



(b)

Figure 6.2 – (a) Schematic view of the sample with the scanned region (*i.e.*, laminography ROI) close to the central hole and the ROI (*i.e.*, DVC ROI). Section of the reconstructed volume with the position of the region of interest. (b) Macroscale force-displacement curve.

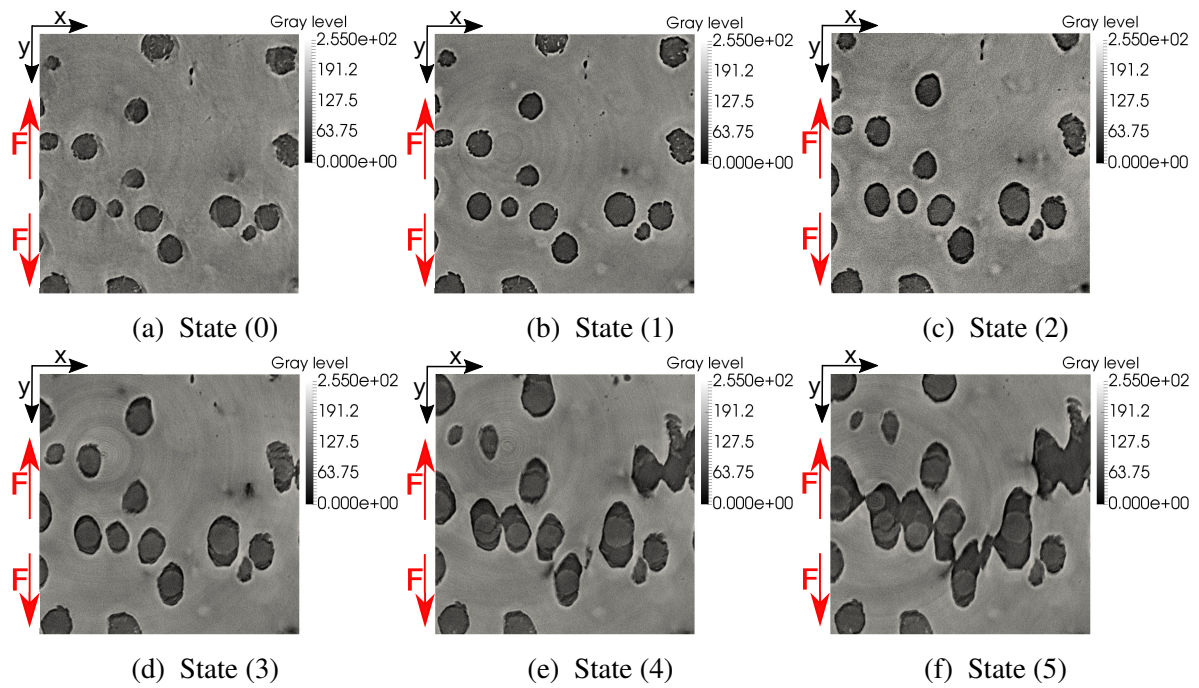


Figure 6.3 – Through thickness section showing nodules embedded in the matrix for the undeformed state (a) and after the first five loading steps (b)-(f).

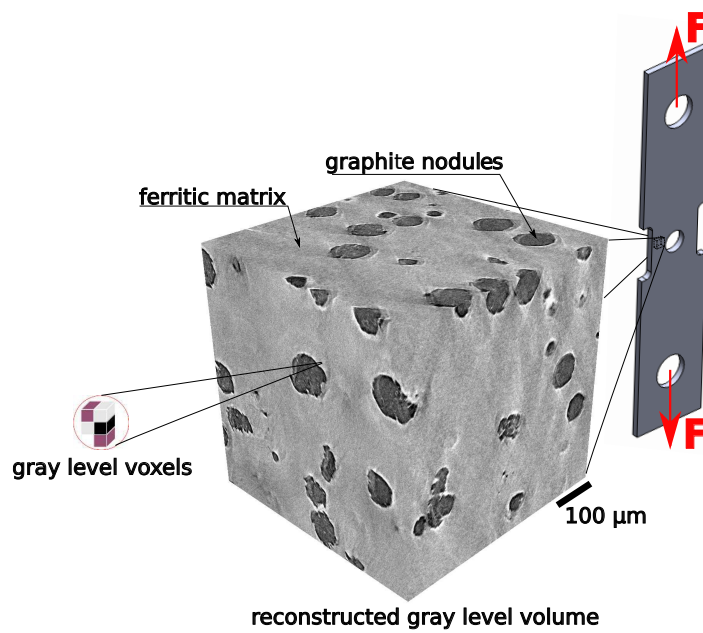


Figure 6.4 – Reconstructed volume as a spatial discrete matrix of gray level values.

[98].

All the results reported hereafter have required the DVC analyses to converge based on the variation of the solution between two iterations of the least squares solver. An additional check is related to the gray level residuals ρ that will be shown in the sequel.

6.1.2.2.2 Link between DVC and numerical simulations The measured displacements are expressed on a regular undeformed mesh made of hexahedral elements. Full-field results written node-wise are provided as .txt output files of DVC and will be used as boundary conditions for the FE micromechanical calculations. Hence, for the first incremental loading step (0)-(1) the results are written on the undeformed frame (0), for the second (1)-(2) on the mesh associated with the microstructure at state (1), and so on. An example is shown in Figure 6.5.

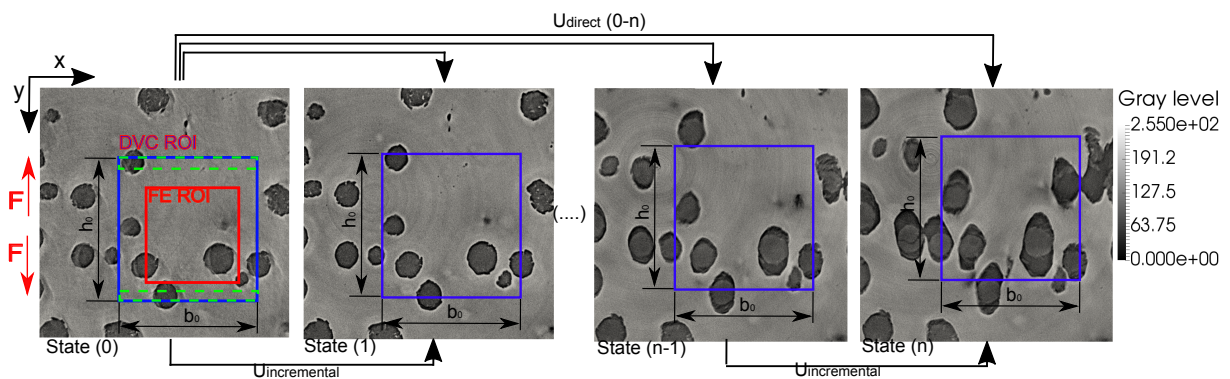


Figure 6.5 – DVC (blue) and FE (red) ROIs at different loading steps. The FE ROI has to remain inside the DVC ROI throughout loading.

Since undeformed meshes (blue DVC ROI) with constant (initial) size are considered at the microstructure state $(n - 1)$ for loading step (n) , with its positions defined relatively to the followed microstructure features, some of the material points present in the DVC ROI at the beginning are lost during the loading history. These regions are depicted with green dashed rectangles in the figure.

Since the material points used for FE computations need to possess a complete kinematic information through the loading history, just an inner part of the original DVC ROI has been utilized for communication between DVC and FE simulations (red FE ROI), where the ROI size reduction is the most significant in the loading direction (y) for which the displacements are the largest.

Once defined, boundaries of the domain are used to extract the corresponding part of the DVC displacement solutions. These displacements are interpolated on the unstructured tetrahedral mesh used in numerical simulations, where they are imposed as Dirichlet boundary conditions. Additionally, because the underlying experiment and consequently DVC calculations are obtained with a small number of loading steps, linear interpolation in time may be necessary to properly prepare boundary conditions for FE computations.

6.1.2.2.3 Uncertainty quantification Uncertainties can be assessed using two methods. These methods rely on two consecutive scans of the unloaded and loaded sample without applying any additional load (0 mm bis) or prescribing rigid body motions between the two acquisitions (0.744 mm bis). The measured displacement fields account for the cumulated effects of laminography and DVC on the measurement uncertainty.

The first analysis considers directly the two displacement fields obtained in these two situations. The first displacement field should be zero, while the second one should have a zero gradient (*i.e.*, strain). This analysis (not reported here) indicates a displacement and strain resolution below the voxel for the present measurements.

The second analysis considers gray level residuals (defined in Subsection 1.1.4). These residuals do not only serve as correlation quality inspector, but they also provide useful tools for sensitive (precise) detection of damage occurrence [282]. In the present case they will also provide an objective way of comparing measured and simulated displacement fields.

The kinematic basis used in the DVC discrete formulation prescribes continuity to the measured displacement field. Any deviation from this requirement (*e.g.*, void nucleation and growth) cannot be properly captured by the underlying kinematics and will be reflected in a local residual increase. Hence, a significant amount of damage growth may deteriorate gray level conservation and possibly DVC convergence. A particular care will be given to the evolution of these residuals during loading. The results regarding gray level residuals are reported in Subsection 6.1.4.

6.1.3 Finite Element simulations

6.1.3.1 Definition of a computational domain

For each experiment, 3D X-ray images are reconstructed at various loading steps. For obvious reasons, it is impossible to systematically capture the same part of the specimen, and some features may go in and out of the images.

Regarding DVC, this is dependent on whether computations are conducted with a direct or incremental scheme (Figure 6.5). The ROI may be different depending on the used method as for example more material points of intermediary images are taken into account by the incremental method.

However, this is not possible for mechanical simulations, namely, the chosen initial FE domain has to remain inside all DVC ROIs throughout the simulation. This is independent of the DVC method (direct or incremental).

In practice, the DVC ROI is chosen as large as possible (ideally, the full X-ray images minus the regions with missing information), and the FE domain for mechanical computations is manually chosen in order to be contained inside all DVC ROIs.

6.1.3.2 Application of boundary conditions

Once an appropriate domain has been chosen and meshed according to the initial image, boundary conditions have to be applied to follow experimental images through each loading step. This problem is split into two operations that are time and spatial interpolations. Neither the time step nor the FE mesh used for mechanical computations will generally match the loading steps used in experiments and the mesh used for DVC.

In practice, a loading step will be split into several time steps, especially at crack initiation. Regarding the FE mesh, it will be fitted to the features of the microstructure, and refined close to interfaces. It is worth noting that such fine meshes are not compatible with standard DVC approaches [280], the reason for that being the fact that the number of voxels per nodal displacement cannot be arbitrarily reduced without additional regularization [101, 280].

The application of boundary conditions is presented in the following for time t , which is not necessarily a time at which a scan was acquired, and for boundary nodes of the FE mesh, which are not necessarily nodes of the DVC mesh. Note that t is an artificial and dimensionless

time linked to the loading steps (*i.e.*, the material behavior is rate-independent). The automatic procedure implemented in the FE code reads:

1. find the two loading steps taken at instants t_a and t_b such that $t_a \leq t < t_b$, with no loading step between t_a and t_b ,
2. read the undeformed DVC mesh and the DVC displacement field at t_a ,
3. perform linear time-interpolation,
4. perform linear (resp. trilinear) space-interpolation by finding for each boundary node of the FE mesh the element of the DVC mesh containing it, and apply linear (resp. trilinear) interpolation inside this element depending on its type.

Operation 1 has linear complexity and negligible cost as the number of loading steps is small. The same remark applies to operations 2 and 3 as the DVC mesh is at least one order of magnitude coarser than the FE mesh (in terms of number of elements). Operation 4, however, requires to localize each node of the FE mesh inside the DVC mesh. Optimized algorithms can be found in the literature to perform such operation in logarithmic time (*e.g.*, by using space partitioning techniques [216]) but were not implemented due to the small size of the DVC mesh compared to the FE mesh. Hence, this operation has a cost proportional to the number of elements in the DVC mesh, and quadratic cost considering it has to be run for all boundary nodes of the FE mesh. This cost would have to be optimized if finer DVC meshes were to be used, especially if those meshes were to have an order comparable to that of the FE mesh.

Last, the displacement field interpolated at the boundary nodes of the FE mesh is prescribed by means of Dirichlet boundary conditions on the whole boundary of the FE domain. Therefore, apart from small differences due to interpolation and remeshing, the boundary of the FE mesh is expected to follow exactly the measured displacement field at each loading steps. The errors that will be measured inside the domain are expected to be mainly due to the mechanical modeling.

6.1.3.3 Constitutive law

As stated in the introduction, graphite nodules are considered as voids in the present computations [266, 267, 268, 269]. These voids are modeled using an isotropic linear elasticity law with very low Young's modulus. With a sufficiently low value, the behavior of a void is obtained. The influence of such penalization technique on void growth was investigated in 2D in previous work at Cemef - MINES ParisTech [5]. This investigation is again carried out for the present 3D computations.

The power law for isotropic hardening of the ferritic matrix was fitted against a stress/strain curve for a purely ferritic material [268]. The obtained values are $\sigma_y = 290$ MPa, $K = 382$ MPa, $n = 0.35$; the Young's modulus $E = 210$ GPa, and Poisson's ratio $\nu = 0.3$.

6.1.3.4 Simulation results

The DVC ROI for which boundary conditions are available is of dimensions up to 532^3 voxels. Finding the largest 3D box included in this ROI and in all ROIs through each loading step was performed manually by launching simulations without meshing any microstructure. Box dimensions were reduced progressively until reaching the above condition. The chosen FE domain is of dimensions $[-245, 200] \times [-17, 200] \times [-245, 245]$ voxels, due to necking in the x -direction and crack opening in the y -direction.

In the following, FE simulation results are presented using this initial domain and, unless otherwise mentioned, DVC boundary conditions using element size 32 voxels and no mechanical regularization. This element size means that each hexahedral element of the DVC mesh is a cube containing $32 \times 32 \times 32$ voxels. Qualitative comparisons with experiments are presented based on 2D slices of the microstructure. Particular interest is given to void volume change (nodules being already replaced by voids in the initial mesh) in order to enable for quantitative comparisons. More precise error measurements are presented in Subsection 6.1.4.

6.1.3.4.1 Mesh generation To show how different meshing parameters can be used in order to capture different scales of the microstructure, three different sets are tested. In the reference configuration $h2$, mesh adaptation parameters are fixed to $h_{min} = 10 \mu\text{m}$, $h_{max} = 50 \mu\text{m}$, $\epsilon_h = 100 \mu\text{m}$, and $h_c = 0.1 \mu\text{m}$. A coarser mesh $h4$ is then obtained by multiplying all these parameters by 2, while a finer mesh $h1$ is based on a division of these parameters by 2. The resulting meshes have 69,010 elements for the coarsest one, 1,857,466 for the finest one, and 387,473 for the reference one.

A sensitivity analysis similar to those presented in Section 3.4 is conducted to check that finer scales are better captured with the finest setting, in the case of nodular cast iron. Therefore, the middle slice of the image is compared to the midsection slice for each obtained mesh in Figure 6.6.

The coarsest result in Figure 6.6(c) gives a rough approximation of the microstructure, while an acceptable description is obtained in the reference mesh (Figure 6.6(b)). Last, no significant difference is observed between the initial image and the finest mesh in Figure 6.6(a) and Figure 6.6(d).

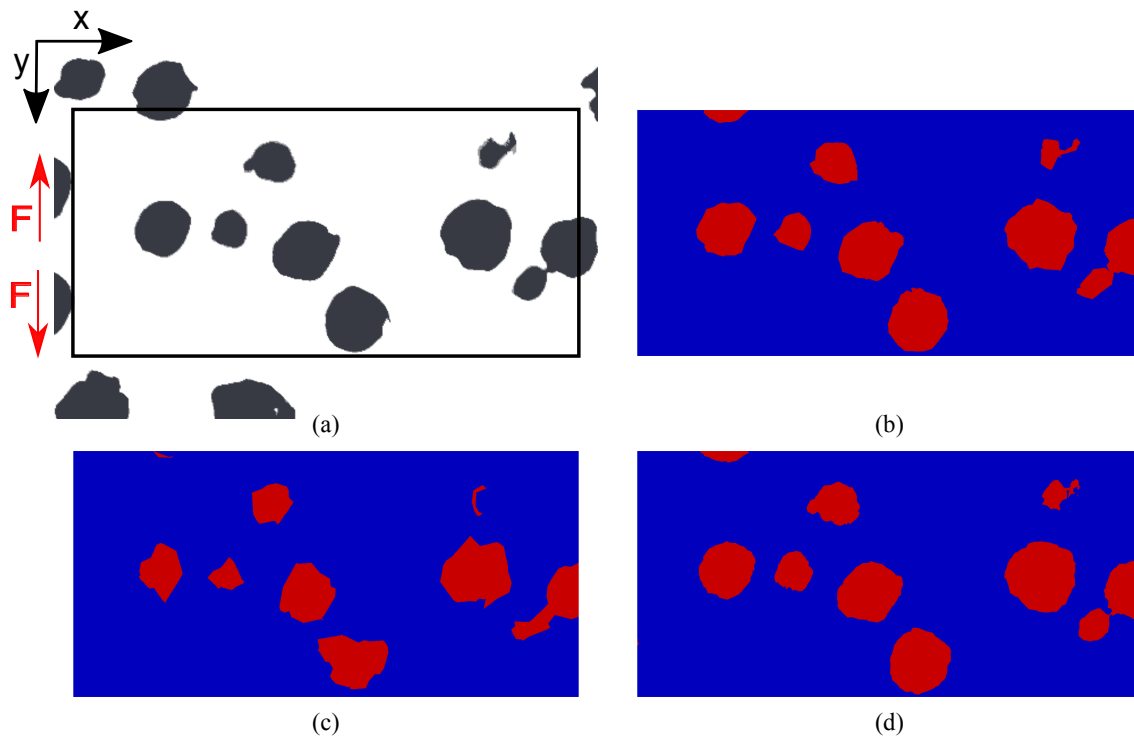


Figure 6.6 – Matrix and nodules at midsection of: (a) the image, (b) the reference mesh $h2$, (c) the coarse mesh $h4$, (d) the fine mesh $h1$.

For FE simulations, mesh quality is of major importance and should be investigated. The quality distribution is presented in Figure 6.7 for the three settings, following the definition in Equation (2.1). Finer meshes induce more elements far from interfaces and render mesh adaptation easier. Therefore, the histogram for the finest mesh is slightly shifted to the right. However, the proportion of elements in the first half of the histogram remains negligible for the three configurations, which proves that accuracy is improved with finer meshes but not at the sacrifice of mesh quality. Though this qualitative comparison suggests to use very fine meshes, it is important to see the influence of these parameters on quantities of interest such as void volume change for example.

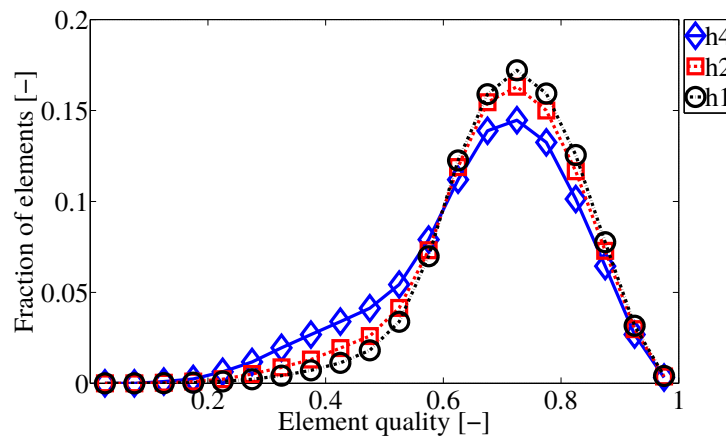


Figure 6.7 – Distribution of element quality at the initial state for the three tested FE mesh settings.

6.1.3.4.2 Choice of numerical parameters To choose appropriate meshing parameters, time step and void penalization coefficient, a sensitivity analysis is conducted.

Meshing parameters are tested using the three meshes defined in the previous section.

Regarding the time step, the reference is identical to that of the reconstructed images, *i.e.*, there are 7 scans, so 6 DVC displacement fields are available and 6 time increments are performed in the FE simulation. Note that scans were not acquired at equidistributed displacement increments as smaller loading steps were performed at the onset of void coalescence (Figure 6.2(b)). A configuration with a time step 10 times smaller is tested (*i.e.*, 60 time increments) to investigate time step influence.

Last, the reference configuration uses a Young's modulus for voids 1,000 times smaller than that of the matrix. A simulation is performed with a penalization of 10,000 to check the influence of this penalization coefficient.

The results are presented in Figure 6.8 in terms of relative void volume change, which is expressed as the void volume divided by the volume of the FE ROI. While the penalization parameter and the time step do not seem to have a significant influence on the results, the mesh size plays a key role. The image import and mesh adaptation methodology introduced in Chapter 3 enable all scales of the initial image to be captured with a finer mesh, and preserve them more efficiently throughout the simulation. Hence, both the initial void volume and its changes during loading are under-estimated with a coarser mesh.

These results suggest that the reference penalization parameter and time step are appropriate for the FE simulations, hence they are used in all following results. However, more accurate error

measurements are necessary to investigate locally the influence of mesh size (Subsection 6.1.4).

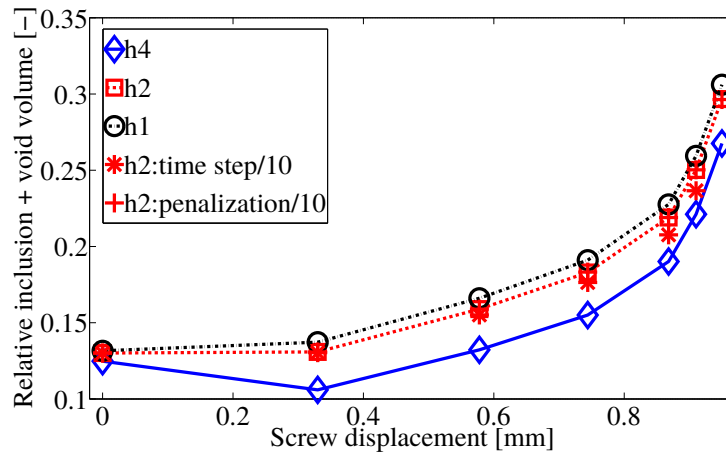


Figure 6.8 – Change of void volume (wrt. total ROI volume) with applied macroscopic displacement for various numerical parameters.

6.1.3.4.3 Discussion To show the interest of the present method linking synchrotron experiments and FE simulations through the use of DVC, it is important to compare the void volume change curves in Figure 6.8 to experimental observations. This is illustrated qualitatively in Figure 6.9, where void growth in the FE simulation using mesh $h1$ is compared with experimental images, while quantitative comparisons are presented in Subsection 6.1.4.

Results in Figure 6.9 suggest that void coalescence is not only due to plasticity, as significant errors can be observed for the last loading steps. Indeed, it is reminded that only a simple von Mises plasticity model with power law hardening is used for the matrix material. It seems that there is either significant matrix softening between neighboring voids, which would imply the presence of a minor void population [137, 248] not captured by X-ray images, or a transition from strained bands to localized fracture of these ligaments.

Inter-void plastic strained bands are clearly visible in Figure 6.10. Comparison with the final crack propagation path in Figure 6.9 reveals the importance of studying more closely the behavior of the matrix in these bands. Crystal plasticity modeling [4] may be important, as grain size in the matrix material is comparable to nodule size [267]. Such discussions are only possible thanks to simulations with real microstructures and measured boundary conditions.

6.1.4 Quantitative comparisons

The whole methodology presented in the previous sections focuses on expressing experiments and FE simulations in the same kinematic space. On the one hand, experimental images are directly exploited by the FE code in order to mesh the initial domain. On the other hand, they are also exploited by DVC in order to compute displacement fields that are then used to drive the FE simulations. In order to check the validity and accuracy of all the computations, these links need to be reversed, as shown in Figure 6.1. The FE simulation results should be compared both against experimental images obtained during loading and measured displacement fields as well. Regarding the validation of DVC measurements, it is common practice to study correlation residuals (Paragraph 6.1.2.2.3), namely, the deformed experimental volumes are corrected using the measured displacement field and compared to the actual reference volume. This operation can

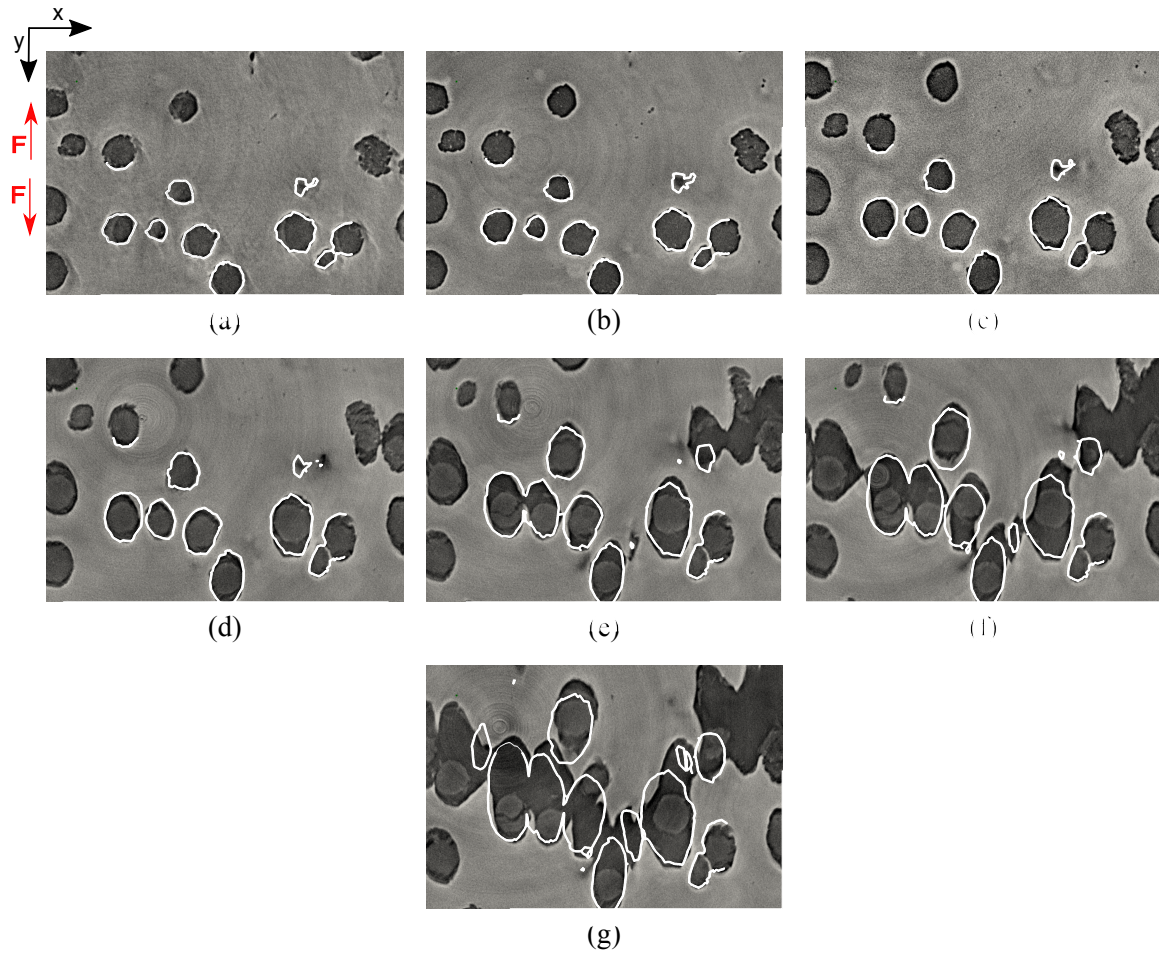


Figure 6.9 – Comparison between the void/matrix interface obtained by the FE simulation (thin white line) and the experimental images at a macroscopic displacement of: (a) $0\ \mu\text{m}$, (b) $330\ \mu\text{m}$, (c) $578\ \mu\text{m}$, (d) $744\ \mu\text{m}$, (e) $868\ \mu\text{m}$, (f) $910\ \mu\text{m}$, (g) $950\ \mu\text{m}$.

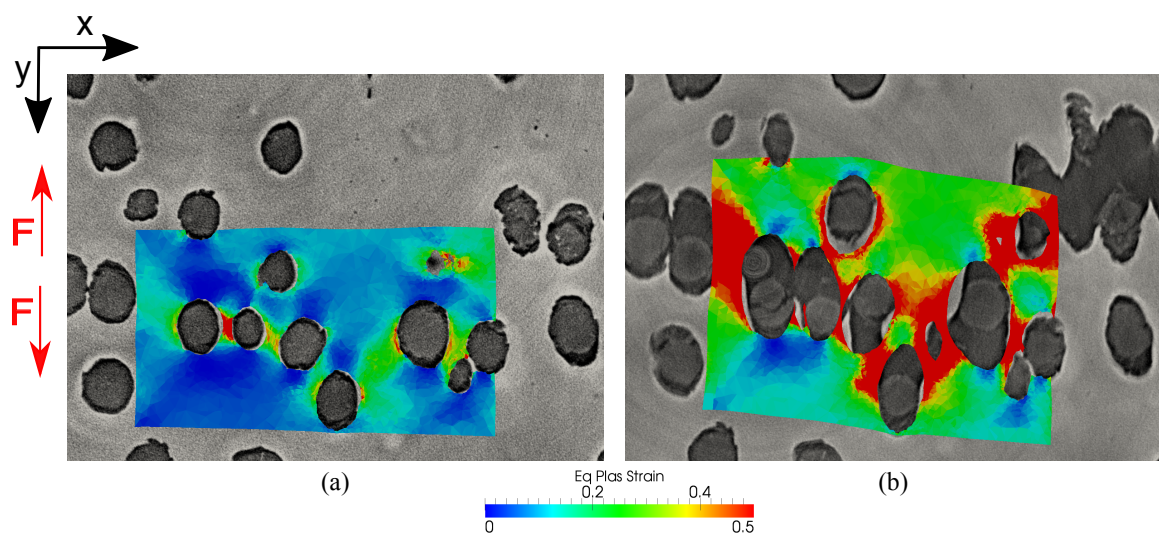


Figure 6.10 – Equivalent plastic strain obtained by the FE simulation superimposed with experimental images at a macroscopic displacement of: (a) $578\ \mu\text{m}$, (b) $910\ \mu\text{m}$.

also be applied to the displacement fields obtained by the FE simulation, *i.e.*, compute gray level residuals for the FE kinematic fields by correcting reconstructed volumes. The corresponding DVC and FE gray level residual fields can then be compared.

DVC displacement fields are applied to the boundaries of the FE domain, but they are also available inside the domain. Hence, DVC and FE kinematic fields can also be interpolated on the same mesh and directly compared.

In the following, displacement fields obtained by DVC are interpolated on the corresponding FE mesh (*i.e.*, unstructured tetrahedral mesh). The meshes are shown in Figure 6.11. The FE domain, which needed to be reduced compared with the DVC ROI for the reasons outlined in Paragraph 6.1.2.2.2 and Paragraph 6.1.3.1, contains the fine mesh h_2 adjusted to the microstructure details as opposed to the structured and coarse DVC mesh.

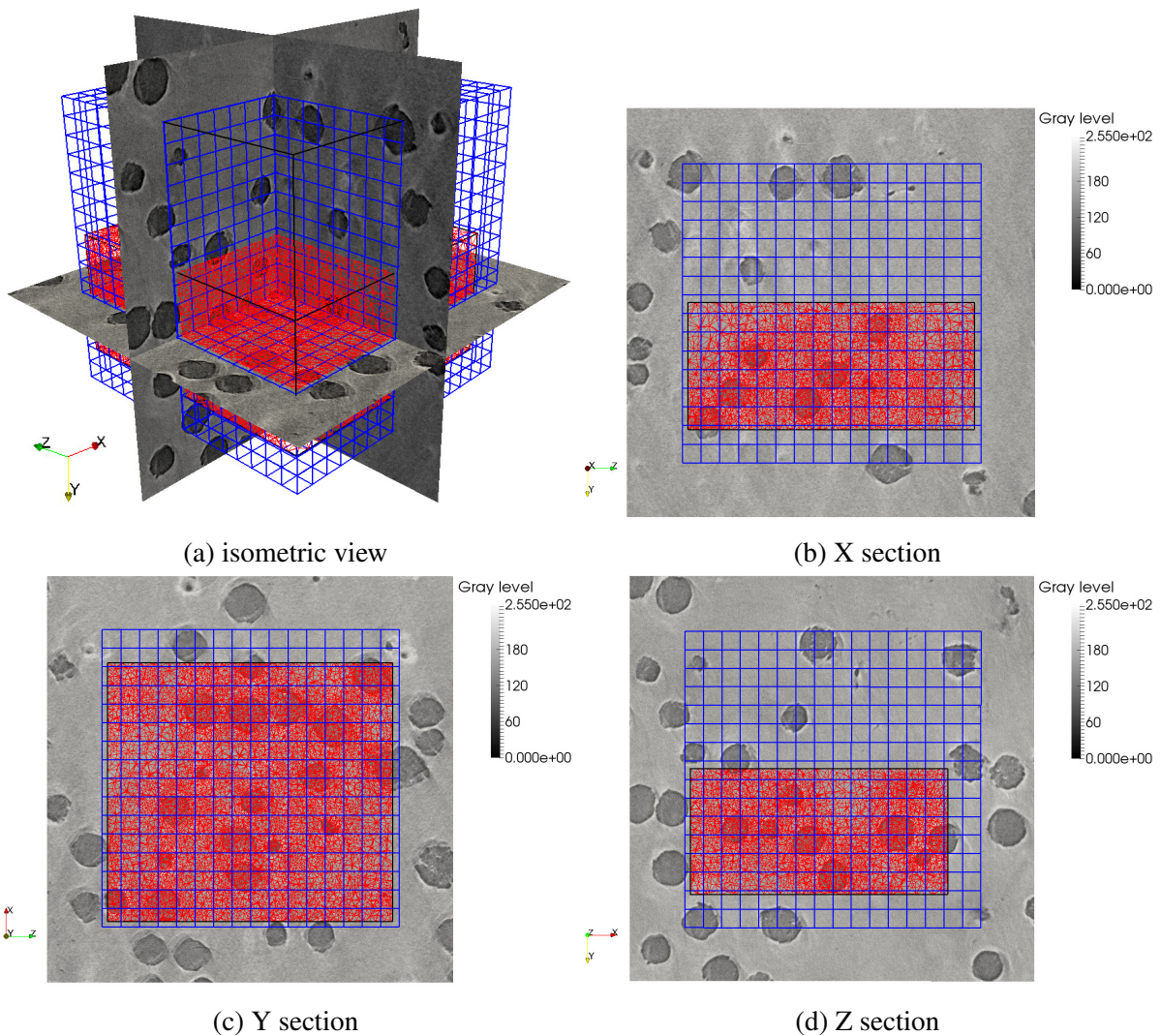


Figure 6.11 – (a) DVC (blue) and FE (red) meshes plotted over the corresponding cast iron microstructure in (a) isometric view and (b-d) sections normal to X , Y and Z axes.

The original FE and DVC interpolated displacement fields are then subtracted yielding the displacement difference field. The displacement fields and their difference are shown in Figure 6.12 for the third loading step on the section normal to the y -direction. The displacement field magnitude shows good match between the two solutions, which is to be expected since measured

boundary conditions are prescribed. The field differences mainly occur in areas close to the nodules (Figure 6.12(c)).

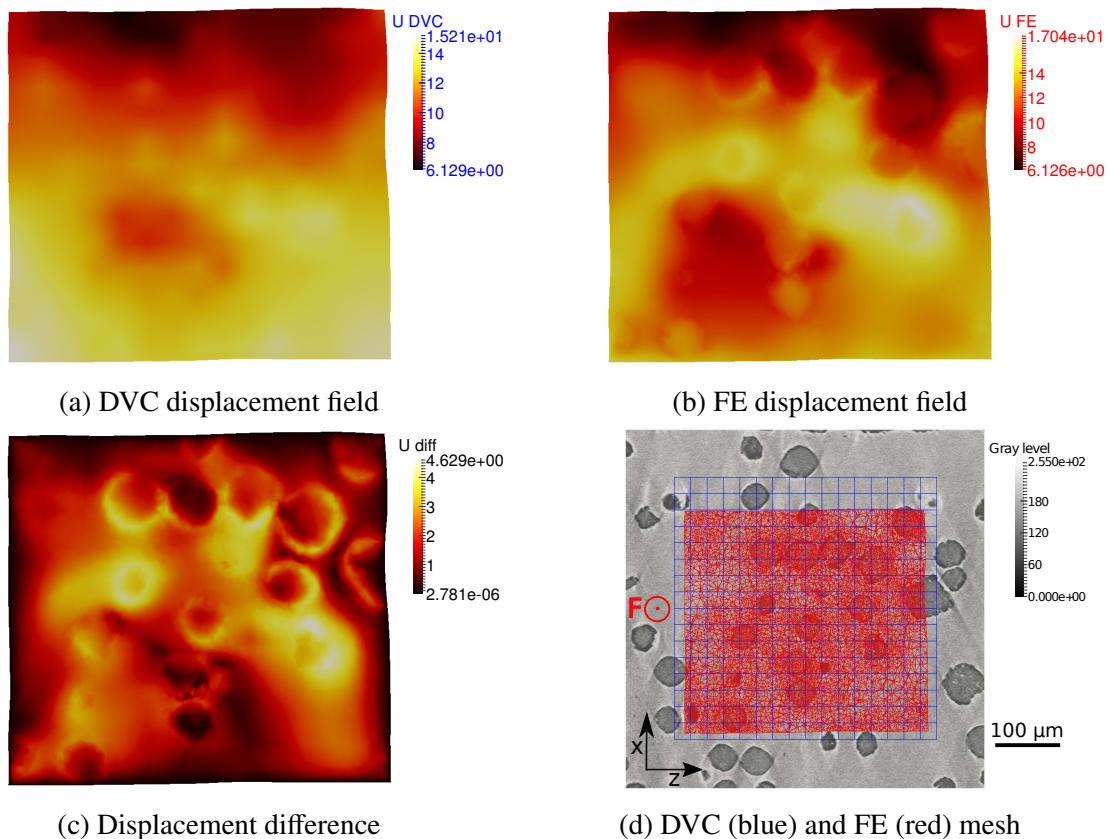


Figure 6.12 – Section normal to y -direction: (a) DVC displacement field magnitude, (b) FE displacement field magnitude, (c) absolute difference between them and (d) DVC and FE meshes for the third loading step. All reported values are expressed in voxels ($1\text{ voxel} \leftrightarrow 1.095\ \mu\text{m}$) and correspond to the FE mesh h_2 .

The displacement difference is characterized by the mean and standard deviation values for the three directions. They are shown in Figure 6.13. It is interesting to normalize standard deviations with the corresponding DVC displacement uncertainty (Figure 6.13(b)). The displacement differences deviate more than the measurement uncertainty meaning the current DVC and FE results are not fully consistent. However, it is worth noting that for the first four steps the differences remain rather small (*i.e.*, less than 5 times the standard displacement resolutions). Conversely, for the last loading step, the agreement is less good. This is due to the fact that significant void growth has occurred (Figure 6.9) and is not fully captured either by DVC or FE simulations.

The influence of the mesh size used in the FE computations is reported in Figure 6.14 using the three settings defined in Paragraph 6.1.3.4.1. The diagrams are showing (a) mean and (b) standard deviation of the displacement differences between measured (via DVC) and FE simulations. The results show there is no significant influence of the mesh size when compared to DVC results. Interestingly, for the last two loading steps, the difference between the three FE simulations increases. This is a further indication that localized phenomena occur and that the FE discretization becomes sensitive to such events.

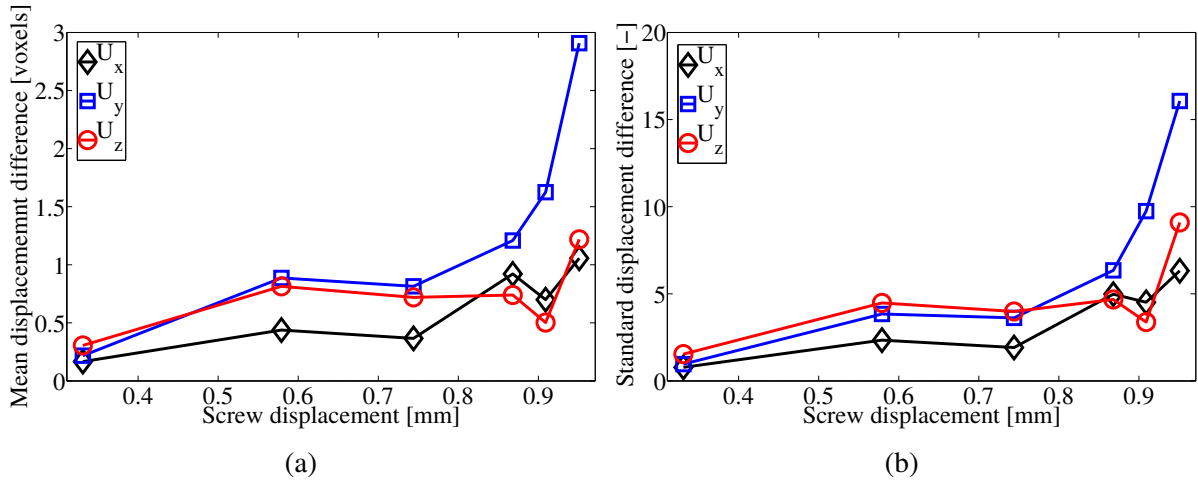


Figure 6.13 – (a) Mean values and (b) standard deviations (in %) of the difference between the measured simulated displacement fields for the FE mesh h_2 . Standard deviations are normalized by the corresponding DVC uncertainties.

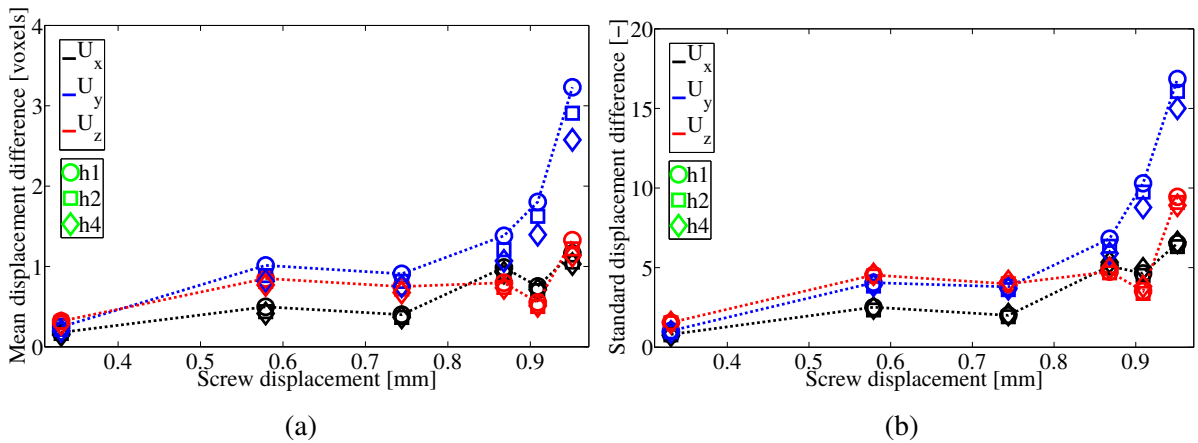


Figure 6.14 – (a) Mean values and (b) standard deviations (in %) of the difference between the measured and simulated displacement fields for different FE mesh sizes. Standard deviations are normalized by the corresponding DVC uncertainties.

Although assessing displacement differences is an interesting piece of information, it is not an objective way of validating FE simulations since the meshes are different in DVC calculations and FE simulations (Figure 6.11). In the following it is proposed to use gray level residuals to compare all results even though the experimental solution is unknown. To validate DVC results, corrected deformed volumes \hat{g} are computed by resorting to measured displacement fields. The same procedure is followed by computing gray level residuals with FE computed displacement fields. The tetrahedral mesh together with the computed displacement values are imported into a newly developed tetrahedral-DVC code [283, 284]. By using the linear shape functions the displacement results are interpolated voxel-wise and the corresponding deformed volume $g(\mathbf{x})$ is corrected by the computed displacement field $\mathbf{u}_{FE}(\mathbf{x})$. The gray level residuals, namely, differences between the reference volume $f(\mathbf{x})$ and corrected deformed volume $g(\mathbf{x} + \mathbf{u}(\mathbf{x}))$ can then be compared for DVC and FE computations.

This procedure is illustrated in Figure 6.15 for the third loading step. The microstructure

section in the reference and deformed states is shown in addition to their raw difference. The latter shows that the motion of the nodules is not accounted for. Figure 6.15(d-e) shows the gray level residual after correcting with the displacement fields measured via DVC and computed with the FE simulation with h_2 mesh. When compared with Figure 6.15(c) it is concluded that DVC and FE results are close to the experiment.

There still are some very small areas close to the nodules interface that are not properly captured by the measured and simulated fields. On the DVC side, this is an indication that debonding has occurred and the displacement continuity associated with the DVC mesh is violated. On the FE side, the hypothesis that the nodules can be approximated by voids may be a possible cause for this difference. The constitutive model chosen for the matrix at this scale and the corresponding material parameters could be additional reasons.

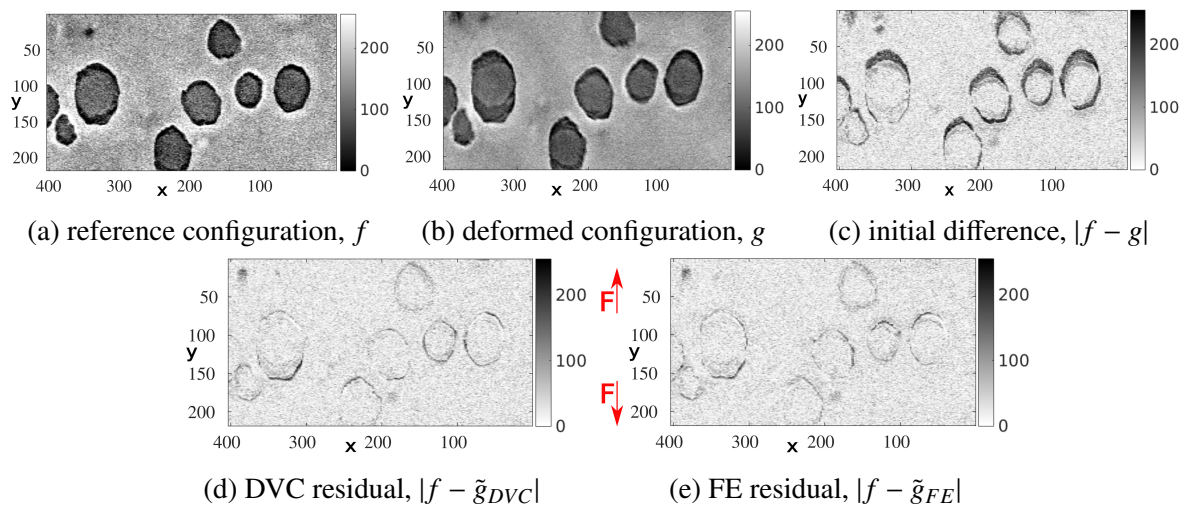


Figure 6.15 – Microstructure section in the (a) reference and (b) deformed states. Absolute gray level differences between the two initial states (c) and after correction with DVC (d) and FE (e) displacements (obtained on h_2 mesh) for third loading step.

The results of Figure 6.15 indicate that DVC and FE results are very close in terms of gray level residuals. This is confirmed by reporting the standard deviations of the residual fields for all the analyzed loading steps (Figure 6.16). These curves are plotted together with the corresponding residuals from the uncertainty analyses of the first and fourth loading steps. First, the DVC and FE residuals have very similar levels for the whole history even though the discretizations are very different. This is mainly due to the fact that measured boundary conditions have been applied to the numerical model. As the screw displacement is increased, the two residuals depart from those observed for the uncertainty analysis. This is an indication that the measured and computed displacements are no longer able to capture all the complex phenomena taking place. Model errors are therefore to be expected. On the DVC side it is related to the coarse and continuous hexahedral discretization.

The influence of the FE mesh is evaluated in Figure 6.17. There is no significant influence of the mesh size on the gray level residuals. The three meshes can be used in the present analyses since they lead to virtually identical global residuals. This last result shows that on the FE side the origin of higher residual is due to the constitutive model that is no longer able to fully capture all the strained bands preceding coalescence mechanisms.

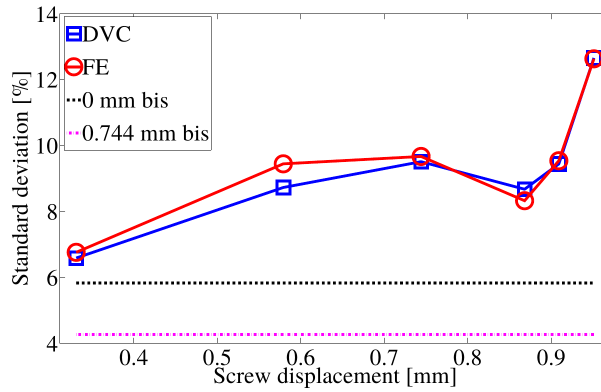


Figure 6.16 – Standard deviation for the dimensionless gray level residual fields for all loading steps (FE results obtained with h_2 mesh). The standard deviations obtained for the repetition scans (0 mm bis) and rigid body motion scans (0.744 mm bis) are given for comparison (Paragraph 6.1.2.2.3).

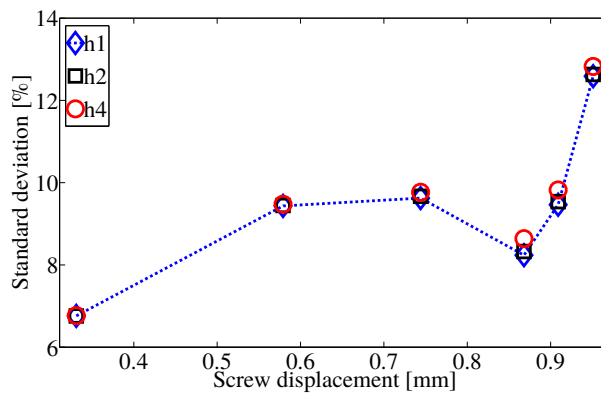


Figure 6.17 – Standard deviation gray level residuals for all loading steps with three different FE discretizations.

From the previous results (Figure 6.16) it is concluded that the FE solution driven by the DVC boundary conditions is close to the DVC measurements, *i.e.*, both yield similar gray level residuals. This result validates the whole numerical procedure. However, it does not necessarily validate the constitutive model since up to now only kinematic fields were probed. Error measurements based purely on kinematic data may not be sufficient because all 6 faces of the FE ROI are constrained. Hence, static data should also be involved in the analysis. This procedure requires the knowledge of stress profiles along the sample ligament to be able to compare experimentally measured macro-forces and calculated static responses from FE simulations on microscopic level (FE ROI scale). A sensitivity analysis regarding FE ROI size should also be considered, because a larger FE ROI would reduce the influence of DVC boundary conditions and may increase errors in FE simulations (Section 6.2).

6.1.5 Conclusion

In this section an innovative validation procedure combining synchrotron laminography, digital volume correlation and FE simulations on the microscale level has been presented (Figure 6.1). Experimental data, namely, reconstructed volumes are collected via laminography and load levels while performing a tensile test on a flat specimen of nodular cast iron with a central hole. Bulk

kinematic fields in the region close to the central hole are measured via DVC. Since high strain levels occur between subsequent scans regularized approaches to DVC are to be used to converge. A stepwise relaxation procedure has been followed ending with unregularized solutions.

The FE mesh is adapted to the real microstructure under the assumption that graphite nodules are considered as voids thanks to the developments presented in Chapter 2 and Chapter 3. The FE simulations are driven by Dirichlet boundary conditions extracted from DVC measurements on all 6 surfaces of the analyzed domain. The results obtained from DVC registrations and FE simulations are then mutually and separately compared with respect to the available experimental information.

DVC results are validated based on correlation residuals, and gray level residuals. The areas of higher residuals correspond to the position of the debonding zones that appear very early on. This is expected as the hexahedral mesh used for DVC computations enforces a continuity constraint on kinematic solutions, which is violated when debonding occurs.

Once validated, DVC measurements are used to drive FE simulations. Added to the fact that the real microstructure is discretized in the FE mesh, heterogeneous displacements prescribed by DVC rely extensively on the robustness of the mesh adaptation methodology developed in the present work (Chapter 2). The latter enables simulations to be performed with significant void growth up to coalescence. While microstructures are often idealized in the literature, these promising results confirm the new possibilities opened by the present developments for numerical modeling of complex 3D microstructures having a complex morphology and undergoing large deformations and complex topological events such as those observed in reality.

DVC and FE results are then compared by direct comparison of the full-field solutions and computation of the gray level residuals. The first method, giving a relative comparison, provides the gap between DVC and FE kinematic fields. It is shown that differences between the two methods are mainly concentrated in the bulk of the inspected region around the nodules, while boundary zones have mostly zero differences because the boundary conditions are measured via DVC.

However, just observing the displacement difference between the two methods does not yield an absolute error. Conversely, the gray level residuals can be computed independently for both approaches. The kinematic fields are probed by computing the deformed volume corrected by the measured or simulated displacement fields. There are, on average, no significant differences between DVC and FE residual fields. Most of them are concentrated around graphite nodules. The small magnitude of the differences between DVC and FE residual fields may be influenced by FE ROI size, which has not been varied in the present section. A larger FE ROI is considered in the following section.

To the authors' best knowledge this is the first time 3D calculations are performed on a real microstructure and by using measured boundary conditions up to large plastic strain. This approach will enable better understanding and modeling of fracture mechanisms at microscale levels. Its interest with respect to other approaches is emphasized in the following section.

6.2 Comparison with other methods

6.2.1 Introduction

As mentioned in the introduction of this chapter, other approaches have been used in the literature to validate ductile fracture models with respect to 3D full field experimental data.

- The most straightforward approach is Direct Numerical Simulation (DNS), where the microstructure of the whole specimen has to be meshed, hence taking into account only microscale constitutive models. Since the whole specimen is simulated, boundary conditions are applied directly at pins, as in the experiment. However, for the specimen considered herein, DNS would have a huge cost regarding both experiments and simulations. Scanning the whole specimen would require multiple scans at each loading step, and this large set of 3D data would then have to be meshed.
- To avoid this huge computational cost, full specimen FE simulations taking into account the microstructure only partially have been considered [86, 248, 258, 263, 264, 265]. In these embedded cell methods (Subsection 1.2.2), microscale constitutive models are used in the ROI where the microstructure is meshed, while homogeneity is assumed in the remainder of the specimen. Thus, an appropriate macroscale constitutive model has to be defined and identified for this out-of-ROI homogeneous material. This approach will be referred to as strong FE (sFE) in the following.
- Opposed to the previous approach, where the ROI mesh is directly embedded in the specimen mesh, the two FE calculations can be weakly coupled. In this weak FE (wFE) approach [18, 82, 262], the specimen scale simulation assumes a homogeneous material in the whole domain. A relevant mechanical field is then transferred from this first simulation to a second simulation at the ROI scale, where the microstructure is meshed. This mechanical field defines the boundary conditions for the micromechanical simulation. As detailed in Subsection 1.2.2, these can be static, kinematic, or a combination of both.
- The method introduced in Section 6.1, referred to as DVC-FE in this section, which has the main advantage that no macroscale constitutive model is required, thus the computational cost remains reasonable as only the ROI is meshed.

The present section aims at showing the interest of the DVC-FE approach by comparisons with standard methods. This investigation is conducted with new experimental results using nodular cast iron specimens with a geometry inspired from Ref. [85]. A first test (A) was performed using small loading steps in order to obtain accurate force measurements and 2D surface images to be exploited thanks to global DIC. The second test (B) was performed using larger loading steps since it was conducted in a synchrotron facility. For this second test, both 3D X-ray scans of the ROI and 2D surface images were acquired (Figure 6.18).

While the DVC-FE methodology presented above uses directly and solely the 3D X-ray data, the two alternatives to obtain boundary conditions for ROI calculations considered in this section (*i.e.*, wFE and sFE) rely on force measurements and 2D surface images. Force measurements are used to identify the behavior of the material at the specimen scale, as well as 2D surface images thanks to a recent Integrated-DIC technique [91]. In the wFE method, an FE simulation of the experiment at the specimen scale is conducted, and calculated displacement fields are used to drive a second FE calculation at the ROI scale. In the sFE method, the ROI is embedded

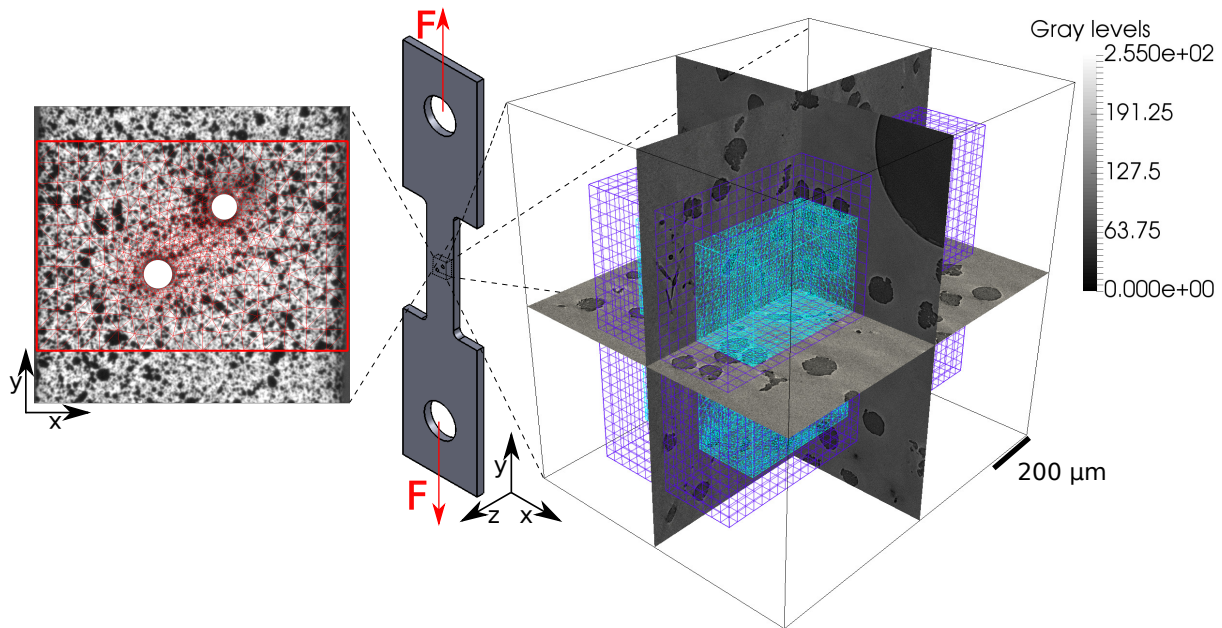


Figure 6.18 – Schematic view of the sample with zoomed region between the holes showing on the right: DVC (blue) and FE (cyan) meshes plotted over the corresponding cast iron microstructure in isometric view. On the left: surface image with speckle pattern and DIC mesh from test (B).

and meshed directly inside the specimen mesh and only one FE simulation is conducted. In this second method, the material behavior is modeled using microscale constitutive models in the ROI, while macroscale constitutive models are used in the rest of the domain.

The studied material is the same as in Section 6.1, only specimen geometry is changed (Figure 6.19). Similarly, graphite nodules are considered as voids in the initial microstructure, so that no void nucleation models are necessary in this section.

The aforementioned approaches with weak (wFE) and strong (sFE) couplings between specimen and ROI calculations are applied to a real 3D microstructure observed thanks to 3D *in-situ* SRCL experiments. The results are then compared to those obtained using the DVC-FE approach [44], showing the interest of this methodology. Details regarding the new experiments are presented in Subsection 6.2.2, while the technical implementation of each approach for boundary conditions is described in Subsection 6.2.3. The results are presented and compared based on error measurements with respect to experimental images in Subsection 6.2.4.

Since the present work focused exclusively on FE simulations and micromechanical modeling, all details regarding the experiments and DVC can be found in the published version of this section [42].

6.2.2 Experiments

The specimen geometry, inspired by the work of Weck et al. [85] is shown in Figure 6.19.

Test (A) was conducted as a pre-test for test (B) to study in detail the particular sample behavior (*i.e.*, to assess the load levels for the scanning procedure). Therefore, identical sample geometry and material were used for test (B). The load/displacement curve for test (A) is shown in Figure 6.21(b).

For test (B), the SRCL procedure was identical to that already described in Subsection 6.1.2, though a recent GPU code helped accelerate significantly the 3D reconstruction step [285]. The reconstructed volume has a size of $1600 \times 1600 \times 1600$ voxels. The physical size (length) of 1

cubic voxel is equal to $1.095 \mu\text{m}$. After scanning the undeformed state (0), additional 12 scans are acquired during the step-wise loading procedure, where the last scan corresponds to the fully opened final crack.

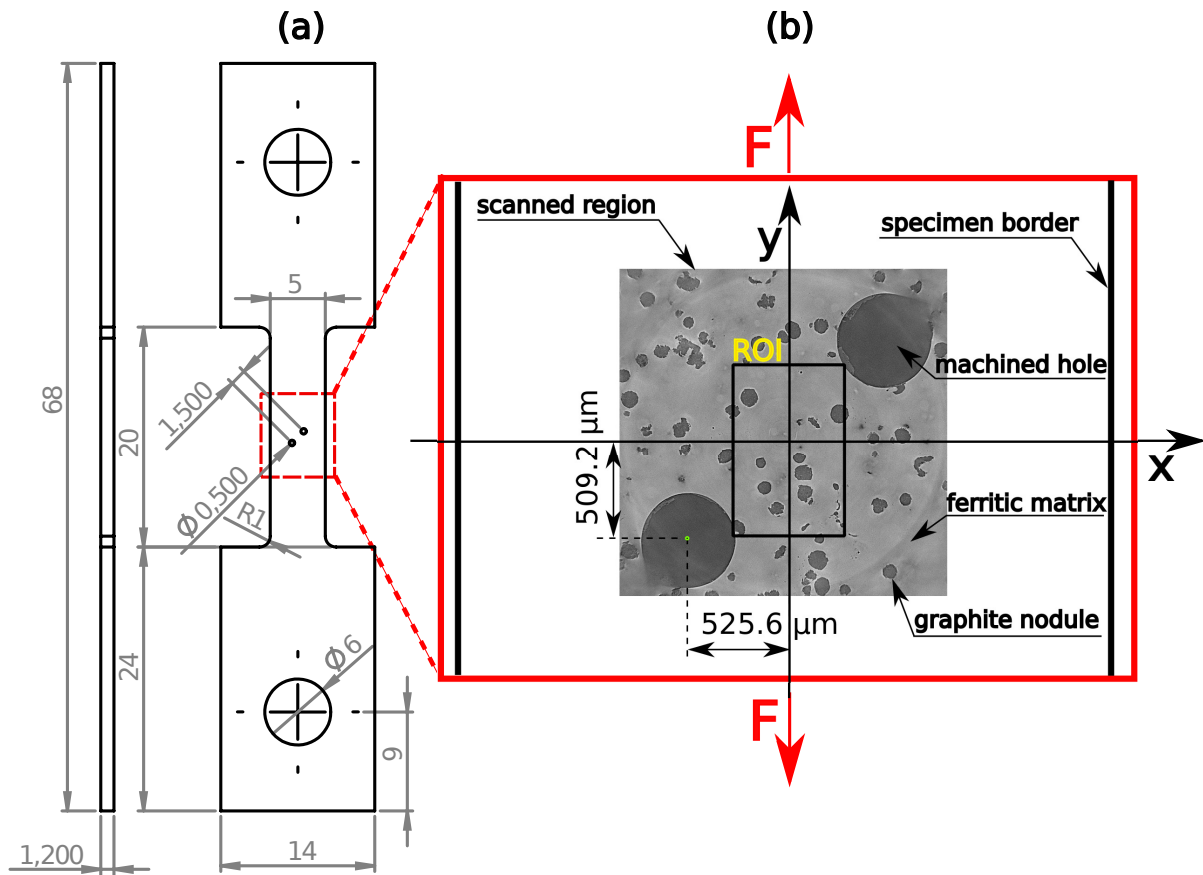


Figure 6.19 – (a) The sample geometry with the scanned region between the pin holes; (b) section of the reconstructed volume with ROI position.

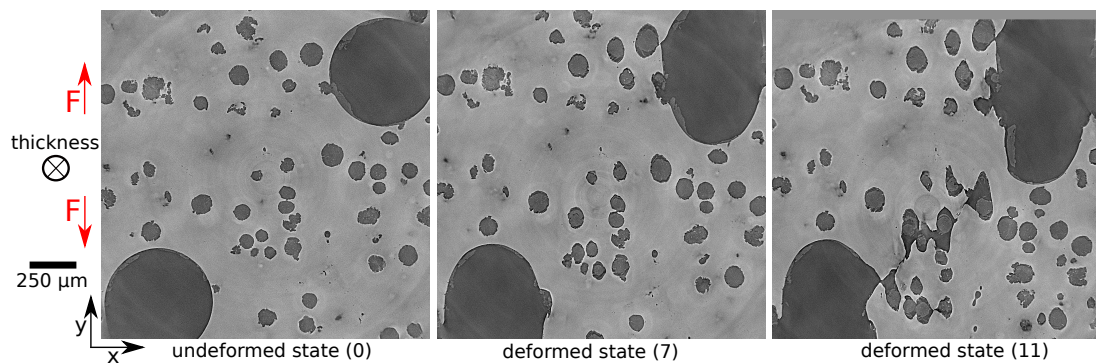


Figure 6.20 – The midthickness section of the reconstructed volume for three different loading steps.

The scanned region incorporates two holes while the ROI employed in DVC and FE calculations is mainly concentrated in the ligament between the holes (Figure 6.18 and Figure 6.19). Since the two machined holes have diameters of $500 \mu\text{m}$, the nodule population (treated

as voids in the FE calculations) in the ligament area with the characteristic size of $60\ \mu\text{m}$ can be considered as a secondary void population. Hence, subsequent concurrent micro and macro plasticity and damage localization phenomena can be observed.

In Reference [85], the authors used machined holes of micrometer size, which made impossible the observation of the secondary void population (this limitation on the size of observable voids is actually due to current imaging techniques [286]). In the present case, the larger size of the holes, and the large size of the graphite nodules allow for such observations.

This is illustrated in Figure 6.20 where mid-thickness sections of the reconstructed volume for the three different load stages are shown. As a consequence of the mentioned multiscale flow conditions, classical void coalescence mechanisms are accompanied by sheet coalescence between the two machined holes that is observed in the last loading step.

6.2.3 Boundary conditions

The first two procedures for boundary conditions presented in this section, namely DVC-FE and wFE, consist in computing displacement fields and then applying these displacement fields as Dirichlet boundary conditions on the whole boundary of the FE mesh of the ROI. The third procedure, namely sFE, consists in a single step where the ROI is already being computed. The three approaches and their implementation are detailed hereafter. Regarding the numerical methods, micromechanical models, and material properties for the matrix that are used inside the ROI, they are the same as those used in Section 6.1.

6.2.3.1 Digital Volume Correlation - Finite Element technique

The DVC method does not differ from that described in Paragraph 6.1.2.2. However, because a larger DVC ROI is used in this section (Figure 6.19), original reconstructed volumes are *a priori* coarsened, *i.e.*, each 8 neighboring voxels are averaged to form one supervoxel. By doing this, file sizes are decreased by a factor of 8 and the overall gradient of gray level fields is more favorable since the ferritic matrix itself is a low contrast material where DVC registration is difficult.

The same DVC uncertainty assessment carried out in Paragraph 6.1.2.2 yields a standard displacement resolution of 0.25 supervoxel for a DVC element size of 16 supervoxels (*i.e.*, 32 voxels) for all three directions.

6.2.3.2 Identification of macroscale material parameters

Both wFE and sFE methods require the identification of material parameters $\{\mathbf{p}\}$ based on experimental measurements acquired during test (A). In the case of wFE, these material parameters are used in the whole domain for the calculation at the specimen scale of test (B). In the case of sFE, these parameters are only used for the homogenized out-of-ROI material, while microscale material parameters are used inside the ROI.

The identification of material parameters can be performed only using force measurements, or using both force measurements and 2D surface images. The two approaches are detailed hereafter.

6.2.3.2.1 Static data A first identification is conducted using standard global optimization methods [90, 287], where the objective function is defined as [92]

$$E(\mathbf{F}(\mathbf{u})) = \frac{\sqrt{\int_0^U (\mathbf{F}(\mathbf{u}) - \mathbf{F}^{exp}(\mathbf{u}))^2 d\mathbf{u}}}{\sqrt{\int_0^U \mathbf{F}^{exp}(\mathbf{u})^2 d\mathbf{u}}} \quad (6.1)$$

where the forces obtained in an FE simulation \mathbf{F} are compared with the sum of reaction forces measured during the experiment \mathbf{F}^{exp} , with an integral on the loading path $[0, U]$. Therefore, only static data acquired during test (A) are taken into account. Note that the displacement \mathbf{u} , and all displacements mentioned in this section, are measured via 2D DIC [278, 279, 288]. These values were determined directly at the upper and lower parts of the mesh presented in Figure 6.21(a). The force/displacement curve based on measurements and simulations is shown in Figure 6.21(b). The experimental data were acquired up to final failure, but the last loading steps of test (B) were discarded for this inverse analysis because no micromechanical simulation is carried out up to final failure in Subsection 6.2.4. The force/displacement curves show that the numerical approximation is very good, but only the macroscopic force is compared. Local measurements are considered in the sequel.

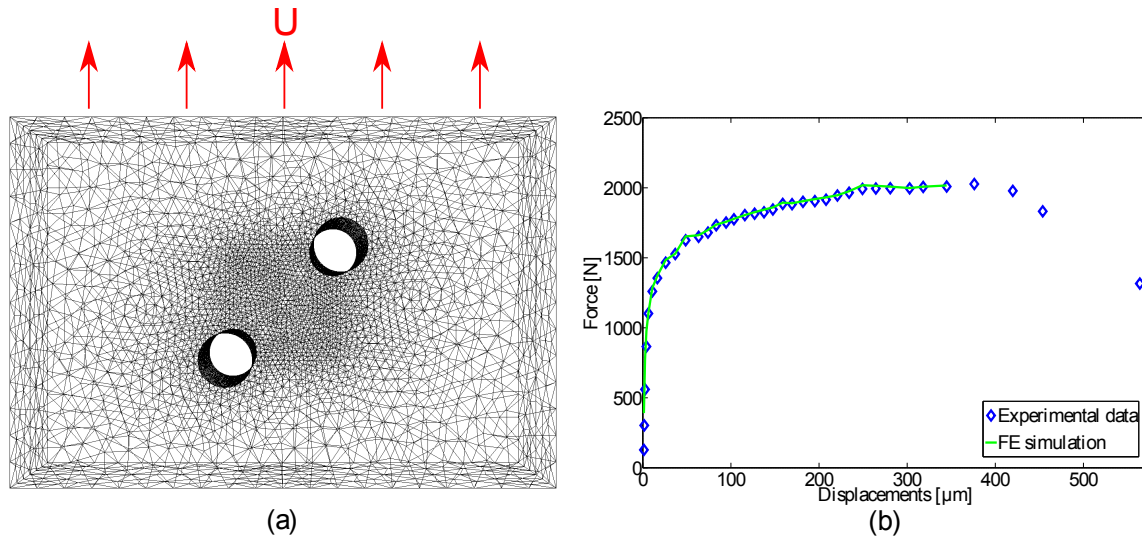


Figure 6.21 – Identification of macroscopic material parameters based on static data of test (A): (a) mesh used for specimen scale calculations, (b) comparison between the simulated force/displacement curve and experimental data.

6.2.3.2.2 Static and kinematic data In order to obtain more realistic material properties more advanced identification techniques can be considered. In Integrated-DIC or DVC [91, 284, 289], both kinematic (*i.e.*, 2D surface images from test (A)) and static (*i.e.*, force measurements from test (A)) data are taken into account. This technique (not detailed here) requires displacement fields to be fully mechanically admissible, *i.e.*, satisfy equilibrium for the chosen constitutive law.

The Integrated-DIC code used herein is a Matlab implementation with C++ kernel (Correli 3.0 [283]) while the accompanying FE simulations are performed using the commercial package Abaqus/Standard. More details about mechanical correlation can be found in Reference [284]. Due to very low sensitivity the Poisson’s ratio had to be fixed in Integrated-DIC to its initial value of 0.28 while the other elasto plastic parameters have been identified.

Material parameters obtained using both identification procedures are given in Table 6.1. Though these parameters may seem to differ notably, the influence of this difference is significant only at low (< 0.2) and very large (> 1) equivalent plastic strain, the latter not being experienced herein. Note that elastic strains are not significant. Hence, the results are not expected to strongly depend on the choice of identification procedure, apart from the first loading steps.

Method	E (GPa)	ν	σ_y (MPa)	K (MPa)	n
Static data	187	0.28	64.4	524	0.19
Integrated-DIC	136	0.28	216	408	0.331
Matrix	210	0.3	290	382	0.35

Table 6.1 – Elasto plastic properties of nodular cast iron obtained using inverse analysis on test (A), first based only on static data, and then also on kinematic data thanks to Integrated-DIC. Material parameters used for the matrix material in micromechanical simulations are reminded in the third line.

6.2.3.3 Weak Finite Element technique

In the wFE technique, a first macroscopic simulation of test (B) has to be conducted at the specimen scale. The material is considered as homogeneous and modeled using the same elasto-plastic model with the power law hardening defined in Equation (4.10) and the two sets of material parameters given in Table 6.1. Since specimens used in tests (A) and (B) had identical geometries, the same mesh as in Figure 6.21(a) is used. The displacement field between each consecutive loading step where 3D X-ray scans were acquired is stored in the reference configuration. These displacements are then interpolated at the boundaries of the ROI during a second FE simulation at the microscale by means of linear interpolation (both meshes being exclusively composed of tetrahedra).

6.2.3.4 Strong Finite Element technique

In the sFE method, a single FE simulation is carried out. This simulation uses a mesh similar to that shown in Figure 6.21(a), with the difference that this time the mesh incorporates the ROI with its microstructure. In the ROI, the material properties correspond to a two-phase matrix/voids material (third line of Table 6.1), while in the rest of the specimen the two sets of material properties given in the first lines of Table 6.1 are considered. Compared to other approaches, this method adds significant computation time, as illustrated by the used mesh of ≈ 1.5 million elements in Figure 6.22. However, it has the advantage that ductile fracture can be studied simultaneously at two scales.

6.2.4 Results

In this subsection, results using the DVC-FE approach are first presented and discussed, as comparisons with experiments are qualitatively and quantitatively possible. Then, comparisons with other approaches are proposed.

6.2.4.1 Digital Volume Correlation - Finite Element coupling

The results using the DVC-FE approach are shown in Figure 6.23, where both void growth and plastic strain are observed. This computation included 100 voids meshed with ≈ 1 million

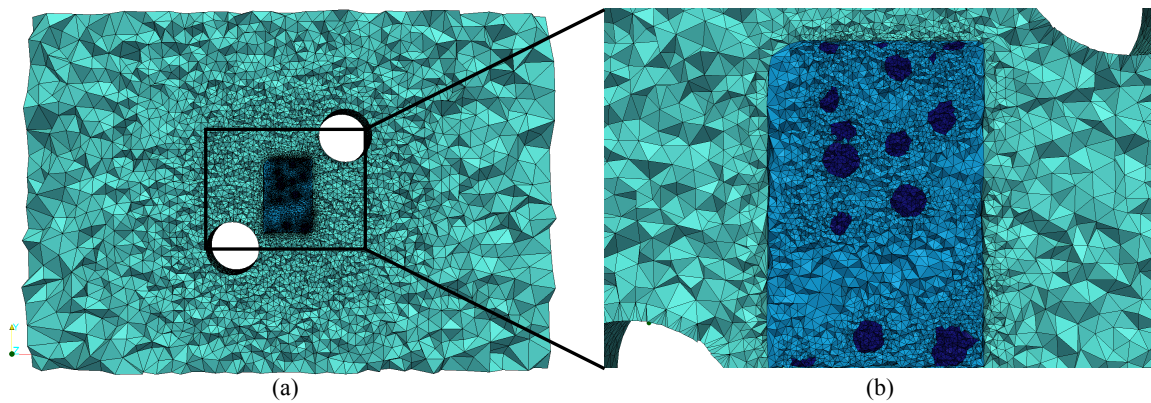


Figure 6.22 – Inside view of the mesh used in sFE calculations: (a) full specimen, (b) zoom on the ROI. The three shades of blue represent, from lighter to darker, the homogenized out-of-ROI material, the matrix, and the graphite nodules (idealized as voids).

elements. The simulation was performed in less than 3 h using 40 Central Processing Units (CPUs). This quite low computation time is very promising in the prospect of applying inverse analyses at the microscale to identify micromechanical properties, especially regarding coalescence modeling.

This is helped by the fact that DVC avoids the requirement of meshing the whole specimen, as in a DNS. In the present case, considering the ratio between the volume of the out-of-ROI material and the volume of the ROI in Figure 6.22, the number of elements that a DNS calculation would require can be estimated at ≈ 100 million elements. Although such calculation is not conducted herein, the aforementioned computation time shows that it could be conducted in the very near future, at least regarding the numerical part, thanks to the numerical methods and parallel computing capabilities demonstrated in this work. However, the DVC-FE approach is, by far, more efficient, as only the DVC ROI has to be modeled in the FE simulation.

Regarding the results obtained with the DVC-FE method, errors can be assessed first qualitatively, for example by comparing the Z midsection of the ROI with experimental images, as shown in Figure 6.24. Since the DVC boundary conditions are expected to follow the experimental images, the matrix/void interfaces in the simulation (in white in the figure) can be superimposed on these images and compared. This figure reveals that interfaces are overall very accurately meshed and tracked during the simulation, up to the last loading step. However, there is an irregularity in the material, namely a non spherical void in the top left region of Figure 6.24. In the undeformed state, this defect is already poorly captured by the meshing technique due to its very small size, and this error accumulates during loading. This figure shows that void growth in the simulations compares well with what is observed in X-ray images.

As presented in Subsection 6.1.4, thanks to the present framework, local comparisons are possible. This is shown in Figure 6.25 as standard deviation of residual fields (normalized by dynamic range of the volume, *i.e.*, 256 gray levels) for DVC and DVC-FE calculations.

It is reminded that theoretically, the DVC-FE curve is not expected to be below the DVC one, since the latter is used to drive the former. The error produced by micromechanical models inside the DVC-FE domain is low and it slightly increases at late loading steps (from $\approx 15\%$ initially to $\approx 20\%$ in late loading steps). A look at the Z midsection in Figure 6.26(a-b) reveals that these differences between simulations (DVC-FE) and experiments (DVC) are concentrated

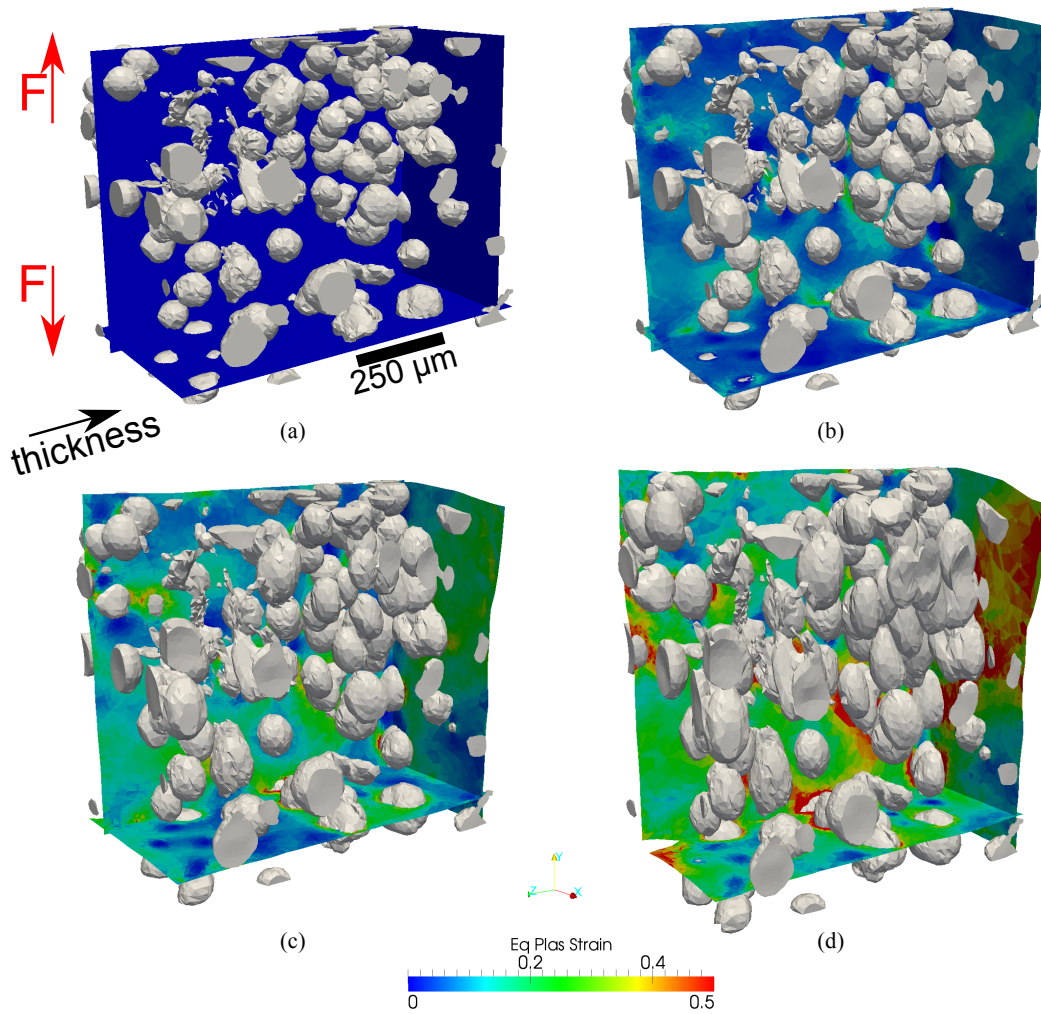


Figure 6.23 – ROI calculation results using the DVC-FE approach showing the 3D meshed voids and the equivalent plastic strain on sections when: (a) $u = 0$ (undeformed state), (b) $u = 83 \mu\text{m}$, (c) $u = 192 \mu\text{m}$, (d) $u = 321 \mu\text{m}$.

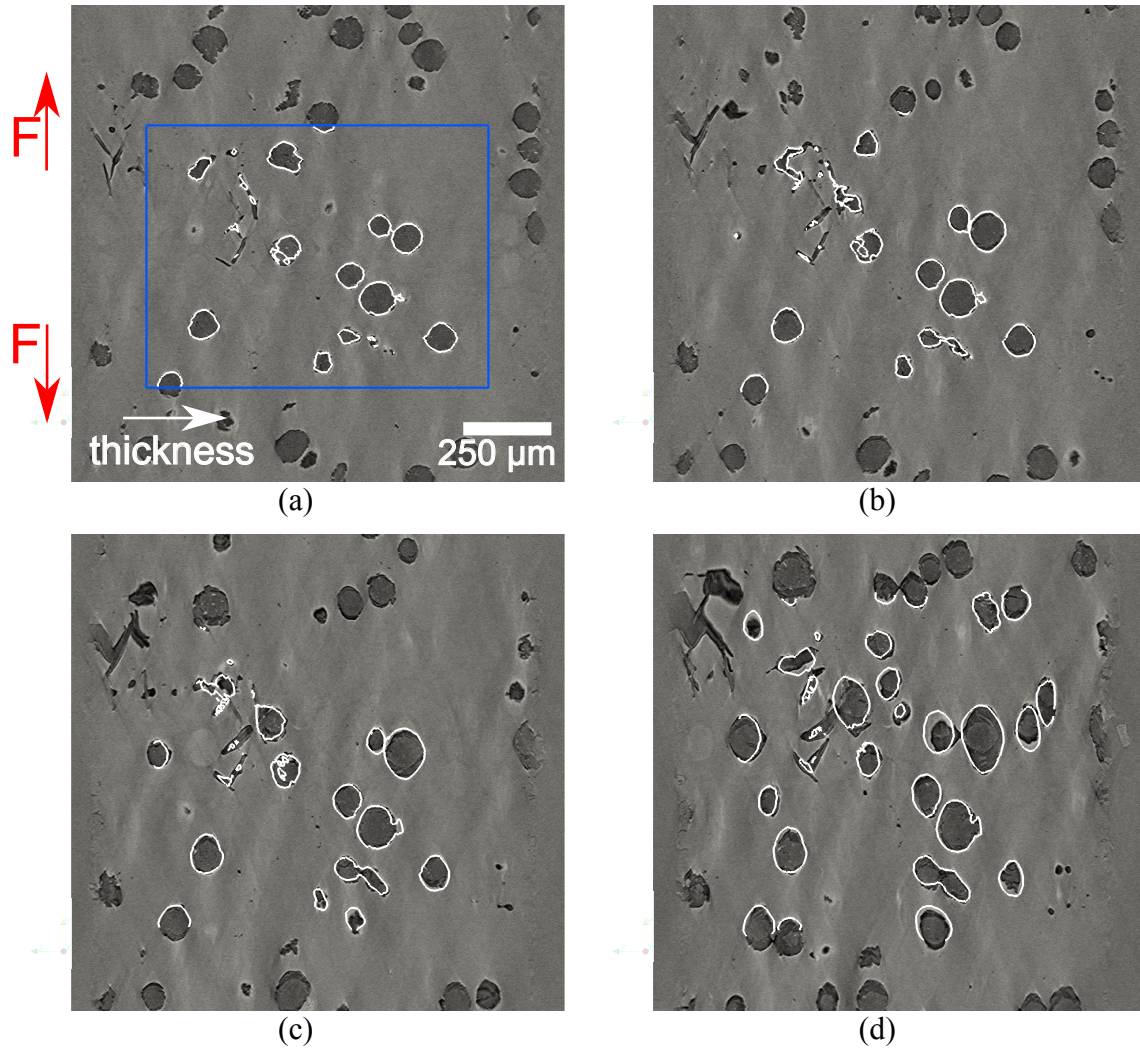


Figure 6.24 – ROI (blue line) calculation results using the DVC-FE approach comparing the numerical matrix/void interface (white line) with experimental images for the X midsection when: (a) $\mathbf{u} = 0$ (undeformed state), (b) $\mathbf{u} = 83 \mu\text{m}$, (c) $\mathbf{u} = 192 \mu\text{m}$, (d) $\mathbf{u} = 321 \mu\text{m}$.

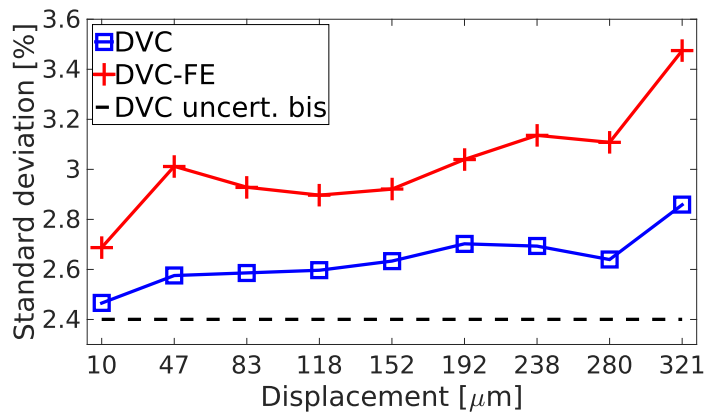


Figure 6.25 – Standard deviation for the dimensionless gray level residual fields for all loading steps. For comparison purposes, the dashed line corresponds to the resolution analysis for the so-called “bis” case (Paragraph 6.2.3.1).

around interfaces. This is expected due to plastic localization.

The growth of a minor void population and damage at a lower scale are certainly also an explanation. These minor voids cannot be observed due to the resolution of the synchrotron imaging technique used herein. The development and application of higher resolution techniques, such as nanolaminography, would be interesting in order to check these assumptions. However, these error measurements will be the basis for modeling and identification of more advanced plasticity and damage models in future work.

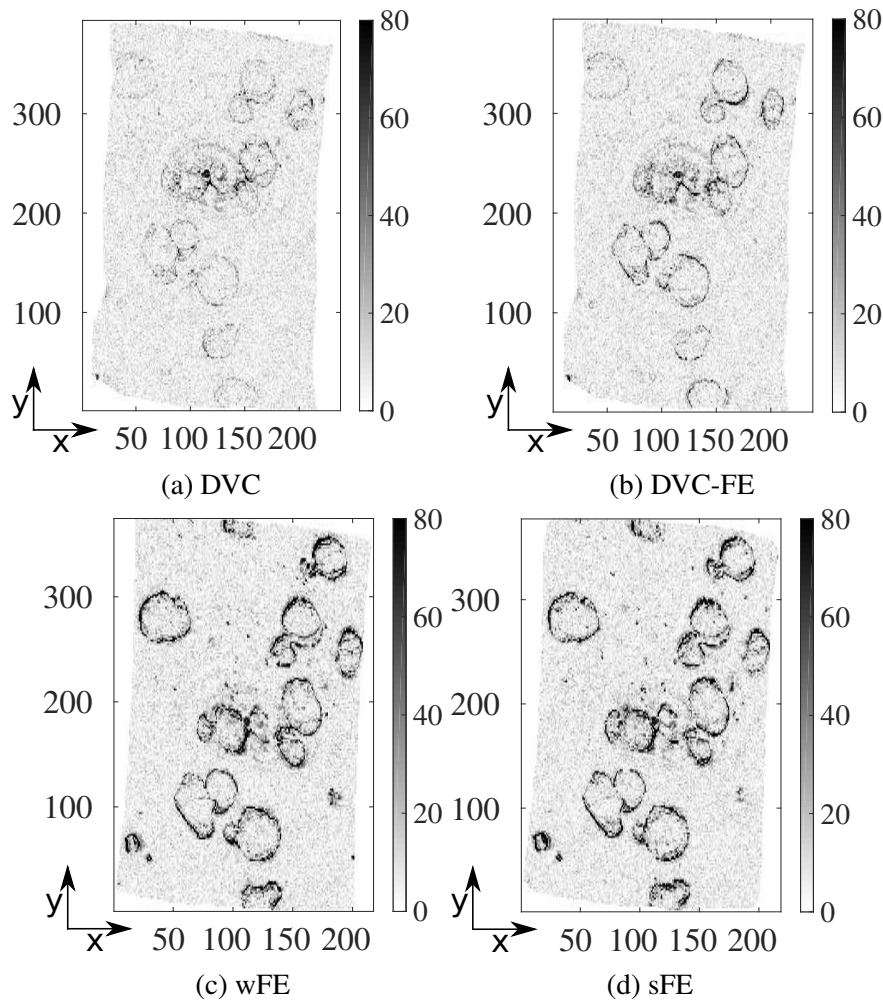


Figure 6.26 – Absolute gray level differences at the Z midsection after correction with DVC (a), DVC-FE (b), wFE (c) and sFE (d) displacements for the ninth loading step. Note that due to different rigid body motions for each simulation, the Z midsections slightly differ.

Once the absolute errors in terms of gray level residuals are estimated, relative comparisons can be shown. DVC and FE kinematic fields are interpolated on the same mesh and directly compared in Figure 6.27(a). Again, it is confirmed that the main differences are concentrated in the debonding zones, while the differences close to the boundaries are mostly zero.

6.2.4.2 Comparisons with other approaches

For quantitative comparisons between the DVC-FE method and its two alternatives used in this section, two approaches are proposed. In the first approach, as commonly carried out by

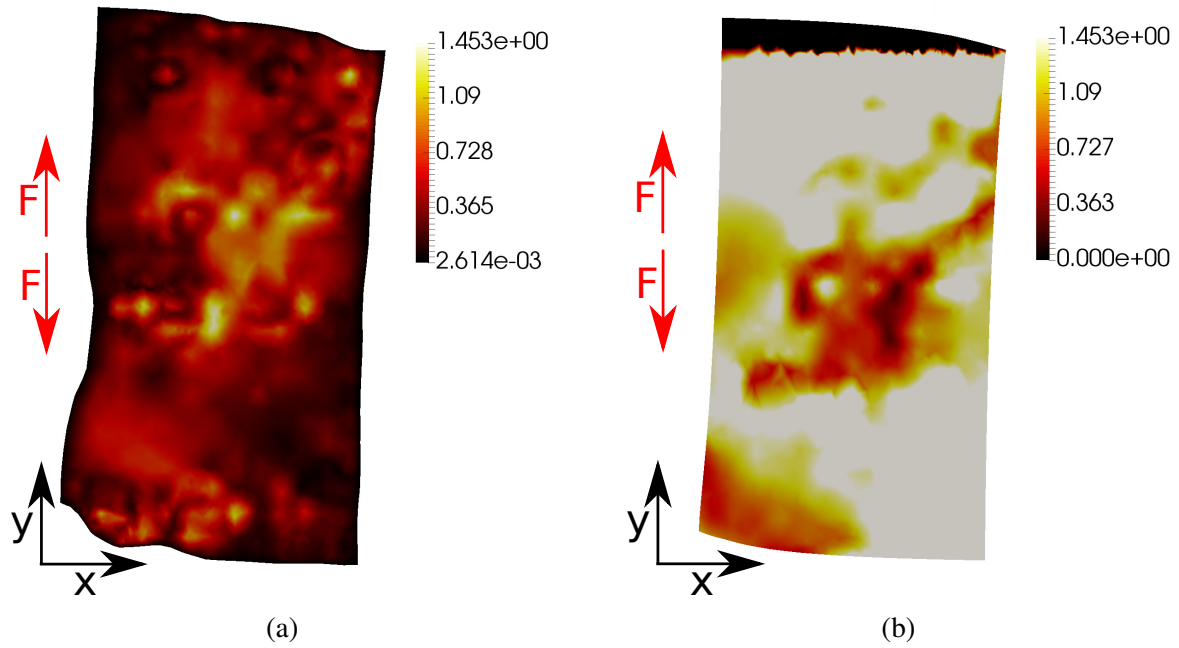


Figure 6.27 – Mid-section normal to z -direction showing absolute difference between: (a) DVC and DVC-FE displacement fields, (b) DVC and wFE displacement fields for the ninth loading step. The black area at the top of sub-figure (b) represents a zone out of the DVC ROI. The color bar range is set according to the data set from sub-figure (a) in order to have more convenient visual comparison. The displacement difference is expressed in supervoxels (1 supervoxel \longleftrightarrow 2.2 μm).

most authors, void growth curves are compared, giving only average quantities and global error measurements [19, 21, 67, 228, 259, 290]. The second approach aims at studying which method is closer to experimental observations based on local differences. These local errors are computed by reducing the kinematic data for each simulation back to gray level residuals. This requires to extend the procedure already applied to DVC and DVC-FE kinematic data to the wFE and sFE methods.

6.2.4.2.1 Global error indicators Void growth is defined by the following relationships

$$f = \frac{\text{void volume}}{\text{ROI volume}}, \text{ void growth} = \frac{f}{f_0}. \quad (6.2)$$

where f_0 denotes the initial void volume fraction. Void growth curves are shown in Figure 6.28. The EXP curve is obtained by computing void growth in processed laminography images (*i.e.*, images with smooth signed distance functions as in Figure 3.18(b)). The 3D box where this experimental void growth is computed remains fixed to the initial ROI. The wFE and sFE curves correspond to simulations using material properties based only on static data (first line of Table 6.1), while the wFE I-DIC and sFE I-DIC curves correspond to simulations using material properties based also on kinematic data thanks to Integrated-DIC (second line of Table 6.1). All numerical results show a significant decrease of the porosity f at the first loading step, which is not observed for the experimental curve. This is due to the fact that the first loading step corresponds to a more significant macroscopic displacement than others, and remeshing is extensively used for all simulations. This remeshing has the consequence that interfaces can be slightly smoothed, and void volume can be diffused.

Apart from this numerical issue, the curves reveal significant void growth with increasing load for DVC-FE and sFE results, while nearly no void growth occurs in the wFE simulation. This effect can be explained by the fact that the computation used to obtain displacement boundary conditions for the wFE simulation does not take into account damage and the subsequent volume change in the ROI. Hence, the displacement fields that are transferred to the ROI in this case are incompressible in the plastic regime, and neither the void volume nor the ROI volume can evolve.

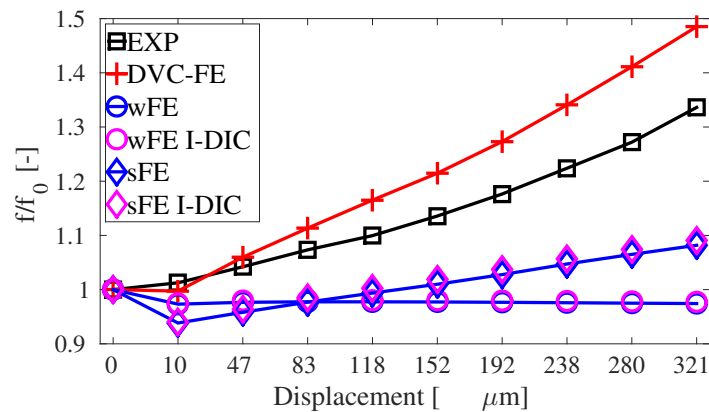


Figure 6.28 – Void volume change curves for all the approaches investigated in this section.

Regarding comparisons with the experimental curve, void growth seems to be overestimated with the DVC-FE method. This can be explained by the fact that nodules are considered as voids in the simulations, while in reality only the voids nucleated after debonding of nodule/matrix interfaces grow (Figure 6.24). Thus, it can be assumed that all curves would have a slightly lower slope if nodules were taken into account. The DVC-FE method is the only one that shows a void growth similar to that observed in the experiment.

The comparison between DVC-FE and sFE results using the proposed procedure shows that although void growth and the compressibility effects induced by the presence of voids are taken into account in the sFE method, this void growth is not as significant as with the DVC-FE method. In particular, the slopes of the wFE and sFE curves are clearly lower than what is observed experimentally. Both results are not improved when using Integrated-DIC material parameters. The influence of material parameters seems to be negligible. This observation remains to be confirmed with local error measurements.

6.2.4.2.2 Local error indicators In order to compare wFE and sFE kinematic fields with X-ray images, the method used to measure gray level residuals associated to DVC-FE results has to be extended to other methods. This is difficult because wFE and sFE meshes do not follow X-ray images. Hence, a methodology has to be defined in order to remove rigid body motions from wFE/sFE calculated displacement fields and allow for a superimposition of wFE/sFE meshes on X-ray images.

First, mean deformation gradients over the ROI for DVC and wFE/sFE displacement fields are calculated. By employing a polar decomposition on the latter, wFE/sFE and DVC rotations are evaluated while the mean values of kinematic fields represent the corresponding translations. Mean wFE/sFE translations and rotations are subtracted from wFE/sFE displacement fields, and replaced by mean translations and rotations associated to the DVC solution.

Hence, from the wFE/sFE displacements fields, rigid body motions originating from the FE

simulations are first eliminated, and then rigid body motions associated with the experiment (*i.e.*, measured with DVC) are applied. This is performed in order to have equal conditions for all presented methods when reducing them to gray level residual images. The resulting errors are shown in Figure 6.29 and Figure 6.26(c-d) while the displacement difference between DVC measurements and wFE calculated fields is shown in Figure 6.27(b).

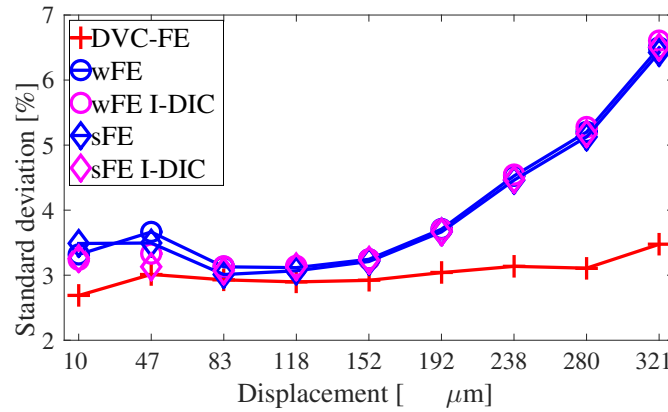


Figure 6.29 – Standard deviation for the dimensionless gray level residual fields for all loading steps and investigated cases.

Surprisingly, although sFE yields slightly better results than wFE, independently of the material parameters, this difference is negligible. This means that although the sFE method predicts a void growth that is globally closer to experimental data, the shape of these voids is inexact. Therefore, errors that do not appear in global measurements are revealed by local measurements, thereby underlining the interest of the present methodology. The small difference between wFE and sFE results could mean that the constitutive model used at the macroscale corresponds well to the homogenized mechanical response obtained in the ROI, where microscale constitutive models are used.

Regarding the comparison between sFE/wFE and DVC-FE, the gap is increasing during the load history, ending with a deviation that is twice higher with the sFE/wFE methods than with the DVC-FE one. This confirms the tendency that was observed based on void growth curves. To have a more precise idea of this gap, the cumulative gray level residuals distribution is shown in Figure 6.30(a) for the last loading step. This difference does not seem significant because it takes into account a large number of supervoxels belonging to the matrix, where contrast is small. This observation is illustrated in Figure 6.30(b), where only gray level residuals higher than 40 are shown, hence discarding most supervoxels of the matrix. The cumulative distribution taking into account only the remaining supervoxels (*i.e.*, close to voids or nodules) is shown in Figure 6.30(c). It reveals a significant difference between the DVC-FE results and those obtained with the sFE/wFE methods. The error is doubled with the latter.

This underlines the inability of macro simulations to precisely describe all the micro localization phenomena occurring in the ROI both between the machined holes and the nodules, and between the nodules themselves. Figure 6.27(b) reveals nearly zero difference in the ligament area, meaning that the macroshear band position (*i.e.*, between the machined holes) and the corresponding kinematics are properly captured with wFE simulations while the out of ligament area contains more significant displacement differences compared with DVC-FE simulations.

Overall, the use of Integrated-DIC material parameters for wFE and sFE methods improves the results. As expected in Paragraph 6.2.3.2, this gain is concentrated at lower strains while at

higher strains the influence of these material parameters is negligible. Paint cracking and subsequent DIC convergence issues from 2D images (test (A)) could be responsible for decreasing Integrated-DIC performance at late loading steps. This observation adds to the interest for the DVC method, which relies directly on the contrast of the material.

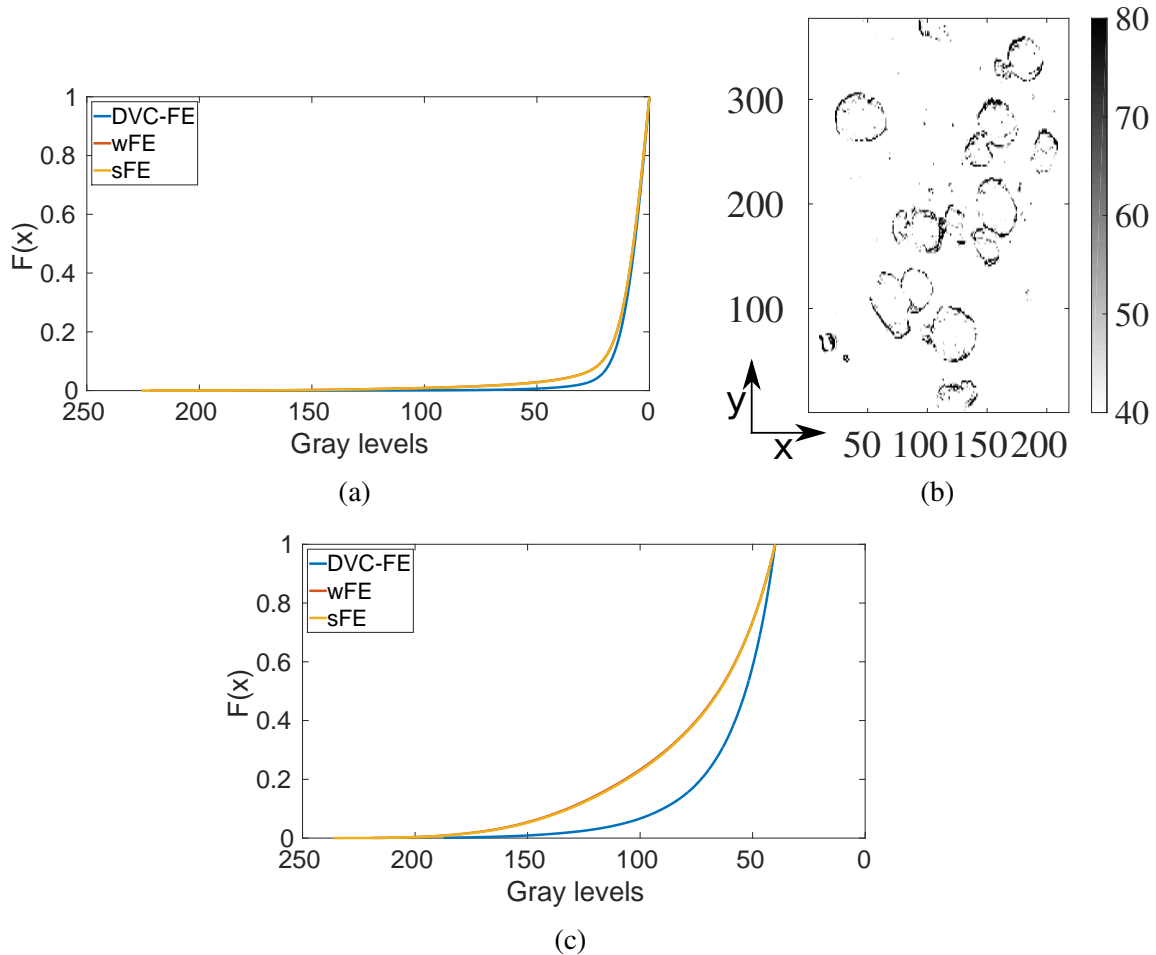


Figure 6.30 – Cumulative distribution of gray level residuals at the last incremental loading step considering: (a) all supervoxels, (c) only supervoxels with gray level residuals higher than 40. In (b), the absolute gray level differences for the sFE method with residuals higher than 40 are shown for the same Z midsection as in Figure 6.26(d).

Therefore, the way the material parameters are identified herein improves the results but only slightly. Using more complex macroscale constitutive models would certainly improve the results obtained using the wFE and sFE methods. This would also increase the need for identification methods such as Integrated-DIC that take into account field measurements. For instance, the inability of both wFE and sFE methods to correctly predict plastic localization could be linked to an anisotropy of the yield surface at the macroscale, due to the presence of the nodules. Damage and the subsequent volume changes of the homogenized material should also be considered, due to debonding of the nodules from the matrix. These remarks stress out the importance of understanding the influence of the microstructure on the mechanical response of the homogenized material. Therefore, a numerical validation procedure for micromechanical simulations that does not rely on any macroscopic constitutive model, such as the DVC-FE method, is of great interest.

6.2.5 Conclusion

The present section compares numerical validation frameworks for micromechanical FE simulations based on synchrotron 3D imaging data. Given a 3D microstructure meshing technique, the aim is to conduct FE simulations in conditions as close as possible to the experiments, and then validate micromechanical models with local error indicators. As DNS is too costly and would require meshes with more than 100 million elements, multiscale methods have been proposed in the literature to avoid meshing the microstructure in the whole specimen.

The method denoted strong FE (sFE) in this section is an embedded cell approach consisting in meshing the microstructure only in a small ROI, and embedding this ROI mesh in a specimen mesh. Macroscale constitutive models are used for the out-of-ROI material, while microscale constitutive models are used inside the ROI. Another method, referred to as weak FE (wFE) in this section, consists in separating the macroscale and microscale problems, by first conducting an FE simulation at the specimen scale, considering a totally homogeneous material, and then using the displacement fields from this first simulation to drive a second simulation at the ROI scale.

A common disadvantage of both sFE and wFE methods is that they depend on a macroscale constitutive model, which is not obvious to choose and then identify, especially when large plastic strains and complex damage phenomena are observed locally. In the experiments presented in this section, the nodular graphite cast iron specimens with a geometry inspired by the work of Weck et al. [85] feature two machined holes (Figure 6.19). Ductile fracture due to the nucleation, growth and coalescence of microscopic voids between the machined holes is observed. Due to the multiscale flow conditions, classical void coalescence mechanisms are accompanied by the sheet coalescence mechanism that is observed in the last loading stage (Figure 6.20). Hence, the proposed experiment enables to observe micro and macro plasticity and damage localization phenomena that remain challenging for micromechanical modeling, especially when multiscale methods are involved.

The DVC-FE method introduced in Section 6.1 is applied in this section and compared with the sFE and wFE methods. The latter two rely on an identification of material parameters at the macroscale, which is performed by either only using force measurements or combining static and kinematic data via Integrated-DIC.

Standard deviations of the gray level residual fields show that the DVC-FE method yields better results than both wFE and sFE methods (Figure 6.29), the gap being increased significantly at later stages of the experiment. The same conclusions are drawn from Figure 6.28 where void growth is shown for the different approaches. While these global measurements indicate a significantly improved prediction of void growth with the sFE method compared to wFE, local measurements based on standard deviation of the gray level residuals prove that this improvement is negligible with both sets of material parameters. This result underlines the importance of considering local error measurements for validating micromechanical simulations, and the interest for experimental-numerical frameworks that allow for such measurements.

Based on these local error indicators, it has been shown that using more sophisticated identification methods such as Integrated-DIC only marginally enhances the results. However, the measured errors remain significant compared to the DVC-FE method, which outlines the inability of Dirichlet conditions calculated by macro-simulations to describe precisely the micro localization effects occurring in the heterogeneous ROI.

Conclusion

Experimental techniques enabling to acquire *in situ* three-dimensional (3D) full field observations of the ductile fracture micromechanisms of voids nucleation, growth and coalescence are now commonly used by multiple authors. In Chapter 4, full field simulations taking into account these mechanisms for large 3D microstructures have been presented. In the present chapter, an experimental-numerical framework has been developed in order to compare experiments and simulations based on 3D full field data.

The proposed technique relies on a key technique, namely Digital Volume Correlation (DVC). 3D X-ray images acquired at consecutive loading steps can be correlated in order to measure 3D full field kinematic data, indicating the displacement fields between these consecutive scans. Uncertainty assessments for two different experiments on the same material confirm the validity of these measurements, and the robustness of the DVC registration method.

The material is nodular cast iron, which at the microscale features a ferritic steel matrix, and graphite nodules that debond very early under tensile loading. Additionally, these nodules are known to have a very low load carrying capacity. Thus, they were considered as voids in this chapter, and no nucleation mechanism was modeled.

Once the initial microstructure in a small Region of Interest (ROI) is meshed, DVC measurements are used as Dirichlet boundary conditions on the whole boundary of this ROI, hence driving the Finite Element (FE) simulations. This method enables to reproduce very accurately the actual loading to which the microstructure is locally subjected. Furthermore, the FE kinematic solution inside the ROI can be compared to DVC measurements, giving a quantitative indicator of the error made by micromechanical models. The FE kinematic solution can also be directly compared to consecutive X-ray images, giving accurate and local error measurements. These FE simulations with complex 3D microstructures and large plastic strains, due to realistic loading conditions, show the potential and robustness of the Level-Set (LS) and mesh adaptation techniques developed in the present work.

Then, comparisons are proposed in this chapter between this new DVC-FE methodology, and conventional methods, both regarding boundary conditions and error measurements. In fact, most previous works have relied on multiscale methods to deduce boundary conditions for micromechanical calculations. Independently on the choice of coupling between macroscale and microscale mechanics, it is shown in this chapter that multiscale schemes cannot capture accurately the complex plastic localization and voids coalescence phenomena occurring in the ROI.

In particular, while most previous works have only considered global error measurements (*i.e.*, with respect to averaged variables), the local error indicators based on DVC can also be applied to micromechanical simulations that are not necessarily driven by DVC. Thus, the errors produced by multiscale schemes can be measured more precisely, revealing that void morphology is not well described locally with these schemes. This is not the case for the DVC-FE method, which yields better predictions, both globally and locally.

Because a simple plasticity model has been used for the matrix material, and nodule behavior has been neglected, there still is a significant gap between DVC-FE and DVC results. Thus, more advanced microscale constitutive models should be studied in the future, especially regarding the modeling of a minor void population. These could be based on the void coalescence models

developed in this work (Chapter 5), or porous plasticity models.

For other materials or loading configurations, the behavior of the nodules should be considered, including debonding or fragmentation mechanisms, as done in Chapter 4. In fact, this DVC-FE approach is likely to be applicable to other materials where micromechanical modeling is gaining an increasing interest, such as metallic foams and composites for instance.

The results presented in this chapter are very promising not only for micromechanical modeling, but also for identification of microscale constitutive models. The latter would rely extensively on the DVC-FE method and its ability to provide experimentally measured boundary conditions for micromechanical simulations, and then compute local and relevant error estimators to assess the validity of these simulations. Integrated 4D analyses [284] will be considered in the future to conduct inverse analyses based on these error measurements and identify material parameters at the microscale.

Section 6.1 is highly inspired from [44]. Section 6.2 is highly inspired from [42].

Chapter 7

Conclusions and outlook

We can only see a short distance ahead, but we can see plenty there that needs to be done.

Alan Turing

7.1	Achievements	254
7.2	Suggestions for future work	256
7.2.1	Mesh generation and adaptation	256
7.2.2	Level-Set reinitialization	257
7.2.3	Computational contact mechanics	260
7.2.4	Micromechanical models and computational fracture mechanics	260
7.2.5	Multiscale methods	262

The main objective of this work was to develop advanced numerical tools in order to model ductile fracture at the microscale. In many forming processes studied at the Center for Material forming - MINES ParisTech (Cemef - MINES ParisTech), metal alloys fail due to the nucleation, growth and coalescence of microscopic cracks and voids.

It has been emphasized in the introduction that it is necessary to better understand and predict the influence of metal forming processes on the microstructure of metallic materials. Additionally, the understanding of the influence of microscopic failure mechanisms on the macroscopic mechanical response of these materials is also of interest.

To reach such ends, the literature review presented in Chapter 1 has shown that recent efforts from the community focus on the microscale aspects of ductile fracture, both regarding experimentation and modeling.

Recent developments in the fields of loading devices and X-ray imaging techniques have enabled the *in situ* three-dimensional (3D) observation of ductile fracture mechanisms at the microscale, for a wide range of metallic materials.

Inspired by the work of Gurson, theoretical approaches have focused on the development of multiscale methods in order to link the macroscopic mechanical response of materials to the microstructure. Because these approaches are based on analytical calculations, they assume very restrictive microstructures and loading conditions. The results obtained using these methods are however very promising.

Therefore, numerical methods that would use the same multiscale framework, but extend the results to arbitrary microstructures and loading conditions are of great interest.

7.1 Achievements

Based on the literature review and the emergent need for more realistic micromechanical simulation tools, the main breakthroughs achieved within this work were the following:

- Discretizing complex three-dimensional (3D) microstructures featuring arbitrary shapes, sizes, and arrangements. Thanks to an innovative coupling between the Level-Set (LS) method and body-fitted Finite Element (FE) meshing techniques, such microstructures can be easily discretized using LS functions, and then meshed explicitly in a single mesh, including voids.
- Developing interface tracking methods to capture the interfaces between the different components of these microstructures and model their deformation, up to large plastic strains. The LS method has been enhanced in the present work by adding a volume conservation constraint to an existing mesh adaptation algorithm. Completed by a mesh motion procedure and an LS reinitialization technique, this methodology can be used in a wide range of applications where large displacements and deformations occur, including complex topological modifications such as void coalescence. This technique is particularly interesting compared to what is existing in the literature as it preserves the advantages of the LS method regarding the modeling of complex topological events, but adds explicitly meshed interfaces and improves volume conservation.
- Capturing and modeling cracks on-the-fly during the simulation. The method proposed in this work consists in representing cracks by LS functions that are then explicitly meshed. The interesting point of this technique is that the subsequent free surfaces can deform until cracks change into voids that start interacting and coalescing. This is helped by the fact that voids are directly embedded in the FE mesh. An innovative computational contact mechanics has also been proposed in order to detect contact events between crack faces, including self-contact.
- Meshing microstructures from 3D X-ray data. Thanks to the developments carried out in the present work, not only can X-ray data be converted into LS functions in order to mesh microstructures from X-ray images, but the mesh size can also be adapted to the multiple scales of the geometry.
- Study micromechanical models for void nucleation and coalescence. Based on the literature, local criteria have been proposed in order to predict particle fragmentation and debonding. Void coalescence has first been assumed to be purely driven by plasticity, and then comparisons with experiments have been used to define a fracture criterion for the intervoid ligament. Results obtained with these models are a major breakthrough with respect to the literature, especially regarding 3D simulations taking into account void nucleation and coalescence at large plastic strains. Comparisons with conventional approaches reveal the importance of considering more advanced micromechanical models and computational methods such as those developed in the present work.
- Comparisons with experiments. The work achieved jointly with the Centre des Matériaux - MINES ParisTech and the Laboratoire de Mécanique et Technologie - ENS Cachan enables for the application of measured boundary conditions to the boundaries of a small Region Of Interest (ROI). Thanks to *in situ* laminography experiments, the latter is observed initially in 3D in order to be meshed with the tools developed in the present

work, and then during loading in order to measure boundary conditions with a Digital Volume Correlation (DVC) method. The robust numerical tools developed in the present work handle accurately the arbitrary shapes arising from X-ray images, and the arbitrary loading conditions given by DVC measurements. This accuracy is validated thanks to local comparisons with experiments. Because FE simulations track the local loading conditions observed in experiments, it is possible to superimpose simulation results and experimental observations, and quantify errors between the two. This powerful procedure is of great interest for identification of material parameters directly at the microscale. Its main advantage with respect to the existing literature is that it does not require any macroscopic measurements or simulations.

This project was particularly important to develop all the necessary numerical tools for modeling failure at the microscale in an accurate way and with acceptable computational cost. It should be noticed that the present work gave rise to several papers in peer-reviewed international journals (2 submitted and 5 already published) and conferences (5 national and 12 international). As illustrated by the fact that the author of the present work was not systematically the lead author or presenter for all these papers and conferences, the present work also led to partnerships. In particular, some numerical methods developed in this work have been and are currently being applied by colleagues to ductile fracture and other applications of materials science and computational thermomechanics in general.

7.2 Suggestions for future work

Multiple points should be studied to improve further the numerical methods and especially the micromechanical models developed in this work. Applications of the present developments to other challenging applications should also be considered. Some of these research topics have been or are being investigated by colleagues at Cemef - MINES ParisTech.

7.2.1 Mesh generation and adaptation

First, the new mesh generation and adaptation methods developed in the present work have been successfully applied to capture new interfaces on-the-fly during simulations, and adapt the mesh up to large plastic strains. These algorithms have been used by colleagues to track interfaces in other applications, namely homogenization of the behavior of the polymer composite meshed in Paragraph 3.4.2.3 [8], and modeling of globularization mechanisms in α/β titanium alloys [56]. The application of these algorithms to fluid-structure interaction would raise no particular difficulty, even with a moving and deforming structure. This has been demonstrated in Appendix A, although the air was not modeled in these simulations and considered as void.

Second, an interesting prospect to the present work, which has actually already been implemented by the present author and tested in 2D, is the meshing of multiple junctions. Thus, applications of the body-fitted meshing and remeshing techniques developed in the present work to crystal plasticity and recrystallization could be addressed in a very near future. Existing techniques based on other meshing tools can be found in [181, 291].

The reader is referred to Paragraph 3.2.3.2 for details on the Eulerian LS method used currently at Cemef - MINES ParisTech for grain growth modeling, and the numerical treatment used to eliminate vacuum regions that are produced due to numerical errors at each transport step. As mentioned in Paragraph 3.2.3.2, this numerical treatment only removes vacuums across edges of the mesh, hence vacuums generally still remain across elements (and faces in 3D). This is illustrated in Figure 7.1(a,b). Using the interface fitting algorithm described in Section 2.1, these vacuums are not eliminated, as shown in Figure 7.1(c,d). Therefore, an interface joining algorithm is necessary.

The main aspect of the interface joining technique proposed in the following to remove these vacuums is that it is purely topological:

1. Each element of the mesh is considered one by one. All intersections between an interface and edges of this element are computed. The barycenter of these intersections is inserted in the mesh, thus splitting this element (*e.g.*, into 3 triangles in 2D, and 4 tetrahedra in 3D). The LS functions to all interfaces that had intersections on edges of this element are set to zero on the inserted node.
2. Each face of the mesh is considered one by one. All intersections between an interface and edges of this face are computed. The barycenter of these intersections is inserted in the mesh, thus splitting this face. The LS functions to all interfaces that had intersections on edges of this face are set to zero on the inserted node.
3. Each edge of the mesh is considered one by one. All intersections between an interface and this edge are computed. The barycenter of these intersections is inserted in the mesh, thus splitting this edge. The LS functions to all interfaces that had intersections on this edge are set to zero on the inserted node.

Note that in 1D, steps 2 and 3 are not necessary as elements are edges, in 2D step 3 is not necessary as faces are edges and in 4D an additional step would be necessary. Each topology is hence considered one by one, starting with the topology of higher dimension. An example of result obtained with this interface joining technique in 2D is shown in Figure 7.1(e,f). All elements of the mesh are colored, hence there is no vacuum. In order to obtain this result, the interface joining step was followed by a mesh adaptation step, which is possible because the mesh adaptation algorithm with volume conservation constraint is compatible as is with multiple junctions.

As suggestions for future work, mesh quality should be investigated and in particular it should be verified that the quality of the mesh can be preserved during deformation. The presence of multiple junctions may have a negative influence on mesh quality. This should especially be validated in 3D. Furthermore, while applying a Lagrangian method to crystal plasticity modeling is conventional, it is more common to use Eulerian methods for recrystallization modeling. However, it has been proved that the remeshing techniques developed in this work could handle complex topological events such as grain nucleation or disappearance.

Recrystallization modeling would additionally rely on the definition of a velocity field at grain boundaries, which would require a robust computation of the local mean curvature of these boundaries. The latter could be performed using geometrical operations, or the Superconvergent Patch Recovery (SPR) technique (Subsection 3.1.3). The same remark would hold in the case of multiphase flows and surface tension modeling. As first tests regarding recrystallization modeling, only contributions due to stored energy could be taken into account, as this approximation avoids the computation of the local mean curvature [2].

Last, as mentioned in Paragraph 4.5.3.7, finer meshes and time steps are necessary to accurately predict fracture instants. Local mesh refinement based once again on the SPR technique could be used, but this time applied to a relevant mechanical field such as the equivalent plastic strain, or a damage indicator.

Using such technique, remeshing would be more frequent, and conservation of history variables would be an issue. The remeshing method developed in the present work helps the conservation of the volume of each phase, but the conservation of other relevant FE fields such as history variables is not accounted for. Adding such constraints to the remesher may render mesh adaptation too difficult. Existing approaches in the literature often rely on the SPR technique described in Subsection 3.1.3 to reduce this diffusion by improving the transport of history variables [292, 293]. Similar techniques have been studied at Cemef - MINES ParisTech in different contexts [294, 295] and have been tested in the present work. An important limitation is that while diffusion is reduced, mechanical variables tend to drift away from equilibrium. This tendency was not investigated further by the present author. Other approaches to this problem consist in using mesh intersection techniques during the transport step [296], or relying on higher-order elements.

7.2.2 Level-Set reinitialization

On the one hand, the new LS reinitialization algorithm presented in Section 3.2 is an interesting improvement over the tools used previously at Cemef - MINES ParisTech because it computes directly the projection of any point onto the interface discretized by the LS method. This has the advantage that the signed distance function to the interface can be computed more accurately, but not at the sacrifice of efficiency thanks to a space partitioning technique.

This algorithm has already been applied successfully to a panel of problems that goes beyond

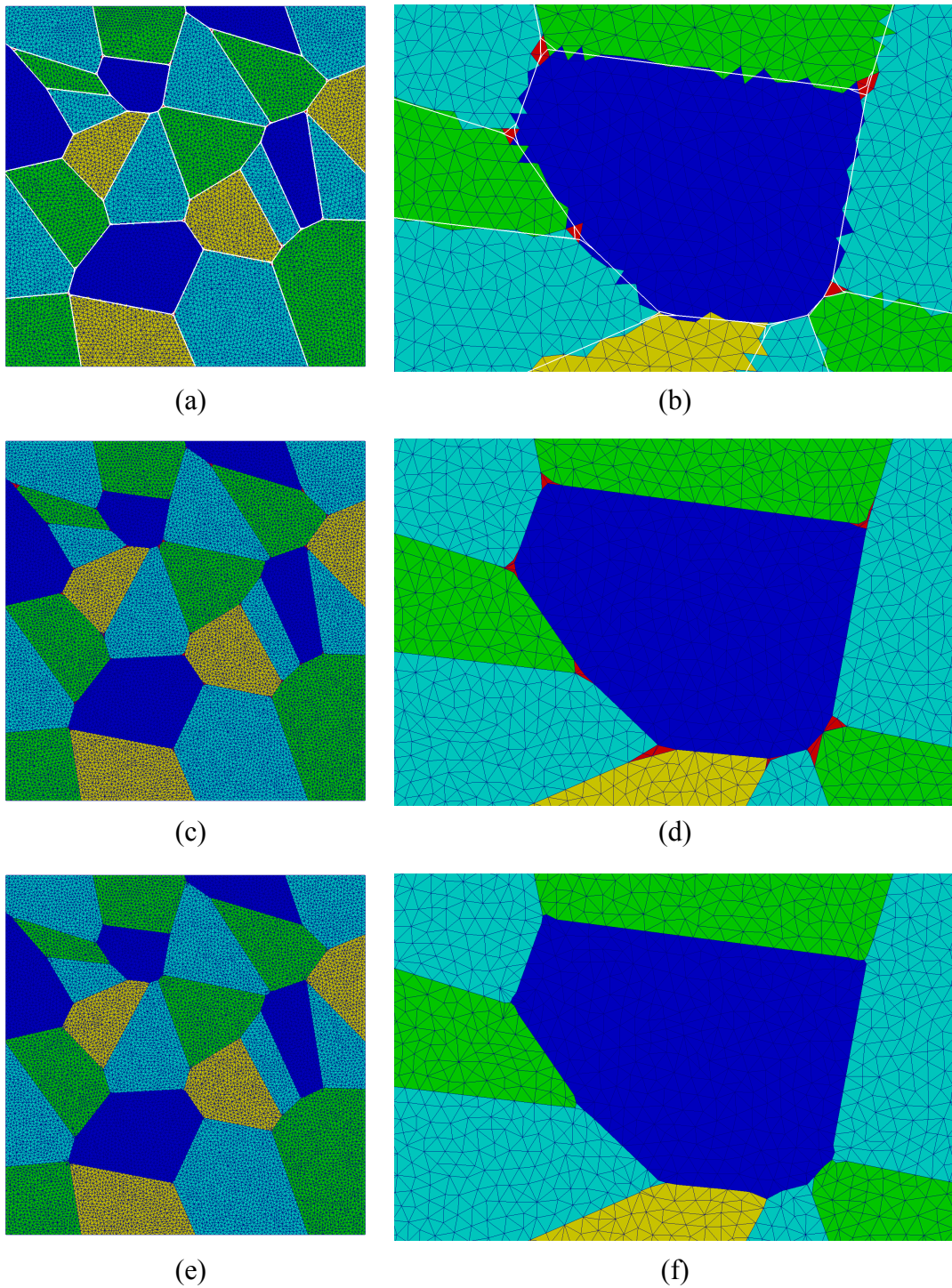


Figure 7.1 – Example of a 2D polycrystal of 25 grains represented by 4 LS functions (blue, cyan, yellow, green). In (a,b), interfaces (white) are implicitly meshed and go across mesh elements, with vacuum regions (red) at some multiple junctions. In (c,d), interfaces are explicitly meshed using the fitting procedure but multiple junctions are not treated, thus vacuum regions remain. In (e,f), interfaces are explicitly meshed using the joining procedure, no vacuum regions remain in the final mesh.

ductile fracture and micromechanics. As detailed in Paragraph 3.2.3.2, the microstructure of polycrystals can be represented in a full field FE simulation using LS functions, that need to be reinitialized when the microstructure evolves due to heat treatments for instance [43]. When these heat treatments are combined with mechanical loading, complex recrystallization phenomena have to be modeled, with the use of crystal plasticity constitutive models [3]. For some materials such as dual phase alloys, globularization or phase transformations may have to be accounted for [56]. Other thermomechanical phenomena, such as phase change and in particular solidification during welding or additive manufacturing processes, have also been modeled by colleagues using the LS method [297, 298, 299]. The LS reinitialization method proposed in this work has been used in all these developments, hence proving its robustness and capabilities in a larger context.

Another interesting possibility offered by this algorithm is that because the projection of each point is available, the gradient of the LS functions can be computed at any point, and in particular at mesh nodes. This operation, which usually requires gradient recovery techniques (Subsection 3.1.3), can hence be solved with the same geometrical accuracy as LS reinitialization, as shown in Figure 7.2. This is very interesting in applications where interface motion is driven by the normal vector to the interface, or other geometrical variables. FE variables can also be transported from the interface to the rest of the domain, by associating these variables to the projections. These extensions of the LS reinitialization algorithm have already been implemented and successfully applied by colleagues to the full field modeling of static recrystallization [3].

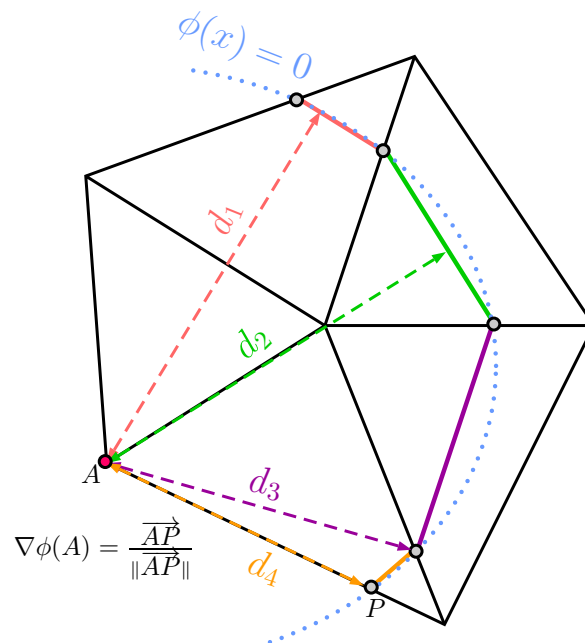


Figure 7.2 – Geometric computation of the gradient of a LS function ϕ at a mesh node A based on its projection P onto the interface. Figure reproduced from [3].

On the other hand, the generalization of this LS reinitialization method to higher-order LS functions could be interesting. The space partitioning technique would still be applied, but the computation of the projection of a given point onto the interface would not result in a linear problem any more. The solution of the subsequent nonlinear problem may raise some

difficulties, but is worth considering to reduce the diffusion induced by the LS method in Eulerian simulations.

7.2.3 Computational contact mechanics

The new contact detection algorithm described in Appendix A is very interesting for a wider range of applications than those discussed in the present work. In particular, the fact that the algorithm is based on local mesh adaptation operations instead of global searches is of great interest in explicit dynamics. When very small time steps are used, algorithms such as the LS reinitialization algorithm discussed above are to be avoided, because their computational cost is insensitive to the time step. The contact detection algorithm proposed in the present work has the advantage that its computational cost decreases with the time step, as mesh nodes move with smaller amplitudes, but not at the sacrifice of robustness.

To illustrate the capabilities of the contact detection algorithm to capture all sorts of contact events, including self-contact, recent results are shown in Figure 7.3. The fall of a spring on rigid stairs is modeled. The result in Figure 7.3(a) features multiple contact and self-contact events, that become even more complex to detect and model when the spring is softer, as in Figure 7.3(b). In these simulations, the mesh is coarsened in the air (considered as void) to reduce the computational cost. Error estimators should be studied in order to refine or coarsen the mesh in preferential directions and help contact detection.

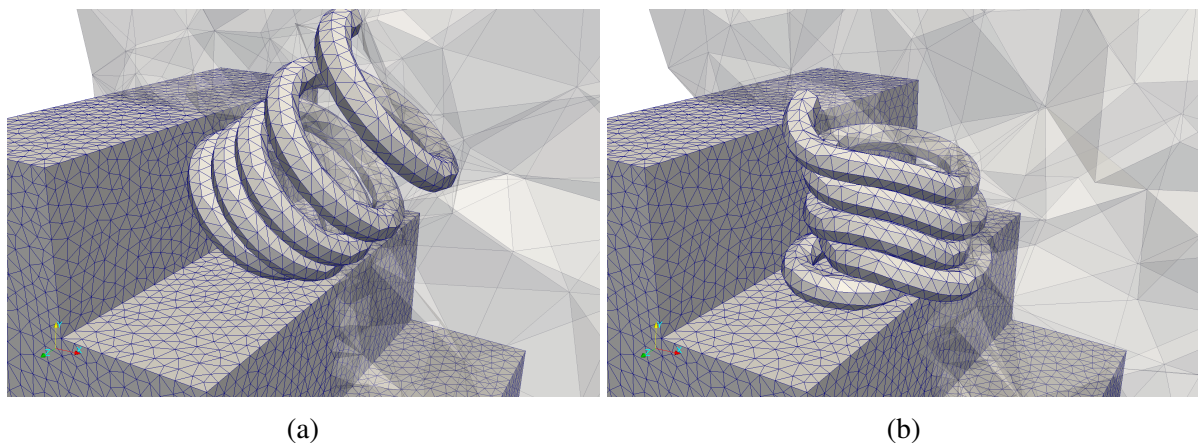


Figure 7.3 – Numerical simulation of the fall of a hard (a) or soft (b) spring on stairs, using the contact detection algorithm proposed in the present work.

Moreover, these results could be improved in many aspects as multiple questions are still open, especially regarding the formulation that has been chosen. This formulation does not take into account large deformations and friction terms, and is known to be over-constrained. All these points should be studied to improve the prediction of contact surfaces and their deformation, and generalize these developments to other applications.

7.2.4 Micromechanical models and computational fracture mechanics

In the first place, micromechanical modeling is a very wide research topic, even when restricted to ductile fracture. Many approaches have been proposed in the literature, but only a few of them take into account the particles and the subsequent particle fragmentation and debonding

phenomena. Large plastic strains and the complex void linkage mechanisms that they imply are also rarely addressed. Thus, the results obtained in the present work are an interesting scientific contribution. Nevertheless, because the focus was on numerical methods for interface modeling and tracking, using the LS method and mesh adaptation to handle large plastic strains and complex fracture events, simple constitutive models were used at the microscale.

Assuming particles as elastic and brittle is well accepted, as they are known to fail before yielding in most metal alloys. However, the use of a von Mises plasticity model for the matrix material should be reconsidered. For many industrial materials, plasticity at the microscale could be more complex, and highly influenced by grain boundaries and local slip directions. Results presented in Chapter 6 also suggest that submicron size voids may be present in some materials, and have a major influence on void coalescence.

In the frame of the present work, crystal plasticity modeling will highly depend on the possibility to reconstruct 3D images of the crystal structure of a material [15, 276]. Such images may also have to be acquired during deformation in order to identify material parameters for crystal plasticity constitutive laws. Otherwise, comparisons with experiments as done in Chapter 6 may not be possible. Computational cost may also be of major influence, as crystal plasticity solvers are known to be very greedy in terms of computational resources [3].

The priority may hence not be crystal plasticity, but porous plasticity. Damage modeling seems to be necessary for the matrix material, as plastic localization does not solely explain the complex intervoid ligament failure mechanisms that were observed in Chapter 6. The easiest manner would be to couple the Lemaitre model used in Chapter 5 to constitutive equations. In order to avoid any mesh dependency, a regularization method would then be necessary [249, 250].

Different levels of couplings between the Lemaitre model and constitutive equations have been implemented in the FE code during previous work at Cemef - MINES ParisTech [115]. An implicit gradient model was used for regularization. These developments could be used and completed with the fracture model proposed in Chapter 5 for the damage-to-fracture transition in intervoid ligaments. However, the use of a Lemaitre damage model at the microscale may be questionable, as it would then be impossible to know the porosity in the material. A regularized Gurson-Tvergaard-Needleman (GTN) model is currently being developed to avoid such issues [55, 61]. Although this model increases significantly the number of material parameters, the numerical validation framework developed in Chapter 6 could provide a powerful tool for the identification of these parameters.

These developments on a regularized GTN model could be an opportunity to consider a large deformation implementation. In fact, the small strain framework used in the present work may lead to significant errors when used with loading conditions experienced in real metal forming processes.

In the second place, in all fracture models, independently on whether fracture was occurring inside particles, at the matrix/particles interface, or inside the matrix, the strain energy release rate was not taken into account. There has been an increasing interest for numerical methods and models that could take into account strain energy release. In particular, Cohesive Zone Models (CZMs) have been widely used. An implementation of these CZMs has been conducted recently by colleagues [54].

As discussed in Chapter 2, these models are to be coupled to advanced computational fracture mechanics tools such as those developed in the present work in order to avoid any mesh dependency. Results obtained by coupling CZMs to the numerical tools developed in the present work are very promising, as arbitrary crack paths can be meshed and then faces along these cracks can be split in order to insert cohesive elements.

This is illustrated in Figure 7.4. As shown in this figure, although fracture was assumed to occur

instantaneously in the present work, there is nothing preventing the use of the proposed numerical methods to model the progressive propagation of a crack across an FE mesh, now accounting for the strain energy release rate. The numerical crack extension length ℓ^F (Chapter 4) is also eliminated. Future work includes the extension of this approach to 3D and large deformations.

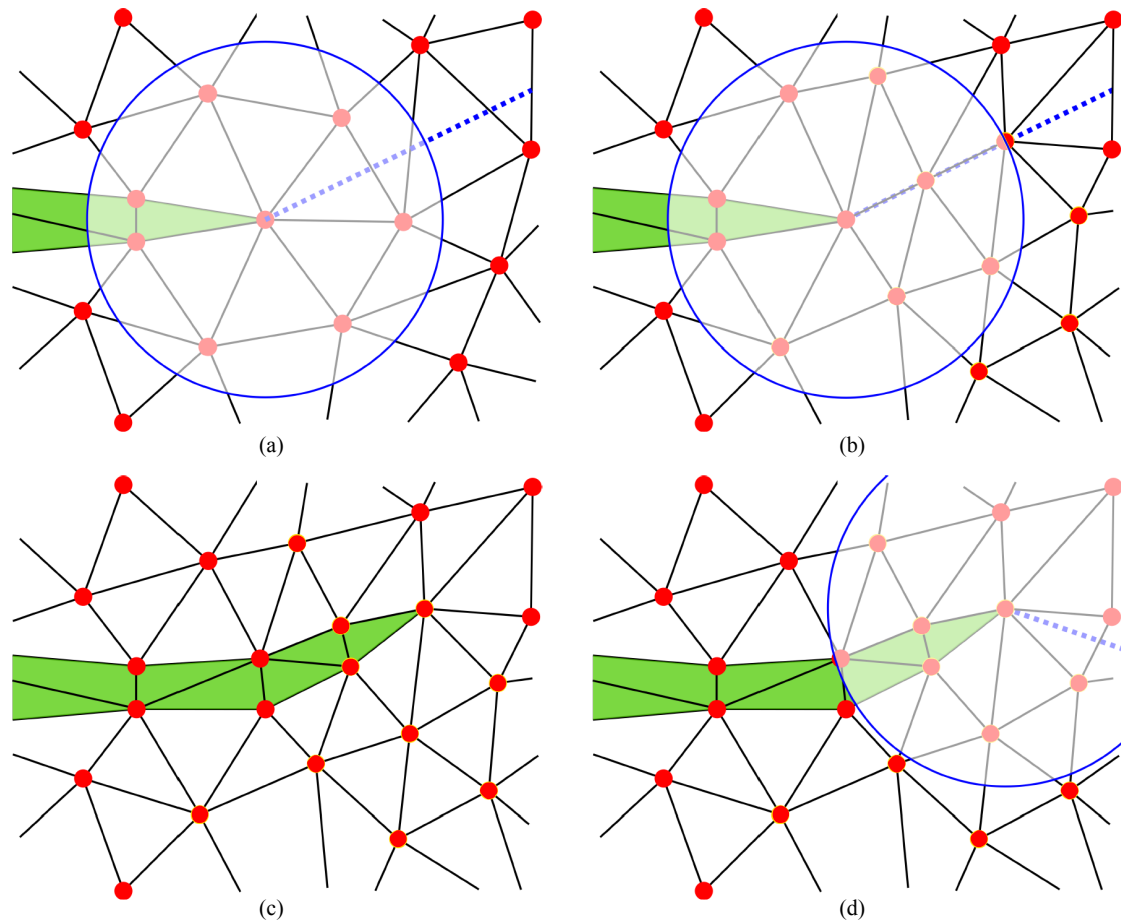


Figure 7.4 – Propagation of a crack with cohesive elements: (a) initial material with existing cohesive elements (green), filter LS function (solid blue line), and new crack LS function defined using fracture or damage-based criteria (dashed blue line), (b) fitting of the mesh to the crack inside the filter, (c) insertion and opening of cohesive elements, (d) next propagation step. Figure reproduced from [54].

7.2.5 Multiscale methods

As mentioned in the introduction of this work, the long term objective of the project in which the present work is included is to improve the prediction of ductile damage and fracture during metal forming processes, especially in the frame of non proportional loading paths. This requires a better understanding of the micromechanics of ductile fracture, thanks to the help of advanced numerical methods such as those developed in Chapter 2, Chapter 3 and Appendix A, and micromechanical models such as those developed in Chapter 4 and Chapter 5. Comparisons with experiments will also play a major role in validating predictions, hence the interest for the methodology introduced in Chapter 6.

Once results are validated at the microscale, the question of applying the acquired knowledge

on ductile fracture mechanisms at the industrial scale will have to be answered. This transfer between microscale and macroscale will also be interesting for materials scientists, who may compare their mean field models to full field numerical simulations. Such comparisons require an accurate measurement of the porosity and the macroscopic stress and strain tensors during deformation. This is easily done by averaging full field numerical results as in Chapter 4, while uncertainties are significantly increased with experimental approaches, especially regarding the porosity [286]. This is exemplified in the following, with a distinction between two objectives, namely the prediction of microstructure evolution, and the prediction of material behavior.

7.2.5.1 Predicting microstructure evolution

On the one hand, the goal could be to predict microstructure evolution, for given macroscopic loading conditions (macro to micro transition). Material parameters for mean field void nucleation, growth, and coalescence models would have to be identified against full field results averaged on the Representative Volume Element (RVE). These models (*e.g.*, the Rice & Tracey void growth model [26]) typically depend on the applied strain and the stress state, that were controlled in RVE calculations using the stress state control algorithm (Section 4.4).

Such an identification has already been carried out at Cemef - MINES ParisTech for void closure under compressive loading [300]. Based on a wide range of RVE simulations results, a new model was proposed, and was proved to give better estimates than those found in the literature for these loading conditions. This framework has been extended recently with an automatic procedure designed to correct material parameters for mean field models thanks to a database of full field simulation results obtained for various loading conditions [301]. The presence of void nucleation and coalescence phenomena does not prevent the application of the same approach to the present case. Thus, it is not discussed further.

7.2.5.2 Predicting material behavior

On the other hand, the goal could be to predict microstructure evolution, and then the effect of this evolution on the macroscopic behavior of the material (macro to micro, and then micro to macro transitions). Material parameters for a mean field porous plasticity model would have to be identified against full field results averaged on the RVE. This is more complex than just an estimation of the porosity, as the objective function that has to be minimized during the identification has to be clarified, as well as the variables for this minimization. Additionally, three mean field models are now necessary.

- A porosity model should be defined. The definition and identification of mean field porosity models based on full field simulations would be conducted separately, as already discussed in Paragraph 7.2.5.1. Thus, in the present paragraph, no approximation is carried out regarding the porosity f^{RVE} , which is taken directly from an RVE simulation.
- A porous plasticity model has to be defined. In the present paragraph, the GTN model is used [35]

$$\psi^{GTN} = \left(\frac{\bar{\Sigma}}{\Sigma_0} \right)^2 + 2q_1^{GTN} f^{RVE} \cosh \left(\frac{3}{2} q_2^{GTN} \frac{\Sigma_m}{\Sigma_0} \right) - 1 - \left(q_1^{GTN} f^{RVE} \right)^2 = 0. \quad (7.1)$$

Normally, this model would require the identification of numerous parameters due to void nucleation, growth and coalescence models. Because the porosity f^{RVE} in Equation (7.1) is taken directly from RVE simulation results, only two material parameters remain, namely

q_1^{GTN} and q_2^{GTN} . The mean stress Σ_m , the equivalent stress $\bar{\Sigma}$, and the yield stress Σ_0 are associated to the GTN model, and not to be confused with RVE simulation results.

- Elasticity and plasticity remain to be defined. Hooke's law for linear isotropic elasticity is used (Equation (1.4)), which adds two material parameters E^{el} and ν^{el} . Once again, only isotropic hardening is taken into account, using a power law (Equation (4.10)), which adds three material parameters Σ_y^{pl} , K^{pl} , and n^{pl} .

RVE simulation results consist of inputs $\{\mathbf{I}\} = \{\Delta E^{RVE}, f^{RVE}\}$ and outputs $\{\mathbf{O}\} = \{\Sigma_m^{RVE}, \bar{\Sigma}^{RVE}\}$, where ΔE^{RVE} is a list of strain increments, and $f^{RVE}, \Sigma_m^{RVE}, \bar{\Sigma}^{RVE}$ are the RVE-averaged results of a full field simulation for these strain increments. A GTN solver has been implemented in a Scilab code [302] based on previous work [32]. Given an initial guess for the set of material parameters $\{\mathbf{p}\} = \{E^{el}, \nu^{el}, \Sigma_y^{pl}, K^{pl}, n^{pl}, q_1^{GTN}, q_2^{GTN}\}$, this solver computes the GTN prediction $\{\mathbf{G}\} = \{\Sigma_m, \bar{\Sigma}\}$ for the inputs $\{\mathbf{I}\}$. The squared difference between the GTN prediction $\bar{\Sigma}$ and RVE simulation outputs $\bar{\Sigma}^{RVE}$ is the objective function to minimize, while the material parameters $\{\mathbf{p}\}$ are the variables for this minimization problem.

If the RVE simulation did not take into account particles, then $E^{el}, \nu^{el}, \Sigma_y^{pl}, K^{pl}, n^{pl}$ would be known as they would correspond to the matrix material. As in this paragraph RVE simulation results from Chapter 4 are considered, the microstructure features particles. Elastic properties E^{el}, ν^{el} and plastic properties $\Sigma_y^{pl}, K^{pl}, n^{pl}$ could be identified separately by conducting RVE simulations with no fracture criteria and no plasticity in the matrix material. This is one added advantage of simulations, because ensuring that the yield stress is not reached in experiments is not as simple [303]. In order to avoid any additional simulations, this multi-step method is not used in the present work and all parameters are identified simultaneously using Scilab's `optim_ga` routine.

Only the macroscopic von Mises equivalent stress is used for error measurements because large differences were observed between RVE and GTN predictions regarding the mean stress. This may be due to the assumption that damage does not affect the elastic part of the constitutive model for the homogeneous material. Additionally, the GTN solver did not converge up to the last loading step for all simulations. This may be due to the high porosity and early coalescence mechanisms observed for the material studied in Chapter 4. Both limitations will be investigated further in the future.

Material parameters computed by the inverse analysis are

$$\{\mathbf{p}^*\} = \left\{ \begin{array}{l} E^{el} = 80\,754 \text{ MPa}, \nu^{el} = 0.30, \\ \Sigma_y^{pl} = 158 \text{ MPa}, K^{pl} = 567 \text{ MPa}, n^{pl} = 0.22, \\ q_1^{GTN} = 0.74, q_2^{GTN} = 1.40 \end{array} \right\}.$$

The simulation results $\{\mathbf{I}\}$ and $\{\mathbf{O}\}$ used for this analysis correspond to the simulation with macroscopic triaxiality ratio $\eta = 0.33$. Computed parameters $\{\mathbf{p}^*\}$ are then used to assess GTN predictions at $\eta = 0$ and $\eta = 0.66$, as shown in Figure 7.5. The curves for the GTN predictions go only up to the last loading step for which the GTN solver converged.

These results show that, with material parameters $\{\mathbf{p}^*\}$, the GTN model overestimates material strength. This error increases with the macroscopic stress triaxiality ratio. Additionally, the GTN model predicts a sudden loss of load carrying capacity, while this is more progressive in RVE simulations.

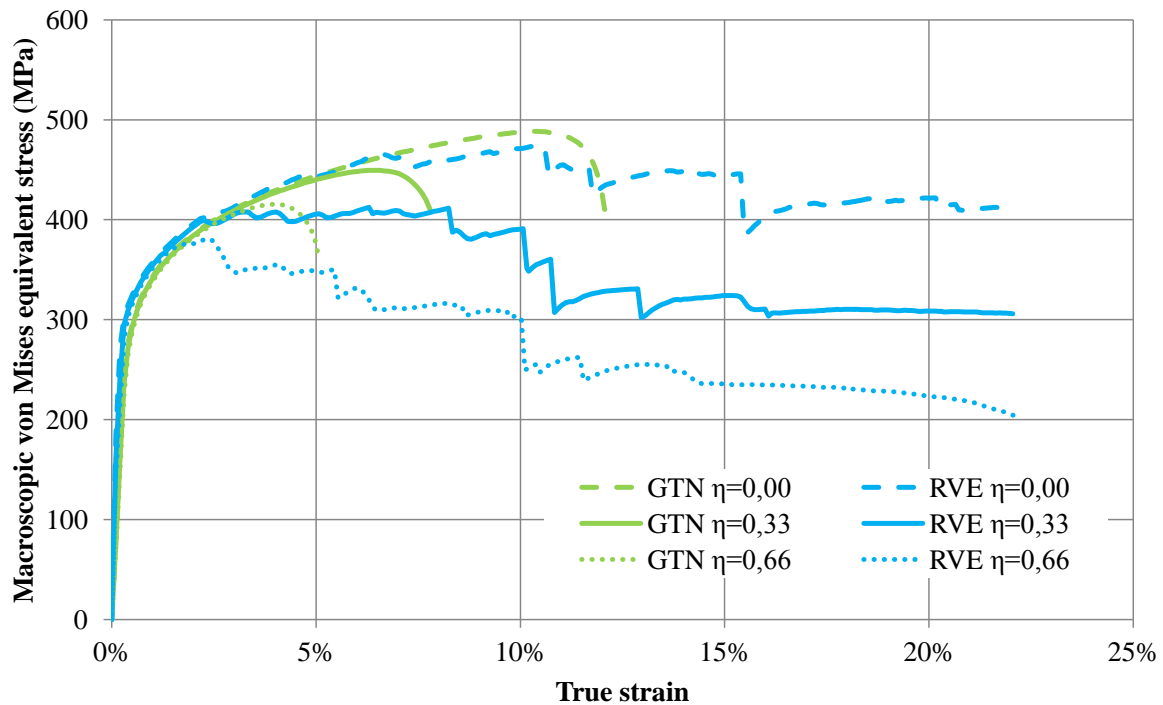


Figure 7.5 – Comparison between the macroscopic von Mises equivalent stress predicted by the GTN model and that averaged during RVE calculations at various macroscopic stress triaxiality ratios η .

While several authors have focused on improving the prediction of the porosity for general stress states, these results seem to indicate that the yield surface could also be improved. Recent extensions of the GTN model will be studied in the future, such as the Gologanu-Leblond-Devaux model [36]. Voids in the RVE simulations may also be distinguished between penny-shaped voids (*i.e.*, fragmentation micro-cracks) and spherical voids (*i.e.*, debonded particles). These two void populations certainly have a different influence on the load carrying capacity of the microstructure.

Finally, in order to reach a wider range of loading conditions than those studied in Chapter 4, it will be important to generalize the stress state control algorithm to two variables (*i.e.*, triaxiality ratio and Lode parameter). An attempt has been made in the present work using a recent non linear optimization library [304]. However, the macroscopic triaxiality ratio and Lode parameter for a given macroscopic strain rate tensor depend highly on the used time step, which is adaptive in the present framework. Consequently, the triaxiality ratio and the Lode parameter oscillate and conventional methods such as the Nelder-Mead algorithm tend to fail. Other approaches should be studied. This may also require to consider an implementation of periodicity constraints for nodes on opposite faces, which was avoided in the present work thanks to assumptions on the microstructure and loading conditions.

A generalization of the stress state control algorithm is also required for an application of the full field simulation tools developed in the present work to industrial processes, which will be considered by colleagues in an upcoming project [305].

Appendix A

An adaptive immersed approach to contact/impact mechanics

Football is not a contact sport, it's a collision sport - dancing is a contact sport.

Vincent Thomas "Vince" Lombardi

Introduction	270
A.1 Contact detection	272
A.1.1 Literature review	272
A.1.2 Proposed method	272
A.2 Contact formulation and solution	276
A.2.1 Literature review	276
A.2.2 Chosen method	277
A.3 Results	280
A.3.1 Contact	280
A.3.2 Impact	282
Conclusion	284

Résumé en français

Dans cette annexe, une nouvelle méthode de détection de contact est proposée. Cette méthode s'inscrit dans un cadre monolithique, où tous les objets à simuler sont immergés dans un unique maillage éléments finis. Les éléments de ce maillage occupés par aucun objet sont appelés éléments de la phase vide, et sont perpétuellement adaptés au cours de la simulation. Ainsi, on s'assure que ces éléments restent aussi réguliers que possible. Lorsque ces éléments prennent une topologie particulière, la notion d'élément de contact est introduite.

Ces éléments de contact sont utilisés pour discrétiser un problème de lagrangien augmenté implicite qui est résolu à l'aide d'un algorithme de Newton-Raphson. Ce dernier est lui-même inclus dans un algorithme itératif d'Uzawa. L'avantage principal de cette méthode est qu'aucune pénétration n'est possible entre les objets, car la méthode peut mesurer ses propres erreurs et automatiquement réduire le pas de temps pour les corriger. Des résultats très prometteurs sont obtenus pour des cas d'application de contact en statique et d'impact en dynamique.

Cette nouvelle méthode de détection de contact est basée sur l'adaptation de maillage, qui est une opération coûteuse et qui requiert de maintenir une certaine distance entre les objets. Ainsi, les éléments de contact ne peuvent pas dégénérer. Cette méthode est néanmoins très intéressante en comparaison avec les approches conventionnelles globales, car l'adaptation de maillage est une opération locale. En particulier, son coût est fortement réduit lorsque les surfaces de contact ne se déplacent ou se déforment que localement et par de très petites amplitudes. En outre, le maillage dans la phase vide est ignoré dans la plupart des opérations coûteuses comme le transfert de champ, puisqu'aucune variable d'histoire ne prend de valeurs dans les éléments de la phase vide.

Bien que les cas d'application présentés dans cette annexe montrent le potentiel de l'approche proposée pour la détection de contact ou d'impact par adaptation de maillage, plusieurs développements sont encore nécessaires. En particulier, sa robustesse est limitée, ce qui empêche de la comparer aux méthodes conventionnelles de détection de contact dans un cadre plus général. Pour commencer, le coût de l'adaptation de maillage pourrait être réduit en utilisant un maillage plus grossier dans la phase vide, ou en étudiant des estimateurs d'erreur pour adapter le maillage de manière anisotrope dans des directions préférentielles et ainsi aider la détection de contact. Ensuite, l'implémentation parallèle de cette méthode de détection de contact s'appuie fortement sur l'implémentation parallèle de l'algorithme d'adaptation de maillage, qui ne permet pas d'atteindre des accélérations optimales. Cette implémentation devrait être améliorée afin d'assurer l'optimalité et la performance à la fois de l'adaptation de maillage et de la détection de contact lors d'exécutions sur grands nombres de processeurs. De par la nature locale de l'algorithme d'adaptation de maillage utilisé dans ce travail, ces résultats devraient être très prometteurs en comparaison avec les approches conventionnelles qui s'appuient sur des recherches globales.

Par ailleurs, la discrétisation face-noeud utilisée dans cette annexe mène à une formulation sur-contrainte. Lorsque viennent s'ajouter les contributions dues à la discrétisation arête-arête supplémentaire en 3D, ce problème ne peut que s'aggraver. Les pistes pour éviter ces difficultés consisteraient à utiliser des éléments quadrangulaires et hexaédriques dans la phase vide, ce qui nécessiterait de généraliser l'algorithme d'adaptation de maillage à ce type d'éléments. L'avantage de ces derniers est qu'ils mènent à une discrétisation face-face qui permet un assemblage plus régulier des termes de contact et une meilleure approximation des surfaces de contact. Une autre possibilité serait de garder des éléments triangulaires et tétraédriques dans la phase vide, mais de les combiner localement pour construire une discrétisation face-face.

Pour finir, le critère utilisé pour automatiquement corriger la détection de contact en réduisant le pas de temps consiste à calculer le volume des éléments déformés. Paradoxalement, cette technique prend naturellement en compte les grandes déformations, ce qui n'est pas le cas de la formulation de lagrangien augmenté utilisée dans cette annexe. Cette formulation devrait donc être améliorée, ce qui pourrait également être une opportunité pour y ajouter les termes de frottement et ainsi s'intéresser à d'autres applications.

Introduction

With the computational fracture mechanics methodology introduced in the present work, a new problem appears, namely contact. In previous work at the Center for Material forming - MINES ParisTech (Cemef - MINES ParisTech) [5, 6], the volume conservation issue raised by the used Level-Set (LS) framework led to diffusion of crack faces whenever they came back into contact. More precisely, when the distance between two interfaces was smaller than mesh size, the phase between these two interfaces ended up being diffused. Physically, this defect led to complete crack closure and healing.

Thanks to the methodology introduced in Chapter 2, diffusion of the void phase is controlled by two parameters V_μ and V_σ . For instance, by fixing $V_\mu = 0$ diffusion never occurs and crack faces can penetrate each other, leading to non physical results and even failure of the mesh adaptation process. Because the conformity criterion in Algorithm 1 is based on volume computations, it cannot deal with zero volume or flipped elements.

An example of a 2D simulation with elements of the void phase about to be flipped is shown in Figure A.1. This has the consequence that nodes of the void/matrix interface will penetrate edges of the void/inclusion interface, and the opposite.

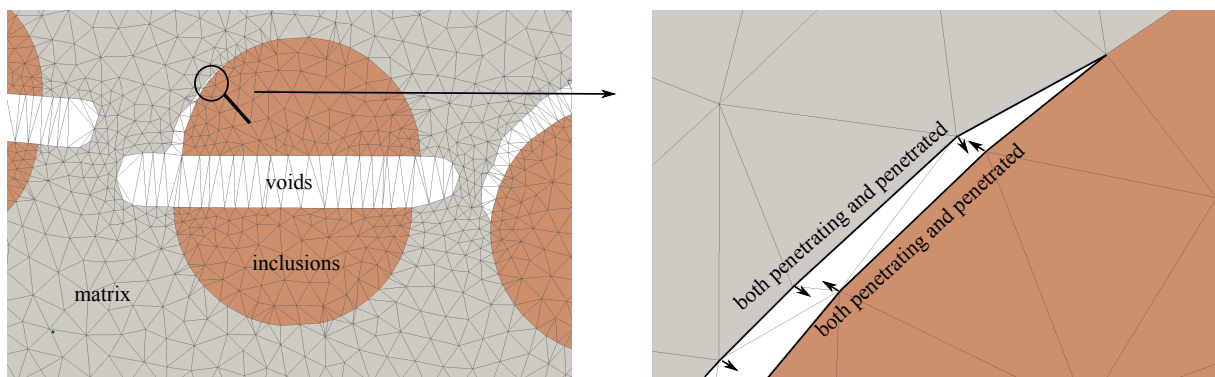


Figure A.1 – Contact situation in a 2D simulation with cracks.

In the following, a short review of computational contact mechanics approaches is presented, with a particular interest for robust methods to systematically prevent penetration. A major difficulty in the present simulations is the occurrence of self-contact, which is contact between two surfaces of the same phase. Friction is not considered in this appendix, but only a frictionless unilateral contact. Hence, the mechanical model has to be improved in order to include a force preventing penetration of crack faces (reaction force), but no force should resist to them sliding against each other (frictional force), or separating from each other (cohesion force). For a wider review of computational contact mechanics, the reader is referred to [306, 307].

As before, the domain is noted Ω , and the boundary of the void phase Γ_v . This boundary is sub-divided into a *penetrating* contact surface $\hat{\Gamma}_c \subset \Gamma_v$ and a *penetrated* contact surface $\Gamma_c \subset \Gamma_v$ that are not known *a priori*, and that are not necessarily exclusive. Standard computational contact mechanics approaches (called contact-impact mechanics in dynamics) are based on three tools:

- contact detection, which usually consists in an $\mathcal{O}(n \log n)$ algorithm similar to the one presented in Section 3.2, where for each *element* of Γ_c , all *elements* of $\hat{\Gamma}_c$ that could potentially come into contact have to be found,

- contact formulation, which consists in assembling contact terms, in an explicit or implicit manner, and with various coupling possibilities,
- contact solution, where the formulation assembled previously is solved using standard solution techniques for constrained problems.

Contact formulation can take into account an implicit velocity field to better predict the actual position of the penetrating and penetrated surfaces, but these surfaces are generally determined explicitly during contact detection. Hence, each *element* K of Γ_c is associated with several *elements* of $\hat{\Gamma}_c$ and a penetration is calculated for each of them. However, the penetration of K by an *element* of $\hat{\Gamma}_c$ with which it was not associated is ignored. In a large deformation context, which is not the case in the present framework, changes of orientation of the contact faces can also be taken into account implicitly, but with the same limitation due to explicit contact detection.

The word *element* is always written in italic in this appendix because different possibilities have been proposed in the literature for the discretization of Γ_c and $\hat{\Gamma}_c$: node-to-node, face-to-node, face-to-face. For historical reasons, the word segment is often preferred by the computational contact mechanics community to refer to a face. The latter is used in this appendix to be consistent with mesh topology vocabulary.

This choice of discretization and explicit or implicit scheme has to be completed with a choice of coupling. The contact constraint can be enforced strongly in the velocity-pressure formulation, by adding supplementary contributions on both left and right hand-sides of the problem, or it can be enforced weakly by only adding terms in the right hand-side of the problem. Intermediary coupling is also possible, with right hand-side terms that are updated with an outer iterative solver.

In the present work, the main contribution regards the contact detection step, while standard methods have been used for contact formulation and solution, highly inspired from previous work [113, 308, 309, 310] and the literature [306, 307].

A.1 Contact detection

A.1.1 Literature review

As stated above, the process of contact detection is explicit, as it is based on the current state of the mesh. If the contact formulation did not enforce strictly contact constraints, it would be necessary to detect *elements* of $\hat{\Gamma}_c$ that have already penetrated Γ_c . Explicit time discretizations, often used in dynamics, have led researchers to investigate suitable contact detection algorithms for this case [311, 312, 313, 314, 315, 316]. In this work, since penetration has to be avoided at all cost, contact constraints will be enforced strictly, hence it is necessary to detect, for each *element* of Γ_c , all the *elements* of $\hat{\Gamma}_c$ for which a reaction force would potentially have to be computed.

A straightforward way of solving this problem would be to look for each *element* of $\hat{\Gamma}_c$, the closest *element* of Γ_c . This method is known as a brute force algorithm and has a cost of $\mathcal{O}(\hat{n}_c n_c)$, \hat{n}_c being the number of *elements* in $\hat{\Gamma}_c$, while n_c is the number of elements in Γ_c . Using space partitioning techniques based on binary trees, this cost can be reduced to $\mathcal{O}(\hat{n}_c \log n_c)$ [306, 316, 317, 318, 319, 320]. Other researchers have developed techniques inspired from the bucket sort algorithm (*also known as* bin sort) [306, 307, 313, 321, 322] and hash tables [323, 324, 325].

This straightforward approach, however, has several flaws, independently of the choice of space partitioning technique. In the case illustrated in Figure A.2(a-c), the closest projection of the green body on the orange body is highlighted in red. Since the motion of the green body is oriented in the direction of the projection, contact is detected and the link between penetrating and penetrated surfaces is always correctly predicted, even if the green body moves directly from (a) to (c).

Now, in the case illustrated in Figure A.2(d-f), the closest projection does not give a correct prediction *a priori*. This is a first flaw of this contact detection technique [316, 326, 327]. However, one could argue that this mistake can be corrected *a posteriori* by performing contact detection again after deformation in Figure A.2(e), realizing that penetration occurred, and going back to Figure A.2(d) with a smaller time step. However, this cannot be detected if the green body moved directly from Figure A.2(d) to Figure A.2(f).

This problem is linked to the prediction of the instant of contact/impact and is very important for thin structures or impact problems in general [316, 327]. Therefore, this contact detection technique has to be used with a very small time step, which generally has to be determined by the user.

An additional limitation of this technique is that, in order to achieve robustness and make sure that contact surfaces are always correctly predicted, even in the case illustrated in Figure A.2(d-f), contact detection has to be performed at each time increment, and even twice per time increment if one wants to predict the issue in Figure A.2(e). Though adaptive strategies have been proposed in the literature to avoid a global search at each time increment, they are known to not yield the same robustness as a global search [307, 313, 314, 318, 321].

A.1.2 Proposed method

In the present work, a new contact detection method is proposed that offers a promising alternative to the straightforward technique described above. The main advantage of this method is that it predicts when contact surfaces are not well predicted as in Figure A.2(d-f), and enables to

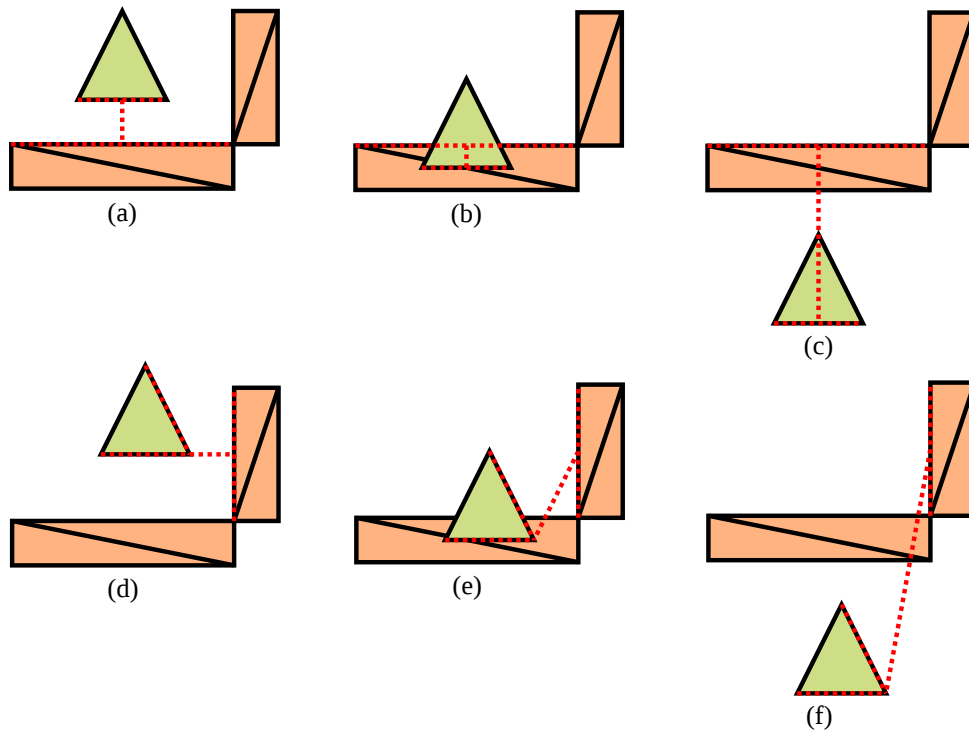


Figure A.2 – Contact detection: (a-c) success, (d-f) failure.

automatically tune the time step. Though this method has costs that are not comparable to the straightforward technique, it has the advantage of enabling local adaptation of contact surfaces, with the same robustness as a global search.

The method originates from a discussion on cohesive elements. These elements are used in computational fracture mechanics to model accurately the progressive loss of load bearing capacity of interfaces [184]. In two dimensions (2D), quadrilateral elements with zero volume are inserted in the initial mesh by splitting faces of each interface that could potentially crack. Crack initiation is modeled by allowing these quadrilateral elements to open progressively with the introduction of a load-displacement constitutive law (as opposed to usual stress-strain laws). However, if compression occurs locally, these cohesive elements can also be used to model contact, as cohesive elements will be flipped in case of penetration. This situation is illustrated in Figure A.3.

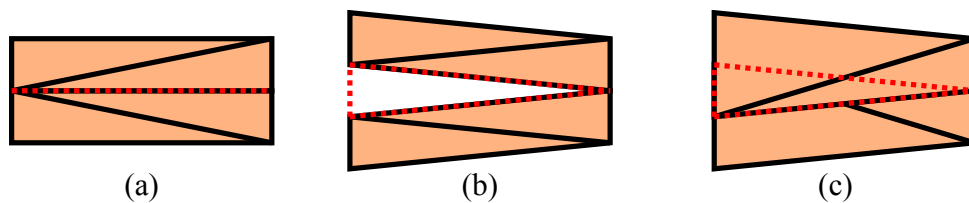


Figure A.3 – Cohesive elements with correct contact prediction: (a) initial mesh with cohesive element in red, (b) crack initiation, (c) inter-penetration of crack faces.

It is assumed that the cohesive element can be used as a contact element, and that the two opposite faces of the contact element are both penetrating and penetrated surfaces, as in Figure A.4(a,b). This is not true if the two opposite faces move or deform significantly and end up not *facing* each other, as in Figure A.4(c). Additionally, the cohesive element could even be flipped

without contact occurring, as in Figure A.4(d).

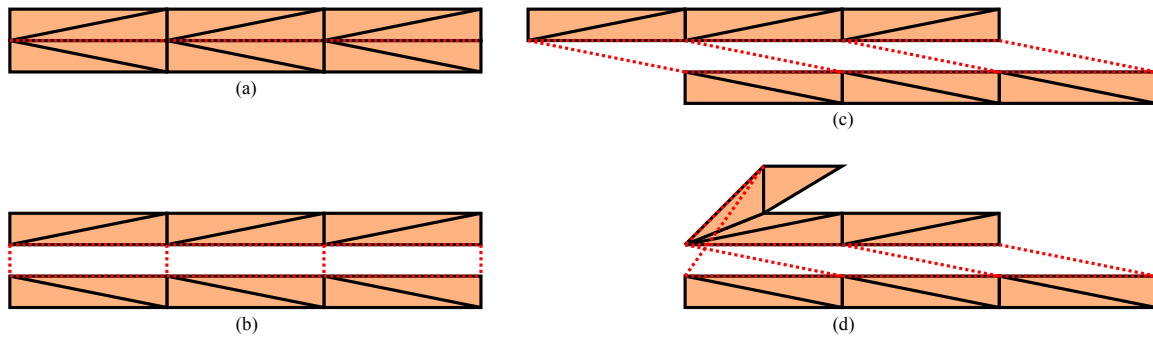


Figure A.4 – Cohesive elements with incorrect contact prediction: (a) initial mesh with cohesive element in red, (b) crack initiation, (c) sliding, contact surfaces are not well predicted, (d) a cohesive element has flipped without contact occurring.

Based on the remarks made above on cohesive elements, it is proposed to apply mesh adaptation to these elements. In the present work, cohesive laws are not considered, but the elements of the void phase are used to predict contact. Adapting these elements with a pure shape criterion ensures that simplexes in the void phase are as regular as possible. For example, in 2D, a regular simplex is an equilateral triangle, which is also a triangle where the orthogonal projection of each node on the opposite face is the middle of this face. A well-shaped element in the void phase is hence a perfect candidate for a contact element, given that one of its nodes belongs to $\hat{\Gamma}_c$, while the face opposing this node belongs to Γ_c .

In 2D, several situations can be met inside each element of the void phase, as illustrated in Figure A.5(a,b). In Figure A.5(b), the green node is potentially in contact with the opposite face, while in Figure A.5(a) two nodes are potentially in contact with their respective opposite faces.

This principle can be extended to three dimensions (3D), as illustrated in Figure A.5(c-e). An additional difficulty in 3D it that an edge-to-edge situation can be met because an edge may penetrate another edge with no node penetrating any face, as shown in Figure A.5(f).

The new method introduced in this appendix enables for a prediction of this situation naturally as these particular contact elements will be automatically generated during mesh adaptation. The listing of these possibilities also naturally introduces the discretization of contact surfaces Γ_c and $\hat{\Gamma}_c$ used in this work, which is a face-to-node discretization, with the particular edge-to-edge case in 3D. As a conclusion, each face of an element of the void phase is associated with the opposite node if both the face and the node are shared with elements of a solid phase. In 3D, each edge of an element of the void phase is associated with the opposite edge if both edges are shared with elements of a solid phase.

The different configurations can be determined in $\mathcal{O}(n_v)$ using only topological operations, by going through all elements of the void phase, and considering the faces (and edges in 3D) of these elements that are shared with a non-void element. The number of elements n_v in the void phase can be reduced by prescribing a coarse mesh size in the void phase, as there is no physical data stored in these elements. Obviously, it is important to consider the cost of mesh adaptation in the void phase. However, this operation does not ask for field transfer, which would require $\mathcal{O}(\hat{n}_v \log n_v)$ operations, as there is no field to transfer in the void phase. Additionally, the cost of mesh adaptation is $\mathcal{O}(n_v)$ if no contact surface moved, and, more generally, it is of linear cost in the parts of the mesh where no contact surface moved.

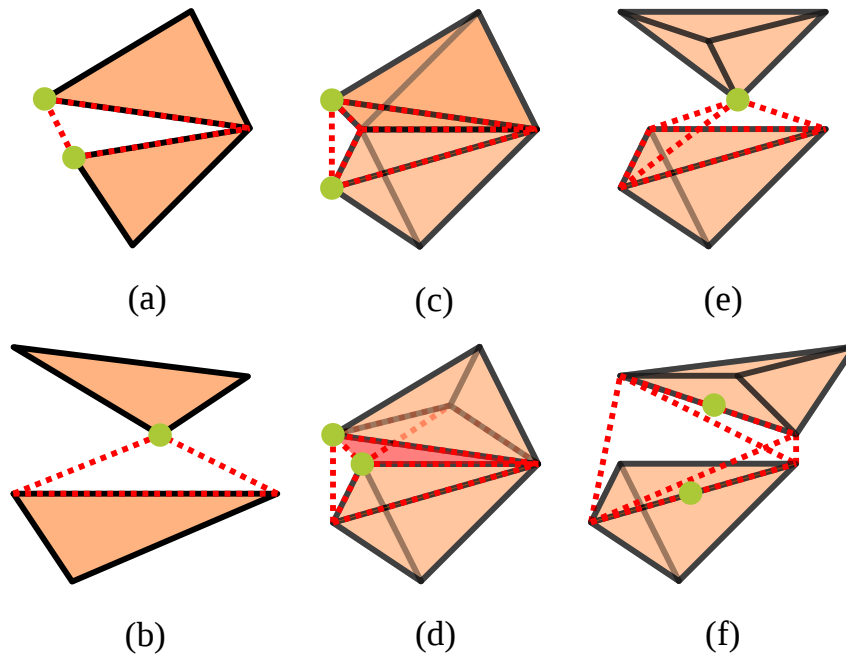


Figure A.5 – Contact element topology: (a) one 2D element with two nodes in $\hat{\Gamma}_c$ and two faces in Γ_c , (b) one 2D element with one node in $\hat{\Gamma}_c$ and one face in Γ_c , (c) one 3D element with two nodes in $\hat{\Gamma}_c$ and two faces in Γ_c , (d) two 3D elements (their common face being highlighted in red) with one node in $\hat{\Gamma}_c$ each and one face in Γ_c each, (e) one 3D element with one node in $\hat{\Gamma}_c$ and one face in Γ_c , (f) one 3D element with two edges in $\hat{\Gamma}_c$ and two edges in Γ_c .

As a conclusion, the proposed contact detection procedure consists in adapting the mesh in the void phase before each mechanical solution, with no field transfer. Then, each element of the void phase is tested against each configuration in Figure A.5. Finally, these configurations are used to compute normal vectors and other quantities of interest for contact formulation, these normal vectors being naturally oriented because the mesh adaptation process produces oriented elements in the void phase.

After contact formulation and solution, the mesh is deformed. If any element of the void phase ends up being flipped (based on a simple volume criterion), it means that penetration occurred and was not detected, as in Figure A.2(d-f), hence the time step can be reduced and the time increment can be restarted. This condition is necessary but not sufficient, as illustrated in Figure A.4(d).

If the maximum displacement of contact surfaces at each time increment is less than the mesh size in the void phase, it is possible to optimize this correction step by taking into account only contact elements (*i.e.*, only the elements of the void phase that participate in the contact formulation). In this case, the mesh motion algorithm (Section 2.3) prevents the remaining elements of the void phase from degenerating.

A.2 Contact formulation and solution

A.2.1 Literature review

Based on the face-to-node and edge-to-edge contact discretization presented above, contact formulation can be described [113, 306, 307, 308, 309, 310]. This formulation introduces a unilateral contact condition in the velocity-pressure formulation corresponding to the mechanical problem, which already accounts for material behavior, equilibrium, and (in)compressibility. Defining d_c as the initial distance between Γ_c and $\hat{\Gamma}_c$, and Δt as the time step, the unilateral contact condition expresses as

$$d_c(\mathbf{x}) + \Delta t(v(\hat{\mathbf{x}}) - v(\mathbf{x})) \cdot n(\mathbf{x}) \leq 0, \mathbf{x} \in \Gamma_c \quad (\text{A.1})$$

where $\hat{\mathbf{x}}$ is a point of $\hat{\Gamma}_c$ suspected to penetrate the contact surface by the contact detection algorithm, and \mathbf{x} is its orthogonal projection on Γ_c . The vector n is normal to Γ_c and oriented outwards with respect to the void phase. Opposed to contact formulations with a rigid body, in the present case $v(\hat{\mathbf{x}})$ is unknown and $\hat{\mathbf{x}}$ will generally also belong to Γ_c . The expression in Equation (A.1) is actually a first order approximation of the actual penetration [113], and the condition can be equivalently expressed as

$$P(\mathbf{x}) = \frac{d_c(\mathbf{x})}{\Delta t} + (v(\hat{\mathbf{x}}) - v(\mathbf{x})) \cdot n(\mathbf{x}), P(\mathbf{x}) \leq 0, \mathbf{x} \in \Gamma_c.$$

This constraint can be enforced through a positive Lagrange multiplier λ , leading to the following Lagrangian formulation [306, 307, 328]

$$\mathcal{L}^\lambda(v, p, \lambda) = \mathcal{L}^{vp}(v, p) + \int_{\Gamma_c} \lambda [P]^+ \quad (\text{A.2})$$

where $[x]^+ = \begin{cases} x, & x > 0 \\ 0, & x \leq 0 \end{cases}$ and \mathcal{L}^{vp} is the functional associated with the velocity-pressure formulation presented in Subsection 1.2.1. Minimization of this functional is usually performed with a Newton-Raphson procedure, where each nonlinear solution step uses a linear approximation. This linear system solved at each nonlinear solution step includes the terms associated with λ and is known to require specific preconditioning treatments. However, the solution that minimizes $\mathcal{L}^\lambda(v, p, \lambda)$ does not allow any penetration and the constraint is exactly verified.

To reduce implementation and preconditioning issues, the constraint can be enforced through penalization [113, 306, 307, 308, 309, 310], with a penalization constant ρ_c

$$\mathcal{L}^{\rho_c}(v, p, \lambda) = \mathcal{L}^{vp}(v, p) + \frac{\rho_c}{2} \int_{\Gamma_c} [P]^{+2}. \quad (\text{A.3})$$

This method relies heavily on the choice of ρ_c , as the accuracy of the formulation is bounded by $\frac{1}{\rho_c}$. A high penalization coefficient is necessary for a good accuracy, but it will also increase the stiffness of the functional and perturb the nonlinear and linear solvers used to minimize it. Opposite to the previous method, this penalized formulation allows penetration and the constraint is not exactly verified.

In an augmented Lagrangian formulation [306, 307, 329, 330, 331], the constraint is enforced through a penalization part and Lagrange multipliers, hence combining Equation (A.3) and Equation (A.2)

$$\mathcal{L}^{\rho_c \lambda}(v, p, \lambda) = \mathcal{L}^{vp}(v, p) + \frac{\rho_c}{2} \int_{\Gamma_c} [P]^{+2} + \int_{\Gamma_c} \lambda [P]^+. \quad (\text{A.4})$$

The role of the penalization part is to accelerate the convergence of the algorithm, as it will account globally for small penetrations. The role of the multiplier part is to account locally for higher penetrations, and ensure that the constraint is exactly verified. Although they guarantee a higher level of accuracy with no penetration, the computational cost of both Lagrangian and augmented Lagrangian methods is far more significant than that of the penalization approach. Opposed to the standard Lagrangian formulation, the augmented Lagrangian one does not modify the number of degrees of freedom in the velocity-pressure problem, but an outer iterative process is necessary to update the Lagrange multipliers.

A.2.2 Chosen method

Due to its easier implementation and the fact that it prevents penetration, the augmented Lagrange formulation is a suitable candidate for the present developments. It is detailed hereafter in the case of the face-to-node and edge-to-edge contact elements. The discretization $\Gamma_{c,h}$ of the contact surface Γ_c is composed of faces of the mesh, and also edges in 3D. These faces and edges do not lie on $\partial\Omega$ because the void phase is meshed. For each of these faces and edges that are marked by the contact detection algorithm, a contact element K is considered, with $\hat{\mathbf{x}}, \mathbf{x} \in K$.

In the face-to-node case, $\hat{\mathbf{x}}$ is a node of K and \mathbf{x} is its orthogonal projection on the opposite face F , n_h being the normal vector to F , oriented outwards with respect to the void phase. A Lagrange multiplier is associated to the face F .

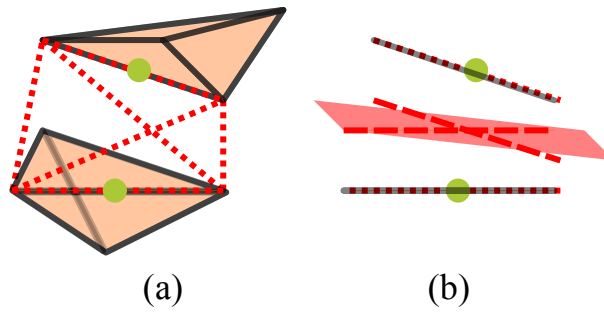


Figure A.6 – Edge-to-edge contact: (a) configuration, (b) definition of contact surface and projection points.

In the edge-to-edge case illustrated in Figure A.6, the normal vector n_h is the normalized cross product of the two edge vectors. The two points $\hat{\mathbf{x}}$ and \mathbf{x} are then located respectively on the penetrating edge and the penetrated one by solving a 2×2 linear system where the solutions are such that $(\hat{\mathbf{x}} - \mathbf{x}) \cdot n_h$ is minimal. A Lagrange multiplier is associated with the penetrated edge. In both cases, the distance $d_{c,h}$ is equal to $(\hat{\mathbf{x}} - \mathbf{x}) \cdot n_h$. The velocity is approximated by v_h and $v_h(\hat{\mathbf{x}})$ is noted \hat{v}_h . Thus, integrals in Equation (A.4) can be discretized

$$\begin{aligned} \frac{\rho_c}{2} \int_{\Gamma_{c,h}} [P_h]^{+2} &= \frac{\rho_c}{2} \int_{\Gamma_{c,h}} \left[\frac{d_{c,h}}{\Delta t} + (\hat{v}_h - v_h) \cdot n_h \right]^{+2}, \\ \int_{\Gamma_{c,h}} \lambda [P_h]^+ &= \int_{\Gamma_{c,h}} \lambda_h \left[\frac{d_{c,h}}{\Delta t} + (\hat{v}_h - v_h) \cdot n_h \right]^+. \end{aligned}$$

The discrete Lagrange multiplier is a vector of size the number of penetrated faces (and edges in 3D). It is not constant per contact element, as each contact element can carry multiple configurations, as in Figure A.5(a). For the sake of completeness, the derivatives of the contact

terms in Equation (A.4) are given below. Since all contact terms are vanishing if the condition in Equation (A.1) is verified, the derivatives are only defined in $\Gamma_{c,h}^+ = \{\mathbf{x} \in \Gamma_{c,h}, P_h(\mathbf{x}) > 0\}$

$$\begin{aligned} \frac{\partial}{\partial v_h} \left(\frac{\rho_c}{2} \int_{\Gamma_{c,h}^+} (P_h)^2 \right) (\delta w_h) &= \rho_c \int_{\Gamma_{c,h}^+} (P_h(v_h)) (D_h(\delta w_h) \cdot n_h), \\ \frac{\partial}{\partial v_h} \left(\int_{\Gamma_{c,h}^+} \lambda (P_h) \right) (\delta w_h) &= \int_{\Gamma_{c,h}^+} \lambda_h (D_h(\delta w_h) \cdot n_h), \end{aligned}$$

where $D_h : \delta w_h \rightarrow \frac{\partial(\hat{v}_h - v_h)}{\partial v_h}(\delta w_h)$. For implementation in a Newton-Raphson solver, the second derivative of the penalty term also has to be computed

$$\frac{\partial^2}{\partial v_h \partial v_h} \left(\frac{\rho_c}{2} \int_{\Gamma_{c,h}^+} (P_h)^2 \right) (\delta w_h, \delta u_h) = \rho_c \int_{\Gamma_{c,h}^+} (D_h(\delta u_h) \cdot n_h) (D_h(\delta w_h) \cdot n_h).$$

These terms are added to the discrete mixed weak form in Equation (1.13)

$$\left\{ \begin{aligned} & \int_{\Omega_h} \left(\frac{\partial s_h}{\partial v_h}(v_h^0) : \dot{\varepsilon}(v_h) \right) : \dot{\varepsilon}(w_h) \\ & \quad - \int_{\Omega_h} p_h \operatorname{div} w_h \\ + \rho_c \int_{\Gamma_{c,h}^+} (D_h(v_h) \cdot n_h) (D_h(w_h) \cdot n_h) &= \int_{\Omega_h} \left(\frac{\partial s_h}{\partial v_h}(v_h^0) : \dot{\varepsilon}(v_h) \right) : \dot{\varepsilon}(w_h) \\ & \quad - \int_{\Omega_h} s_h(v_h^0) : \dot{\varepsilon}(w_h) \\ & \quad + \int_{\partial\Omega_h} w_h \cdot (\sigma_h n_h) \\ & \quad + \rho_c \int_{\Gamma_{c,h}^+} (D_h(v_h^0) \cdot n_h) (D_h(w_h) \cdot n_h) \\ & \quad - \rho_c \int_{\Gamma_{c,h}^+} (P_h(v_h^0)) (D_h(w_h) \cdot n_h) \\ & \quad - \int_{\Gamma_{c,h}^+} \lambda_h (D_h(w_h) \cdot n_h), \forall w_h \in \mathcal{V}_h, \\ - \int_{\Omega_h} q_h \operatorname{div}(v_h) - \int_{\Omega_h} \frac{\dot{p}_h}{\mathcal{X}} q_h &= 0, \forall q_h \in \mathcal{P}_h. \end{aligned} \right. \quad (\text{A.5})$$

The nonlinear penalization term is hence strongly coupled to the Newton-Raphson solver, while the Lagrange multiplier part yields only a right hand-side term. The solution of this term is based on an outer Uzawa iteration consisting in a projection onto the contact constraint

$$\lambda_h \leftarrow \lambda_h + \rho_c P_h(v_h), \quad (\text{A.6})$$

where v_h is the solution obtained at convergence of the Newton-Raphson algorithm applied on Equation (A.5). A certain number of remarks have to be made regarding this methodology.

First, this augmented Lagrangian formulation is standard, and is well-known to lead to an over-constrained problem due to the choice of discretization [329, 332, 333, 334]. It can be proved that the number of constraints (or, equivalently, the number of configurations), will generally be greater than the number of degrees of freedom, leading to artificially rigid contact

surfaces [309].

Strategies to avoid this problem include coloring algorithms which enable to discriminate contact surfaces into masters and slaves, and assemble contact constraints only for one of the two categories. In order to obtain a symmetric formulation, this procedure can be applied in a two-pass algorithm where the roles are then switched [311, 315, 321, 335].

A more robust solution with improved prediction of interface deformation, especially in case of friction and other important physical phenomena at contact surfaces, is given by mortar elements, which are based on a face-to-face discretization [306, 307, 319, 329]. Studying the compatibility of this method with the contact detection algorithm introduced in this appendix will be considered in future work (Chapter 7). For instance, quadrangular or hexahedral contact elements could be used instead of triangles and tetrahedra, as mesh adaptation algorithms compatible with such elements have been studied recently in the literature [336]. More simply, the discretization of the contact surface with mortar elements could be built by considering the neighborhood of each triangular and tetrahedral contact element.

Second, some particularities have to be taken into account due to the original contact detection algorithm introduced in this appendix. First, the outer Uzawa iteration is also in charge of reducing the time step if convergence is reached but a contact element is being flipped. Then, the initial distance between contact surfaces $d_{c,h}$ is artificially increased with a small thickness ϵ_c in order to detect penetration slightly before it actually occurs, and maintain a small thickness in contact elements, preventing them from degenerating. Degenerated contact elements would lead to a failure of the mesh adaptation algorithm. In practice, a value of ϵ_c at least one order smaller than the mesh size is chosen.

A.3 Results

In this section, numerical experiments are carried out to test the contact detection algorithm and show its ability to predict self-contact and impact instants. All 2D calculations are carried out in plane strain. The penalization coefficient ρ_c is fixed to 100, and the condition for convergence of the Uzawa loop is that the predicted penetration should be less than $0.5\epsilon_c$. It is stopped after 20 iterations if this condition has not been met.

Because these simulations only feature small deformations, remeshing is only applied in the void phase. This remeshing is applied at the beginning of each increment for contact detection, and at the end of some increments depending on the mesh motion algorithm. The β coefficient for the latter is set to 0.5.

A.3.1 Contact

The contact problem studied in this subsection features two incompressible elastic bodies with different Young's moduli. The geometry, shown in Figure A.7, is constructed so that body 2 will move towards body 1, until contact, and will then deform it until it comes into contact with itself. Thus, a constant velocity $V_X = (-0.5, 0)$ is imposed at the right face of body 2, and another constant velocity $V_Y = (0, -0.5)$ is imposed at its top face. The (non-dimensional) time step is fixed initially to 0.01 and then varies due to the contact solution algorithm.

A 3D configuration is also tested, by considering the same case with a thickness of 0.2 m. Both contact instants, first of body 2 with body 1, and then of body 1 with itself, are to be captured. The Young's moduli of the two bodies are shown in Figure A.7. A uniform isotropic mesh size of 80 μm is used in the whole domain. The contact thickness ϵ_c is fixed to 0.8 mm in 2D and 8 mm in 3D. It is higher in 3D because the volume of a regular tetrahedron is necessarily smaller than the surface of a triangle of same size.

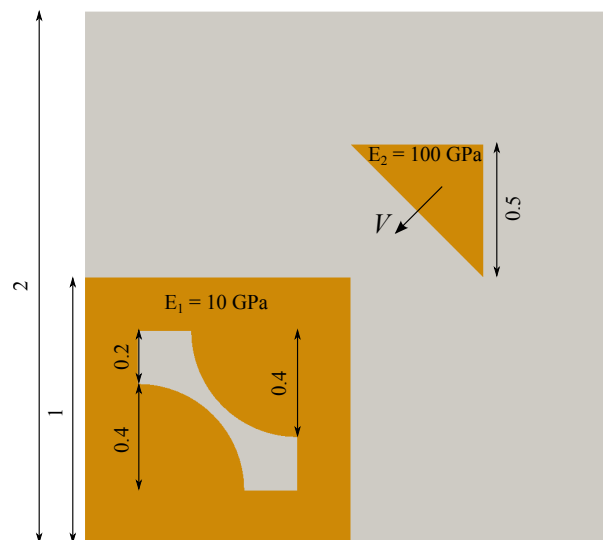


Figure A.7 – Contact test case, with solids in gold and void phase in light gray. All distances are in meters.

The 2D and 3D geometries after both contacts are shown in Figure A.8. Although no element got flipped in both calculations, all steps of the 3D one did not converge in 20 iterations. Thus, some elements reached a thickness lower than $0.5\epsilon_c$ at some points of the simulation. This

is an issue that is likely to be due to the presence of Lagrange multipliers at faces and edges. These supplementary constraints at edges can only aggravate the over-constrained aspect of the augmented Lagrange formulation.

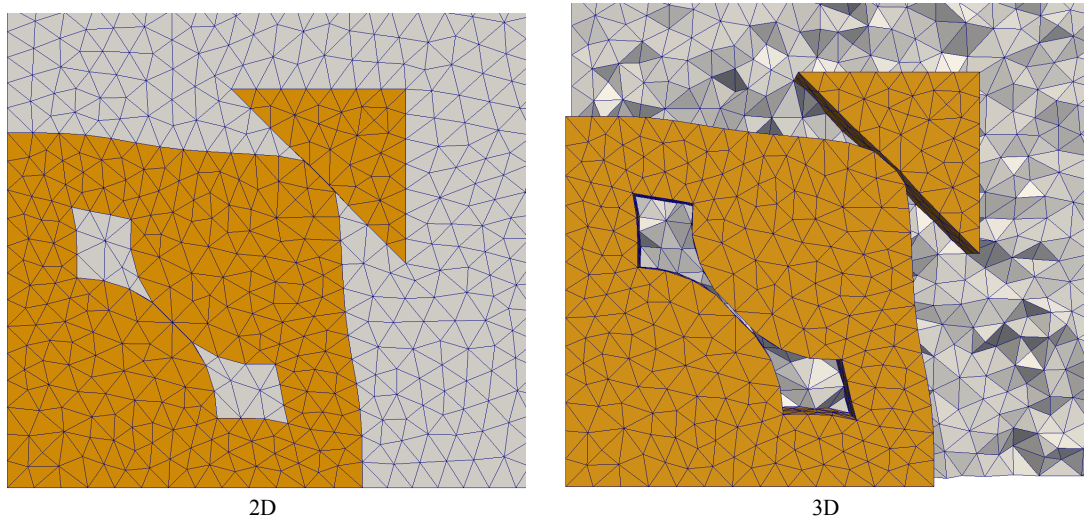


Figure A.8 – Results in 2D and 3D at $t = 0.7$ for the contact test case, with solids in gold and void phase in light gray.

The true stresses at all time steps are shown in Figure A.9 for the 2D calculation. It is defined as the vertical force on the left and bottom faces of body 2, divided by the respective areas of these faces. Each dot on this curve represents an increment of the simulation, which gives an idea of time step change. While contact detection is directly correct for the first contact instant, the time step has to be decreased for the second one.

This first experiment shows both interesting capabilities of the proposed contact detection approach, and limitations. Improvements of the contact formulation will be necessary to solve convergence issues in 3D.

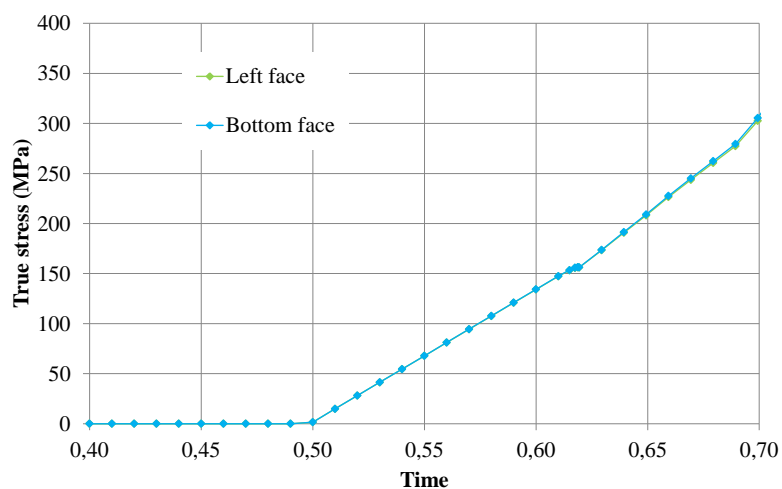


Figure A.9 – True stress measured at the left and bottom faces of body 1 for the 2D contact test case.

A.3.2 Impact

In the following tests, the static formulation in Equation (A.5) is extended to the dynamic case by adding an inertia term $\int_{\Omega_h} \rho \dot{v}_h w_h$ on the left-hand side, ρ being the density of the material.

This term is discretized with an implicit Euler scheme. A volume force term $\int_{\Omega_h} \rho g w_h$ associated with gravity is also added, with $g = 10 \text{ m s}^{-2}$.

The studied impact problem is the fall of a random arrangement of spherical balls with random sizes on a rigid ground. The balls are modeled as incompressible elastic solids with a Young's modulus of 100 GPa and a density of 1000 kg m^{-3} . The Young's modulus for the ground is fixed to a very high value of 100 TPa in order to limit the deformation of the ground (its density is the same as the one used for the balls).

Regarding numerical parameters, the time step is fixed initially to 0.01 s, and a uniform isotropic mesh size of 4 mm is used in the whole domain. The contact thickness is set to 0.4 mm. The simulation is stopped when one of the balls touches the boundary of the domain. The mesh at different points of the simulation is shown in Figure A.10. The number of elements in this mesh is around 200000 and does not vary significantly during the simulation.

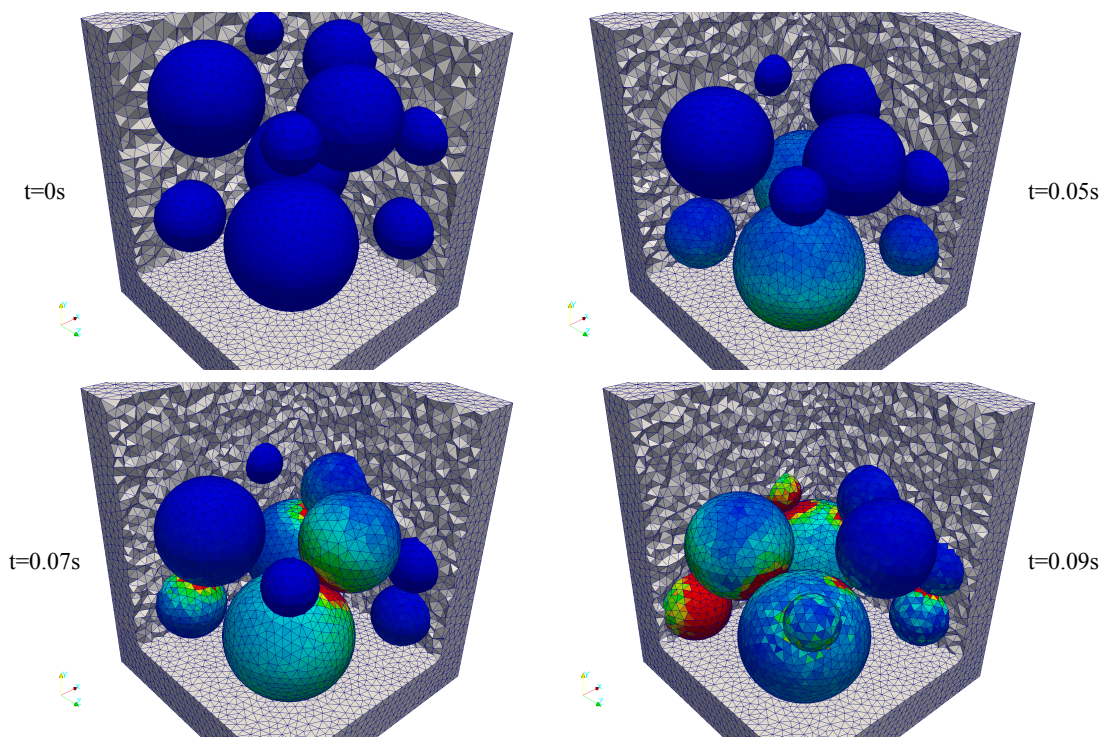


Figure A.10 – Result of the impact test case. Balls are colored from blue to red depending on stress intensity, red indicating higher stresses (in magnitude).

An important advantage of the present framework is that all balls are considered as a single material and not independent bodies, so that in the implementation contact between the balls is detected no differently than self-contact. Moreover, the use of a single mesh is very interesting for distributed computations, as partitioning is easier with a single mesh than several ones. In particular, the parallel implementation of contact detection is helped by the fact that mesh adaptation only uses local operations, while global search algorithms used by standard contact

detection techniques are quite complex to implement in parallel. The parallel efficiency of these algorithms is also highly dependent on the partitioning strategy.

The performance of the present contact detection method in parallel is assessed by performing the same simulation but using more than 1 Central Processing Unit (CPU). The speedup obtained using 2 CPUs instead of 1 is 1.5, which means that there is an acceleration, but is poor (it should be closer to 2). Increasing the number of CPUs to 4, a speedup of 3.1 is measured, and then 5.6 using 8 CPUs. These measurements show that using mesh adaptation to detect contact is interesting from a parallel computing point of view, which is very promising for industrial applications such as powder compaction, where contacts between a large number of grains have to be modeled. The parallel implementation of the mesh adaptation algorithm should be revisited in order to improve these results.

The proposed approach performs well on this 3D problem with multiple impacts, as all increments converged in less than 20 iterations of the Uzawa algorithm, and most of them required only a few iterations. The main difference between static and dynamic tests is that in the latter the time step has a direct influence on contact solution, as the displacement of the two bodies is directly reduced. In statics, the motion of one of the bodies is reduced, but due to springback the displacement of the deformed body may be independent on the time step. As a conclusion, while results in dynamic tests are promising, a more robust strategy than reducing the time step should be studied to help contact detection in the static case.

Conclusion

In this appendix, a new contact detection method has been proposed. This method requires to immerse all bodies that could potentially enter into contact in a single mesh (monolithic approach). The elements of this mesh occupied by no body, called void phase elements, are constantly being adapted in order to have simplexes as regular as possible. When some specific configurations are encountered in these elements (Figure A.5), the notion of contact element is introduced.

These contact elements are used to discretize an implicit augmented Lagrangian formulation that is solved thanks to a Newton-Raphson procedure, which is itself included in an Uzawa iterative scheme. The main advantage of this method is that no penetration is possible, as the method can detect its own failure and automatically reduce the time step to correct itself. Promising results are obtained with applications not only in static problems but also in impact mechanics.

The method is based on mesh adaptation, which is a costly operation and requires to maintain a small thickness between bodies to prevent degeneration of contact elements. However, the costs are reduced with no sacrifice on robustness when contact surfaces only move locally or slightly, in comparison with a global search. Additionally, the mesh in the void phase is ignored in most Finite Element (FE) operations such as field transfer, since no history data is stored in these elements.

Though the numerical experiments presented in this appendix show the potential of the proposed adaptive immersed approach to contact/impact mechanics, several developments are necessary in order to improve its robustness, and assess completely its interest with respect to more standard contact detection techniques.

First, the cost of mesh adaptation could be reduced using a coarser mesh size in the void phase, or studying error estimators to adapt the mesh in specific directions and help contact detection. Second, the parallel implementation of this approach relies on the parallel implementation of the mesh adaptation algorithm (Section 2.5), which does not show optimal parallel efficiency. This should be improved in order to ensure the performance of the method in massively parallel computations. Due to the local nature of the mesh adaptation algorithm, results are likely to be very promising with respect to standard approaches that are based on global searches.

Third, the face-to-node discretization used in the present work results in an over-constrained formulation. The contributions due to the supplementary edge-to-edge discretization in 3D can only aggravate this issue. This could be improved by using quadrangular and hexahedral elements, but then defining mesh adaptation methods that could handle them. These elements would yield a face-to-face discretization and enable to assemble the contact constraints on a better approximation of the contact surfaces. Another possibility would be to adapt the mesh with simplex elements and then build a face-to-face discretization by combining simplexes.

Finally, the test used to automatically correct contact detection by reducing the time step consists in computing the volume of deformed elements. This naturally takes into account large deformations, while the contact formulation assumes small deformations. The formulation should be upgraded to eliminate this paradox. Such study could be an opportunity to integrate frictional terms in the formulation.

Bibliography

- [1] P.-O. Bouchard, L. Bourgeon, H. Lachapèle, E. Maire, C. Verdu, R. Forestier, and R. E. Logé. “On the influence of particle distribution and reverse loading on damage mechanisms of ductile steels”. In: *Materials Science and Engineering: A* 496.1-2 (2008), pages 223–233. doi: [10.1016/j.msea.2008.05.033](https://doi.org/10.1016/j.msea.2008.05.033) (cited on pages [10](#), [32](#)).
- [2] M. Bernacki, Y. Chastel, T. Coupez, and R. E. Logé. “Level set framework for the numerical modelling of primary recrystallization in polycrystalline materials”. In: *Scripta Materialia* 58.12 (2008), pages 1129–1132. doi: [10.1016/j.scriptamat.2008.02.016](https://doi.org/10.1016/j.scriptamat.2008.02.016) (cited on pages [10](#), [103](#), [110](#), [111](#), [257](#)).
- [3] B. Scholtes, R. Boulais-Sinou, A. Settefrati, D. Pino Muñoz, I. Poitroult, A. Montouchet, N. Bozzolo, and M. Bernacki. “3D level set modeling of static recrystallization considering stored energy fields”. In: *Computational Materials Science* 122 (2016), pages 57–71. doi: [10.1016/j.commatsci.2016.04.045](https://doi.org/10.1016/j.commatsci.2016.04.045) (cited on pages [10](#), [259](#), [261](#)).
- [4] H. Resk, L. Delannay, M. Bernacki, T. Coupez, and R. E. Logé. “Adaptive mesh refinement and automatic remeshing in crystal plasticity finite element simulations”. In: *Modelling and Simulation in Materials Science and Engineering* 17.7 (2009), page 075012. doi: [10.1088/0965-0393/17/7/075012](https://doi.org/10.1088/0965-0393/17/7/075012) (cited on pages [10](#), [60](#), [227](#)).
- [5] E. Roux, M. Bernacki, and P.-O. Bouchard. “A level-set and anisotropic adaptive remeshing strategy for the modeling of void growth under large plastic strain”. In: *Computational Materials Science* 68 (2013), pages 32–46. doi: [10.1016/j.commatsci.2012.10.004](https://doi.org/10.1016/j.commatsci.2012.10.004) (cited on pages [10](#), [14](#), [40](#), [57](#), [60](#), [70](#), [94](#), [116](#), [224](#), [270](#)).
- [6] E. Roux, M. Shakoor, M. Bernacki, and P.-O. Bouchard. “A new finite element approach for modelling ductile damage void nucleation and growth—analysis of loading path effect on damage mechanisms”. In: *Modelling and Simulation in Materials Science and Engineering* 22.7 (2014), page 075001. doi: [10.1088/0965-0393/22/7/075001](https://doi.org/10.1088/0965-0393/22/7/075001) (cited on pages [10](#), [14](#), [17](#), [40](#), [56](#), [58](#), [60](#), [70](#), [94](#), [159](#), [270](#)).
- [7] K. Hitti, P. Laure, T. Coupez, L. Silva, and M. Bernacki. “Precise generation of complex statistical Representative Volume Elements (RVEs) in a finite element context”. In: *Computational Materials Science* 61 (2012), pages 224–238. doi: [10.1016/j.commatsci.2012.04.011](https://doi.org/10.1016/j.commatsci.2012.04.011) (cited on pages [10](#), [44](#)).
- [8] I. Coppo. “Generation and homogenization of RVEs for a polymer composite with discontinuous reinforcements”. Post Master’s Degree. Ecole Nationale Supérieure des Mines de Paris, 2015-2016 (cited on pages [10](#), [130](#), [256](#)).
- [9] T. F. Morgeneyer, J. Besson, H. Proudhon, M. J. Starink, and I. Sinclair. “Experimental and numerical analysis of toughness anisotropy in AA2139 Al-alloy sheet”. In: *Acta Materialia* 57.13 (2009), pages 3902–3915. doi: [10.1016/j.actamat.2009.04.046](https://doi.org/10.1016/j.actamat.2009.04.046) (cited on pages [11](#), [25](#), [215](#)).

- [10] A. Hosokawa, D. S. Wilkinson, J. Kang, and E. Maire. “Effect of triaxiality on void growth and coalescence in model materials investigated by X-ray tomography”. In: *Acta Materialia* 60.6-7 (2012), pages 2829–2839. doi: [10.1016/j.actamat.2012.01.048](https://doi.org/10.1016/j.actamat.2012.01.048) (cited on pages 11, 30).
- [11] B. L. Boyce, B. G. Clark, P. Lu, J. D. Carroll, and C. R. Weinberger. “The Morphology of Tensile Failure in Tantalum”. In: *Metallurgical and Materials Transactions A* 44.10 (2013), pages 4567–4580. doi: [10.1007/s11661-013-1814-8](https://doi.org/10.1007/s11661-013-1814-8) (cited on page 11).
- [12] N. Tutyshkin, W. H. Müller, R. Wille, and M. Zapara. “Strain-induced damage of metals under large plastic deformation: Theoretical framework and experiments”. In: *International Journal of Plasticity* 59 (2014), pages 133–151. doi: [10.1016/j.ijplas.2014.03.011](https://doi.org/10.1016/j.ijplas.2014.03.011) (cited on page 11).
- [13] I. Westermann, K. O. Pedersen, T. Furu, T. Børvik, and O. S. Hopperstad. “Effects of particles and solutes on strength, work-hardening and ductile fracture of aluminium alloys”. In: *Mechanics of Materials* 79 (2014), pages 58–72. doi: [10.1016/j.mechmat.2014.08.006](https://doi.org/10.1016/j.mechmat.2014.08.006) (cited on page 11).
- [14] D. O. Fernandez and R. Boeri. “Study of the fracture of ferritic ductile cast iron under different loading conditions”. In: *Fatigue & Fracture of Engineering Materials & Structures* 38.5 (2015), pages 610–620. doi: [10.1111/ffe.12266](https://doi.org/10.1111/ffe.12266) (cited on page 11).
- [15] W. Ludwig, A. King, P. Reischig, M. Herbig, E. M. Lauridsen, S. Schmidt, H. Proudhon, S. Forest, P. Cloetens, S. Rolland Du Roscoat, J.-Y. Buffière, T. J. Marrow, and H. F. Poulsen. “New opportunities for 3D materials science of polycrystalline materials at the micrometre lengthscale by combined use of X-ray diffraction and X-ray imaging”. In: *Materials Science and Engineering: A* 524.1-2 (2009), pages 69–76. doi: [10.1016/j.msea.2009.04.009](https://doi.org/10.1016/j.msea.2009.04.009) (cited on pages 11, 261).
- [16] T. F. Morgeneyer, L. Helfen, I. Sinclair, H. Proudhon, F. Xu, and T. Baumbach. “Ductile crack initiation and propagation assessed via in situ synchrotron radiation-computed laminography”. In: *Scripta Materialia* 65.11 (2011), pages 1010–1013. doi: [10.1016/j.scriptamat.2011.09.005](https://doi.org/10.1016/j.scriptamat.2011.09.005) (cited on pages 11, 25, 214).
- [17] A. Hosokawa, D. S. Wilkinson, J. Kang, and E. Maire. “Onset of void coalescence in uniaxial tension studied by continuous X-ray tomography”. In: *Acta Materialia* 61.4 (2013), pages 1021–1036. doi: [10.1016/j.actamat.2012.08.002](https://doi.org/10.1016/j.actamat.2012.08.002) (cited on pages 11, 25, 27, 30, 215).
- [18] M. Kaye, C. Puncreobutr, P. D. Lee, D. S. Balint, T. Connolly, D. Farrugia, and J. Lin. “A new parameter for modelling three-dimensional damage evolution validated by synchrotron tomography”. In: *Acta Materialia* 61.20 (2013), pages 7616–7623. doi: [10.1016/j.actamat.2013.08.065](https://doi.org/10.1016/j.actamat.2013.08.065) (cited on pages 11, 214, 235).
- [19] D. Seo, H. Toda, M. Kobayashi, K. Uesugi, A. Takeuchi, and Y. Suzuki. “Three-Dimensional Investigation of Void Coalescence in Free-Cutting Steel using X-ray Tomography”. In: *ISIJ International* 55.7 (2015), pages 1483–1488. doi: [10.2355/isijinternational.55.1483](https://doi.org/10.2355/isijinternational.55.1483) (cited on pages 11, 25, 27, 215, 245).
- [20] F. Hannard, T. Pardoën, E. Maire, C. Le Bourlot, R. Mokso, and A. Simar. “Characterization and micromechanical modelling of microstructural heterogeneity effects on ductile fracture of 6xxx aluminium alloys”. In: *Acta Materialia* 103 (2016), pages 558–572. doi: [10.1016/j.actamat.2015.10.008](https://doi.org/10.1016/j.actamat.2015.10.008) (cited on pages 11, 25, 27, 32).

- [21] L. Babout, Y. Bréchet, E. Maire, and R. Fougères. “On the competition between particle fracture and particle decohesion in metal matrix composites”. In: *Acta Materialia* 52.15 (2004), pages 4517–4525. doi: [10.1016/j.actamat.2004.06.009](https://doi.org/10.1016/j.actamat.2004.06.009) (cited on pages 11, 25, 27, 29, 32, 139, 142, 215, 245).
- [22] T. F. Morgeneyer, T. Taillandier-Thomas, L. Helfen, T. Baumbach, I. Sinclair, S. Roux, and F. Hild. “In situ 3-D observation of early strain localization during failure of thin Al alloy (2198) sheet”. In: *Acta Materialia* 69 (2014), pages 78–91. doi: [10.1016/j.actamat.2014.01.033](https://doi.org/10.1016/j.actamat.2014.01.033) (cited on pages 11, 25–27, 30, 32, 33, 214).
- [23] S. Fayolle. “Etude de la modélisation de la pose et de la tenue mécanique des assemblages par déformation plastique : application au rivetage auto-poinçonneur”. PhD thesis. Ecole Nationale Supérieure des Mines de Paris, 2008 (cited on pages 12, 13, 35).
- [24] J.-M. Gachet. “Intégration de la phase de mise en forme dans le dimensionnement de flasques de sièges automobile”. PhD thesis. Ecole Nationale Supérieure des Mines de Paris, 2013 (cited on pages 12, 13).
- [25] F. A. McClintock. “A Criterion for Ductile Fracture by the Growth of Holes”. In: *Journal of Applied Mechanics* 35.2 (1968), page 363. doi: [10.1115/1.3601204](https://doi.org/10.1115/1.3601204) (cited on pages 13, 24, 45, 214).
- [26] J. R. Rice and D. M. Tracey. “On the ductile enlargement of voids in triaxial stress fields”. In: *Journal of the Mechanics and Physics of Solids* 17.3 (1969), pages 201–217. doi: [10.1016/0022-5096\(69\)90033-7](https://doi.org/10.1016/0022-5096(69)90033-7) (cited on pages 13, 24, 45, 46, 141, 194, 214, 263).
- [27] L. Kachanov. “Time of the Rupture Process under Creep Conditions”. In: *Bull. SSR Acad. Sci., Division of Technical Sciences* 8 (1958), pages 26–31 (cited on page 13).
- [28] J. Lemaitre and J.-L. Chaboche. “Phenomenological approach of damage rupture”. In: *Journal de Mécanique Appliquée* 2.3 (1978), pages 317–365 (cited on pages 13, 194).
- [29] P.-O. Bouchard. “Contribution à la Modélisation Numérique en Mécanique de la Rupture et Structures Multimatériaux”. PhD thesis. Ecole Nationale Supérieure des Mines de Paris, 2000 (cited on page 13).
- [30] B. Picqué. “Experimental study and numerical simulation of iron oxide scales mechanical behavior in hot rolling”. PhD thesis. Ecole Nationale Supérieure des Mines de Paris, 2004 (cited on page 13).
- [31] L. Bourgeon. “Etude et modélisation des mécanismes d’endommagement en forge à froid”. PhD thesis. Ecole Nationale Supérieure des Mines de Paris, 2010 (cited on page 13).
- [32] T.-S. Cao. “Modeling ductile damage for complex loading paths”. PhD thesis. Ecole Nationale Supérieure des Mines de Paris, 2013 (cited on pages 13, 35, 264).
- [33] A. L. Gurson. “Plastic Flow and Fracture Behavior of Ductile Materials Incorporating Void Nucleation, Growth, and Interaction”. PhD thesis. Brown University, 1975 (cited on pages 13, 24, 45, 47, 141, 191, 194).
- [34] V. Tvergaard. “Influence of voids on shear band instabilities under plane strain conditions”. In: *International Journal of Fracture* 17.4 (1981), pages 389–407. doi: [10.1007/BF00036191](https://doi.org/10.1007/BF00036191) (cited on page 13).

- [35] V. Tvergaard and A. Needleman. “Analysis of the cup-cone fracture in a round tensile bar”. In: *Acta Metallurgica* 32.1 (1984), pages 157–169. doi: [10.1016/0001-6160\(84\)90213-X](https://doi.org/10.1016/0001-6160(84)90213-X) (cited on pages 13, 263).
- [36] M. Gologanu, J.-B. Leblond, and J. Devaux. “Approximate models for ductile metals containing non-spherical voids—Case of axisymmetric prolate ellipsoidal cavities”. In: *Journal of the Mechanics and Physics of Solids* 41.11 (1993), pages 1723–1754. doi: [10.1016/0022-5096\(93\)90029-F](https://doi.org/10.1016/0022-5096(93)90029-F) (cited on pages 13, 47, 265).
- [37] A. A. Benzerga and J.-B. Leblond. “Ductile Fracture by Void Growth to Coalescence”. In: *Advances in Applied Mechanics* 44 (2010), pages 169–305. doi: [10.1016/S0065-2156\(10\)44003-X](https://doi.org/10.1016/S0065-2156(10)44003-X) (cited on pages 14, 27, 31, 45, 47, 48, 138, 140, 141, 144, 148, 191).
- [38] A. Pineau, A. A. Benzerga, and T. Pardoen. “Failure of metals I – Brittle and ductile fracture”. In: *Acta Materialia* January (2016). doi: [10.1016/j.actamat.2015.12.034](https://doi.org/10.1016/j.actamat.2015.12.034) (cited on pages 14, 31, 47, 148, 191, 204).
- [39] M. Shakoor, B. Scholtes, P.-O. Bouchard, and M. Bernacki. “An efficient and parallel level set reinitialization method – Application to micromechanics and microstructural evolutions”. In: *Applied Mathematical Modelling* 39.23-24 (2015), pages 7291–7302. doi: [10.1016/j.apm.2015.03.014](https://doi.org/10.1016/j.apm.2015.03.014) (cited on pages 17, 133).
- [40] M. Shakoor, M. Bernacki, and P.-O. Bouchard. “A new body-fitted immersed volume method for the modeling of ductile fracture at the microscale: Analysis of void clusters and stress state effects on coalescence”. In: *Engineering Fracture Mechanics* 147 (2015), pages 398–417. doi: [10.1016/j.engfracmech.2015.06.057](https://doi.org/10.1016/j.engfracmech.2015.06.057) (cited on pages 17, 89, 133, 210).
- [41] M. Shakoor, P.-O. Bouchard, and M. Bernacki. “An adaptive Level-Set Method with enhanced volume conservation for simulations in multiphase domains”. In: *International Journal for Numerical Methods in Engineering* (2016). doi: [10.1002/nme.5297](https://doi.org/10.1002/nme.5297) (cited on pages 17, 89).
- [42] M. Shakoor, A. Buljac, J. Neggers, F. Hild, T. F. Morgeneyer, L. Helfen, M. Bernacki, and P.-O. Bouchard. “On the choice of boundary conditions for micromechanical simulations based on synchrotron 3D imaging”. In: *International Journal of Solids and Structures* (Submitted) (cited on pages 17, 126, 133, 236, 251).
- [43] B. Scholtes, M. Shakoor, A. Settefrati, P.-O. Bouchard, N. Bozzolo, and M. Bernacki. “New finite element developments for the full field modeling of microstructural evolutions using the level-set method”. In: *Computational Materials Science* 109 (2015), pages 388–398. doi: [10.1016/j.commatsci.2015.07.042](https://doi.org/10.1016/j.commatsci.2015.07.042) (cited on pages 17, 56, 133, 259).
- [44] A. Buljac, M. Shakoor, J. Neggers, M. Bernacki, P.-O. Bouchard, L. Helfen, T. F. Morgeneyer, and F. Hild. “Numerical Validation Framework for Micromechanical Simulations based on Synchrotron 3D Imaging”. In: *Computational Mechanics* (Submitted) (cited on pages 17, 133, 219, 236, 251).
- [45] M. Shakoor, M. Bernacki, and P.-O. Bouchard. “Numerical modelling of ductile damage at the microscale in a level set framework”. In: *International CAE Conference (CAE)*. Verona (Italy), Oct. 27–28, 2014 (cited on page 17).
- [46] M. Shakoor, M. Bernacki, and P.-O. Bouchard. “An adaptive body-fitted monolithic method for modeling the fracture of heterogeneous microstructures”. In: *International Conference on Computational Modeling of Fracture and Failure of Materials and Structures (CFRAC)*. Paris (France), June 3–5, 2015 (cited on page 18).

- [47] M. Shakoор, M. Bernacki, and P.-O. Bouchard. “Modeling of ductile fracture mechanisms at the microscale using a new adaptive body-fitted monolithic method”. In: *International Conference on Computational Plasticity (COMPLAS)*. Barcelona (Spain), Sept. 1–3, 2015 (cited on page 18).
- [48] M. Shakoор, M. Bernacki, and P.-O. Bouchard. “An adaptive body-fitted monolithic method for modeling the fracture of heterogeneous microstructures”. In: *World Congress on Computational Mechanics (WCCM)*. Seoul (Korea), July 24–29, 2016 (cited on page 18).
- [49] M. Shakoор, M. Bernacki, E. Roux, and P.-O. Bouchard. “Numerical modelling of the effect of non-proportional loading on ductile fracture at the microscale”. In: *European Conference on Fracture (ECF)*. Trondheim (Norway), June 30–July 4, 2014 (cited on page 18).
- [50] M. Shakoор, M. Bernacki, and P.-O. Bouchard. “Analysis of void clusters arrangements on coalescence using a new body-fitted immersed volume method for the modeling of ductile fracture at the microscale”. In: *IUTAM Symposium: Ductile Fracture and Localization*. Paris (France), Mar. 27–28, 2015 (cited on page 18).
- [51] B. Scholtes, M. Shakoор, N. Bozzolo, P.-O. Bouchard, A. Settefrati, and M. Bernacki. “Advances in Level-Set modeling of recrystallization at the polycrystal scale - Development of the Digi- μ software”. In: *International ESAFORM Conference on Material Forming (ESAFORM)*. Graz (Austria), Apr. 15–17, 2015 (cited on page 18).
- [52] M. Shakoор, M. Bernacki, and P.-O. Bouchard. “Micromechanical modelling of ductile fracture mechanisms using a new body-fitted immersed volume method”. In: *International Conference on Computational Modeling of Fracture and Failure of Materials and Structures (CFRAC)*. Paris (France), June 3–5, 2015 (cited on page 18).
- [53] P.-O. Bouchard, M. Shakoор, V. M. Trejo Navas, and M. Bernacki. “Numerical modeling of failure mechanisms in complex heterogeneous microstructures”. In: *European Conference on Fracture (ECF)*. Catania (Italy), June 20–24, 2016 (cited on page 18).
- [54] D. Pino Muñoz, M. Shakoор, M. Bernacki, and P.-O. Bouchard. “Towards a mesh independent fracture modeling method using cohesive elements”. In: *European Conference on Fracture (ECF)*. Catania (Italy), June 20–24, 2016 (cited on pages 18, 261, 262).
- [55] V. M. Trejo Navas, M. Shakoор, M. Bernacki, and P.-O. Bouchard. “Ductile fracture – Influence of heterogeneous microstructure on nucleation, growth and coalescence mechanisms”. In: *International Conference on Numerical Methods in Industrial Forming Processes (NUMIFORM)*. Troyes (France), July 4–7, 2016 (cited on pages 18, 261).
- [56] D. Polychronopoulou, N. Bozzolo, D. Pino Muñoz, J. Bruchon, M. Shakoор, Y. Millet, C. Dumont, I. Freiherr von Thüngen, R. Besnard, and M. Bernacki. “Introduction to the level-set full field modeling of laths spheroidization phenomenon in α/β titanium alloys”. In: *International Conference on Numerical Methods in Industrial Forming Processes (NUMIFORM)*. Troyes (France), July 4–7, 2016 (cited on pages 18, 256, 259).
- [57] M. Shakoор, P.-O. Bouchard, and M. Bernacki. “Modélisation numérique de l’endommagement ductile à l’échelle des microstructures”. In: *Journées Matériaux Numériques (JMN)*. St-Aignan-sur-Cher (France), Feb. 3–5, 2015 (cited on page 19).

- [58] M. Shakoор, M. Bernacki, and P.-O. Bouchard. “Une nouvelle méthode de volume immergé pour la modélisation numérique de l’endommagement ductile à l’échelle des microstructures”. In: *Colloque national en calcul des structures (CSMA)*. Giens (France), May 18–22, 2015 (cited on page 19).
- [59] P.-O. Bouchard, M. Shakoор, and M. Bernacki. “3D modeling of ductile fracture at the microscale using a new body-fitted mesh adaptation technique”. In: *Workshop SF2M/MECAMAT*. Paris (France), Nov. 30–Dec. 1, 2015 (cited on page 19).
- [60] A. Buljac, M. Shakoор, J. Neggers, M. Bernacki, P.-O. Bouchard, L. Helfen, T. F. Morgeneyer, and F. Hild. “Micromechanical simulations based on laminography 3D imaging: experimental/numerical framework”. In: *Workshop SF2M/MECAMAT*. Paris (France), Sept. 15–16, 2016 (cited on page 19).
- [61] V. M. Trejo Navas, M. Shakoор, M. Bernacki, and P.-O. Bouchard. “Ductile fracture - Influence of heterogeneous microstructure on nucleation, growth and coalescence mechanisms”. In: *Workshop SF2M/MECAMAT*. Paris (France), Sept. 15–16, 2016 (cited on pages 19, 261).
- [62] A. Myagotin, A. Voropaev, L. Helfen, D. Hänschke, and T. Baumbach. “Efficient Volume Reconstruction for Parallel-Beam Computed Laminography by Filtered Backprojection on Multi-Core Clusters”. In: *IEEE Trans. Image Process.* 22.12 (2013), pages 5348–5361 (cited on page 25).
- [63] T. F. Morgeneyer, L. Helfen, H. Mubarak, and F. Hild. “3D Digital Volume Correlation of Synchrotron Radiation Laminography Images of Ductile Crack Initiation: An Initial Feasibility Study”. In: *Experimental Mechanics* 53.4 (2012), pages 543–556. doi: [10.1007/s11340-012-9660-y](https://doi.org/10.1007/s11340-012-9660-y) (cited on pages 25, 26, 33).
- [64] T. Ueda, L. Helfen, and T. F. Morgeneyer. “In situ laminography study of three-dimensional individual void shape evolution at crack initiation and comparison with GTN-type simulations”. In: *Acta Materialia* 78 (2014), pages 254–270. doi: [10.1016/j.actamat.2014.06.029](https://doi.org/10.1016/j.actamat.2014.06.029) (cited on pages 25, 32, 214).
- [65] A. Buljac, T. Taillandier-Thomas, T. F. Morgeneyer, L. Helfen, S. Roux, and F. Hild. “Slant strained band development during flat to slant crack transition in AA 2198 T8 sheet: in situ 3D measurements”. In: *International Journal of Fracture* (2015). doi: [10.1007/s10704-015-0052-z](https://doi.org/10.1007/s10704-015-0052-z) (cited on pages 25, 33, 214).
- [66] L. Babout, E. Maire, J.-Y. Buffière, and R. Fougères. “Characterization by X-ray computed tomography of decohesion, porosity growth and coalescence in model metal matrix composites”. In: *Acta Materialia* 49.11 (2001), pages 2055–2063. doi: [10.1016/S1359-6454\(01\)00104-5](https://doi.org/10.1016/S1359-6454(01)00104-5) (cited on pages 27, 30, 154, 155, 214).
- [67] D. Seo, H. Toda, M. Kobayashi, K. Uesugi, A. Takeuchi, and Y. Suzuki. “In Situ Observation of Void Nucleation and Growth in a Steel using X-ray Tomography”. In: *ISIJ International* 55.7 (2015), pages 1474–1482. doi: [10.2355/isijinternational.55.1474](https://doi.org/10.2355/isijinternational.55.1474) (cited on pages 27, 214, 215, 245).
- [68] L. Babout, E. Maire, and R. Fougères. “Damage initiation in model metallic materials: X-ray tomography and modelling”. In: *Acta Materialia* 52.8 (2004), pages 2475–2487. doi: [10.1016/j.actamat.2004.02.001](https://doi.org/10.1016/j.actamat.2004.02.001) (cited on pages 27, 29, 138, 139, 142, 155).

- [69] P. Ganguly and W. J. Poole. “Rearrangement of local stress and strain fields due to damage initiation in a model composite system”. In: *Computational Materials Science* 34.2 (2005), pages 107–122. doi: [10.1016/j.commatsci.2004.12.062](https://doi.org/10.1016/j.commatsci.2004.12.062) (cited on pages [27](#), [29](#), [138](#), [139](#), [144](#)).
- [70] D. Lassance, D. Fabregue, F. Delannay, and T. Pardoen. “Micromechanics of room and high temperature fracture in 6xxx Al alloys”. In: *Progress in Materials Science* 52.1 (2007), pages 62–129. doi: [10.1016/j.pmatsci.2006.06.001](https://doi.org/10.1016/j.pmatsci.2006.06.001) (cited on pages [27](#), [28](#), [138](#), [140](#), [141](#), [144](#)).
- [71] C. Landron, E. Maire, O. Bouaziz, J. Adrien, L. Lecarme, and A. Bareggi. “Validation of void growth models using X-ray microtomography characterization of damage in dual phase steels”. In: *Acta Materialia* 59.20 (2011), pages 7564–7573. doi: [10.1016/j.actamat.2011.08.046](https://doi.org/10.1016/j.actamat.2011.08.046) (cited on pages [27–29](#), [138](#), [140](#), [141](#)).
- [72] N. Kanetake, M. Nomura, and T. Choh. “Continuous observation of microstructural degradation during tensile loading of particle reinforced aluminum matrix composites”. In: *Materials Science and Technology* 11.December (1995), pages 1246–1252 (cited on page [28](#)).
- [73] F. M. Beremin. “Cavity Formation from Inclusions in Ductile Fracture of A508 Steel”. In: *Metallurgical Transactions A* 12.05 (1981), pages 723–731 (cited on pages [28](#), [139–141](#)).
- [74] J. Fitoussi, N. Bourgeois, G. Guo, and D. Baptiste. “Prediction of the anisotropic damaged behavior of composite materials: introduction of multilocal failure criteria in a micro-macro relationship”. In: *Computational Materials Science* 5.1-3 (1996), pages 87–100. doi: [10.1016/0927-0256\(95\)00061-5](https://doi.org/10.1016/0927-0256(95)00061-5) (cited on pages [28](#), [29](#), [139](#), [142](#), [144](#)).
- [75] S. Balasivanandha Prabu and L. Karunamoorthy. “Microstructure-based finite element analysis of failure prediction in particle-reinforced metal–matrix composite”. In: *Journal of Materials Processing Technology* 207.1-3 (2008), pages 53–62. doi: [10.1016/j.jmatprotec.2007.12.077](https://doi.org/10.1016/j.jmatprotec.2007.12.077) (cited on pages [28](#), [29](#), [139](#)).
- [76] G. G. Sozhamannan, S. B. Prabu, and R. Paskaramoorthy. “Failures analysis of particle reinforced metal matrix composites by microstructure based models”. In: *Materials & Design* 31.8 (2010), pages 3785–3790. doi: [10.1016/j.matdes.2010.03.025](https://doi.org/10.1016/j.matdes.2010.03.025) (cited on pages [28](#), [29](#), [139](#)).
- [77] M. N. Shabrov, E. Sylven, S. Kim, D. H. Sherman, L. Chuzhoy, C. L. Briant, and A. Needleman. “Void Nucleation by Inclusion Cracking”. In: *Metallurgical and Materials Transactions A* 35.06 (2004), pages 1745–1755 (cited on pages [28](#), [139](#), [140](#)).
- [78] L. Babout. “Etude par tomographie X et modélisation de l’endommagement de matériaux métalliques modèles”. PhD thesis. Institut National des Sciences Appliquées de Lyon, 2002 (cited on pages [28](#), [29](#), [139](#), [141](#), [142](#)).
- [79] B. J. Lee and M. E. Mear. “Stress concentration induced by an elastic spheroidal particle in a plastically deforming solid”. In: *Journal of the Mechanics and Physics of Solids* 47 (1999), pages 1301–1336 (cited on pages [28](#), [29](#), [138](#), [139](#), [141](#), [143–145](#)).
- [80] J. Q. Qi, H. W. Wang, C. M. Zou, W. Q. Wei, and Z. J. Wei. “Temperature dependence of fracture behavior of in situ synthesized TiC/Ti-alloy matrix composite”. In: *Materials Science and Engineering: A* 528.25-26 (2011), pages 7669–7673. doi: [10.1016/j.msea.2011.06.077](https://doi.org/10.1016/j.msea.2011.06.077) (cited on page [28](#)).

- [81] M. H. Zhang and J. K. Chen. “Analysis of interfacial fracture strength of an inclusion in a polymeric composite considering cohesive force”. In: *Computational Materials Science* 61 (2012), pages 6–11. doi: [10.1016/j.commatsci.2012.03.017](https://doi.org/10.1016/j.commatsci.2012.03.017) (cited on page 29).
- [82] J. P. Bandstra, D. A. Koss, A. Geltmacher, P. Matic, and R. K. Everett. “Modeling void coalescence during ductile fracture of a steel”. In: *Materials Science and Engineering: A* 366.2 (2004), pages 269–281. doi: [10.1016/j.msea.2003.08.018](https://doi.org/10.1016/j.msea.2003.08.018) (cited on pages 30, 214, 235).
- [83] A. Weck and D. S. Wilkinson. “Experimental investigation of void coalescence in metallic sheets containing laser drilled holes”. In: *Acta Materialia* 56.8 (2008), pages 1774–1784. doi: [10.1016/j.actamat.2007.12.035](https://doi.org/10.1016/j.actamat.2007.12.035) (cited on pages 30, 194, 197–199, 204, 214).
- [84] A. Weck, T. H. R. Crawford, A. Borowiec, D. S. Wilkinson, and J. S. Preston. “Femtosecond laser-based fabrication of a new model material to study fracture”. In: *Applied Physics A* 86.1 (2006), pages 55–61. doi: [10.1007/s00339-006-3730-x](https://doi.org/10.1007/s00339-006-3730-x) (cited on pages 30, 197).
- [85] A. Weck, D. S. Wilkinson, E. Maire, and H. Toda. “Visualization by X-ray tomography of void growth and coalescence leading to fracture in model materials”. In: *Acta Materialia* 56.12 (2008), pages 2919–2928. doi: [10.1016/j.actamat.2008.02.027](https://doi.org/10.1016/j.actamat.2008.02.027) (cited on pages 30, 191, 194, 197, 235, 236, 238, 249).
- [86] A. Hosokawa, D. S. Wilkinson, J. Kang, M. Kobayashi, and H. Toda. “Void growth and coalescence in model materials investigated by high-resolution X-ray microtomography”. In: *International Journal of Fracture* 181.1 (2013), pages 51–66. doi: [10.1007/s10704-013-9820-9](https://doi.org/10.1007/s10704-013-9820-9) (cited on pages 30, 191, 192, 235).
- [87] A. G. Weck. “The Role of Coalescence on Ductile Fracture”. PhD thesis. McMaster University, 2007 (cited on pages 30, 31, 192, 197, 199, 201).
- [88] A. A. Benzerga, J. Besson, and A. Pineau. “Anisotropic ductile fracture”. In: *Acta Materialia* 52.15 (2004), pages 4623–4638. doi: [10.1016/j.actamat.2004.06.020](https://doi.org/10.1016/j.actamat.2004.06.020) (cited on pages 31, 191).
- [89] C. Tekoglu, J. W. Hutchinson, and T. Pardoen. “On localization and void coalescence as a precursor to ductile fracture.” In: *Philosophical transactions. Series A, Mathematical, physical, and engineering sciences* 373.2038 (2015). doi: [10.1098/rsta.2014.0121](https://doi.org/10.1098/rsta.2014.0121) (cited on pages 31–33, 47, 191, 192).
- [90] M. Grédiac, F. Hild, and A. Pineau, editors. *Full-Field Measurements and Identification in Solid Mechanics*. Hoboken, NJ USA: John Wiley & Sons, Inc., 2013. doi: [10.1002/9781118578469](https://doi.org/10.1002/9781118578469) (cited on pages 33, 238).
- [91] F. Mathieu, H. Leclerc, F. Hild, and S. Roux. “Estimation of Elastoplastic Parameters via Weighted FEMU and Integrated-DIC”. In: *Experimental Mechanics* 55.1 (2015), pages 105–119. doi: [10.1007/s11340-014-9888-9](https://doi.org/10.1007/s11340-014-9888-9) (cited on pages 33, 235, 239).
- [92] E. Roux and P.-O. Bouchard. “On the interest of using full field measurements in ductile damage model calibration”. In: *International Journal of Solids and Structures* 72 (2015), pages 50–62. doi: <http://dx.doi.org/10.1016/j.ijsolstr.2015.07.011> (cited on pages 33, 238).
- [93] B. K. Bay, T. S. Smith, D. P. Fyhrie, and M. Saad. “Digital volume correlation: three-dimensional strain mapping using X-ray tomography”. In: *Experimental Mechanics* 39 (1999), pages 217–226 (cited on page 33).

- [94] T. S. Smith, B. K. Bay, and M. M. Rashid. “Digital volume correlation including rotational degrees of freedom during minimization”. In: *Experimental Mechanics* 42.3 (2002), pages 272–278 (cited on page 33).
- [95] M. Bornert, J. M. Chaix, P. Doumalin, J. C. Dupré, T. Fournel, D. Jeulin, E. Maire, M. Moreaud, and H. Moulinec. “Mesure tridimensionnelle de champs cinématiques par imagerie volumique pour l’analyse des matériaux et des structures”. In: *Instrumentation, Mesure, Métrologie* 4 (2004), pages 43–88 (cited on page 33).
- [96] E. Verhulp, B. van Rietbergen, and R. Huiskes. “A three-dimensional digital image correlation technique for strain measurements in microstructures”. In: *J. Biomech.* 37.9 (2004), pages 1313–1320 (cited on page 33).
- [97] S. Roux, F. Hild, P. Viot, and D. Bernard. “Three-dimensional image correlation from X-ray computed tomography of solid foam”. In: *Composites Part A: Applied Science and Manufacturing* 39.8 (2008), pages 1253–1265. doi: [10.1016/j.compositesa.2007.11.011](https://doi.org/10.1016/j.compositesa.2007.11.011) (cited on pages 33, 217, 219).
- [98] J. Rannou, N. Limodin, J. Réthoré, A. Gravouil, W. Ludwig, M.-C. Baietto-Dubourg, J.-Y. Buffière, A. Combescure, F. Hild, and S. Roux. “Three dimensional experimental and numerical multiscale analysis of a fatigue crack”. In: *Computer Methods in Applied Mechanics and Engineering* 199.21-22 (2010), pages 1307–1325. doi: [10.1016/j.cma.2009.09.013](https://doi.org/10.1016/j.cma.2009.09.013) (cited on pages 33, 217, 222).
- [99] A. Bouterf, S. Roux, F. Hild, J. Adrien, E. Maire, and S. Meille. “Digital Volume Correlation Applied to X-ray Tomography Images from Spherical Indentation Tests on Lightweight Gypsum”. In: *Strain* 50 (2014), pages 444–453. doi: [10.1111/str12101](https://doi.org/10.1111/str12101) (cited on pages 33, 217).
- [100] T. Taillandier-Thomas, S. Roux, T. F. Morgeneyer, and F. Hild. “Localized strain field measurement on laminography data with mechanical regularization”. In: *Nuclear Instruments and Methods in Physics Research Section B: Beam Interactions with Materials and Atoms* 324 (2014), pages 70–79. doi: [10.1016/j.nimb.2013.09.033](https://doi.org/10.1016/j.nimb.2013.09.033) (cited on pages 33, 219).
- [101] H. Leclerc, J.-N. Périé, S. Roux, and F. Hild. “Voxel-Scale Digital Volume Correlation”. In: *Experimental Mechanics* 51.4 (2011), pages 479–490. doi: [10.1007/s11340-010-9407-6](https://doi.org/10.1007/s11340-010-9407-6) (cited on pages 33, 219, 223).
- [102] V. Kouznetsova, M. G. D. Geers, and W. A. M. Brekelmans. “Multi-scale constitutive modelling of heterogeneous materials with a gradient-enhanced computational homogenization scheme”. In: *International Journal for Numerical Methods in Engineering* 54.8 (2002), pages 1235–1260. doi: [10.1002/nme.541](https://doi.org/10.1002/nme.541) (cited on pages 34, 41).
- [103] P. Ponte Castañeda. “Second-order homogenization estimates for nonlinear composites incorporating field fluctuations: II—applications”. In: *Journal of the Mechanics and Physics of Solids* 50.4 (2002), pages 759–782. doi: [10.1016/S0022-5096\(01\)00098-9](https://doi.org/10.1016/S0022-5096(01)00098-9) (cited on pages 34, 41).
- [104] V. G. Kouznetsova, M. G. D. Geers, and W. A. M. Brekelmans. “Multi-scale second-order computational homogenization of multi-phase materials: a nested finite element solution strategy”. In: *Computer Methods in Applied Mechanics and Engineering* 193.48-51 (2004), pages 5525–5550. doi: [10.1016/j.cma.2003.12.073](https://doi.org/10.1016/j.cma.2003.12.073) (cited on pages 34, 41).

- [105] F. Vernerey, W. K. Liu, and B. Moran. “Multi-scale micromorphic theory for hierarchical materials”. In: *Journal of the Mechanics and Physics of Solids* 55.12 (2007), pages 2603–2651. doi: [10.1016/j.jmps.2007.04.008](https://doi.org/10.1016/j.jmps.2007.04.008) (cited on page 34).
- [106] K. Danas and P. Ponte Castañeda. “Influence of the Lode parameter and the stress triaxiality on the failure of elasto-plastic porous materials”. In: *International Journal of Solids and Structures* 49.11-12 (2012), pages 1325–1342. doi: [10.1016/j.ijsolstr.2012.02.006](https://doi.org/10.1016/j.ijsolstr.2012.02.006) (cited on pages 34, 41, 47).
- [107] E. Bosco, V. G. Kouznetsova, and M. G. D. Geers. “Multi-scale computational homogenization - localization for propagating discontinuities using X-FEM”. In: *International Journal for Numerical Methods in Engineering* 102.3-4 (2015), pages 496–527. doi: [10.1002/nme.4838](https://doi.org/10.1002/nme.4838) (cited on pages 34, 41).
- [108] C. Mcveigh, F. Vernerey, W. K. Liu, B. Moran, and G. B. Olson. “An interactive microvoid shear localization mechanism in high strength steels”. In: *Journal of the Mechanics and Physics of Solids* 55.2 (2007), pages 225–244. doi: [10.1016/j.jmps.2006.08.002](https://doi.org/10.1016/j.jmps.2006.08.002) (cited on pages 34, 48, 49, 138).
- [109] C. McVeigh and W. K. Liu. “Linking microstructure and properties through a predictive multiresolution continuum”. In: *Computer Methods in Applied Mechanics and Engineering* 197.41-42 (2008), pages 3268–3290. doi: [10.1016/j.cma.2007.12.020](https://doi.org/10.1016/j.cma.2007.12.020) (cited on pages 34, 41).
- [110] K. Matous, M. Kulkarni, and P. Geubelle. “Multiscale cohesive failure modeling of heterogeneous adhesives”. In: *Journal of the Mechanics and Physics of Solids* 56.4 (2008), pages 1511–1533. doi: [10.1016/j.jmps.2007.08.005](https://doi.org/10.1016/j.jmps.2007.08.005) (cited on pages 34, 41).
- [111] V. P. Nguyen, O. Lloberas-Valls, M. Stroeven, and L. J. Sluys. “Homogenization-based multiscale crack modelling: From micro-diffusive damage to macro-cracks”. In: *Computer Methods in Applied Mechanics and Engineering* 200.9-12 (2011), pages 1220–1236. doi: [10.1016/j.cma.2010.10.013](https://doi.org/10.1016/j.cma.2010.10.013) (cited on pages 34, 41).
- [112] H. J. Böhm, editor. *Mechanics of Microstructured Materials*. Springer Vienna, 2004. ISBN: 978-3-211-24154-7. doi: [10.1007/978-3-7091-2776-6](https://doi.org/10.1007/978-3-7091-2776-6) (cited on pages 34, 41–44, 49).
- [113] K. Mocellin. “Contribution à la simulation numérique tridimensionnelle du forgeage à chaud : étude du contact et calcul multigrille”. PhD thesis. Ecole Nationale Supérieure des Mines de Paris, 1999 (cited on pages 35, 271, 276).
- [114] P.-O. Bouchard, F. Bay, Y. Chastel, and I. Tovenca. “Crack propagation modelling using an advanced remeshing technique”. In: *Computer Methods in Applied Mechanics and Engineering* 189.3 (2000), pages 723–742. doi: [10.1016/S0045-7825\(99\)00324-2](https://doi.org/10.1016/S0045-7825(99)00324-2) (cited on pages 35, 58, 80, 82, 86).
- [115] R. El Khaoulani. “Prédiction fiable de l’endommagement ductile par la méthode des éléments finis mixtes : endommagement non local et adaptation de maillage”. PhD thesis. Ecole Nationale Supérieure des Mines de Paris, 2010 (cited on pages 35, 194, 261).
- [116] C. Gruau. “Génération de métriques pour adaptation anisotrope de maillages, applications à la mise en forme des matériaux”. PhD thesis. Ecole Nationale Supérieure des Mines de Paris, 2004 (cited on pages 35, 66).

- [117] O. Basset. “Simulation Numérique d’Ecoulements MultiFluides sur Grille de Calcul”. PhD thesis. Ecole Nationale Supérieure des Mines de Paris, 2006, pages 145–166 (cited on page 35).
- [118] O. Desmaison. “Modélisation numérique d’un procédé de soudage hybride arc / laser en approche Level Set : application au soudage multi-passes de tôles d’acier de forte épaisseur”. PhD thesis. Ecole Nationale Supérieure des Mines de Paris, 2013, pages 75–86 (cited on page 35).
- [119] A. Ern and J.-L. Guermond. *Theory and Practice of Finite Elements*. Volume 159. Applied Mathematical Sciences. New York, NY: Springer New York, 2004. ISBN: 978-1-4419-1918-2. doi: [10.1007/978-1-4757-4355-5](https://doi.org/10.1007/978-1-4757-4355-5) (cited on pages 37, 97).
- [120] O. C. Zienkiewicz, R. L. Taylor, and J. Z. Zhu. *The Finite Element Method: Its Basis and Fundamentals*. Elsevier, 2013. ISBN: 978-1-85617-633-0. doi: [10.1016/B978-1-85617-633-0.00019-8](https://doi.org/10.1016/B978-1-85617-633-0.00019-8) (cited on pages 37, 97, 98).
- [121] D. Boffi, F. Brezzi, L. F. Demkowicz, R. G. Durán, R. S. Falk, and M. Fortin. *Mixed Finite Elements, Compatibility Conditions, and Applications*. Volume 1939. Lecture Notes in Mathematics. Berlin, Heidelberg: Springer Berlin Heidelberg, 2008. doi: [10.1007/978-3-540-78319-0](https://doi.org/10.1007/978-3-540-78319-0) (cited on page 38).
- [122] C. Aliaga. “Simulation numérique par éléments finis en 3D du comportement thermomécanique au cours du traitement thermique d’aciers : application à la trempe de pièces forgées ou coulées”. PhD thesis. Ecole Nationale Supérieure des Mines de Paris, 2000 (cited on page 38).
- [123] E. Perchat. “MINI-élément et factorisation incomplètes pour la parallélisation d’un solveur de Stokes 2D : application au forgeage”. PhD thesis. Ecole Nationale Supérieure des Mines de Paris, 2004 (cited on page 38).
- [124] R. H. Wagoner and J.-L. Chenot. *Metal Forming Analysis*. Cambridge University Press, 2001. ISBN: 9780521017725 (cited on page 38).
- [125] T. Coupez, H. Digonnet, and R. Ducloux. “Parallel meshing and remeshing”. In: *Applied Mathematical Modelling* 25.2 (2000), pages 153–175. doi: [10.1016/S0307-904X\(00\)00045-7](https://doi.org/10.1016/S0307-904X(00)00045-7) (cited on pages 39, 84, 175).
- [126] S. Balay, S. Abhyankar, M. F. Adams, J. Brown, P. Brune, K. Buschelman, L. Dalcin, V. Eijkhout, W. D. Gropp, D. Kaushik, M. G. Knepley, L. C. McInnes, K. Rupp, B. F. Smith, S. Zampini, H. Zhang, and H. Zhang. *PETSc Web page*. <http://www.mcs.anl.gov/petsc>. 2016. URL: <http://www.mcs.anl.gov/petsc> (cited on pages 40, 44, 176).
- [127] M. Bornert, E. Hervé, C. Stolz, and A. Zaoui. “Self-Consistent Approaches and Strain Heterogeneities in Two-Phase Elastoplastic Materials”. In: *Applied Mechanics Reviews* 47.1S (1994), S66. doi: [10.1115/1.3122824](https://doi.org/10.1115/1.3122824) (cited on pages 40, 215).
- [128] M. Dong and S. Schmauder. “Modeling of metal matrix composites by a self-consistent embedded cell model”. In: *Acta Materialia* 44.6 (1996), pages 2465–2478. doi: [10.1016/1359-6454\(95\)00345-2](https://doi.org/10.1016/1359-6454(95)00345-2) (cited on pages 40, 215).
- [129] M. Grigorovitch and E. Gal. “The local response in structures using the Embedded Unit Cell Approach”. In: *Computers & Structures* 157 (2015), pages 189–200. doi: [10.1016/j.compstruc.2015.05.006](https://doi.org/10.1016/j.compstruc.2015.05.006) (cited on page 40).

- [130] J. C. Michel and P. Suquet. “Computational analysis of nonlinear composite structures using the nonuniform transformation field analysis”. In: *Computer Methods in Applied Mechanics and Engineering* 193.48-51 (2004), pages 5477–5502. doi: [10.1016/j.cma.2003.12.071](https://doi.org/10.1016/j.cma.2003.12.071) (cited on page 41).
- [131] C. Oskay and J. Fish. “Eigendeformation-based reduced order homogenization for failure analysis of heterogeneous materials”. In: *Computer Methods in Applied Mechanics and Engineering* 196.7 (2007), pages 1216–1243. doi: [10.1016/j.cma.2006.08.015](https://doi.org/10.1016/j.cma.2006.08.015) (cited on page 41).
- [132] P. Ladevèze, J.-C. Passieux, and D. Néron. “The LATIN multiscale computational method and the Proper Generalized Decomposition”. In: *Computer Methods in Applied Mechanics and Engineering* 199.21-22 (2010), pages 1287–1296. doi: [10.1016/j.cma.2009.06.023](https://doi.org/10.1016/j.cma.2009.06.023) (cited on page 41).
- [133] T. Dillard, S. Forest, and P. Ienny. “Micromorphic continuum modelling of the deformation and fracture behaviour of nickel foams”. In: *European Journal of Mechanics - A/Solids* 25.3 (2006), pages 526–549. doi: [10.1016/j.euromechsol.2005.11.006](https://doi.org/10.1016/j.euromechsol.2005.11.006) (cited on page 41).
- [134] J. C. Michel, H. Moulinec, and P. Suquet. “Effective properties of composite materials with periodic microstructure: a computational approach”. In: *Computer Methods in Applied Mechanics and Engineering* 172.1-4 (1999), pages 109–143. doi: [10.1016/S0045-7825\(98\)00227-8](https://doi.org/10.1016/S0045-7825(98)00227-8) (cited on pages 41, 43, 44).
- [135] T. Kanit, F. N’Guyen, S. Forest, D. Jeulin, M. Reed, and S. Singleton. “Apparent and effective physical properties of heterogeneous materials: Representativity of samples of two materials from food industry”. In: *Computer Methods in Applied Mechanics and Engineering* 195.33-36 (2006), pages 3960–3982. doi: [10.1016/j.cma.2005.07.022](https://doi.org/10.1016/j.cma.2005.07.022) (cited on pages 41–44).
- [136] J. P. Bandstra and D. A. Koss. “On the influence of void clusters on void growth and coalescence during ductile fracture”. In: *Acta Materialia* 56.16 (2008), pages 4429–4439. doi: [10.1016/j.actamat.2008.05.009](https://doi.org/10.1016/j.actamat.2008.05.009) (cited on page 43).
- [137] L. Zybelle, G. Hütter, T. Linse, U. Mühlich, and M. Kuna. “Size effects in ductile failure of porous materials containing two populations of voids”. In: *European Journal of Mechanics - A/Solids* 45 (2014), pages 8–19. doi: [10.1016/j.euromechsol.2013.11.006](https://doi.org/10.1016/j.euromechsol.2013.11.006) (cited on pages 43, 47, 227).
- [138] D. N. Ilin and M. Bernacki. “Advancing layer algorithm of dense ellipse packing for generating statistically equivalent polygonal structures”. In: *Granular Matter* 18.3 (2016), page 43. doi: [10.1007/s10035-016-0646-9](https://doi.org/10.1007/s10035-016-0646-9) (cited on page 44).
- [139] J. A. Oliveira, J. Pinho-da-Cruz, and F. Teixeira-Dias. “Asymptotic homogenisation in linear elasticity. Part II: Finite element procedures and multiscale applications”. In: *Computational Materials Science* 45.4 (2009), pages 1081–1096. doi: [10.1016/j.commatsci.2009.01.027](https://doi.org/10.1016/j.commatsci.2009.01.027) (cited on page 44).
- [140] H. J. Kim and C. C. Swan. “Voxel-based meshing and unit-cell analysis of textile composites”. In: *International Journal for Numerical Methods in Engineering* 56.7 (2003), pages 977–1006. doi: [10.1002/nme.594](https://doi.org/10.1002/nme.594) (cited on page 44).
- [141] F. Fritzen, T. Böhlke, and E. Schnack. “Periodic three-dimensional mesh generation for crystalline aggregates based on Voronoi tessellations”. In: *Computational Mechanics* 43.5 (2009), pages 701–713. doi: [10.1007/s00466-008-0339-2](https://doi.org/10.1007/s00466-008-0339-2) (cited on page 44).

- [142] J.-B. Leblond. *Mécanique de la rupture fragile et ductile*. Hermes Science Publications, 2003. ISBN: 2-7462-0751-6 (cited on page 45).
- [143] P.-G. Vincent. “Modélisation micromécanique de la croissance et de la percolation de pores sous pression dans une matrice céramique à haute température”. PhD thesis. Université d’Aix-Marseille I, 2007 (cited on page 45).
- [144] J.-B. Leblond and L. Morin. “Gurson’s Criterion and Its Derivation Revisited”. In: *Journal of Applied Mechanics* 81.5 (2014), page 051012. doi: [10.1115/1.4026112](https://doi.org/10.1115/1.4026112) (cited on pages 45–48).
- [145] D. Lassance, F. Scheyvaerts, and T. Pardoen. “Growth and coalescence of penny-shaped voids in metallic alloys”. In: *Engineering Fracture Mechanics* 73.8 (2006), pages 1009–1034. doi: [10.1016/j.engfracmech.2005.12.004](https://doi.org/10.1016/j.engfracmech.2005.12.004) (cited on pages 47–49, 191).
- [146] C. Tekoglu and T. Pardoen. “A micromechanics based damage model for composite materials”. In: *International Journal of Plasticity* 26.4 (2010), pages 549–569. doi: [10.1016/j.ijplas.2009.09.002](https://doi.org/10.1016/j.ijplas.2009.09.002) (cited on page 47).
- [147] T. Pardoen and J. W. Hutchinson. “An extended model for void growth and coalescence”. In: *Journal of the Mechanics and Physics of Solids* 48.12 (2000), pages 2467–2512. doi: [10.1016/S0022-5096\(00\)00019-3](https://doi.org/10.1016/S0022-5096(00)00019-3) (cited on pages 47, 191).
- [148] F. Scheyvaerts, P. R. Onck, C. Tekoglu, and T. Pardoen. “The growth and coalescence of ellipsoidal voids in plane strain under combined shear and tension”. In: *Journal of the Mechanics and Physics of Solids* 59.2 (2011), pages 373–397. doi: [10.1016/j.jmps.2010.10.003](https://doi.org/10.1016/j.jmps.2010.10.003) (cited on pages 47, 49, 191).
- [149] T.-S. Cao, C. Bobadilla, P. Montmitonnet, and P.-O. Bouchard. “A comparative study of three ductile damage approaches for fracture prediction in cold forming processes”. In: *Journal of Materials Processing Technology* 216 (2015), pages 385–404. doi: [10.1016/j.jmatprotec.2014.10.009](https://doi.org/10.1016/j.jmatprotec.2014.10.009) (cited on page 47).
- [150] K. Nahshon and J. W. Hutchinson. “Modification of the Gurson Model for shear failure”. In: *European Journal of Mechanics, A/Solids* 27.1 (2008), pages 1–17. doi: [10.1016/j.euromechsol.2007.08.002](https://doi.org/10.1016/j.euromechsol.2007.08.002) (cited on page 47).
- [151] J. Dahl, K. L. Nielsen, and V. Tvergaard. “Effect of Contact Conditions on Void Coalescence at Low Stress Triaxiality Shearing”. In: *Journal of Applied Mechanics* 79.2 (2012), page 021003. doi: [10.1115/1.4005565](https://doi.org/10.1115/1.4005565) (cited on page 47).
- [152] V. Tvergaard. “Behaviour of porous ductile solids at low stress triaxiality in different modes of deformation”. In: *International Journal of Solids and Structures* 60-61 (2015), pages 28–34. doi: [10.1016/j.ijsolstr.2015.01.027](https://doi.org/10.1016/j.ijsolstr.2015.01.027) (cited on page 47).
- [153] J. Besson and C. Guillemer-Neel. “An extension of the Green and Gurson models to kinematic hardening”. In: *Mechanics of Materials* 35.1-2 (2003), pages 1–18. doi: [10.1016/S0167-6636\(02\)00169-2](https://doi.org/10.1016/S0167-6636(02)00169-2) (cited on page 47).
- [154] X.-P. Xu and A. Needleman. “Void nucleation by inclusion debonding in a crystal matrix”. In: *Modelling and Simulation in Materials Science and Engineering* 1.2 (1993), pages 111–132. doi: [10.1088/0965-0393/1/2/001](https://doi.org/10.1088/0965-0393/1/2/001) (cited on page 47).
- [155] J. Y. Shu. “Scale-dependent deformation of porous single crystals”. In: *International Journal of Plasticity* 14.10-11 (1998), pages 1085–1107. doi: [10.1016/S0749-6419\(98\)00048-5](https://doi.org/10.1016/S0749-6419(98)00048-5) (cited on page 47).

- [156] G. P. Potirniche, J. L. Hearndon, M. F. Horstemeyer, and X. W. Ling. “Lattice orientation effects on void growth and coalescence in fcc single crystals”. In: *International Journal of Plasticity* 22.5 (2006), pages 921–942. doi: [10.1016/j.ijplas.2005.06.003](https://doi.org/10.1016/j.ijplas.2005.06.003) (cited on page 47).
- [157] U. Borg, C. F. Niordson, and J. W. Kysar. “Size effects on void growth in single crystals with distributed voids”. In: *International Journal of Plasticity* 24.4 (2008), pages 688–701. doi: [10.1016/j.ijplas.2007.07.015](https://doi.org/10.1016/j.ijplas.2007.07.015) (cited on page 47).
- [158] K.-C. Liao, J. Pan, and S. C. Tang. “Approximate yield criteria for anisotropic porous ductile sheet metals”. In: *Mechanics of Materials* 26.4 (1997), pages 213–226. doi: [10.1016/S0167-6636\(97\)00033-1](https://doi.org/10.1016/S0167-6636(97)00033-1) (cited on page 47).
- [159] A. A. Benzerga and J. Besson. “Plastic potentials for anisotropic porous solids”. In: *European Journal of Mechanics - A/Solids* 20.3 (2001), pages 397–434. doi: [10.1016/S0997-7538\(01\)01147-0](https://doi.org/10.1016/S0997-7538(01)01147-0) (cited on page 47).
- [160] V. Monchiet, O. Cazacu, E. Charkaluk, and D. Kondo. “Macroscopic yield criteria for plastic anisotropic materials containing spheroidal voids”. In: *International Journal of Plasticity* 24.7 (2008), pages 1158–1189. doi: [10.1016/j.ijplas.2007.08.008](https://doi.org/10.1016/j.ijplas.2007.08.008) (cited on page 47).
- [161] F. Reusch, B. Svendsen, and D. Klingbeil. “Local and non-local Gurson-based ductile damage and failure modelling at large deformation”. In: *European Journal of Mechanics - A/Solids* 22.6 (2003), pages 779–792. doi: [10.1016/S0997-7538\(03\)00070-6](https://doi.org/10.1016/S0997-7538(03)00070-6) (cited on page 47).
- [162] M. G. D. Geers, R. L. J. M. Ubachs, and R. A. B. Engelen. “Strongly non-local gradient-enhanced finite strain elastoplasticity”. In: *International Journal for Numerical Methods in Engineering* 56.14 (2003), pages 2039–2068. doi: [10.1002/nme.654](https://doi.org/10.1002/nme.654) (cited on page 47).
- [163] J. Wen, Y. Huang, K. C. Hwang, C. Liu, and M. Li. “The modified Gurson model accounting for the void size effect”. In: *International Journal of Plasticity* 21.2 (2005), pages 381–395. doi: [10.1016/j.ijplas.2004.01.004](https://doi.org/10.1016/j.ijplas.2004.01.004) (cited on page 47).
- [164] D. Fabrègue and T. Pardoen. “A constitutive model for elastoplastic solids containing primary and secondary voids”. In: *Journal of the Mechanics and Physics of Solids* 56.3 (2008), pages 719–741. doi: [10.1016/j.jmps.2007.07.008](https://doi.org/10.1016/j.jmps.2007.07.008) (cited on pages 47–49, 192).
- [165] F. Alauzet, P. J. Frey, P. L. George, and B. Mohammadi. “3D transient fixed point mesh adaptation for time-dependent problems: Application to CFD simulations”. In: *Journal of Computational Physics* 222.2 (2007), pages 592–623. doi: [10.1016/j.jcp.2006.08.012](https://doi.org/10.1016/j.jcp.2006.08.012) (cited on page 56).
- [166] D.-L. Quan, T. Toulorge, E. Marchandise, J.-F. Remacle, and G. Bricteux. “Anisotropic mesh adaptation with optimal convergence for finite elements using embedded geometries”. In: *Computer Methods in Applied Mechanics and Engineering* 268 (2014), pages 65–81. doi: [10.1016/j.cma.2013.09.007](https://doi.org/10.1016/j.cma.2013.09.007) (cited on pages 56, 60, 97, 103, 116).
- [167] T. de Geus. “From damage to fracture, from micro to macro: a systematic study of ductile fracture in multi-phase microstructures”. PhD thesis. Technische Universiteit Eindhoven, 2016. ISBN: 9789491909344 (cited on page 56).

- [168] M. Bernacki, H. Resk, T. Coupez, and R. E. Logé. “Finite element model of primary recrystallization in polycrystalline aggregates using a level set framework”. In: *Modelling and Simulation in Materials Science and Engineering* 17.6 (2009), page 064006. doi: [10.1088/0965-0393/17/6/064006](https://doi.org/10.1088/0965-0393/17/6/064006) (cited on pages 56, 60, 80).
- [169] N. Sukumar, D. L. Chopp, N. Moës, and T. Belytschko. “Modeling holes and inclusions by level sets in the extended finite-element method”. In: *Computer Methods in Applied Mechanics and Engineering* 190.46-47 (2001), pages 6183–6200. doi: [10.1016/S0045-7825\(01\)00215-8](https://doi.org/10.1016/S0045-7825(01)00215-8) (cited on pages 56, 58, 60, 70, 71, 103).
- [170] S. Osher and J. A. Sethian. “Fronts propagating with curvature-dependent speed: Algorithms based on Hamilton-Jacobi formulations”. In: *Journal of Computational Physics* 79.1 (1988), pages 12–49. doi: [10.1016/0021-9991\(88\)90002-2](https://doi.org/10.1016/0021-9991(88)90002-2) (cited on page 56).
- [171] W. J. Boettinger, J. A. Warren, C. Beckermann, and A. Karma. “Phase-field simulation of solidification”. In: *Annual Review of Materials Research* 32.1 (2002), pages 163–194. doi: [10.1146/annurev.matsci.32.101901.155803](https://doi.org/10.1146/annurev.matsci.32.101901.155803) (cited on page 56).
- [172] L.-Q. Chen. “Phase-field models for microstructure evolution”. In: *Annual Review of Materials Research* 32.1 (2002), pages 113–140. doi: [10.1146/annurev.matsci.32.112001.132041](https://doi.org/10.1146/annurev.matsci.32.112001.132041) (cited on page 56).
- [173] C. W. Hirt and B. D. Nichols. “Volume of fluid (VOF) method for the dynamics of free boundaries”. In: *Journal of Computational Physics* 39.1 (1981), pages 201–225. doi: [10.1016/0021-9991\(81\)90145-5](https://doi.org/10.1016/0021-9991(81)90145-5) (cited on page 56).
- [174] M. J. Borden, C. V. Verhoosel, M. A. Scott, T. J. R. Hughes, and C. M. Landis. “A phase-field description of dynamic brittle fracture”. In: *Computer Methods in Applied Mechanics and Engineering* 217-220 (2012), pages 77–95. doi: [10.1016/j.cma.2012.01.008](https://doi.org/10.1016/j.cma.2012.01.008) (cited on page 56).
- [175] C. Miehe, F. Welschinger, and M. Hofacker. “Thermodynamically consistent phase-field models of fracture: Variational principles and multi-field FE implementations”. In: *International Journal for Numerical Methods in Engineering* 83.10 (2010), pages 1273–1311. doi: [10.1002/nme.2861](https://doi.org/10.1002/nme.2861) (cited on page 56).
- [176] M. Sussman. “A second order coupled level set and volume-of-fluid method for computing growth and collapse of vapor bubbles”. In: *Journal of Computational Physics* 187.1 (2003), pages 110–136. doi: [10.1016/S0021-9991\(03\)00087-1](https://doi.org/10.1016/S0021-9991(03)00087-1) (cited on page 56).
- [177] D. Enright, R. Fedkiw, J. Ferziger, and I. Mitchell. “A Hybrid Particle Level Set Method for Improved Interface Capturing”. In: *Journal of Computational Physics* 183.1 (2002), pages 83–116. doi: [10.1006/jcph.2002.7166](https://doi.org/10.1006/jcph.2002.7166) (cited on pages 56, 76).
- [178] S. E. Hieber and P. Koumoutsakos. “A Lagrangian particle level set method”. In: *Journal of Computational Physics* 210.1 (2005), pages 342–367. doi: [10.1016/j.jcp.2005.04.013](https://doi.org/10.1016/j.jcp.2005.04.013) (cited on page 56).
- [179] X. Zheng, J. Lowengrub, A. Anderson, and V. Cristini. “Adaptive unstructured volume remeshing – II: Application to two- and three-dimensional level-set simulations of multiphase flow”. In: *Journal of Computational Physics* 208.2 (2005), pages 626–650. doi: [10.1016/j.jcp.2005.02.024](https://doi.org/10.1016/j.jcp.2005.02.024) (cited on page 56).
- [180] M. Sussman. “A parallelized, adaptive algorithm for multiphase flows in general geometries”. In: *Computers & Structures* 83.6-7 (2005), pages 435–444. doi: [10.1016/j.compstruc.2004.06.006](https://doi.org/10.1016/j.compstruc.2004.06.006) (cited on page 56).

- [181] H. Hallberg. “A modified level set approach to 2D modeling of dynamic recrystallization”. In: *Modelling and Simulation in Materials Science and Engineering* 21.8 (2013), page 085012. doi: [10.1088/0965-0393/21/8/085012](https://doi.org/10.1088/0965-0393/21/8/085012) (cited on pages 56, 82, 103, 104, 256).
- [182] G. Compère, J.-F. Remacle, and E. Marchandise. “Transient Mesh Adaptivity with Large Rigid-Body Displacements”. In: *Proceedings of the 17th International Meshing Roundtable*. Edited by R. V. Garimella. Berlin, Heidelberg: Springer Berlin Heidelberg, 2008, pages 213–230. doi: [10.1007/978-3-540-87921-3_{_}13](https://doi.org/10.1007/978-3-540-87921-3_{_}13) (cited on pages 56, 63, 72, 75, 76, 78).
- [183] F. Alauzet. “A changing-topology moving mesh technique for large displacements”. In: *Engineering with Computers* 30.2 (2013), pages 175–200. doi: [10.1007/s00366-013-0340-z](https://doi.org/10.1007/s00366-013-0340-z) (cited on pages 56, 75, 76, 78).
- [184] M. Ortiz and A. Pandolfi. “Finite-deformation irreversible cohesive elements for three-dimensional crack-propagation analysis”. In: *International Journal for Numerical Methods in Engineering* 44.9 (1999), pages 1267–1282. doi: [10.1002/\(SICI\)1097-0207\(19990330\)44:9<1267::AID-NME486>3.0.CO;2-7](https://doi.org/10.1002/(SICI)1097-0207(19990330)44:9<1267::AID-NME486>3.0.CO;2-7) (cited on pages 58, 144, 273).
- [185] T. N. Bittencourt, P. A. Wawrzynek, A. R. Ingraffea, and J. L. Sousa. “Quasi-automatic simulation of crack propagation for 2D LEFM problems”. In: *Engineering Fracture Mechanics* 55.2 (1996), pages 321–334. doi: [10.1016/0013-7944\(95\)00247-2](https://doi.org/10.1016/0013-7944(95)00247-2) (cited on pages 58, 86).
- [186] B. J. Carter, P. A. Wawrzynek, and A. R. Ingraffea. “Automated 3-D crack growth simulation”. In: *International Journal for Numerical Methods in Engineering* 47.1-3 (2000), pages 229–253. doi: [10.1002/\(SICI\)1097-0207\(20000110/30\)47:1/3<229::AID-NME769>3.0.CO;2-2](https://doi.org/10.1002/(SICI)1097-0207(20000110/30)47:1/3<229::AID-NME769>3.0.CO;2-2) (cited on pages 58, 86).
- [187] H. R. Javani, R. H. J. Peerlings, and M. G. D. Geers. “Three-dimensional finite element modeling of ductile crack initiation and propagation”. In: *Advanced Modeling and Simulation in Engineering Sciences* 3.1 (2016), page 19. doi: [10.1186/s40323-016-0071-y](https://doi.org/10.1186/s40323-016-0071-y) (cited on page 58).
- [188] N. Moës, J. Dolbow, and T. Belytschko. “A finite element method for crack growth without remeshing”. In: *International Journal for Numerical Methods in Engineering* 46.1 (1999), pages 131–150. doi: [10.1002/\(SICI\)1097-0207\(19990910\)46:1<131::AID-NME726>3.0.CO;2-J](https://doi.org/10.1002/(SICI)1097-0207(19990910)46:1<131::AID-NME726>3.0.CO;2-J) (cited on page 58).
- [189] P. Laure, G. Baume, O. Basset, L. Silva, and T. Coupez. “Numerical methods for solid particles in particulate flow simulations”. In: *Revue européenne de mécanique numérique* 16.3-4 (2007), pages 365–383. doi: [10.3166/remn.16.365-383](https://doi.org/10.3166/remn.16.365-383) (cited on page 60).
- [190] Z. Sun, R. E. Logé, and M. Bernacki. “3D finite element model of semi-solid permeability in an equiaxed granular structure”. In: *Computational Materials Science* 49.1 (2010), pages 158–170. doi: [10.1016/j.commatsci.2010.04.042](https://doi.org/10.1016/j.commatsci.2010.04.042) (cited on page 60).
- [191] L. Silva, R. Valette, P. Laure, and T. Coupez. “A new three-dimensional mixed finite element for direct numerical simulation of compressible viscoelastic flows with moving free surfaces”. In: *International Journal of Material Forming* 5.1 (2011), pages 55–72. doi: [10.1007/s12289-011-1030-2](https://doi.org/10.1007/s12289-011-1030-2) (cited on pages 60, 80).

- [192] C. Geuzaine and J.-F. Remacle. “Gmsh: A 3-D finite element mesh generator with built-in pre- and post-processing facilities”. In: *International Journal for Numerical Methods in Engineering* 79.11 (2009), pages 1309–1331. doi: [10.1002/nme.2579](https://doi.org/10.1002/nme.2579) (cited on pages [60](#), [76](#), [124](#), [169](#), [170](#)).
- [193] K. J. Fidkowski and D. L. Darmofal. “A triangular cut-cell adaptive method for high-order discretizations of the compressible Navier–Stokes equations”. In: *Journal of Computational Physics* 225.2 (2007), pages 1653–1672. doi: [10.1016/j.jcp.2007.02.007](https://doi.org/10.1016/j.jcp.2007.02.007) (cited on page [60](#)).
- [194] C. Gruau and T. Coupez. “3D tetrahedral, unstructured and anisotropic mesh generation with adaptation to natural and multidomain metric”. In: *Computer Methods in Applied Mechanics and Engineering* 194.48-49 (2005), pages 4951–4976. doi: [10.1016/j.cma.2004.11.020](https://doi.org/10.1016/j.cma.2004.11.020) (cited on pages [62](#), [63](#)).
- [195] C. Dobrzynski and P. Frey. “Anisotropic Delaunay Mesh Adaptation for Unsteady Simulations”. In: *Proceedings of the 17th International Meshing Roundtable*. Edited by R. V. Garimella. Berlin, Heidelberg: Springer Berlin Heidelberg, 2008, pages 177–194. doi: [10.1007/978-3-540-87921-3](https://doi.org/10.1007/978-3-540-87921-3) (cited on page [63](#)).
- [196] B. M. Klingner and J. R. Shewchuk. “Aggressive Tetrahedral Mesh Improvement”. In: *Proceedings of the 16th International Meshing Roundtable*. Springer Berlin Heidelberg, 2008. Chapter Session 1A, pages 3–23. doi: [10.1007/978-3-540-75103-8_1](https://doi.org/10.1007/978-3-540-75103-8_1) (cited on pages [63](#), [72](#)).
- [197] ISO. *ISO/IEC 9899:1999*. Technical report. Geneva, Switzerland: International Organization for Standardization, 1999 (cited on page [66](#)).
- [198] D. A. Di Pietro, S. Lo Forte, and N. Parolini. “Mass preserving finite element implementations of the level set method”. In: *Applied Numerical Mathematics* 56.9 (2006), pages 1179–1195. doi: [10.1016/j.apnum.2006.03.003](https://doi.org/10.1016/j.apnum.2006.03.003) (cited on pages [75](#), [76](#)).
- [199] R. Löhner, J. R. Cebral, F. E. Camelli, S. Appanaboyina, J. D. Baum, E. L. Mestreau, and O. A. Soto. “Adaptive embedded and immersed unstructured grid techniques”. In: *Computer Methods in Applied Mechanics and Engineering* 197.25-28 (2008), pages 2173–2197. doi: [10.1016/j.cma.2007.09.010](https://doi.org/10.1016/j.cma.2007.09.010) (cited on page [76](#)).
- [200] J. Bruchon and T. Coupez. “A numerical strategy for the direct 3D simulation of the expansion of bubbles into a molten polymer during a foaming process”. In: *International Journal for Numerical Methods in Fluids* 57.8 (2008), pages 977–1003. doi: [10.1002/flid.1660](https://doi.org/10.1002/flid.1660) (cited on page [80](#)).
- [201] H. Digonnet, L. Silva, and T. Coupez. “Massively parallel computation on anisotropic meshes”. In: *6th International Conference on Adaptive Modeling and Simulation, AD-MOS 2013*. Edited by J. P. Moitinho de Almeida, P. Díez, C. Tiago, and N. Parés. Lisbon, Portugal, 2013, pages 199–211 (cited on page [85](#)).
- [202] Y. Belhamadia, A. Fortin, and E. Chamberland. “Anisotropic mesh adaptation for the solution of the Stefan problem”. In: *Journal of Computational Physics* 194.1 (2004), pages 233–255. doi: [10.1016/j.jcp.2003.09.008](https://doi.org/10.1016/j.jcp.2003.09.008) (cited on pages [98](#), [99](#)).
- [203] Y. Zhang, C. Bajaj, and B.-S. Sohn. “3D Finite Element Meshing from Imaging Data.” In: *Computer methods in applied mechanics and engineering* 194.48-49 (2005), pages 5083–5106. doi: [10.1016/j.cma.2004.11.026](https://doi.org/10.1016/j.cma.2004.11.026) (cited on pages [98](#), [99](#), [124](#), [125](#)).

- [204] B. Pouliot, M. Fortin, A. Fortin, and E. Chamberland. “On a new edge-based gradient recovery technique”. In: *International Journal for Numerical Methods in Engineering* 93.1 (2013), pages 52–65. doi: [10.1002/nme.4374](https://doi.org/10.1002/nme.4374) (cited on page 99).
- [205] A. Yazid, N. Abdelkader, and H. Abdelmadjid. “A state-of-the-art review of the X-FEM for computational fracture mechanics”. In: *Applied Mathematical Modelling* 33.12 (2009), pages 4269–4282. doi: [10.1016/j.apm.2009.02.010](https://doi.org/10.1016/j.apm.2009.02.010) (cited on page 103).
- [206] M. Bernacki, R. E. Logé, and T. Coupez. “Level set framework for the finite-element modelling of recrystallization and grain growth in polycrystalline materials”. In: *Scripta Materialia* 64.6 (2011), pages 525–528. doi: [10.1016/j.scriptamat.2010.11.032](https://doi.org/10.1016/j.scriptamat.2010.11.032) (cited on pages 103, 115).
- [207] A. L. Cruz-Fabiano, R. E. Logé, and M. Bernacki. “Assessment of simplified 2D grain growth models from numerical experiments based on a level set framework”. In: *Computational Materials Science* 92 (2014), pages 305–312. doi: [10.1016/j.commatsci.2014.05.060](https://doi.org/10.1016/j.commatsci.2014.05.060) (cited on pages 103, 115).
- [208] J. A. Sethian. “A fast marching level set method for monotonically advancing fronts.” In: *Proceedings of the National Academy of Sciences* 93.4 (1996), pages 1591–1595. doi: [10.1073/pnas.93.4.1591](https://doi.org/10.1073/pnas.93.4.1591) (cited on page 103).
- [209] R. Kimmel and J. A. Sethian. “Computing geodesic paths on manifolds”. In: *Proceedings of the National Academy of Sciences* 95.15 (1998), pages 8431–8435. doi: [10.1073/pnas.95.15.8431](https://doi.org/10.1073/pnas.95.15.8431) (cited on page 103).
- [210] J. A. Sethian and A. Vladimirsky. “Fast methods for the Eikonal and related Hamilton-Jacobi equations on unstructured meshes.” In: *Proceedings of the National Academy of Sciences of the United States of America* 11 (2000), pages 5699–703. doi: [10.1073/pnas.090060097](https://doi.org/10.1073/pnas.090060097) (cited on page 103).
- [211] M. Sussman, P. Smereka, and S. Osher. “A Level Set Approach for Computing Solutions to Incompressible Two-Phase Flow”. In: *Journal of Computational Physics* 114.1 (1994), pages 146–159. doi: [10.1006/jcph.1994.1155](https://doi.org/10.1006/jcph.1994.1155) (cited on pages 103, 104).
- [212] R. N. Elias, M. A. D. Martins, and A. L. G. A. Coutinho. “Simple finite element-based computation of distance functions in unstructured grids”. In: *International Journal for Numerical Methods in Engineering* 72.9 (2007), pages 1095–1110. doi: [10.1002/nme.2079](https://doi.org/10.1002/nme.2079) (cited on page 104).
- [213] M. W. Jones, J. A. Baerentzen, and M. Sramek. “3D distance fields: a survey of techniques and applications”. In: *IEEE Transactions on Visualization and Computer Graphics* 12.4 (2006), pages 581–599. doi: [10.1109/TVCG.2006.56](https://doi.org/10.1109/TVCG.2006.56) (cited on page 104).
- [214] O. Fortmeier and H. Martin Bucker. “Parallel re-initialization of level set functions on distributed unstructured tetrahedral grids”. In: *Journal of Computational Physics* 230.12 (2011), pages 4437–4453. doi: [10.1016/j.jcp.2011.02.005](https://doi.org/10.1016/j.jcp.2011.02.005) (cited on page 104).
- [215] D. H. Eberly and P. J. Schneider. *Geometric Tools for Computer Graphics*. Kaufmann, Morgan, 2003, pages 1–1043 (cited on page 104).
- [216] J. L. Bentley. “Multidimensional binary search trees used for associative searching”. In: *Communications of the ACM* 18.9 (1975), pages 509–517. issn: 00010782. doi: [10.1145/361002.361007](https://doi.org/10.1145/361002.361007) (cited on pages 105, 224).
- [217] T. Coupez. “Metric construction by length distribution tensor and edge based error for anisotropic adaptive meshing”. In: *Journal of Computational Physics* 230.7 (2011), pages 2391–2405. doi: [10.1016/j.jcp.2010.11.041](https://doi.org/10.1016/j.jcp.2010.11.041) (cited on page 112).

- [218] J. E. Burke and D. Turnbull. “Recrystallization and grain growth”. In: *Progress in Metal Physics* 3 (1952), pages 220–292. doi: [10.1016/0502-8205\(52\)90009-9](https://doi.org/10.1016/0502-8205(52)90009-9) (cited on page 115).
- [219] J. R. Shewchuk. “Delaunay refinement algorithms for triangular mesh generation”. In: *Computational Geometry* 22.1-3 (2002), pages 21–74. doi: [10.1016/S0925-7721\(01\)00047-5](https://doi.org/10.1016/S0925-7721(01)00047-5) (cited on page 124).
- [220] T. Toulorge, J. Lambrechts, and J.-F. Remacle. “Optimizing the geometrical accuracy of curvilinear meshes”. In: *Journal of Computational Physics* 310 (2016), pages 361–380. doi: [10.1016/j.jcp.2016.01.023](https://doi.org/10.1016/j.jcp.2016.01.023) (cited on page 124).
- [221] P. G. Young, T. B. H. Beresford-West, S. R. L. Coward, B. Notarberardino, B. Walker, and A. Abdul-Aziz. “An efficient approach to converting three-dimensional image data into highly accurate computational models.” In: *Philosophical transactions. Series A, Mathematical, physical, and engineering sciences* 366.1878 (2008), pages 3155–73. doi: [10.1098/rsta.2008.0090](https://doi.org/10.1098/rsta.2008.0090) (cited on pages 124, 125).
- [222] J.-X. Zhao. “Development of numerical tools for mesh generation/adaptation applied imaging”. PhD thesis. Ecole Nationale Supérieure des Mines de Paris, 2016 (cited on pages 124, 125).
- [223] J. Schindelin, I. Arganda-Carreras, E. Frise, V. Kaynig, M. Longair, T. Pietzsch, S. Preibisch, C. Rueden, S. Saalfeld, B. Schmid, J.-Y. Tinevez, D. J. White, V. Hartenstein, K. Eliceiri, P. Tomancak, and A. Cardona. “Fiji: an open-source platform for biological-image analysis”. In: *Nature Methods* 9.7 (2012), pages 676–682. doi: [10.1038/nmeth.2019](https://doi.org/10.1038/nmeth.2019) (cited on page 124).
- [224] C. A. Schneider, W. S. Rasband, and K. W. Eliceiri. “NIH Image to ImageJ: 25 years of image analysis”. In: *Nature Methods* 9.7 (2012), pages 671–675. doi: [10.1038/nmeth.2089](https://doi.org/10.1038/nmeth.2089) (cited on page 124).
- [225] G. Odin, C. Savoldelli, P.-O. Bouchard, and Y. Tillier. “Determination of Young’s modulus of mandibular bone using inverse analysis.” In: *Medical engineering & physics* 32.6 (2010), pages 630–7. doi: [10.1016/j.medengphy.2010.03.009](https://doi.org/10.1016/j.medengphy.2010.03.009) (cited on pages 128, 129).
- [226] V. Fabre. “Etude de l’endommagement en fatigue d’un composite thermoplastique à fibres courtes - cas du polyamide 6,6 renforcé de fibres de verre courtes”. PhD thesis. Ecole Nationale Supérieure des Mines de Paris, 2015 (cited on pages 128, 131).
- [227] A. Eckschlager, W. Han, and H. J. Böhm. “A unit cell model for brittle fracture of particles embedded in a ductile matrix”. In: *Computational Materials Science* 25.1-2 (2002), pages 85–91. doi: [10.1016/S0927-0256\(02\)00252-5](https://doi.org/10.1016/S0927-0256(02)00252-5) (cited on page 138).
- [228] C. Landron, O. Bouaziz, E. Maire, and J. Adrien. “Characterization and modeling of void nucleation by interface decohesion in dual phase steels”. In: *Scripta Materialia* 63.10 (2010), pages 973–976. doi: [10.1016/j.scriptamat.2010.07.021](https://doi.org/10.1016/j.scriptamat.2010.07.021) (cited on pages 138, 141, 215, 245).
- [229] C. Landron, O. Bouaziz, E. Maire, and J. Adrien. “Experimental investigation of void coalescence in a dual phase steel using X-ray tomography”. In: *Acta Materialia* 61.18 (2013), pages 6821–6829. doi: [10.1016/j.actamat.2013.07.058](https://doi.org/10.1016/j.actamat.2013.07.058) (cited on page 138).

- [230] T. W. J. De Geus, R. H. J. Peerlings, and M. G. D. Geers. “Microstructural topology effects on the onset of ductile failure in multi-phase materials – A systematic computational approach”. In: *International Journal of Solids and Structures* 67-68 (2015), pages 326–339. doi: [10.1016/j.ijsolstr.2015.04.035](https://doi.org/10.1016/j.ijsolstr.2015.04.035) (cited on page 138).
- [231] R. Miller, M. Ortiz, R. Phillips, V. Shenoy, and E. B. Tadmor. “Quasicontinuum models of fracture and plasticity”. In: *Engineering Fracture Mechanics* 61.3-4 (1998), pages 427–444. doi: [10.1016/S0013-7944\(98\)00047-2](https://doi.org/10.1016/S0013-7944(98)00047-2) (cited on page 138).
- [232] Y. J. Wei and L. Anand. “Grain-boundary sliding and separation in polycrystalline metals: application to nanocrystalline fcc metals”. In: *Journal of the Mechanics and Physics of Solids* 52.11 (2004), pages 2587–2616. doi: [10.1016/j.jmps.2004.04.006](https://doi.org/10.1016/j.jmps.2004.04.006) (cited on page 138).
- [233] T. R. Bieler, P. Eisenlohr, F. Roters, D. Kumar, D. E. Mason, M. A. Crimp, and D. Raabe. “The role of heterogeneous deformation on damage nucleation at grain boundaries in single phase metals”. In: *International Journal of Plasticity* 25.9 (2009), pages 1655–1683. doi: [10.1016/j.ijplas.2008.09.002](https://doi.org/10.1016/j.ijplas.2008.09.002) (cited on page 138).
- [234] Y. Wang and J. Li. “Phase field modeling of defects and deformation”. In: *Acta Materialia* 58.4 (2010), pages 1212–1235. doi: [10.1016/j.actamat.2009.10.041](https://doi.org/10.1016/j.actamat.2009.10.041) (cited on page 138).
- [235] A. S. Argon and R. Safoglu. “Cavity Formation from Inclusions in Ductile Fracture”. In: *Metallurgical Transactions A* 6.apr (1975), pages 828–837 (cited on page 140).
- [236] A. L. Helbert, X. Feaugas, and M. Clavel. “Effects of microstructural parameters and back stress on damage mechanisms in α/β titanium alloys”. In: *Acta Materialia* 46.3 (1998), pages 939–951. doi: [10.1016/S1359-6454\(97\)00288-7](https://doi.org/10.1016/S1359-6454(97)00288-7) (cited on pages 140, 141).
- [237] S. K. Yerra, G. Martin, M. Véron, Y. Bréchet, J. D. Mithieux, L. Delannay, and T. Pardoen. “Ductile fracture initiated by interface nucleation in two-phase elastoplastic systems”. In: *Engineering Fracture Mechanics* 102 (2013), pages 77–100. doi: [10.1016/j.engfracmech.2013.02.028](https://doi.org/10.1016/j.engfracmech.2013.02.028) (cited on pages 141, 144).
- [238] Y. Charles, R. Estevez, Y. Bréchet, and E. Maire. “Modelling the competition between interface debonding and particle fracture using a plastic strain dependent cohesive zone”. In: *Engineering Fracture Mechanics* 77.4 (2010), pages 705–718. doi: [10.1016/j.engfracmech.2009.11.012](https://doi.org/10.1016/j.engfracmech.2009.11.012) (cited on pages 142, 144).
- [239] J. Fitoussi, G. Guo, and D. Baptiste. “Determination of a tridimensional failure criterion at the fibre/matrix interface of an organic-matrix/discontinuous-reinforcement composite”. In: *Composites Science and Technology* 56 (1996), pages 755–760 (cited on page 144).
- [240] Y. Bao and T. Wierzbicki. “On fracture locus in the equivalent strain and stress triaxiality space”. In: *International Journal of Mechanical Sciences* 46.1 (2004), pages 81–98. doi: [10.1016/j.ijmecsci.2004.02.006](https://doi.org/10.1016/j.ijmecsci.2004.02.006) (cited on pages 150, 194, 214).
- [241] Y. Bao and T. Wierzbicki. “A Comparative Study on Various Ductile Crack Formation Criteria”. In: *Journal of Engineering Materials and Technology* 126.3 (2004), page 314. doi: [10.1115/1.1755244](https://doi.org/10.1115/1.1755244) (cited on pages 150, 194).
- [242] P. Ludwik. *Elemente der technologischen Mechanik*. Leipzig (Germany): Verlag Von Julius Springer, 1909, page 32 (cited on page 153).

- [243] P. F. Thomason. *Ductile fracture of metals*. Pergamon Press, 1990. ISBN: 0080401783 (cited on pages 191, 214).
- [244] A. A. Benzerga. “Micromechanics of coalescence in ductile fracture”. In: *Journal of the Mechanics and Physics of Solids* 50.6 (2002), pages 1331–1362. doi: [10.1016/S0022-5096\(01\)00125-9](https://doi.org/10.1016/S0022-5096(01)00125-9) (cited on page 191).
- [245] L. Lecarme, C. Tekoglu, and T. Pardoen. “Void growth and coalescence in ductile solids with stage III and stage IV strain hardening”. In: *International Journal of Plasticity* 27.8 (2011), pages 1203–1223. doi: [10.1016/j.ijplas.2011.01.004](https://doi.org/10.1016/j.ijplas.2011.01.004) (cited on page 191).
- [246] L. Morin, J.-B. Leblond, A. A. Benzerga, and D. Kondo. “A unified criterion for the growth and coalescence of microvoids”. In: *Journal of the Mechanics and Physics of Solids* (2016), pages 1–18. doi: [10.1016/j.jmps.2016.01.013](https://doi.org/10.1016/j.jmps.2016.01.013) (cited on page 191).
- [247] K. L. Nielsen and V. Tvergaard. “Failure by void coalescence in metallic materials containing primary and secondary voids subject to intense shearing”. In: *International Journal of Solids and Structures* 48.9 (2011), pages 1255–1267. doi: [10.1016/j.ijsolstr.2011.01.008](https://doi.org/10.1016/j.ijsolstr.2011.01.008) (cited on page 192).
- [248] G. Hütter, L. Zybelle, and M. Kuna. “Size effects due to secondary voids during ductile crack propagation”. In: *International Journal of Solids and Structures* 51.3-4 (2014), pages 839–847. doi: [10.1016/j.ijsolstr.2013.11.012](https://doi.org/10.1016/j.ijsolstr.2013.11.012) (cited on pages 192, 215, 227, 235).
- [249] R. H. J. Peerlings, R. De Borst, W. A. M. Brekelmans, and J. H. P. De Vree. “Gradient enhanced damage for quasi-brittle materials”. In: *International Journal for Numerical Methods in Engineering* 39.19 (1996), pages 3391–3403. doi: [10.1002/\(SICI\)1097-0207\(19961015\)39:19<3391::AID-NME7>3.0.CO;2-D](https://doi.org/10.1002/(SICI)1097-0207(19961015)39:19<3391::AID-NME7>3.0.CO;2-D) (cited on pages 192, 261).
- [250] R. H. J. Peerlings, M. G. D. Geers, R. De Borst, and W. A. M. Brekelmans. “A critical comparison of nonlocal and gradient-enhanced softening continua”. In: *International Journal of Solids and Structures* 38.44-45 (2001), pages 7723–7746. doi: [10.1016/S0020-7683\(01\)00087-7](https://doi.org/10.1016/S0020-7683(01)00087-7) (cited on pages 192, 261).
- [251] Z. P. Bažant and M. Jirásek. “Nonlocal Integral Formulations of Plasticity and Damage: Survey of Progress”. In: *Journal of Engineering Mechanics* 128.11 (2002), pages 1119–1149. doi: [10.1061/\(ASCE\)0733-9399\(2002\)128:11\(1119\)](https://doi.org/10.1061/(ASCE)0733-9399(2002)128:11(1119)) (cited on page 192).
- [252] N. Moës, C. Stolz, P.-E. Bernard, and N. Chevaugeon. “A level set based model for damage growth: The thick level set approach”. In: *International Journal for Numerical Methods in Engineering* 86.3 (2011), pages 358–380. doi: [10.1002/nme.3069](https://doi.org/10.1002/nme.3069) (cited on page 192).
- [253] H.-B. Mühlhaus and E. C. Alfantis. “A variational principle for gradient plasticity”. In: *International Journal of Solids and Structures* 28.7 (1991), pages 845–857. doi: [10.1016/0020-7683\(91\)90004-Y](https://doi.org/10.1016/0020-7683(91)90004-Y) (cited on page 192).
- [254] R. De Borst and H.-B. Mühlhaus. “Gradient-dependent plasticity: Formulation and algorithmic aspects”. In: *International Journal for Numerical Methods in Engineering* 35.3 (1992), pages 521–539. doi: [10.1002/nme.1620350307](https://doi.org/10.1002/nme.1620350307) (cited on page 192).
- [255] W. D. Nix and H. Gao. “Indentation size effects in crystalline materials: A law for strain gradient plasticity”. In: *Journal of the Mechanics and Physics of Solids* 46.3 (1998), pages 411–425. doi: [10.1016/S0022-5096\(97\)00086-0](https://doi.org/10.1016/S0022-5096(97)00086-0) (cited on page 192).

- [256] H. Gao. “Mechanism-based strain gradient plasticity: I. Theory”. In: *Journal of the Mechanics and Physics of Solids* 47.6 (1999), pages 1239–1263. doi: [10.1016/S0022-5096\(98\)00103-3](https://doi.org/10.1016/S0022-5096(98)00103-3) (cited on page 192).
- [257] N. A. Fleck and J. W. Hutchinson. “A reformulation of strain gradient plasticity”. In: *Journal of the Mechanics and Physics of Solids* 49.10 (2001), pages 2245–2271. doi: [10.1016/S0022-5096\(01\)00049-7](https://doi.org/10.1016/S0022-5096(01)00049-7) (cited on page 192).
- [258] Y. Alinaghian, M. Asadi, and A. Weck. “Effect of pre-strain and work hardening rate on void growth and coalescence in AA5052”. In: *International Journal of Plasticity* 53 (2014), pages 193–205. doi: [10.1016/j.ijplas.2013.08.007](https://doi.org/10.1016/j.ijplas.2013.08.007) (cited on pages 197, 215, 235).
- [259] J. Fansi, T. Balan, X. Lemoine, E. Maire, C. Landron, O. Bouaziz, M. Ben Bettaieb, and A. M. Habraken. “Numerical investigation and experimental validation of physically based advanced GTN model for DP steels”. In: *Materials Science and Engineering: A* 569 (2013), pages 1–12. doi: [10.1016/j.msea.2013.01.019](https://doi.org/10.1016/j.msea.2013.01.019) (cited on pages 214, 215, 245).
- [260] G. Requena, E. Maire, C. Leguen, and S. Thuillier. “Separation of nucleation and growth of voids during tensile deformation of a dual phase steel using synchrotron microtomography”. In: *Materials Science and Engineering: A* 589 (2014), pages 242–251. doi: [10.1016/j.msea.2013.09.084](https://doi.org/10.1016/j.msea.2013.09.084) (cited on page 214).
- [261] M. Dunand and D. Mohr. “Hybrid experimental-numerical analysis of basic ductile fracture experiments for sheet metals”. In: *International Journal of Solids and Structures* 47.9 (2010), pages 1130–1143. doi: [10.1016/j.ijsolstr.2009.12.011](https://doi.org/10.1016/j.ijsolstr.2009.12.011) (cited on page 214).
- [262] V. Tvergaard and J. W. Hutchinson. “Two mechanisms of ductile fracture: Void by void growth versus multiple void interaction”. In: *International Journal of Solids and Structures* 39.13-14 (2002), pages 3581–3597. doi: [10.1016/S0020-7683\(02\)00168-3](https://doi.org/10.1016/S0020-7683(02)00168-3) (cited on pages 214, 235).
- [263] R. Tian, S. Chan, S. Tang, A. M. Kopacz, J. S. Wang, H. J. Jou, L. Siad, L. E. Lindgren, G. B. Olson, and W. K. Liu. “A multiresolution continuum simulation of the ductile fracture process”. In: *Journal of the Mechanics and Physics of Solids* 58.10 (2010), pages 1681–1700. doi: [10.1016/j.jmps.2010.07.002](https://doi.org/10.1016/j.jmps.2010.07.002) (cited on pages 215, 235).
- [264] S. Tang, A. M. Kopacz, S. Chan O’Keeffe, G. B. Olson, and W. K. Liu. “Three-dimensional ductile fracture analysis with a hybrid multiresolution approach and microtomography”. In: *Journal of the Mechanics and Physics of Solids* 61.11 (2013), pages 2108–2124. doi: [10.1016/j.jmps.2013.07.007](https://doi.org/10.1016/j.jmps.2013.07.007) (cited on pages 215, 235).
- [265] S. C. O’Keeffe, S. Tang, A. M. Kopacz, J. Smith, D. J. Rowenhorst, G. Spanos, W. K. Liu, and G. B. Olson. “Multiscale ductile fracture integrating tomographic characterization and 3-D simulation”. In: *Acta Materialia* 82 (2015), pages 503–510. doi: [10.1016/j.actamat.2014.09.016](https://doi.org/10.1016/j.actamat.2014.09.016) (cited on pages 215, 235).
- [266] M. J. Dong, C. Prioul, and D. François. “Damage effect on the fracture toughness of nodular cast iron: Part I. Damage characterization and plastic flow stress modeling”. In: *Metallurgical and Materials Transactions A* 28.11 (1997), pages 2245–2254. doi: [10.1007/s11661-997-0182-7](https://doi.org/10.1007/s11661-997-0182-7) (cited on pages 215, 224).

- [267] G. Hütter, L. Zybelle, and M. Kuna. “Micromechanisms of fracture in nodular cast iron: From experimental findings towards modeling strategies – A review”. In: *Engineering Fracture Mechanics* 144 (2015), pages 118–141. doi: [10.1016/j.engfracmech.2015.06.042](https://doi.org/10.1016/j.engfracmech.2015.06.042) (cited on pages 215, 224, 227).
- [268] K. S. Zhang, J. B. Bai, and D. François. “Ductile fracture of materials with high void volume fraction”. In: *International Journal of Solids and Structures* 36.23 (1999), pages 3407–3425. doi: [10.1016/S0020-7683\(98\)00157-7](https://doi.org/10.1016/S0020-7683(98)00157-7) (cited on pages 215, 224).
- [269] N. Bonora and A. Ruggiero. “Micromechanical modeling of ductile cast iron incorporating damage. Part I: Ferritic ductile cast iron”. In: *International Journal of Solids and Structures* 42.5-6 (2005), pages 1401–1424. doi: [10.1016/j.ijstr.2004.07.025](https://doi.org/10.1016/j.ijstr.2004.07.025) (cited on pages 215, 224).
- [270] L. Helfen, A. Myagotin, P. Pernot, M. DiMichiel, P. Mikulík, A. Berthold, and T. Baumbach. “Investigation of hybrid pixel detector arrays by synchrotron-radiation imaging”. In: *Nuclear Instruments and Methods in Physics Research Section A: Accelerators, Spectrometers, Detectors and Associated Equipment* 563.1 (2006), pages 163–166. doi: [10.1016/j.nima.2006.01.085](https://doi.org/10.1016/j.nima.2006.01.085) (cited on page 217).
- [271] L. Helfen, T. F. Morgeneyer, F. Xu, M. N. Mavrogordato, I. Sinclair, B. Schillinger, and T. Baumbach. “Synchrotron and neutron laminography for three-dimensional imaging of devices and flat material specimens”. In: *International Journal of Materials Research (formerly Zeitschrift fuer Metallkunde)* 103.02 (2012), pages 170–173. doi: [10.3139/146.110668](https://doi.org/10.3139/146.110668) (cited on page 217).
- [272] V. Maurel, L. Helfen, F. N’Guyen, A. Koster, M. Di Michiel, T. Baumbach, and T. F. Morgeneyer. “Three-dimensional investigation of thermal barrier coatings by synchrotron-radiation computed laminography”. In: *Scripta Materialia* 66.7 (2012), pages 471–474. doi: [10.1016/j.scriptamat.2011.12.021](https://doi.org/10.1016/j.scriptamat.2011.12.021) (cited on page 217).
- [273] D. J. Bull, L. Helfen, I. Sinclair, S. M. Spearing, and T. Baumbach. “A comparison of multi-scale 3D X-ray tomographic inspection techniques for assessing carbon fibre composite impact damage”. In: *Composites Science and Technology* 75 (2013), pages 55–61. doi: [10.1016/j.compscitech.2012.12.006](https://doi.org/10.1016/j.compscitech.2012.12.006) (cited on page 217).
- [274] P. Reischig, L. Helfen, A. Wallert, T. Baumbach, and J. Dik. “High-resolution non-invasive 3D imaging of paint microstructure by synchrotron-based X-ray laminography”. In: *Applied Physics A* 111.4 (2013), pages 983–995. doi: [10.1007/s00339-013-7687-2](https://doi.org/10.1007/s00339-013-7687-2) (cited on page 217).
- [275] F. Xu, L. Helfen, T. Baumbach, and H. Suhonen. “Comparison of image quality in computed laminography and tomography”. In: *Optics Express* 20.2 (2012), page 794. doi: [10.1364/OE.20.000794](https://doi.org/10.1364/OE.20.000794) (cited on pages 217, 219).
- [276] H. Proudhon, J. Li, P. Reischig, N. Guéninchault, S. Forest, and W. Ludwig. “Coupling Diffraction Contrast Tomography with the Finite Element Method”. In: *Advanced Engineering Materials* 18.6 (2016), pages 903–912. doi: [10.1002/adem.201500414](https://doi.org/10.1002/adem.201500414) (cited on pages 217, 261).
- [277] C. C. Roth and D. Mohr. “Ductile fracture experiments with locally proportional loading histories”. In: *International Journal of Plasticity* 79 (2016), pages 328–354. doi: [10.1016/j.ijplas.2015.08.004](https://doi.org/10.1016/j.ijplas.2015.08.004) (cited on page 219).

- [278] G. Besnard, F. Hild, and S. Roux. ““Finite-Element” Displacement Fields Analysis from Digital Images: Application to Portevin–Le Châtelier Bands”. In: *Experimental Mechanics* 46.6 (2006), pages 789–803. doi: [10.1007/s11340-006-9824-8](https://doi.org/10.1007/s11340-006-9824-8) (cited on pages [219](#), [239](#)).
- [279] F. Hild and S. Roux. “Comparison of Local and Global Approaches to Digital Image Correlation”. In: *Experimental Mechanics* 52.9 (2012), pages 1503–1519. doi: [10.1007/s11340-012-9603-7](https://doi.org/10.1007/s11340-012-9603-7) (cited on pages [219](#), [239](#)).
- [280] H. Leclerc, J.-N. Périé, F. Hild, and S. Roux. “Digital volume correlation: what are the limits to the spatial resolution?” In: *Mechanics & Industry* 13.6 (2012), pages 361–371. doi: [10.1051/meca/2012025](https://doi.org/10.1051/meca/2012025) (cited on pages [219](#), [223](#)).
- [281] Z. Tomičević, F. Hild, and S. Roux. “Mechanics-aided digital image correlation”. In: *The Journal of Strain Analysis for Engineering Design* 48.5 (2013), pages 330–343. doi: [10.1177/0309324713482457](https://doi.org/10.1177/0309324713482457) (cited on page [219](#)).
- [282] Z. Tomičević, J. Kodvanj, and F. Hild. “Characterization of the nonlinear behavior of nodular graphite cast iron via inverse identification: Analysis of biaxial tests”. In: *European Journal of Mechanics - A/Solids* 59 (2016), pages 195–209. doi: [10.1016/j.euromechsol.2016.03.006](https://doi.org/10.1016/j.euromechsol.2016.03.006) (cited on page [223](#)).
- [283] H. Leclerc, J. Neggers, F. Mathieu, S. Roux, and F. Hild. “Correli 3.0”. IDDN . FR . 001 . 520008 . 000 . S . P . 2015 . 000 . 31500. Agence pour la Protection des Programmes, Paris (France), 2015 (cited on pages [231](#), [239](#)).
- [284] F. Hild, A. Bouterf, L. Chamoin, H. Leclerc, F. Mathieu, J. Neggers, F. Pled, Z. Tomičević, and S. Roux. “Toward 4D mechanical correlation”. In: *Advanced Modeling and Simulation in Engineering Sciences* 3.1 (2016), page 17. doi: [10.1186/s40323-016-0070-z](https://doi.org/10.1186/s40323-016-0070-z) (cited on pages [231](#), [239](#), [251](#)).
- [285] M. Vogelgesang, T. Farago, T. F. Morgeneyer, L. Helfen, T. dos Santos Rolo, A. Myagotin, and T. Baumbach. “Real-time image-content-based beamline control for smart 4D X-ray imaging”. In: *Journal of Synchrotron Radiation* 23.5 (2016), pages 1–10. doi: [10.1107/S1600577516010195](https://doi.org/10.1107/S1600577516010195) (cited on page [236](#)).
- [286] C. C. Tasan, J. P. M. Hoefnagels, and M. G. D. Geers. “Identification of the continuum damage parameter: An experimental challenge in modeling damage evolution”. In: *Acta Materialia* 60.8 (2012), pages 3581–3589. doi: [10.1016/j.actamat.2012.03.017](https://doi.org/10.1016/j.actamat.2012.03.017) (cited on pages [238](#), [263](#)).
- [287] R. Storn and K. Price. “Differential Evolution - A Simple and Efficient Heuristic for Global Optimization over Continuous Spaces”. In: *Journal of Global Optimization* 11.4 (1997), pages 341–359. doi: [10.1023/A:1008202821328](https://doi.org/10.1023/A:1008202821328) (cited on page [238](#)).
- [288] M. Kahziz, T. F. Morgeneyer, M. Mazière, L. Helfen, O. Bouaziz, and E. Maire. “In situ 3D Synchrotron Laminography Assessment of Edge Fracture in Dual-Phase Steels: Quantitative and Numerical Analysis”. In: *Experimental Mechanics* 56.2 (2016), pages 177–195. doi: [10.1007/s11340-015-0076-3](https://doi.org/10.1007/s11340-015-0076-3) (cited on page [239](#)).
- [289] J. Neggers, J. P. M. Hoefnagels, M. G. D. Geers, F. Hild, and S. Roux. “Time-resolved integrated digital image correlation”. In: *International Journal for Numerical Methods in Engineering* 103.3 (2015), pages 157–182. doi: [10.1002/nme.4882](https://doi.org/10.1002/nme.4882) (cited on page [239](#)).

- [290] T.-S. Cao, E. Maire, C. Verdu, C. Bobadilla, P. Lasne, P. Montmitonnet, and P.-O. Bouchard. “Characterization of ductile damage for a high carbon steel using 3D X-ray micro-tomography and mechanical tests – Application to the identification of a shear modified GTN model”. In: *Computational Materials Science* 84 (2014), pages 175–187. doi: [10.1016/j.commatsci.2013.12.006](https://doi.org/10.1016/j.commatsci.2013.12.006) (cited on page 245).
- [291] S. Dancette, A. Browet, G. Martin, M. Willemet, and L. Delannay. “Automatic processing of an orientation map into a finite element mesh that conforms to grain boundaries”. In: *Modelling and Simulation in Materials Science and Engineering* 24.5 (2016), page 055014. doi: [10.1088/0965-0393/24/5/055014](https://doi.org/10.1088/0965-0393/24/5/055014) (cited on page 256).
- [292] J. Mediavilla, R. H. J. Peerlings, and M. G. D. Geers. “A robust and consistent remeshing-transfer operator for ductile fracture simulations”. In: *Computers & Structures* 84.8-9 (2006), pages 604–623. doi: [10.1016/j.compstruc.2005.10.007](https://doi.org/10.1016/j.compstruc.2005.10.007) (cited on page 257).
- [293] H. R. Javani, R. H. J. Peerlings, and M. G. D. Geers. “Consistent remeshing and transfer for a three dimensional enriched mixed formulation of plasticity and non-local damage”. In: *Computational Mechanics* 53.4 (2013), pages 625–639. doi: [10.1007/s00466-013-0922-z](https://doi.org/10.1007/s00466-013-0922-z) (cited on page 257).
- [294] K. W. Kpodzo. “Accélération des calculs pour la simulation du laminage à pas de pèlerin en utilisant la méthode multimallages”. PhD thesis. Ecole Nationale Supérieure des Mines de Paris, 2014 (cited on page 257).
- [295] S. Kumar, L. Fourment, and S. Guerdoux. “Parallel, second-order and consistent remeshing transfer operators for evolving meshes with superconvergence property on surface and volume”. In: *Finite Elements in Analysis and Design* 93 (2015), pages 70–84. doi: [10.1016/j.finel.2014.09.002](https://doi.org/10.1016/j.finel.2014.09.002) (cited on page 257).
- [296] P. E. Farrell, M. D. Piggott, C. C. Pain, G. J. Gorman, and C. R. Wilson. “Conservative interpolation between unstructured meshes via supermesh construction”. In: *Computer Methods in Applied Mechanics and Engineering* 198.33-36 (2009), pages 2632–2642. doi: [10.1016/j.cma.2009.03.004](https://doi.org/10.1016/j.cma.2009.03.004) (cited on page 257).
- [297] T. T. M. Nguyen. “Multiscale finite element modeling of macrosegregation and grain transport”. PhD thesis. Ecole Nationale Supérieure des Mines de Paris, 2015 (cited on page 259).
- [298] A. Saad. “Numerical modelling of macrosegregation formed during solidification with shrinkage using a Level Set approach”. PhD thesis. Ecole Nationale Supérieure des Mines de Paris, 2016 (cited on page 259).
- [299] Q. Chen, G. Guillemot, C.-A. Gandin, and M. Bellet. “Finite element modeling of deposition of ceramic material during SLM additive manufacturing”. In: *International Conference on Numerical Methods in Industrial Forming Processes (NUMIFORM)*. Troyes (France), July 4–7, 2016 (cited on page 259).
- [300] M. Saby. “Compréhension et modélisation des mécanismes de refermeture de porosité dans les procédés de mise en forme des métaux à chaud”. PhD thesis. Ecole Nationale Supérieure des Mines de Paris, 2013 (cited on page 263).
- [301] A. Chbihi, P.-O. Bouchard, M. Bernacki, and D. Pino Muñoz. “Influence of Lode angle on modelling of void closure in hot metal forming processes”. In: *Finite Elements in Analysis and Design* (Submitted) (cited on page 263).

- [302] Scilab Enterprises. *Scilab: Le logiciel open source gratuit de calcul numérique*. Scilab Enterprises. Orsay, France, 2012. URL: <http://www.scilab.org> (cited on page 264).
- [303] J. Besson, C. Berdin, S. Bugat, R. Desmorat, F. Feyel, S. Forest, E. Lorentz, E. Maire, T. Pardoen, A. Pineau, and B. Tanguy. *Local approach to fracture*. Presses des Mines, 2004. ISBN: 9782911762550 (cited on page 264).
- [304] S. G. Johnson. *The NLopt nonlinear-optimization package*. <http://ab-initio.mit.edu/nlopt>. 2014. URL: <http://ab-initio.mit.edu/nlopt> (cited on page 265).
- [305] S. Delchambre. “Prediction of void nucleation in Fe-TiB₂ steel during cold forming process via microscopic simulations”. Post Master’s Degree. Ecole Nationale Supérieure des Mines de Paris, 2016-2017 (cited on page 265).
- [306] P. Wriggers. *Computational Contact Mechanics*. Berlin, Heidelberg: Springer Berlin Heidelberg, 2006. doi: [10.1007/978-3-540-32609-0](https://doi.org/10.1007/978-3-540-32609-0) (cited on pages 270–272, 276, 279).
- [307] V. A. Yastrebov. “Computational contact mechanics: geometry, detection and numerical techniques”. PhD thesis. Ecole Nationale Supérieure des Mines de Paris, 2011 (cited on pages 270–272, 276, 279).
- [308] J. A. P. Barboza. “Traitement de contact entre corps déformables et calcul parallèle pour la simulation 3D du forgeage multicorps”. PhD thesis. Ecole Nationale Supérieure des Mines de Paris, 2004 (cited on pages 271, 276).
- [309] S. Popa. “Quasi-Symmetrical contact algorithm and recurrent boundary conditions: application to 3D metal forging simulations”. PhD thesis. Ecole Nationale Supérieure des Mines de Paris, 2005 (cited on pages 271, 276, 279).
- [310] M. Hachani. “Amélioration de la modélisation de contact pour les procédés à faible zone de contact”. PhD thesis. Ecole Nationale Supérieure des Mines de Paris, 2011 (cited on pages 271, 276).
- [311] T. Belytschko and M. O. Neal. “Contact-impact by the pinball algorithm with penalty and Lagrangian methods”. In: *International Journal for Numerical Methods in Engineering* 31.3 (1991), pages 547–572. doi: [10.1002/nme.1620310309](https://doi.org/10.1002/nme.1620310309) (cited on pages 272, 279).
- [312] J. G. Malone and N. L. Johnson. “A Parallel Finite Element Contact / Impact Algorithm for Non-Linear Explicit Transient Analysis : Part I-the Search Algorithm and Contact Mechanics”. In: *International Journal for Numerical Methods in Engineering* 590.December 1992 (1994), pages 559–590 (cited on page 272).
- [313] M. Oldenburg and L. Nilsson. “The position code algorithm for contact searching”. In: *International Journal for Numerical Methods in Engineering* 37.3 (1994), pages 359–386. doi: [10.1002/nme.1620370302](https://doi.org/10.1002/nme.1620370302) (cited on page 272).
- [314] F. Wang, J. Cheng, and Z. Yao. “FFS contact searching algorithm for dynamic finite element analysis”. In: *International Journal for Numerical Methods in Engineering* 52.7 (2001), pages 655–672. doi: [10.1002/nme.221](https://doi.org/10.1002/nme.221) (cited on page 272).
- [315] G. Frenning. “An efficient finite/discrete element procedure for simulating compression of 3D particle assemblies”. In: *Computer Methods in Applied Mechanics and Engineering* 197.49-50 (2008), pages 4266–4272. doi: [10.1016/j.cma.2008.05.002](https://doi.org/10.1016/j.cma.2008.05.002) (cited on pages 272, 279).

- [316] A. M. Aragón and J.-F. Molinari. “A hierarchical detection framework for computational contact mechanics”. In: *Computer Methods in Applied Mechanics and Engineering* 268 (2014), pages 574–588. doi: [10.1016/j.cma.2013.10.001](https://doi.org/10.1016/j.cma.2013.10.001) (cited on page 272).
- [317] J. Bonet and J. Peraire. “An alternating digital tree (ADT) algorithm for 3D geometric searching and intersection problems”. In: *International Journal for Numerical Methods in Engineering* 31.1 (1991), pages 1–17. doi: [10.1002/nme.1620310102](https://doi.org/10.1002/nme.1620310102) (cited on page 272).
- [318] Y. T. Feng and D. R. J. Owen. “An augmented spatial digital tree algorithm for contact detection in computational mechanics”. In: *International Journal for Numerical Methods in Engineering* 55.2 (2002), pages 159–176. doi: [10.1002/nme.502](https://doi.org/10.1002/nme.502) (cited on page 272).
- [319] B. Yang and T. A. Laursen. “A large deformation mortar formulation of self contact with finite sliding”. In: *Computer Methods in Applied Mechanics and Engineering* 197.6-8 (2008), pages 756–772. doi: [10.1016/j.cma.2007.09.004](https://doi.org/10.1016/j.cma.2007.09.004) (cited on pages 272, 279).
- [320] J. Choi, H. S. Ryu, C. W. Kim, and J. H. Choi. “An efficient and robust contact algorithm for a compliant contact force model between bodies of complex geometry”. In: *Multibody System Dynamics* 23.1 (2010), pages 99–120. doi: [10.1007/s11044-009-9173-3](https://doi.org/10.1007/s11044-009-9173-3) (cited on page 272).
- [321] D. J. Benson and J. O. Hallquist. “A single surface contact algorithm for the post-buckling analysis of shell structures”. In: *Computer Methods in Applied Mechanics and Engineering* 78.2 (1990), pages 141–163. doi: [10.1016/0045-7825\(90\)90098-7](https://doi.org/10.1016/0045-7825(90)90098-7) (cited on pages 272, 279).
- [322] S. H. Paik, J. J. Moon, S. J. Kim, and M. Lee. “Parallel performance of large scale impact simulations on Linux cluster super computer”. In: *Computers & Structures* 84.10-11 (2006), pages 732–741. doi: [10.1016/j.compstruc.2005.11.013](https://doi.org/10.1016/j.compstruc.2005.11.013) (cited on page 272).
- [323] S. P. Wang and E. Nakamachi. “The inside-outside contact search algorithm for finite element analysis”. In: *International Journal for Numerical Methods in Engineering* 40.19 (1997), pages 3665–3685. doi: [10.1002/\(SICI\)1097-0207\(19971015\)40:19<3665::AID-NME234>3.0.CO;2-K](https://doi.org/10.1002/(SICI)1097-0207(19971015)40:19<3665::AID-NME234>3.0.CO;2-K) (cited on page 272).
- [324] A. Munjiza and K. R. F. Andrews. “NBS contact detection algorithm for bodies of similar size”. In: *International Journal for Numerical Methods in Engineering* 43.1 (1998), pages 131–149. doi: [10.1002/\(SICI\)1097-0207\(19980915\)43:1<131::AID-NME447>3.0.CO;2-S](https://doi.org/10.1002/(SICI)1097-0207(19980915)43:1<131::AID-NME447>3.0.CO;2-S) (cited on page 272).
- [325] H. Mazhar, T. Heyn, and D. Negrut. “A scalable parallel method for large collision detection problems”. In: *Multibody System Dynamics* 26.1 (2011), pages 37–55. doi: [10.1007/s11044-011-9246-y](https://doi.org/10.1007/s11044-011-9246-y) (cited on page 272).
- [326] Z. Zhi-Hua and L. Nilsson. “A contact searching algorithm for general contact problems”. In: *Computers & Structures* 33.1 (1989), pages 197–209. doi: [10.1016/0045-7949\(89\)90141-7](https://doi.org/10.1016/0045-7949(89)90141-7) (cited on page 272).
- [327] P. Flores and J. Ambrósio. “On the contact detection for contact-impact analysis in multibody systems”. In: *Multibody System Dynamics* 24.1 (2010), pages 103–122. doi: [10.1007/s11044-010-9209-8](https://doi.org/10.1007/s11044-010-9209-8) (cited on page 272).
- [328] P. Hild. “Problèmes de contact unilatéral et maillages éléments finis incompatibles”. PhD thesis. Université Paul Sabatier de Toulouse, 1998 (cited on page 276).

- [329] J. C. Simo, P. Wriggers, and R. L. Taylor. “A perturbed Lagrangian formulation for the finite element solution of contact problems”. In: *Computer Methods in Applied Mechanics and Engineering* 50.2 (1985), pages 163–180. doi: [10.1016/0045-7825\(85\)90088-X](https://doi.org/10.1016/0045-7825(85)90088-X) (cited on pages [276](#), [278](#), [279](#)).
- [330] P. Alart and A. Curnier. “A mixed formulation for frictional contact problems prone to Newton like solution methods”. In: *Computer Methods in Applied Mechanics and Engineering* 92.3 (1991), pages 353–375. doi: [10.1016/0045-7825\(91\)90022-X](https://doi.org/10.1016/0045-7825(91)90022-X) (cited on page [276](#)).
- [331] J. C. Simo and T. A. Laursen. “An augmented lagrangian treatment of contact problems involving friction”. In: *Computers & Structures* 42.1 (1992), pages 97–116. doi: [10.1016/0045-7949\(92\)90540-G](https://doi.org/10.1016/0045-7949(92)90540-G) (cited on page [276](#)).
- [332] P. Papadopoulos and R. L. Taylor. “A mixed formulation for the finite element solution of contact problems”. In: *Computer Methods in Applied Mechanics and Engineering* 94.3 (1992), pages 373–389. doi: [10.1016/0045-7825\(92\)90061-N](https://doi.org/10.1016/0045-7825(92)90061-N) (cited on page [278](#)).
- [333] P. Papadopoulos and R. L. Taylor. “A simple algorithm for three-dimensional finite element analysis of contact problems”. In: *Computers & Structures* 46.6 (1993), pages 1107–1118. doi: [10.1016/0045-7949\(93\)90096-V](https://doi.org/10.1016/0045-7949(93)90096-V) (cited on page [278](#)).
- [334] M. A. Crisfield. “Re-visiting the contact patch test”. In: *International Journal for Numerical Methods in Engineering* 48.3 (2000), pages 435–449. doi: [10.1002/\(SICI\)1097-0207\(20000530\)48:3<435::AID-NME891>3.0.CO;2-V](https://doi.org/10.1002/(SICI)1097-0207(20000530)48:3<435::AID-NME891>3.0.CO;2-V) (cited on page [278](#)).
- [335] E. Bittencourt and G. J. Creus. “Finite element analysis of three-dimensional contact and impact in large deformation problems”. In: *Computers & Structures* 69.2 (1998), pages 219–234. doi: [10.1016/S0045-7949\(98\)00008-X](https://doi.org/10.1016/S0045-7949(98)00008-X) (cited on page [279](#)).
- [336] T. Baudouin, J.-F. Remacle, E. Marchandise, F. Henrotte, and C. Geuzaine. “A frontal approach to hex-dominant mesh generation”. In: *Advanced Modeling and Simulation in Engineering Sciences* 1.1 (2014), page 8. doi: [10.1186/2213-7467-1-8](https://doi.org/10.1186/2213-7467-1-8) (cited on page [279](#)).

Résumé

L'objectif de cette thèse de doctorat est de contribuer à une meilleure compréhension et modélisation de la rupture ductile lors de la mise en forme des métaux. Cette mise en forme se réalise en général par une série de chargements thermomécaniques où de multiples paramètres comme le type et la direction de chargement varient. Des outils de simulations prédictifs sont nécessaires pour modéliser les mécanismes de rupture, et ensuite optimiser les coûts de production.

La rupture ductile des matériaux métalliques est précédée par la détérioration progressive de leur capacité de charge due à la germination, croissance, et coalescence de cavités microscopiques. Dans ce travail, une approche micromécanique est développée afin de conduire des simulations éléments finis réalistes et à champ complet de la rupture ductile à l'échelle microscopique. Des méthodes de génération et d'adaptation de maillage s'appuyant sur des fonctions de niveau sont proposées pour discrétiser la microstructure. Avec ces méthodes, les propriétés géométriques des fonctions de niveau sont conservées, ainsi que le volume et la morphologie de chaque composante de la microstructure, et ce pour de grandes déformations plastiques. Ces méthodes numériques sont étendues pour permettre la modélisation de fissures aux interfaces entre certaines composantes de la microstructure, ou à l'intérieur même de ces composantes. Une nouvelle méthode de détection de contact par adaptation de maillage est aussi développée.

L'intérêt de ces développements numériques et modèles micromécaniques est démontré tout d'abord pour des microstructures générées statistiquement. Ensuite, une nouvelle méthodologie est proposée pour modéliser des microstructures réelles (laminographie *in-situ*) avec des conditions aux limites mesurées expérimentalement (corrélation d'images volumiques).

Mots Clés

Rupture ductile, endommagement, micromécanique, remaillage, interfaces, fonctions de niveau

Abstract

The present PhD thesis aims at a better understanding and modeling of ductile fracture during the forming of metallic materials. These materials are typically formed using series of thermomechanical loads where many parameters such as loading type and direction vary. Predictive numerical tools are necessary to model fracture mechanisms, and then optimize production costs.

Ductile fracture in metallic materials is the result of a progressive deterioration of their load carrying capacity due to the nucleation, growth, and coalescence of microscopic voids. In this work, a micromechanical approach is developed in order to conduct realistic full field finite element simulations of ductile fracture at the microscale. Meshing and remeshing methods relying on the use of Level-Set functions are proposed to discretize the microstructure. Thanks to these methods, the geometric properties of Level-Set functions are preserved, as well as the volume and morphology of each component of the microstructure, even at large plastic strains. These numerical methods are extended to account for cracks and model the failure of some components of the microstructure, or interfaces between them. A new contact detection method based on mesh adaptation is also developed.

The interest of these numerical developments and micromechanical models is first demonstrated at the scale of representative volume elements with statistically generated microstructures. Then, a new methodology is proposed to conduct simulations of real microstructures observed via *in-situ* X-ray laminography, with boundary conditions that are measured using digital volume correlation techniques.

Keywords

Ductile fracture, damage, micromechanics, remeshing, interfaces, level-set